UNIVERSITE DE BOURGOGNE FRANCHE-COMTE
UFR SCIENCES DE LA VIE, DE LA TERRE ET DE L'ENVIRONNEMENT

THÈSE

Pour obtenir le grade de

Docteur de l'Université de Bourgogne Franche-Comté

Discipline : Géodynamique des Enveloppes Supérieures

par

M. Gwénaël CARAVACA

Le dix juillet deux mille dix-sept

4D paleoenvironmental evolution of the Early Triassic Sonoma Foreland Basin

(western USA)

Soutenue publiquement devant un jury composé des membres suivants :

Dr. A. Brayard, *chargé de recherche CNRS*	Université de Bourgogne	Directeur de thèse
Dr. C. Thomazo, *maître de conférences*	Université de Bourgogne	Co-encadrant
Dr. S. Bourquin, *directrice de recherche CNRS*	Université de Rennes 1	Rapporteur
Pr. F. Boulvain, *professeur ordinaire*	Université de Liège (Belgique)	Rapporteur
Pr. E. Vennin, *professeur*	Université de Bourgogne	Examinateur
Dr. G. Escarguel, *maître de conférences*	Université Claude Bernard Lyon1	Examinateur
Pr. M. Guiraud, *professeur*	Université de Bourgogne	Invité

UNIVERSITE DE BOURGOGNE FRANCHE-COMTE
UFR SCIENCES DE LA VIE, DE LA TERRE ET DE L'ENVIRONNEMENT

DISSERTATION

Submitted in partial fulfillment of the requirements of degree of

Doctor of Philosophy at the Université de Bourgogne Franche-Comté

In Upper envelopes geodynamics

by

M. Gwénaël CARAVACA

On July the tenth, two thousand and seventeen

4D paleoenvironmental evolution of the Early Triassic Sonoma Foreland Basin (western USA)

Publicly presented in front of the board of examiners composed by:

Dr. A. Brayard, *chargé de recherche CNRS*	Université de Bourgogne	Lead supervisor
Dr. C. Thomazo, *maître de conférences*	Université de Bourgogne	Co-supervisor
Dr. S. Bourquin, *directrice de recherche CNRS*	Université de Rennes 1	Reviewer
Pr. F. Boulvain, *professeur ordinaire*	Université de Liège (Belgique)	Reviewer
Pr. E. Vennin, *professeur*	Université de Bourgogne	Examiner
Dr. G. Escarguel, *maître de conférences*	Université Claude Bernard Lyon1	Examiner
Pr. M. Guiraud, *professeur*	Université de Bourgogne	Guest

To my grand-father, Yves.

Acknowledgements

First and foremost, I wish to thank the members of the board of examiners, Dr. Sylvie Bourquin and Pr. Frédéric Boulvain, for accepting to review this dissertation. Thank you for your time and your expertise that are both much appreciated.

I thank my co-authors, and now I am overcoming the PhD student status, my colleagues: Dr. Laetitia Le Pourhiet, Dr. Anne-Sabine Grosjean, Dr. Gilles Escarguel, Dr. Daniel A. Stephen, M. James F. Jenks and M. Kevin G. Bylund. Thanks to all of you for your comments, suggestions and help in writing, revising, rerevising, rererevising the manuscripts representing our collaborative works.

I thank Dr. Nicolas Olivier, formerly in Lyon, now in Clermont-Ferrand, the first (in the long list…) of my supervisors, back when I started it all in Lyon. I remember you Nicolas, helping to build my bed during my first days in the capital of the Gaul.

Then comes Pr. Emmanuel Fara who has been over my shoulder since my first term in Dijon. I started looking at dinosaur footprints, now I am presenting a PhD dissertation, let's say that I did take some steps too.

I would like to thank my fellow PhD students, M. Paul Perron, M. (soon to be Dr.) Pierre-Alexandre Teboul and M. (yet another soon to be Dr.) Romain Jattiot. Taking some moments to talk with you guys were refreshing breathes (well, maybe not when Pierre-Alexandre was smoking nearby…).

I wish to thank Mrs. Florence Euvrard for our casual early talks on the fourth floor.

I also remember the time when Dr. Alexis N'Dongo was my partner in front of me in our "southerners only" office. He left for Gabon last year, but he was a good friend here.

To thank M. Ludovic Bruneau and M. Théophile Cocquerez, I will yell "BAAAAASTOOOON !!!", our rallying cry when it comes to annihilate some civilizations in eponymous strategy game during some memorable and outstanding evenings.

While I am now in Dijon, I do not forget where I came from. For that, I want to address my thoughts to Dr. Carine Lézin and Pr. Bernard Andreu. They guided me and Harmonie into Sedimentology and Paleoenvironment reconstructions while completing our Bachelor of Science in Toulouse, and advised us to go far away in Burgundy. How right they were to do so…

I want to add a word for Dr. René Cubaynes who taught me while I was in my last year of high school. Thank you for pushing me into this adventure, or should I say: Tibi gratias ago magister, salve !

Before I started by PhD, I was very skeptical toward Geochemistry. I was among those telling that "geochemists are making a curve with only two dots". Then I worked with Dr. Christophe Thomazo. Now I am not telling that anymore. Now I am telling that "you need to watch for the error bars before plotting a curve between two points!". Thank you, Christophe, for making me liking Geochemistry, it was not that easy and you succeeded!

I could not decently not talk about my chief-supervisor, my overseer, my boss, in a word, Grand Moff Dr. Arnaud Brayard. I remember that day back in July 2013, I came back from a failed application for a PhD position in Toulouse when you asked me to come and see you, regarding a project, about paleoenvironmental reconstructions of some remote and foreign basin, on another continent. And here we stand. Nearly 4 years later, we have worked together and we have learnt to know each other. From rough beginnings, I am now proud to have "served" under you command, glad to have been your student, and I could not thank you enough for your dedication to my success.

Now, some words for a fellow southerner, exiled in this misty and wet country just like me. I respect the man as much as I admire the professor and his qualities. Pr. Michel Guiraud "picked" me when I finished my first year of Master's degree to work along him on passive margins. Since then we never stop sharing thoughts on geodynamical topics, and I cannot say how much I have learnt from him. Even these recent couple years he was present, helping me in my PhD works to point some unexpected results. Thank you, Michel, for "picking" me up then, and thank you for all you do now.

Finally, it is starting to be difficult to find the right words, the fair ones. I know what I owe and who I owe to be the scientist I am becoming. And I owe a lot to Pr. Emmanuelle Vennin. For 6 years, she has told me a major part of what I know. She helped me in my work, she went mad at me when I was silly and deserved it, but she always was there when I needed it most. To be honest, this acknowledgement should be done around 7.20 AM, before coffee break, the preferred time to talk and work. Thank you, Emmanuelle, for everything.

Above and beyond the professional world, there are close relatives. Without them, I am not sure I could have survived those 3 years or so.

I want to thank M. Jérémy Deroire and Dr. Benjamin Pierrat, for our lunch-times. From polite colleagues, then good buddies, I think we grew real friends and your support in any occasion was always cheerily and gladly welcome.

Aside my friends in office, I have also two very close friends outside, "in real life", but I don't know if it still the real life when I am with them after all… M. Loan Pras, M. Jean-Christophe Laborde, thank you for your unconditional support, for being present here, physically or not, for befriending me.

I am not the person I am without some history and education. My mother and father told me most things, and the first was to be curious about all things. Now, after all these years, I remain curious, but I am curious especially about rocks. Thank you Mum and Dad for always encouraging me in my way, no matter what happens.

Harmonie, I want you to be addressed at last, but not least. You are with me. Every day, in good and bad moment, and oh frak there were a lot of bad days during my thesis! Still, you are with me. I cannot thank you for your support, your kindness and your presence, because there is no word strong enough. I can just say that without you, not only it would not be the same, but I would not have succeeded.

Résumé étendu

Introduction : la Terre au Trias inférieur et la reconquête après l'extinction fini-Permienne

Situé après la limite entre le Paléozoïque et le Mésozoïque, le Trias inférieur est un intervalle court (~4Ma seulement ; Ovtcharova *et al.*, 2006 ; Galfetti *et al.*, 2007a ; Baresel *et al.*, 2017). Lors de la transition entre le Permien et le Trias (PTB), la configuration tectonique de la Terre était différente, et la plupart des masses continentales étaient rassemblées en un seul super continent, la Pangée, lui-même entouré par un unique océan global, la Panthalassa (e.g., Murphy & Nance, 2008 ; Murphy *et* al., 2009 ; Stampfli *et al*., 2013).

Lors de cette transition et durant le Trias inférieur, un évènement volcanique majeur, la mise en place de la grande province ignée de Sibérie (e.g., Ivanov *et al.*, 2009, 2013), a conduit à l'émission de grande quantité de gaz à effet de serre (e.g., Galfetti *et al.*, 2007b ; Romano *et al.*, 2013). Ceux-ci ont contribué à l'acidification de la colonne d'eau et à l'augmentation des températures consécutivement à l'injection de CO_2 dans l'atmosphère (e.g., Galfetti *et al.*, 2007b ; Sun *et* al., 2012 ; Romano *et al.*, 2013).

Les perturbations environnementales qui en découlèrent ont eu des conséquences sur les milieux de dépôts associés à cette période, mais également sur les écosystèmes. Elles sont supposées avoir contribué à la mise en place de conditions délétères pour les organismes et avoir perduré durant tout le Trias inférieur, restreignant ainsi la rediversification biologique d'après-crise (e.g., Pruss & Bottjer, 2004 ; Fraiser & Bottjer, 2007 ; Bottjer *et al.*, 2008 ; Algeo *et al.*, 2011 ; Meyer *et al.*, 2011 ; Bond & Wignall, 2014 ; Song *et al.*, 2014).

La limite PT fut le théâtre de la plus importante et la plus destructrice crise biologique du Phanérozoïque, et fut responsable de la disparition de plus de 90% des espèces marines (Raup, 1979), ou encore de la perte d'environ 50% des familles de tétrapodes continentaux (Benton & Newell, 2014), pour ne citer que ces deux exemples. De nombreux groupes ont été oblitérés durant cette extinction, comme par exemple les groupes caractéristiques du Paléozoïque tels que les coraux tabulés ou encore les trilobites (Sepkoski, 2002). Cependant, si la Vie a failli s'éteindre à l'aube du Mésozoïque, celle-ci a tout de même pu se reconstruire, au prix d'une rediversification communément admise comme lente et difficile dans des conditions environnementales délétères (e.g., Twitchett, 1999 ; Fraiser & Bottjer, 2007 ; Meyer *et al.*, 2011 ; Chen & Benton, 2012).

De grands paradigmes sont couramment associés à la rediversification du Trias inférieur (illustrés dans la Figure R.1a) :

- La présence de taxons « désastre », représentant des organismes opportunistes et généralistes qui auraient proliféré à la suite de la libération de niches écologiques laissées vacantes par les métazoaires disparus (e.g. ; Schubert & Bottjer, 1992, 1995 ; Rodland & Bottjer, 2001 ; He *et al.*, 2007) ;
- Des faciès dit « anachroniques », composés de récifs exclusivement microbiens tels ceux trouvés dans les dépôts Précambriens (e.g., Schubert & Bottjer, 1992 ; Woods *et al.*, 1999 ; Pruss & Bottjer, 2005 ; Pruss *et al.*, 2005 ; Woods, 2009) ;
- Un effet « Lilliput », soit un nanisme généralisé des faunes présentes (e.g., Urbanek, 1993 ; Hautmann & Nützel, 2005 ; Payne, 2005 ; Twitchett, 2007 ; Fraiser *et al.*, 2011 ; Metcalfe *et al.*, 2011 ; Song *et al.*, 2011) ;
- Une anoxie/euxinie généralisée dans le domaine marin, y compris littoral (e.g., Isozaki, 1997 ; Meyer *et al.*, 2011 ; Song *et al.*, 2012 ; Grasby *et al.*, 2013).

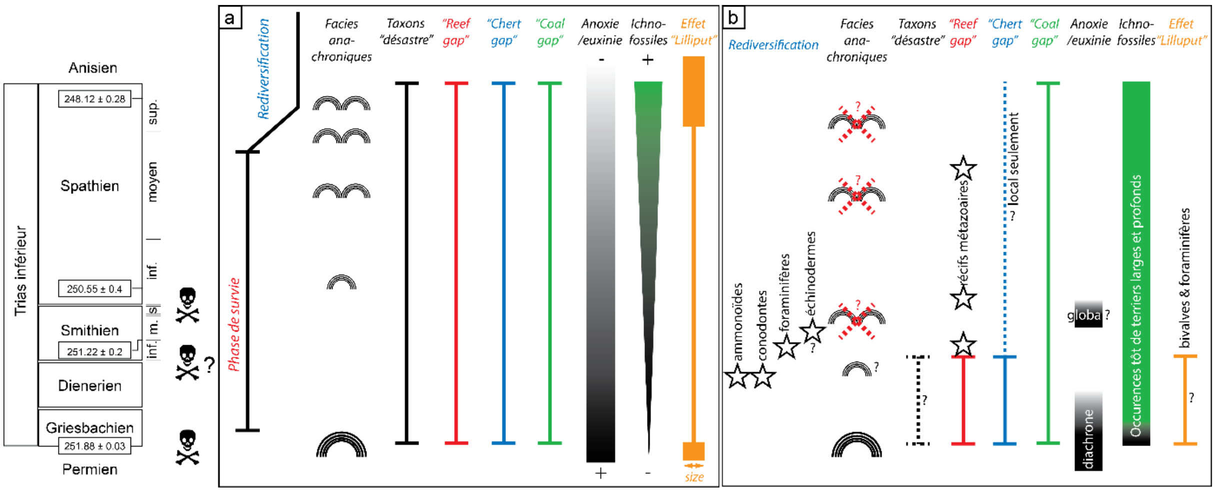

Fig. R.1 : a) Représentation synthétique des principaux paradigmes communément acceptés pour la rediversification biologique au cours du Trias inférieur. b) Représentation synthétique de ces mêmes paradigmes, révisés selon les données récemment recueillies dans le bassin ouest-américain (d'après Brayard, 2015). Inf. : inférieur ; m. : moyen ; s./sup. : supérieur.

Cependant, de nombreuses études récentes viennent questionner ces paradigmes et montrent que non seulement les conditions paléoenvironnementales n'étaient pas si délétères qu'envisagé, mais qu'en plus, la rediversification fut explosive pour certains groupes nekto-pélagiques (e.g., Orchard, 2007 ; Brayard *et al.*, 2009 ; Brühwiler *et al.*, 2010 ; Brayard & Bucher, 2015).

Ainsi la réévaluation de ces paradigmes (Fig. R.1b) permet d'entrevoir un Trias inférieur bien plus diversifié et dynamique que précédemment décrit, avec des écosystèmes complexes présents très peu de temps après la crise PTB (~1,5 Ma après seulement, e.g., Brayard *et al.*, 2011, 2017).

Tout particulièrement, les données en provenance du bassin ouest-américain viennent supporter ces nouveaux modèles d'une rediversification rapide au cours du Trias inférieur. Ceci est relativement paradoxal car c'est précisément sur la base de données issues de ce même bassin que certains des premiers paradigmes sur le Trias inférieur ont été initialement édictés (e.g., Schubert & Bottjer, 1992 ; Fraiser & Bottjer, 2004 ; Pruss & Bottjer, 2004 ; voir Brayard, 2015 pour une discussion).

Cependant, le bassin ouest-américain reste encore aujourd'hui mal contraint d'un point de vue paléoenvironnemental, ainsi que du point de vue de son évolution spatio-temporelle, notamment géodynamique. Le besoin de caractériser cette évolution 4D apparaît donc clairement ainsi que de comprendre les mécanismes de contrôle sous-jacents afin de caractériser l'environnement régional dans lequel la rediversification a eu lieu, et ainsi déchiffrer les liens potentiels entre milieux de dépôt et communautés biologiques.

Pour ce faire, une étude intégrée inédite est mise en œuvre. L'utilisation conjointe de méthodes sédimentologiques, paléontologiques, géochimiques, structurales et cartographiques, mais également la spatialisation des données à l'aide d'un logiciel SIG, permet d'étudier l'évolution 4D du bassin à différentes échelles (de l'affleurement au bassin), dans le but de déterminer les facteurs de contrôle de ce bassin, ainsi que leurs influences à différentes échelles sur les milieux de dépôts rencontrés dans le bassin.

• Le bassin ouest-américain dans le temps et au Trias inférieur

Le bassin étudié se situe à l'Ouest des Etats-Unis d'Amérique. La zone d'étude correspond environ à un rectangle large de 600 km et haut de 1000 km, recouvrant intégralement l'Utah, le sud-est de l'Idaho, l'ouest du Wyoming, l'est du Nevada, ainsi que les bordures frangeantes de l'Arizona au Sud et du Colorado à l'Est (Fig. R.2a).

Ce bassin est le produit d'une très longue et complexe histoire tectono-sédimentaire, qui se reflète dans la variété des terrains rencontrés. Celle-ci a débuté il y a environ 2 milliards d'années lors de l'emplacement des terranes Mojave et Yavapai contre la terrane Wyoming (Whitmeyer & Karlstrom, 2007). Cet évènement structural majeur s'est déroulé au cours du Paléoprotérozoïque (Fig. R.2b) et a permis la formation du socle du bassin, mais également généré de nombreuses faiblesses lithosphériques qui ont eu des impacts ultérieurs lors de l'évolution de ce bassin (e.g., Peterson, 1977).

Depuis la mise en place de son socle au Paléoprotérozoïque et jusqu'à nos jours, le bassin ouest-américain a connu une histoire structurale composée d'une succession de phases d'orogénèses et de quiescences tectoniques (Fig. R.2b ; e.g., Dickinson, 2004, 2006, 2013). Ces évènements structuraux ont été influencés par les terranes lithosphériques formant le socle de la région et ont contribué à la formation de bassins sédimentaires, notamment le bassin de foreland de Sonoma (Sonoma Foreland Basin, SFB) au cours du Trias inférieur, et qui est l'objet de ce travail. Ces différents évènements se succèdent comme suit (Fig. R.2b) :

- Mise en place des terranes lithosphériques et formation du socle durant le Paléoprotérozoïque (Whitmeyer & Karlstrom, 2007) ;
- Fragmentation (par rifting) du supercontinent Rodinia et formation d'une marge passive à haut potentiel de sédimentation (anciennement connue sous le nom de « Cordilleran miogeocline », e.g., Clark, 1957) ;
- Orogénèse Antler : mise en place de l'Allochtone Roberts Mountains dans l'actuel Nevada et création d'un bassin de foreland dans la zone d'étude (Utah et Idaho) au cours du Dévonien tardif et du Carbonifère basal (Burchfiel & Davies, 1975 ; Speed & Sleep, 1982 ; Oldow *et al.*, 1989 ; Smith *et al.*, 1993 ; Dickinson, 2004, 2006, 2013) ;
- Orogénèse des Montagnes Rocheuses Ancestrales dans la région des Montagnes Rocheuses actuelles (Est et Sud-Est du bassin ouest-américain, ~Colorado) durant le Carbonifère tardif et jusqu'au Permien moyen (e.g., Ye *et al.*, 1996 ; Dickerson, 2003). Cette phase orogénique est accompagnée d'une quiescence dans l'ancien bassin de foreland Antler (dans l'Utah) ;
- Orogénèse Sonoma, à la transition Permien/Trias, qui voit la mise en place de l'Allochtone Golconda également dans l'actuel Nevada (de façon similaire à l'Allochtone Roberts Mountains), et qui provoque la formation du SFB étudié dans ce travail ;
- Les orogénèses Sevier et Laramide, se déroulant durant le Crétacé et la première moitié du Paléogène. Elles sont le résultat de la migration vers l'Est du slab de la plaque Farallon, subductée « à plat » sous le craton Nord-Américain (Burchfiel & Davis, 1975 ; Dickinson, 2006, 2013). Ces orogénèses se manifestent de façon différente. L'évènement Sevier provoque la formation d'une chaîne de chevauchement de type « thin-skin », encore visible à l'heure actuelle (la chaîne Sevier, dans l'Est de l'Utah), de forme arquée du fait de taux de raccourcissement différentiels le long de son front (Dickinson, 2006, 2013 ; Yonkee & Weil, 2010 ; Yonkee *et al.*, 2014). L'évènement Laramide a lui contribué à la formation des Montagnes Rocheuses actuelles, du fait de la propagation de contraintes compressives intracontinentales (Burchfiel & Davies, 1975 ; Oldow, 1984 ; Oldow *et al.*, 1989 ; Speed & Silberling, 1989 ; Ye *et al.*, 1996 ; Ingersoll, 2008 ; Dickinson, 2013) ;
- Enfin, l'extension de la province Basin & Range, dans l'actuel Nevada et l'Ouest de l'Utah, a débuté au cours du Néogène et se poursuit encore à l'heure actuelle. Cette extension résulte de la relaxation des contraintes transtensionnelles horizontales héritées de la subduction Farallon, et se caractérise par une extension tardi-orogénique due à un étalement gravitaire des reliefs formés précédemment (e.g., Malavieille, 1993 ; Parsons *et al.*, 1994 ; Gans & Bohrson, 1998 ; Dickinson, 2002, 2006).

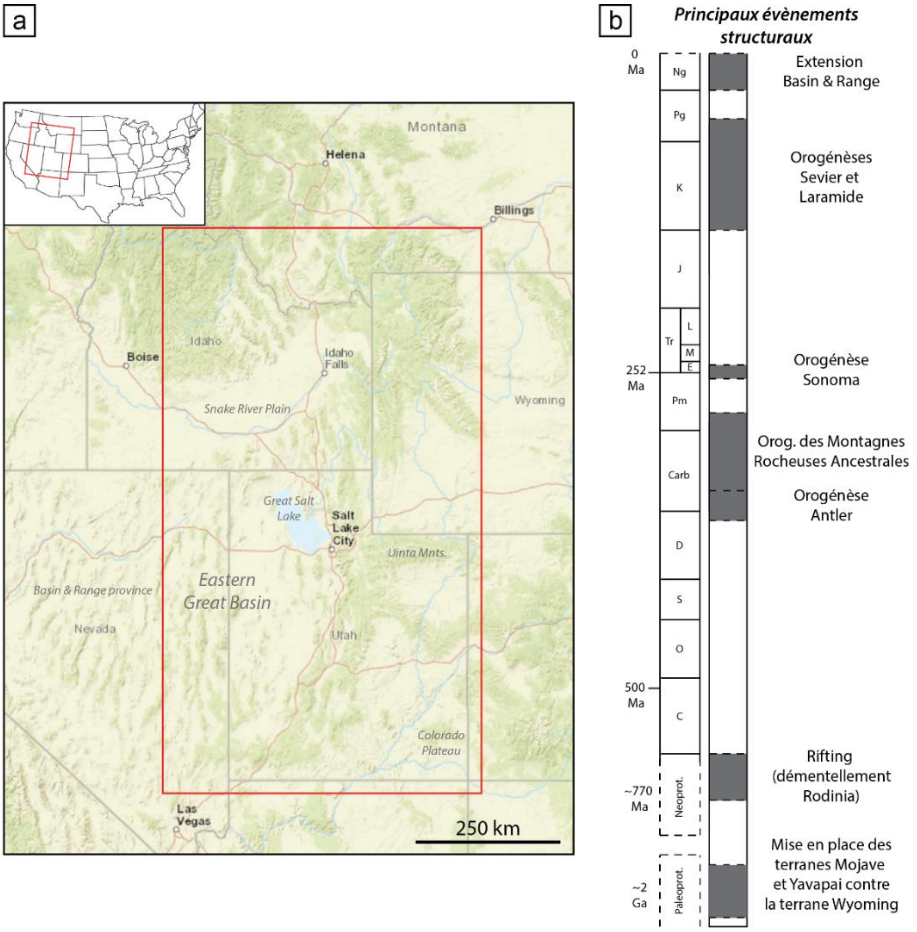

Figure R.2 : a) Carte géographique de l'Ouest américain montrant la position et l'extension de la zone d'étude. b) Chronostratigraphie simplifiée des principaux évènements structuraux survenus dans le bassin ouest-américain depuis sa formation au Paléoprotérozoïque (d'après Oldow *et al.*, 1989 ; Whitmeyer & Karlstrom, 2007 ; Dickinson, 2013).

Le bassin ouest-américain au Trias inférieur, ou SFB, s'est donc formé à la suite d'évènements géodynamiques complexes. Cependant, ces derniers sont encore mal contraints, et des interrogations subsistent quant aux mécanismes exacts de sa formation, de son évolution, ainsi que de son impact sur les environnements de dépôts du bassin. Ceux-ci sont connus depuis de nombreuses années au travers de travaux sédimentologiques mais également paléontologiques (e.g., Kummel, 1954, 1957 ; Schubert & Bottjer, 1992 ; Paull & Paull, 1991, 1994 ; Fraiser & Bottjer, 2004 ; Pruss & Bottjer, 2004).

En effet, le SFB présente un enregistrement fossile et sédimentaire exceptionnel du Trias inférieur, et constitue ainsi un bassin important dans l'étude de la rediversification biologique après la PTB. De plus, ce bassin a été la source des données ayant permis la proposition de nombreux paradigmes admis pour le Trias inférieur.

Cet enregistrement, bien que de qualité, montre cependant une particularité importante et intéressante, bien que peu documentée. En effet, il existe une dichotomie entre les parties Nord et Sud du bassin. Celle-ci est visible aussi bien dans le registre fossile que dans le registre sédimentaire.

Dans le registre fossile, deux communautés distinctes bien documentées permettent notamment de la mettre en évidence : le groupe nekto-pélagique des ammonoïdes, et les communautés récifales microbiennes. En ce qui concerne les ammonoïdes, des études récentes et en cours (e.g., Jattiot *et al.*, *in prep.*) montrent que certains genres d'ammonoïdes sont géographiquement ségrégués. C'est notamment le cas des genres *Wyomingites*, dont l'extension géographique est restreinte à la partie Nord du bassin (Fig. R.3), et *Guodunites*, qui au contraire est cantonné dans la partie Sud du SFB (Fig. R.3). En ce qui concerne les communautés microbiennes, leurs dépôts permettent également de faire une distinction N/S. Dans le sud du SFB, de puissantes séries de calcaires microbiens massifs (Fig. R.3), montrant une grande diversité de macro- et de mésostructures, peuvent être observées dans le registre sédimentaire (e.g., Brayard *et al.*, 2013 ; Olivier *et al.*, 2014, 2016, cf. appendice 1 ; Vennin *et al.*, 2015). Au contraire, la partie Nord du bassin semble être dépourvue de tels dépôts (Fig. R.3). Enfin, la partie centrale du bassin montre quant à elle des dépôts de type MISS (microbially-induced sedimentary structures, ou structures sédimentaires induites par l'activité microbiennes), témoignant de la présence d'une activité microbienne différente de celle observée dans le Sud (Fig. R.3).

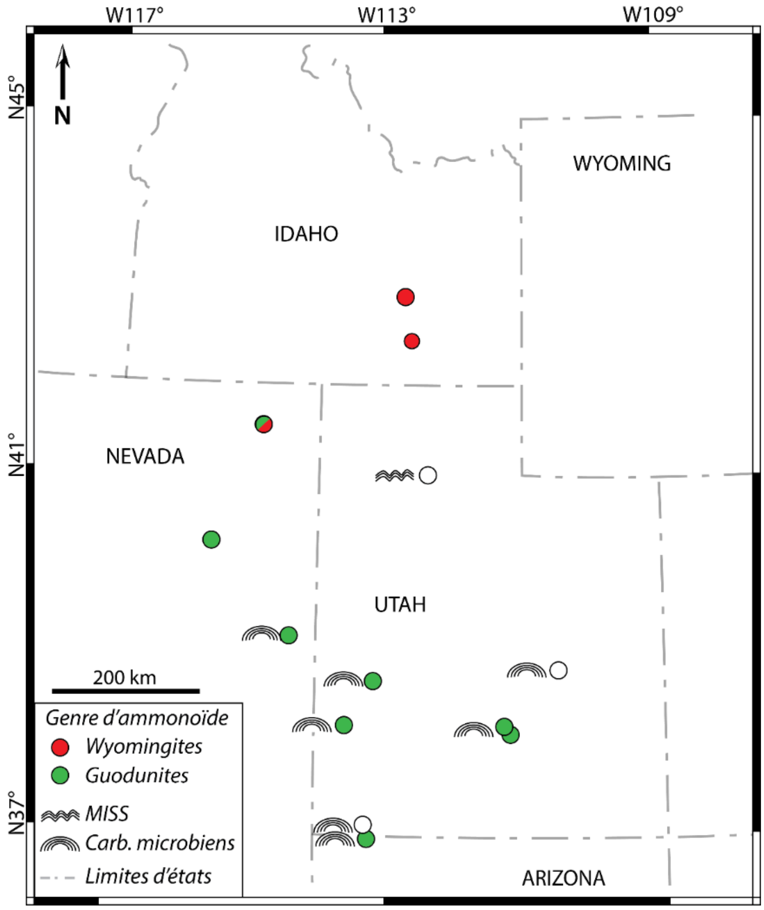

Figure R.3 : Carte paléogéographique illustrant la répartition spatiale de certains genres d'ammonoïdes et des dépôts microbiens, montrant une ségrégation Nord/Sud marquée (d'après Brayard et al., 2013 ; Olivier et al., 2014, 2016, cf. appendice 1 ; Vennin et al., 2015 ; Grosjean *et al.*, *in prep*. ; Jattiot *et al.*, *in prep*.).

Dans le registre sédimentaire, la distinction N/S est mise en évidence par une différence de lithologie, particulièrement visible jusqu'au Smithien moyen (Fig. R.4). Dans le Sud du SFB, la lithologie dominante est constituée de « red beds », dépôts terrigènes fin (siltites à grès fins) caractérisant un environnement de transition, continental à marin, et de dépôts microbiens (Fig. R.3). Ces faciès sont caractéristiques du Groupe Moenkopi (*sensu* Lucas *et al.*, 2007 ; Fig. R.4a). Sur le même intervalle, la partie Nord du bassin enregistre le dépôt de siltites fines, ressemblant aux « red beds » sans en avoir la coloration rougeâtre caractéristique. Ces dépôts présentent clairement une affinité marine de par leur contenu bioclastique tel des coquilles fragmentées de bivalves (e.g., Kummel, 1957 ; Caravaca *et al.*, 2017, cf. section III.A). Ces dépôts sont caractéristiques des formations Dinwoody et Woodside (Fig. R.4).

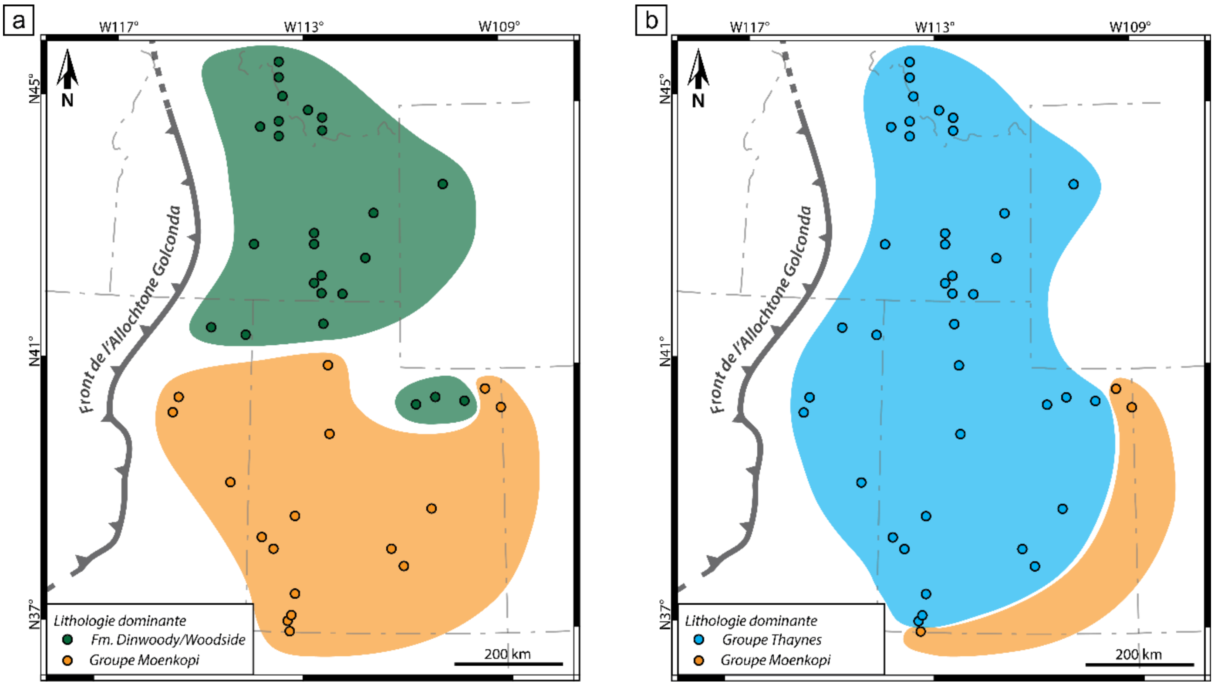

Figure R.4 : Cartes paléogéographique de la distribution spatiale des principales formations lithologiques au cours du Trias inférieur. a) Distribution spatiale des formations Woodside et Dinwoody, et du Groupe Moenkopi jusqu'au Smithien moyen-tardif. b) Distribution spatiale des restes du Groupe Moenkopi et du Groupe Thaynes à partir du Smithien tardif et durant le Spathien basal.

Au cours du Smithien terminal, une transgression de troisième ordre reconnue régionalement (Embry, 1997 ; Vennin *et al.*, 2015) est responsable de l'ennoiement de la quasi-totalité du SFB. Du fait de l'arrivée de conditions marines franches, le dépôt des carbonates bioclastiques ouverts du Groupe Thaynes (*sensu* Lucas *et al.*, 2007 ; Fig. R.4b) est alors possible dans quasiment tout le bassin.

Bien que de nombreuses études aient été menées sur le SFB, la plupart d'entre elles sont relativement anciennes, incomplètes, incorrectes, ou traitent de sujets variés ne permettant pas d'obtenir une image précise de l'évolution des milieux de dépôt à différentes échelles de temps et d'espace. De plus, il apparaît que les travaux précédents sur le SFB n'ont jamais tenu compte de la paléogéographie exacte du bassin au Trias inférieur, car aucune reconstruction palinspastique n'a été proposée jusqu'à aujourd'hui. Ces problématiques sont donc adressées dans ce travail.

• Enregistrement et évolution du signal géochimique dans le SFB

Bien que l'enregistrement sédimentaire et paléontologique du SFB ait été très étudié, les études géochimiques restent quant à elles anecdotiques, malgré leur importance capitale dans l'interprétation des environnements de dépôts. Seuls Marenco *et al.* (2008, 2012) avaient proposé des études limitées spatialement et temporellement sur les enregistrements élémentaires du carbone organique et du soufre, ainsi que le signal isotopique $\delta^{34}S$. Récemment, Thomazo *et al.* (2016) ont proposé une étude à haute résolution de l'entièreté de la coupe de Minersville dans la partie Sud du SFB.

Ainsi, ce travail propose de détailler le signal géochimique de trois coupes : Hot Springs (HS ; Caravaca *et al.*, 2017, cf. section III.A), Lower Weber Canyon (LWC ; Grosjean *et al.*, *in prep.*) et Minersville (MV, Thomazo *et al.*, 2016), représentant les parties Nord, centrale et Sud du SFB, respectivement (Fig. R.5), ceci afin d'analyser le registre géochimique à l'échelle du bassin. Pour cela, les paires d'isotopes du carbone (carbonate et matière organique) sont mesurées sur toutes ces coupes ainsi que les éléments traces et majeurs (T&M). Les signaux géochimiques de HS et LWC représentent une étude et des données originales, tandis que le signal carbone de MV est repris de Thomazo *et al.* (2016). Cependant, les concentrations en élément T&M de MV sont originales à ce travail.

La coupe de HS se situe dans l'extrême Sud-Est de l'Idaho, dans la partie Nord du SFB (Fig. R.5). Son épaisse succession sédimentaire (~900m) permet d'obtenir un enregistrement à haute-résolution temporelle de l'intervalle allant du Permien moyen (à supérieur ?) jusqu'au Spathien inférieur.

Les milieux de dépôts observés à HS sont ceux d'une rampe interne peu profonde, montrant un approfondissement relatif mais progressif depuis la base du Trias. Cet approfondissement est caractérisé par des conglomérats cédant la place à de fins niveaux dolosilteux, puis à des niveaux plus énergétiques de shoals ooïdiques, jusqu'à un maximum d'ennoiement autour de la limite Smithian/Spathien (SSB). Cette dernière est ici marquée par la présence sous-jacente de nombreux spécimens d'ammonoïdes appartenant aux bancs à *Meekoceras*. Au-dessus, le milieu reste encore sous influences marines franches au court du Spathien inférieur.

L'enregistrement géochimique de HS se révèle relativement bien préservé, avec des indices de remobilisation secondaire ponctuels, suggérant un enregistrement « primaire » dans cette partie du bassin (Fig. R.5).

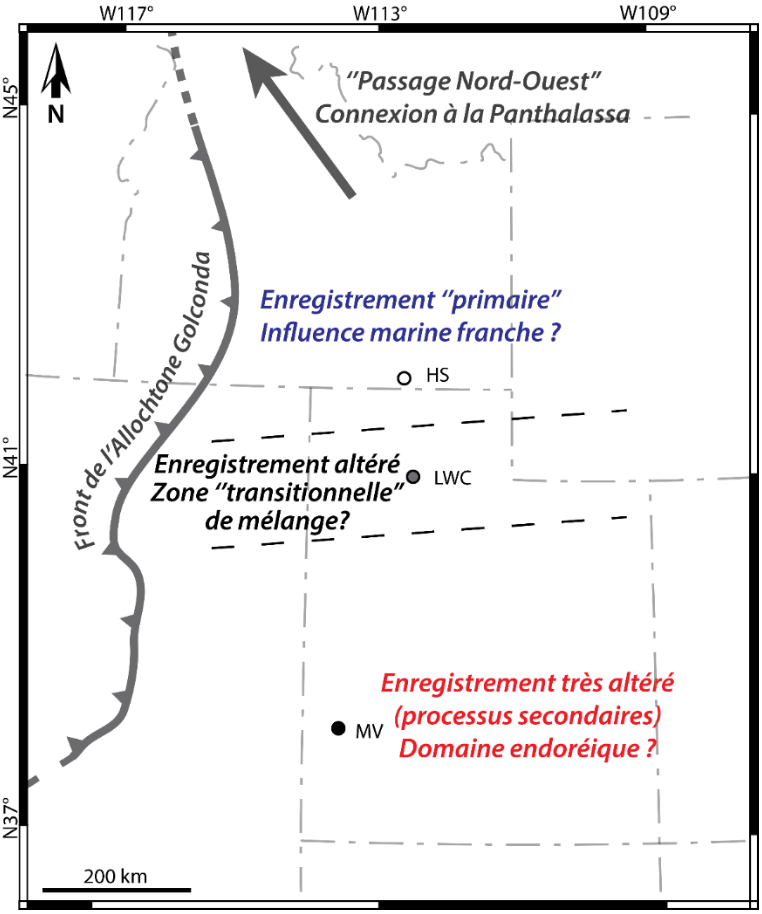

Figure R.5 : Carte montrant la position des coupes de HS, LWC et MV, représentant les parties Nord, centrale et Sud du SFB, respectivement. Les signaux géochimiques montrent une préservation différentielle en fonction de leur position dans le bassin du fait de variations dans les processus secondaires en lien avec les environnements de dépôts locaux.

Le signal des paires d'isotopes du carbone montre le couplet d'excursion négative et positive caractéristique à l'échelle mondiale du Smithien moyen et de la SSB (e.g., Galfetti *et al.*, 2007b ; Romano *et al.*, 2012 ; Grasby *et al.*, 2013). La coévolution des signaux du carbonate et de la matière organique indique également une origine potentiellement exogénique de ces perturbations, et donc une influence du cycle global du carbone, sur cette enregistrement (Zeebe, 2012). Cependant, nos travaux sur la coupe de HS ont montré que dans le détail ce signal était également contrôlé par des facteurs locaux, comme la variation des apports en carbone d'origine terrigène. Ceci remet donc en question le caractère global de ce signal et l'établissement de corrélation à l'échelle planétaire sur sa base.

L'analyse des éléments T&M de HS n'a pas permis de mettre en évidence la présence d'une anoxie marquée dans la colonne d'eau, contrairement à ce qui est décrit dans la littérature pour le Trias inférieur (e.g., Isozaki, 1997 ; Meyer *et al.*, 2011 ; Sun *et al.*, 2012). Seuls quelques rares épisodes de conditions suboxiques à l'interface eau/sédiment peuvent être identifiés par de faibles pics de la concentration en U (e.g., Sauvage *et al.*, 2013).

La coupe de LWC se situe dans le Nord de l'Utah, dans la partie centrale du SFB (Fig. R.5). Moins épaisse que HS (~290 m d'épaisseur), elle enregistre des milieux de dépôts similaires de rampe interne. Cependant, les faciès rencontrés sont différents. La succession sédimentaire débute par un épais niveau de red beds terrigènes (>40 m), représentant un milieu transitionnel continental à marin, d'une unité peu profonde de dolosiltites, puis enfin d'une unité d'alternances marno-calcaires autour de la SSB, indiquant une ouverture vers des conditions plus marines accompagnant une tendance transgressive. Enfin, la dernière unité représentant le Spathien inférieur est composée de dépôts de milieux de rampe moyenne dominés par la boue, enregistrant localement des niveaux de tempestites (Grosjean *et al.*, *in prep.*).

L'enregistrement géochimique est à LWC moins complet qu'à HS. Seuls les paires d'isotopes du carbone ont été étudiés. Le signal du carbone ne montre pas de coévolution entre le carbonate et la matière organique. Si le couplet d'excursions négative et positive caractéristique du Smithien moyen et de la SSB est bien identifiable dans l'enregistrement organique, il est plus difficile à observer dans l'enregistrement du carbonate. En effet, plusieurs outliers négatifs viennent perturber le signal autour de la SSB.

Des processus secondaires semblent altérer fortement le signal géochimique de la coupe de LWC (Fig. R.5). Cette hypothèse est supportée par une covariation des signaux $\delta^{13}C_{carb}$ et $\delta^{18}O_{carb}$ au sein d'une des unités lithologiques. Si l'interprétation de LWC en tant que signal global du cycle du carbone est de fait impossible, ces résultats suggèrent une forte influence des processus locaux (y compris secondaires) sur l'enregistrement et la préservation des signaux géochimiques.

La coupe de MV se situe dans le Sud-Ouest de l'Utah, dans la partie Sud du SFB (Fig. R.5). Les 160 m de cette coupe enregistrent des dépôts dont la base est constituée de red beds transitionnels correspondant au Dienerien supérieur (?) et au Smithian inférieur. Viennent ensuite des dépôts de carbonates microbiens de milieu intertidal à supratidal, puis des mudstones laminés déposés dans un contexte de rampe moyenne à externe, et un intervalle SSB caractérisé par des marnes de rampe externe (offshore inférieur). Enfin, le Spathien inférieur est représenté par un dépôt de mudstones de rampe externe, avec localement des passées tempestitiques.

Comme à LWC, l'enregistrement des paires d'isotopes du carbone ne montre pas de coévolution entre le carbonate et la matière organique, à ceci près que c'est l'enregistrement du carbonate qui montre le couplet habituel représentant le Smithien moyen et la SSB, alors que le signal organique ne montre aucune variation. Le signal apparaît donc altéré par des processus secondaires, ce qui est confirmé par plusieurs corrélations entre les signaux $\delta^{13}C_{carb}$ et $\delta^{18}O_{carb}$ et le rapport élémentaire Mn/Sr notamment (Thomazo *et al.*, 2016).

Par ailleurs, les éléments T&M mettent en évidence la présence de plusieurs épisodes suboxiques le long de la coupe de MV par l'intermédiaire du signal élémentaire de l'U. Les résultats présentés par Thomazo *et al.*, (2016) montrent que ces épisodes suboxiques seraient associés au métabolisme de bactéries sulfato-réductrices dans la partie supérieure des sédiments lors de la diagénèse précoce.

Ces différents résultats montrent que le signal géochimique des paires d'isotopes du carbone dans le SFB semble plus répondre à des forçages locaux liés aux conditions du milieu de dépôt, qu'à un forçage global lié au cycle exogénique du carbone. Cependant, une influence de ce dernier ne peut être formellement écartée.

Le signal géochimique n'est pas altéré de la même façon dans tout le SFB : un « gradient » d'altération peut être supposé, depuis un signal « primaire » au Nord, vers un signal de plus en plus altéré vers le Sud (Fig. R.5). Il apparaît donc qu'une distinction géochimique existe entre les parties Nord et Sud du bassin (Fig. R.5). Cette différenciation peut avoir été générée par des disparités dans la connexion des réservoirs du SFB : si le Nord du SFB est de tous temps connecté à la Panthalassa par un « passage Nord-Ouest » (Fig. R.5 ; Colpron & Nelson, 2009), ce n'est pas le cas du Sud du SFB avant le Smithien tardif, quand la connexion se fait consécutivement à la transgression régionale de troisième ordre (e.g., Vennin *et al.*, 2015). Une composante endoréique est ainsi peut-être à considérer dans cette partie Sud plus restreinte du SFB (Fig. R.5)

- Contrôle géodynamique du bassin

Les différents enregistrements sédimentaires, paléontologiques mais également géochimiques montrent tous l'existence d'une distinction entre les parties Nord et Sud du bassin. Cependant, les connaissances actuelles du SFB, de son évolution géodynamique et de ses paramètres de contrôle au premier ordre ne permettent pas d'expliquer l'origine de cette différence.

Une étude intégrée, utilisant des approches sédimentologiques, paléontologiques, géophysiques, géodynamiques, cartographiques et structurales, a été menée sur l'ensemble du bassin afin de tenter de déterminer quels étaient les facteurs de contrôles sur l'évolution contrastée des parties Nord et Sud du SFB. Une modélisation numérique a également été menée pour caractériser les facteurs de contrôle incriminés. Pour cela, une base de données de 43 coupes réparties dans l'entièreté du SFB a été établie (Fig. R.6). Ces coupes ont été biostratigraphiquement corrélées à l'aide de zones d'ammonoïdes (Brayard *et al.*, 2013). L'intervalle ainsi considéré correspond au Trias inférieur depuis sa base représentée à l'échelle régionale par la discontinuité Permien/Trias (PTU ; Brayard *et al.*, 2013), et jusqu'à la fin du Smithien (intervalle PTU-Smithien). Lorsque cela était possible, cet intervalle inclut la base du Spathien jusqu'à la zone à *Columbites* (Brayard *et al.*, 2013 ; Jenks *et al.*, 2013).

Afin d'obtenir une image non biaisée de la paléogéographie du SFB durant le Trias inférieur, une reconstitution palinspastique du bassin a été réalisée en se basant sur des données issues de la littérature (e.g., DeCelles & Coogan, 2006 ; Schelling *et al.*, 2007 ; Yonkee & Weil, 2010 ; Yonkee *et al.*, 2014), mais également en réalisant des « coupes équilibrées », permettant d'horizontaliser les terrains déformés (dans notre cas résultant de la mise en place de la chaîne de chevauchement Sevier durant le Mésozoïque) et ainsi de connaître la valeur estimée du transport tectonique subit par les terrains incriminés. Cette carte (Fig. R.6) permet donc de replacer les affleurements étudiés dans leur position d'origine, ce qui représente une première pour cet intervalle de temps et ce bassin.

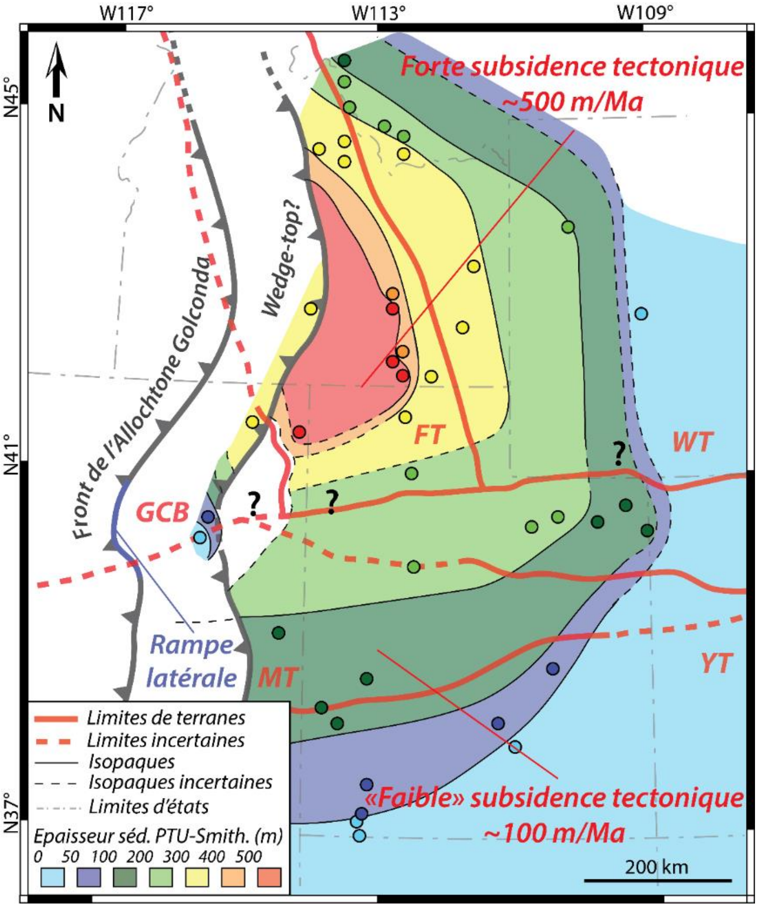

Figure R.6 : Carte paléogéographique isopaque de la distribution spatiale de l'épaisseur sédimentaire pour l'intervalle PTU-Smithien, montrant des différences marquées d'épaisseur entre le Nord et le Sud du SFB (d'après Caravaca *et al.*, *in press*, cf ; section IV). Cette différence est également mise en exergue par une forte variation du taux de subsidence tectonique. Le front de l'Allochtone Golconda montre la présence dans sa partie centrale d'une rampe latérale vraisemblablement héritée des discontinuités du socle lithosphérique. Celui-ci est d'ailleurs composé par 5 terranes d'âges (et donc de comportement rhéologique) différents : GCB : Grouse Creek Block ; FT : Farmington Terrane ; WT : Wyoming Terrane ; MT : Mojave Terrane ; YT : Yavapai Terrane.

Cette nouvelle paléogéographie nous a permis de réaliser une carte de la répartition spatiale de l'épaisseur sédimentaire pour l'intervalle PTU-Smithien (Fig. R.6). Sur cette carte isopaque, il est possible de remarquer une fois encore la distinction entre le Sud et le Nord du bassin. Le Sud du bassin est caractérisé par une tendance d'approfondissement progressif vers le Nord-Ouest, depuis des épaisseurs sédimentaires de quelques dizaine au plus de mètres sur les bordures sud et est du bassin, jusqu'à une profondeur maximum d'environ 250 m (Fig. R.6). Au contraire, le Nord du SFB est caractérisé par un approfondissement plus brutal vers l'Ouest, et dont les valeurs sont comprises entre 300 et ~600 m (Fig. R.6).

Une analyse de backstripping sur 4 coupes représentatives du bassin a également permis de calculer les taux de subsidence dans le SFB. Ainsi, les valeurs obtenues pour la subsidence tectonique, qui est la composante principale de la subsidence totale dans ce bassin au cours du Trias inférieur, varient depuis ~100 m/Ma dans la partie Sud du bassin et jusqu'à ~500 m/Ma dans la partie Nord (Fig. R.6). L'analyse de backstripping a également pu mettre en évidence et donc confirmer la nature foreland du bassin de Sonoma, ce qui restait encore très débattu (e.g., Ingersoll, 2008). Néanmoins, si la nature foreland du bassin permet d'expliquer la subsidence tectonique comme étant d'origine flexurale à la suite de la mise en place d'une charge topographique représentée par l'Allochtone Golconda (Fig. R.6), cela n'explique en rien la différenciation N/S observée.

Pour tenter de trouver une explication, nous nous sommes intéressés au socle du bassin. En effet, celui-ci est formé par 5 terranes lithosphériques d'âges différents (Fig. R.6) : les terranes Archéennes Wyoming (WT) et Grouse Creek Block (GCB), les terranes Paléoprotérozoique Mojave (MT) et Yavapai (YT), et enfin la zone mobile Mésoprotérozoïque Farmington (FT). Du fait de leur âge différent, il est attendu un comportement rhéologique différent de leur part, lié à leur épaisseur (épaisseur élastique Te) et ainsi à leur rigidité (e.g., Artemieva & Mooney, 2002). De fait, les terranes anciennes (Archéennes et Paléoprotérozoïques) sont froides, épaisses et très résistantes à la déformation et à la flexuration, tandis que les terranes « juvéniles » (depuis le Mésoprotérozoïque) sont moins épaisses, plus chaudes et donc moins résistantes à la déformation et à la flexuration. Il apparaît ainsi que cette différence rhéologique peut se révéler capitale dans le contrôle de la flexuration, et par conséquent de la subsidence tectonique durant le développement du SFB au Trias inférieur.

Comme ces différences rhéologiques remontent au Mésoprotérozoïque, il est fort probable qu'elles aient impacté le bassin également bien avant la mise en place du SFB au cours du Trias inférieur. Paulsen & Marshak (1999) ont aussi montré l'existence d'une rampe latérale dans le front de la chaîne Sevier au niveau des Monts Wasatch (au Nord-Est de Salt Lake City), résultant d'une variation de distribution spatiale de l'épaisseur sédimentaire. En effet, il existe un lien entre la longueur d'onde de propagation d'une contrainte compressive et l'épaisseur du socle sous-jacent au niveau du front de décollement : plus l'épaisseur sera élevée, plus la propagation de la contrainte sera grande, et plus le transport tectonique sera important. Or, la présence d'un haut topographique dans la zone centrale du bassin a été mise en évidence durant le Paléozoïque (Peterson, 1977), et un différentiel d'épaisseur sédimentaire est bien identifié. Ainsi, en la présence d'une épaisseur sédimentaire plus élevée au Nord du bassin, le transport tectonique est plus important dans cette même partie Nord du bassin pour la Sevier. Suivant ce raisonnement et les données de distribution spatiale de l'épaisseur sédimentaire pour le Paléozoïque, nous proposons la présence d'une rampe latérale dans le front de chevauchement de l'Allochtone Golconda au niveau de la partie centrale du SFB (Fig. R.6). Une hétérogénéité spatiale était donc vraisemblablement présente dans l'allochtone, provoquant de fait une variation spatiale de la charge sédimentaire qui a pu être répercutée dans la réponse flexurale de la lithosphère du SFB.

Pour vérifier ces hypothèses, une modélisation numérique du comportement rhéologique du bassin flexural en réponse à la mise en place d'un allochtone est réalisée. Ainsi, plusieurs hypothèses ont été testées :

- Socle du bassin hétérogène et allochtone homogène ;
- Socle du bassin homogène et allochtone hétérogène ;
- Socle du bassin et allochtone hétérogènes tous les deux.

La modélisation numérique a montré que le modèle dont les résultats se rapprochaient le plus des observations de terrain de l'épaisseur sédimentaire étaient ceux produits par le modèle impliquant une hétérogénéité à la fois dans le socle du bassin (et donc des terranes ayant un comportement rhéologique différent) et dans la distribution spatiale de l'allochtone (avec donc une charge topographique variant dans l'espace). Dans le même temps, la surcharge sédimentaire provoquée par le dépôt de séries sédimentaires durant le fonctionnement et le remplissage du bassin a été écartée car étant insuffisante à provoquer un tel différentiel de subsidence entre le Nord et le Sud.

Ainsi, cette étude intégrée a pu montrer le rôle précédemment insoupçonné de l'héritage sur la mise en place et le développement du SFB, résultant des variations de rhéologie des terranes composant le socle. C'est ainsi que le contrôle prépondérant au premier ordre de la subsidence différentielle dans le SFB apparaît comme étant de nature lithosphérique, et permet la distinction de deux dynamiques différentes et propres pour chacune des parties Nord et Sud du bassin.

• 2 sous-bassins

L'étude comparée et intégrée des enregistrements sédimentaires, des registres fossiles, des signaux géochimiques et des paramètres géodynamiques et structuraux indique qu'il n'existe pas un seul SFB, mais deux sous-bassins reliés durant le Trias inférieur.

En effet, de telles différences dans les communautés (e.g., ammonoïdes et microbes ; Fig. R.3), dans les lithologies observées (e.g., formations marines Dinwoody/Woodside *vs* formation terrigène Moenkopi ; Fig. R.4) ou dans la préservation du signal géochimique (forte altération *vs* bonne préservation ; Fig. R.5), ne peut s'expliquer en la présence d'un seul et unique système sédimentaire. Il apparaît donc nécessaire de distinguer deux sous-bassins : le Nord-SFB et le Sud-SFB (Fig. R.7).

Ces deux sous-bassins, partagent des caractères communs (e.g., réservoir géochimique élémentaire, milieux de dépôts peu profond), mais demeurent distincts dans leur évolution géodynamique au cours du Trias inférieur.

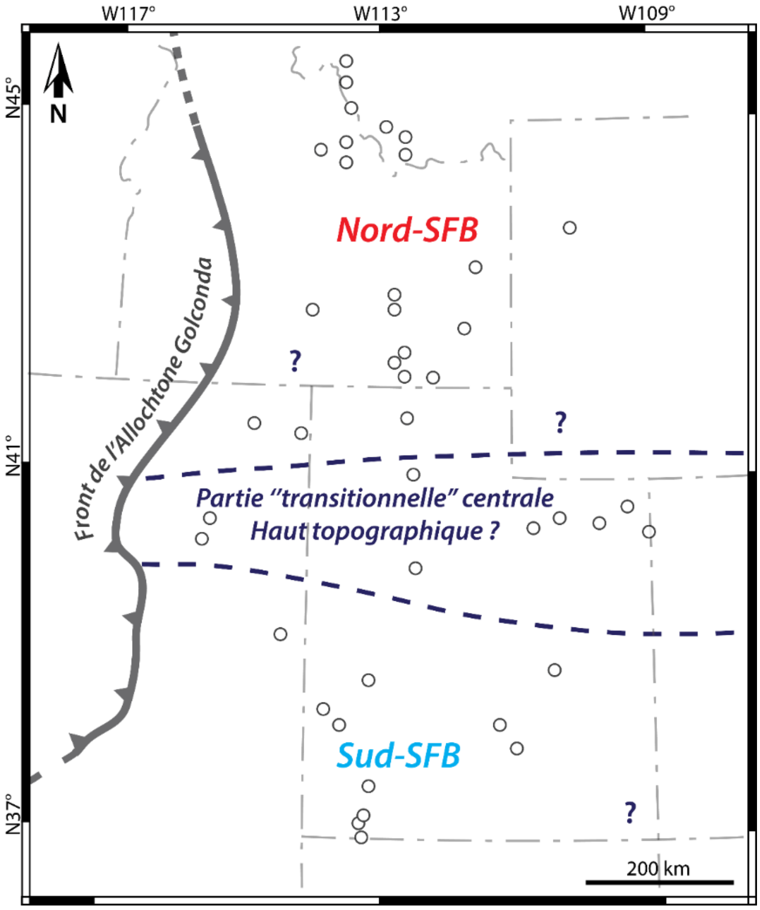

Figure R.7 : Nouvelle paléogéographie révisée du SFB, montrant la distinction entre le Nord-SFB et le Sud-SFB, délimitée par une zone centrale « transitionnelle » (et potentiellement un haut topographique)

Une partie centrale « transitionnelle » du SFB reste pour l'heure actuelle toujours mal contrainte à bien des égards. Par exemple, d'un point de vue sédimentaire, l'absence d'affleurements qualitatifs dans cette région ne permet pas de caractériser les paléoenvironnements et/ou le signal géochimique de cette zone de façon exhaustive. La présence supposée d'un haut topographique dans ce secteur (Fig. R.7) implique donc de concentrer une partie des futurs efforts de recherche sur cette région pour parfaire la compréhension de l'évolution 4D du SFB.

La connaissance de cette dernière est indispensable pour fournir un cadre paléoenvironnemental précis dans lequel analyser la rediversification biologique post-crise PTB, à une échelle régionale. Il sera alors intéressant de déchiffrer et de caractériser de façon plus précise les potentielles interactions et rétroactions entre les communautés biologiques et leur environnement de dépôt.

Mots-clés : Sonoma Foreland Basin, Ouest USA, Trias inférieur, étude intégrée, sédimentologie, géochimie, paléontologie, géologie structurale, modélisation numérique, SIG, cartographie géologique, reconstitutions paléoenvironnementales

Abstract

In the wake of the Mesozoic, the Early Triassic (~251.95 Ma) corresponds to the aftermath of the most severe mass extinction of the Phanerozoic: the end-Permian crisis, when life was nearly obliterated (e.g., 90% of marine species disappeared). Consequences of this mass extinction are thought to have prevailed for several millions of years, implying a delayed recovery lasting the whole Early Triassic, if not more.

Several paradigms have been established and associated to a delayed biotic recovery scenario expected to have resulted from harsh and deleterious paleoenvironments. These paradigms include a global anoxia in the marine realm, a “Lilliput” effect, and the presence of “disaster” taxa and “anachronistic” facies. However, recent works have shown a more complex global scheme for the Early Triassic recovery, and that a reevaluation of these paradigms was needed. Especially, new data from the western USA basin were critical in re-addressing these paradigms.

The western USA basin is the result of a long tectono-sedimentary history that started 2 Gyr ago by the amalgamation of different lithospheric terranes forming its basement. A succession of orogenies and quiescence phases led to the formation of several successive basins in the studied area, and traces of this important geodynamical activity are still present today. The Sonoma orogeny occurred about 252 Ma in response to the eastward migration of drifting arcs toward the Laurentian craton. As a result, compressive constrains lead to the obduction of the Golconda Allochthon above the west-Pangea margin in present-day Nevada. Emplacement of this topographic load provoked the lithosphere flexuration beneath present-day Utah and Idaho to form the Sonoma Foreland Basin (SFB) studied in this work.

The SFB recorded an excellent fossil and sedimentary record of the Early Triassic. A relatively high and complex biotic diversity has been observed there leading to describe a rapid and explosive recovery for some groups (e.g., ammonoids) in this basin after the end-Permian crisis. The sedimentary record is also well developed and has been studied extensively for a long time. Overall, these studies notably documented a marked difference between the northern and southern sedimentary succession within the basin, whose origin was poorly understood.

This work therefore aims to characterize the various depositional settings in the Early Triassic SFB, as well as their paleogeographical distribution. Their controlling factors are also studied based on an original integrated method using sedimentological, paleontological, geochemical, geodynamical, structural and cartographic analyses.

Aside the fossil and sedimentary discrepancy between the northern and the southern parts of the SFB, geochemical analyses provide new insights supporting this N/S dichotomy. This study also questions the validity of the geochemical signal as a tool for global correlation, as it appears to mainly reflect local forcing parameters.

The geodynamical framework of the SFB was also investigated along with a numerical modelling of the rheological behavior of the basin. This work distinguishes the northern and southern parts of the basin based on markedly distinct tectonic subsidence rates during the Early Triassic: ~500 m/Myr in the northern part *vs* ~100m/Myr in the southern part. Origin of this remarkable difference is found in inherited properties of the basin basement itself. Indeed, different ages and therefore, rheological behaviors (i.e., rigidity to deformation and flexuration) of the basement lithospheric terranes act as a major controlling factor over the spatial distribution of the subsidence, and therefore of the sedimentary deposition. The lithosphere heritage is thus of paramount importance in the formation, development and spatio-temporal evolution of the SFB.

This work leads to a new paleogeographical representation of the Sonoma Foreland Basin and its multi-parameter controlling factors. We highlight the importance of the local parameters in influencing the development and 4D evolution of the depositional settings. In turn, this evolution is likely of prime importance in understanding the rhythms and modalities of the biotic recovery observed in the SFB. Finally, we now distinguish two distinct sub-basins in this area: the North-SFB and the South-SFB with contrasted Early Triassic geobiological evolution.

Keywords: Sonoma Foreland Basin, western USA, Early Triassic, integrated study, sedimentology, geochemistry, paleontology, structural geology, numerical modelling, GIS, geological mapping, paleoenvironmental reconstructions

Contents

I. GENERAL & CONTEXTUAL INTRODUCTION 14

A. The Early Triassic Earth: from one world to another 16

- Early Triassic 101: when? 16
- Global paleogeographic reconstructions of the Early Triassic Earth 17
- Geochemical record at the PTB and during its aftermath: a succession of isotopic excursions 18
- Climate and temperature variations 19

B. Focus on the "post-apocalyptic" Early Triassic world 21

- The Permian/Triassic boundary crisis 21
- Common paradigms associated to the "delayed recovery" 23
- Evidence for an alternative scenario 25

C. Methodology of the integrated approach 31

II. THE WESTERN USA SONOMA FORELAND BASIN 36

A. A brief overview of a 2Ga-long history: a geodynamically active region 38

- Location and extent of the western USA basin 38
- History of the western USA Basin since the Proterozoic 41

B. The Early Triassic SFB: State of the art57

- Location and extent of the SFB 57
- Spatial heterogeneities in SFB studies 57
- A marked dichotomy in the SFB sedimentary record 59
- The N/S dichotomy is also visible in the fossil record 61
- Misinterpretations and gap in the geological history of the SFB 65

III. GEOCHEMICAL PARAMETERS OF THE SFB WATER COLUMN 68

A. Northern SFB signal: Hot Springs 70

B. Central SFB signal: Lower Weber Canyon 84

- Introductory remarks and geological setting 84
- Paired carbon isotopic signal 86
- Preservation of the isotopic signal. 89

C. Southern SFB signal: Minersville 90

- Introductory remarks and geological setting 90
- Paired carbon isotopic signal 92
- Preservation of the isotopic signal. 93
- Trace and major elements 97
- Interpretation of the MV geochemical signal: only local? 102

D. Characterization of the basin-scale geochemical signal 102

- Carbon isotopic record 103
- Trace and major elements occurrences and concentrations 107
- Geochemical discrimination between a southern and a northern sub-basin in the SFB 111
- SFB versus global Early Triassic geochemical record 112

IV. CHARACTERIZATION OF THE MAIN CONTROLLING FACTORS OVER THE SFB SEDIMENTARY RECORD 114

V. SYNTHESIS/CONCLUSIONS SFB OR SFBs? 144

A. Evidence for two sub-basins 146
- Paleontological record 146
- Sedimentary record 148
- Geochemical record 149
- Geodynamical framework of the SFB 151
- Perspectives on basin paleogeography 153

B. Ongoing work: expected impact on the 4D evolution of depositional settings in the North- and South-SFB 155

C. Larger implications for the Early Triassic time interval 162

D. Other general and conceptual perspectives 163

REFERENCES 166

APPENDICES 194

Appendix 1: Characterization of the sedimentary record and depositional environments of the Torrey area (south-central Utah) 196

Appendix 2: Supplementary material belonging to the article “Early Triassic fluctuations of the global carbon cycle: new evidence from paired carbon isotopes in the western USA basin” (see section III.A) 224

Appendix 3: Supplementary material belonging to the article “Controlling factors for differential subsidence in the Sonoma Foreland Basin (Early Triassic, western USA)” (see section IV) 233

Tables

- Table I.C.1: Synthetic list of the various disciplinary fields, techniques and methods used in this integrated basin-scale study of the SFB. 33
- Table III.B.1. Geochemical data with $\delta^{13}C_{org}$, $\delta^{13}C_{carb}$, $\Delta^{13}C_{carb-org}$, $\delta^{18}O_{carb}$ and carbonate ($CaCO_3$) contents (after Grosjean et al., in prep.). 88
- Table III.C.1. Geochemical data with $\delta^{13}C_{org}$, $\delta^{13}C_{carb}$, $\Delta^{13}C_{carb-org}$, Total Organic Carbon (TOC) content, $\delta^{18}O_{carb}$ and carbonate ($CaCO_3$) contents (after Thomazo et al., 2016). 95
- Table III.C.2: Geochemical data with trace and major elements results. 100
- Table V.B.1: Main facies associations and depositional settings observed in the SFB during the middle-late Smithian interval (references are given within the table). 158

Illustrations

- Fig. I.A.1: Simplified chronostratigraphic chart of the Early Triassic. Skulls: major biotic crises. Radiometric ages after Ovtcharova et al. (2006), Galfetti et al. (2007b) and Baresel et al. (2014).. 16
- Fig. I.A.2: Paleogeographic reconstruction of the Earth during the Early Triassic (after Blakey, 2013).. 17
- Fig. I.A.3: Worldwide Early Triassic variations of the $\delta^{13}C$ signal on both the organic matter and carbonates. Red boxes highlight the Dienerian/Smithian boundary (DSB) and Smithian/Spathian boundary (SSB) isotopic events. Data after Galfetti et al. (2007b), Hermann et al. (2011), Sun et al. (2012), Grasby et al. (2013) and Thomazo et al. (2013). l.: lower; mi.: middle; u.: upper.. 18
- Fig. I.A.4: Simplified relative temperature trend during the Early Triassic obtained using the δ18Ocp signal (obtained from conodont pectiniform elements, after Romano et al., 2013). Several episodes of climatic changes are obvious, notably a cooling phase in the Dienerian and an important warming during the middle Smithian followed by a cooling at the SSB. 20
- Fig. I.B.1: Humoristic sketch of the end-Permian mass extinction. Characteristic Paleozoic organisms such as trilobites and tabulate corals disappeared at that time. 21
- Fig. I.B.2: Synthetic flow chart summarizing some of the proposed cause-and-effect relationships during the end-Permian mass extinction and the Early Triassic “delayed” recovery. This chart highlights a major role of the Siberian LIP episode over environmental perturbations (after Bond & Wignall, 2014). 23
- Fig. I.B.3: a) Synthetic representation of the main paradigms usually accepted concerning the Early Triassic recovery. b) Synthetic representation of these paradigms revised with recent data from the western USA basin (after Brayard, 2015)... 24
- Fig. I.B.4: a) Example of a depositional setting in the Torrey area (western USA basin, after Olivier et al., 2016, see appendix 1) showing laterally heterogenous and diachroneous presence of microbial communities during the middle Smithian (facies F2 and F3). The model highlights the contemporaneity of the microbial deposits with diverse benthic metazoan organisms b) Schematic evolution of the main microbial limestones facies in the same locality (western USA basin, after Olivier et al., 2016, see appendix 1) showing associations of microbial deposits with metazoan faunas, as well as the various types of microbial communities. See Olivier et al. (2016, see appendix 1) for details. c) Illustration of Smithian sponge-dominated metazoan associations as reef-builders in southwestern Utah (after Brayard et al., 2011) 26

- Fig. I.B.5: a) Photograph of the modern reef-building microbialites in the Great Salk Lake (Utah, USA; courtesy of Dr. Anthony Bouton). b) Relative abundance of microbial carbonates in reefs during the Phanerozoic compared to the marine metazoan generic diversity (after Riding, 2006). This chart shows that microbial carbonates may be present in the aftermath of some mass extinctions (e.g., Late Ordovician or end-Permian), but not all, and when present, they do not always show an increase in proportion. 27
- Fig. I.B.6: Various (ichno-)fossils recently found in the western USA basin highlighting the diversity of Early Triassic ecosystems of this area. a) Large burrows (centimetric-diameter) in carbonated beds of the Timpoweap Canyon (southwestern Utah, USA; after Olivier et al., 2014). b) Some large-sized specimens (pluri-centimetric) of Smithian gastropods from southwestern Utah (after Brayard et al., 2010). Scale bars are 10 mm. c) Illustration of various and well-preserved specimens from the "Paris biota" (southeastern Idaho, after Brayard et al., 2017), which shows a highly diversified early Spathian ecosystem. Scale bars are 10mm. 30
- Figure I.C.1: Illustration of the multi-scale character of the study, from basin-scale to microfacies analysis (location map after Caravaca et al., in press a, see section IV; geological map after Oriel & Platt, 1980). 31
- Figure I.C.2: Map of the study area showing location of sampled sections used in this work. 32
- Figure II.A.1: Simplified tectonic map of the western USA showing the present-day configuration of the lithospheric basement and the main geodynamical structures (modified after Jones, 2013). The red box highlights the location of the studied area in this work........ 39
- Figure II.A.2: Topographic map of the studied area (base map World Street Map ©ESRI). ... 39
- Figure II.A.3: Simplified chronostratigraphy of the successive structuring events in the western USA Basin since the Paleoproterozoic (after Oldow et al., 1989; Whitmeyer & Karlstrom, 2007; Dickinson, 2013). 41
- Figure II.A.4: Map of lithospheric terranes of the western USA during emplacement of the Paleoproterozoic Mojave and Yavapai terranes against the Archean Grouse Creek Block and Wyoming Terrane (after Whitmeyer & Karlstrom, 2007). 42
- Figure II.A.5: a) Paleogeographic reconstruction of the western USA during the Cambrian (Blakey, 2013). b) Simplified Cambrian map of the western USA, highlighting the presence of the "Miogeocline" passive margin formed during the fragmentation of the supercontinent Rodinia (after Blakey, 2013; Dickinson, 2013). c) W-E lithospheric cross-section, showing the characteristic geometry of the "Miogeocline" passive margin (after Ingersoll, 2008). 43
- Figure II.A.6: a) Paleogeographic reconstruction of the western USA during the Late Devonian (Blakey, 2013). b) Simplified Late Devonian map of the western USA, showing the location of

the Roberts Mountain Allochthon and the resulting Antler Foreland Basin. Presence of volcanic arcs is also reported in the oceanic domain (e.g., Sierran/Klamath), as well as an opening ocean (Slide Mountain Ocean) in a back-arc configuration relative to the Antler orogen (after Burchfield & Royden, 1991; Colpron & Nelson, 2009; Blakey, 2013; Dickinson, 2013). c) W-E lithospheric cross-section of the area, showing the Roberts Mountain Allochthon obducted onto the Laurentia craton and the opening Slide Mountain Ocean in a back-arc configuration (Havallah Basin; after Ingersoll, 2008). d) Paleogeographic map of the western margin of the Laurentian continent with a focus on the study area. This map shows first steps of the opening of the Slide Mountain Ocean, with dotted line representing locus of back-arc rift (Colpron et al., 2007). 45

- Figure II.A.7: a) Paleogeographic reconstruction of the western USA during the late Carboniferous (Pennsylvanian; Blakey, 2013). b) Simplified map of the western USA during the late Carboniferous (Pennsylvanian) showing the location of the Slide Mountain Ocean and bordering volcanic arcs of the Sonomia micro-plate to the West (Klamath arc). Primordial Ancestral Rocky Mountains (ARM) uplifts are located in the southeastern part of the study area (after Colpron et al., 2007; Blakey, 2013; Dickinson, 2013). c) W-E lithospheric cross-section of the area (after Ingersoll, 2008). d) Paleogeographic map of the western margin of the Laurentian continent with focus on the study area (Colpron et al., 2007)....................... 46
- Figure II.A.8: a) Paleogeographic reconstruction of the western USA during the Early Permian (Blakey, 2013). b) Simplified map of the western USA during the Early Permian showing the location of northwesternmost ARM uplifts and the presence of the marine Oquirrh Basin. The Slide Mountain Ocean is closing, with the Klamath volcanic arc of the Sonomia micro-plate migrating toward the Laurentian margin (after Ye et al., 1996; Dickerson, 2003; Ingersoll, 2008; Colpron et al., 2007; Blakey, 2013; Dickinson, 2013). c) W-E lithospheric cross-section of the area showing basement uplifts of the ARM, the position of the Oquirrh Basin and the closure of the Slide Mountain Ocean through a westward-dipping subduction under the Klamath volcanic arc of the Sonomia micro-plate (after Ingersoll, 2008). d) Paleogeographic map of the ARM uplifts between the studied area and the Ouachita-Marathon orogenic belt in southeastern Laurentia (Dickerson, 2003). 48
- Figure II.A.9: a) Paleogeographic reconstruction of the western USA during the Early Triassic (Blakey, 2013). b) Simplified Early Triassic map of the western USA showing the location of the Golconda Allochthon and the resulting Sonoma Foreland Basin (SFB). The Sonomia micro-plate had been amalgamated to the Laurentian craton, leading to the formation of the Golconda Allochthon. Relics of ARM uplifts are still present in the southeastern end of the SFB (after Ingersoll, 2008; Colpron et al., 2007; Blakey, 2013; Dickinson, 2013). c) W-E

lithospheric cross-section of the area showing the GA obducted onto the Laurentia craton while the Sonoma micro-plate is amalgamated to the craton. The Slide Mountain Ocean is assumed to be present as a lithospheric wedge between the Laurentian and Sonoman plates (after Ingersoll, 2008). d) Paleogeographic map of the western margin of the Laurentian continent with a focus on the study area. This map shows the closure of the Slide Mountain Ocean and the amalgamation of volcanic arcs (Sierra and Klamath; Colpron et al., 2007)..... 50

- Figure II.A.10: a) Simplified Early Triassic paleogeographic map of the SFB, with locations of the reconstructed GA and Koipato volcanic Formation (after Caravaca et al., in press a, see section IV). b) and c) Proposed model for syn- and late-orogenic evolution of the GA thrust belt. b) During syn-orogenic interval, horizontal tectonic forces (Ft) generated a relief by emplacement of the GA, leading to the formation of the SFB and allowing thickening of the underlying crust. c) During the late-orogenic interval, horizontal tectonic forces are not sufficient enough to compensate and overthrow the vertical gravitational forces (Fg) exerted by the mass of the obducted material, leading to a thinning of the crust (e.g., Malavieille et al., 1990; Malavieille, 1993). This thinning caused an isostatic rebound with a partial melting of the crust, responsible for the onset of rhyolitic volcanism in the area (Koipato Fm.; Vetz, 2011).. 52
- Figure II.A.11: a) Paleogeographic reconstruction of the western USA during the Cretaceous (Blakey, 2013). b) Simplified Cretaceous map of the western USA highlighting the presence of the Sevier thrust-and-fold belt (TFB) and the ensuing Sevier foreland Basin (i.e., the “Western Interior Seaway”; after Blakey, 2008, 2013; Ingersoll, 2008; Miall, 2010; Dickinson, 2013). c) W-E lithospheric cross-section of the area showing the Sevier thrust-and-fold belt emplaced onto the North American craton and the eastward-dipping subduction of the Farallon plate (after Ingersoll, 2008)... 53
- Figure II.A.12: a) Paleogeographic reconstruction of the western USA during the Eocene (Blakey, 2013). b) Simplified Eocene map of the western USA highlighting the presence of the Sevier thrust-and-fold belt, Rocky Mountains and Colorado Plateau uplifts (e.g., Oldow, 1984; Ye et al., 1996; Paulsen & Marshak, 1999; Ingersoll, 2008; Blakey, 2013; Dickinson, 2013). c) W-E lithospheric cross-section highlighting the “flat” slab subduction of the Farallon plate (after Ingersoll, 2008)... 54
- Figure II.A.13: a) Paleogeographic reconstruction of the western USA during the Oligocene (Blakey, 2013). b) Simplified map of the western USA during the Oligocene to present-day, showing the extensional Basin and Range province (Blakey, 2013; Dickinson, 2013). c) W-E lithospheric cross-section showing the impacts of the extensional Basin and Range province and the formation of many half-graben basins (after Ingersoll, 2008).................................. 56

- Figure II.B.1: a) Early Triassic location of the SFB (after Brayard et al., 2013). b) Simplified paleogeographic map of the SFB with position of the reconstructed GA and relic ARM uplifts (after Caravaca et al., in press a, see section IV). The "northwestern passage" (after Colpron & Nelson, 2009) is expected to be the only connection between the SFB and the open Panthalassa Ocean during this interval. 58
- Figure II.B.2: Illustration (non-exhaustive) of various published works on the western USA Basin showing location of some studied outcrops. The map also highlights some areas devoid of Early Triassic outcrops. 59
- Figure II.B.3: a) Simplified litho- and chronostratigraphic subdivisions in the Early Triassic SFB. Main ammonoid markers (late Smithian Anasibirites and early Spathian Columbites) are used for biostratigraphical correlation (timeframe from Brayard et al., 2013). Radiometric ages: (1) from Baresel et al., 2017; (2) and (3) from Galfetti et al., 2007a. b) Lithostratigraphic columns for eight selected sections in the SFB, with biostratigraphic correlation (after Caravaca et al., in press a, see section IV). These columns illustrate the discrepancies in dominant lithologies and in thickness of the sedimentary record between the northern and southern parts of the SFB. Basal and biostratigraphic correlation using timeframe after Brayard et al. (2013). RC: Rock Canyon, CR: Confusion Range, PR: Pahvant Range, M: Minersville, T: Torrey, LWC: Lower Weber Canyon, HS: Hot Springs, SC: Sheep Creek. 62
- Figure II.B.4: Photographs of different outcrops in the SFB showing variations in dominant lithologies and sedimentary thicknesses (after Caravaca et al., in press a, see section IV). a) Panorama of Rock Canyon (RC) outcrop, showing plurimetric beds of conglomerates from the basal Moenkopi Group. b) Detail photograph of the conglomerate from RC. c) Photograph of the terrigenous red beds of the Moenkopi Group at Lower Weber Canyon (LWC). d) Panorama of the limestones beds of the Thaynes Group limestones at LWC. e) Panorama of the Moenkopi Group at Minersville (M), showing succession of terrigenous red beds and microbial limestones. f) Panorama of the transition between Moenkopi and Thaynes Groups showing succession of microbial and bioclastic limestones at M. g) Photograph of the marine siltstones of the Dinwoody and Woodside Formations at Hot Springs (HS). h) Panorama of the HS section, showing succession of limestone levels of the Thaynes Group bioclastic limestones. Position of the illustrated sections is indicated on the map in Fig. II.B.3b. 63

- Figure II.B.5: Map illustrating the spatial distribution of some organisms (ammonoids and microbial limestones) found in the SFB and displaying a segregation between the northern and southern parts of the basin (after Brayard et al., 2013; Olivier et al., 2014, 2016, see appendix 1; Vennin et al., 2015; Jattiot et al., in prep.). 64

- Figure II.B.6: Examples of “erroneous” non-palinspastically reconstructed, and therefore, non-paleogeographic interpretations of the SFB. a) Isopach map of the Dinwoody Fm. (Kummel, 1957). b) Spatial extent of the end-Smithian transgression (Paull & Paull, 1993). c, d) Spatial distribution of oversimplified facies belts of the Thaynes Group during the Smithian (Goodspeed & Lucas, 2007; Brayard et al., 2013). 66
- Figure III.B.1: a) Map of the studied area and location of the Lower Weber Canyon section. b) Synthetic log of the complete Lower Weber Canyon section (after Grosjean et al., in prep.). Synthetic ammonoid biozonation after Brayard et al. (2013); Meekoceras: Meekoceras beds; Ana.: Anasibirites kingianus beds. c) Detail log and position of geochemical samples for the SSB transition of the Lower Weber Canyon section. Up. Sm.: upper Smithian; SSB: Smithian/Spathian Boundary. 85
- Figure III.B.2: Carbon and oxygen isotopes record, carbonate and total organic contents chemostratigraphy in the Lower Weber Canyon section. Open symbols in SSB units bear uncertainties due to potential secondary alteration. 87
- Figure III.B.3: Isotopic and elementary geochemical parameters of the Lower Weber Canyon section. a) $\delta^{13}C_{carb}$ vs $\delta^{13}C_{org}$.b) $\delta^{13}C_{carb}$ vs $CaCO_3$ content. c) $\delta^{13}C_{carb}$ vs $\delta^{18}O_{carb}$. A positive correlation is observed between $\delta^{13}C_{carb}$ vs $\delta^{18}O_{carb}$ within Unit A. 89
- Figure III.C.1: a) Map of the studied area and location of the Minersville section. b) Synthetic log of the Minersville section showing the sequential framework, facies, lithologies and depositional settings (after Vennin et al., 2015). Synthetic ammonoid biozonation after Brayard et al. (2013); V.u.: Vercherites undulatus beds; I.b.: Inyoites beaverensis beds; O.: Owenites beds; A.k.: Anasibirites kingianus beds; Xe: Xenoceltitidae “gen. indet.” A beds. SSB: Smithian/Spathian Boundary. 91
- Figure III.C.2: Carbon and oxygen isotopes record, carbonate and total organic contents chemostratigraphy in the Minersville section (after Thomazo et al., 2016)........................... 93
- Figure III.C.3: Isotopic and elementary geochemical parameters of the Minersville section (after Thomazo et al., 2016). a) δ13Corg vs δ13Ccarb. b) Mn content vs δ13Ccarb. c) Mn/Sr ratio vs δ18Ocarb. d) δ13Corg vs Total Organic Carbon (TOC) content. Uncertainties are smaller than the symbol size. 96
- Figure III.C.4: Chemostratigraphy of selected trace and major elements in the Minersville section, listed after their detrital and authigenic origin. 98
- Figure III.D.1: Simplified lithological columns and biostratigraphic correlation based on Anasibirites beds for the Minersville, Lower Weber Canyon and Hot Springs sections, representing southern, central and northern parts of the SFB, respectively. The base of the

sections corresponds to the regionally recognized Permian/Triassic unconformity (Brayard et al., 2013). 103

- Figure III.D.2: Early Triassic variations of the δ13C signal for both carbonates and organic matter in the SFB based on the HS, LWC and MV studied sections. Open symbols in LWC record units bear uncertainties due to potential secondary alteration. Radiochronologic ages after Ovtcharova et al. (2006), Galfetti et al. (2007a) and Baresel et al. (2017). L.: lower; mi. middle; u. upper; SSB: Smithian/Spathian boundary. 105
- Figure III.D.3: Early Triassic variations of the Δ13C signal in the SFB based on the HS, LWC and MV studied sections. Open symbols in LWC record units bear uncertainties due to potential secondary alteration. Radiochronologic ages after Ovtcharova et al. (2006), Galfetti et al. (2007a) and Baresel et al. (2017). L.: lower; mi. middle; u. upper; SSB: Smithian/Spathian boundary. 106
- Figure III.D.4: Chemostratigraphy of the detrital trace and major elements in the HS and MV sections. 108
- Figure III.D.5 Chemostratigraphy of the authigenic trace and major elements in the HS and MV sections. SSB: Smithian/Spathian boundary. 110
- Figure V.A.1: Paleogeographic map illustrating the spatial distribution of some ammonoids genera and microbial deposits and displaying a segregation between the northern and southern parts of the basin (after Brayard et al., 2013; Olivier et al., 2014, 2016; Vennin et al., 2015; Grosjean et al., in prep.; Jattiot et al., in prep.). 147
- Figure V.A.2: Paleogeographic maps of the spatial distribution of the Early Triassic dominant lithological formations in the SFB. a) Spatial distribution of the Dinwoody and Woodside formations and of the Moenkopi Group until the middle-late Smithian. b) Spatial distribution of the remaining Moenkopi Group and of the Thaynes Group during late Smithian and early Spathian. 149
- Figure V.A.3: Map of the studied area with location of the HS, LWC and MV section, representing northern, central “transitional” and southern parts of the SFB, respectively. SFB geochemical signals record differential preservation of the primary depositional signatures and imprint by local secondary processes. 150

- Figure V.A.4: Isopach map of the sedimentary thicknesses recorded for the PTU-Smithian interval, showing marked differences in sedimentary thicknesses between northern and southern parts of the SFB (after Caravaca et al., in press a, see section IV). Red lines indicate the limits of lithospheric terranes; GCB: Grouse Creek Block; FT: Farmington Terrane; WT: Wyoming Terrane; MT: Mojave Terrane; YT: Yavapai Terrane. 152

- Figure V.A.5: Revised paleogeography for the SFB, showing a distinction between the North-SFB and South-SFB, delimited by a central "transitional" part (potentially a topographic high). 154
- Figure V.B.1: Simplified synthetic depositional model for the main facies associations FA1 to FA7 (Table 7.B.1) described for the middle-late Smithian interval in the SFB. FWWB: Fair weather wave base; SWB: Storm wave base. 155
- Figure V.B.2: Preliminary representation of the spatial distribution of the main depositional settings in the SFB during the Owenites beds (middle Smithian, after Brayard et al., 2013). A North/South distinction is evidenced by this map, with restriction of the FA3 microbial association to the South-SFB, while the North-SFB exclusively displays the FA2 peritidal association and FA7 deep offshore conditions. 159
- Figure V.B.3: Preliminary representation of the spatial distribution of the main depositional settings in the SFB during the Anasibirites beds (late Smithian, after Brayard et al., 2013). Southeastward migration of the FA5 is clearly evidenced by this map and marks lateral evolution and migration of specific depositional conditions with time........ 160

I. GENERAL & CONTEXTUAL INTRODUCTION

A. The Early Triassic Earth: from one world to another

Early Triassic 101: when?

At the boundary between the two longest eras of the Phanerozoic (the Paleozoic and Mesozoic, respectively), the Early Triassic is a key period in the installation of modern ecosystems. However, this interval remains enigmatic on many points. The Early Triassic immediately follows the most catastrophic known biotic crisis of the living history on Earth at the Permian/Triassic boundary (PTB) some ~251.95 Myr ago (Baresel *et al.*, 2017) that provoked annihilation of ~90% of marine species (to be further discussed in section I.B; e.g., Raup, 1979).

Even if of paramount importance, this period is one of the shortest epoch subdivisions, spanning only ~5 million years (Ovtcharova *et al.*, 2006, Galfetti *et al.*, 2007a, Baresel *et al.*, 2017; Fig. I.A.1). The Early Triassic is subdivided into two stages, the Induan and Olenekian, that are themselves split into two substages each: the Griesbachian and Dienerian, and the Smithian and Spathian, respectively. It is worth noting that the Spathian accounts for more than half of the entire Early Triassic (Fig. I.A.1). The four substages subdivision is the most widely used timeframe because its boundaries are well defined in terms of successive abiotic and biotic events. The Smithian/Spathian boundary event is a good example as it records a faunal turnover coeval with climatic and environmental changes recorded by various isotopic markers (e.g., Brayard *et al.*, 2006; Romano *et al.*, 2013).

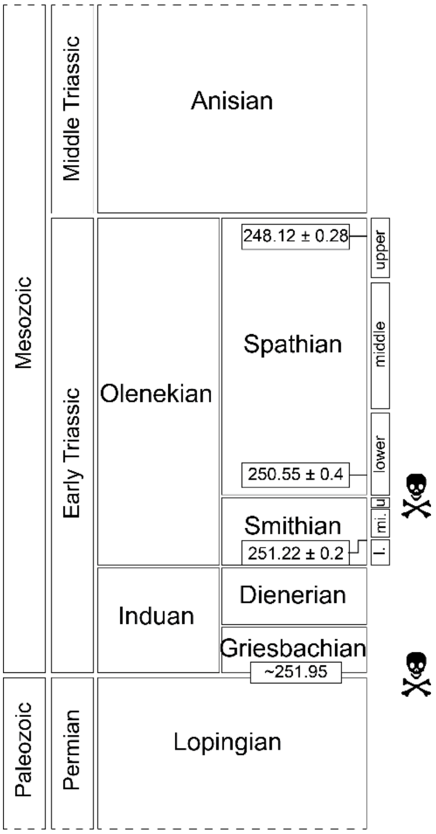

Fig. I.A.1: Simplified chronostratigraphic chart of the Early Triassic. Skulls: major biotic crises. Radiometric ages after Ovtcharova *et al.* (2006), Galfetti *et al.* (2007b) and Baresel *et al.* (2017).

- Global paleogeographic reconstructions of the Early Triassic Earth

During the Early Triassic, the face of our planet was very different from today. Starting in the Permian, convergence and amalgamation of most continental landmasses, along with the closures of the Rheic and Iapetus oceans, lead to the formation of one supercontinent named Pangea (e.g., Murphy & Nance, 2008; Murphy *et* al., 2009; Stampfli *et al.*, 2013). This supercontinent was roughly oriented along a North/South trending axis between both poles of the planet (Fig. I.A.2). It was surrounded by a large ocean called Panthalassa and included an interior Tethyan sea formed during the Permian over the remnants of the lost Rheic ocean on the eastern margin of the Pangea (Fig. I.A.2; Metcalfe, 1994). Some continental arc terranes that were not amalgamated drifted along inaccurate positions in the Panthalassa, as a consequence of the complex interplay of exterior oceanic subductions, such as the Stikinia and Quesnellia terranes off the western margin of Pangea (Fig. I.A.2; Johnston & Borel, 2007; Cocks & Torsvik, 2011; Stampfli *et al.*, 2013).

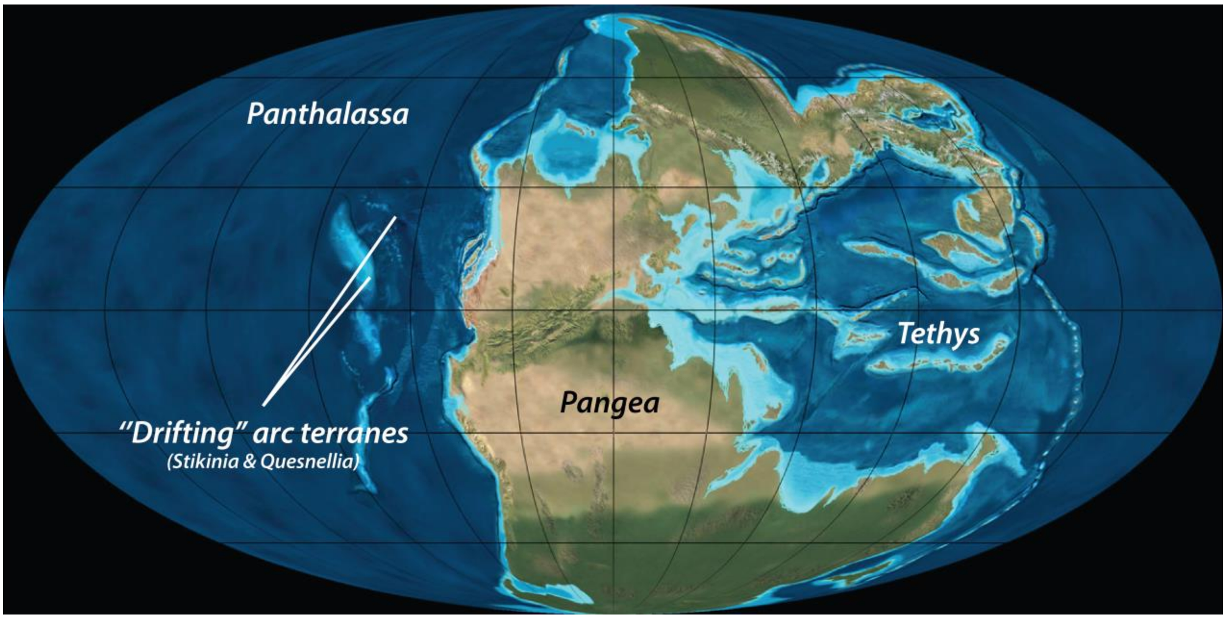

Fig. I.A.2: Paleogeographic reconstruction of the Earth during the Early Triassic (after Blakey, 2013).

This configuration of continental masses had several consequences such as drastic modifications of the oceanic and atmospheric circulations, leading to marked variations in climate during the late Permian-Early Triassic interval (Parrish, 1993; Veevers, 1994; Tabor & Montañez, 2002). These climatic fluctuations were also responsible for important changes in depositional environments both onshore (e.g., Permian equatorial monsoonal activity changes; Tabor & Montañez, 2002) and offshore (e.g., anoxia of the deep ocean and shallow platforms at the PTB and during the Early Triassic; Isozaki, 1997). Moreover, they likely had a strong influence on ecosystems before, during and after the mass extinction event. Large-scale injections of greenhouse gas released from the Siberian traps volcanism at the PTB are a major additional climate forcing at that time leading to increase in pCO_2, acidification of the water column or increase in atmospheric and sea surface temperatures for example (e.g., Galfetti *et al.*, 2007b; Sun *et* al., 2012; Romano *et al.*, 2013).

Geochemical record at the PTB and during its aftermath: a succession of isotopic excursions

Payne *et al.* (2004) were among the first to document the variations of the carbon isotopic record throughout the Early Triassic, and many other studies have followed since then (e.g., Galfetti *et al.*, 2007b; Hermann *et al.*, 2011; Sun *et* al., 2012; Grasby *et al.*, 2013; Romano *et al.*, 2013; Thomazo *et al.*, 2016). They all show some of the largest Phanerozoic carbon isotopic excursions both in the $\delta^{13}C_{carb}$ and $\delta^{13}C_{org}$ signals (Fig. I.A.3.). They were interpreted as variations within the relative size of the inorganic *versus* organic carbon reservoirs and thus, in the carbon cycle evidencing complex environmental perturbations during the post-crisis interval.

Among these excursions, two events marked by shifts in both the carbonate and organic $\delta^{13}C$ records are noticeable: a potential Dienerian/Smithian boundary (DSB) episode, and a conspicuous Smithian/Spathian boundary (SSB) excursion (Fig. I.A.3).

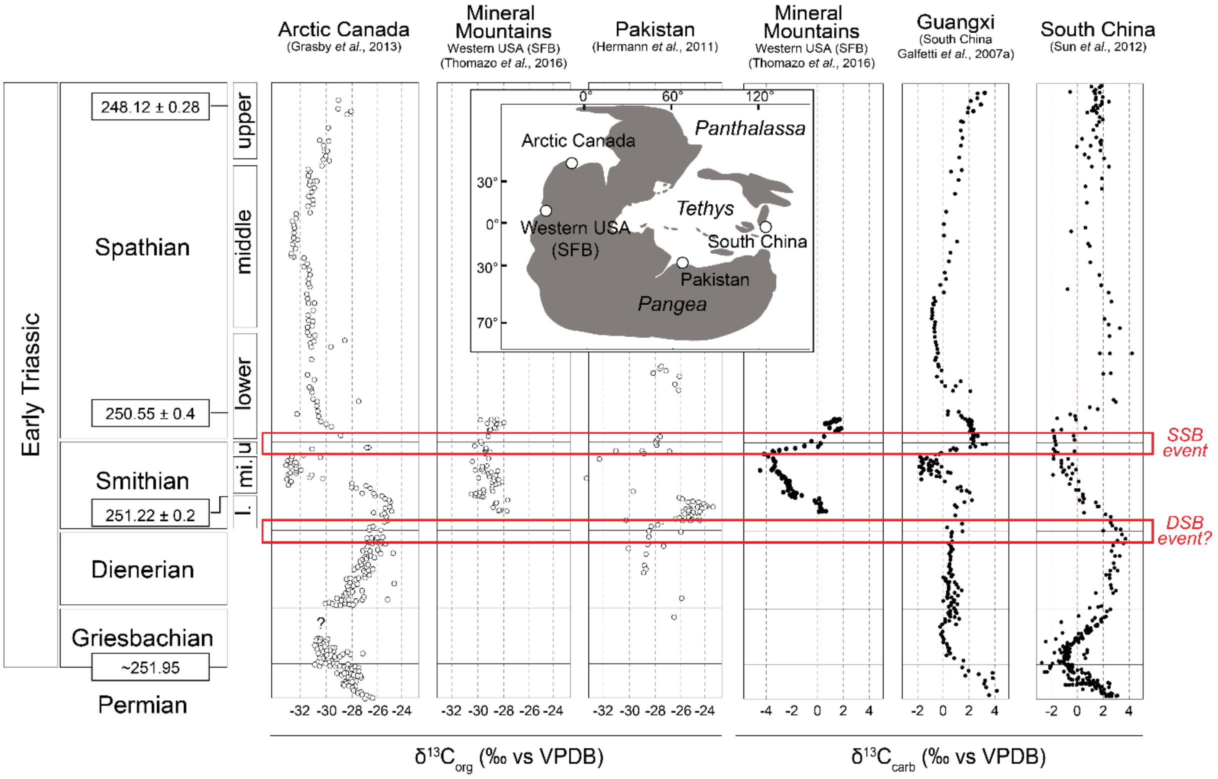

Fig. I.A.3: Worldwide Early Triassic variations of the $\delta^{13}C$ signal on both the organic matter and carbonates. Red boxes highlight the Dienerian/Smithian boundary (DSB) and Smithian/Spathian boundary (SSB) isotopic events. Data after Galfetti *et al.* (2007b), Hermann *et al.* (2011), Sun *et al.* (2012), Grasby *et al.* (2013) and Thomazo *et al.* (2013). l.: lower; mi.: middle; u.: upper.

Around the DSB, a relatively small positive excursion (~2 to 4‰) was identified within some sections such as in Arctic Canada, in Pakistan and in South China (Fig. I.A.3; Payne *et al.*, 2004; Galfetti *et al.*, 2007b; Hermann *et al.*, 2011; Grasby *et al.*, 2013). This excursion is visible on both carbonate and organic matter signals but apparently does not occur in all sections. This questions its global nature vs. local controlled forcing parameters (e.g., Klaebe *et al.*, 2017; Thomazo *et al.*, 2016; Caravaca *et al.*, 2017, section III.A). The relative concomitance of this isotopic shift with changes in ammonoid faunas (Brühwiler et al., 2010) suggests a potential important environmental perturbation at that time.

The second and most important Early Triassic geochemical event is an isotopic couplet of a negative and a positive shifts during the middle Smithian to early Spathian interval. First, a strong negative shift is recorded in the middle Smithian (up to ~-8‰ in the δ^{13}Corg signal of distal shelf deposits from Arctic Canada; Fig. I.A.3). Then, a positive excursion is recorded at the SSB (up to ~6‰ in organic reservoir from Arctic Canada, but also in δ^{13}Ccarb signal from outer ramp deposits from western USA Basin; Fig. I.A.3). These isotopic swings are recorded globally in various settings, in both Panthalassic and Tethyan outcrops and at various latitudes (e.g., Payne *et al.*, 2004; Galfetti *et al.*, 2007b; Hermann *et al.*, 2011; Sun *et al.*, 2012; Grasby *et al.*, 2013; Romano *et al.*, 2013; Thomazo *et al.*, 2016). The absolute magnitude of these excursions varies however form sections to sections and often between the carbonate and organic matter reservoirs of the same section (Fig. I.A.3).

Concomitant biotic changes are observed to these isotopic excursions, such as a marked extinction of ammonoids and conodonts during the late Smithian suggesting severe causal environmental perturbations (e.g., Orchard, 2007; Goudemand *et al.*, 2008; Brayard, 2015). This highlights a strong link between environmental conditions and the tempo and modalities of the post-crisis biotic recovery.

Nevertheless, the timing of these variations in the carbon cycle is yet to be accurately determined, along with the precise nature of the forcing parameters behind these isotopic excursions (e.g., Thomazo *et al.*, 2016). Indeed, origin of these variations has often been linked to the late eruptions of the Siberian traps throughout the Early Triassic (e.g., Galfetti *et al.*, 2007b; Sun *et al.*, 2012; Romano *et al.*, 2013). However, the differences observed between organic and carbonate δ^{13}C signals both at the local and global scales question the importance of local controlling factors on these signals, as recently evidenced by Klaebe *et al*. (2017) or more specifically for the western USA basin by Thomazo *et al.* (2016). The recognition and detailed characterization of such controlling factors acting at various spatio-temporal scales is therefore critical to understand the environmental frame of this period.

- Climate and temperature variations

Early Triassic temperature variations have been recently determined by a few authors (Sun *et al.*, 2012; Romano *et al.*, 2013) using the δ^{18}O signal on conodont phosphate from the Tethys realm (Fig. I.A.4).

These works show important and recurrent variations of the relative temperatures during the Early Triassic, with a global cooling during the Dienerian, and an important warming followed by a cooling during the middle Smithian and at the SSB, respectively (Fig. I.A.4). These changes in temperatures are thought to be a direct consequence of variations in pCO_2 in relation to the abovementioned Siberian large igneous province (LIP) degassing (e.g., Romano *et al.*, 2013). It is worth noting that these abrupt changes in temperatures appear contemporaneous to known isotopic events and biotic changes. However, these temperature fluctuations are presently documented only from the Tethyan realm and need to be confirmed at a more global scale.

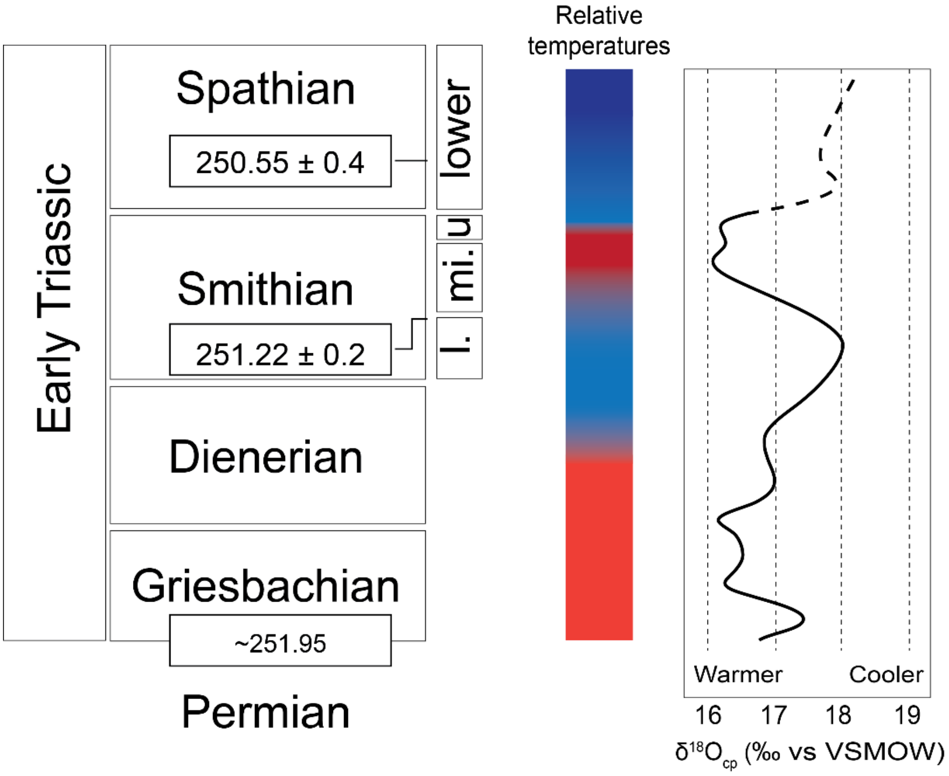

Fig. I.A.4: Simplified relative temperature trend during the Early Triassic obtained using the δ18Ocp signal (obtained from conodont pectiniform elements, after Romano *et al.*, 2013). Several episodes of climatic changes are obvious, notably a cooling phase in the Dienerian and an important warming during the middle Smithian followed by a cooling at the SSB.

These large-scale fluctuations of the global carbon cycle and of temperatures, associated with other events such as marked changes in sedimentary deposits, lead numerous authors to describe the Early Triassic interval as a period of “deleterious” environmental conditions (e.g., Pruss & Bottjer, 2004; Fraiser & Bottjer, 2007; Bottjer *et al.*, 2008; Algeo *et al.*, 2011; Meyer *et al.*, 2011; Bond & Wignall, 2014; Song *et al.*, 2014). Thus, they usually conclude to a strong impact of these harsh conditions over ecosystems during the entire Early Triassic, and especially consider a “delayed biotic recovery” scenario in the aftermath of the end-Permian mass extinction.

B. Focus on the “post-apocalyptic” Early Triassic world

• The Permian/Triassic boundary crisis

At the transition between Paleozoic and Mesozoic eras occurred the most important and severe known mass extinction that impact almost every living groups on both marine and terrestrial realms. For instance, this event resulted in the disappearance of more than 90% of the marine species (Raup, 1979), and the loss of ~50% of continental tetrapod families (Benton & Newell, 2014) and ~30% of insect orders (Labandeira & Sepkoski, 1993).

This mass extinction is also marked by the obliteration of typical Paleozoic organisms such as trilobites, tabulate corals or fusulinid foraminifers (Fig. I.B.1; Sepkoski, 2002). This event was also a trigger for major ecological replacements known as the “Mesozoic Marine Revolution” (Vermeij, 1977). Changes occurring in continental ecosystems lead for example to the replacement of pelycosaurs by therapsids, which will later give birth to modern mammals (Fig. I.B.1; Benton *et al.*, 2004; Cowen, 2013).

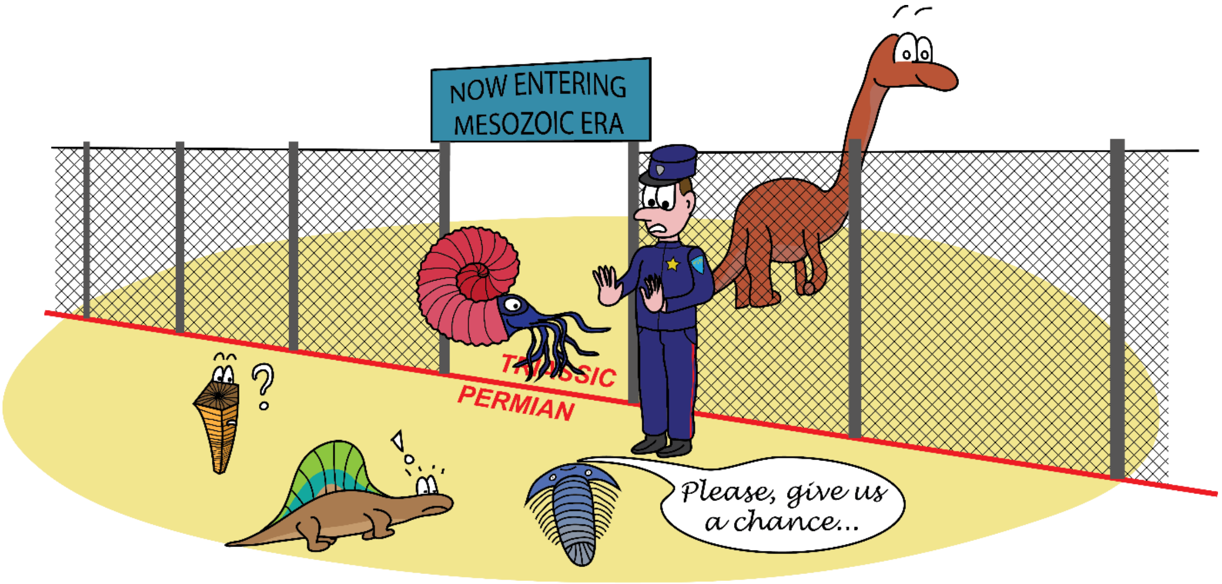

Breaking news: Many groups are refused entry through the Permian/Triassic border...

Fig. I.B.1: Humoristic sketch of the end-Permian mass extinction. Characteristic Paleozoic organisms such as trilobites and tabulate corals disappeared at that time.

While this biological crisis was exceptional given its consequences on ecosystems, its causes are still hardly debated (see e.g. recent reviews by Benton & Twitchett, 2003; Erwin, 2006; Payne & Clapham, 2012). Various and non-exclusive potential causes have been proposed:

- Intermittent or prolonged (up to a few million years long) marine anoxia developing up on the Panthalassa and on Tethyan carbonated platforms (e.g., Isozaki, 1997; Kato *et al*., 2002; Grasby *et al*., 2013; Sun *et al*., 2015);
- Shallow marine euxinia developing up to the photic zone (e.g., Grice et al., 2005; Hays *et al*., 2007);
- Acidification of the water column (e.g., Payne *et al.,* 2010; Clarkson *et al*., 2015);
- Hypercapnia (Knoll *et al*., 2007);
- Reduced atmospheric O2 (e.g., Weidlich *et al*., 2003; Kaiho & Koga, 2013);
- Methane release (e.g., Krull & Retallack, 2000; Krull *et al*., 2000; Majorowicz *et al*., 2014);
- Ozone depletion (Beerling *et al*., 2007; Lamarque *et al*., 2007);
- Global warming (e.g., Sun *et al.*, 2012; Romano et al., 2013, Benton & Newell, 2014);
- Microbial methanogenic bursts (Rohtman *et al*., 2014);
- Poisoning blooms (Wu *et al*., 2014);
- Sudden massive terrestrial influxes (e.g., Algeo & Twitchett, 2010; Algeo *et al*., 2011);
- Seismites & tsunamites (Brookfield *et al*, 2013; Krystyn *et al*., 2014);
- Bolide impact (e.g., Kaiho *et al.*, 2001; Becker *et al*., 2004; Tohver *et al*., 2012, 2013).

The massive volcanic eruptions linked to the Siberian LIP appear as a robust triggering mechanism behind the various environmental perturbations at that time. These result from the huge volume of greenhouse gas and halocarbons directly released into the atmosphere. This influx to the atmosphere has been proposed to reflect both the Earth mantle reservoir, but also the alteration of evaporites and organic-rich sediment during magma ascend through older sedimentary deposits (e.g., Ivanov *et al*., 2009, 2013; Wignall, 2007; Svensen *et al*., 2009; Korte *et al*., 2010; Iacono-Marziano *et al*., 2012; Ogden & Sleep, 2012; Konstantinov *et al*., 2014). Moreover, many of the mechanisms mentioned above can be a (direct) consequence of the Siberian LIP emplacement. These numerous feedbacks have been synthetized by Wignall (2001), Algeo *et al.* (2011) and more recently by Bond & Wignall (2014), and are illustrated in the Figure I.B.2.

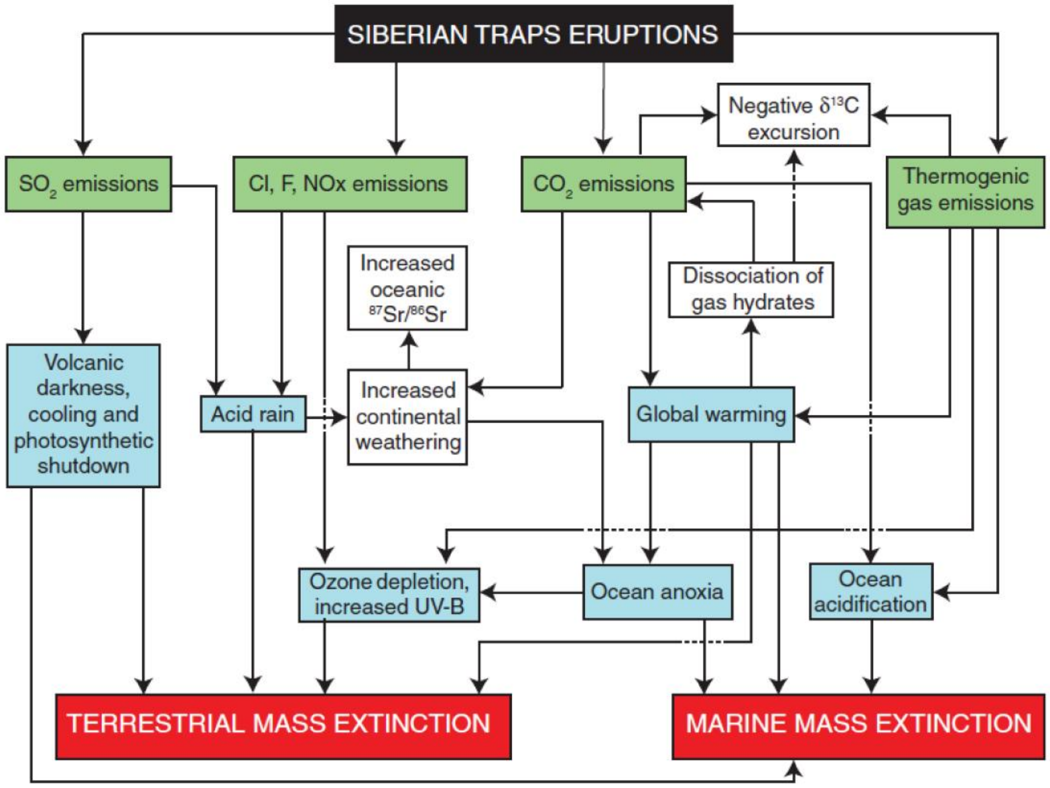

Fig. I.B.2: Synthetic flow chart summarizing some of the proposed cause-and-effect relationships during the end-Permian mass extinction and the Early Triassic “delayed” recovery. This chart highlights a major role of the Siberian LIP episode over environmental perturbations (after Bond & Wignall, 2014).

The Siberian LIP episode was not strictly restricted to the PTB (*sensu stricto*) and given the kinetics of the referred mechanisms, the entire Early Triassic is probably influenced by this episode as well (e.g., Payne *et al.*, 2004; Payne & Kump, 2007; Romano *et al.*, 2013; Bond & Wignall, 2014).

- Common paradigms associated to the “delayed recovery”

The Early Triassic is usually portrayed as a “post-apocalyptic” world from both an environmental and biotic points of view. That is, “deleterious” conditions are thought to prevail until at least the Middle Triassic, meanwhile the recovery of ecosystems after this crisis is usually assumed to span at least the entire Early Triassic if not more (e.g., Twitchett, 1999; Fraiser & Bottjer, 2007; Meyer *et al.*, 2011; Chen & Benton, 2012).

Associated to this ecocide scenario, other paradigms have been commonly assumed based on the fossil record and unusual sedimentary deposits found in Early Triassic exposures worldwide: presence of “disaster taxa” and “anachronistic facies”, “Lilliput effect”, “chert gap”, “coal gap” and finally “anoxia/euxinia” and “superanoxic ocean” (Fig. I.B.3). Early Triassic communities are generally described as poorly diversified, with abundant opportunistic and generalist organisms. Noteworthy, some of the Early Triassic paradigms have been first proposed on the basis of data from the western USA Basin, and then extrapolated to a global scale (e.g., Schubert & Bottjer, 1992; Fraiser & Bottjer, 2004; Pruss & Bottjer, 2004). Divergent observations from these paradigms such as highly diversified faunas in the Griesbachian are often assumed to be local exceptions representing refugia in a globally unhospitable marine realm (e.g., Beatty *et al.*, 2008; Zonneveld *et al.*, 2010).

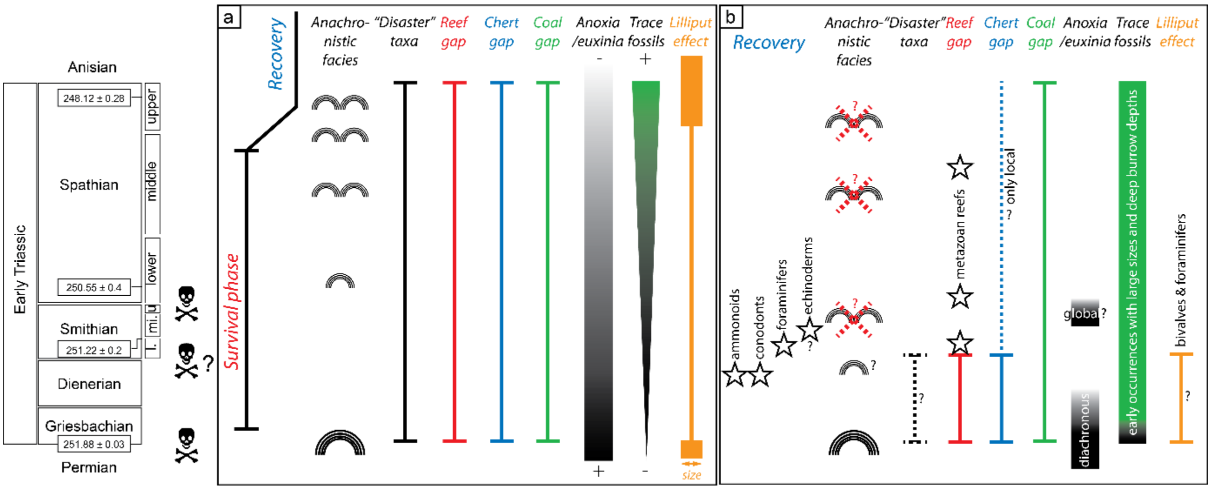

Fig. I.B.3: a) Synthetic representation of the main paradigms usually accepted concerning the Early Triassic recovery. b) Synthetic representation of these paradigms revised with recent data from the western USA basin (after Brayard, 2015).

Main Early Triassic paradigms represented in Figure I.B.3 are:

- "Disaster taxa": Early Triassic ecosystems are often described to be mainly composed of opportunistic and generalist organisms, such as Claraia for bivalves or Lingula for brachiopods, and by microbial communities in the marine realm. They are thought to have proliferated because of the potential absence of competition in their respective ecological niches, but also given to their abilities to adapt to various extreme environemental conditions (e.g.; Schubert & Bottjer, 1992, 1995; Rodland & Bottjer, 2001; He *et al.*, 2007);
- "Anachronistic facies" and "reef gap": reef-building metazoan associations are thought to have been replaced by microbial deposits. These microbial-dominated facies and bioconstructions are called "anachronistic facies" due to their resemblance with e.g. some Precambrian facies composed exclusively by microorganisms (e.g., Schubert & Bottjer, 1992; Woods *et al.*, 1999; Pruss & Bottjer, 2005; Pruss *et al.*, 2005; Woods, 2009). The absence of metazoan reefs (made by corals or sponges for example) is often cited as an evidence for the delayed recovery scenario, their reappearance during the Middle Triassic serving as a marker for the end of the "protracted" recovery (e.g., Flügel, 2002; Payne *et al.*, 2006);
- "Lilliput effect": many of the surviving organisms found in Early Triassic series are often considered to have undergone a drastic body-size reduction, and notably the benthic organisms (e.g., Urbanek, 1993; Hautmann & Nützel, 2005; Payne,

2005; Twitchett, 2007; Fraiser *et al*., 2011; Metcalfe *et al*., 2011; Song *et al*., 2011);

- “Chert gap”: by comparison with the Permian, Early Triassic sediments show rare siliceous deposits (e.g., Beauchamp & Baud, 2002; Sperling & Ingle, 2006).
- “Coal gap”; no coal or peat-forming plant deposits have been reported so far from the Early Triassic (Veevers *et al*., 1994, Retallack *et al*., 1996);
- “Anoxia/euxinia” and “Superanoxic ocean”: several authors interpreted the Early Triassic to be marked by continuous or recurrent anoxic/euxinic events at a global scale (e.g., Isozaki, 1997; Meyer *et al*., 2011; Song *et al*., 2012; Grasby *et al*., 2013). The absence of trace fossil, or their low diversity when present within this interval, is usually interpreted as a consequence of low O2 concentrations in the bottom waters. (e.g., Twitchett & Wignall, 1996).

Many studies challenged the “delayed recovery” scenario and associated paradigms in the last years. Recent advances on this issue were notably made within the western USA Basin.

• Evidence for an alternative scenario

Contrary to the “delayed recovery” scenario, several studies have shown an “explosive” rediversification during the Early Triassic for nekto-pelagic groups such as conodonts (Orchard, 2007) or ammonoids (e.g., Brayard *et al.*, 2009). The latter are a striking example for a rapid recovery: they almost disappeared during the PTB crisis, but reached a high richness level during the Smithian, less than ~1.5 Myr after the PTB (e.g., Brayard *et al.*, 2009; Brühwiler *et al.*, 2010; Brayard & Bucher, 2015; Brayard, 2015). Recovery of some benthic communities seems also to have been rapid e.g. for foraminifers (Payne *et al.*, 2011; Song *et al.*, 2011), bivalves and gastropods (Kaim *et al.*, 2010; Hautmann *et al.*, 2011; Hofmann *et al.*, 2014) or trace fossil makers (e.g., Hofmann *et al.*, 2011). However, trends observed on benthic faunas are still hardly debated and remain relatively fuzzy.

“Anachronistic facies” were interpreted to result from the harsh environmental conditions prevailing during the Early Triassic (e.g., Schubert & Bottjer, 1992; Woods *et al.*, 1999; Pruss & Bottjer, 2005; Pruss *et al.*, 2005; Mary & Woods, 2008; Woods, 2009). However, recent studies in the western USA basin documented a laterally heterogeneous and diachroneous depositional pattern for these microbial deposits (Figs. I.B.4a and I.B.4b; e.g.; Olivier *et al.*, 2014, 2016, see appendix 1; Vennin *et al.*, 2015). This therefore challenges common interpretations of these microbial deposits as corresponding to peculiar deleterious environmental conditions.

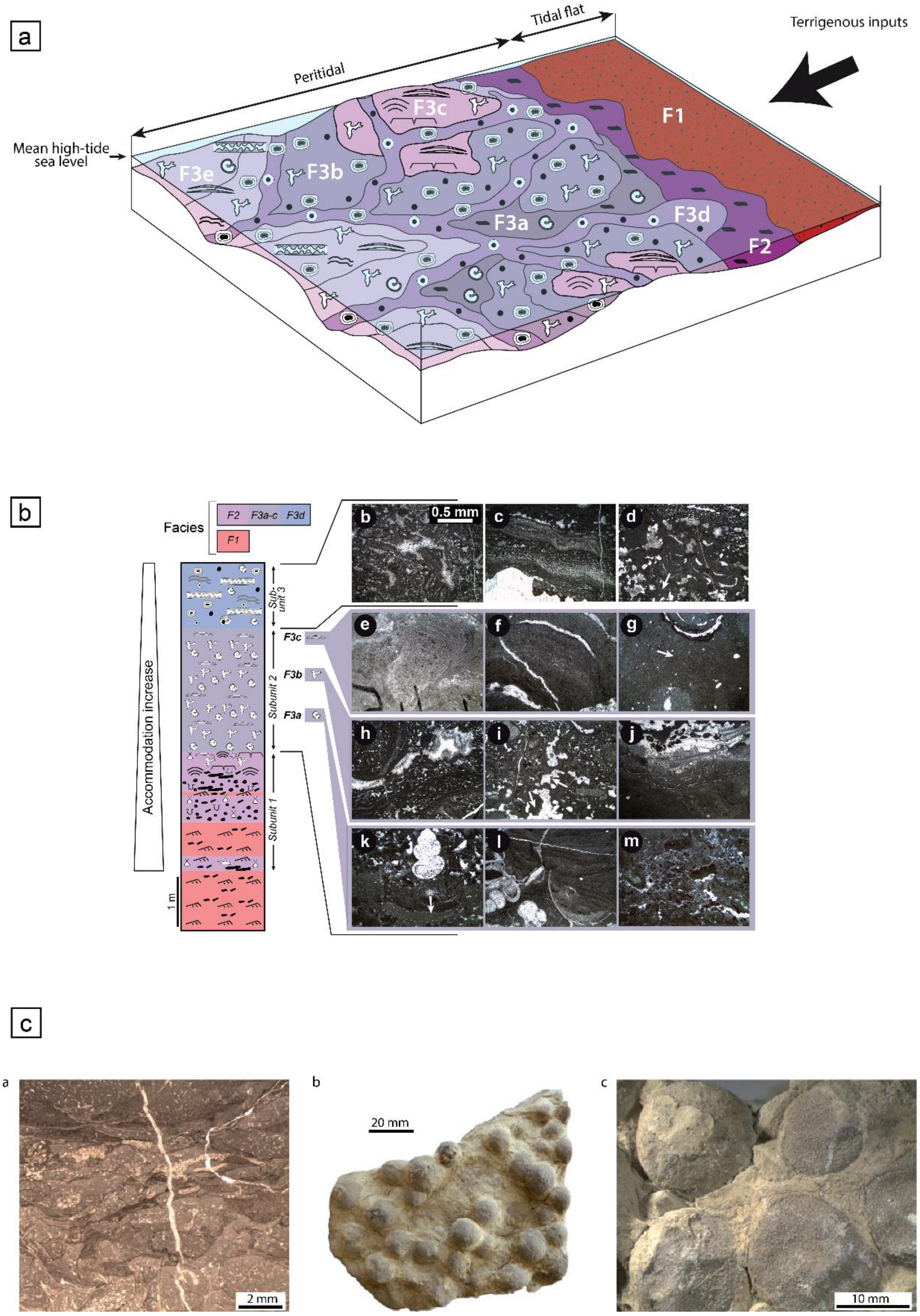

Fig. I.B.4: a) Example of a depositional setting in the Torrey area (western USA basin, after Olivier et al., 2016, see appendix 1) showing laterally heterogenous and diachroneous presence of microbial communities during the middle Smithian (facies F2 and F3). The model highlights the contemporaneity of the microbial deposits with diverse benthic metazoan organisms b) Schematic evolution of the main microbial limestones facies in the same locality (western USA basin, after Olivier *et al*., 2016, see appendix 1) showing associations of microbial deposits with metazoan faunas, as well as the various types of microbial communities. See Olivier *et al.* (2016, see appendix 1) for details. c) Illustration of Smithian sponge-dominated metazoan associations as reef-builders in southwestern Utah (after Brayard *et al*., 2011)

Moreover, diversified microbial deposits were found in association with diversified metazoan faunas (Figure I.B.4; Olivier *et al.*, 2014, 2016, see appendix 1; Vennin *et al.*, 2015) in the western USA basin, questioning the pertinence of the notion of “anachronistic facies” as such deposits are supposed to lack of metazoan inhabitants. The western USA basin notably revealed that *in situ* metazoan reef-building communities also existed. Various inhabitants such as sponges (Fig. I.B.4c), serpulids, bivalves, gastropods, cephalopods, echinoderms, ostracods, conodonts or foraminifers testimony for complex and diversified ecosystems (e.g., Brayard *et al.*, 2011; Olivier *et al.*, 2014, 2016, see appendix 1; Brayard, 2015; Vennin *et al.*, 2015). Earliest metazoan reefs are reported from the early Smithian and persisted through the Spathian (e.g., Brayard, 2015), shortening the “exclusively microbial” interval (e.g., Flügel, 2002) and restricting it only to the earliest Triassic (Kershaw *et al.*, 2007, 2009).

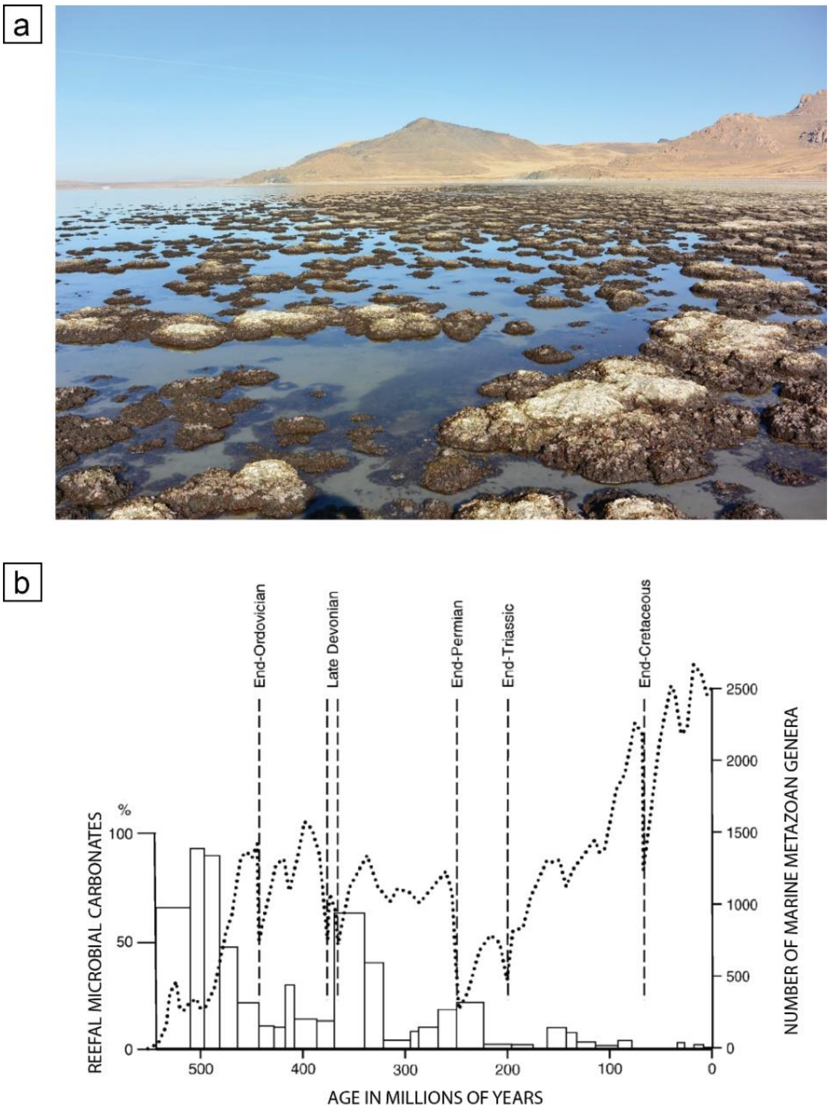

Fig. I.B.5: a) Photograph of the modern reef-building microbialites in the Great Salk Lake (Utah, USA; courtesy of Dr. Anthony Bouton). b) Relative abundance of microbial carbonates in reefs during the Phanerozoic compared to the marine metazoan generic diversity (after Riding, 2006). This chart shows that microbial carbonates may be present in the aftermath of some mass extinctions (e.g., Late Ordovician or end-Permian), but not all, and when present, they do not always show an increase in proportion.

In addition, modern examples of well-developed microbial-dominated deposits associated with metazoan organisms can be currently found in various environments including but not restricted to lagoons in Polynesia (Sprachta *et al.*, 2001), the warm water of the Bahamas (e.g., Dupraz *et al.*, 2004; Myshrall *et al.*, 2010), the hypersaline lakes of the Great Salt Lake (USA, Fig. I.B.5a; e.g., Bouton *et al.*, 2016), or the alkaline Satonda Crater Lake in Indonesia (Arp *et al.*, 2003). The environmental significance of the Early Triassic microbial deposits and the controlling factors behind their presence thus remains an open question (e.g., Vennin *et al.*, 2015 and Olivier *et al.*, 2016, see appendix 1, for the western USA basin). However, deciphering interactions between microbial deposits and their environments is therefore crucial to understand the Early Triassic recovery dynamics.

Finally, microbial deposits are not always characteristic of deleterious and/or post-crisis environments as commonly previously thought (e.g., Flügel, 2002; Riding, 2006). Reef-building microbial systems have been present throughout most of the Phanerozoic, either associated or not with metazoan organisms (e.g., Riding., 2006). Figure I.B.5b shows their development may follow mass extinction events (e.g., Late Ordovician or end-Permian), but this is not always true.

The absence or rarity of trace fossils has been used to argue for anoxic/euxinic conditions in the marine realm (e.g., Twitchett & Wignall, 1996). However, recent findings have demonstrated the increasing presence of trace fossils and deep burrows within Early Triassic series (e.g., Beatty *et al*., 2008; Chen *et al*., 2012; Olivier *et al*., 2014). Some authors nevertheless consider these unusual trace concentrations as corresponding to refugia zones (e.g., Beatty *et al*., 2008; Zonneveld *et al*., 2010). Recent studies in the western USA basin show the presence of important networks of centimetric-diameter burrows within Smithian series (Fig. I.B.6a; Olivier *et al*. 2014, 2016, see appendix 1). These observations hint toward a sustained infaunal activity. They are also associated with diversified bioclastic levels in adjacent beds, questioning the deleterious environmental conditions attributed to the water column.

Finally, another commonly accepted paradigm, the “Lilliput effect”, that has been also suggested for some other post-crisis intervals (e.g., Late Ordovician crisis; Huang *et al*., 2010), was recently questioned owing to fossils from the western USA basin. Brayard *et al*. (2010, 2015) showed that gastropod assemblages were not “unusually small” (Fraiser & Bottjer, 2004) when compared to Permian, later Mesozoic or modern gastropod assemblages. Additionally, the presence of numerous pluri-centimetric large gastropod specimens named “Gulliver” (Fig. I.B.5c) does not support a “Lilliput effect” for this clade, which probably results from a marked bias in sampling intensity (Brayard *et al*., 2015).

A highly diversified marine ecosystem was also recently found in early Spathian strata of the western USA basin (Brayard *et al*., 2017). Abundant remains of various and sometimes unexpected groups have been unearthed in southern Idaho. Benthic organisms exhibiting an exceptional preservation, such as crustaceans or echinoderms (crinoids, ophiuroids), were sampled (Fig. I.B.6c). Nekto-pelagic organisms were also present and diversified: for instance, sharks, bony fishes and ammonoids. Ichthyosaur remains were also reported from coeval neighboring localities (e.g., Massare & Callaway, 1994; Romano *et al*., 2012; Brayard *et al*., 2017). These findings point toward a rapid recovery and rediversification for these groups after the PTB, at least in this basin, and show that complex ecosystems – from primary producers to predators – were already developed at that time (e.g., Brayard *et al*., 2017).

All these evidence from the western USA basin do not support commonly accepted Early Triassic paradigms, as well as several other data from various locations worldwide (e.g., Wheeley & Twitchett, 2005; Beatty *et al*, 2008; Hautmann *et al.*, 2011, Hofmann *et al.*, 2011). It therefore clearly appears these paradigms needed to be reevaluated and revised as to propose a new and more accurate interpretation of the Early Triassic “fast and diverse” biotic recovery, as illustrated in Figure I.B.3b.

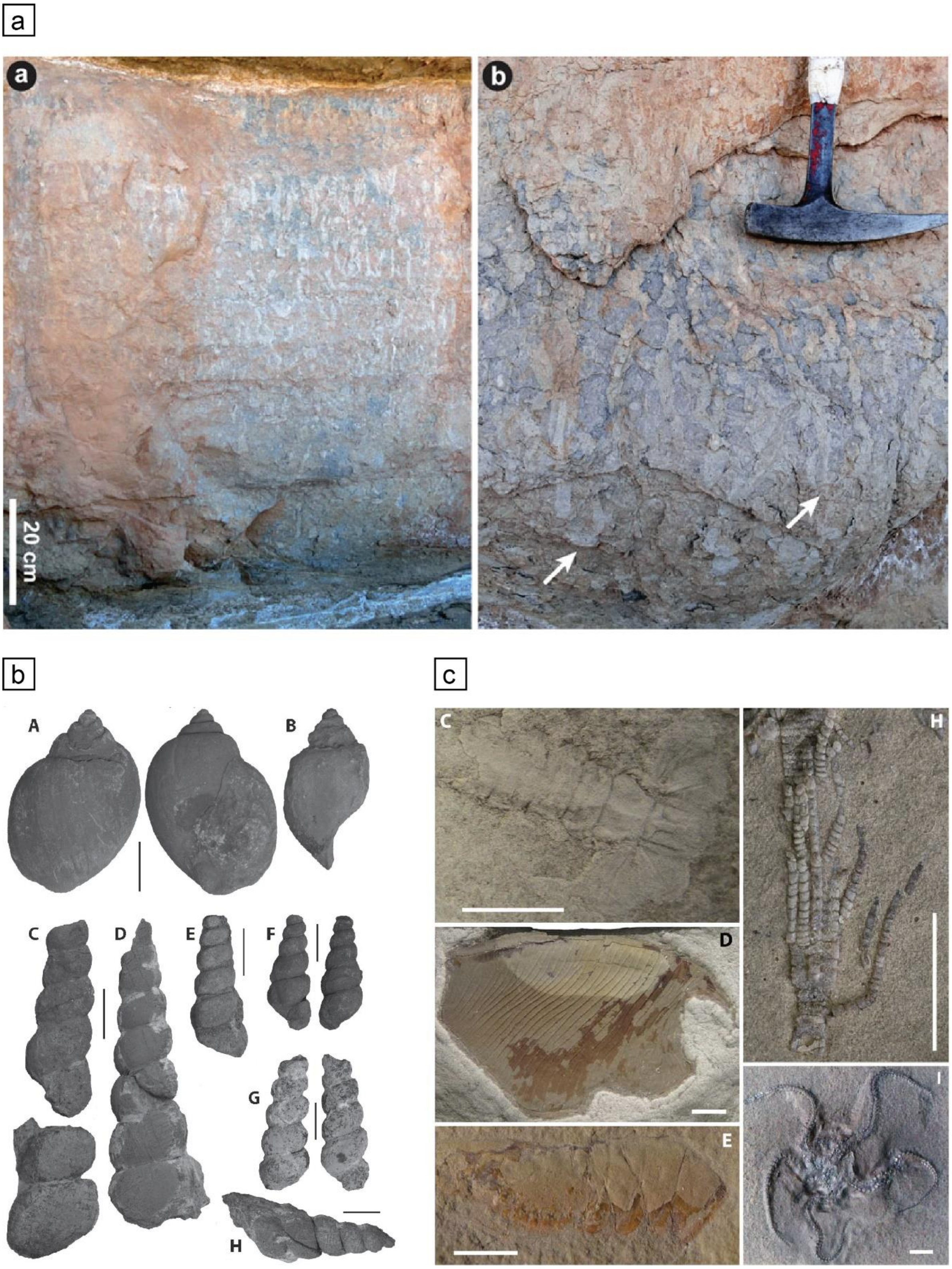

Fig. I.B.6: Various (ichno-)fossils recently found in the western USA basin highlighting the diversity of Early Triassic ecosystems of this area. a) Large burrows (centimetric-diameter) in carbonated beds of the Timpoweap Canyon (southwestern Utah, USA; after Olivier *et al.*, 2014). b) Some large-sized specimens (pluri-centimetric) of Smithian gastropods from southwestern Utah (after Brayard *et al.*, 2010). Scale bars are 10 mm. c) Illustration of various and well-preserved specimens from the "Paris biota" (southeastern Idaho, after Brayard *et al.*, 2017), which shows a highly diversified early Spathian ecosystem. Scale bars are 10mm.

C. Methodology of the integrated approach

The originality of this work is based on an integrative and multi-scale study of the western USA basin, using regional, local, macro- and microscopical data (Fig. I.C.1) analyzed through a large panel of methods and techniques. **The aim of this integrated study is to understand the dynamics of the basin as a whole.**

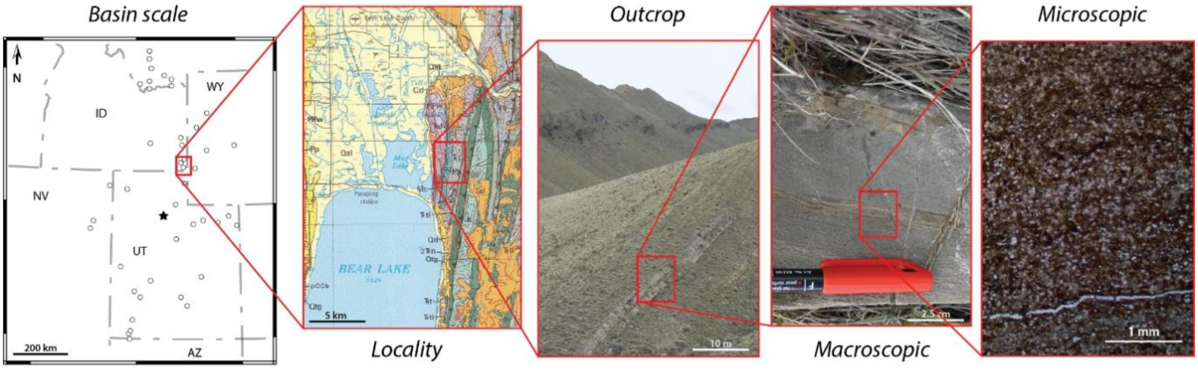

Figure I.C.1: Illustration of the multi-scale character of the study, from basin-scale to microfacies analysis (location map after Caravaca *et al.*, *in press*, see section IV; geological map after Oriel & Platt, 1980).

To achieve this goal, new original data have been collected throughout the basin by our research team (Fig. I.C.2), and were investigated using a wide-range of disciplinary fields including sedimentology, paleontology, geochemistry, tectonics and structural geology. The consequent spatialization of the geological information provides answers to questions raised by empiric observations of the Early Triassic record within the western USA basin (see section II.B).

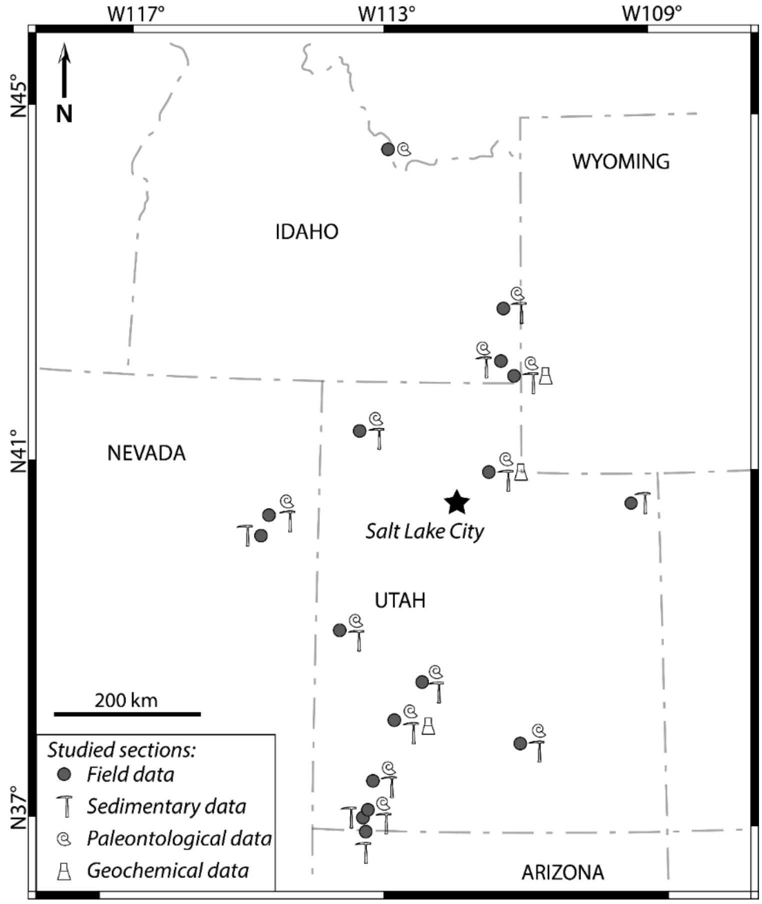

Figure I.C.2: Map of the study area showing location of sampled sections used in this work.

The Table I.C.1 lists the various approaches used in this work and their purpose/application in the reconstruction of the basin and its paleoenvironments. Detailed and complete descriptions of techniques as well as their aim and limitations are embedded in the corpus of the enclosed published articles (see Caravaca *et al.*, 2017, *in press*, section III.A and IV).

basin-scale study of the SFB.

Disciplinary field	Techniques/methods	Use/aim	Scale
Sedimentology	Fieldwork	Sample collecting/logging	Outcrop to locality
	Geological mapping of formations and groups	Paleogeographic reconstructions	Locality to basin
	Macro-/Microfacies analysis	Depositional setting reconstructions	Outcrop to basin
		Lithostratigraphic correlations	Locality to basin
	Backstripping	Determination of sedimentation rates	Outcrop to basin
Geochemistry	Paired carbon isotopes	Chemostratigraphic correlations	Locality to global
		Determination of variations in carbon reservoir	Outcrop to basin
	Trace & Major element concentrations	Determination of redox state of the water-column	Outcrop to basin
		Determination of paleoproductivity in the water-column	Outcrop to basin
		Estimation of the terrigenous influx	Outcrop to basin
	Carbonate content (wt. %)	Estimation of the carbonate factory	Outcrop to basin
Paleontology	Fossil sampling/identification	Biostratigraphy (dating and correlations)	Locality to global
		Paleoenvironment reconstructions	Outcrop to basin
	Ichnofossil identification	Paleoenvironment reconstructions	Outcrop to basin
Structural Geology/Tectonics	Geophysical data interpretations (airmag/gravity anomaly maps)	Lithospheric mapping	Basin
		Determination of lithospheric composition and weaknesses	Basin
	Geological mapping and regional cross-sections	Palinspastic reconstructions (paleogeography)	Locality to basin
	Flexural modeling	Determination of rheological behavior of the lithosphere	Basin
Data integration and spatialization	Geographic Information System (Global Mapper software)	Paleogeographic mapping	Locality to basin
		Palinspastic reconstructions	Locality to basin
		Database	Outcrop to basin

Table I.C.1: Synthetic list of the various disciplinary fields, techniques and methods used in this integrated

Recent evidence therefore gives a picture of Early Triassic organisms more diversified and resilient than previously thought, at least in the western USA basin. The various and often diversified ecosystems (e.g., Brayard et al.*, 2017), microbial communities (Vennin* et al.*, 2015), and laterally evolving depositional settings (e.g., Kummel, 1954, 1957; Goodspeed & Lucas, 2007; Olivier* et al.*, 2014, 2016, see appendix 1) found in this basin make it a key area to decipher regional patterns and processes underlying the biotic recovery.*

Our research team has documented an excellent fossil and sedimentary record in the western USA Basin during the past years. However, these gathered data also exhibit conspicuous differences within the basin, especially between its southern and northern parts. For instance, differences in fossil assemblages and in nature and characteristics of the sedimentary formations have been pointed out (e.g., Brayard et al.*, 2013; Jattiot* et al.*,* in press*). This possible segregation of the western USA basin into two sub-basins was rarely documented nor discussed before. Additionally, it raises the question of a potential effect of the local/regional environmental conditions on the observed recovery tempo and on the emergence of unexpected complex ecosystems in this basin.*

In order to answer these new issues and seek out the controlling mechanisms at the basin scale underlying the formation and evolution of environments, an integrated study is needed including e.g. paleontology, sedimentology and geochemistry. To achieve this goal, several fields were investigated starting with the structural and tectono-sedimentary history of the region and the characterization of its heritage. Then, a comprehensive synthesis of the regional sedimentary record was made to describe and decipher the spatio-temporal variations of the depositional settings. Additionally, the geochemical record of the basin was surveyed to identify potential parameters of the water column and the sediment/bottom waters interface. Finally, the first order mechanisms controlling the spatio-temporal development and evolution of the entire western USA Basin were investigated.

II. THE WESTERN USA SONOMA FORELAND BASIN

Based on the different available works on the western USA Basin, and recent publications from our research team, the western USA appear as an appropriate place to study the Early Triassic biotic recovery and to decipher the potential underlying mechanisms (e.g., Brayard *et al*., 2013, 2017; Olivier *et al*., 2014, 2016, see appendix 1; Vennin *et al*., 2015; Thomazo *et al*., 2016; see section I.B). Nevertheless, a detailed environmental and paleogeographic framework for this basin during the Early Triassic interval is still missing.

A brief review of previous works on the tectonic structuring of this basin is therefore necessary to determine the different lacks in our understanding of the regional paleoenvironment distribution at that time.

A. A brief overview of a 2Ga-long history: a geodynamically active region

- Location and extent of the western USA basin

The western USA Basin (as understood in this work) corresponds to the eastern part of the Great Basin, a depressed, mostly desertic and endorheic area ranging from the Colorado Plateau and Wasatch (Rocky) Mountains in eastern Utah, to the Sierra Nevada mountains in western California. Its northern part is bounded by the Columbia volcanic Plateaus in Oregon and Snake River Plain in Idaho. Most part of the Great Basin lies today as an extensional domain most commonly known as the Basin & Range Province (Fig. II.A.1; e.g., Dickinson 2004, 2006, 2013).

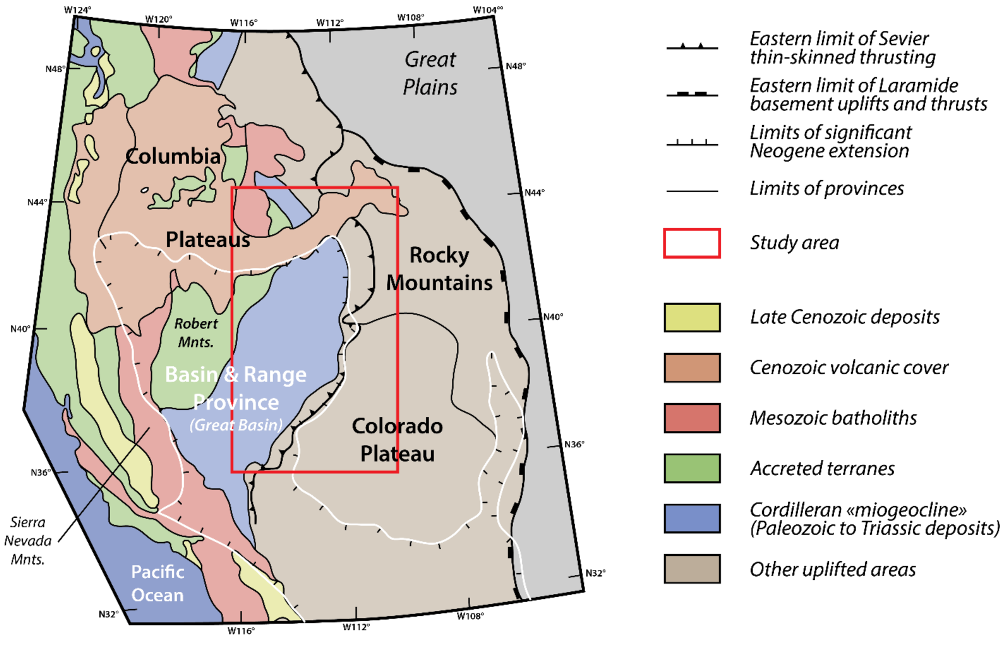

Figure II.A.1: Simplified tectonic map of the western USA showing the present-day configuration of the lithospheric basement and the main geodynamical structures (modified after Jones, 2013). The red box highlights the location of the studied area in this work.

The studied area, referred to as the western USA Basin, roughly corresponds to a 1000 x 600 km vertical rectangle encompassing Utah, southeastern Idaho, and parts of eastern Nevada and western Wyoming (Fig. II.A.2). This basin displays a ~2 Gyr-long and complex geodynamic history since the Proterozoic, which is still active today. This evolution is notably marked by a succession of various orogenies, basin formations, volcanic events, or accretion of lithospheric terranes (Fig. II.A.3; e.g.; Blakey, 2008; Ingersoll, 2008; Dickinson, 2013).

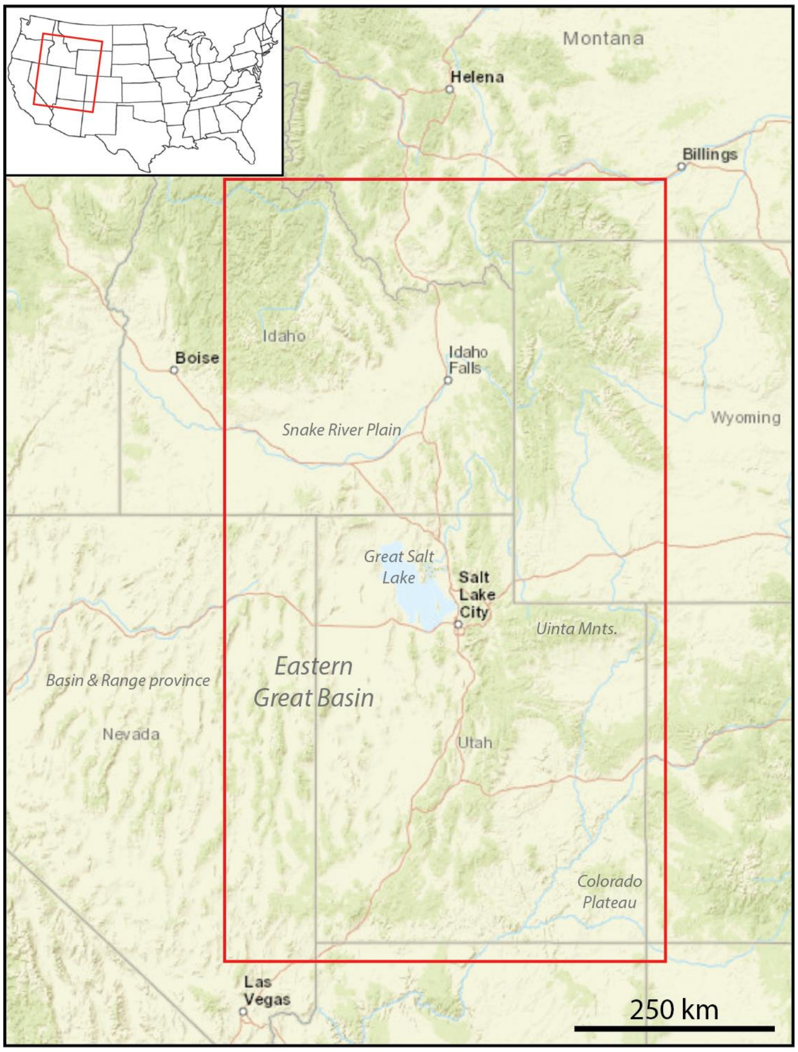

Figure II.A.2: Topographic map of the studied area (base map World Street Map ©ESRI).

These different tectono-sedimentary episodes contributed to the formation of a "mosaic" of terrains in this region (Fig. II.A.1), highlighting the various origin and nature of the basement in the western USA Basin and its surroundings. If an important Phanerozoic sedimentary cover is present within the entire basin (e.g., Dickinson, 2006, 2013), the accretion of exotic terranes and the successive orogenies were the source of important compressional as well as extensional deformations that markedly modified this cover (e.g., displacement, erosion, deformation). Consequently, paleogeographic reconstructions of this area can be somewhat “blurred” and difficult to define.

Additionally, inherited structures due to this active geodynamic frame had a direct impact on sedimentary patterns encountered in this region (e.g., Peterson, 1977 for the Paleozoic) and/or on the controlling factors behind them, therefore highlighting the need to decipher the successive events that occurred within this area.

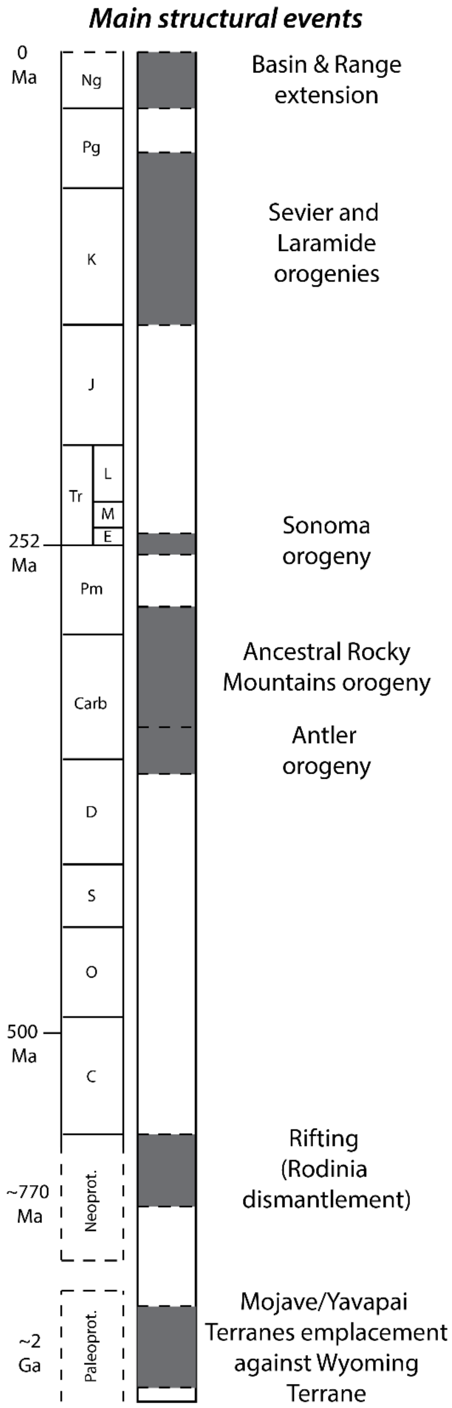

Figure II.A.3: Simplified chronostratigraphy of the successive structuring events in the western USA Basin since the Paleoproterozoic (after Oldow *et al.*, 1989; Whitmeyer & Karlstrom, 2007; Dickinson, 2013).

History of the western USA Basin since the Proterozoic

The successive geodynamic events underwent by the western USA Basin mainly result from the formation and interplay of the different lithospheric terranes constituting its basement (e.g., Whitmeyer & Karlstrom, 2007; Lund *et al.*, 2015), indicating a major role of the heritage in the structural processes that shaped the basin through time. This section lists the main structural events in this region since the Proterozoic, with a focus on those that occurred before the Early Triassic and may have had a strong influence on the development and evolution of the basin during this interval. Contrary to some of previous references (e.g., Dickinson, 2013), simplified tectonic maps illustrated in Figures II.A.4 to II.A.13 do not present palinspastically restored state borders to facilitate the intuitive understanding of the position of the different structural features relative to the modern geography.

Paleoproterozoic formation of the basement

The first structuring of the western USA Basin dates back to Paleoproterozoic times and took place ~2 Ga for the oldest. Supposedly during the Neoarchean to Paleoproterozoic interval, the Grouse Creek Block was indirectly emplaced against the Wyoming craton (Whitmeyer & Karlstrom, 2007; Fig. II.A.4). Lying between these two blocks is the Farmington terrane, a mobile belt made of reworked Archean crust (Fig. II.A.4; Yonkee & Weil, 2015; Lund *et al.*, 2015). Its formation most probably results from the emplacement of the two Archean blocks.

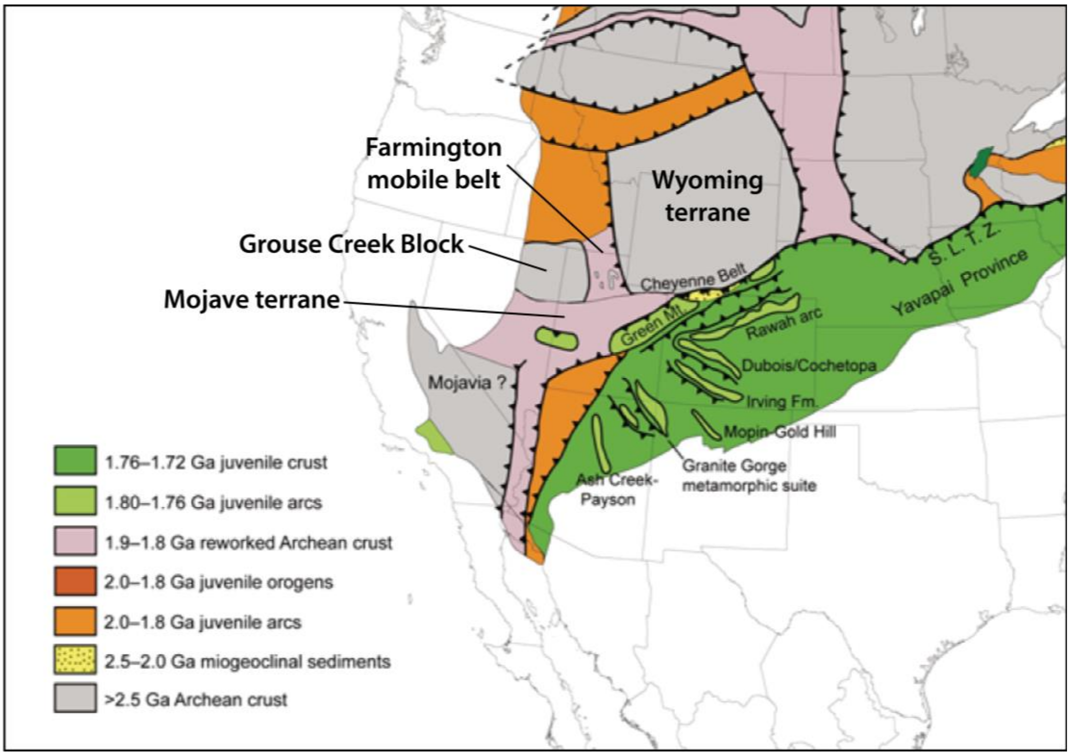

Figure II.A.4: Map of lithospheric terranes of the western USA during emplacement of the Paleoproterozoic Mojave and Yavapai terranes against the Archean Grouse Creek Block and Wyoming Terrane (after Whitmeyer & Karlstrom, 2007).

Then, Paleoproterozoic Mojave and associated Yavapai terranes were formed and emplaced against the Archean Wyoming craton and Grouse Creek Block terranes (Figs. II.A.3 and II.A.4; Whitmeyer & Karlstrom, 2007; Lund *et al.*, 2015). This event generated multiple lithospheric fault zones along which later reactivations were possible during deformational episodes (Oldow *et al.*, 1989; Dickerson, 2003).

Additionally, during following Mesoproterozoic times, at least one intense episode of metamorphism took place in the Farmington terrane, as shown by metamorphism ages of about ~1.64 Ma (Mueller *et al.*, 2011).

All these old structuring events are of paramount importance in the geodynamical history of the basin. Indeed, tectonic constraints and/or metamorphism underwent by the basement left a lasting heritage in the form of lithospheric faults or weaknesses (e.g., Chardon *et al.*, 2009; Cagnard *et al.*, 2011), which were reactivated during following tectonic events (such as orogenies). This heritage is assumed to have played a role in the development and evolution of the western USA sedimentary basins (e.g., Paulsen & Marshak, 1999).

- *Rodinia fragmentation and formation of a passive margin*

The tectono-sedimentary history during the subsequent Proterozoic times remains poorly known due to the lack of sedimentary remnants of these periods. However, it is assumed that at least two rifting events took place in the North American/Laurentian craton during this period: a first one during the Mesoproterozoic and the second during the Neoproterozoic (~770 Ma; Fig. II.A.3). These events are most probably linked to the fragmentation of the supercontinent Rodinia (Burchfiel & Davis, 1975; Oldow *et al.*, 1989; Dickinson, 2006; Yonkee & Weil, 2010).

A passive margin thus formed on the edge of the Laurentian continental plate along the Wasatch hinge line (Fig. II.A.5; Burchfiel & Davies, 1975, Dickinson, 2006). At that time, open-marine conditions and a sedimentation showing a deepening trend toward the West developed upon this westward thinning crust, thanks to the post-rift thermal subsidence and then, sedimentary loading.

The long period of tectonic quiescence following the formation of this passive margin lasted until the Late Devonian (~380 Ma; Fig. II.A.2) and corresponds to the deposition of a thick sedimentary prism on the West, formerly known as the “Cordilleran Miogeocline” and upon which younger series lies unconformably (Fig. II.A.5b; Clark, 1957; Paull & Paull, 1991; Dickinson, 2006, 2013).

- *The Antler orogeny*

Starting in the Late Devonian and until the late early Carboniferous, the Antler orogeny marks the beginning of a period of nearly continuous structural events that are still acting today (Fig. II.A.3).

The Antler orogeny was caused by the convergence and accretion of exotic island-arcs against the western margin of the Laurentian craton (Figs. II.A.6a and II.A.6b) during the late Devonian and continued during the Mississippian with the onset of subduction and obduction processes until the early Pennsylvanian (Burchfiel & Davies, 1975; Speed & Sleep, 1982; Oldow *et al.*, 1989; Smith *et al.*, 1993; Dickinson, 2004, 2006, 2013). The Antler orogeny mainly took place in Central Nevada, but also influenced a region extending from Idaho to California and to Utah eastward (Fig. II.A.6).

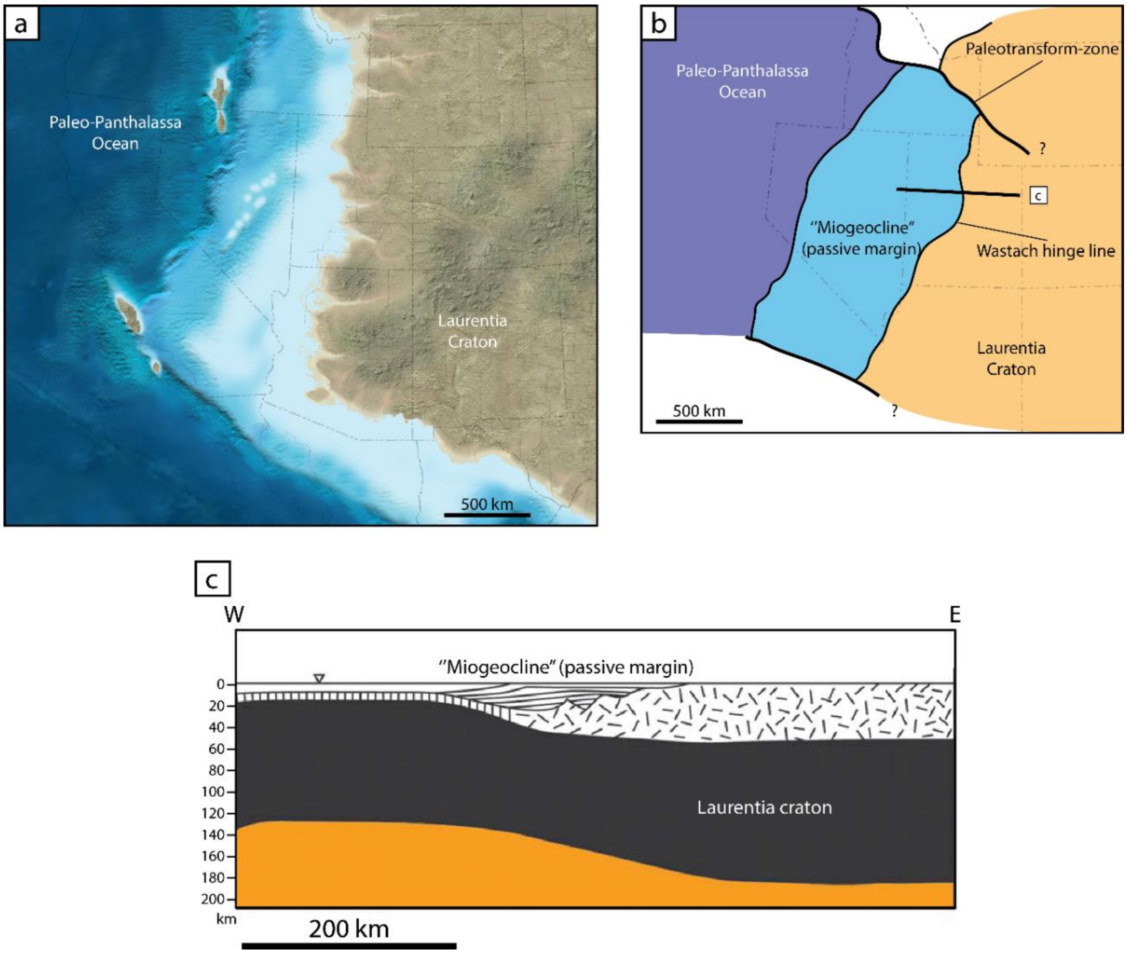

Figure II.A.5: a) Paleogeographic reconstruction of the western USA during the Cambrian (Blakey, 2013). b) Simplified Cambrian map of the western USA, highlighting the presence of the "Miogeocline" passive margin formed during the fragmentation of the supercontinent Rodinia (after Blakey, 2013; Dickinson, 2013). c) W-E lithospheric cross-section, showing the characteristic geometry of the "Miogeocline" passive margin (after Ingersoll, 2008).

Two hypotheses were proposed regarding parameters controlling the subduction occurring mainly in central Nevada during the Antler orogeny. The main issue being to determine whether the downgoing slab was plunging eastward (e.g., Burchfiel & Davies, 1975) or westward (e.g., Speed & Sleep, 1982; Trexler & Nitchman, 1990; Ingersoll, 2008). The most commonly accepted hypothesis is the second one, involving a subducted continental plate driven westward under a migratory exotic arc (Fig. II.A.6c; Trexler & Nitchman, 1990; Dickinson, 2004, 2006; Ingersoll, 2008). A back-arc extensional domain between the Antler assemblage and the Sierran/Klamath volcanic arcs, the Havallah Basin, also started to develop at that time as part of the newly-formed Slide Mountain Ocean (Fig. II.A.6d; Burchfield & Royden, 1991; Ingersoll, 2008, Colpron *et al.*, 2007).

The Antler orogeny is characterized by the emplacement of a large obducted accretionary prism presently located in Central Nevada (i.e., Roberts Mountains Thrust, Fig. II.A.1; Burchfiel & Davis, 1975; Speed & Sleep, 1982; Speed & Silberling, 1989; Burchfiel & Royden, 1991). The Roberts Mountains Allochthon led to the formation of the N/S-trending westward-dipping Antler Foreland Basin over the Laurentian continent (Fig. II.A.6; Speed & Sleep, 1982; Trexler & Nitchman, 1990; Burchfiel & Royden, 1991; Smith *et al.*, 1993; Dickinson, 2004, 2006, 2013; Blakey, 2008; Ingersoll, 2008). This basin witnessed the deposition of progressively shallowing-up open-marine sedimentary series (e.g., Trexler & Nitchman, 1990; Snyder *et al.*, 2003)

- *Havallah basin and development of the Slide Mountain Ocean*

Immediately following the Antler orogeny during the Carboniferous, the Havallah Basin system continued to develop west of the Roberts Mountain Allochthon (Fig. II.A.7). This basin corresponds to the southernmost part of an opening oceanic system spreading during that period: the Slide Mountain Ocean (Colpron *et al.*, 2007).

This micro-oceanic plate spread between the Laurentian craton to the East and the (Paleo-) Panthalassa to the West. Its western border was notably composed by exotic volcanic arcs like the Sierran and Klamath arcs of the Sonomia micro-plate (Speed, 1979; Colpron *et al.*, 2007), while its eastern border was the relics of the Robert Mountains Allochthon, the latter having stopped uplift since the inversion of the main horizontal constraints and undergoing erosion with time (Fig. II.A.7, e.g., Blakey, 2013).

The Havallah Basin served as a depocenter for marine sediments that were later scraped off during formation of the accretionary prism later thrusted into the Golconda Allochthon during the next Sonoma orogeny during the Permian-Triassic transition.

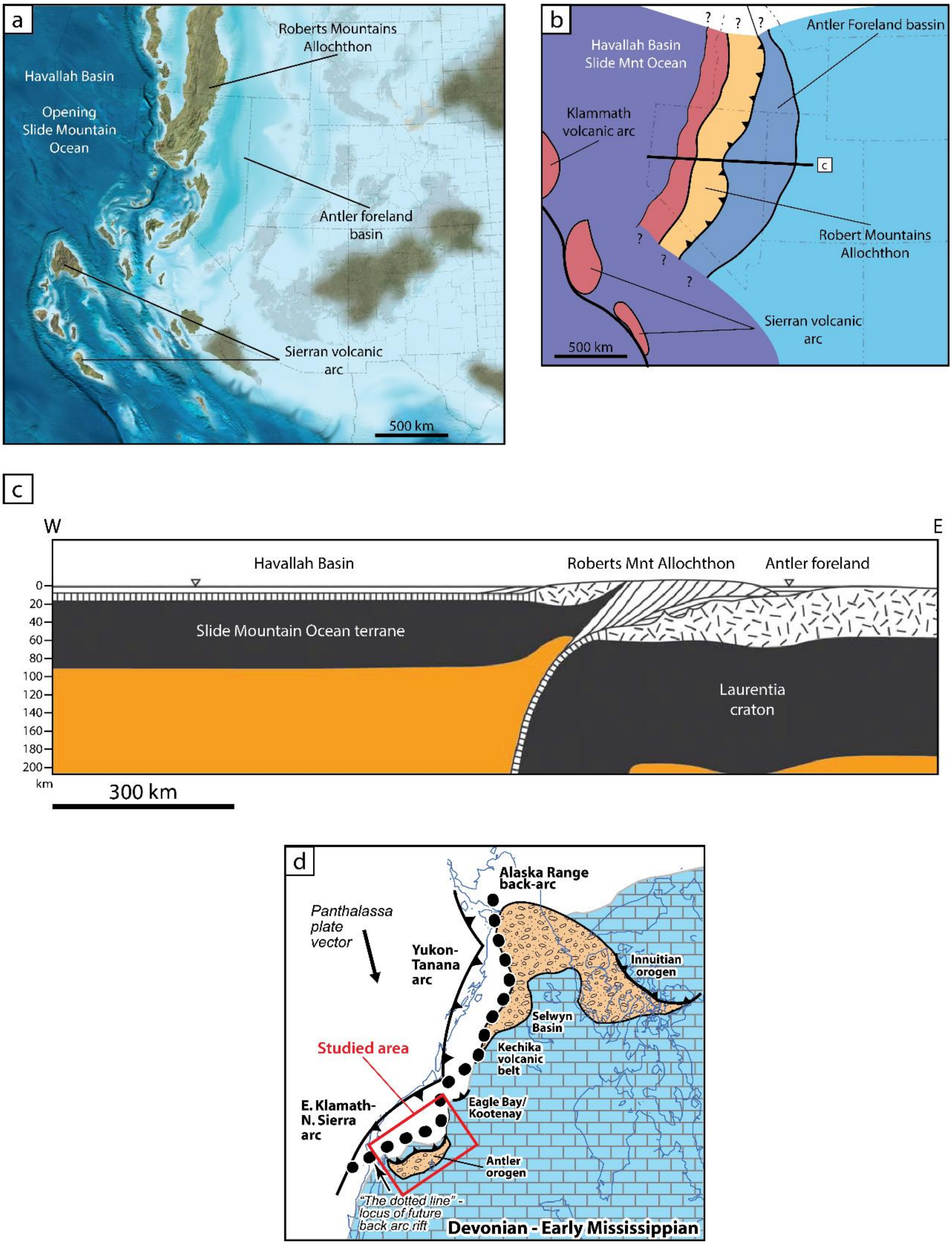

Figure II.A.6: a) Paleogeographic reconstruction of the western USA during the Late Devonian (Blakey, 2013). b) Simplified Late Devonian map of the western USA, showing the location of the Roberts Mountain Allochthon and the resulting Antler Foreland Basin. Presence of volcanic arcs is also reported in the oceanic domain (e.g., Sierran/Klamath), as well as an opening ocean (Slide Mountain Ocean) in a back-arc configuration relative to the Antler orogen (after Burchfield & Royden, 1991; Colpron & Nelson, 2009; Blakey, 2013; Dickinson, 2013). c) W-E lithospheric cross-section of the area, showing the Roberts Mountain Allochthon obducted onto the Laurentia craton and the opening Slide Mountain Ocean in a back-arc configuration (Havallah Basin; after Ingersoll, 2008). d) Paleogeographic map of the western margin of the Laurentian continent with a focus on the study area. This map shows first steps of the opening of the Slide Mountain Ocean, with dotted line representing locus of back-arc rift (Colpron *et al.*, 2007).

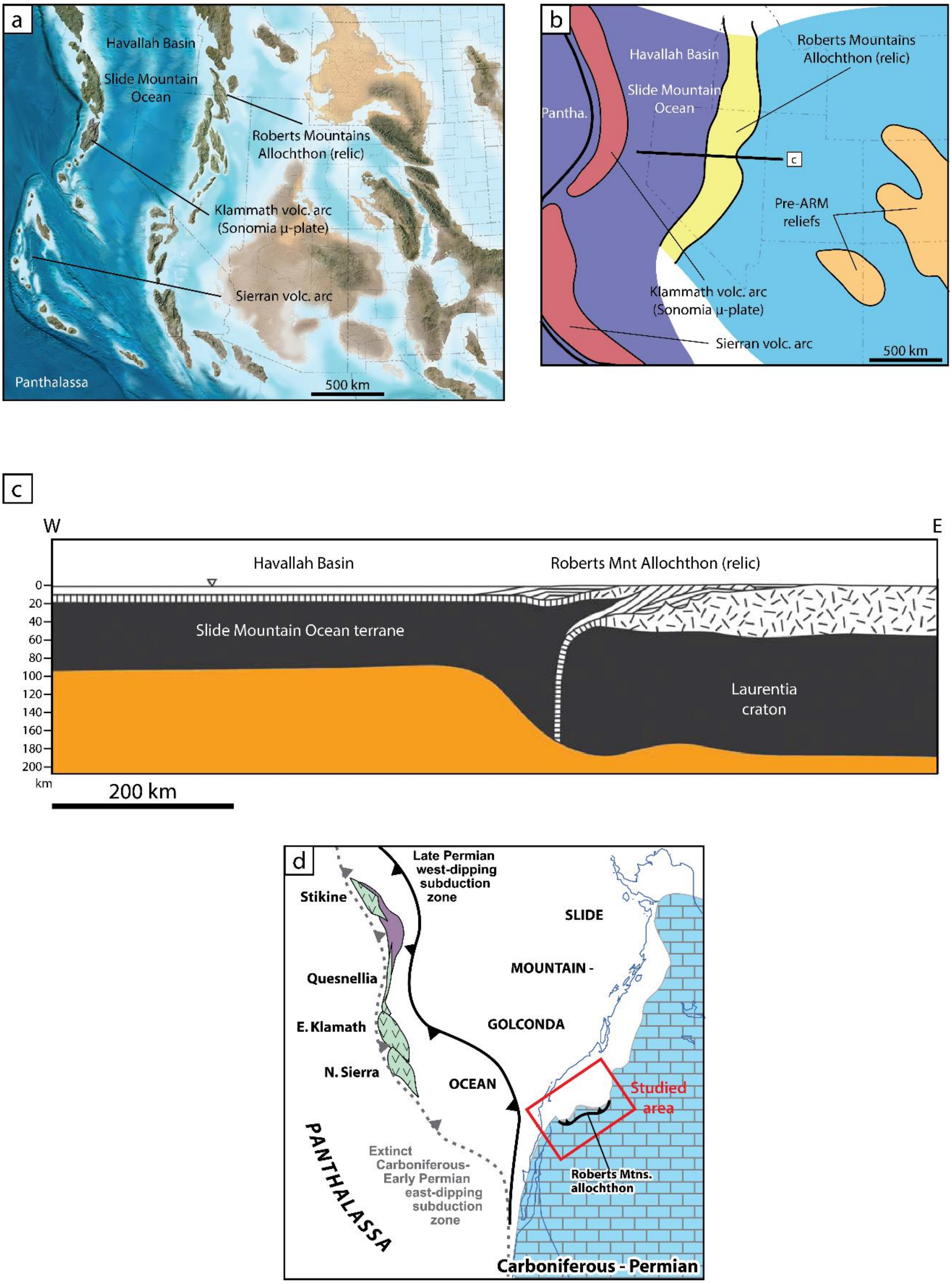

Figure II.A.7: a) Paleogeographic reconstruction of the western USA during the late Carboniferous (Pennsylvanian; Blakey, 2013). b) Simplified map of the western USA during the late Carboniferous (Pennsylvanian) showing the location of the Slide Mountain Ocean and bordering volcanic arcs of the Sonomia micro-plate to the West (Klamath arc). Primordial Ancestral Rocky Mountains (ARM) uplifts are located in the southeastern part of the study area (after Colpron *et al*., 2007; Blakey, 2013; Dickinson, 2013). c) W-E lithospheric cross-section of the area (after Ingersoll, 2008). d) Paleogeographic map of the western margin of the Laurentian continent with focus on the study area (Colpron *et al.*, 2007).

- *The Ancestral Rocky Mountains orogeny*

The Ancestral Rocky Mountains (ARM) orogeny occurred in the eastern part of the studied region (Fig. II.A.8) and ranged from the early Carboniferous up to the early to mid-Permian (~350 to 270 Ma; Fig. II.A.3). This mountain-building event resulted from a succession of crustal uplifts across the Laurentian continent, between the southeastern border of the Antler Foreland Basin in present-day Utah, to the Ouachita-Marathon orogenic belt in present-day Texas (Fig. II.B.8d). This orogen is linked to important long-range intra-cratonic deformations. Indeed, transtensional and transpressional constrains along with lithospheric buckling resulted from the Laurentia-Gondwana continental collision (Kluth & Coney, 1981; Ye *et al.*, 1996; Geslin *et al.*, 1998; Dickerson, 2003; Blakey, 2008; Dickinson, 2006, 2013). However, the detailed chain of events and strength components responsible for the orogeny are still debated today (e.g., Foley *et al.*, 2016).

The resulting chain probably showed a marked topographic relief, some of which could have persisted until the Early Triassic (Kluth & Coney, 1981; Blakey, 2008). Most of these crustal uplifts were emplaced according to lithospheric weaknesses inherited from the Proterozoic structural heritage (Kluth & Coney, 1981; Dickerson, 2003). In the study area, most remarkable uplifts related to the ARM are the Kaibab/Defiance and Uncompahgre uplifts (in its southern and eastern parts, respectively; Figs. II.B.8a and II.B.8b). These reliefs were important enough to last until the Early Triassic and likely had a major role in terrigenous inputs into the Permian to Triassic basins of the region (Dickinson, 2013; 2014 *pers. com.*).

Many sedimentary basins formed during the Carboniferous-Permian interval (Dickerson, 2003). For instance, the Permian Oquirrh Basin (Fig. II.A.8) probably resulted from the complex interplay between intracratonic deformations to the East and the reactivation of Antler faults to the West (Geslin *et al.*, 1998: fig. 12; Trexler & Nitchman, 1990; Dickerson, 2003; Blakey, 2008). This highly subsiding basin recorded up to 6 km of marine strata (Walker, 1985; Yonkee & Weil, 2015). Additionally, by the Middle Permian, reversion of the subduction polarity under the volcanic arcs (formerly eastward dipping see Fig. II.A.7d and now westward dipping in a similar fashion to the subduction during Antler orogeny) lead to the rapid closure of the Slide Mountain Ocean. Exotic volcanic arcs of the Sonomia micro-plate consequently converged toward the Laurentian craton (Fig. II.A.8c; Colpron *et al.*, 2007)

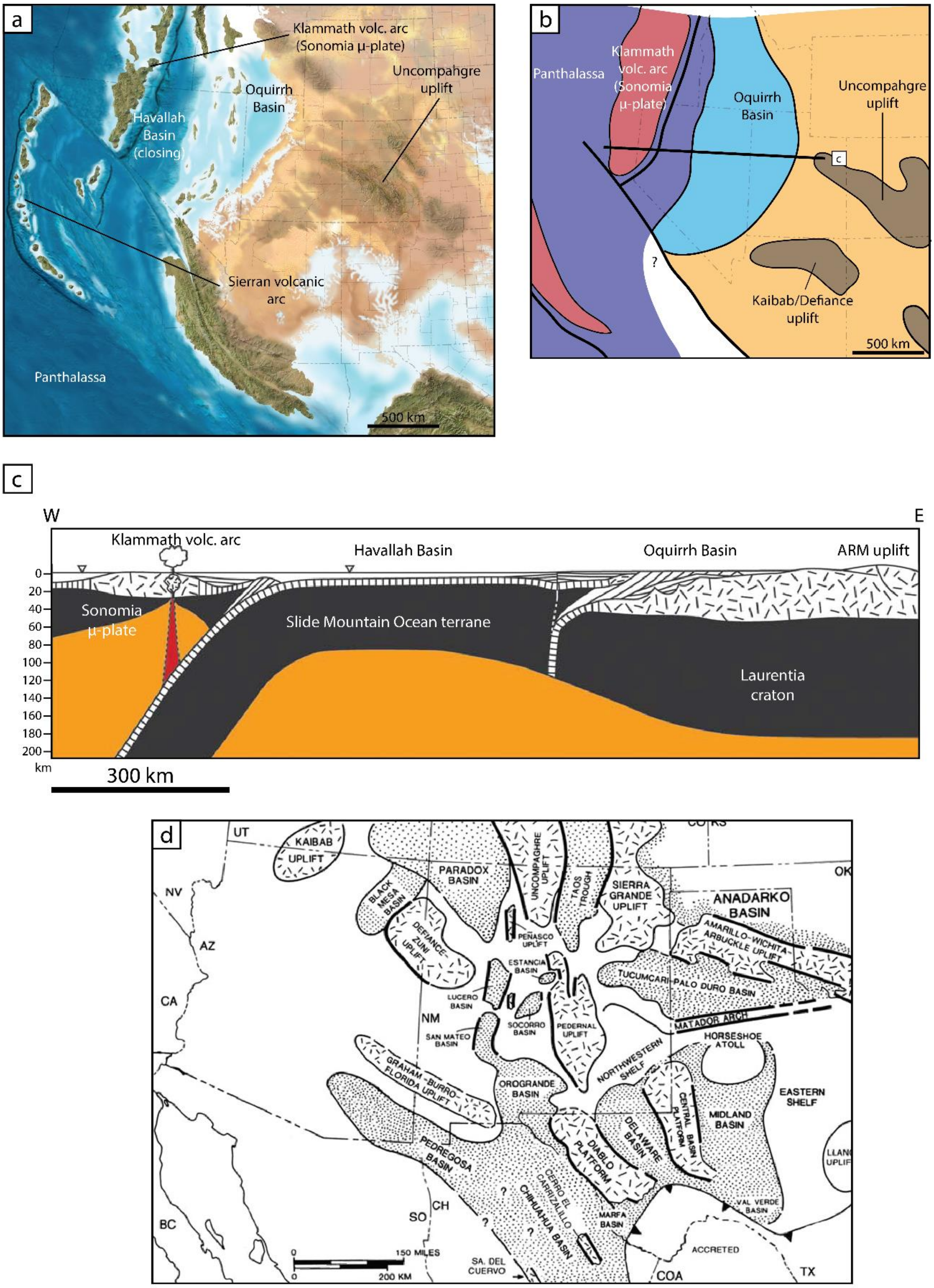

Figure II.A.8: a) Paleogeographic reconstruction of the western USA during the Early Permian (Blakey, 2013). b) Simplified map of the western USA during the Early Permian showing the location of northwesternmost ARM uplifts and the presence of the marine Oquirrh Basin. The Slide Mountain Ocean is closing, with the Klamath volcanic arc of the Sonomia micro-plate migrating toward the Laurentian margin (after Ye *et al.*, 1996; Dickerson, 2003; Ingersoll, 2008; Colpron *et al.*, 2007; Blakey, 2013; Dickinson, 2013). c) W-E lithospheric cross-section of the area showing basement uplifts of the ARM, the position of the Oquirrh Basin and the closure of the Slide Mountain Ocean through a westward-dipping subduction under the Klamath volcanic arc of the Sonomia micro-plate (after Ingersoll, 2008). d) Paleogeographic map of the ARM uplifts between the studied area and the Ouachita-Marathon orogenic belt in southeastern Laurentia (Dickerson, 2003).

- *The Sonoma orogeny and the formation of the Early Triassic Sonoma Foreland Basin*

This orogeny is still hardly known and debated (e.g., Ingersoll, 2008). Indeed, only a very few remnants are visible today. The Sonoma orogeny occurred ~100 Ma after the Antler orogeny, around the PTB (Fig. II.A.3). Similarly to the Antler orogeny, the Sonoma orogeny results from the eastward migration and accretion of exotic island-arc systems, here belonging to the Sonomia microplate (Klamath volcanic arc) onto the Laurentian craton (Fig. II.A.9; Burchfiel & Davis, 1975; Speed & Silberling, 1989; Blakey, 2008; Ingersoll, 2008; Dickinson, 2006, 2013).

The Sonoma orogeny is characterized by thrusting of an accretionary prism obducted above the continental crust and known as the Golconda Allochthon (GA, Fig. II.A.9; e.g., Speed & Silberling, 1989; Dickinson, 2013). It is worth noting that this allochthon is emplaced in the same area than the older Roberts Mountains Allochthon (Figs. II.A.7 to II.A.9). The GA accretionary prism likely resulted from scraping of the marine sediments deposited in the Slide Mountain Ocean during the episodic westward-dipping subduction that lead to the closure of this micro-ocean (Gabrielse *et al.*, 1983; Oldow *et al.*, 1989; Speed & Silberling, 1989; Dickinson, 2004, 2006, 2013; Ingersoll, 2008; Colpron *et al.*, 2007).

GA is thought to have initiated the formation of a foreland basin: the Sonoma Foreland Basin (Dickinson, 2006, 2013; Blakey, 2008; Ingersoll, 2008), which recorded sediments deposited during the Early Triassic. However, the location and extent of the GA is determined on the field by only a few remnants (e.g. the Koipato volcanic formation, see below), which are presently located in Central Nevada (Fig. II.A.10a; Snyder & Brueckner, 1983; Walker, 1985; Schweickert & Lahren, 1987; Oldow *et al.*, 1989; Dickinson, 2006, 2013; Blakey, 2008; Ingersoll, 2008). Remnants of the GA, if any, are yet to be found in the northern part of the basin, especially in Idaho (Schweickert & Lahren, 1987; Oldow *et al.*, 1989).

Precise mechanisms behind the formation and evolution of the Sonoma Foreland Basin remain to be precisely characterized (see section IV).

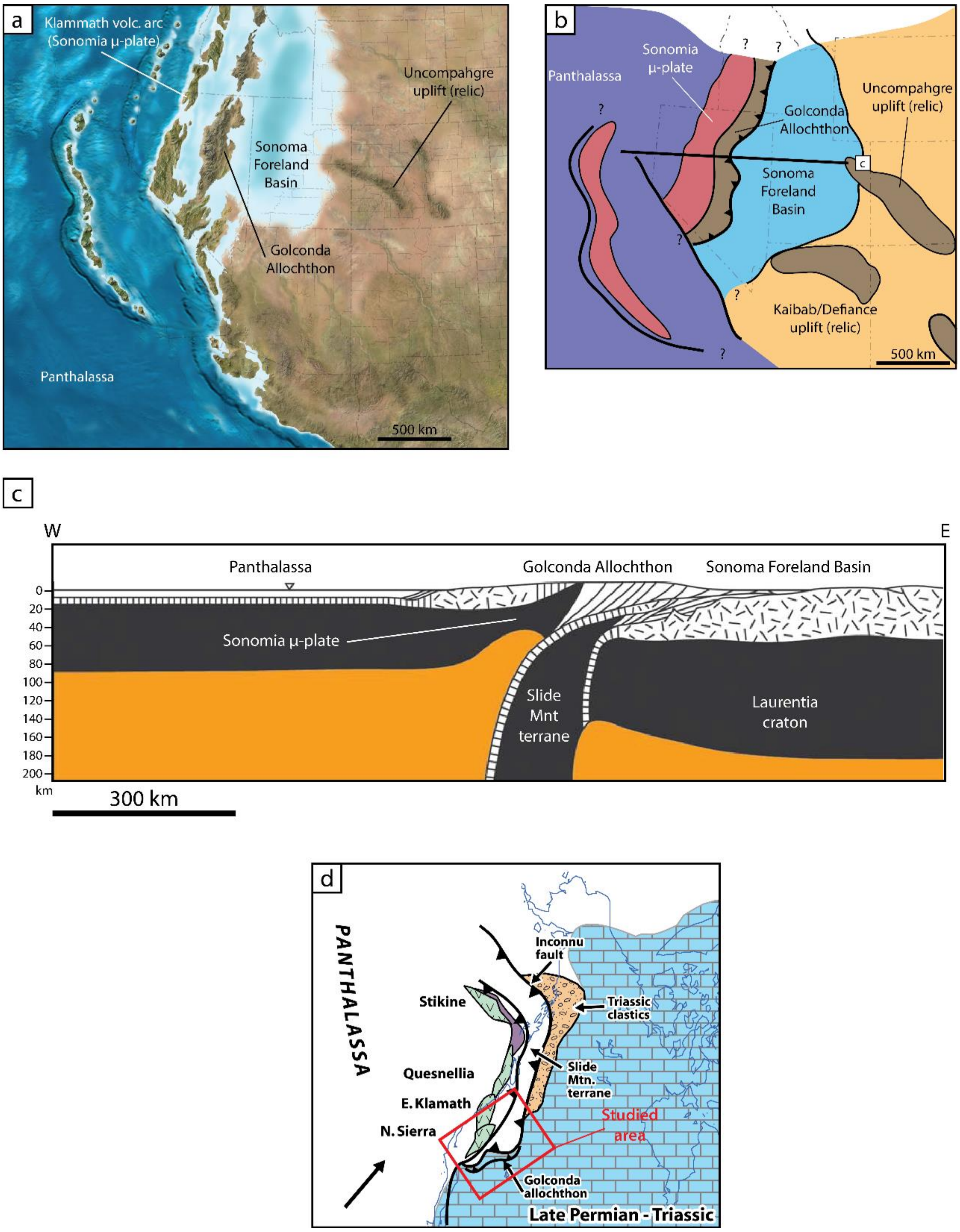

Figure II.A.9: a) Paleogeographic reconstruction of the western USA during the Early Triassic (Blakey, 2013). b) Simplified Early Triassic map of the western USA showing the location of the Golconda Allochthon and the resulting Sonoma Foreland Basin (SFB). The Sonomia micro-plate had been amalgamated to the Laurentian craton, leading to the formation of the Golconda Allochthon. Relics of ARM uplifts are still present in the southeastern end of the SFB (after Ingersoll, 2008; Colpron *et al*., 2007; Blakey, 2013; Dickinson, 2013). c) W-E lithospheric cross-section of the area showing the GA obducted onto the Laurentia craton while the Sonoma micro-plate is amalgamated to the craton. The Slide Mountain Ocean is assumed to be present as a lithospheric wedge between the Laurentian and Sonoman plates (after Ingersoll, 2008). d) Paleogeographic map of the western margin of the Laurentian continent with a focus on the study area. This map shows the closure of the Slide Mountain Ocean and the amalgamation of volcanic arcs (Sierra and Klamath; Colpron *et al*., 2007).

- *The Koipato volcanic Formation*

The main controversy regarding the existence and extent the Sonoma Foreland Basin as a true foreland basin is related to the poor field evidence indicating a relief sufficient enough to provoke a lithospheric flexuration (e.g., Oldow *et al.*, 1989; Speed & Silberling, 1989; Wyld, 1991). Among the rare field evidence is the presence of the Koipato volcanic Formation in present-day central Nevada, being one of the GA remnants (Fig. II.A.10a; Vetz, 2011). At this place, remnants of the allochthon are sealed by an unconformably lying rhyolitic formation, presumably emplaced by the end of the Sonoma orogeny (Vetz, 2011). A minimum age of Anisian (~248 Ma, Middle Triassic) is given to this volcanic formation using U-Pb zircon geochronology (Vetz, 2011) and confirmed by the occurrence of Anisian ammonoids in the overlying sedimentary series (Nichols & Silberling, 1977; Bucher, 1988; Vetz, 2011). Nevertheless, the potential presence of older ammonoid faunas is not to be discarded.

The presence of such volcanism is of major importance regarding the late orogenic history of the allochthon and its demise. Vetz (2011) described this formation as a volcanic (locally intrusive) felsic to rhyolitic unit, bearing a high $^{87}Sr/^{86}Sr$ ratio (0.7089 – 0.7126) and fairly negative εNd values (-9.73 – -12.89). This peculiar type of magmatism and volcanism points toward a late orogenic context (Malavieille *et al.*, 1990; Malavieille, 1993; Innocent *et al.*, 1994; Yang *et al.*, 2008; Valenzuela *et al.,* 2011). Based on this volcanic-type occurrence, a new and original model explaining the late-orogenic evolution of the GA and the presence of the associated Koipato volcanism can be proposed here based on similar examples in the literature (e.g., Thorpe *et al.*, 1989; Malavieille, 1993; Innocent *et al.*, 1994; Riley *et al.*, 2001; Valenzuela *et al.*, 2011; Figs. II.A.10b and II.A.10c).

During the Sonoma orogeny, horizontal tectonic forces (Ft) are important and lead to the formation of a relief, in this case by thrusting of GA above the North American continental margin (Fig. II.A.10b). These forces are higher than the vertical load exerted by the mass of the relief (gravitational forces, Fg). Consequently, the lithospheric crust is thickened. By the end of the orogeny, vertical Fg become preponderant compared to horizontal Ft in the allochthon. Therefore, gravity collapse of the relief occurs, leading to a late-orogenic extension and thinning of the crustal lithosphere (thinning being emphasized by relief erosion; Fig. II.A.10c). These movements are characterized by normal-faulting (syn-volcanism normal faulting was documented in the Koipato Fm. by Vetz, 2011), as well as by a return to isostatic equilibrium with a shallowing of the asthenosphere (Fig. II.A.10c; e.g., Malavieille *et al.*, 1990; Malavieille, 1993, Innocent *et al.*, 1994). This asthenospheric shallowing is then responsible for an enhanced thermicity leading to the partial melting of the basal continental crust, most probably at the origin of the rhyolitic volcanism reported for the Koipato formation.

This model is in agreement with the proposition of a marked relief for the Golconda Allochthon. It has therefore to not be neglected in the context of the formation of a flexural foreland basin in the studied area during the Early Triassic. Moreover, this relief may have also contributed to the terrigenous inputs within the SFB, similarly to the ARM relic uplifts on the opposite side of the basin.

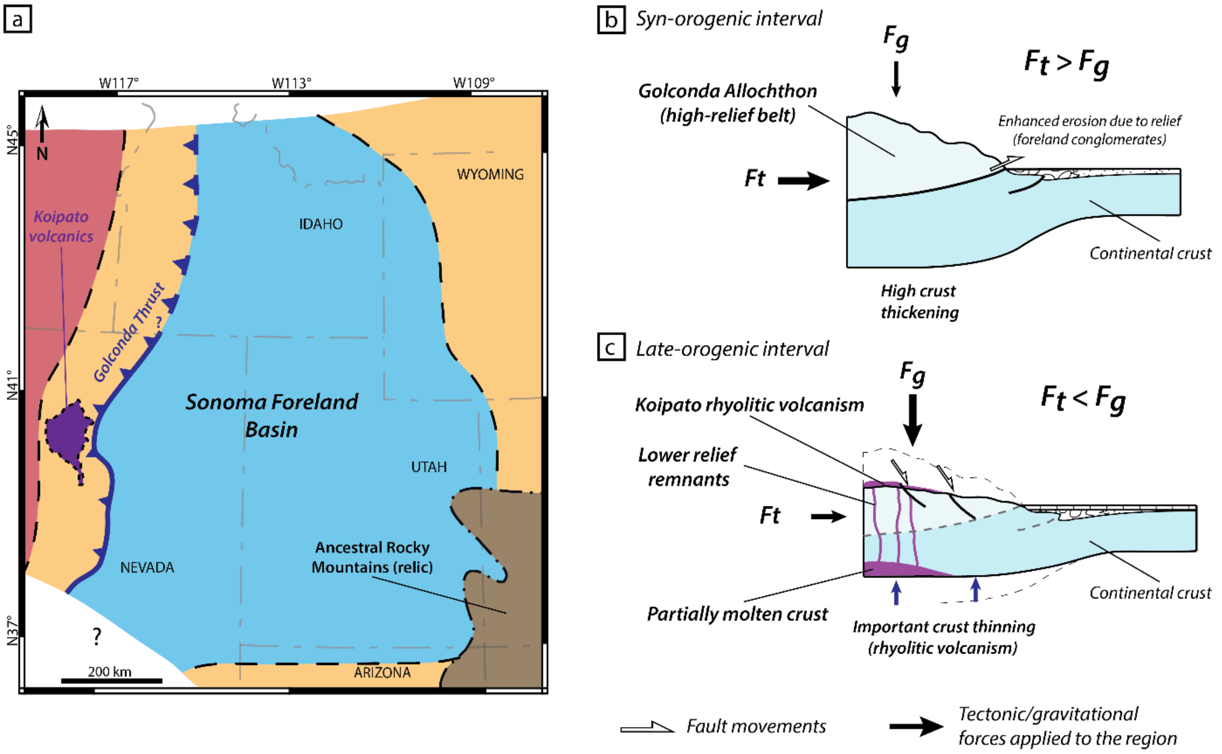

Figure II.A.10: a) Simplified Early Triassic paleogeographic map of the SFB, with locations of the reconstructed GA and Koipato volcanic Formation (after Caravaca et al., in press a, see section IV). b) and c) Proposed model for syn- and late-orogenic evolution of the GA thrust belt. b) During syn-orogenic interval, horizontal tectonic forces (Ft) generated a relief by emplacement of the GA, leading to the formation of the SFB and allowing thickening of the underlying crust. c) During the late-orogenic interval, horizontal tectonic forces are not sufficient enough to compensate and overthrow the vertical gravitational forces (Fg) exerted by the mass of the obducted material, leading to a thinning of the crust (e.g., Malavieille *et al*., 1990; Malavieille, 1993). This thinning caused an isostatic rebound with a partial melting of the crust, responsible for the onset of rhyolitic volcanism in the area (Koipato Fm.; Vetz, 2011).

- *The Sevier orogeny: a thin-skin thrust-and-fold belt*

The Sevier orogeny is Early Cretaceous to Eocene in age (~140 to ~50 Ma; Fig. II.A.3). East-West compressive constraints formed a large thrust-and-fold belt, which is still present today and constitutes the eastern border of the Great Basin (Figs. II.A.1 and II.A.11; Dickinson, 2006, 2013; Yonkee & Weil, 2010; Yonkee *et al.*, 2014). The Sevier orogeny originated from the ongoing eastward subduction of the Farallon oceanic plate under the North American continental plate, with a slab drag causing superficial compressional deformations and shortenings (Fig. II.A.11c; Burchfiel & Davis, 1975; Dickinson, 2006, 2013). The Sevier belt was important enough to trigger the formation of an important and famous foreland basin known as the Western Interior Seaway (e.g., Blakey, 2008; Ingersoll, 2008; Miall, 2010; Dickinson, 2013). Although this basin originated in the same area than the predecessor Antler and Sonoma foreland basins (Miall, 2010), it mainly differs by its much larger extension and the eastern position of its main depocenter.

This orogen was responsible for displacement of many older terrains (such as the Triassic sedimentary series), which resulted in the loss of the original paleogeographic signal corresponding to these intervals (e.g., Dickinson, 2006, 2013). Palinspastic reconstructions of the area for these intervals are thus mandatory. This thrust-and-fold belt is not homogeneous along its N/S trending front, with varying estimated tectonic shortenings and eastward displacement of terrains reaching up to 140 km (DeCelles & Coogan, 2006; Schelling *et al.*, 2007; Dickinson, 2006, 2013; Yonkee & Weil, 2010, 2015; Yonkee *et al.*, 2014). Northern and southern parts of the Sevier belt are separated by a conspicuous recess formed by a lateral ramp and located west of the Uinta Mountains ("Uinta Recess", Fig. II.A.11b). Its formation results from inherited features of the basement (e.g., Mukul & Mitra, 1988; Lawton *et al.*, 1994; Paulsen & Marshak, 1999; Wilkerson *et al.*, 2002).

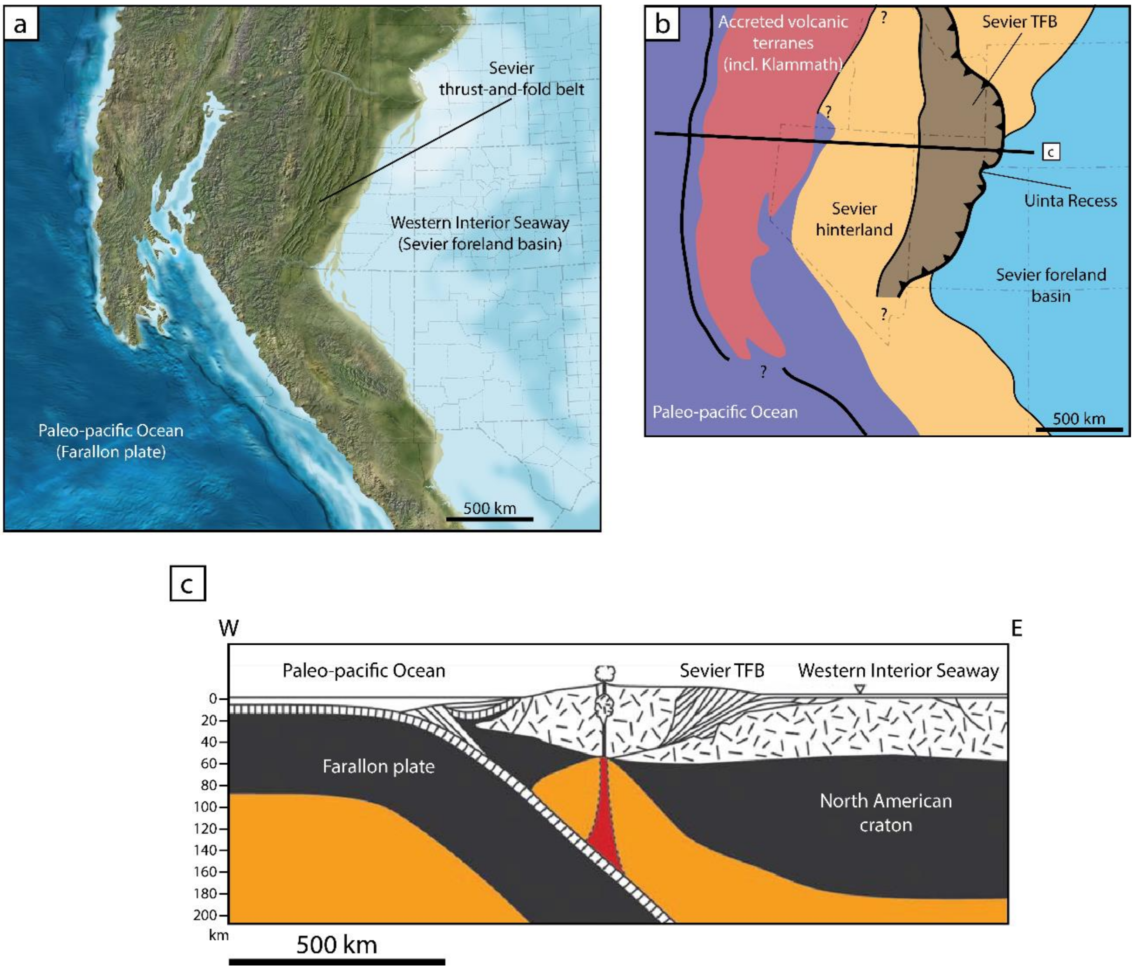

Figure II.A.11: a) Paleogeographic reconstruction of the western USA during the Cretaceous (Blakey, 2013). b) Simplified Cretaceous map of the western USA highlighting the presence of the Sevier thrust-and-fold belt (TFB) and the ensuing Sevier foreland Basin (i.e., the "Western Interior Seaway"; after Blakey, 2008, 2013; Ingersoll, 2008; Miall, 2010; Dickinson, 2013). c) W-E lithospheric cross-section of the area showing the Sevier thrust-and-fold belt emplaced onto the North American craton and the eastward-dipping subduction of the Farallon plate (after Ingersoll, 2008).

- *The Laramide orogeny and the formation of the present-day Rockies:*

During the same Early Cretaceous to Eocene interval (Fig. II.A.3), the Laramide orogeny occurred East and Southeast of the study area, and reactivated most basal crustal uplifts set during the ARM orogeny. This structural event led to the formation of the modern Rocky Mountains overlapping older structures, especially in the Colorado Plateau (Fig. II.A.12; Oldow *et al.*, 1989; Ye *et al.*, 1996; Dickinson, *pers. com.* 2015).

This orogen resulted from continuous compressional constraints due to the "flat" subduction of the Farallon plate after the main Sevier events, because the intraplate compressional deformation had to be accommodated. This was possible notably through the thrusting and reactivation of earlier ARM crustal uplifts (Burchfiel & Davies, 1975; Oldow, 1984; Oldow *et al.*, 1989; Speed & Silberling, 1989, Ye *et al.*, 1996; Dickinson, 2004;), as well as the reactivation of Proterozoic inherited structures (e.g., uplift of the Uinta Mountains along Proterozoic fault-lines; Paulsen & Marshak, 1999). The "flat" Farallon slab also played a role in contributing to the regional uplift, especially to the Colorado Plateau uplift (Fig. II.A.12c; e.g., Ye *et al.*, 1996; Ingersoll, 2008; Dickinson, 2013).

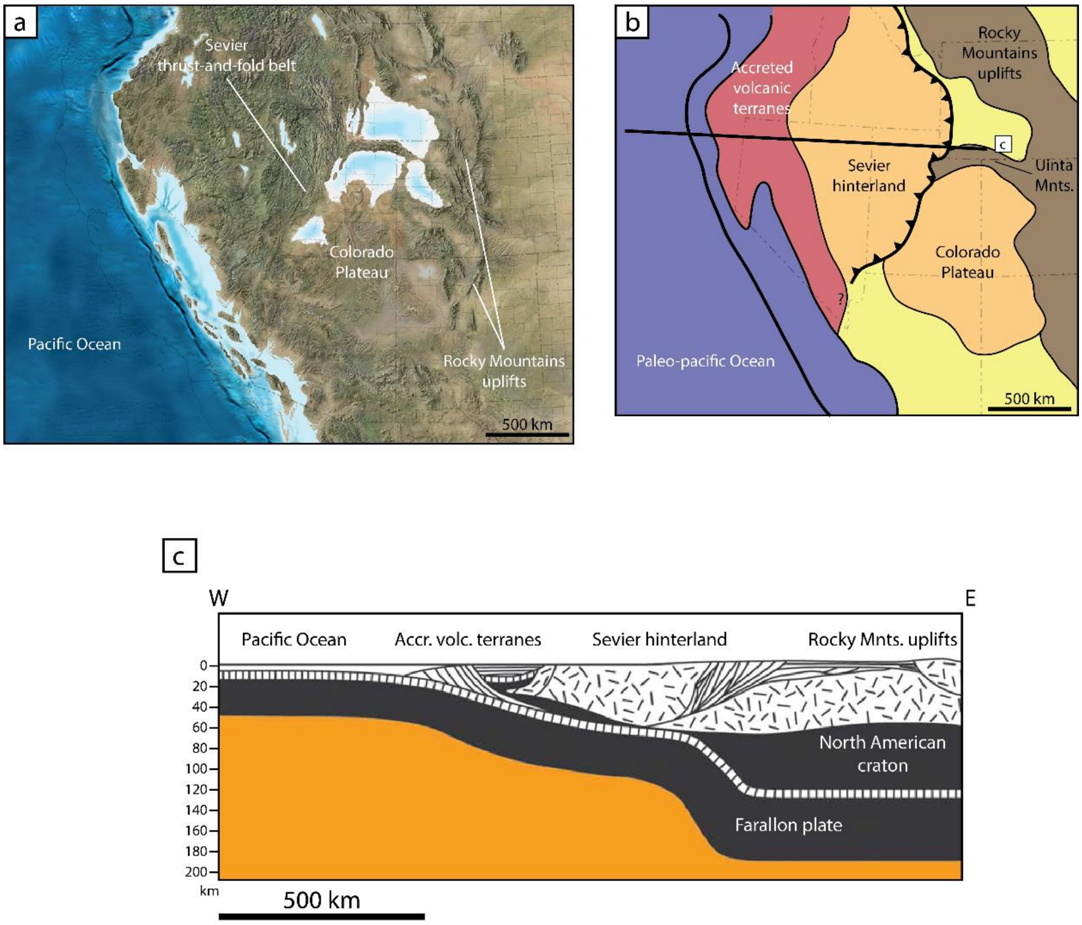

Figure II.A.12: a) Paleogeographic reconstruction of the western USA during the Eocene (Blakey, 2013). b) Simplified Eocene map of the western USA highlighting the presence of the Sevier thrust-and-fold belt, Rocky Mountains and Colorado Plateau uplifts (e.g., Oldow, 1984; Ye *et al.*, 1996; Paulsen & Marshak, 1999; Ingersoll, 2008; Blakey, 2013; Dickinson, 2013). c) W-E lithospheric cross-section highlighting the "flat" slab subduction of the Farallon plate (after Ingersoll, 2008).

- *Basin and Range extensional Province*

Finally, extensional constrains in the Basin and Range Province started by the Neogene (~20 Ma; Fig. II.A.2) and are still active today (Oldow *et al.*, 1989; DeCelles & Coogan, 2006; Dickinson, 2002, 2006, 2013). This province is characterized by normal-faulting, half-graben formation (e.g., Bear Lake, southeastern Idaho) terrain movements and seismic activity (e.g., Evans *et al.*, 2003). This extension is mainly set in a large area covering Nevada and Utah and comprised between the Sevier belt and Colorado Plateau to the East, and the Sierra Mountains to the West (Figs. II.A.1 and II.A.13).

This extension is the result of internal forces (Kreemer & Hammond, 2007) that generated transtensional stresses and pure shear after the relaxation of compressive stresses due to the subduction of the Farallon plate (Parsons *et al.*, 1994; Gans & Bohrson, 1998; Dickinson, 2002, 2006). However, the precise origins of these extensional constrains are still discussed and several possible mechanisms were proposed including: (1) a mantellic wide "rift-like" process with ascent and underplating of mantellic material leading to thermal lamination of the lithosphere (Lachenbruch & Morgan, 1990; Parsons *et al.*, 1994, Gans & Bohrson, 1998); (2) a mechanical origin with the extension occurring in a late orogenic context due to the instability and gravity collapse of the thickened lithospheric crust in Nevada and westernmost Utah (Fletcher& Hallet, 1983; Malavieille, 1993; Zandt *et al.*, 1995). A combination of these two potential mechanisms cannot be discarded. Nevertheless, the easternmost borders of the basin (e.g., Colorado Plateau or Sevier belt to the East) are not affected by these displacements (Fig. II.A.13; Dickinson, 2006, 2013).

It is also worth noting that this extension reactivated in inversion some of the thrust faults created during the Sevier orogeny (Coney, 1987; Dickinson, 2006, 2013).

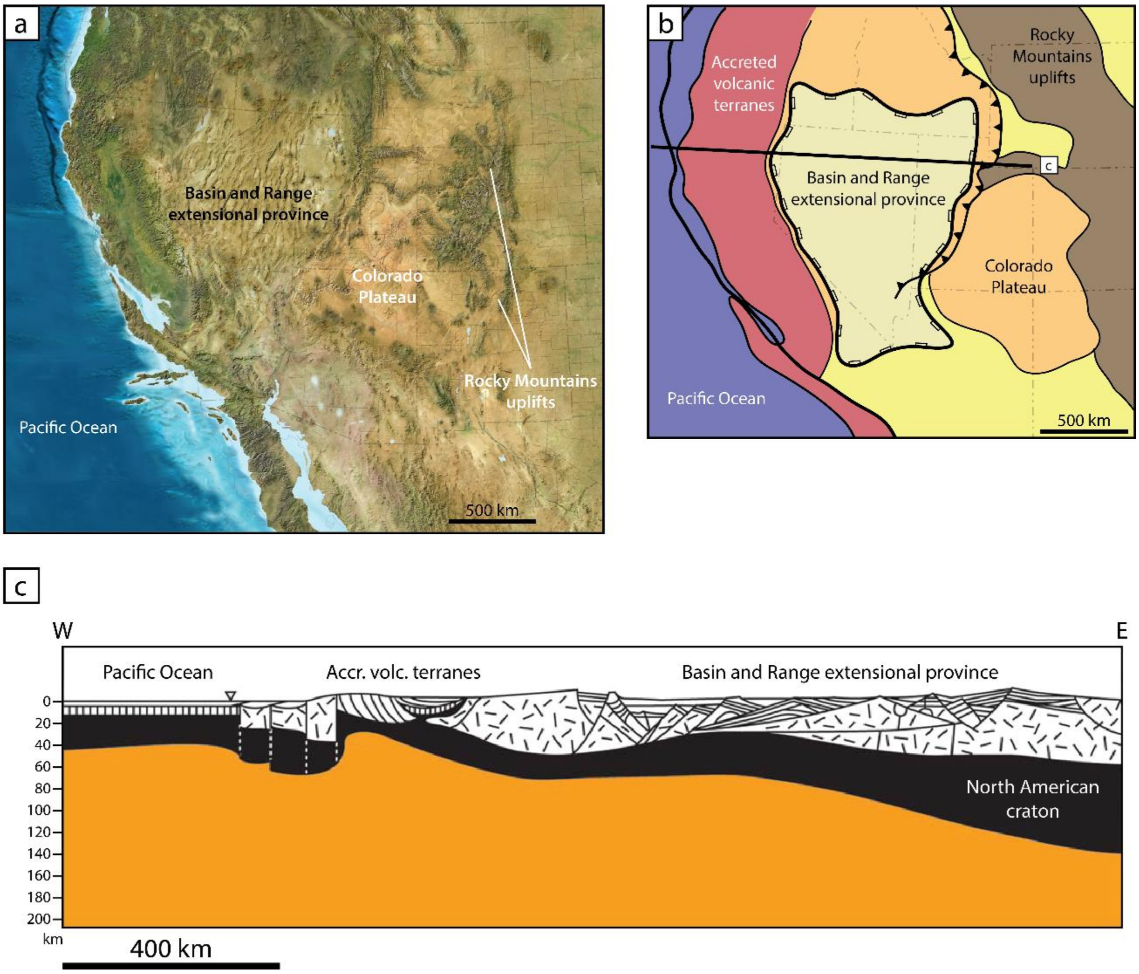

Figure II.A.13: a) Paleogeographic reconstruction of the western USA during the Oligocene (Blakey, 2013). b) Simplified map of the western USA during the Oligocene to present-day, showing the extensional Basin and Range province (Blakey, 2013; Dickinson, 2013). c) W-E lithospheric cross-section showing the impacts of the extensional Basin and Range province and the formation of many half-graben basins (after Ingersoll, 2008).

B. The Early Triassic SFB: State of the art

Location and extent of the SFB

The SFB was located in the northern intertropical zone on the western Pangea margin during the Early Triassic (Fig. II.B.1a). It results from the emplacement of GA during the Sonoma orogeny around the PTB (see section above). The SFB shows an excellent fossil and sedimentary records from the PTB until the Spathian (fourth substage of the Early Triassic), with mainly transitional continental/marine to shallow marine depositional settings (e.g., Kummel, 1954, 1957, Paull & Paull, 1993; Lucas *et al.*, 2007; Brayard *et al.*, 2013; Olivier *et al.*, 2016, see appendix 1).

During the maximum inundation of the end-Smithian (e.g., Embry, 1997; Brayard *et al.*, 2013; Vennin *et al.*, 2015), the SFB stretched from the GA reliefs on the West, to the ARM remnants on the Southeast (e.g., the Uncompahgre uplift, Fig. II.B.1b). Northeastern and eastern borders are not (yet) precisely constrained due to the lack of studies and the continental nature of easternmost deposits blurring the paleogeographic signal (e.g., Kummel, 1954, 1957; Heckert *et al.*, 2015). The Southern border is also a transitional continental to marine zone with possibly some of the northwesternmost ARM remnants making a (undocumented) relief barrier in present-day southern Utah (e.g., Blakey, 2008; Dickinson, 2013). The northern part of the SFB is commonly thought to have been the unique connection with the open Panthalassa Ocean through a "northwestern passage" made by the last relics of the Slide Mountain Ocean (Colpron & Nelson, 2009), granting open-marine conditions to spread into the basin from the North (e.g., Kummel, 1957; Paull & Paull, 1994, Goodspeed & Lucas, 2007). The southwesternmost end of the basin still remains to be documented. Additionally, the SFB is wider in its southern part (~600 km-wide) than its in northern part (~400 km-wide; Fig. II.B.1b).

Despite numerous studies, the detailed paleogeography of the SFB is still poorly constrained and needs careful re-investigations, as the spatio-temporal distribution of sedimentary deposits have been previously established almost only for the northern part of the basin (e.g., Kummel, 1957; Paull & Paull, 1994).

Spatial heterogeneities in SFB studies

Despite its importance for its fossil record on the Early Triassic biotic recovery, the knowledge acquired on the SFB is somewhat scattered and restricted. The SFB was the topic of numerous but spatially-uneven paleontological and sedimentary works during the past decades (Fig. II.B.2).

Paleontological works mainly focus on the Early Triassic biotic recovery. In that, many recent studies have been published giving a renewed portray of the basin (e.g., Brayard *et al.*, 2006, 2009, 2010, 2013 or 2017, but also Goodspeed & Lucas, 2007, McGowan *et al.*, 2009; Hofmann *et al.*, 2014 or Jattiot *et al.*, 2016, *in prep.*). Nevertheless, these publications do not concern the basin at a whole. Only a few exceptions such as Brayard *et al.* (2013) dealing with biostratigraphical timeframe and correlation for of the southern part of the SFB results from rather large analyses, but not a the basin-scale so far.

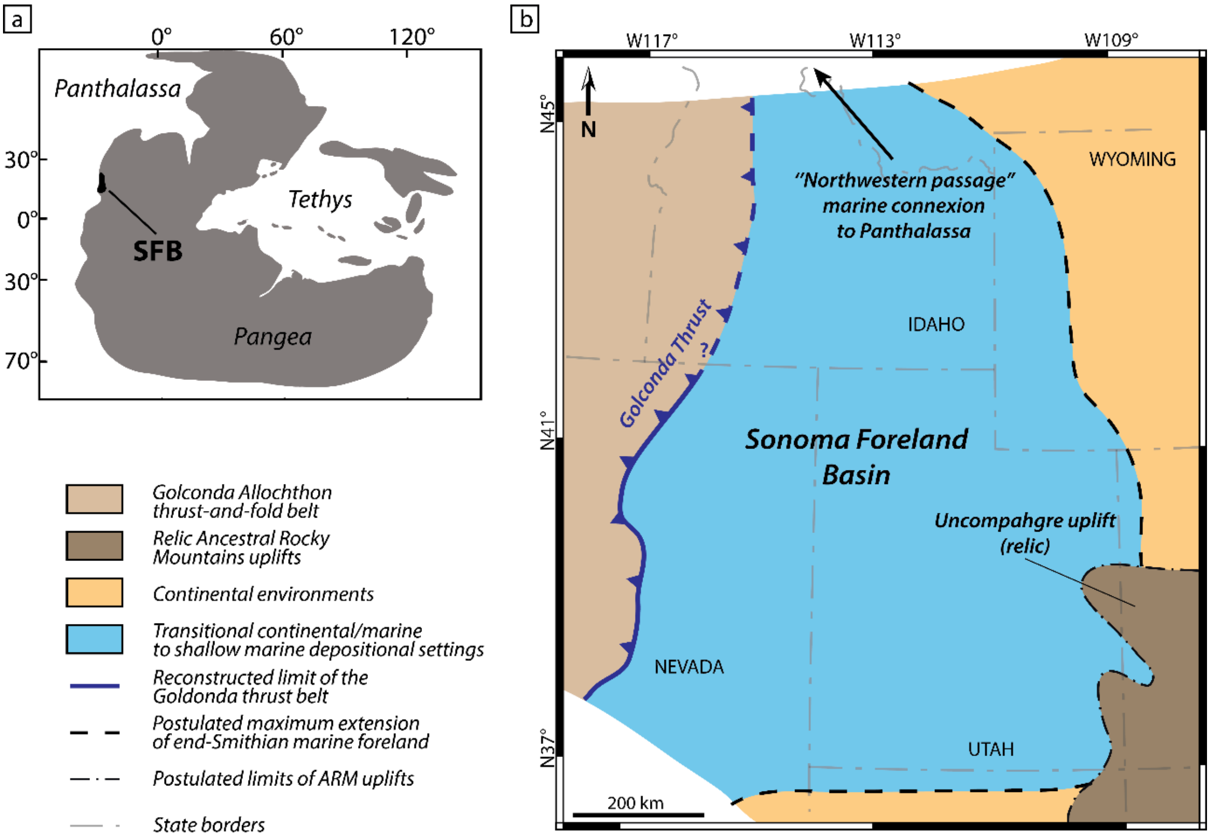

Figure II.B.1: a) Early Triassic location of the SFB (after Brayard et al., 2013). b) Simplified paleogeographic map of the SFB with position of the reconstructed GA and relic ARM uplifts (after Caravaca *et al.*, *in press* a, see section IV). The "northwestern passage" (after Colpron & Nelson, 2009) is expected to be the only connection between the SFB and the open Panthalassa Ocean during this interval.

Sedimentological studies are also less abundant and often older: most sedimentary studies done on the SFB date back from before 2005 (Fig. II.B.2), with important syntheses such as Kummel's work published in the fifties (Kummel 1954, 1957). If some of these studies were done with a regional overlook (e.g., Kummel, 1954, 1957; Paull & Paull, 1991, 1994), the vast majority of sedimentological works were based on a specific topic such as the SFB petroliferous potential (Blakey, 1977), formational lithology (Blakey, 1974; Paull & Paull, 1993) or on specific restricted areas (Davidson, 1967; Goodspeed & Lucas, 2007), even for the most recent works (e.g., Olivier *et al.*, 2014, 2016, see appendix 1; Heckert *et al.*, 2015). A true modern basin-scale reappraisal of the sedimentary record is therefore lacking.

Additionally, geochemical studies on basin Early Triassic exposures are nearly inexistent (Fig. II.B.2) with exception of e.g. Thomazo *et al.* (2016). This is all the more surprising given the fact that some of the commonly accepted paradigms for the Early Triassic recovery were seminally based on the SFB record (e.g., Schubert & Bottjer, 1992; Fraiser & Bottjer, 2004; Pruss & Bottjer, 2004).

Finally, the intense tectonics recorded during the Mesozoic and Cenozoic (notably during the Sevier orogeny), but also the volcanic episodes (emplacement of the Snake River Plain in southern Idaho) may have led to a potential loss in the Triassic record. However, some areas in the basin still remain under-explored or under-sampled, such as the northwestern Utah (Fig. II.B.2) and deserve a better look.

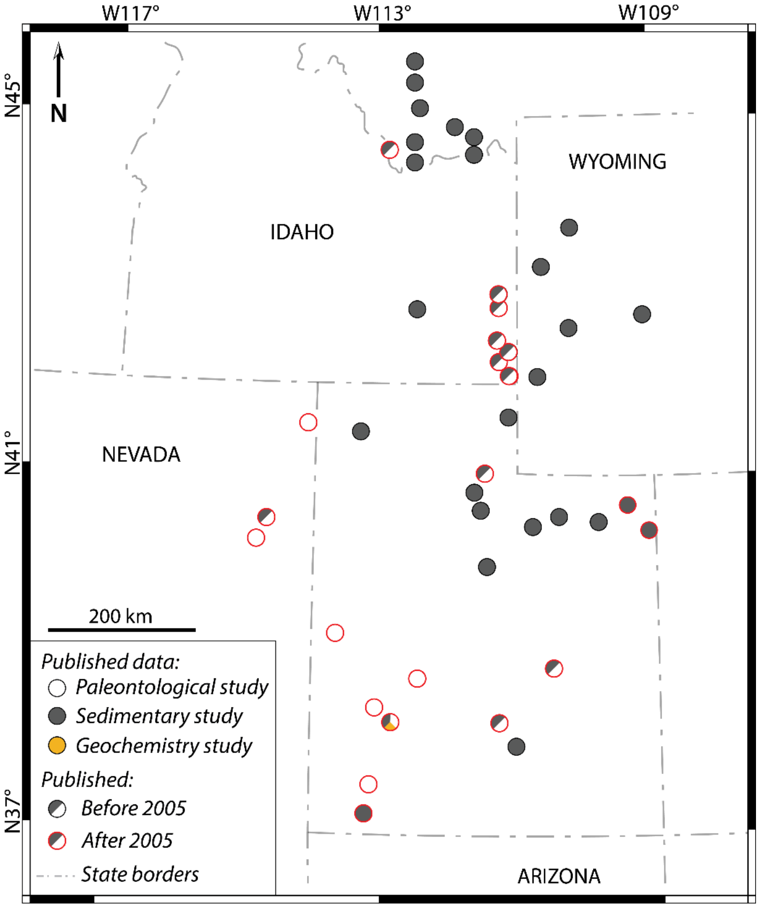

Figure II.B.2: Illustration (non-exhaustive) of various published works on the western USA Basin showing location of some studied outcrops. The map also highlights some areas devoid of Early Triassic outcrops.

- A marked dichotomy in the SFB sedimentary record

The sedimentary record of the SFB is considered as almost continuous throughout the basin, with only local erosion surfaces being under the temporal resolution of ammonoid biozones for the Early Triassic (e.g., Kummel, 1957; Paull & Paull, 1993; Lucas *et al.*, 2007; Brayard *et al.*, 2013; Olivier *et al.*, 2014, 2016, see appendix 1; Vennin *et al.*, 2015, Davydov *et al.*, 2016). The very base of this record is formed by the regional Permian/Triassic unconformity (PTU, Brayard *et al.*, 2013), which is diachroneous within the basin, locally showing important hiatus in the basal Early Triassic at some places, especially in the southern part of the basin (e.g., the Torrey area in southeastern Utah; Olivier *et al.*, 2016, see appendix 1). Nonetheless, some recent data suggest that a few exposures may have preserved a continuous record from the Late Permian to the Early Triassic, notably in Idaho (Davydov *et al.*, 2016) or in western Utah (e.g., Minersville area; Vennin *et al.*, 2015; ongoing work), allowing to track the crucial changes in depositional settings during the PTB mass extinction event and its aftermath.

Despite the somewhat outdated sedimentary studies of the basin (Fig. II.B.2; e.g., Newel & Kummel, 1942; Kummel, 1954, 1957, Blakey, 1974), authors behind these works had done a thorough and precise description of the different lithofacies encountered in the SFB. Using this database, some marked discrepancies can be observed in term of dominant lithologies and thickness of the Early Triassic sedimentary record, evidencing a conspicuous dichotomy between the northern and southern parts of the SFB (Fig. II.B.3). Surprisingly, this observation at the scale of the basin was only elusively addressed until recently.

In its southern part (Figs. II.B.3 and II.B.4), the basin is mainly filled with few tenths of meters of transitional continental to marine coarse sandstones to conglomerates known as "red beds" of the Moenkopi Group (Figs. II.B.4a-c and II.B.4e; *sensu* Lucas *et al.*, 2007; Brayard *et al.*, 2013, Olivier *et al.*, 2016, see appendix 1). At the top of the Moenkopi Group, metric-scale beds of intertidal microbial limestones can be observed (Figs. II.B.3 and II.B.4e; Brayard *et al.*, 2013; Vennin *et al.*, 2015; Olivier *et al.*, 2016, see appendix 1). The upper part of this sedimentary pile is characterized by also few tenths of meters of open-marine bioclastic limestones (locally shales) of the Thaynes Group (Figs. II.B.3, II.B.4d and II.B.4f; *sensu* Lucas *et al.*, 2007), marking the maximum flooding of the Smithian third-order transgression and the maximum reach of marine facies in the southern part of the SFB (Embry, 1997; Vennin *et al.*, 2015). This late Smithian flooding event is characterized by the presence of the ammonoid genus *Anasibirites* throughout the basin (Fig. II.B.3a; Lucas *et al.*, 2007; Brayard *et al.*, 2013; Jattiot *et al.*, 2015, *in press*).

In the northern part of the basin (Figs. II.B.3 and II.B.4), the sedimentary record mainly differs at its base by the presence of the Dinwoody and Woodside Formations in place of the Moenkopi Group, which are characterized by several tenths to hundreds of meters of fine marine siltstones (Figs. II.B.3, and II.B.4g; Kummel, 1954, 1957; Sadler, 1981; Paull & Paull, 1991; Caravaca *et al.*, 2017, see section III.A). Above these formations, the sedimentary record resembles the one observed in the southern part and corresponds to the open-marine bioclastic limestones and shales of the Thaynes Group (Figs. II.B.3, II.B.4d and II.B.4h) reaching up to several tenths to hundreds of meters-thick.

Noteworthy, no microbial activity has been found so far in the northern part of the basin, with exception of the Lower Weber Canyon outcrop displaying microbially induced sedimentary structures (MISS) but no microbial limestones as described in southern part of the basin (LWC in Figs. II.B.3 and II.B.4; Grosjean *et al.*, *in prep*.). Interestingly, this outcrop displays shared characteristics with the southern type of sedimentary record (such as presence of terrigenous “red beds” deposits), and might be representative of a “transition zone” between the two parts of the SFB.

The distinction and characterization of the depositional settings for these two different North and South areas, as well as their evolution and their potentially local controlling parameters are therefore worth of attention to decipher mechanisms forming such discrepancy.

- The N/S dichotomy is also visible in the fossil record

As evoked above in section I.B., the Early Triassic SFB fossil record is relatively abundant throughout the entire basin (Fig. I.B.9). Nevertheless, distribution and abundance of some documented taxa apparently follow the N/S dichotomy observed in the sedimentary record.

Noteworthy, the presence of mineralizing microbial communities is well established in the southern part of the basin, with various outcrops of different ages displaying m-thick beds of microbial limestones (Fig. II.B.5, e.g.; Pruss & Payne, 2009; Marenco *et al.*, 2012; Brayard *et al.*, 2013; Woods, 2013; Olivier *et al.*, 2014, 2016, cf. appendix 1; Vennin *et al.*, 2015). In turn, outcrops in the northern SFB seem devoid of any similar microbial limestone deposition (e.g., Kummel, 1957; Paull & Paull, 1991; Jenks *et al.*, 2013; Caravaca *et al.*, 2017, see section III.A).

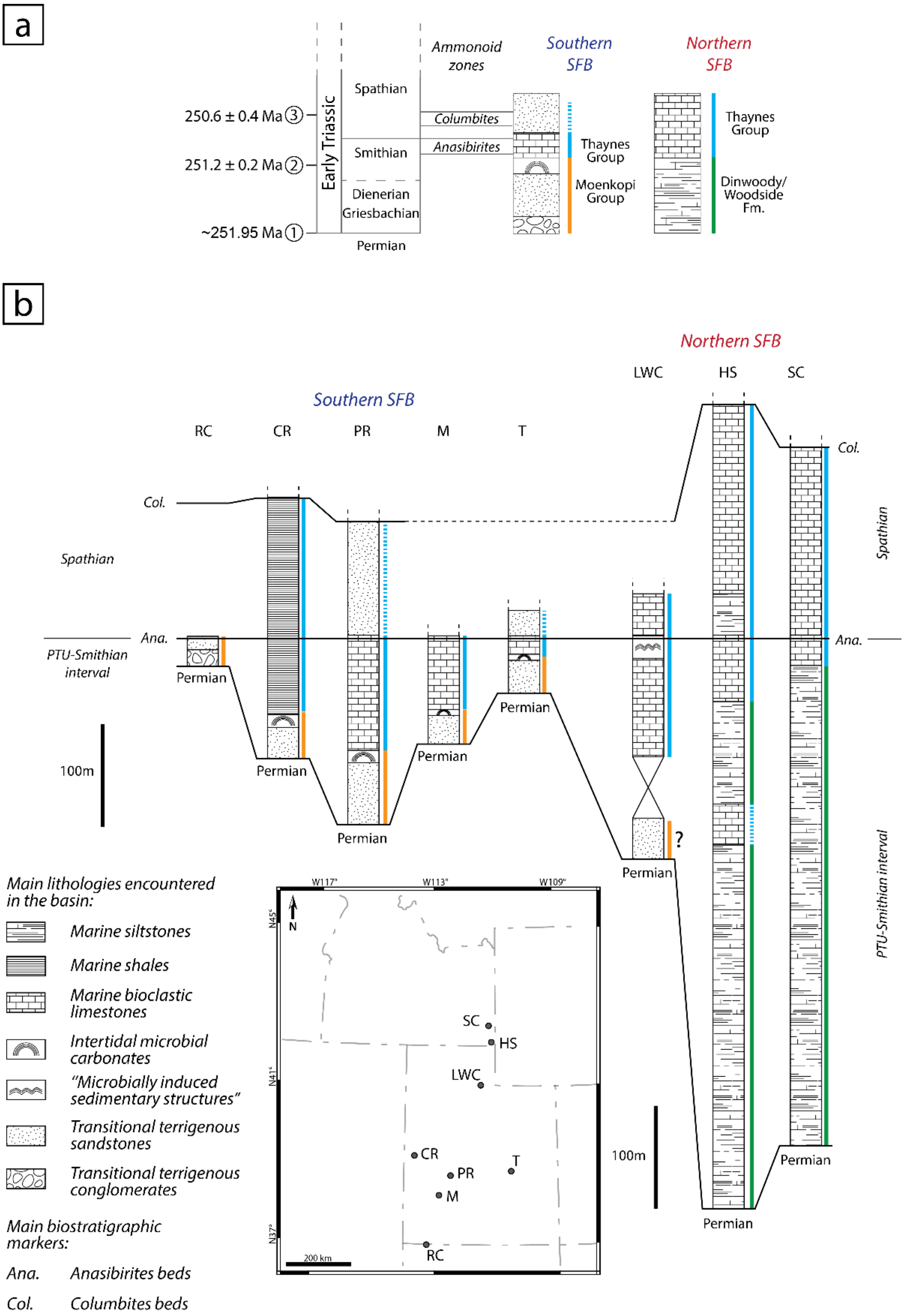

Figure II.B.3: a) Simplified litho- and chronostratigraphic subdivisions in the Early Triassic SFB. Main ammonoid markers (late Smithian *Anasibirites* and early Spathian *Columbites*) are used for biostratigraphical correlation (timeframe from Brayard *et al.*, 2013). Radiometric ages: (1) from Baresel *et al.*, 2017; (2) and (3) from Galfetti *et al.*, 2007a. b) Lithostratigraphic columns for eight selected sections in the SFB, with biostratigraphic correlation (after Caravaca *et al.*, *in press*, see section IV). These columns illustrate the discrepancies in dominant lithologies and in thickness of the sedimentary record between the northern and southern parts of the SFB. Basal and biostratigraphic correlation using timeframe after Brayard *et al.* (2013). RC: Rock Canyon, CR: Confusion Range, PR: Pahvant Range, M: Minersville, T: Torrey, LWC: Lower Weber Canyon, HS: Hot Springs, SC: Sheep Creek.

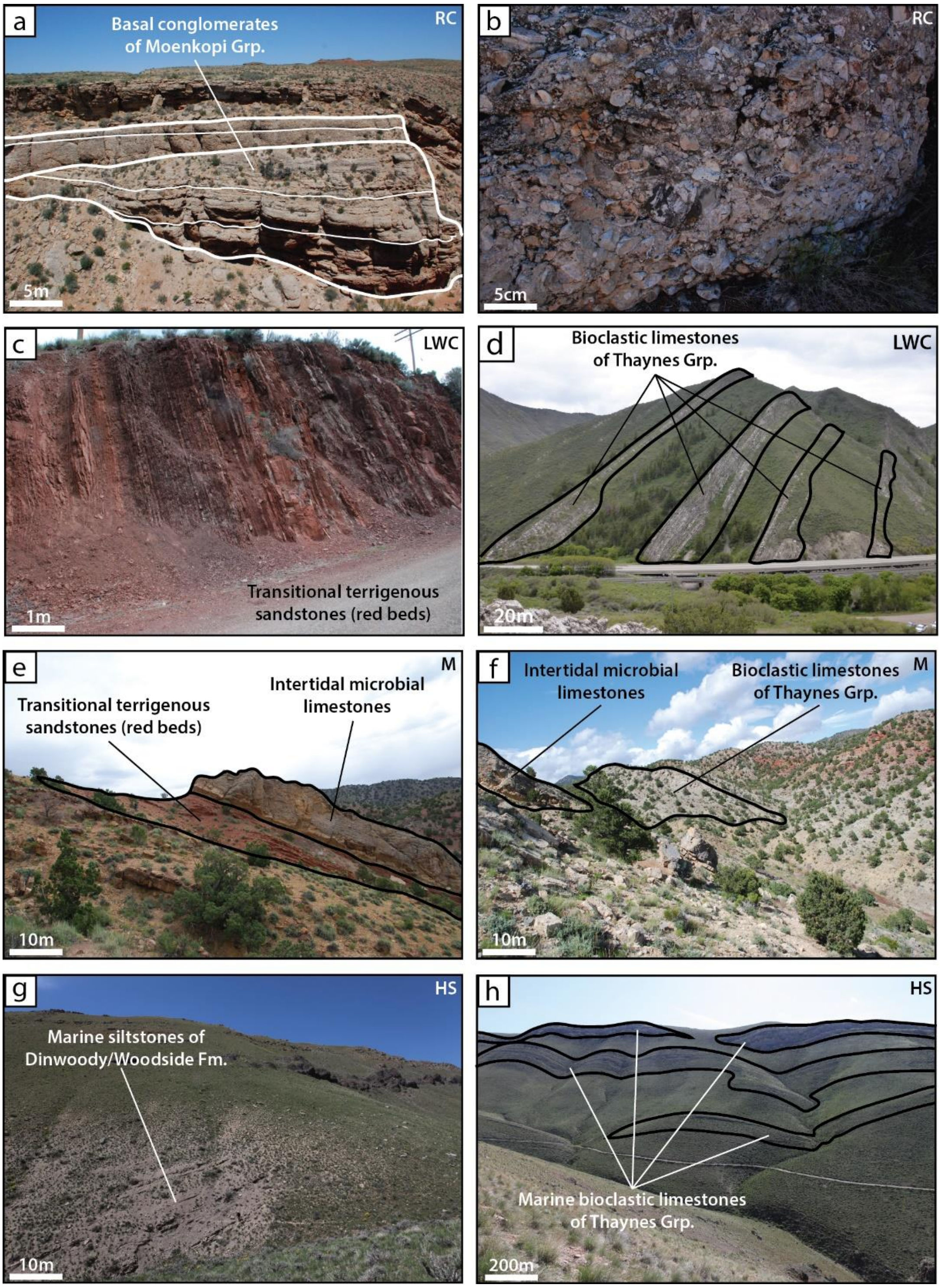

Figure II.B.4: Photographs of different outcrops in the SFB showing variations in dominant lithologies and sedimentary thicknesses (after Caravaca *et al.*, *in press*, see section IV). a) Panorama of Rock Canyon (RC) outcrop, showing plurimetric beds of conglomerates from the basal Moenkopi Group. b) Detail photograph of the conglomerate from RC. c) Photograph of the terrigenous red beds of the Moenkopi Group at Lower Weber Canyon (LWC). d) Panorama of the limestones beds of the Thaynes Group limestones at LWC. e) Panorama of the Moenkopi Group at Minersville (M), showing succession of terrigenous red beds and microbial limestones. f) Panorama of the transition between Moenkopi and Thaynes Groups showing succession of microbial and bioclastic limestones at M. g) Photograph of the marine siltstones of the Dinwoody and Woodside Formations at Hot Springs (HS). h) Panorama of the HS section, showing succession of limestone levels of the Thaynes Group bioclastic limestones. Position of the illustrated sections is indicated on the map in Fig. II.B.3b.

Ongoing works (Jattiot *et al.*, *in prep.*) on the spatio-temporal distribution and abundance of ammonoids within the basin also strongly support this dichotomy hypothesis, showing a clear segregation between some ammonoid genera: for instance, *Wyomingites* is restricted to the northern part of the SFB while *Guodunites* is exclusively present in the southern part (Fig. II.B.5, Jattiot *et al.*, *in prep.*). In terms of abundance, ammonoids also exhibit strong gradients between the northern and the southern parts of the SFB.

This subdivision overlaps with the sedimentary record thus highlighting the tight links between depositional settings and their faunal content. The impact of the local environmental conditions on fossil assemblages is therefore an important factor to be considered.

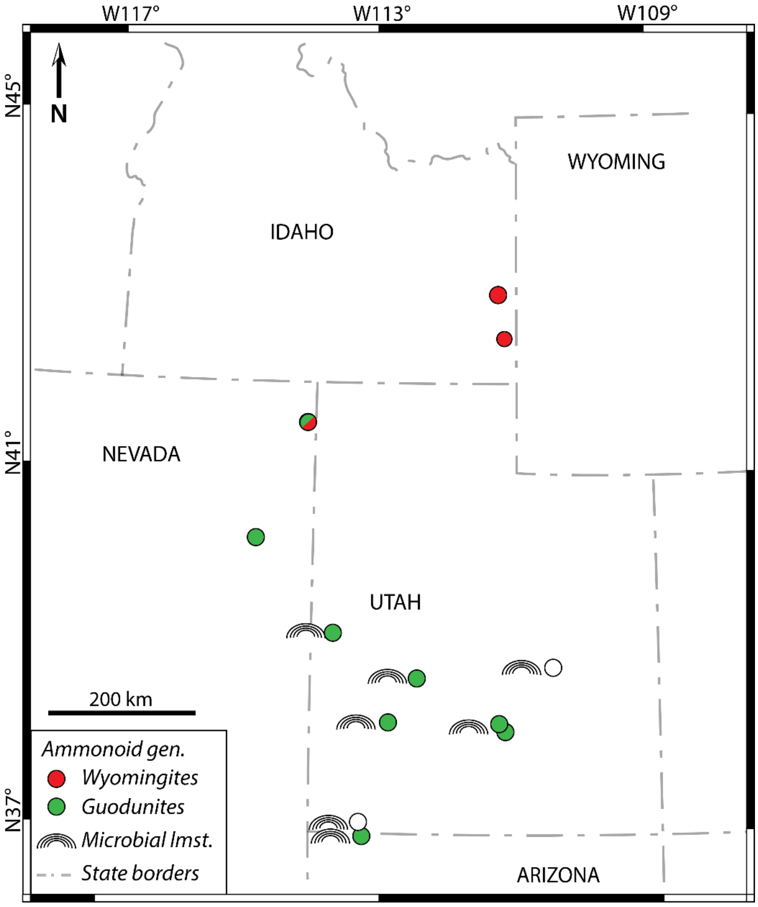

Figure II.B.5: Map illustrating the spatial distribution of some organisms (ammonoids and microbial limestones) found in the SFB and displaying a segregation between the northern and southern parts of the basin (after Brayard *et al.*, 2013; Olivier *et al.*, 2014, 2016, see appendix 1; Vennin *et al.*, 2015; Jattiot *et al.*, *in prep.*).

- Misinterpretations and gap in the geological history of the SFB

Based on the available literature, the SFB remains poorly constrained. Works on the SFB are lacunar and some are outdated and need revisions and reevaluation using modern methods and new field data.

Particularly, the geodynamic evolution of the region related to the foreland basin system during the Sonoma orogeny has not yet been carefully studied notwithstanding its fundamental implications on local paleoenvironmental conditions and their impact on the regional Early Triassic biotic recovery (see e.g. Vennin *et al.*, 2015, for local implication on the development of microbial mats, or Brayard *et al.,* 2017, for locally highly diversified fauna). Moreover, inheritance and role of the basement were not enough taken into account as a major parameter controlling the evolution of the basin and potentially northern and southern sub-basins.

Additionally, regional studies display a strong paleogeographic bias. Indeed, some studies on the northern part of the SFB (e.g. Kummel 1954, 1957; Fig. II.B.6a), or about transgressive episodes in the SFB (Paull & Paull 1993, 1994; Fig. II.B.6b), have been done based on modern positions of exposures and without taking into account the Early Triassic paleogeography of the basin. Outcrops are thus considered at their present-day position and maps are then drawn based on those positions (e.g., Paull & Paull, 1993). As many SFB outcrops are situated in highly tectonized areas and have underwent compressional stresses and transport during the Mesozoic and Cenozoic eras, palinspastic reconstructions are therefore needed to use the actual paleogeography of the SFB at the time of deposition.

Imprecisions concerning the regional facies and evolution of the depositional settings also arose from this lack of a basin-scale integrated work (Figs. II.B.6c and II.B.6d). Reality of the paleoenvironments, their position within the basin, and the potential local controlling factor(s) have to be studied and detailed using a wide range of data (e.g., paleontological, sedimentological or geochemical).

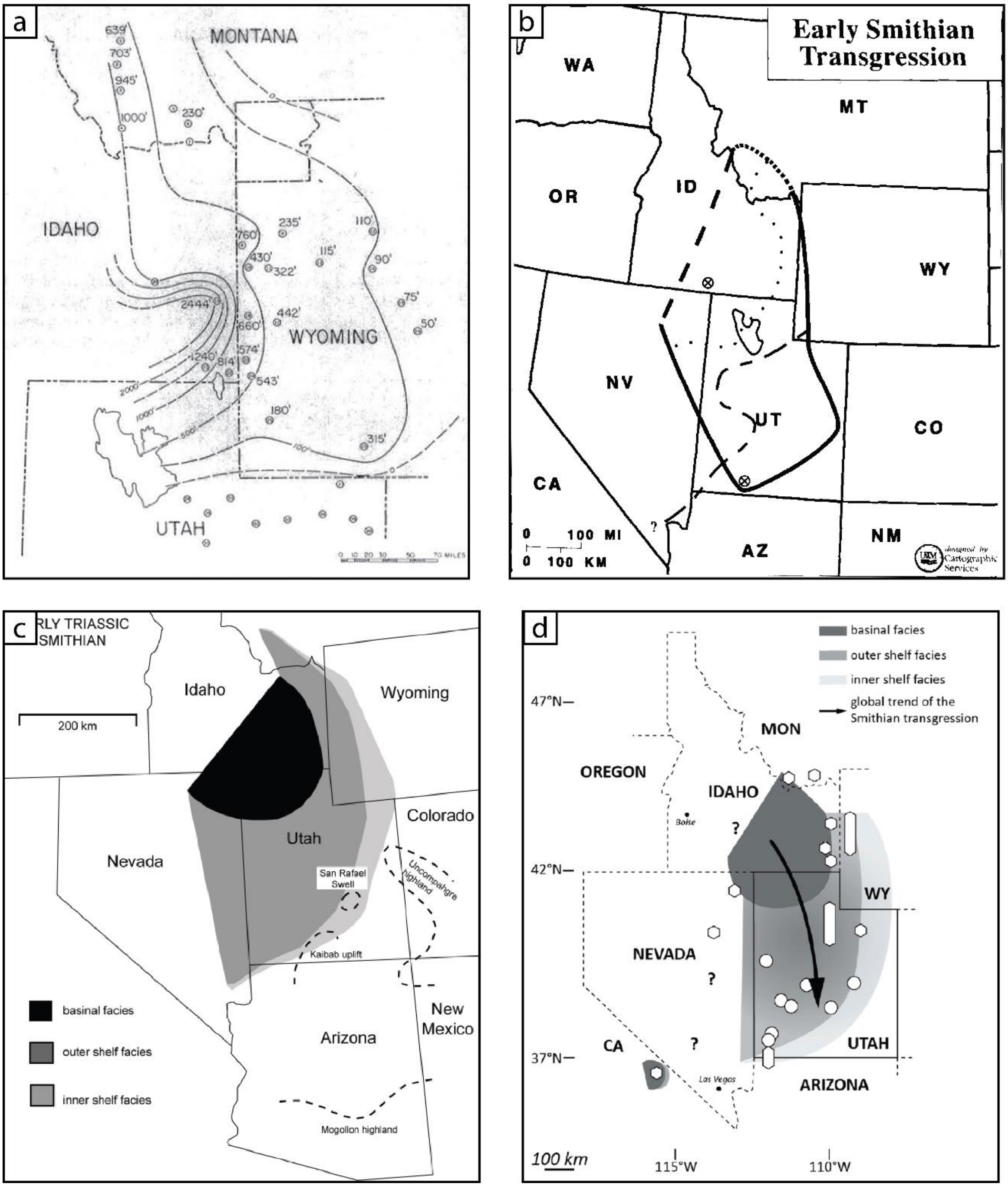

Figure II.B.6: Examples of “erroneous” non-palinspastically reconstructed, and therefore, non-paleogeographic interpretations of the SFB. a) Isopach map of the Dinwoody Fm. (Kummel, 1957). b) Spatial extent of the end-Smithian transgression (Paull & Paull, 1993). c, d) Spatial distribution of oversimplified facies belts of the Thaynes Group during the Smithian (Goodspeed & Lucas, 2007; Brayard *et al.*, 2013).

The western USA Basin exists since the Paleoproterozoic and had a long and complex tectono-sedimentary history that is still active today. Consequently, a strong heritage is present in this region and has played a considerable role throughout the long history of this basin. If many structural events have been tracked down since the first emplacement of the basin basement, some episodes nevertheless remain poorly constrained such as the Sonoma orogeny that occurred at the Permian/Triassic transition.

The Sonoma Foreland Basin (SFB) exhibits an excellent fossil and sedimentary record, being of first importance in the current debate on the Early Triassic biotic recovery. However, previous lacunar studies on this basin left numerous questions on its paleoenvironments and their evolution unanswered. This is especially obvious when documenting the discrepancy in sedimentary record and fossil assemblages existing between the northern and southern parts of the SFB.

Using an original and integrated approach, this work aims to provide a new accurate paleogeographic view of the SFB and its depositional settings, as well as their spatio-temporal evolution. Additionally, this works will focus on the heritage of the region to evaluate (i) if this one possibly exerted a control over the observed North-South discrepancies, and (ii) if yes, what could have been its precise role because it was likely a major control over the geodynamical history of the region up to today.

III. GEOCHEMICAL PARAMETERS OF THE SFB WATER COLUMN

Very few geochemical studies have been conducted within the SFB in the past years despite (i) the growing interest for this area, (ii) the importance of chemostratigraphy for worldwide correlations, and (iii) the significance of geochemistry in addressing the evolution of the paleoenvironment during the Early Triassic. Marenco *et al.* (2008, 2012) provided a few interpretations on the geochemical record of the SFB, but they were spatially and temporally very restricted, as well as focusing on C and S elementary concentrations. Basin-scale analyses covering large intervals within the Early Triassic and using a multi-proxy approach are yet to be conducted in the basin. Only Thomazo *et al.* (2016) proposed such a study of the Minersville section in the southern part of the SFB.

In this chapter, samples from three distant sections covering the Smithian-Spathian transition are analyzed for their geochemical record: Hot Springs (southeastern Idaho), which represents the northern part of the SFB; Lower Weber Canyon (northern Utah) representing a central "transitional (?)" part of the SFB; and Minersville (southwestern Utah) as representative of the southern part of the SFB. These three sections allow to get a larger sight of the SFB record from a geochemical point of view.

Both the paired carbon isotopes record and the concentrations of trace and major (T&M) elements are studied and compared to obtain information on the detailed local evolution of the carbon cycle, detrital fluxes, paleoproductivity and paleoredox conditions in the water column at basin scale.

A. Northern SFB signal: Hot Springs

The northern part of the SFB is represented by the Hot Springs (HS) section located in southeasternmost Idaho. This site was first studied for its sedimentary record by Kummel (1957), where a thick succession is documented for the Early Triassic. Recently, a few paleontological studies (e.g., Romano *et al.*, 2012; Hofmann *et al.*, 2014) were carried out on this section, but its geochemical record remained unstudied until this work.

High-resolution sedimentary and geochemical analyses were performed on a ~900 m-thick section from the Permian up to the lower Spathian, using both paired carbon isotopes and T&M elements. Results and interpretations are presented in Caravaca *et al.*, 2017:

Global and Planetary Change 154 (2017) 10–22

Contents lists available at ScienceDirect

Global and Planetary Change

journal homepage: www.elsevier.com/locate/gloplacha

Early Triassic fluctuations of the global carbon cycle: New evidence from paired carbon isotopes in the western USA basin

Gwénaël Caravaca[a,*], Christophe Thomazo[a], Emmanuelle Vennin[a], Nicolas Olivier[b], Théophile Cocquerez[a], Gilles Escarguel[c], Emmanuel Fara[a], James F. Jenks[d], Kevin G. Bylund[e], Daniel A. Stephen[f], Arnaud Brayard[a]

[a] Biogéosciences UMR6282, CNRS, Univ. Bourgogne Franche-Comté, 6 Boulevard Gabriel, 21000 Dijon, France
[b] Laboratoire Magmas et Volcans, Univ. Clermont Auvergne, CNRS, 6 Avenue Blaise Pascal, 63178 Aubière Cedex, France
[c] Univ. Claude Bernard Lyon 1, CNRS, ENTPE, UMR 5023 LEHNA, 69622 Villeurbanne Cedex, France
[d] 1134 Johnson Ridge Lane, West Jordan, UT 84084, USA
[e] 140 South 700 East, Spanish Fork, UT 84660, USA
[f] Department of Earth Science, Utah Valley University, Orem, UT 84058, USA

ARTICLE INFO

Keywords:
Early Triassic
Paired carbon isotopes
Net isotopic effect
Western USA basin
Smithian
Spathian

ABSTRACT

In the aftermath of the catastrophic end-Permian mass extinction, the Early Triassic records recurrent perturbations in the carbon isotope signal, most notably during the Smithian and through the Smithian/Spathian Boundary (SSB; ~1.5 myr after the Permian/Triassic boundary), which show some of the largest excursions of the Phanerozoic. The late Smithian also corresponds to major biotic turnovers and environmental changes, such as temperature fluctuations, that deeply impacted the recovery after the end-Permian mass extinction. Here we document the paired carbon isotope signal along with an analysis of the trace and major elements at the long-known Hot Springs section (southeastern Idaho, USA). This section records Early Triassic sediments from the Griesbachian-Dienerian up to the lower Spathian. We show that the organic and carbonate $\delta^{13}C$ variations mirror the signals identified at a global scale. Particularly, the middle Smithian-SSB event represented by a negative-positive isotopic couplet is well identified and is not of diagenetic origin. We also document a positive excursion potentially corresponding to the Dienerian/Smithian Boundary. Observed Smithian-Spathian excursions are recorded similarly in both the organic and carbonate reservoirs, but the organic matter signal systematically shows unexpectedly dampened variations compared to its carbonate counterpart. Additionally, we show that variations in the net isotopic effect (i.e., $\Delta^{13}C$) probably resulted from a complex set of forcing parameters including either a mixing between terrestrial and marine organic matter depending on the evolution of the depositional setting, or variations in the biological fractionation. We establish that the $\Delta^{13}C$ signal cannot be directly related to CO_2-driven temperature variations at Hot Springs. Even though the carbon isotope signal mirrors the Early Triassic variations known at the global scale, the Hot Springs signal probably also reflects local influences on the carbon isotopes that are neither diagenetic nor representative of the global exogenic carbon cycle.

1. Introduction

The Early Triassic (~252 to ~247 Ma; Galfetti et al., 2007a; Baresel et al., 2017) is generally portrayed as a time interval of high ecological stress in the aftermath of the end-Permian mass extinction. This interval is also characterized by large-scale fluctuations of the carbon cycle and harsh marine conditions, including a combination of ocean acidification, euxinia, extreme seawater temperature and fluctuating productivity (e.g., Payne and Clapham, 2012; Song et al., 2012; Sun et al., 2012; Romano et al., 2013; Pietsch and Bottjer, 2014). Various geochemical analyses indicate that fluctuations in sea surface temperatures (SST) continued throughout the Early Triassic, sometimes being associated with large and rapid $\delta^{13}C$ shifts (Payne et al., 2004; Galfetti et al., 2007a; Grasby et al., 2013; Sun et al., 2012; Romano et al., 2013) and marked extinction events (e.g., Orchard, 2007; Brayard et al., 2009; Hochuli et al., 2016). Several works have documented a marked $\delta^{13}C$ negative excursion during the middle Smithian, immediately followed by a positive excursion across the Smithian/Spathian Boundary (SSB) in

---

[*] Corresponding author.
E-mail address: gwenael.caravaca@u-bourgogne.fr (G. Caravaca).

http://dx.doi.org/10.1016/j.gloplacha.2017.05.005
Received 1 February 2017; Received in revised form 17 May 2017; Accepted 17 May 2017

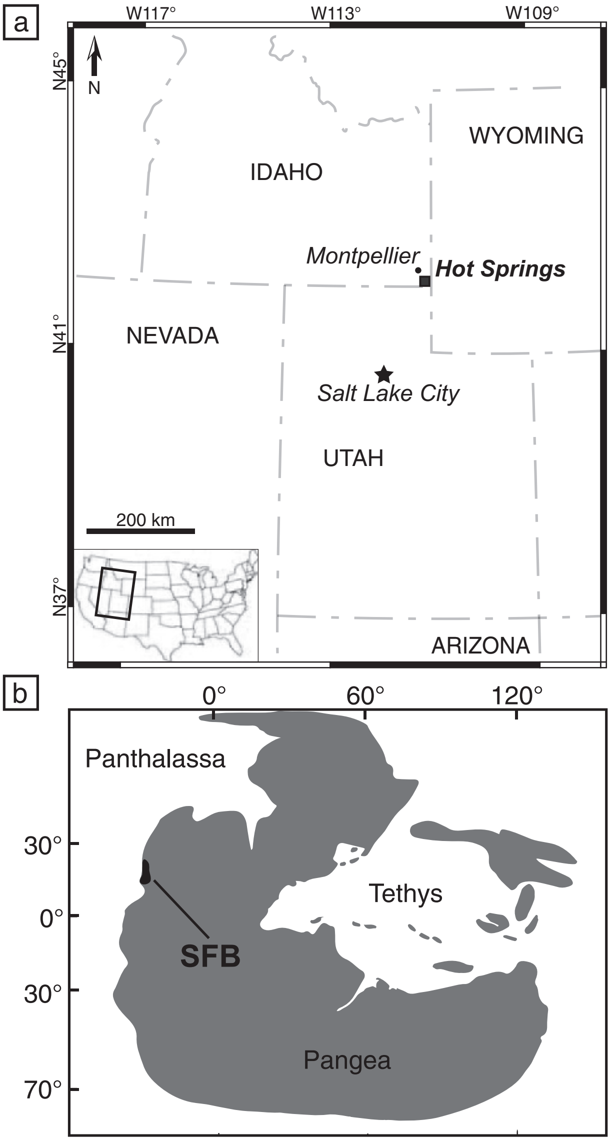

Fig. 1. (a) Map of the studied area and location of the Hot Springs section. (b) Early Triassic location of the Sonoma Foreland Basin.

different paleoenvironments within the Tethys and northern Panthalassa (Payne et al., 2004; Galfetti et al., 2007a, 2007b; Horacek et al., 2007a, 2007b, 2009; Hermann et al., 2011; see also Fig. 1 in Thomazo et al., 2016). This global signal is measured either on carbonate or organic matter (e.g., Grasby et al., 2013). However, it is rarely documented in both reservoirs simultaneously (see discussion in Thomazo et al., 2016). The observed signal is thus commonly interpreted to result from variations in the $\delta^{13}C$ of the seawater dissolved inorganic carbon (DIC) reservoir (e.g., Zeebe, 2012). Proposed triggering mechanisms for the middle Smithian negative excursion involve (i) a massive release of ^{12}C-enriched CO_2 from volcanogenic (Sobolev et al., 2011) or thermogenic (Payne and Kump, 2007) sources, or (ii) a decrease in the organic carbon flux buried in the sedimentary record (Payne et al., 2004; Meyer et al., 2011). Concomitant periods of sustained authigenic carbonate production, decoupled from the seawater DIC reservoir, have also been documented based on carbon and sulfur isotope signals (Thomazo et al., 2016). Globally, the carbon isotope signal around the Dienerian/Smithian Boundary is less known than for the middle Smithian and the SSB due to worldwide uncertainties of biostratigraphy, synchronicity and magnitude of observed $\delta^{13}C$ excursions (e.g., Horacek et al., 2007b).

Greenhouse climate conditions prevailed during the middle-upper Smithian, in combination with anoxia on some shelf environments and potential acidification of surface waters due to elevated pCO_2 attributed to large-scale greenhouse gas injections from the Siberian traps (Galfetti et al., 2007a; Romano et al., 2013). These harsh conditions may have turned lethal for marine faunas (Song et al., 2009; Sun et al., 2012; Pietsch and Bottjer, 2014; Pietsch et al., 2016). Relative cooling events are observed during the lower Smithian and lower Spathian. They are interpreted to result from the drawdown of CO_2 by an enhanced biological pump (Payne and Kump, 2007). The global scenario arising from these studies is therefore a direct link between potential temperature variations and fluctuations in the exogenic carbon cycle: the "cool" lower Smithian and lower Spathian could be associated with a sustained biological pump and high $\delta^{13}C$ records, disrupted by a warming event during the middle-upper Smithian triggered by ^{12}C-enriched CO_2 atmospheric releases due to intense volcanism. These fluctuations may have generated a biotic crisis during the upper Smithian.

Direct access to the geological record of CO_2 concentrations is a challenging question (e.g., Retallack, 2001). However, coupled carbon isotope data from organic matter and carbonate measured in pristine rocks (i.e., not affected by diagenetic remobilization) can provide insights about changing concentrations of dissolved CO_2 in the ocean ($[CO_2]_{aq}$) (Hayes et al., 1999; Sansjofre et al., 2011). Indeed, the carbon isotope difference measured between carbonates and organic matter, $\Delta^{13}C_{carb-org}$, strongly depends on the $[CO_2]_{aq}$ (Hayes et al., 1999). Only a few studies reported paired carbon measurements performed on the same samples through the critical Smithian-Spathian transition (Brühwiler et al., 2009; Hermann et al., 2011; Meyer et al., 2013; Sun et al., 2015; Thomazo et al., 2016). Additionally, available $\Delta^{13}C_{carb-org}$ datasets from these studies cannot be used to reconstruct $[CO_2]_{aq}$ on the Smithian-Spathian interval because the resolution of the sampling is not sufficient (Brühwiler et al., 2009; Hermann et al., 2011; Meyer et al., 2013; Sun et al., 2015) or because of the secondary (e.g., diagenetic) modification of the isotopic record (Thomazo et al., 2016). Here we perform high-resolution measurements of the paired carbon isotope signal together with elementary (trace and major elements) compositions of 177 pristine samples encompassing the middle to upper (?) Permian to lower Spathian interval at the Hot Springs section (southeastern Idaho, USA). We show that the carbon isotope signals of both carbonate and organic matter are primary and are coupled through multiple $\delta^{13}C$ excursions. Our results reveal that the magnitudes of the isotopic shifts are dampened in the organic matter reservoir compared to its inorganic carbonate counterpart. The resulting variations in the $\Delta^{13}C_{carb-org}$ signal are discussed in terms of mixing with the detrital flux of organic matter and changes in biological fractionation.

2. Geological settings

Sampling has been carried out on the Permian to lower Spathian sedimentary succession of the Hot Springs (HS) section (GPS coordinates: N42.114299°, W-111.249599°; ~24 km south of Montpelier, Idaho, Fig. 1a). These sediments reflect deposition within the highly-subsiding northern part of the shallow Sonoma Foreland Basin (SFB) (Kummel, 1954, 1957; Caravaca et al., in press). This basin was located on the western Pangea margin at a near-equatorial position during the Early Triassic (Fig. 1b). The base of the section encompasses middle to upper(?) Permian sediments characterized by phosphatic spiculites of the Phosphoria Fm. (Wardlaw and Collison, 1986; Carrol et al., 1998), and the major regional Permian-Triassic unconformity (PTU; Brayard et al., 2013). Recent findings by Davydov et al. (2016) suggested the potential existence of a continuous Permian-Triassic (PT) record in neighboring localities of southernmost Idaho. However, at HS, only evidence for a discontinuity has been observed between Permian and Triassic sediments. For instance, conglomerates reworking phosphatic clasts from the underlying Phosphoria Fm. occur at the base of the Triassic part of the section (see below and Paull and Paull, 1986; Wignall and Hallam, 1992). No accurate age is known for deposits

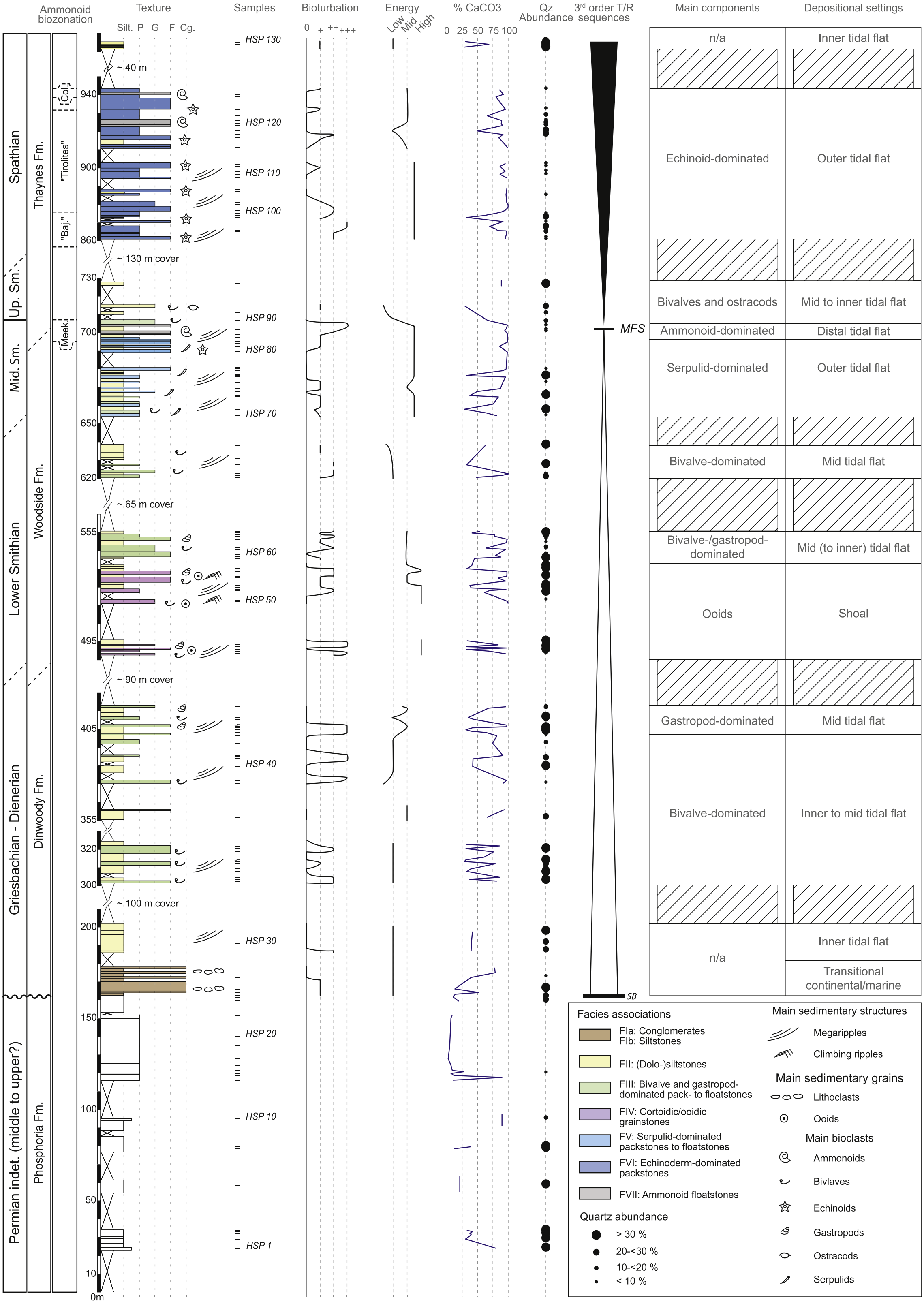

Fig. 2. Synthetic log of the Hot Springs section showing the stratigraphic position of ammonoid beds and geochemical samples. The sequential framework, facies and depositional settings, as well as carbonate contents (% $CaCO_3$) are indicated (see Table 1 and Supplementary Table S1 for details). Formations after Kummel (1954) and Wardlaw and Collison (1986). Synthetic ammonoid biozonation after Guex et al. (2010), Brayard et al. (2013), and Jenks et al. (2013); Meek.: *Meekoceras* beds; "Baj.": "*Bajarunia*" beds; "Tirolites": "*Tirolites*" beds; Col.: *Columbites* beds. Mid. Sm.: middle Smithian; Up. Sm.: upper Smithian. MFS: Maximum Flooding Surface. (For interpretation of the references to color in this figure legend, the reader is referred to the web version of this article.)

immediately below the PTU, but following Davydov et al. (2016), part of them might be Upper Permian in age. Permian part of the hiatus included within the PTU is therefore hard to precisely constrain, but might be of long duration regarding the Late Permian.

The siltstones and carbonates of the Early Triassic Dinwoody, Woodside and Thaynes formations at the HS section were deposited in proximal marine environments (Kummel, 1954) and illustrate the global rise in sea level recorded for the Early Triassic (Haq et al., 1987; Embry, 1997). No marked unconformity can be observed between each successive formation along the section and at the scale of southeastern Idaho (e.g., Kummel, 1957; Paull and Paull, 1993) and no major erosion nor reworked material can be observed within these levels. The upper part of the HS section is biostratigraphically well calibrated using the regional synthetic frame including the successive middle Smithian to lower Spathian ammonoid *Meekoceras*, "*Bajarunia*", "*Tirolites*" and *Columbites* beds, which are commonly found in the SFB (Kummel, 1954, 1957; Guex et al., 2010; Brayard et al., 2013; Jenks et al., 2013; Jattiot et al. in press; Fig. 2). Lower strata of the Dinwoody Fm. are Griesbachian to Dienerian based on the occurrence of *Claraia* and lingulid beds (e.g., Kummel, 1954, 1957). This is supported by the presence of conodonts *Hindeodus typicalis* and *Isarcella isarca* in the basal beds indicating a mid-Griesbachian age (Paull et al., 1985). Usually, the lower boundary of the Thaynes Fm. is regionally identified at the base of the Smithian ledge-forming *Meekoceras* beds for convenience. However, these limestone deposits are included within a high-order sequence in continuity with underlying rocks (e.g., Embry, 1997) and only represent part of the early-middle Smithian (Jattiot et al. in press). It thus implies that the Dienerian/Smithian boundary (DSB) as well as the lower to middle Smithian transition at HS are mainly recognized using regional lithostratigraphy (after e.g. Kummel, 1954, 1957) and also by chemostratigraphy using comparisons with known global carbon isotopic signals (e.g., Payne et al., 2004; Galfetti et al., 2007a; Richoz et al., 2007; Horacek et al., 2009; Hermann et al., 2011; Grasby et al., 2013). Comparisons with other known carbon isotopic signals worldwide indicate that the Dienerian to middle Smithian transition is probably an expanded succession at HS. This is in agreement with the high sedimentation rates reported for this place and time interval (~650 m/Myr, Caravaca et al., in press). As the DSB is not yet formally defined based on biostratigraphical markers (see proposals of Tong et al., 2004; Krystyn et al., 2007 and Richoz et al., 2007), we determined its approximate position by using a positive $\delta^{13}C$ excursion, as observed at some other localities (e.g., Horacek et al., 2007a, 2007b, 2007c; Hermann et al., 2011; Clarkson et al., 2013; Metcalfe et al., 2013). Overall, the HS section shows an almost continuous Early Triassic succession up to the middle Spathian, although minor hiatuses under the temporal resolution of this work might exist without significant consequence on our interpretations of the geochemical trends.

3. Sedimentary features and depositional environment

The Early Triassic part of the HS section consists of a succession of fine marine siltstones (Griesbachian to early Smithian; historically assigned to the Dinwoody and Woodside Fms. of Kummel, 1954, 1957) and bioclastic carbonates (Smithian-Spathian Thaynes Fm.), with an increasing amount of carbonate components toward the top of the section (Fig. 2). The depositional environments reflect a large and shallow inner ramp evolving from an embayment system to an open tidal flat. Seven facies (FI to FVII, Table 1) help to discriminate three main environmental domains: (1) transitional continental to marine, (2) tidal flat and (3) open marine.

3.1. Transitional continental to marine environment

At the very base of the section, channelized dm-thick conglomerates (FI; Fig. 2, Table 1) are composed of pluri-centimetric clasts. Channels (FIa) are embedded in siltstones (FIb) and barren of faunas. Clasts observed in conglomerate facies FIa are derived from the underlying Permian Phosphoria Fm. and indicate a local reworking of this material. The low biotic content (rare bivalves), the channelized conglomerates and the silt-dominated facies argue for a transitional continental to marine domain in a flood plain embayment.

3.2. Tidal flat

The tidal flat environment is characterized by five facies consisting of mixed siliciclastic and carbonate components that together indicate a transition from inner to outer tidal flat settings. The vertical and lateral successions of facies suggest a "facies mosaic" pattern (as illustrated in Wright and Burgess, 2005; Vennin et al., 2015; Olivier et al., 2016). The (dolo)siltstones (FII; Fig. 2, Table 1) show rare organisms, mud-draping, rare dm- to pluri-metric megaripples and locally-abundant bioturbations and indicate the most proximal, low to moderate energy and tide-dominated conditions. Its terrigenous content (up to > 30%, Fig. 2) mainly consists of sub-rounded (locally sub-angular) quartz grains, with a mean size around 70 μm. Mica and glauconite grains can also be found locally. The bivalve and gastropod-rich facies (FIII; Fig. 2, Table 1) is associated with dm- to m-thick beds of dolosiltstones (facies FII, Fig. 2). It shows dm- to pluri-metric megaripples. The presence of mud-drapes, mudclasts and bidirectional laminations argues for a tide-dominated environment (Johnson and Baldwin, 1996). These facies correspond to inner to mid tidal flat settings. They vertically change into cortoidic and ooidic packstones to grainstones (FIV; Fig. 2, Table 1) deposited in subtidal high-energy shoals, as indicated by the presence of type 1 ooids (Strasser, 1986). The serpulid-dominated packstones to floatstones (FV; Fig. 2, Table 1) display the highest carbonate content of the whole section (up to ~99%), and are associated with the presence of hummocky cross-stratifications and bioclast-dominated tempestitic beds. The echinoderm-dominated packstones (FVI; Fig. 2, Table 1) are marked by a recrudescence of terrigenous inputs during the lower Spathian (compared to the middle-upper Smithian). Both serpulid- and echinoderm-dominated facies display dm- to m-megaripples and represent outer tidal flat settings.

3.3. Open marine environment

The more open marine conditions recorded in the section correspond to the middle Smithian ammonoid floatstones (FVII; Fig. 2, Table 1). These beds show accumulations of ammonoid shells, as well as intense bioturbation. They correspond to the maximum flooding surface recorded at HS (Fig. 2). This agrees with the regional 3rd order cyclicity observed elsewhere in the basin (e.g., Mineral Mountains area, Vennin et al., 2015) or at a larger scale (Embry, 1997). This facies represents distal tidal flat settings.

4. Analytical methods

A total of 177 bulk rock samples were collected. Bulk rock samples were sorted to eliminate recrystallizations and calcified veins, and then powdered to < 60 μm using a ring and puck mill at the Biogéosciences Laboratory of the Université de Bourgogne Franche-Comté, Dijon, France. Organic carbon isotope compositions ($\delta^{13}C_{org}$) and Total Organic Carbon (TOC) contents were measured on carbonate-free residues. Sample powders reacted with HCl (6 N) at room temperature for 24 h followed by 4 h at 80 °C to remove carbonate phases (Thomazo et al., 2009). Residues were rinsed with deionized distilled water until neutral, centrifuged (3500 rpm for 5 min), and dried at 50 °C overnight. Aliquots of dried decarbonated samples (~3–60 mg) were then weighed in tin capsules. TOC content and $\delta^{13}C_{org}$ measurements were performed at the Biogéosciences Laboratory of the Université de Bourgogne Franche-Comté, Dijon, France, on a Vario MICRO cube elemental analyzer (Elementar, Hanau, Germany) coupled in contin-

Table 1
Description and characterization of the 7 facies identified in the Hot Springs section and their corresponding depositional settings.

Facies	Biotic components	Non–biotic elements	Matrix	Preservation	Structures	Energy	Depositional setting	Main environmental domains
FI: (a) Conglomerates and (b) siltstones	Rare bivalves, vertebrate fragments	(a) Sub–rounded to sub–angular clasts, phosphatic grains, ooids, peloids; (b) quartz grains	(a) and (b) Peloids and silts	(a) Broken shells	(a) Erosion base, matrix supported, m–to dam channels; (b) silty facies	High (a) to low (b)	Flood plain embayment;	Transitional continental to marine environment
FII: (a) (Dolo–) siltstones and (b) Ostracod–rich laminated mudstones	Bivalves, and (b) ostracods	(a) Sub–rounded silty terrigenous elements (mainly quartz, micas), rare peloids and glauconite grains; (b) Dolo–mudstones	Micrite and microsparite, dolomite	Locally fragmented shells, bioturbation	(a) Mud drapes, planar to oblique laminations, loading structures, ripples and dm–to m–megaripples; (b) laminated dolomudstones with fenestral porosity (possible microbial structures?)	Low to medium	Inner tidal flat	Tidal flat
FIII: Bivalve and gastropod–dominated packstones to floatstones	Bivalves, gastropods, rare echinoderms and very rare serpulids	Terrigenous silty grains (quartz, mica), mudclasts, phosphatic grains	Microdolomite	Bioturbation (high intensity), locally oriented and disarticulated bivalves, fragmented and complete gastropods, "umbrella" structures under valves	Dm–to m (locally pluri–m) megaripples, mud drapes	Medium to high	Mid tidal flat	
FIV: Cortoidic/ooidic packstonesto grainstones	Bivalves, gastropods, echinoderms, rare vertebrate fragments	Cortoids, ooids (type 1, Strasser, 1986), peloids, phosphatic and quartz grains	Peloids or micrite, microsparite	Fragmented and disarticulated shells	Ripples, climbing ripples, m–to pluri–m megaripples	High to very high	Shoal	
FV: Serpulid–dominated packstones to floatstones	Serpulids, echinoderms, bivalves, gastropods, rare foraminifera	Rare terrigenous silty grains	Micrite, microdolomicrite	Fragmented echinoderms, coalescent reworked serpulids, bioturbation	Bioclast–dominated tempestites (showing grading), HCS (dm–high)	Medium to high	Outer tidal flat	
FVI: Echinoderm–dominated packstones	Echinoderms, bivalves, gastropods and rare brachiopods(?)	Quartz grains	Micrite and microdolomite	Bioturbation (local high intensity),	Ripples and dm–to m–megaripples	High		
FVII: Ammonoid floatstones	Ammonoids, serpulids, echinoderms, bivalves and gastropods	Rare peloids	Micrite	complete and oriented ammonoids	Bioaccumulations	Medium	Distal tidal flat	Open marine environment

uous flow mode to an IsoPrime stable isotope ratio mass spectrometer (Isoprime, Manchester, UK). USGS40 certified reference material (C = 40.8 wt%; $\delta^{13}C_{VPDB} = -26.2‰$) was used for calibration. The carbon isotopic composition is expressed in delta notation and reported in permil (‰) relative to the Vienna Pee Dee Belemnite (VPDB) standard; external reproducibility based on duplicate analyses of samples is better than ± 0.2‰ (1σ). Results are reported in Supplementary Table S1.

Carbonate carbon and oxygen isotope analyses ($\delta^{13}C_{carb}$ and $\delta^{18}O_{carb}$) were carried out on powdered bulk-rock samples at the Biogéosciences Laboratory of the Université de Bourgogne Franche-Comté, Dijon, France. The samples (300 to 6000 μg) were loaded into septum screwed glass tubes for isotopic analyses. The tubes were flushed via the autosampler with He and evacuated to remove atmospheric gases. Each sample was reacted with 500 μl of 100% phosphoric acid at 90 °C for 17 min using an online carbonate preparation line coupled to an Isoprime Elementar mass spectrometer (Isoprime, Manchester, UK). Inorganic carbonate content (% $CaCO_3$) was quantified manometrically from the CO_2 yield; all isotopic values are reported in the standard δ-notation in permil (‰) relative to VPDB by assigning a $\delta^{13}C$ value of $+1.95‰$ and a $\delta^{18}O$ value of $-2.20‰$ to the NBS19 international standard. The long-term reproducibility of the NBS19 replicate analyses (three months) is better than ± 0.1‰ (1σ) and ± 0.12‰ (1σ) for carbon and oxygen isotopes, respectively. Results are reported in Supplementary Table S1.

Major and trace element analyses were performed on 108 selected samples using an ICP-MS at the Activation Laboratory (Actlabs) in Ancaster, Canada. The method used is Lithium Metaborate/Tetraborate Fusion ICP and ICP-MS. Reproducibility was checked by seven duplicate and replicate analyses of laboratory standards, and is better than

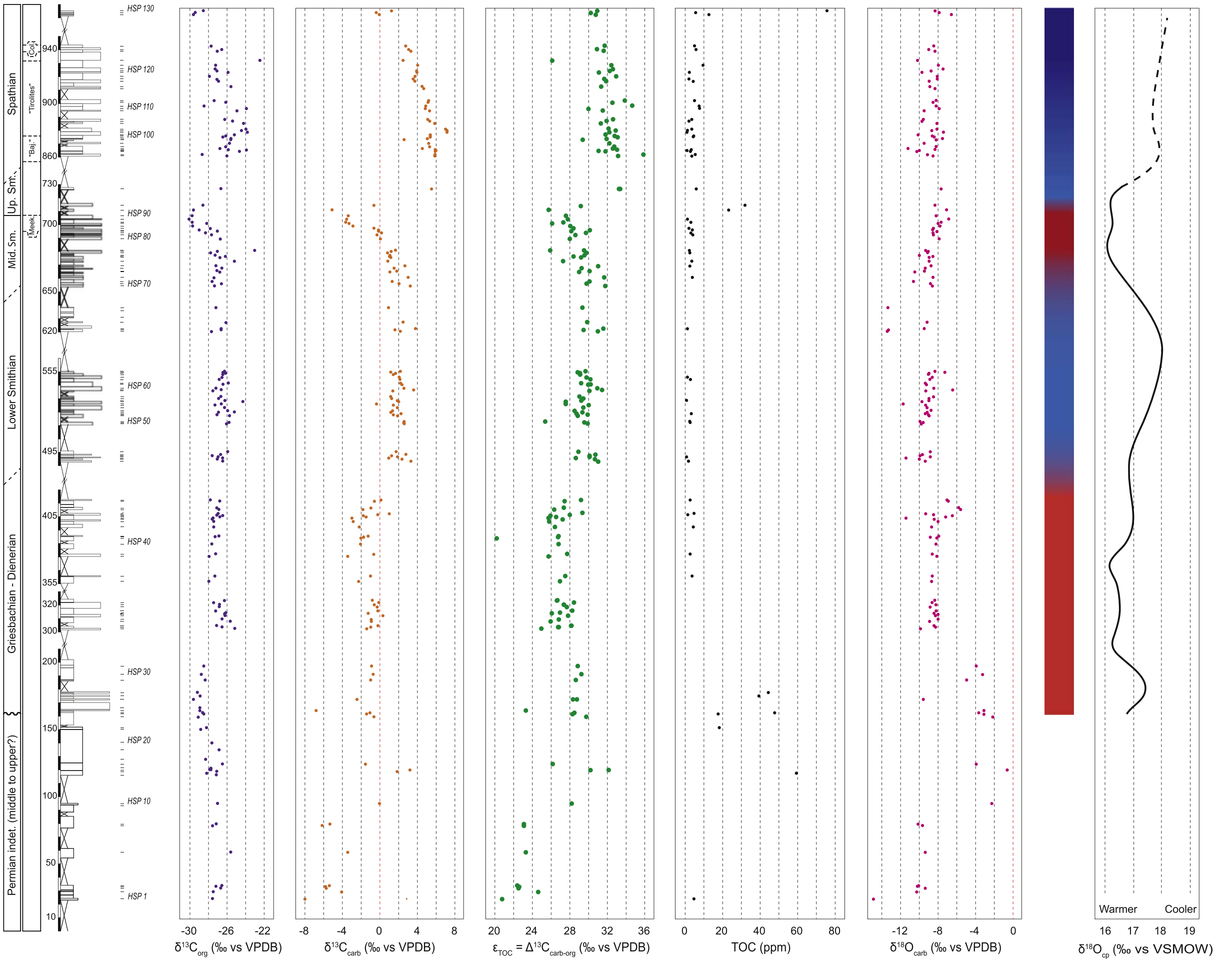

Fig. 3. $\delta^{13}C_{org}$, $\delta^{13}C_{carb}$ and net isotopic effect $\Delta^{13}C_{carb\text{-}org}$ ($= \varepsilon_{TOC}$) with Total Organic Carbon (TOC) contents and $\delta^{18}O_{carb}$ signal in the Hot Springs section. 2 outliers have been removed for clarity (see Supplementary Table S1). $\delta^{18}O_{cp}$ (obtained from conodont pectiniform elements) and paleotemperature trends for the Early Triassic are added and modified after Romano et al. (2013). (For interpretation of the references to color in this figure legend, the reader is referred to the web version of this article.)

2% (1σ) for major and trace elements. Results are reported in Supplementary Table S2.

5. Results

5.1. Carbonate concentration and isotope signal

Overall, carbonate concentration shows an important variability with a mean value of 66.4 (± 29.4 wt%, 1σ, Fig. 2, Supplementary Table S1). Highest concentrations are reached in serpulid- and ammonoid-dominated facies (FV and FVII, Fig. 2) near and within the *Meekoceras* beds (middle Smithian), with lasting high carbonate concentrations up to 99.0 wt%. The $\delta^{13}C_{carb}$ values vary from − 8.0 to + 7.2‰, with a mean value of 1.0 (± 3.1‰, 1σ, Fig. 3, Supplementary Table S1). The $\delta^{13}C_{carb}$ signal records three significant variations along the section: a ^{13}C-enrichment across the potential Dienerian/Smithian Boundary (DSB); a negative isotopic excursion during the middle Smithian, followed by a positive peak across the SSB; and a decreasing trend (^{12}C-enrichment) toward the top of the section. The $\delta^{18}O_{carb}$ signal ranges from − 14.9 to − 0.6‰, with a mean value of − 8.5‰ (± 1.9‰, 1σ, Fig. 3 & Supplementary Table S1). No significant trend is observed throughout the Triassic part of the section, but strong covariation of the $\delta^{13}C_{carb}$ and of the $\delta^{18}O_{carb}$ signals is evidenced during the Permian interval (Fig. 3). The positive trend in $\delta^{13}C_{carb}$ observed here through the DSB is in agreement with several signals reported worldwide (e.g., Horacek et al., 2007a, 2007b, 2007c; Richoz et al., 2007; Hermann et al., 2011; Clarkson et al., 2013; Metcalfe et al., 2013). The identified DSB shift is of smaller magnitude than that of the SSB (Fig. 3).

5.2. Organic matter concentration and isotope signals

Overall, the TOC concentration ranges from 1.0 to 75.6 ppm, with a mean value of 9.2 ppm (± 15.0 ppm, 1 σ, Fig. 3, Supplementary Table S1). The TOC concentration shows low values and almost no variation along the section, except for an important peak in the upper Smithian (32.0 ppm), and small-scale variations during the Permian (from ~30 to 60 ppm). Throughout the section, the $\delta^{13}C_{org}$ ranges from − 30.1 to − 22.4‰, with a mean value of − 27.0 (± 1.3‰, 1 σ, Fig. 3, Supplementary Table S1). The $\delta^{13}C_{org}$ signal records similar variations to that of the $\delta^{13}C_{carb}$ signal except for the DSB where no variation is observed. A negative isotopic excursion during the middle Smithian, followed by a positive peak across the SSB is observed, as well as a decreasing trend (^{12}C-enrichment) toward the top of the section.

5.3. Paired carbon isotopes signal

The $\Delta^{13}C_{carb\text{-}org}$ signal shows a strong variability between 18.95 and 34.6‰, with a mean value of 27.8 (± 2.7‰, 1σ, Fig. 3, Supplementary Table S1). Its evolution follows that of the above-mentioned $\delta^{13}C_{carb}$ and $\delta^{13}C_{org}$ signals, with three significant excursions along the section. First, a large increase in $\Delta^{13}C_{carb\text{-}org}$ values is observed across the DSB. Second, a coeval and equally important decrease is demonstrated during the middle Smithian, immediately followed by a positive peak

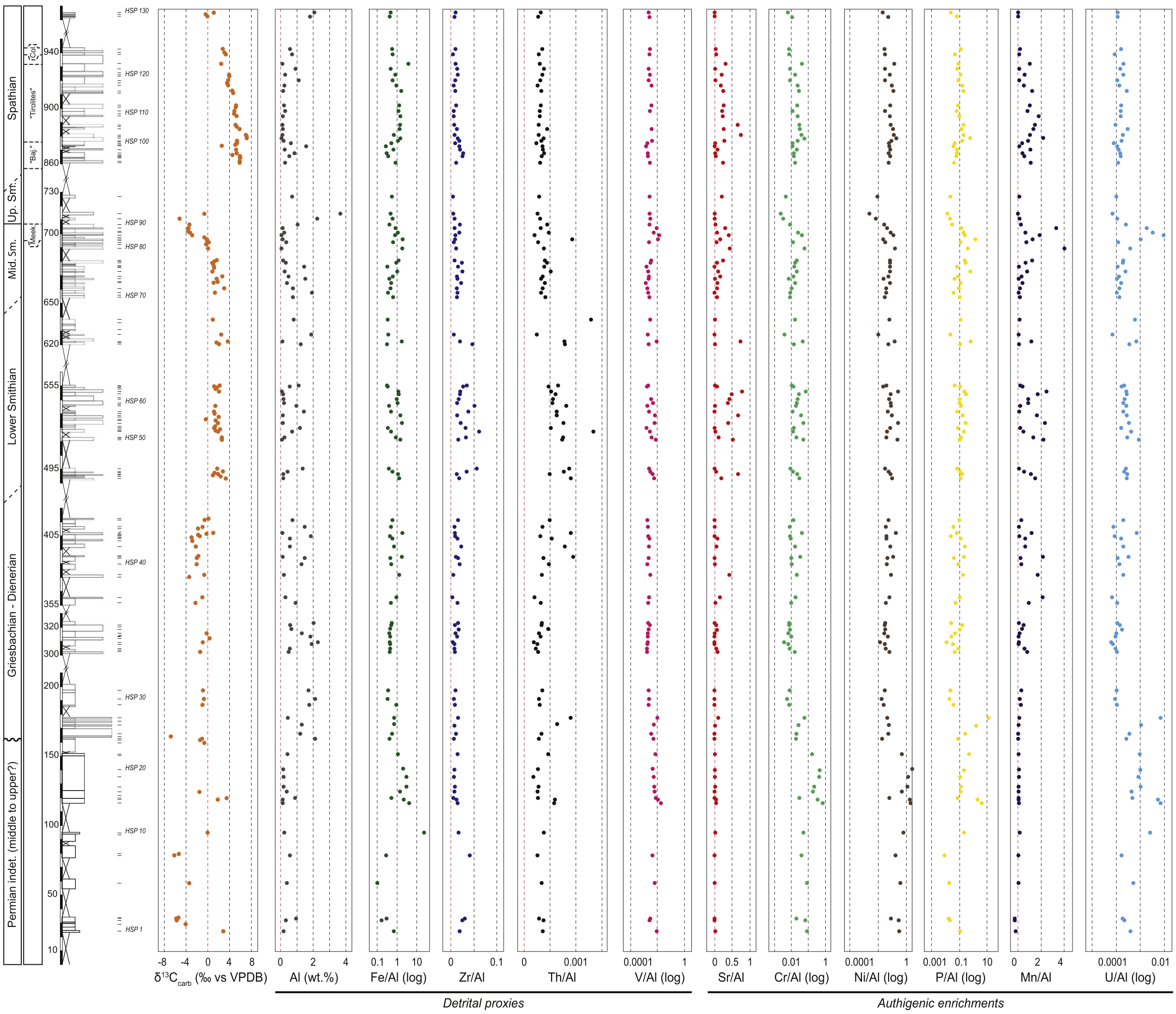

Fig. 4. Fluctuations in trace and major elements in the Hot Springs section, listed after their detrital and authigenic origin. The carbonate carbon isotope signal is also given as a chemostratigraphic reference. Uncertainties are smaller than the symbol size. 5 outliers have been removed for clarity (see Supplementary Table S2). (For interpretation of the references to color in this figure legend, the reader is referred to the web version of this article.)

across the SSB; and a decreasing trend can be seen toward the top of the section.

5.4. Concentrations in major and trace elements

5.4.1. Detrital proxies

While Al concentrations are given in wt%, other major and trace element proportions are expressed as Al-normalized ratios to avoid a potential dilution effect (Tribovillard et al., 2006). Correlations between major and trace elements and Al concentrations are given in the form of the Spearman correlation coefficient (r) and their associated *p*-value (*p*).

Al concentrations range from 0.1 to 3.7%, with a mean value of 0.7 (± 0.7%, 1σ, Fig. 4, Supplementary Table S2) and show no significant variation along the section with the exception of a peak within the upper Smithian. Because Al is typically of detrital origin and usually immobile during diagenesis (Böning et al., 2004), a cross-plot of a given element versus Al concentrations indicates whether the element concentration is dominantly controlled by the detrital flux or not. Here, Fe/Al, V/Al, Th/Al and Zr/Al ratios show a strong correlation with Al concentrations ($r = 0.80^{***}$ for Fe/Al, $r = 0.81^{***}$ for V/Al, $r = 0.91^{***}$ for Th/Al and $r = 0.86^{***}$ for Zr/Al). This suggests that these elements are associated with the Al flux, and have thus mainly a detrital origin. The Fe/Al ratio ranges from 0.1 to 21.4, with a mean value of 1.0 (± 2.1, 1σ, Fig. 4, Supplementary Table S2). The V/Al ratio ranges from 1.33×10^{-3} to 18.07×10^{-3}, with a mean value of 3.67×10^{-3} (± 2.86×10^{-3}, 1σ, Fig. 4, Supplementary Table S2). The Th/Al ratio ranges from 0.18×10^{-3} to 1.33×10^{-3}, with a mean value of 0.44×10^{-3} (± 0.22×10^{-3}, 1σ, Fig. 4, Supplementary Table S2). The Zr/Al ratio ranges from 3.71×10^{-3} to 61.59×10^{-3}, with a mean value of 15.94×10^{-3} (± 10.91×10^{-3}, 1σ, Fig. 4, Supplementary Table S2). These signals show no significant variation along the section, except for the V/Al ratio that displays a weak peak in the *Meekoceras* beds (middle Smithian).

5.4.2. Authigenic enrichments

The Mn/Al, P/Al, Sr/Al, Cr/Al, Ni/Al and U/Al ratios (Fig. 4, Supplementary Table S2) are not significantly correlated to Al concentrations ($r = -0.03$, $p = 0.77$ for Mn/Al, $r = 0.51^{***}$ for P/Al, $r = -0.44^{***}$ for Sr/Al, $r = 0.55^{***}$ for Cr/Al, $r = 0.50^{***}$ for Ni/Al, $r = 0.57^{***}$ for U/Al). This indicates authigenic enrichments related to variations in the paleoenvironmental conditions. The Mn/Al ratio ranges from 0 (HSP 4) to 4.0 (HSP 80), with a mean value of 0.6 (± 0.8, 1σ, Fig. 4, Supplementary Table S2). This signal barely varies along the section, except in the *Meekoceras* beds (middle Smithian) where small-scale variations are recorded. The P/Al ratio ranges from 0.01 to 13.47, with a mean value of 0.34 (± 1.38, 1σ, Fig. 4, Supplementary Table S23). P/Al ratio shows a significant decrease within the upper Smithian interval. Another increase of the P/Al ratio is documented within the "*Bajarunia*" beds (lower Spathian). The Sr/Al ratio ranges from 3.78×10^{-3} to 771.42×10^{-3}, with a mean value of 133.61×10^{-3} ($\pm 188.60 \times 10^{-3}$, 1σ, Fig. 4, Supplementary Table S2), with no important variation along the section. The Cr/Al ratio ranges from 2.18×10^{-3} to 665.42×10^{-3}, with a mean value of 41.66×10^{-3} ($\pm 93.54 \times 10^{-3}$, 1σ, Fig. 4, Supplementary Table S2). This signal shows no significant variation until the upper Smithian where a marked decrease is observed. The latter is immediately followed by an increase across the SSB. Ni/Al ratio ranges from 2.45×10^{-3} to 2492.77×10^{-3}, with a mean value of 155.49×10^{-3} ($\pm 360.46 \times 10^{-3}$, 1 σ, Fig. 4, Supplementary Table S2), showing a similar evolution to the Cr/Al ratio signal with no significant variation until the upper Smithian, where a marked decrease is observed. Ni/Al ratio values increase again across the SSB. The U/Al ratio ranges from 0.06×10^{-3} to 9.15×10^{-3}, with a mean value of 0.58×10^{-3} ($\pm 1.39 \times 10^{-3}$, 1σ, Fig. 4, Supplementary Table S2). U/Al ratio values do not show any noticeable variation except across the middle-upper Smithian transition where a significant peak is observed.

6. Interpretations

6.1. Evolution of the depositional environment

The HS depositional environment corresponds to a shallow inner ramp evolving from an embayment system to an open tidal flat during the Early Triassic. The observed mosaic facies pattern exhibits important vertical and lateral changes reflecting fluctuations in bathymetry and hydrodynamism. The HS section also exhibits mixed terrigenous and carbonate contents composed of (dolo-)siltstones and mud to bioclastic limestone layers. The fine grained terrigenous components may have originated from eastern and/or southern sources such as the Uncompahgre high of remnant Ancestral Rocky Mountains (Kluth and Coney, 1981; Blakey, 2008). The presence of sedimentary structures such as ripples or megaripples highlights episodes of important hydrodynamism. Bioturbation occurs throughout the entire section with varying intensity, even within bioclastic free layers (Fig. 2), suggesting oxygenated bottom-waters during deposition.

The Griesbachian-Dienerian to lower Smithian interval corresponds to a transgressive trend demonstrated by depositional conditions deeper than the ones observed at the very base of the section near the PTU (Fig. 2). The tidal flat records stronger hydrodynamic conditions as shown by the presence of ooid-rich shoals in the lowest Smithian (FIV in Table 1 and Fig. 2). The middle Smithian is characterized by the maximum carbonate content within the serpulid-rich and ammonoid-rich beds (FV and FVII in Table 1 and Fig.2). While included in the transgressive trend, Facies FV (Table 1) marks the outermost tidal flat settings, whereas a maximum of accommodation occurs at the level of the *Meekoceras* beds immediately before the upper Smithian. The upper Smithian corresponds to the maximum extent of the inundated area within the basin and it is characterized by an important flooding of the ramp and of the continental borders (e.g., Blakey, 2008; Brayard et al., 2013; Olivier et al., 2014, 2016; Vennin et al., 2015). Consequently, reworking of continental soils in the most proximal zones of the whole basin may have occurred in the upper Smithian, as argued by evidence of influx of terrestrial organic remains found in the northern part of the basin at some restricted places (personal observations). The lower Spathian marks a return to outer tidal flat conditions characterized by echinoderm-dominated carbonated beds (FVI) associated with and evolving toward an increase in fine terrigenous siliciclastic material (FII; Table 1, Fig. 2). This indicates the onset of a regressive trend after the maximum flooding that occurred during the upper Smithian (Fig. 2).

6.2. Major and trace elements

6.2.1. Detrital influx

Th and Zr are thought to have a siliciclastic origin and are thus interpreted to be linked to potential terrigenous inputs when they are correlated to Al concentrations (Rachold and Brumsack, 2001; Sauvage et al., 2013). In the HS section, these elements show a strong correlation to Al (see Section 5.4.1.). They can therefore be considered as good proxies for detrital influxes. Additionally, the V/Al ratio is strongly correlated to Al (see Section 5.4.1.), likely indicating a terrigenous origin of V, even if this trace element is usually used as a paleoredox marker (e.g., Tribovillard et al., 2006, 2008). The Zr/Al, Th/Al and V/Al ratios show restricted ranges of variation throughout the entire section (Fig. 4). This is in agreement with the observed continuous and homogenous clastic inputs (quartz- and mica-rich) and granulometry (FII; Table 1, Fig. 2). A relative stability in source and/or grain size of the clastic inputs can be inferred (Calvert et al., 1996), suggesting continuous continental weathering conditions.

6.2.2. Paleoproductivity

P/Al and Ni/Al ratios are used as proxies for variations in primary productivity if they are not correlated to Al concentration (i.e., representing an authigenic accumulation; Tribovillard et al., 2006). Phosphorous is a micronutrient, which is mainly incorporated by the phytoplankton. Enrichments of P within sediments are therefore usually interpreted as evidence of a high organic matter (OM) supply, in a productive environment such as present-day coastal upwelling zones (Calvert and Pedersen, 1993; Algeo and Maynard, 2004; Tribovillard et al., 2006; Sauvage et al., 2013). Withdrawal of Ni from the water column and scavenging within the OM is responsible for the sedimentary accumulation of Ni (Nameroff et al., 2004; Naimo et al., 2005; Tribovillard et al., 2006; Sauvage et al., 2013). Variations of these elements can therefore be used to infer variations in OM supply and burial, and thus may be interpreted in terms of primary productivity pulses.

At HS, both P/Al and Ni/Al ratios show weak variations, except in the upper Smithian-lower Spathian interval, where a noticeable decrease in P/Al and Ni/Al ratios is observed across the middle/upper Smithian transition. These variations cannot result from lithological differences as facies observed in this part of the section are similar, being mainly represented by serpulid- and ammonoid-dominated packstones to floatstones (FV and FVII, Fig. 2). Thus, these P/Al and Ni/Al fluctuations can be linked to a change in productivity.

However, these variations may also result from early diagenesis and remineralization of the OM under reducing conditions, especially if they are concomitant with a change in anoxic condition markers (e.g., U; Sauvage et al., 2013). The presence of a concomitant peak in the U/Al signal (Fig. 4) may argue in favor of the remobilization of the P rather than for a primary signal. Ni can be incorporated into sulfides under locally euxinic conditions within the sediment (Tribovillard et al., 2006). P is known to be easily released under anoxic conditions, remobilized and then enriched within the pore-water in the absence of high primary productivity (Benitez-Nelson, 2000; Tribovillard et al., 2006). The reliability of P as a proxy for paleoproductivity is therefore questionable here. The absence of coeval increase between the TOC content and Ni/Al and P/Al ratios better argues for remineralization processes rather than variation in paleoproductivity (Sauvage et al., 2013).

6.2.3. Paleoredox conditions

Sedimentary analyses support well-oxygenated conditions for the water column and the bottom waters throughout the entire section. The analyses of Redox Sensitive Trace Elements (RSTE) such as Mn, U, V and Mo can help to document short-lived episodes of reducing conditions at the bottom-water/sediment interface and in the upper early diagenetic sediment (Algeo and Maynard, 2004; Algeo and Lyons, 2006; Tribovillard et al., 2006; Riquier et al., 2006; Sauvage et al., 2013). Here, Mo was under the detection limit and the V/Al ratio is used as a detritism proxy due to its high correlation to Al. Conversely, Mn/Al and U/Al ratios are barely correlated to Al (see Section 5.4.2).

Both the Mn/Al and U/Al ratios show narrow ranges of variations, except for the serpulid-rich and ammonoid-rich beds (including the middle Smithian *Meekoceras* beds, Figs. 2, 4). There, the U/Al ratio shows a pronounced peak, concomitant with the short-lived peak in P/Al ratio. This U enrichment can reflect dysoxic/anoxic conditions (Calvert and Pedersen, 1993; Algeo and Maynard, 2004; Tribovillard et al., 2006; Sauvage et al., 2013). The unique significant enrichment in the V/Al ratio is documented from the same interval, probably resulting from the V sensitivity to authigenic concentration in reducing environments. A slight concomitant enrichment in the Mn/Al ratio also occurs within the *Meekoceras* beds. During episodes of dysoxic/anoxic conditions, depletion in Mn concentration (associated with enrichment in U) is however expected (Mangini et al., 2001; Kuhn et al., 2005; Westermann et al., 2010; Sauvage et al., 2013). Here, a strong correlation ($r = 0.91$***) between the Mn concentration and the $CaCO_3$ content is observed, suggesting that the Mn concentration reflects lithological variation rather than paleoredox conditions (Pratt et al., 1991). Finally, paleoredox markers indicate that some transient and slightly dysoxic/anoxic condition could have developed within the sediment or at the bottom-water/sediment interface within the interval including the *Meekoceras* beds.

6.2.4. *The peculiar case of chromium*

Cr fluctuations are difficult to interpret in terms of paleoenvironments as they can reflect both detritism and paleoredox conditions (Tribovillard et al., 2006, 2008). At HS, the Cr is only correlated to Al concentration and Th/Al ratio ($r = 0.55$*** and $r = 0.53$***, respectively). Moreover, Cr variations do not mirror those for detrital markers such as Zr/Al or Th/Al ratios. Thus, Cr accumulation may at least partially correspond to an authigenic enrichment. Additionally, Cr is strongly correlated to Ni (Fig. 4, $r = 0.93$***). In the presence of certain dissolved metals (Ni, Pb, Cu), Cr can form $MeCrO_4$ complexes (Tribovillard et al., 2008). Formation of such complexes is mediated by the presence of H_2S as a by-product of bacterial sulfate-reduction (BSR), or resulting from the mixing and reworking of the stocked sedimentary H_2S (Tribovillard et al., 2008). We hypothesize that the formation of $MeCrO_4$ complexes, and more particularly complexes involving Ni, were potentially triggered by pulses of reducing H_2S-rich conditions within the sediment.

6.3. *Carbon isotope records*

6.3.1. *Preservation of isotope signals*

6.3.1.1. *Carbonate*. The carbonate isotope signal is sensitive to diagenesis and prone to change due to circulation of diagenetic fluids and/or processes of dissolution/recrystallization forming secondary carbonates (Sansjofre et al., 2011 and references therein). Most of the time, carbon content in fluids and fluid/rock ratios are low compared to the high carbon content of carbonate rocks and cannot modify significantly their carbon isotope composition. However, when diagenetic fluids are enriched in DIC of organic origin (i.e. with low $\delta^{13}C$), both $\delta^{13}C_{carb}$ and $\delta^{18}O_{carb}$ are likely to be overprinted and it is usually admitted that a positive correlation between $\delta^{13}C_{carb}$ and $\delta^{18}O_{carb}$ or a positive trend between $\delta^{13}C_{carb}$ and carbonate content indicate a diagenetic overprint (Sansjofre et al., 2011). Figure 5a and b show no correlation between $\delta^{13}C_{carb}$ *versus* $\%CaCO_3$ and $\delta^{13}C_{carb}$ *versus* $\delta^{18}O_{carb}$, respectively, during the Triassic interval, suggesting a $\delta^{13}C_{carb}$ signal inherited from the water column and immune from late remobilization processes. However, the Permian record displays a positive correlation ($r = 0.75$**) between $\delta^{13}C_{carb}$ and $\delta^{18}O_{carb}$, interpreted as a secondary process overprint of the signal (Fig. 5b). Due to the presence of diagenetic artifacts in the Permian signal, we therefore cannot use these data to reconstruct the evolution of HS paleoenvironments for this time interval.

The diagenetic overprint of $\delta^{13}C_{carb}$ can also be tested using the Mn/Sr ratio. During alteration by meteoric water, Sr is expelled from carbonate while Mn is incorporated, thus increasing the Mn/Sr ratio (Banner and Hanson, 1990). The observed Mn/Sr ratio is extremely low ($Mn/Sr < < 2$). Moreover, no correlation between the Mn/Sr ratio and $\delta^{13}C_{carb}$ or $\delta^{18}O_{carb}$ is observed (Fig. 5c and d), with the exception of a positive correlation ($r = 0.78$*) between the Mn/Sr ratio and $\delta^{18}O_{carb}$ for Permian samples, highlighting secondary processes for this time interval only (Fig. 5d). However, given the small amount of available points for this interval, this result should be taken with caution. Variations of the $\delta^{13}C_{carb}$ signal are also independent of facies or lithological changes (Figs. 2, 3). Thus, no local or facies-dependent effects (e.g., preferential fluid circulation due to porosity) significantly imprint the $\delta^{13}C_{carb}$ signal. Moreover, the evolution of the $\delta^{13}C$ signal at HS is comparable to signals identified in other basins worldwide, with a marked negative excursion during the middle Smithian, followed by a positive excursion through the SSB (Fig. 6). Finally, no diagenetic overprint on the Early Triassic $\delta^{13}C_{carb}$ is demonstrated at HS, and its similar evolution with $\delta^{13}C_{carb}$ records from other sections worldwide is interpreted as indicating a primary $\delta^{13}C_{carb}$ signal.

6.3.1.2. *Organic matter*. The reliability of $\delta^{13}C_{org}$ to reflect the carbon isotope composition of photosynthetic primary productivity depends on the magnitude of the isotope offsets associated with depositional and post-depositional processes: (i) OM bacterial degradation and secondary OM inputs by heterotrophic and chemoautotrophic organisms during the early diagenesis *s.l.*, (ii) thermal maturation of the OM during burial diagenesis and/or metamorphism, (iii) *syn*- or post-depositional oxidative alteration, and (iv) emplacement of hydrocarbon from another source rock.

Overall, Early Triassic samples from the western USA SFB show low OM concentrations (Supplementary Table S1; Thomazo et al., 2016). Their $\delta^{13}C_{org}$ signal has therefore often been overlooked, their low TOC content casting doubt on the primary significance of the $\delta^{13}C_{org}$. Nevertheless, recent studies have shown that $\delta^{13}C_{org}$ signals can have a primary significance even at low TOC contents (Eigenbrode et al., 2008; Oehlert and Swart, 2014; Sansjofre et al., 2011; Johnston et al., 2012; Thomazo et al., 2009, 2016). At HS, the absence of correlation between the $\delta^{13}C_{org}$ and the TOC content argues against a substantial alteration of the $\delta^{13}C_{org}$ signal (Fig. 7). Similar to the $\delta^{13}C_{carb}$ signal, no significant variation due to changes in lithology and/or in facies is observed and the negative-positive couplet of carbon isotopes excursions during the middle Smithian and the SSB is recognized in the OM reservoir (Fig. 6). These are evidence for a pristine record of the $\delta^{13}C_{org}$ signal.

6.3.2. *Interpretation of the paired carbon isotope signal*

A parallel evolution of the $\delta^{13}C_{carb}$ and $\delta^{13}C_{org}$ signals is expected when perturbations of the biogeochemical carbon cycle are linked to the exogenic carbon cycle (Meyer et al., 2013). Paired organic and carbonate carbon isotopes recorded from the same sample are therefore crucial to distinguish the secular evolution of the carbon cycle (Payne et al., 2004; Payne and Kump, 2007; Meyer et al., 2011; Sobolev et al., 2011) from potential early or burial diagenetic processes (Hayes and Waldbauer, 2006; Derry, 2010; Schrag et al., 2013; Thomazo et al., 2016). Identified $\delta^{13}C_{carb}$ anomalies show a tight coupling with the $\delta^{13}C_{org}$ signal at the middle Smithian-SSB, but not at the DSB. Isotopic covariance in both carbonate and OM reservoirs is particularly well documented at a fine stratigraphic scale, such as the swings in $\delta^{13}C$ in the middle Smithian-lower Spathian transition (Figs. 3, 6), suggesting a relatively well-mixed marine DIC reservoir during this interval.

The observed co-variation of carbon isotope signals for the Smithian-Spathian interval contrasts with models requiring a large dissolved organic carbon (DOC) pool (Rothman et al., 2003). Indeed,

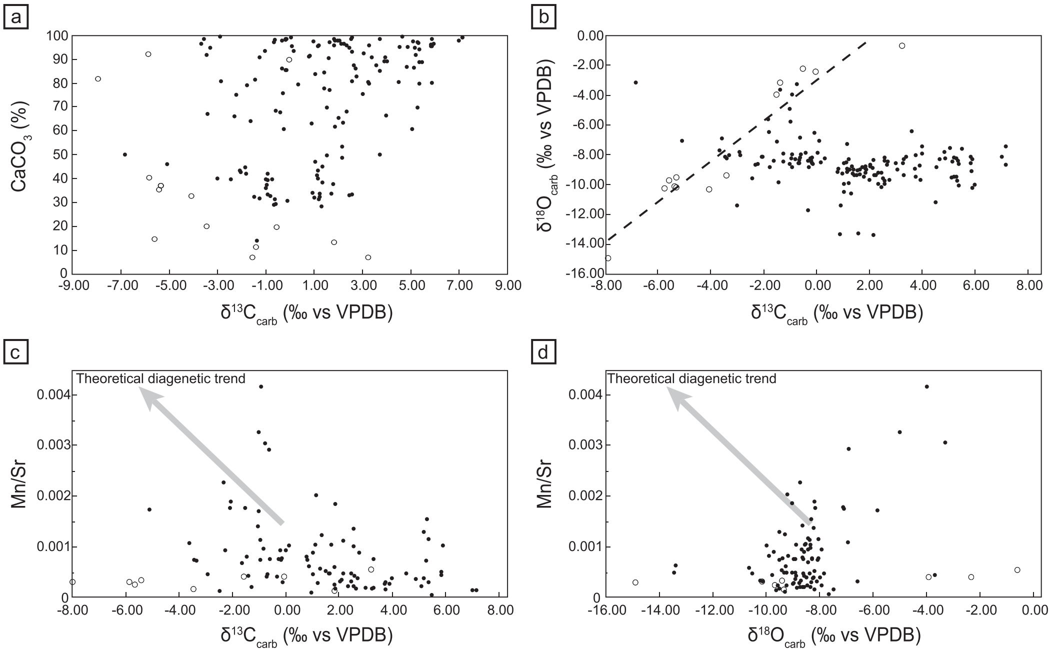

Fig. 5. Cross-plots for isotopic and elementary geochemical parameters. Black dots represent Triassic samples while open circles represent Permian samples. (a) $\delta^{13}C_{carb}$ vs $CaCO_3$ content; (b) $\delta^{13}C_{carb}$ vs $\delta^{18}O_{carb}$; (c) $\delta^{13}C_{carb}$ vs Mn/Sr; (d) $\delta^{18}O_{carb}$ vs Mn/Sr. Theoretical diagenetic trend on (c) and (d) after Sansjofre et al. (2011). $\delta^{13}C_{carb}$ or $\delta^{18}O_{carb}$ do not follow any diagenetic trend; no correlation is observed for Triassic samples; Permian samples show a correlation between $\delta^{13}C_{carb}$ and $\delta^{18}O_{carb}$ signals, and between $\delta^{18}O_{carb}$ and Mn/Sr signals.

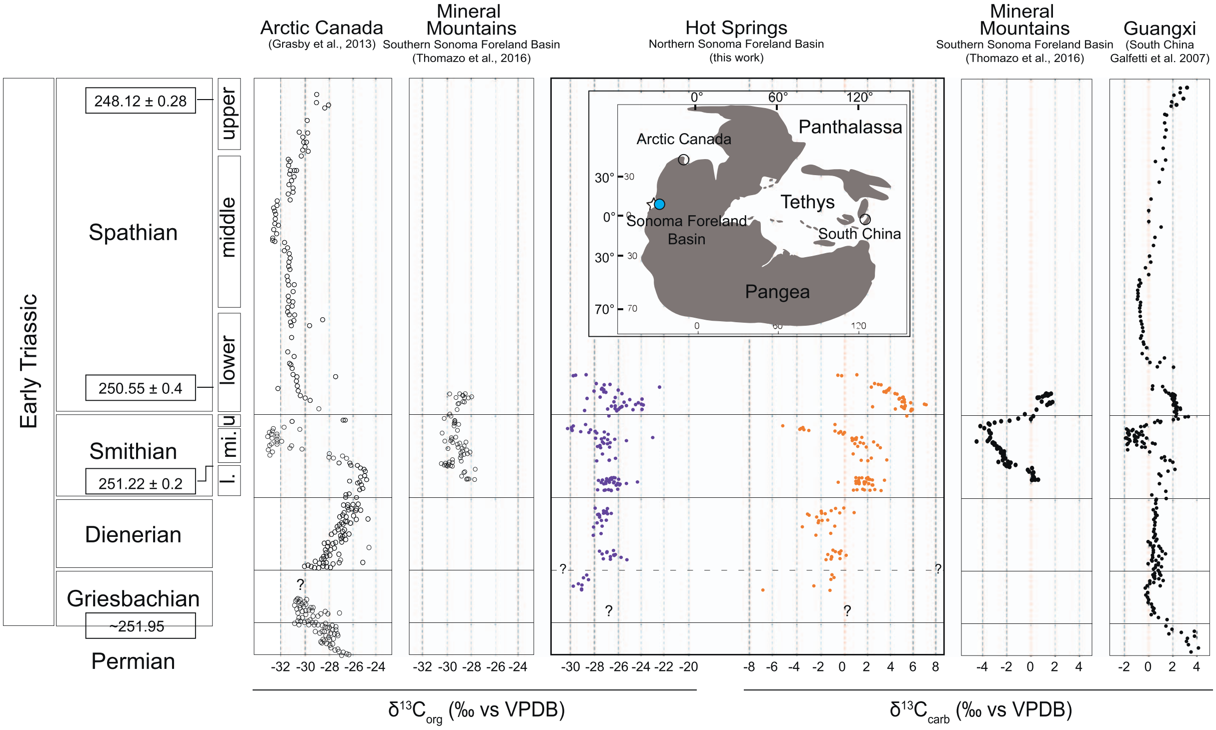

Fig. 6. Worldwide Early Triassic variations of the $\delta^{13}C$ signal for both carbonates and organic matter. Figure modified after Thomazo et al. (2016). Radiochronologic ages after Ovtcharova et al. (2006), Galfetti et al. (2007a) and Baresel et al. (2017). L.: lower; mi.: middle; u.: upper. (For interpretation of the references to color in this figure legend, the reader is referred to the web version of this article.)

the oxidation of such a large reservoir would generate a negative $\delta^{13}C_{carb}$ excursion without changing the $\delta^{13}C_{org}$ (McFadden et al., 2008; Swanson-Hysell et al., 2008). Moreover, the DOC hypothesis implies pronounced changes in the redox balance of the whole basin. Theoretical kinetic considerations are also at odds with the DOC hypothesis as a trigger for the Early Triassic carbon isotope swings (Thomazo et al., 2016). Interestingly, while $\delta^{13}C_{carb}$ - $\delta^{13}C_{org}$ covariation is well characterized at HS, dissimilar net isotopic offsets ($\Delta^{13}C_{carb\text{-}org}$) are associated with the DSB, the middle Smithian and the SSB. The $\delta^{13}C_{org}$ signal is dampened compared to the $\delta^{13}C_{carb}$ (Figs. 3, 6). Variations in the net isotopic effect ($\varepsilon_{TOC} = \Delta^{13}C_{carb\text{-}org}$) can reflect: (i) a diagenetic smoothing of the $\delta^{13}C_{org}$ signal, (ii) variations in the kinetic fractionation associated with carbon fixation (i.e. photosynthesis), or (iii) contamination with a secondary source of organic carbon. The absence of correlation between the $\delta^{13}C_{org}$ and the TOC content (Fig. 7) supports a pristine record of the $\delta^{13}C_{org}$ and indicates that no diagenetic

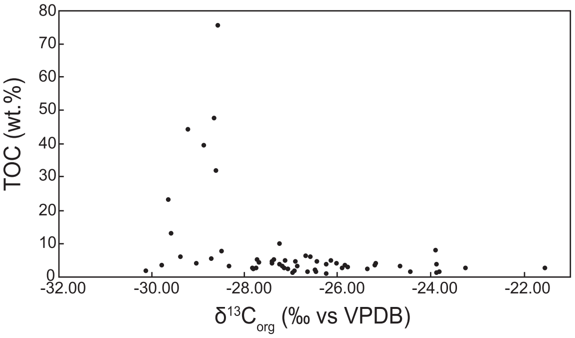

Fig. 7. $\delta^{13}C_{org}$ vs TOC content cross-plot. No correlation can be observed.

alteration has modified the OM isotopic signal at HS.

The photosynthetic fractionation of carbon can vary over time according to the concentration of dissolved CO_2 in the ocean $[CO_2]_{aq}$ and associated controlling mechanisms, including: the temperature, the growth rates of microorganisms (noted as μm) and changes in cell geometries (Hayes et al., 1999). Popp et al. (1998) showed that the photosynthetic fractionation and $\mu m/[CO_2]_{aq}$ are negatively correlated and that species-specific cell geometry determines the slope of the regression line. Based on this relationship, the lowering of surface water $[CO_2]_{aq}$ is expected to generate a decrease in ε_{TOC} at constant growth rate. Additionally, the $\delta^{13}C_{org}$ signal should record a larger shift than carbonates. Conversely, an increase in cellular growth rates tends to significantly reduce ε_{TOC} at moderate atmospheric CO_2 level ($<$ 1500 ppmv).

The observed $\Delta^{13}C_{carb\text{-}org}$ variations may reflect Early Triassic changes in sea surface temperatures as documented by Sun et al. (2012) and Romano et al. (2013) (Fig. 3). The middle Smithian negative $\delta^{13}C$ excursion is interpreted to reflect a temperature increase due to CO_2 injections from the Siberian traps (Sun et al., 2012; Romano et al., 2013). Ensuing extreme greenhouse climate conditions are suggested to have triggered lethal conditions for marine faunas such as anoxia on shelf environments and acidification of surface waters (biocalcification crisis) due to elevated CO_2 (hypercapnia) (e.g. Sun et al., 2012; Pietsch and Bottjer, 2014). At HS, decreases in ε_{TOC} are associated with warm temperatures and ε_{TOC} increases are concomitant with cooler episodes (Fig. 3). The $\Delta^{13}C_{carb\text{-}org}$ changes are thus difficult to explain in the light of temperature variations only. Extensive volcanogenic ^{12}C-enriched CO_2 degassing is consistent with $\delta^{13}C_{carb}$ and $\delta^{13}C_{org}$ Smithian negative signals. However, this should promote in turn a ε_{TOC} increase due to increasing surface water $[CO_2]_{aq}$.

The SSB $\delta^{13}C$ positive excursion is usually said to reflect an increase in primary productivity (Payne and Kump, 2007). Our results agree with this interpretation as increasing TOC contents are associated with $\delta^{13}C_{carb}$ and $\delta^{13}C_{org}$ positive excursions (Fig. 3). An enhanced biological pump is therefore most likely associated with, and contributes to a drawdown of global CO_2 and cooling. The surface water $[CO_2]_{aq}$ must have therefore decreased and consequently, the ε_{TOC} as well. This expected evolution is in contradiction with our observed trend in ε_{TOC} (Fig. 3). Assuming an upper Smithian stratified ocean returning to a more oxidizing state (i.e. ventilation) as suggested by Tian et al. (2014) and Sun et al. (2015), an increase of nutrient inputs into shallow environments is expected to be associated with an increase in μm (Joachimski et al., 2002). Therefore, lowered ε_{TOC} values should be observed, independently of any change in global CO_2. Since an increase in ε_{TOC} is observed at HS, neither changes in $[CO_2]_{aq}$ nor nutrient availability is suggested by paired carbon isotope variations at the DSB, middle Smithian and SSB transitions.

A lowered net isotopic effect is recorded during warm periods (Figs. 3, 6). This can be partly explained by a significant increase in the contribution of the cyanobacterial biomass to the TOC. Indeed, the maximum fractionation factor for cyanobacteria is smaller than for eukaryotic algae (Joachimski et al., 2002). Since photosynthetic fractionation of some modern cyanobacteria is independent of the dissolved $[CO_2]_{aq}$, a bloom of cyanobacteria among the primary producers during harsh (high temperature and low pH) and mesotrophic conditions may explain our results, especially the ε_{TOC} signal that does not reflect a CO_2-dependant increase in temperature. The HS section does not show sedimentological evidence of cyanobacterial blooms through the middle-upper Smithian interval. However, several microbial deposits were described throughout the SFB for this same interval (e.g., Brayard et al., 2013; Olivier et al., 2014, 2016; Vennin et al., 2015).

In some cases, $\Delta^{13}C_{carb\text{-}org}$ variations can reflect a contamination by a secondary source of organic carbon, from the erosion of organic-rich sediments or the migration of hydrocarbons within the basin (Johnston et al., 2012). Thus, mixing of the water column DIC reservoir with exogenous sources of carbon can buffer the $\delta^{13}C_{org}$ signal, especially when TOC values are low. Overall, Early Triassic primary carbon isotope signals of terrestrial and marine OM have been reported to vary around − 22‰ and around − 32‰, respectively (Hermann et al., 2011). We observed a $\delta^{13}C_{org}$ positive excursion that is dampened compared to the $\delta^{13}C_{carb}$ at the DSB (Figs. 3, 6). Such a variation in paired carbon isotopes, decoupled in magnitude, may correspond to a greater contribution of marine OM compared to terrestrial OM at this time. A decrease of the terrestrial OM contribution to the sedimentary TOC at the DSB is also in accordance with facies and paleoenvironmental changes that evolve toward more open marine conditions, as indicated by a change from bioclast-dominated to ooid-dominated facies (Fig. 2, Table 1). The globally recognized negative $\delta^{13}C$ excursion during the middle Smithian is recorded in both carbon reservoirs at HS. However, the amplitude of the ^{12}C–enrichment is lower in the OM. This result is difficult to explain if we hypothesize variations in the relative OM contributors (marine versus terrestrial). According to other known carbon isotope signals of terrestrial and marine OM at that time (Hermann et al., 2011), an increasing contribution of terrestrial OM would be expected to account for a lowered ε_{TOC} signal. The middle-upper Smithian transition at HS corresponds to the maximum transgressive event (Fig. 2). In such a transgressive trend, an increase in terrestrial OM contribution to the sedimentary record is not expected. However, evidence for influx of terrestrial organic remains associated with potential reworking of continental soils is observed in the northern part of the SFB at some restricted places in the uppermost Smithian (personal observations). The subsequent positive $\delta^{13}C$ shift through the SSB is recorded in both carbon reservoirs, with differing amplitudes of variation between carbonate and OM reservoirs and showing a more pronounced excursion in the $\delta^{13}C_{carb}$ signal. The lower Spathian exhibits an increase in terrigenous material compared to the middle-upper Smithian around the *Meekoceras* zone (Fig. 2), but again hypothesis of the mixing of terrestrial and marine OM cannot explain the observed $\Delta^{13}C_{carb\text{-}org}$ signal. Both positive excursions associated with the increase in TOC is however consistent with previous interpretations that suggested a drawdown of CO_2 by an enhanced biological pump (Payne and Kump, 2007).

Recently, some authors (e.g., Klaebe et al., 2017) have demonstrated that local parameters exert an important influence on the carbon isotope record, sometimes enough to overprint any global control. Here, while positive and negative excursions might be rooted to global changes, their expression may vary from one reservoir to another (i.e. carbonate and OM) due to locally-controlled parameters such as ecological structure (primary producers) and sedimentary processes. Thus, the use of the $\Delta^{13}C_{carb\text{-}org}$ signal as a direct tracer of the Early Triassic global $[CO_2]_{aq}$ and sea surface temperature should be taken with great caution.

7. Conclusions

Early Triassic sediments of the Hot Springs section were deposited on a large and shallow inner ramp, evolving from a transitional continental to marine embayment to a more open tidal flat. The maximum of the transgressive trend was reached during the middle-upper Smithian transition.

The paired carbon isotope record and trace and major elements highlight the following features for the sedimentary succession at HS:

- No water column anoxia/euxinia is observed, in agreement with sedimentary structures and biotic associations attesting to vigorous hydrodynamic conditions. Transient and weak dysoxic/anoxic conditions may have developed within the sediment or at the bottom-water/sediment interface during the middle-upper Smithian interval.
- Known worldwide carbon isotope fluctuations for the Smithian and Spathian are recognized in both OM and carbonate $\delta^{13}C$ reservoirs.
- Additionally, a positive excursion near the Dienerian/Smithian Boundary is documented on the carbonate $\delta^{13}C$ signal.
- The $\delta^{13}C$ signal at HS is not of secondary process/diagenetic origin, but rather primary and representative of a pristine record in both reservoirs.
- An increase in primary productivity may be responsible for the positive $\delta^{13}C$ excursion observed in the upper Smithian and through the SSB, as a concomitant increase in TOC content is observed.
- At HS, variations in the net isotopic effect cannot be directly related to CO_2 driven temperature variations, but they better reflect changes in OM sources: marine vs. terrestrial sources and/or the primary producers (e.g. cyanobacteria) origin.
- Finally, local influences on the carbon isotope signals, which are neither diagenetic nor representative of the global exogenic cycle, have probably largely contributed to the HS geochemical signatures. These signals could thus primarily reflect fluctuating local parameters.

Acknowledgements

This work was supported by the French Agence Nationale de la Recherche (ANR) project AFTER (ANR-13-JS06-0001-01). A.-S. Grosjean is thanked for discussions. This is a contribution to the FEDER Bourgogne Franche-Comté. We also thank two anonymous reviewers for constructive comments that helped to improve the manuscript. The Hot Springs section is located on US public land under the stewardship of the Bureau of Land Management (BLM) of the US Department of the Interior; access to this land is gratefully acknowledged.

Appendix A. Supplementary data

Supplementary data to this article can be found online at http://dx.doi.org/10.1016/j.gloplacha.2017.05.005.

References

Algeo, T.J., Lyons, T.W., 2006. Mo–total organic carbon covariation in modern anoxic marine environments: implications for analysis of paleoredox and paleohydrographic conditions. Paleoceanography 21 (1).

Algeo, T.J., Maynard, J.B., 2004. Trace-element behavior and redox facies in core shales of Upper Pennsylvanian Kansas-type cyclothems. Chem. Geol. 206 (3), 289–318.

Banner, J.L., Hanson, G.N., 1990. Calculation of simultaneous isotopic and trace element variations during water-rock interaction with applications to carbonate diagenesis. Geochim. Cosmochim. Acta 54 (11), 3123–3137.

Baresel, B., Bucher, H., Brosse, M., Cordey, F., Guodun, K., Schaltegger, U., 2017. Precise age for the Permian-Triassic boundary in South China from high-precision U-Pb geochronology and Bayesian age-depth modeling. Solid Earth Discuss. 8 (2), 361–378.

Benitez-Nelson, C.R., 2000. The biogeochemical cycling of phosphorus in marine systems. Earth Sci. Rev. 51 (1), 109–135.

Blakey, R.C., 2008. Pennsylvanian-Jurassic Sedimentary Basins of the Colorado Plateau and Southern Rocky Mountains Sedimentary Basins of the World. Elsevier, Amsterdam, Netherlands, Netherlands, pp. 245–296.

Böning, P., Brumsack, H.-J., Böttcher, M.E., Schnetger, B., Kriete, C., Kallmeyer, J., Borchers, S.L., 2004. Geochemistry of Peruvian near-surface sediments. Geochim. Cosmochim. Acta 68 (21), 4429–4451.

Brayard, A., Escarguel, G., Bucher, H., Monnet, C., Brühwiler, T., Goudemand, N., Galfetti, T., Guex, J., 2009. Good genes and good luck: ammonoid diversity and the end-Permian mass extinction. Science 325 (5944), 1118–1121.

Brayard, A., Bylund, K.G., Jenks, J.F., Stephen, D.A., Olivier, N., Escarguel, G., Fara, E., Vennin, E., 2013. Smithian ammonoid faunas from Utah: implications for early Triassic biostratigraphy, correlation and basinal paleogeography. Swiss J. Paleontol. 132 (2), 141–219.

Brühwiler, T., Goudemand, N., Galfetti, T., Bucher, H., Baud, A., Ware, D., Hermann, E., Hochuli, P.A., Martini, R., 2009. The Lower Triassic sedimentary and carbon isotope records from Tulong (South Tibet) and their significance for Tethyan palaeoceanography. Sediment. Geol. 222 (3), 314–332.

Calvert, S., Pedersen, T., 1993. Geochemistry of recent oxic and anoxic marine sediments: implications for the geological record. Mar. Geol. 113 (1), 67–88.

Calvert, S., Bustin, R., Ingall, E., 1996. Influence of water column anoxia and sediment supply on the burial and preservation of organic carbon in marine shales. Geochim. Cosmochim. Acta 60 (9), 1577–1593.

Caravaca, G., Brayard, A., Vennin, E., Guiraud, M., Le Pourhiet, L., Grosjean, A.-S., Thomazo, C., Olivier, N., Fara, E., Escarguel, G., Bylund, K.G., Jenks, J.F., Stephen, D.A., 2017. Controlling factors for differential subsidence in the Sonoma Foreland Basin (Early Triassic, western USA). Geol. Mag. 1–25. http://dx.doi.org/10.1017/S0016756817000164. (in press).

Carrol, A.R., Stephens, N.P., Hendrix, M.S., Glenn, C.R., 1998. Eolian-derived siltstone in the Upper Permian Phosphoria Formation: implications for marine upwelling. Geology 26 (11), 1023–1026.

Clarkson, M., Richoz, S., Wood, R.A., Maurer, F., Krystyn, L., McGurty, D.J., Astratti, D., 2013. A new high-resolution $\delta^{13}C$ record for the Early Triassic: insights from the Arabian Platform. Gondwana Res. 24 (1), 233–242.

Davydov, V.I., Crowley, J.L., Schmitz, M.D., Snyder, W.S., 2016. New U-Pb constraints identify the end-Guadalupian and possibly end-Lopingian extinction events conceivably preserved in the passive margin of North America: implication for regional tectonics. Geol. Mag. 1–13. http://dx.doi.org/10.1017/S0016756816000959.

Derry, L.A., 2010. A burial diagenesis origin for the Ediacaran Shuram–Wonoka carbon isotope anomaly. Earth Planet. Sci. Lett. 294 (1), 152–162.

Eigenbrode, J.L., Freeman, K.H., Summons, R.E., 2008. Methylhopane biomarker hydrocarbons in Hamersley Province sediments provide evidence for Neoarchean aerobiosis. Earth Planet. Sci. Lett. 273 (3), 323–331.

Embry, A.F., 1997. Global sequence boundaries of the Triassic and their identification in the western Canada sedimentary basin. Bull. Can. Petrol. Geol. 45 (4), 415–433.

Galfetti, T., Bucher, H., Ovtcharova, M., Schaltegger, U., Brayard, A., Brühwiler, T., Goudemand, N., Weissert, H., Hochuli, P.A., Cordey, F., Guodun, K., 2007a. Timing of the Early Triassic carbon cycle perturbations inferred from new U-Pb ages and ammonoid biochronozones. Earth Planet. Sci. Lett. 258 (3–4), 593–604.

Galfetti, T., Hochuli, P.A., Brayard, A., Bucher, H., Weissert, H., Vigran, J.O., 2007b. Smithian-Spathian boundary event: evidence for global climatic change in the wake of the end-Permian biotic crisis. Geology 35 (4), 291–294.

Grasby, S., Beauchamp, B., Embry, A., Sanei, H., 2013. Recurrent Early Triassic ocean anoxia. Geology 41 (2), 175–178.

Guex, J., Hungerbühler, A., Jenks, J.F., O'Dogherty, L., Atudorei, V., Taylor, D.G., Bucher, H., Bartolini, A., 2010. Spathian (Lower Triassic) Ammonoids from Western USA (Idaho, California, Utah and Nevada). Institut de géologie et paléontologie, Université de Lausanne.

Haq, B.U., Hardenbol, J., Vail, P.R., 1987. Chronology of fluctuating sea levels since the Triassic. Science 235 (4793), 1156–1167.

Hayes, J.M., Waldbauer, J.R., 2006. The carbon cycle and associated redox processes through time. Philos. Trans. R. Soc. Lond. B 361 (1470), 931–950.

Hayes, J.M., Strauss, H., Kaufman, A.J., 1999. The abundance of ^{13}C in marine organic matter and isotopic fractionation in the global biogeochemical cycle of carbon during the past 800 Ma. Chem. Geol. 161 (1), 103–125.

Hermann, E., Hochuli, P.A., Méhay, S., Bucher, H., Brühwiler, T., Ware, D., Hautmann, M., Roohi, G., Yaseen, A., 2011. Organic matter and palaeoenvironmental signals during the early Triassic biotic recovery: the Salt Range and Surghar Range records. Sediment. Geol. 234 (1), 19–41.

Hochuli, P.A., Sanson-Barrera, A., Schneebeli-Hermann, E., Bucher, H., 2016. Severest crisis overlooked—worst disruption of terrestrial environments postdates the Permian–Triassic mass extinction. Sci. Report. 6. http://dx.doi.org/10.1038/srep28372.

Horacek, M., Brandner, R., Abart, R., 2007a. Carbon isotope record of the P/T boundary and the Lower Triassic in the Southern Alps: evidence for rapid changes in storage of organic carbon. Palaeogeogr. Palaeoclimatol. Palaeoecol. 252 (1), 347–354.

Horacek, M., Richoz, S., Brandner, R., Krystyn, L., Spötl, C., 2007b. Evidence for recurrent changes in Lower Triassic oceanic circulation of the Tethys: the $\delta^{13}C$ record from marine sections in Iran. Palaeogeogr. Palaeoclimatol. Palaeoecol. 252 (1), 355–369.

Horacek, M., Wang, X., Grossman, E.L., Richoz, S., Cao, Z., 2007c. The carbon-isotope curve from the Chaohu section, China: different trends at the Induan–Olenekian Boundary or diagenesis. Albertiana 35, 41–45.

Horacek, M., Koike, T., Richoz, S., 2009. Lower Triassic $\delta^{13}C$ isotope curve from shallow-marine carbonates in Japan, Panthalassa realm: confirmation of the Tethys $\delta^{13}C$ curve. J. Asian Earth Sci. 36 (6), 481–490.

Jattiot, R., Bucher, H., Brayard, A., Brosse, M., Jenks, J., Bylund, K.G., 2017. Smithian ammonoid faunas from northeastern Nevada: implications for Early Triassic biostratigraphy and correlation within the western USA basin. Palaeontogr. Abt. A. http://dx.doi.org/10.1127/pala/2017/0070. (in press).

Jenks, J., Guex, J., Hungerbühler, A., Taylor, D.G., Bucher, H., 2013. Ammonoid biostratigraphy of the Early Spathian *Columbites parisianus* Zone (Early Triassic) at Bear Lake Hot Springs, Idaho. N. M. Mus. Nat. Hist. Sci. Bull. 61, 268–283.

Joachimski, M., Pancost, R., Freeman, K., Ostertag-Henning, C., Buggisch, W., 2002. Carbon isotope geochemistry of the Frasnian–Famennian transition. Palaeogeogr. Palaeoclimatol. Palaeoecol. 181 (1), 91–109.

Johnson, H., Baldwin, C., 1996. Shallow Clastic Seas. Sedimentary Environments: Processes, Facies and Stratigraphy. 3. pp. 232–280.

Johnston, D.T., Macdonald, F.A., Gill, B., Hoffman, P., Schrag, D.P., 2012. Uncovering the Neoproterozoic carbon cycle. Nature 483 (7389), 320–323.

Klaebe, R., Kennedy, M., Jarrett, A., Brocks, J., 2017. Local paleoenvironmental controls on the carbon-isotope record defining the Bitter Springs Anomaly. Geobiology 15 (1), 65–80.

Kluth, C.F., Coney, P.J., 1981. Plate tectonics of the ancestral Rocky Mountains. Geology 9 (1), 10–15.

Krystyn, L., Bhargava, O.N., Richoz, S., 2007. A candidate GSSP for the base of the Olenekian stage: Mud at Pin Valleay; district Lahul & Spiti, Himachal Pradesh (western Himalaya), India. Albertiana 35, 5–29.

Kuhn, O., Weissert, H., Föllmi, K.B., Hennig, S., 2005. Altered carbon cycling and trace-metal enrichment during the late Valanginian and early Hauterivian. Eclogae Geol. Helv. 98 (3), 333–344.

Kummel, B., 1954. Triassic Stratigraphy of Southeastern Idaho and Adjacent Areas. US Government Printing Office.

Kummel, B., 1957. Paleoecology of Lower Triassic formations of southeastern Idaho and adjacent areas. Geol. Soc. Am. Mem. 67, 437–468.

Mangini, A., Jung, M., Laukenmann, S., 2001. What do we learn from peaks of uranium and of manganese in deep sea sediments? Mar. Geol. 177 (1), 63–78.

McFadden, K.A., Huang, J., Chu, X., Jiang, G., Kaufman, A.J., Zhou, C., Yuan, X., Xiao, S., 2008. Pulsed oxidation and biological evolution in the Ediacaran Doushantuo Formation. Proc. Natl. Acad. Sci. 105 (9), 3197–3202.

Metcalfe, I., Nicoll, R., Willink, R., Ladjavadi, M., Grice, K., 2013. Early Triassic (Induan–Olenekian) conodont biostratigraphy, global anoxia, carbon isotope excursions and environmental perturbations: new data from Western Australian Gondwana. Gondwana Res. 23 (3), 1136–1150.

Meyer, K., Yu, M., Jost, A., Kelley, B., Payne, J., 2011. $\delta^{13}C$ evidence that high primary productivity delayed recovery from end-Permian mass extinction. Earth Planet. Sci. Lett. 302 (3), 378–384.

Meyer, K.M., Yu, M., Lehrmann, D., Van de Schootbrugge, B., Payne, J., 2013. Constraints on Early Triassic carbon cycle dynamics from paired organic and inorganic carbon isotope records. Earth Planet. Sci. Lett. 361, 429–435.

Naimo, D., Adamo, P., Imperato, M., Stanzione, D., 2005. Mineralogy and geochemistry of a marine sequence, Gulf of Salerno, Italy. Quat. Int. 140, 53–63.

Nameroff, T., Calvert, S., Murray, J., 2004. Glacial-interglacial variability in the eastern tropical North Pacific oxygen minimum zone recorded by redox-sensitive trace metals. Paleoceanography 19 (1). http://dx.doi.org/10.1029/2003PA000912.

Oehlert, A.M., Swart, P.K., 2014. Interpreting carbonate and organic carbon isotope covariance in the sedimentary record. Nat. Commun. 5. http://dx.doi.org/10.1038/ncomms5672.

Olivier, N., Brayard, A., Fara, E., Bylund, K.G., Jenks, J.F., Vennin, E., Stephen, D.A., Escarguel, G., 2014. Smithian shoreline migrations and depositional settings in Timpoweap Canyon (Early Triassic, Utah, USA). Geol. Mag. 151 (5), 938–955.

Olivier, N., Brayard, A., Vennin, E., Escarguel, G., Fara, E., Bylund, K.G., Jenks, J.F., Caravaca, G., Stephen, D.A., 2016. Evolution of depositional settings in the Torrey area during the Smithian (Early Triassic, Utah, USA) and their significance for the biotic recovery. Geol. J. 51 (4), 600–626.

Orchard, M.J., 2007. Conodont diversity and evolution through the latest Permian and Early Triassic upheavals. Palaeogeogr. Palaeoclimatol. Palaeoecol. 252 (1), 93–117.

Ovtcharova, M., Bucher, H., Schaltegger, U., Galfetti, T., Brayard, A., Guex, J., 2006. New Early to Middle Triassic U–Pb ages from South China: calibration with ammonoid biochronozones and implications for the timing of the Triassic biotic recovery. Earth Planet. Sci. Lett. 243 (3), 463–475.

Paull, R.K., Paull, R.A., 1986. Epilogue for the Permian — a retrospective view from the Triassic in western Cordillera. Univ. Wyo. Contrib. Geol. 24, 243–252.

Paull, R.A., Paull, R.K., 1993. Interpretation of Early Triassic nonmarine–marine relations, Utah, USA. N. M. Mus. Nat. Hist. Sci. Bull. 3, 403–409.

Paull, R.K., Paull, R.A., Anderson, A.L., 1985. Conodont biostratigraphy and depositional history of the Lower Triassic Dinwoody Formation in the Meade Plate, southeastern Idaho. Utah Geol. Assoc. Publ. 14, 55–65.

Payne, J.L., Clapham, M.E., 2012. End-Permian mass extinction in the oceans: an ancient analog for the twenty-first century? Annu. Rev. Earth Planet. Sci. 40, 89–111.

Payne, J.L., Kump, L.R., 2007. Evidence for recurrent Early Triassic massive volcanism from quantitative interpretation of carbon isotope fluctuations. Earth Planet. Sci. Lett. 256 (1), 264–277.

Payne, J.L., Lehrmann, D.J., Wei, J., Orchard, M.J., Schrag, D.P., Knoll, A.H., 2004. Large perturbations of the carbon cycle during recovery from the end-Permian extinction. Science 305 (5683), 506–509.

Pietsch, C., Bottjer, D.J., 2014. The importance of oxygen for the disparate recovery patterns of the benthic macrofauna in the Early Triassic. Earth Sci. Rev. 137, 65–84.

Pietsch, C., Petsios, E., Bottjer, D.J., 2016. Sudden and extreme hyperthermals, low-oxygen, and sediment influx drove community phase shifts following the end-Permian mass extinction. Palaeogeogr. Palaeoclimatol. Palaeoecol. 451, 183–196.

Popp, B.N., Laws, E.A., Bidigare, R.R., Dore, J.E., Hanson, K.L., Wakeham, S.G., 1998. Effect of phytoplankton cell geometry on carbon isotopic fractionation. Geochim. Cosmochim. Acta 62 (1), 69–77.

Pratt, L.M., Force, E.R., Pomerol, B., 1991. Coupled manganese and carbon-isotopic events in marine carbonates at the Cenomanian-Turonian boundary. J. Sediment. Res. 61 (3).

Rachold, V., Brumsack, H.-J., 2001. Inorganic geochemistry of Albian sediments from the Lower Saxony Basin NW Germany: palaeoenvironmental constraints and orbital cycles. Palaeogeogr. Palaeoclimatol. Palaeoecol. 174 (1), 121–143.

Retallack, G.J., 2001. A 300-million-year record of atmospheric carbon dioxide from fossil plant cuticles. Nature 411 (6835), 287–290.

Richoz, S., Krystyn, L., Horacek, M., Spötl, C., 2007. Carbon isotope record of the Induan-Olenekian candidate GSSP Mud and comparison with other sections. Albertiana 35, 35–40.

Riquier, L., Tribovillard, N., Averbuch, O., Devleeschouwer, X., Riboulleau, A., 2006. The Late Frasnian Kellwasser horizons of the Harz Mountains (Germany): two oxygen-deficient periods resulting from different mechanisms. Chem. Geol. 233 (1), 137–155.

Romano, C., Goudemand, N., Vennemann, T.W., Ware, D., Schneebeli-Hermann, E., Hochuli, P.A., Brühwiler, T., Brinkmann, W., Bucher, H., 2013. Climatic and biotic upheavals following the end-Permian mass extinction. Nat. Geosci. 6 (1), 57–60.

Rothman, D.H., Hayes, J.M., Summons, R.E., 2003. Dynamics of the Neoproterozoic carbon cycle. Proc. Natl. Acad. Sci. 100 (14), 8124–8129.

Sansjofre, P., Ader, M., Trindade, R.I.F., Elie, M., Lyons, J., Cartigny, P., Nogueira, A.C.R., 2011. A carbon isotope challenge to the snowball Earth. Nature 478 (7367), 93–96.

Sauvage, L., Riquier, L., Thomazo, C., Baudin, F., Martinez, M., 2013. The late Hauterivian Faraoni "Oceanic Anoxic Event" at Río Argos (southern Spain): an assessment on the level of oxygen depletion. Chem. Geol. 340, 77–90.

Schrag, D.P., Higgins, J.A., Macdonald, F.A., Johnston, D.T., 2013. Authigenic carbonate and the history of the global carbon cycle. Science 339 (6119), 540–543.

Sobolev, S.V., Sobolev, A.V., Kuzmin, D.V., Krivolutskaya, N.A., Petrunin, A.G., Arndt, N.T., Radko, V.A., Vasiliev, Y.R., 2011. Linking mantle plumes, large igneous provinces and environmental catastrophes. Nature 477 (7364), 312–316.

Song, H., Tong, J., Chen, Z., 2009. Two episodes of foraminiferal extinction near the Permian–Triassic boundary at the Meishan section, South China. Aust. J. Earth Sci. 56 (6), 765–773.

Song, H., Wignall, P.B., Tong, J., Bond, D.P.G., Song, H., Lai, X., Zhang, K., Wang, H., Chen, Y., 2012. Geochemical evidence from bio-apatite for multiple oceanic anoxic events during Permian–Triassic transition and the link with end-Permian extinction and recovery. Earth Planet. Sci. Lett. 353, 12–21.

Strasser, A., 1986. Ooids in Purbeck limestones (lowermost Cretaceous) of the Swiss and French Jura. Sedimentology 33 (5), 711–727.

Sun, Y., Joachimski, M.M., Wignall, P.B., Yan, C., Chen, Y., Jiang, H., Wang, L., Lai, X., 2012. Lethally hot temperatures during the Early Triassic greenhouse. Science 338 (6105), 366–370.

Sun, Y., Wignall, P.B., Joachimski, M.M., Bond, D.P.G., Grasby, S.E., Sun, S., Yan, C.B., Wang, L.N., Chen, Y.L., Lai, X.L., 2015. High amplitude redox changes in the late Early Triassic of South China and the Smithian–Spathian extinction. Palaeogeogr. Palaeoclimatol. Palaeoecol. 427, 62–78.

Swanson-Hysell, N., Maloof, A., Halverson, G., Hurtgen, M., 2008. Covariation in the Carbon Isotopes of Carbonate and Organic Carbon Across the Neoproterozoic Bitter Springs Stage. AGU Fall Meeting Abstractspp. 1414.

Thomazo, C., Ader, M., Farquhar, J., Philippot, P., 2009. Methanotrophs regulated atmospheric sulfur isotope anomalies during the Mesoarchean (Tumbiana formation, Western Australia). Earth Planet. Sci. Lett. 279 (1), 65–75.

Thomazo, C., Vennin, E., Brayard, A., Bour, I., Mathieu, O., Elmeknassi, S., Olivier, N., Escarguel, G., Bylund, K.G., Jenks, J., 2016. A diagenetic control on the Early Triassic Smithian–Spathian carbon isotopic excursions recorded in the marine settings of the Thaynes Group (Utah, USA). Geobiology 14 (3), 220–236.

Tian, L., Tong, J., Algeo, T.J., Song, H., Song, H., Chu, D., Shi, L., Bottjer, D.J., 2014. Reconstruction of Early Triassic ocean redox conditions based on framboidal pyrite from the Nanpanjiang Basin, South China. Palaeogeogr. Palaeoclimatol. Palaeoecol. 412, 68–79.

Tong, J., Zakharov, Y.D., Orchard, M.J., Hongfu, Y., Hansen, H.J., 2004. Proposal of Chaohu Section as the GSSP candidate of the Induan-Olenekian Boundary. Albertiana 29, 13–28.

Tribovillard, N., Algeo, T.J., Lyons, T., Riboulleau, A., 2006. Trace metals as paleoredox and paleoproductivity proxies: an update. Chem. Geol. 232 (1), 12–32.

Tribovillard, N., Bout-Roumazeilles, V., Algeo, T., Lyons, T.W., Sionneau, T., Montero-Serrano, J.C., Riboulleau, A., Baudin, F., 2008. Paleodepositional conditions in the Orca Basin as inferred from organic matter and trace metal contents. Mar. Geol. 254 (1), 62–72.

Vennin, E., Olivier, N., Brayard, A., Bour, I., Thomazo, C., Escarguel, G., Fara, E., Bylund, K.G., Jenks, J.F., Stephen, D.A., Hofman, R., 2015. Microbial deposits in the aftermath of the end-Permian mass extinction; a diverging case from the Mineral Mountains (Utah, USA). Sedimentology 62 (3), 753–792.

Wardlaw, B.R., Collison, J.W., 1986. Paleontology and depositon of the Phosphoria formation. Contrib. Geol. 24 (2), 36.

Westermann, S., Caron, M., Fiet, N., Fleitmann, D., Matera, V., Adatte, T., Föllmi, K.B., 2010. Evidence for oxic conditions during oceanic anoxic event 2 in the northern Tethyan pelagic realm. Cretac. Res. 31 (5), 500–514.

Wignall, P.B., Hallam, A., 1992. Anoxia as a cause of the Permian/Triassic mass extinction: facies evidence from northern Italy and the western United States. Palaeogeogr. Palaeoclimatol. Palaeoecol. 93 (1), 21–46.

Wright, V.P., Burgess, P.M., 2005. The carbonate factory continuum, facies mosaics and microfacies: an appraisal of some of the key concepts underpinning carbonate sedimentology. Facies 51 (1–4), 17–23.

Zeebe, R.E., 2012. History of seawater carbonate chemistry, atmospheric CO2, and ocean acidification. Annu. Rev. Earth Planet. Sci. 40, 141–165.

To sum up, the HS section shows a carbon isotope record mirroring the globally recognized couplet of a negative and a positive excursion before and across the SSB in both carbonate and organic matter (OM) reservoirs. However, the OM signal shows systematically dampened values compared to the carbonate signal. Variations in $\Delta^{13}C_{carb-org}$ probably resulted from a complex set of forcing parameters depending on the evolution of the locally-controlled depositional system rather than on the global exogenic carbon cycle.

No water-column anoxia has been evidenced in HS, but transient and episodic suboxic conditions may have developed at the bottom-water/sediment interface, as evidence by the T&M elements concentrations (e.g., U/Al ratio).

These results highlight the primary role of local forcing parameter upon the geochemical signal of the HS section, especially on variations of the paired carbon signal, which appears as not fully representative of the global exogenic cycle nor of diagenetic origin.

B. Central SFB signal: Lower Weber Canyon

• Introductory remarks and geological setting

The central part of the SFB is worth of interest as potentially corresponding to a "transitional" area given its rather intermediate position within the basin. Its record is represented by data from the Lower Weber Canyon (LWC) section located in northern Utah (Fig. III.B.1a). The sedimentary succession and the paired carbon isotopic record presented in this chapter are preliminary results to be more detailed and interpreted in Grosjean *et al*. (*in prep*.). LWC T&M elements will not be described as they were exclusively measured on the carbonate fraction of the samples and not on bulk rock samples like in HS and MV, preventing any direct comparison.

The LWC section is composed by sediments characteristic of both the Early Triassic Moenkopi (basal "red beds"; Fig. III.B.1b) and Thaynes Groups (*sensu* Lucas *et al*., 2007; Grosjean *et al*., *in prep*.; Thomazo *et al*., *in prep*.). The section represents the Smithian-Spathian interval (Fig. III.B.1b).

Out of the ~290 m-thick LWC section (Fig. III.B.1b), this work focuses on a ~19 m-thick succession from the middle Smithian to the early Spathian centered onto the SSB (Fig. III.B.1c). This succession comprises three main lithostratigraphic units. Unit A is composed by dolosiltstones, interbedded with microbially induced sedimentary structures (MISS). Several storm-induced events are visible, as evidenced by bioclastic accumulations, and are interpreted as marine incursion into the peritidal domain characterized by deposits of Unit A. SSB unit shows carbonate-marls alternations corresponding to the late Smithian, as confirmed by the presence of Anasibirites ammonoids ("Ana." In Fig. III.B.1b; Brayard *et al*., 2013). These levels represent an opening towards more marine conditions in a tide-influenced bioclastic mid-ramp. Finally, Unit B is dominated by fine calcarenite layers interbedded in marl-rich sediments. This units represents deeper mud-dominated mid-ramp settings, and also record storm-induced deposits (Grosjean *et al., in prep*.).

Thirty-nine carbonate fraction samples were collected and powdered for geochemical analyses (carbon isotope signal, oxygen isotope signal and carbonate content) using the same protocol as described in Caravaca *et al.* (2017, see section III.A).

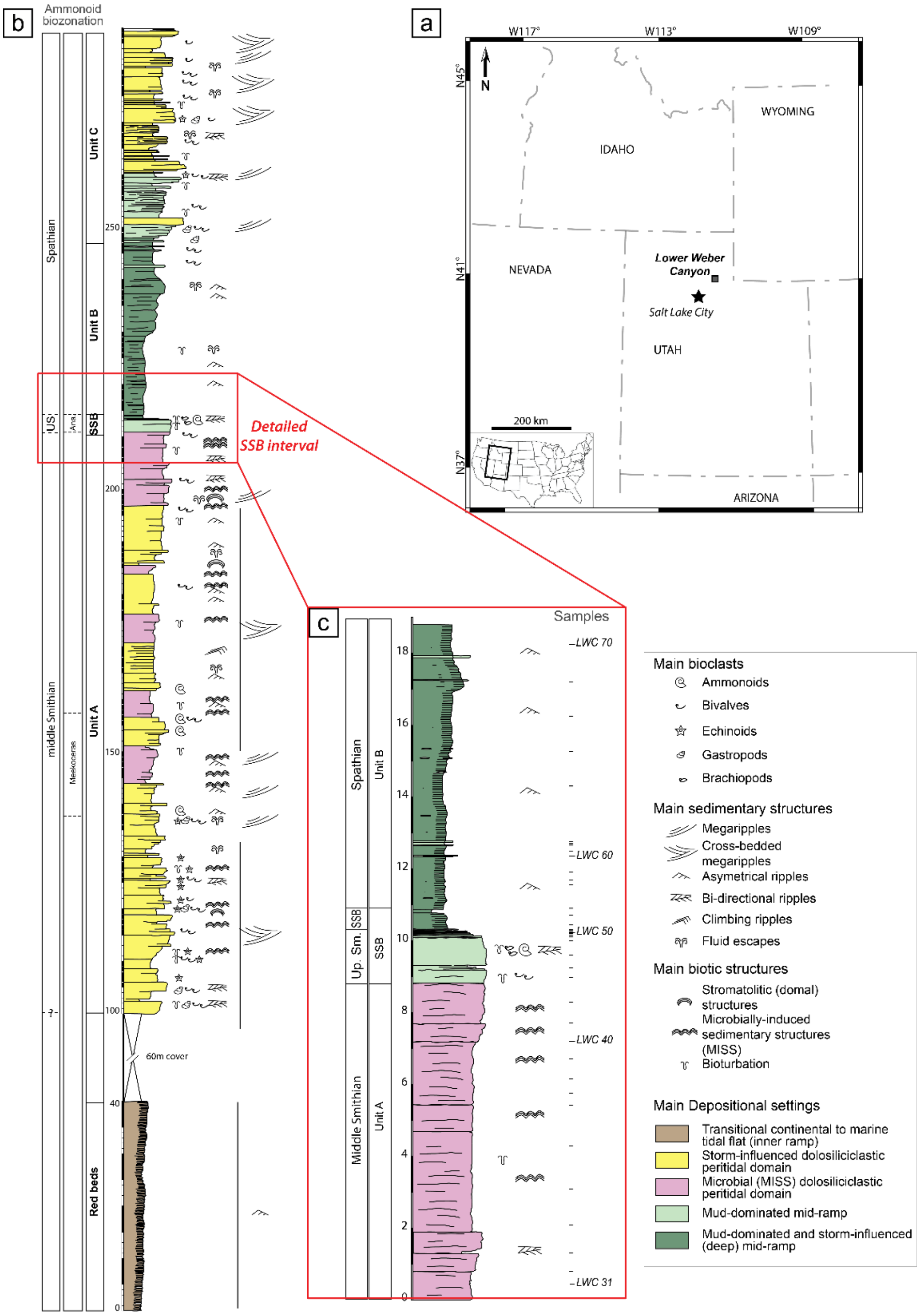

Figure III.B.1: a) Map of the studied area and location of the Lower Weber Canyon section. b) Synthetic log of the complete Lower Weber Canyon section (after Grosjean *et al., in prep*.). Synthetic ammonoid biozonation after Brayard *et al.* (2013); Meekoceras: Meekoceras beds; Ana.: Anasibirites kingianus beds. c) Detail log and position of geochemical samples for the SSB transition of the Lower Weber Canyon section. Up. Sm.: upper Smithian; SSB: Smithian/Spathian Boundary.

- Paired carbon isotopic signal

The $\delta^{13}C_{org}$ values vary from -32.2 to -28.3‰, with a mean value of -30.2 (± 0.8‰, 1σ, Fig. III.B.2, Table III.B.1). The OM record shows only slight variations along the succession. A decrease can be observed during the interval up to the base of the upper Smithian, followed by an increase through the upper Smithian and across the SSB. The rest of the Spathian unit does not show any marked variation. This signal corresponds to the known carbon isotopic couplet of negative and positive shifts across the SSB but remains rather small in absolute magnitude (e.g.; Galfetti *et al.*, 2007b; Grasby *et al.*, 2013; see Fig. 6 in Caravaca *et al.*, 2017, see section III.A).

The $\delta^{13}C_{carb}$ values vary from -5.9 to -0.3‰, with a mean value of -2.4 (± 1.4‰, 1σ, Fig. III.B.2, Table III.B.1). The $\delta^{13}C_{carb}$ signal shows no marked variations during the middle Smithian (with values around -3.0‰), and during the Spathian (with values around -1.0‰; Fig. III.B.2). However, four important negative outliers are observed at the top of the SSB Unit (down to -5.9‰, Fig. III.B.2), embedded within a noticeable increase in $\delta^{13}C_{carb}$ values. This trend in the $\delta^{13}C_{carb}$ signal looks similar to the well-established global signal for carbon isotopic signal during the Smithian-Spathian transition evidencing a positive isotopic excursion across the SSB (e.g.; Galfetti *et al.*, 2007b; Grasby *et al.*, 2013; see Fig. 6 in Caravaca *et al.*, 2017, see section III.A). However, variations remain small compared to other sections in the SFB and worldwide, and dampened down isotope signal may be the result of high sedimentation rates or a secondary alteration of the signal.

The $\Delta^{13}C_{carb\text{-}org}$ values vary from 24.9 to 31.0 ‰, with a mean value of 28.1 (± 1.4‰, 1σ, Fig. III.B.2, Table III.B.1). The difference shows a relative stability, and no significant trend can be observed along the LWC section. However, a group of negative values is present at the top of the upper Smithian interval but it is mirroring that of the $\delta^{13}C_{carb}$ signal (SSB Unit, Fig. III.B.2). Its primary origin is thus to be demonstrated.

The $\delta^{18}O_{carb}$ values vary from -12.3 to -7.8 ‰, with a mean value of -9.9 (± 1.2‰, 1σ, Fig. III.B.2, Table III.B.1). This signal shows a parallel evolution to the $\delta^{13}C_{carb}$ with a decreasing trend during the Smithian, followed by an increase at the SSB. However, a closely correlated evolution is not observed.

The carbonate concentration shows an important variability (from 6.0 to 93.0%), with a mean value of 41.6 (± 27.0%, 1σ, Fig. III.B.2, Table III.B.1). Highest proportion of carbonate is reached in SSB Unit within the late Smithian interval reflecting variations in the dominant lithologies (Fig. III.B.2).

The $\delta^{13}C_{carb}$ and the $\delta^{13}C_{org}$ signals do not follow a straight parallel evolution and do not show any covariation (Fig. III.B.3a). As a covariation is expected between carbonate and OM isotopic signals (e.g., Zeebe, 2012), the LWC isotopic signal may not record the exogenic carbon cycle, but in turn may correspond to local conditions and/or secondary processes overprint.

Because only the $\delta^{13}C_{org}$ signal seems to follow the recognized couplet of negative and isotopic shifts characteristic of the middle Smithian–SSB interval, this questions the preservation of the $\delta^{13}C_{carb}$ record and its accuracy, particularly given the small magnitude isotopic shift observed at the top of the LWC late Smithian interval (Fig. III.C.2).

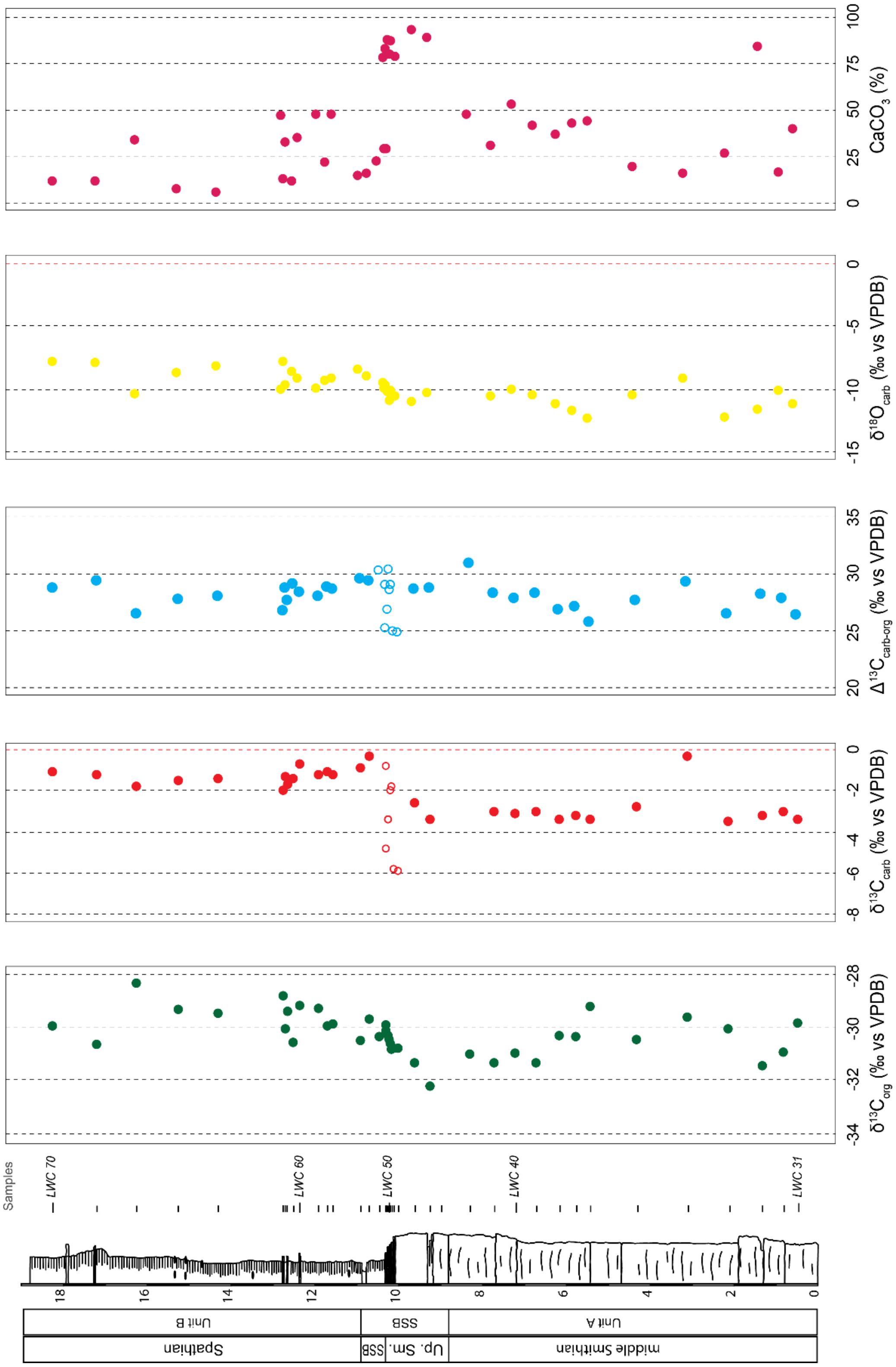

Figure III.B.2: Carbon and oxygen isotopes record, carbonate and total organic contents chemostratigraphy in the Lower Weber Canyon section. Open symbols in SSB units bear uncertainties due to potential secondary alteration.

	Sample	$\delta^{13}C_{org}$ ‰ vs VPDB ± 0,80	$\delta^{13}C_{carb}$ ‰ vs VPDB ± 1,40	$\Delta^{13}C_{carb-org}$ ‰ vs VPDB ± 1,44	$\delta^{18}O_{carb}$ ‰ vs VPDB ± 1,19	$CaCO_3$ % ± 26,95
Unit B	LWC70	-29,92	-1,10	28,82	-7,80	12,00
	LWC69	-30,64	-1,20	29,44	-7,90	12,00
	LWC68	-28,34	-1,80	26,54	-10,40	34,00
	LWC67	-29,33	-1,50	27,83	-8,70	8,00
	LWC66	-29,46	-1,40	28,06	-8,20	6,00
	LWC64	-28,80	-2,00	26,80	-10,00	47,00
	LWC63	-30,06	-1,30	28,76	-7,80	13,00
	LWC62	-29,37	-1,70	27,67	-9,70	33,00
	LWC61	-30,56	-1,40	29,16	-8,60	12,00
	LWC60	-29,15	-0,70	28,45	-9,10	35,00
	LWC59	-29,26	-1,20	28,06	-9,90	48,00
	LWC58	-29,93	-1,10	28,83	-9,30	22,00
	LWC57	-29,88	-1,20	28,68	-9,10	48,00
SSB	LWC55	-30,48	-0,90	29,58	-8,40	15,00
	LWC54	-29,69	-0,30	29,39	-9,00	16,00
	LWC53	-30,35	N/A	30,35	N/A	23,00
	LWC52	-30,10	-4,80	25,30	-9,50	78,00
	LWC51	-29,90	-0,80	29,10	-9,90	29,00
	LWC50	-30,29	-3,40	26,89	-9,70	83,00
	LWC49b	-30,43	N/A	30,43	N/A	29,00
	LWC49	-30,61	-2,00	28,61	-10,20	88,00
	LWC48	-30,82	-1,80	29,02	-10,90	80,00
	LWC47	-30,76	-5,80	24,96	-10,10	87,00
	LWC46	-30,78	-5,90	24,88	-10,60	79,00
	LWC45	-31,31	-2,60	28,71	-11,00	93,00
	LWC44	-32,21	-3,40	28,81	-10,30	89,00
Unit A	LWC42	-30,98	N/A	30,98	N/A	48,00
	LWC41	-31,34	-3,00	28,34	-10,60	31,00
	LWC40	-30,97	-3,10	27,87	-10,00	53,00
	LWC39	-31,33	-3,00	28,33	-10,50	42,00
	LWC38	-30,31	-3,40	26,91	-11,20	37,00
	LWC37	-30,34	-3,20	27,14	-11,70	43,00
	LWC36	-29,22	-3,40	25,82	-12,30	44,00
	LWC35	-30,46	-2,80	27,66	-10,50	20,00
	LWC34	-29,59	-0,30	29,29	-9,10	16,00
	LWC33	-30,05	-3,50	26,55	-12,20	27,00
	LWC32	-31,45	-3,20	28,25	-11,60	84,00
	LWC30	-30,91	-3,00	27,91	-10,10	17,00
	LWC31	-29,83	-3,40	26,43	-11,20	40,00

Table III.B.1. Geochemical data with $\delta^{13}C_{org}$, $\delta^{13}C_{carb}$, $\Delta^{13}C_{carb-org}$, $\delta^{18}O_{carb}$ and carbonate ($CaCO_3$) contents (after Grosjean *et al.*, *in prep.*).

- Preservation of the isotopic signal

The figure III.B.3b does not show marked correlation between the $\delta^{13}C_{carb}$ signal and the carbonate content (% $CaCO_3$). The figure III.B.3c however shows a positive correlation between the $\delta^{13}C_{carb}$ signal and the $\delta^{18}O_{carb}$ signal within Unit A. This therefore indicates an absence of sensible diagenetic overprint within SSB Unit and Unit B (Sansjofre *et al.*, 2011), while Unit A might have suffered substantial remobilization.

Additionally, the presence of several successive outliers in the $\delta^{13}C_{carb}$ signal argues for underlying secondary processes that may have blurred at least part of the isotopic signal at LWC. Further tests (e.g., Mn/Sr ratio *vs* $\delta^{13}C_{carb}$ and $\delta^{18}O_{carb}$) will be performed throughout the succession.

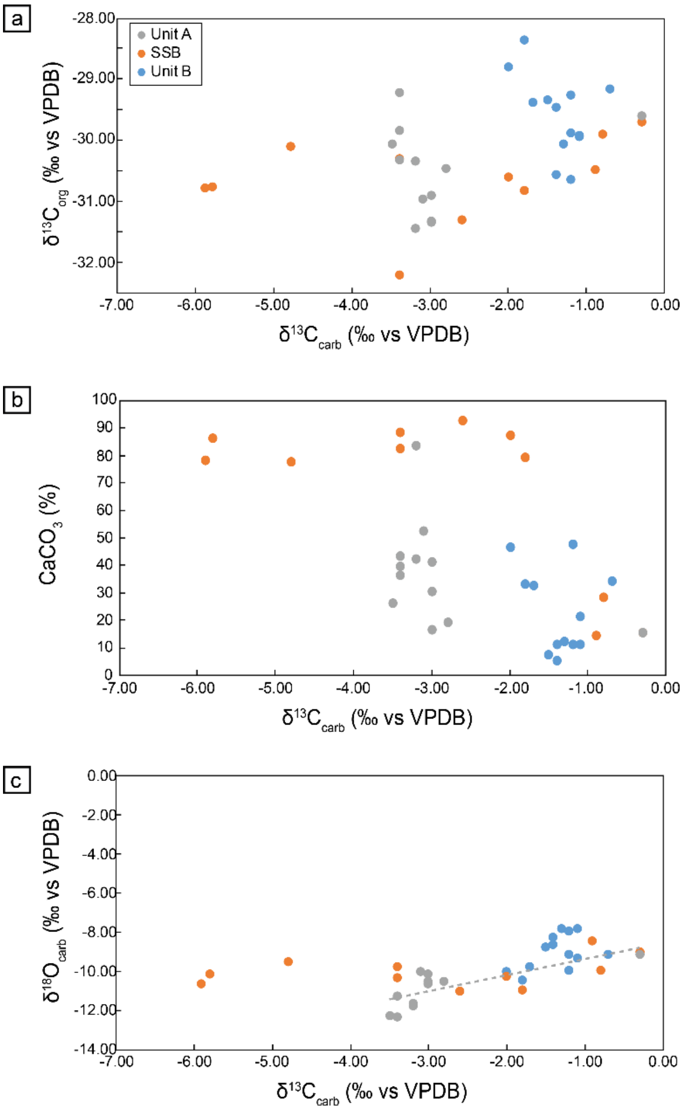

Figure III.B.3: Isotopic and elementary geochemical parameters of the Lower Weber Canyon section. a) $\delta^{13}C_{carb}$ vs $\delta^{13}C_{org}$.b) $\delta^{13}C_{carb}$ vs $CaCO_3$ content. c) $\delta^{13}C_{carb}$ vs $\delta^{18}O_{carb}$. A positive correlation is observed between $\delta^{13}C_{carb}$ vs $\delta^{18}O_{carb}$ within Unit A.

C. Southern SFB signal: Minersville

- Introductory remarks and geological setting

The southern SFB geochemical record is represented by data from the Minersville (MV) section, located in southwestern Utah (Fig. III.C.1a). This section was thoroughly studied by Thomazo *et al.* (2016). Main results and interpretations of their work regarding the carbon isotopic signal and its preservation are summed up in the following lines. However, descriptions of the T&M elements were absent from the initial publication of Thomazo *et al.* (2016) and provided here.

The MV section reflects deposition of the Early Triassic Thaynes Group (*sensu* Lucas *et al.*, 2007) within shallow marine environments of the SFB (Vennin *et al.*, 2015; Thomazo *et al.*, 2016). The sedimentary succession of the MV section has been described by Vennin *et al.* (2015) and it mainly represents the Smithian and part of the Spathian (Fig. III.B.1b; Brayard *et al.*, 2011, 2013; Vennin *et al.*, 2015; Thomazo *et al.*, 2016).

This ~160 m-thick section is divided into 5 main parts: basal red beds, Units A, B and C, and SSB (Smithian/Spathian boundary; Fig. III.C.1b). Red beds consist in Late Dienerian (?) to Smithian inner ramp transitional continental to shallow marine (deltaic?) fine terrigenous (dolo-)siltstones. Unit A is dominated by microbial limestones deposited under intertidal to supratidal inner ramp settings, evolving into tide-dominated bioclastic shoreface levels. Unit B is composed of mudstones, finely laminated and represents homogeneous outer to mid-ramp upper offshore settings. Some storm-induced beds are locally present. The SSB interval is made of marls deposited under outer ramp lower offshore environments, below the storm wave base and corresponds to the maximum inundation described in this part of the SFB so far (e.g., Brayard *et al.*, 2013; Vennin *et al.*, 2015). Finally, Unit C ranges from outer ramp mudstones with local storm-induced levels (resembling those of Unit B) to subtidal microbial carbonates of outer to mid-ramp environments (Vennin *et al.*, 2015; Thomazo *et al.*, 2016). A third order sequential trend is visible along the MV section, with the regional maximum flooding surface (MFS; e.g., Embry, 1997) occurring in the SSB interval.

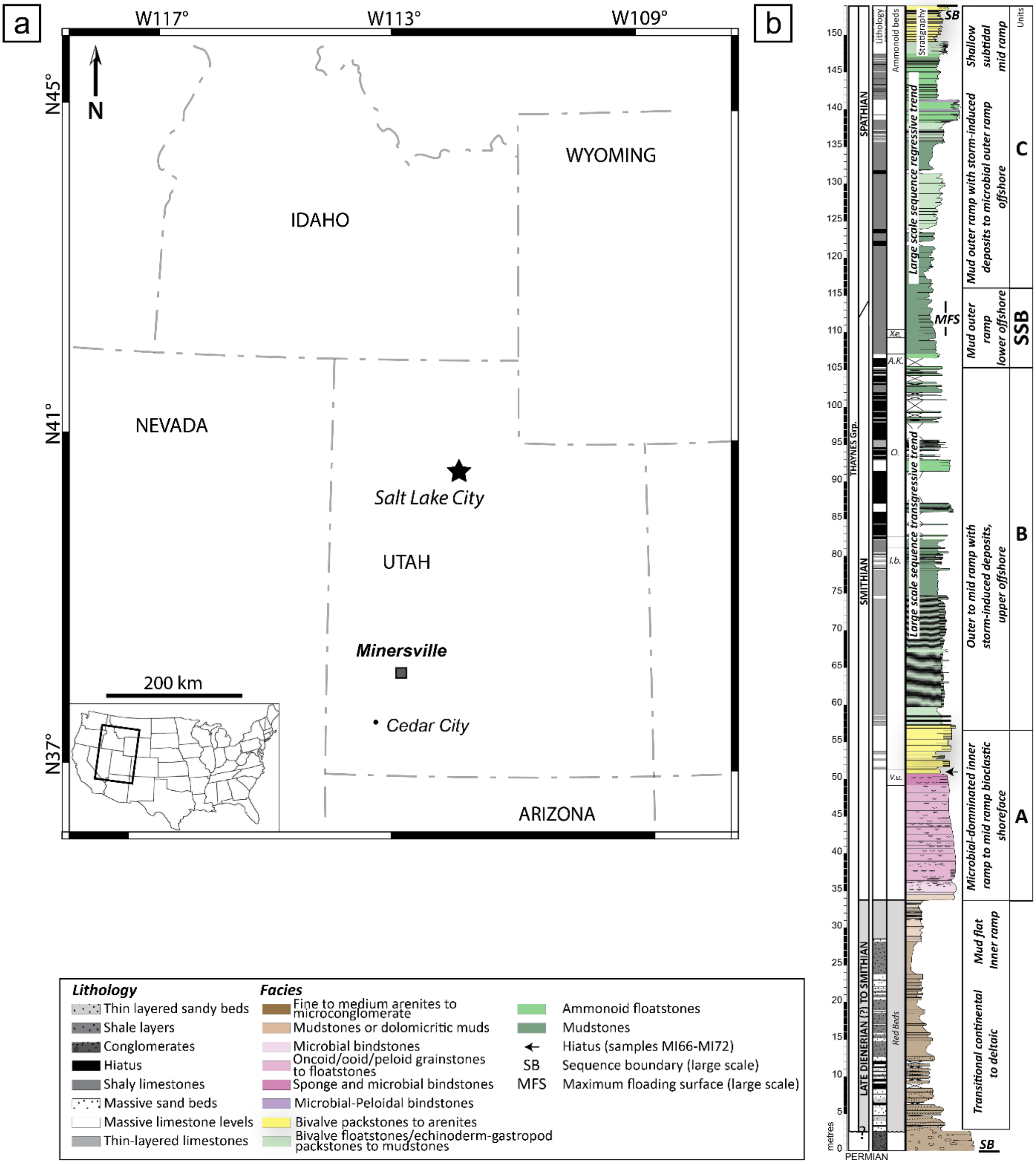

Figure III.C.1: a) Map of the studied area and location of the Minersville section. b) Synthetic log of the Minersville section showing the sequential framework, facies, lithologies and depositional settings (after Vennin *et al*., 2015). Synthetic ammonoid biozonation after Brayard *et al.* (2013); V.u.: Vercherites undulatus beds; I.b.: Inyoites beaverensis beds; O.: Owenites beds; A.k.: Anasibirites kingianus beds; Xe: Xenoceltitidae "gen. indet." A beds. SSB: Smithian/Spathian Boundary.

Eighty-four bulk rock samples were collected and powdered for geochemical analyses (carbon isotope signal, oxygen isotope signal, total organic carbon and carbonate contents and seventy were selected for T&M elements analyses) using the same protocol as described in Caravaca *et al.* (2017, see section III.A).

• Paired carbon isotopic signal

The $\delta^{13}C_{org}$ values vary from -30.5 to -27.7‰, with a mean value of -29.1 (± 0.7‰, 1σ, Fig. III.C.2, Table III.C.1). This organic matter (OM) signal show little variation contrary to the $\delta^{13}C_{carb}$ signal, and does not seem to parallel it either.

The $\delta^{13}C_{carb}$ values vary from -4.5 to 1.8‰, with a mean value of -1.1 (± 1.8‰, 1σ, Fig. III.C.2, Table III.C.1). The $\delta^{13}C_{carb}$ signal shows a decreasing trend during the Smithian interval, followed by an increase through the SSB (Fig. III.C.2). This pattern follows the well-known global signal for the carbon isotopic signal during the Smithian-Spathian interval, which usually evidences a couplet of negative and positive isotopic excursions before and across the SSB, respectively (e.g.; Galfetti *et al.*, 2007b; Grasby *et al.*, 2013; see Fig. 6 in Caravaca *et al.*, *in press* b, see section III.A).

The $\Delta^{13}C_{carb-org}$ values vary from 25.2 to 31.0 ‰, with a mean value of 27.7 (± 1.6‰, 1σ, Fig. III.C.2, Table III.C.1). The ratio follows rather closely the $\delta^{13}C_{carb}$ signal, due to the relative "flatness" of the OM isotope signal. It shows a general decreasing trend during the Smithian interval, and a marked increased from the SSB upwards (Fig. III.C.2). The signal remains stable during the subsequent Spathian interval.

The total organic carbon (TOC) content varies between 0.02 and 0.4 wt.% with a mean value of 0.1 (± 0.1 wt.%, 1σ, Fig. III.C.2, Table III.C.1). The TOC content shows two peaks at the top of unit A in the bioclastic limestones, and at the very top of the unit B, just before the SSB interval, concomitantly of the reversal of the isotopic trend (negative to positive shift) in the $\delta^{13}C_{carb}$ signal (Fig. III.C.2).

The $\delta^{18}O_{carb}$ values vary from -13.8 to -8.6‰, with a mean value of -11.1 (± 1.3‰, 1σ, Fig. III.C.2, Table III.C.1). This signal shows an evolution parallel to that of the $\delta^{13}C_{carb}$ with a decreasing trend during the Smithian, followed by an increased at the SSB. However, a closely correlated evolution is not observed.

The carbonate concentration shows an important variability along the section (from 44.7 to 98.7%), with a mean value of 78.3 (± 15.3%, 1σ, Fig. III.C.2, Table III.C.1). The highest proportion of carbonate is reached within Units A and C and within the SSB interval (Fig. III.C.2).

Figure III.C.3a shows a cross plot of the $\delta^{13}C_{carb}$ and $\delta^{13}C_{org}$ values. It highlights that both OM and carbonate carbon isotopic signals are correlated in Unit A (r = 0.87***) and display similar evolution. This is expected when recording variations of the dissolved inorganic carbon (DIC) reservoir, thus representing variations of the global exogenic carbon cycle (e.g., Zeebe, 2012). The isotopic signal of this Unit A shows a decreasing trend as commonly observed for the Smithian (e.g., Galfetti *et al.*, 2007b, Grasby *et al.*, 2013), and usually interpreted to be related to thermogenic/volcanogenic release of ^{12}C-enriched carbon in relation to the Siberian traps volcanism (e.g., Sobolev *et al.*, 2011). However, the lack of correlation between $\delta^{13}C_{carb}$ and $\delta^{13}C_{org}$ values in the rest of the MV section (Fig. III.C.3a) raises the question of the preservation of the isotopic signal.

- Preservation of the isotopic signal

Mn content and Mn/Sr ratio were investigated (Figs. III.C.3b and III.C.3c). High Mn content and a strong negative correlation between Mn content and the $\delta^{13}C_{carb}$ in Unit B ($r = -0.91$***; Fig. III.C.3b) may be indicative of an enhanced Mn flux to the system. Additionally, high Mn/Sr ratios (from 3.4 to 13.1, higher than 2; Fig. III.C.3c) and their correlation with $\delta^{18}O_{carb}$ ($r = 0.90$***; Fig. III.C.3c) may record the influence of reducing fluids during burial diagenesis (e.g., Kaufman & Knoll, 1995).

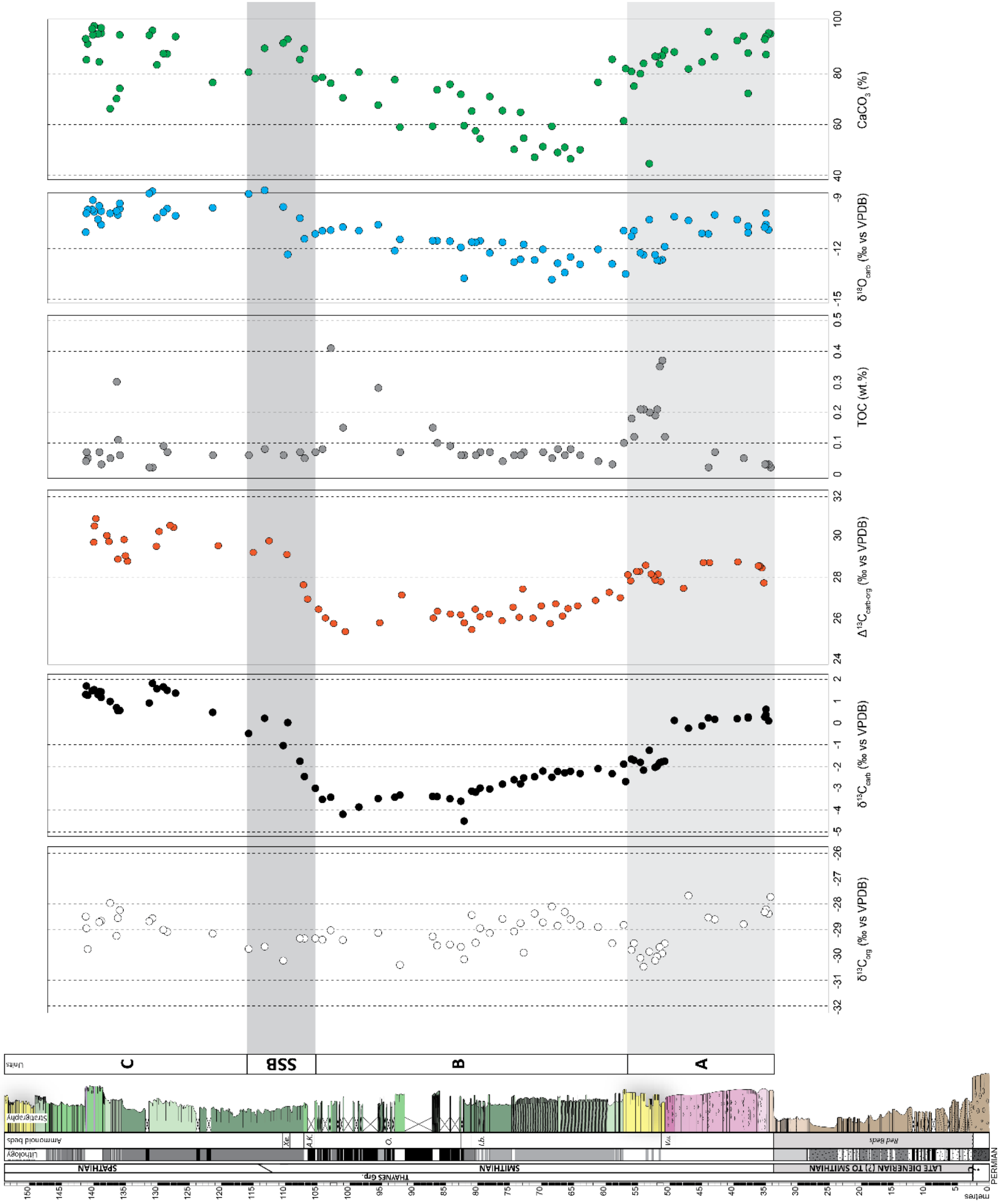

Figure III.C.2: Carbon and oxygen isotopes record, carbonate and total organic contents chemostratigraphy in the Minersville section (after Thomazo *et al.*, 2016)

	Sample	$\delta^{13}C_{org}$	$\delta^{13}C_{carb}$	$\Delta^{13}C_{carb-org}$	TOC	$\delta^{18}O_{carb}$	$CaCO_3$
		‰ vs VPDB	‰ vs VPDB	‰ vs VPDB	wt.%	‰ vs VPDB	%
		± 0,67	± 1,85	± 1,61	± 0,09	± 1,28	± 15,32
Unit A	MI40	N/A	N/A	N/A	N/A	N/A	N/A
	MI237	-27,72	N/A	27,72	0,02	N/A	95,70
	MI45	-28,38	0,09	28,47	0,03	-10,93	96,00
	MI245a	-28,21	0,37	28,58	0,03	-9,92	87,50
	MI245b	N/A	0,62	N/A	N/A	-10,59	94,59
	MI51	-28,32	0,27	28,59	0,03	-10,75	93,44
	MI54a	N/A	0,22	N/A	N/A	-11,07	72,25
	MI54b	N/A	0,27	N/A	N/A	-10,69	88,11
	MI248	-28,79		28,79	0,05	N/A	94,80
	MI57	N/A	0,19	N/A	N/A	-10,30	93,00
	MI59	-28,60	0,16	28,76	0,07	-10,02	86,61
	MIA1-4	-28,53	0,23	28,76	0,02	-11,14	96,50
	MIA1	N/A	-0,14	N/A	N/A	-11,11	84,53
	MI62	-27,67	-0,25	27,42	N/A	-10,35	81,86
	MI66	N/A	0,11	N/A	N/A	-10,12	88,50
	MI72a	-29,55	-1,76	27,79	0,12	-11,89	89,10
	MI74	-29,94	-1,78	28,16	0,37	-12,66	87,10
	MI77	-29,69	-1,83	27,86	0,35	-12,71	83,80
	MI75	-30,06	-1,99	28,07	0,21	-12,68	86,70
	MI76	-30,22	-2,04	28,18	0,19	-12,37	86,80
	MI79	-29,87	-1,26	28,61	0,20	-10,30	44,67
	MI80	-30,46	-2,17	28,29	0,21	-12,38	84,00
	MI81	-30,12	-1,81	28,31	0,21	-12,26	80,00
	MI82	-29,54	-1,71	27,83	0,12	-10,96	75,08
	MI83	-29,80	-1,66	28,14	0,18	-11,28	80,84
	MI84	N/A	-2,69	N/A	N/A	-13,50	81,95
Unit B	MI85	-28,82	-1,89	26,93	0,10	-10,95	61,44
	MI87	-29,54	-2,33	27,21	0,03	-12,91	85,63
	MI88	-28,90	-2,10	26,80	0,04	-12,05	76,63
	MI89	-28,83	-2,32	26,51	0,06	-12,93	50,12
	MI92	-28,60	-2,22	26,38	0,08	-12,50	46,52
	MI93	-28,31	-2,29	26,02	0,06	-13,42	51,06
	MI95	-28,85	-2,23	26,62	0,08	-12,87	49,04
	MI96	-28,10	-2,49	25,61	0,05	-13,83	59,33
	MI97	-28,72	-2,21	26,51	0,07	-12,05	51,34
	MI98	-28,37	-2,47	25,90	N/A	-12,68	47,15
	MI100	-29,91	-2,52	27,39	0,07	-11,76	54,67
	MI101	-28,75	-2,80	25,95	0,06	-12,64	64,83
	MI102	-29,08	-2,61	26,47	0,06	-12,80	50,27
	MI103	-28,58	-2,81	25,77	0,04	-11,63	65,47
	MI105	-29,14	-3,03	26,11	0,07	-12,26	70,97
	MI106	-28,95	-2,99	25,96	0,07	-11,55	54,47

	MI107	-29,52	-3,18	26,34	0,06	-11,64	57,54
	MI108	-28,43	-3,13	25,30	N/A	-11,62	65,30
	MI109	-30,17	-4,50	25,67	0,06	-13,75	59,59
	MI111	-29,68	-3,59	26,09	0,06	-11,93	71,87
	MI113	-29,59	-3,48	26,11	0,09	-11,57	75,82
	MI112	-29,63	-3,38	26,25	0,10	-11,54	73,67
	MI114	-29,27	-3,37	25,90	0,15	-11,54	59,36
	MI115	-30,39	-3,31	27,08	0,07	-11,46	58,97
	MI117	N/A	-3,41	N/A	N/A	-12,13	77,63
	MI118	-29,13	-3,47	25,66	0,28	-10,60	67,66
	MI119	N/A	-3,86	N/A	N/A	-10,95	80,56
	MI120	-29,41	-4,19	25,22	0,15	-10,74	70,57
	MI122	-29,03	-3,41	25,62	0,41	-10,92	76,24
	MI123	-29,40	-3,51	25,89	0,08	-10,96	78,59
SSB	MI124	-29,35	-3,00	26,35	0,07	-11,14	78,09
	MI126	-29,35	-2,46	26,89	0,05	-11,43	89,72
	MI127	-29,35	-1,76	27,59	0,07	-10,21	85,55
	MI150	N/A	0,01	N/A	N/A	-12,35	93,52
	MI129	-30,22	-1,04	29,18	0,06	-9,55	92,01
	MI130	-29,67	0,21	29,88	0,08	-8,57	89,97
	MI151	-29,76	-0,49	29,27	0,06	-8,78	80,59
Unit C	MI153	-29,16	0,48	29,64	0,06	-9,60	76,51
	MI154	N/A	1,36	N/A	N/A	-10,07	94,57
	MI155	-29,09	1,49	30,58	0,07	-9,65	87,74
	MI156	-29,01	1,65	30,66	0,09	-9,86	87,88
	MI157b	N/A	1,56	N/A	N/A	-10,19	83,45
	MI158	-28,56	1,81	30,37	0,02	-8,63	96,95
	MI159	-28,68	0,91	29,59	0,02	-8,76	95,11
	MI160	-28,24	0,57	28,81	0,06	-9,66	74,20
	MI180	N/A	0,57	N/A	N/A	-9,34	95,20
	MI161	-28,55	0,56	29,11	0,11	-10,02	54,85
	MI162	-29,25	0,70	29,95	0,30	-9,80	70,18
	MI163	-27,96	0,98	28,94	0,05	-9,93	66,24
	MI164	-28,66	1,16	29,82	0,03	-10,60	95,80
	MI179	N/A	1,42	N/A	N/A	-9,80	98,00
	MI166	-28,71	1,43	30,14	0,07	-9,49	84,63
	MI165	N/A	1,30	N/A	N/A	-10,28	95,61
	MI167	N/A	1,52	N/A	N/A	-9,84	98,74
	MI194	N/A	1,49	N/A	N/A	-9,15	95,20
	MI168	N/A	1,47	N/A	N/A	-9,71	97,60
	MI170	-29,77	1,26	31,03	0,05	-9,71	91,69
	MI171	-28,95	1,69	30,64	0,07	-9,93	85,45
	MI173	-28,49	1,30	29,79	0,04	-11,04	93,70

Table III.C.1. Geochemical data with $\delta^{13}C_{org}$, $\delta^{13}C_{carb}$, $\Delta^{13}C_{carb-org}$, Total Organic Carbon (TOC) content, $\delta^{18}O_{carb}$ and carbonate ($CaCO_3$) contents (after Thomazo *et al.*, 2016).

The overall low TOC content and the absence of correlation with the $\delta^{13}C_{org}$ signal (Fig. III.C.3d) suggest that an input of OM or an increasing contribution of a dissolved organic carbon (DOC) pool are underlying processes that cannot explain the decoupling and variations of the carbon isotope signal in the MV section.

The observed precipitation of Mn-bearing carbonate and the development of a redox-gradient in surface sediments (Thomazo *et al.*, 2016) indicate the potential presence of suboxic conditions at the bottom water/sediment interface (Tribovillard *et al.*, 2006), particularly throughout Unit B. Associated large pyrite framboids within Unit B (>20µm; Thomazo *et al.*, 2016: fig. 5) are also common diagenetic features formed under oxygen-depleted conditions at the redox boundary (Wilkin & Barnes, 1997). However, a detailed analysis on evolution of framboid size distribution is needed to firmly confirm this hypothesis.

Nevertheless, these results hint toward a remobilization within the first few cm of sediment during the early diagenesis in suboxic conditions, supposedly under the control of bacterially-induced sulfato-reduction (BSR) processes (Thomazo *et al.*, 2016).

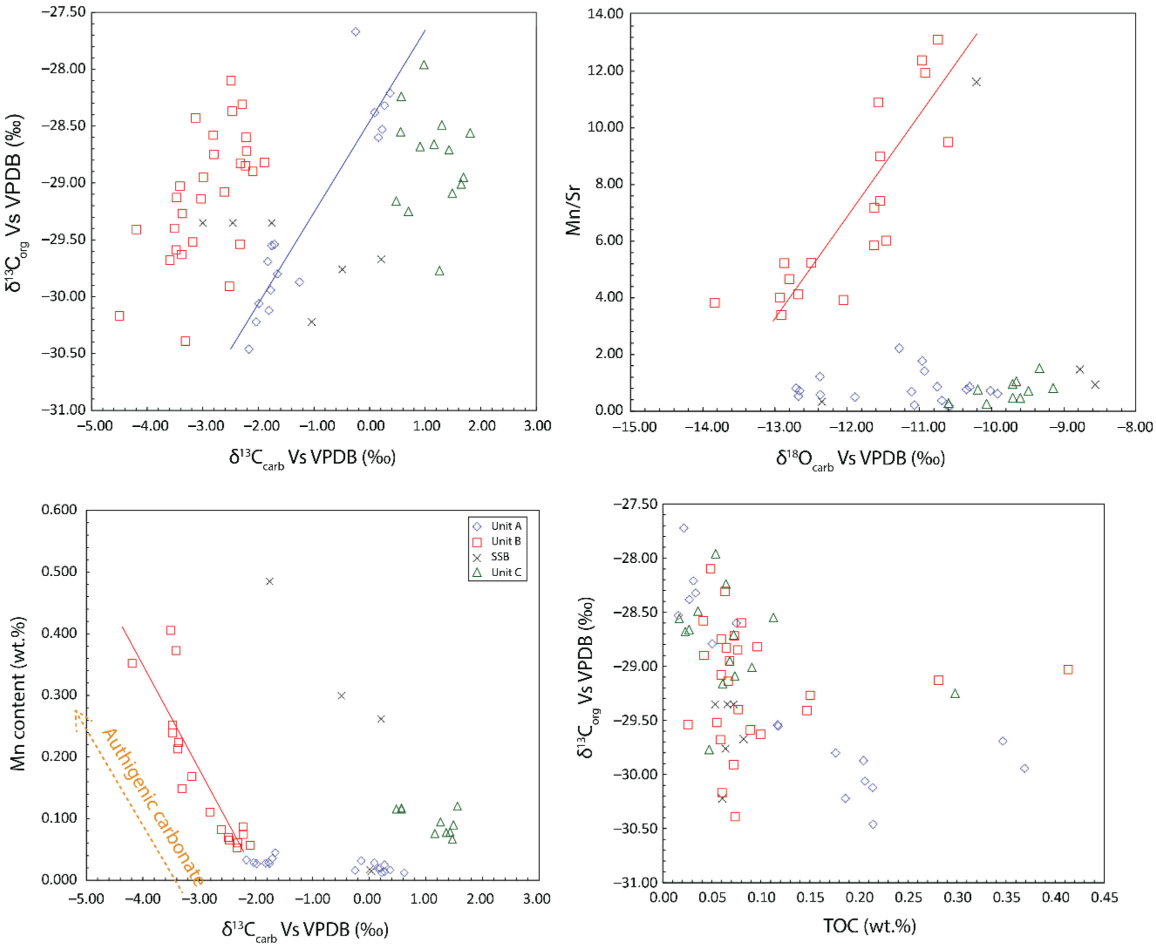

Figure III.C.3: Isotopic and elementary geochemical parameters of the Minersville section (after Thomazo *et al.*, 2016). a) $\delta^{13}C_{org}$ vs $\delta^{13}C_{carb}$. b) Mn content vs $\delta^{13}C_{carb}$. c) Mn/Sr ratio vs $\delta^{18}O_{carb}$. d) $\delta^{13}C_{org}$ vs Total Organic Carbon (TOC) content. Uncertainties are smaller than the symbol size.

- Trace and major elements

T&M elements are commonly used to track down variations in terrigenous inputs, redox conditions and/or paleoproductivity (e.g., Tribovillard *et al.*, 2006, 2008; Sauvage *et al*., 2013). Because Al is usually of detrital origin and most of the time immobile during diagenetic processes, its concentration (wt.%) is used to decipher the terrigenous input (Böning *et al.*, 2004). A cross-plot of a given element *versus* Al concentration therefore indicates whether the concentration of this element is controlled by detrital flux when associated with Al, or conversely is due to an authigenic enrichment (e.g., Sauvage *et al.*, 2013; Caravaca *et al.*, *in press* b, see section III.A). Additionally, proportions of T&M elements are given under the form of an Al-normalized ratio to avoid any dilution effect (Tribovillard *et al.*, 2006). Correlations between T&M elements and Al are expressed using the Spearman correlation coefficient (r) and its associated probability.

- *Detrital proxies and influx*

Al concentrations range from 0.1 to 2.4 wt.%, with a mean value of 0.7 (± 0.5 wt.%, 1σ, Fig. III.C.4, Table III.C.2), and show no significant variation along the MV section. An increase in Al concentration with more scattered values is nonetheless visible in Spathian samples, with no incidence on the general trend of the detrital proxies.

Fe/Al, Zr/Al, Th/Al, Ti/Al and V/Al ratios show a strong correlation to Al concentration (r = 0.71*** for Fe/Al, r = 0.77*** for Zr/Al, 0.88*** for Th/Al, r = 0.96*** for Ti/Al, r = 0.87*** for V/Al, r = 0.77*** for Zr/Al, 0.88*** for Th/Al). Zr, Th and Ti are usually interpreted as terrigenous proxies for the detrital fraction when correlated to Al due to their siliciclastic origin (Rachold & Brumsack, 2001; Sauvage *et al.*, 2013). However, V is rather representative of the redox conditions of the water column (e.g., Tribovillard *et al.*, 2006, 2008; Sauvage *et al.*, 2013). The Fe/Al ratio values ranges from 0.2 to 2.8, with a mean value of 0.6 (± 0.4, 1σ, Fig. III.C.4, Table III.C.2). The Zr/Al ratio ranges from 3.1 x10-3 to 1.4 x10-1, with a mean value of 1.2 x10-2 (± 1.8 x10-2, 1σ, Fig. III.C.4, Table III.C.2). The Th/Al ratio ranges from 1.9 x10-4 to 9.5 x10-4, with a mean value of 3.4 x10-4 (± 1.5 x10-4, 1σ, Fig. III.C.4, Table III.C.2). The Ti/Al ratio ranges from 0.1 to 0.3, with a mean value of 0.1 (± 0.04, 1σ, Fig. III.C.4, Table III.C.2). Finally, the V/Al ratio ranges from 1.4 x10-3 to 8.1 x10-3, with a mean value of 3.4 x10-3 (± 1.5 x10-3, 1σ, Fig. III.C.4; Table III.C.2).

As observed in the HS section (Caravaca *et al.*, 2017, see section III.A), the correlation of V with Al makes this element a marker of the terrigenous fluxes. Ti/Al, Zr/Al, Th/Al and V/Al show no marked variation throughout the entire MV section, except for a slight positive peak in Ti/Al, Zr/Al and Th/Al ratios at the very base of the Unit B. This slight increase, followed a rapid decrease and return to mean values for these different ratios, may be linked to the change in lithology occurring at the transition between Units A and B and renewed terrigenous inputs at that time. Otherwise, rest of the section shows a relative stability in terrigenous inputs, as evidenced by the absence of variation in the Al concentration. This suggests continuous continental weathering conditions during the recorded interval (Calvert *et al.*, 1996).

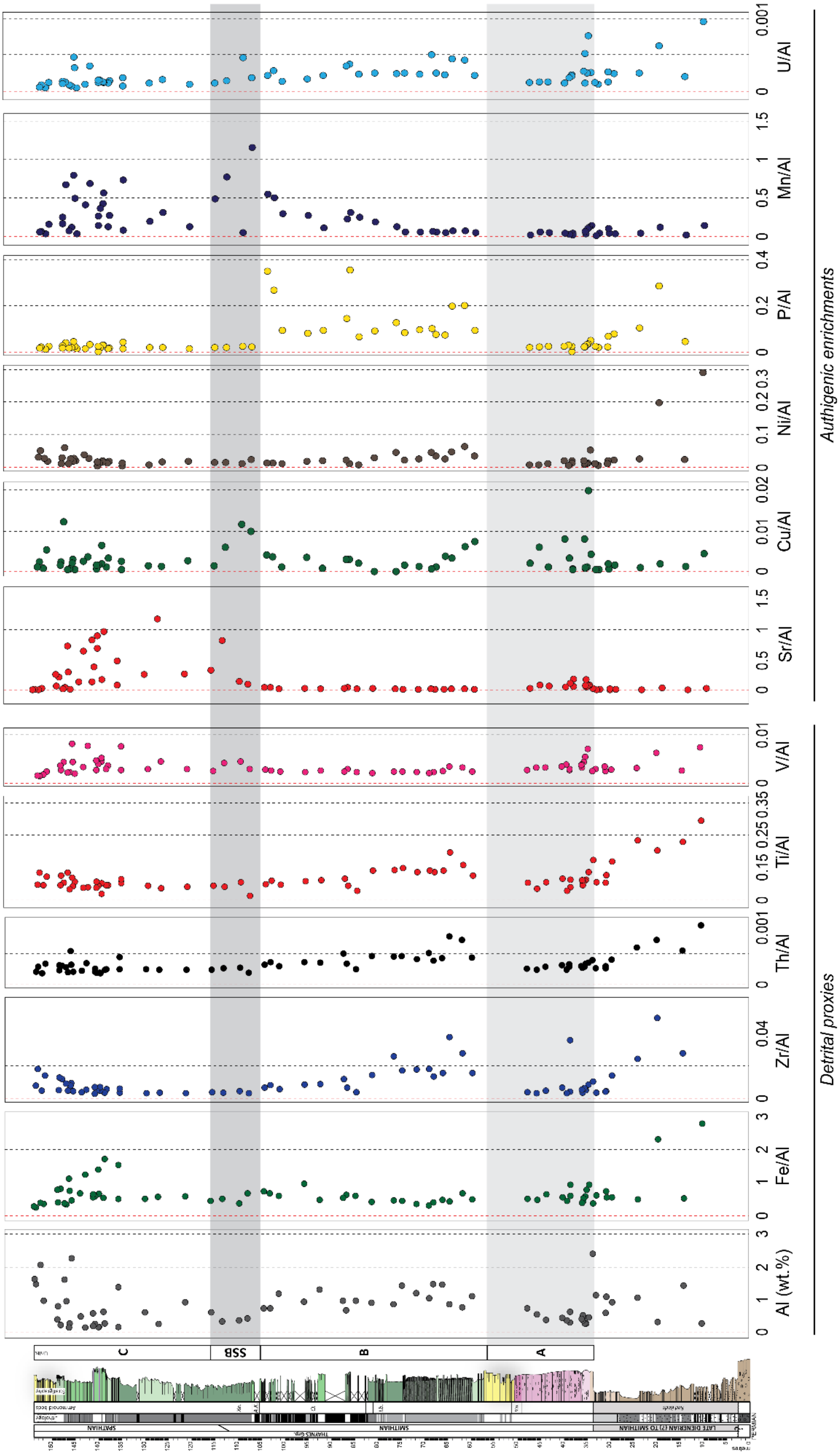

Figure III.C.4: Chemostratigraphy of selected trace and major elements in the Minersville section, listed after their detrital and authigenic origin.

	Sample	Al (Wt. %)	Fe/Al	Zr/Al	Th/Al	Ti/Al	V/Al	Sr/Al	Cu/Al	Ni/Al	P/Al	Mn/Al	U/Al
		± 0,52	± 0,43	± 1,83E-02	± 1,47E-04	± 4,00E-02	± 1,50E-03	± 2,70E-01	± 3,34E-03	± 4,06E-02	± 9,68E-02	± 0,24	± 1,64E-04
Unit A	MI5	0,273	2,80	1,42E-01	9,54E-04	2,95E-01	7,34E-03	2,75E-02	4,40E-03	2,91E-01	5,60E-01	0,14	9,54E-04
	MI7	1,426	0,51	2,81E-02	5,47E-04	2,29E-01	2,59E-03	6,31E-03	1,26E-03	2,31E-02	4,44E-02	0,02	2,03E-04
	MI15	0,320	2,32	5,00E-02	7,18E-04	2,02E-01	6,25E-03	3,87E-02	1,87E-03	1,98E-01	2,86E-01	0,12	6,25E-04
	MI19	1,053	0,46	2,48E-02	5,98E-04	2,34E-01	3,04E-03	7,88E-03	8,55E-04	2,50E-02	1,04E-01	0,04	2,56E-04
	MI24	0,913	0,54	1,42E-02	4,05E-04	1,68E-01	2,74E-03	1,11E-02	1,53E-03	2,15E-02	7,89E-02	0,03	2,41E-04
	MI25	1,082	0,54	4,62E-03	2,96E-04	1,25E-01	2,40E-03	7,30E-03	6,47E-04	1,85E-02	6,85E-02	0,04	1,29E-04
	MI22	0,595	0,72	4,37E-03	2,69E-04	1,03E-01	3,36E-03	1,90E-02	1,85E-03	1,02E-02	2,20E-02	0,11	2,69E-04
	MI35	1,135	0,60	3,79E-03	2,64E-04	1,03E-01	2,82E-03	1,03E-02	3,52E-04	5,11E-03	1,73E-02	0,04	9,69E-05
	MI38	2,405	0,35	1,07E-02	3,99E-04	1,73E-01	2,41E-03	2,83E-03	4,99E-04	1,04E-02	2,45E-02	0,01	1,21E-04
	MI40	0,453	0,92	8,62E-03	3,54E-04	1,35E-01	7,07E-03	2,61E-02	4,20E-03	5,28E-02	4,82E-02	0,14	2,65E-04
	MI237	0,262	0,76	5,34E-03	3,44E-04	1,12E-01	5,34E-03	8,51E-02	1,98E-02	1,15E-02	3,33E-02	0,12	7,63E-04
	MI45	0,275	0,56	6,54E-03	2,91E-04	1,09E-01	4,36E-03	7,34E-02	1,09E-03	9,81E-03	3,17E-02	0,10	2,54E-04
	MI245a	0,511	0,42	4,70E-03	2,74E-04	1,06E-01	3,13E-03	5,36E-02	7,83E-04	8,62E-03	2,14E-02	0,03	1,17E-04
	MI245b	0,365	0,50	3,83E-03	2,74E-04	9,35E-02	3,83E-03	1,78E-01	8,22E-04	1,29E-02	2,39E-02	0,03	5,20E-04
	MI51	0,402	0,37	5,72E-03	2,98E-04	1,10E-01	3,73E-03	7,31E-02	7,96E-03	1,91E-02	2,17E-02	0,06	2,73E-04
	MI54a	0,304	0,59	3,61E-02	3,29E-04	8,86E-02	2,63E-03	1,85E-01	6,57E-04	1,97E-02	1,43E-03	0,04	2,30E-04
	MI54b	0,619	0,93	4,36E-03	2,91E-04	1,11E-01	2,91E-03	5,94E-02	4,84E-04	1,13E-02	2,47E-02	0,02	2,10E-04
	MI248	0,365	0,43	3,29E-03	2,46E-04	7,71E-02	3,83E-03	1,17E-01	3,29E-03	5,20E-03	2,99E-02	0,03	1,92E-04
	MI57	0,442	0,54	6,79E-03	3,17E-04	1,14E-01	3,39E-03	5,30E-02	7,92E-03	1,99E-02	2,47E-02	0,05	1,13E-04
	MI59	0,376	0,63	5,06E-03	2,93E-04	1,04E-01	3,19E-03	7,08E-02	1,06E-03	9,58E-03	2,32E-02	0,05	1,33E-04
	MIA1	0,542	0,46	3,32E-03	2,40E-04	8,29E-02	3,13E-03	8,41E-02	5,90E-03	7,19E-03	2,01E-02	0,06	1,29E-04
	MI62	0,728	0,49	4,12E-03	2,61E-04	1,02E-01	2,61E-03	2,89E-02	2,06E-03	6,87E-03	1,80E-02	0,02	1,24E-04
Unit B	MI87	1,106	0,46	1,59E-02	4,34E-04	1,25E-01	2,35E-03	1,40E-02	7,32E-03	3,43E-02	9,27E-02	0,05	2,17E-04
	MI88	0,767	0,66	2,83E-02	7,17E-04	1,56E-01	3,13E-03	1,88E-02	5,99E-03	6,31E-02	2,02E-01	0,07	4,30E-04
	MI89	0,852	0,41	3,80E-02	7,75E-04	1,96E-01	3,40E-03	1,77E-02	3,17E-03	4,74E-02	2,00E-01	0,07	4,46E-04
	MI92	1,455	0,45	1,58E-02	4,26E-04	1,40E-01	2,40E-03	9,76E-03	3,71E-03	2,39E-02	7,35E-02	0,05	2,27E-04
	MI95	1,482	0,39	1,38E-02	3,91E-04	1,35E-01	2,23E-03	1,12E-02	1,01E-03	3,33E-02	7,51E-02	0,06	2,56E-04
	MI96	1,037	0,29	1,85E-02	5,11E-04	1,39E-01	2,02E-03	1,74E-02	5,78E-04	4,51E-02	1,01E-01	0,07	5,01E-04
	MI98	1,196	0,34	1,82E-02	4,10E-04	1,35E-01	2,26E-03	1,32E-02	1,17E-03	2,41E-02	9,67E-02	0,05	2,34E-04
	MI102	1,434	0,43	1,74E-02	4,60E-04	1,48E-01	2,30E-03	1,23E-02	1,53E-03	2,19E-02	8,22E-02	0,06	2,51E-04
	MI103	0,857	0,44	2,64E-02	4,55E-04	1,41E-01	2,33E-03	2,19E-02	0,00E+00	4,44E-02	1,27E-01	0,13	2,45E-04
	MI108	0,905	0,40	1,48E-02	4,64E-04	1,40E-01	1,99E-03	2,59E-02	0,00E+00	2,88E-02	9,16E-02	0,19	2,54E-04
	MI113	0,963	0,57	3,95E-03	2,49E-04	7,65E-02	2,28E-03	2,27E-02	1,97E-03	6,96E-03	6,57E-02	0,25	2,39E-04
	MI112	0,675	0,62	6,82E-03	3,41E-04	9,24E-02	2,82E-03	4,25E-02	2,96E-03	9,63E-03	3,56E-01	0,32	3,70E-04
	MI114	0,971	0,51	1,22E-02	5,05E-04	1,15E-01	2,37E-03	2,56E-02	2,99E-03	2,09E-02	1,44E-01	0,23	3,50E-04
	MI115	1,305	0,46	9,12E-03	3,53E-04	1,10E-01	2,53E-03	1,89E-02	7,67E-04	1,92E-02	9,37E-02	0,11	2,22E-04
	MI118	0,929	0,95	8,61E-03	3,66E-04	1,06E-01	2,26E-03	2,85E-02	3,34E-03	1,83E-02	7,99E-02	0,27	1,72E-04
	MI120	1,188	0,59	5,81E-03	3,03E-04	9,58E-02	2,36E-03	2,26E-02	1,01E-03	1,01E-02	9,18E-02	0,30	1,43E-04
	MI122	0,738	0,66	8,26E-03	3,66E-04	1,09E-01	2,57E-03	4,23E-02	3,52E-03	1,29E-02	2,69E-01	0,50	2,84E-04

	MI123	0,733	0,73	6,82E-03	3,27E-04	9,73E-02	2,73E-03	4,46E-02	3,96E-03	1,21E-02	3,51E-01	0,55	2,18E-04
SSB	MI127	0,418	0,66	3,35E-03	1,91E-04	6,16E-02	2,87E-03	9,97E-02	9,81E-03	2,37E-02	2,09E-02	1,16	1,91E-04
	MI150	0,365	0,35	4,66E-03	2,74E-04	1,03E-01	4,38E-03	1,45E-01	1,15E-02	1,01E-02	2,39E-02	0,05	4,66E-04
	MI130	0,336	0,49	3,87E-03	2,68E-04	8,92E-02	4,17E-03	8,28E-01	5,95E-03	1,34E-02	1,95E-02	0,78	1,49E-04
	MI151	0,611	0,42	4,09E-03	2,45E-04	9,22E-02	2,45E-03	3,31E-01	1,31E-03	1,29E-02	1,78E-02	0,49	1,15E-04
Unit C	MI153	0,918	0,56	3,48E-03	2,40E-04	9,01E-02	2,83E-03	2,71E-01	2,61E-03	1,68E-02	1,43E-02	0,13	9,80E-05
	MI154	0,249	0,55	3,62E-03	2,41E-04	8,43E-02	4,42E-03	1,18E+00	1,21E-03	1,57E-02	1,75E-02	0,31	1,61E-04
	MI157b	0,603	0,49	3,31E-03	2,49E-04	9,24E-02	2,82E-03	2,60E-01	1,33E-03	6,63E-03	1,81E-02	0,20	1,16E-04
	MI160	1,376	0,49	3,78E-03	2,47E-04	1,00E-01	2,69E-03	7,99E-02	4,36E-04	3,27E-03	1,27E-02	0,08	7,27E-05
	MI180	0,159	1,52	6,30E-03	4,41E-04	1,13E-01	7,56E-03	4,86E-01	2,52E-03	1,13E-02	4,12E-02	0,74	1,89E-04
	MI164	0,275	1,72	5,81E-03	2,54E-04	9,36E-02	3,63E-03	9,69E-01	3,27E-03	1,82E-02	1,59E-02	0,28	1,45E-04
	MI166	0,627	0,52	3,83E-03	2,39E-04	9,37E-02	2,87E-03	1,75E-01	1,12E-03	1,15E-02	1,39E-02	0,12	1,12E-04
	MI194	0,159	0,64	5,04E-03	1,89E-04	6,79E-02	4,41E-03	6,95E-01	1,89E-03	1,95E-02	2,75E-02	0,57	1,26E-04
	MI168	0,156	1,39	7,05E-03	1,92E-04	9,98E-02	5,12E-03	9,01E-01	6,40E-03	1,54E-02	2,80E-02	0,43	1,28E-04
	MI170	0,257	0,57	5,06E-03	1,95E-04	9,34E-02	3,90E-03	3,85E-01	1,56E-03	1,13E-02	1,70E-02	0,37	1,56E-04
	MI225	0,574	0,53	3,13E-03	2,61E-04	8,66E-02	2,61E-03	1,38E-01	5,22E-04	3,48E-03	1,14E-03	0,14	1,22E-04
	MI169	0,193	0,63	7,25E-03	2,07E-04	1,05E-01	4,66E-03	8,33E-01	1,55E-03	1,50E-02	2,26E-02	0,26	1,55E-04
	MI197	0,143	1,22	5,60E-03	3,50E-04	8,81E-02	7,70E-03	6,45E-01	3,50E-03	2,73E-02	3,05E-02	0,69	3,50E-04
	MI200	0,490	0,66	3,88E-03	2,25E-04	8,69E-02	3,27E-03	1,36E-01	2,45E-03	3,76E-02	1,34E-02	0,41	1,02E-04
	MI206	2,263	0,44	4,64E-03	2,12E-04	1,05E-01	1,94E-03	1,14E-02	4,86E-04	2,00E-02	1,25E-02	0,03	5,30E-05
	MI202	0,275	0,74	9,81E-03	3,27E-04	9,15E-02	4,36E-03	2,97E-01	2,91E-03	2,65E-02	2,38E-02	0,50	3,27E-04
	MI203	0,148	1,11	8,10E-03	5,40E-04	1,17E-01	8,10E-03	7,36E-01	2,02E-03	1,69E-02	4,42E-02	0,80	4,72E-04
	MI205	0,950	0,31	4,95E-03	2,00E-04	8,14E-02	2,21E-03	4,07E-02	6,32E-04	2,40E-02	1,84E-02	0,12	7,37E-05
	MI181	1,609	0,34	9,45E-03	2,86E-04	1,34E-01	2,11E-03	2,31E-02	4,35E-04	1,02E-02	1,63E-02	0,08	9,32E-05
	MI209	0,230	0,79	1,22E-02	3,04E-04	1,02E-01	4,34E-03	2,11E-01	1,22E-02	5,95E-02	3,79E-02	0,68	1,30E-04
	MI211	0,799	0,39	1,30E-02	3,13E-04	1,24E-01	2,63E-03	6,56E-02	2,38E-03	2,83E-02	2,73E-02	0,16	1,38E-04
	MI187	0,386	0,77	5,18E-03	2,33E-04	9,46E-02	3,62E-03	2,61E-01	1,55E-03	9,58E-03	1,69E-02	0,25	1,04E-04
	MI214	0,969	0,34	1,45E-02	3,41E-04	1,21E-01	2,37E-03	2,50E-02	5,27E-03	1,74E-02	2,48E-02	0,16	1,24E-04
	MI 215	2,056	0,37	5,06E-03	1,90E-04	9,36E-02	1,75E-03	5,74E-03	6,81E-04	2,67E-02	1,06E-02	0,03	5,35E-05
	MI220	1,474	0,23	1,85E-02	2,92E-04	1,34E-01	1,36E-03	1,10E-02	2,37E-03	5,10E-02	2,07E-02	0,07	8,82E-05
	MI218	1,635	0,26	8,13E-03	2,08E-04	9,53E-02	1,47E-03	7,89E-03	1,10E-03	2,99E-02	1,47E-02	0,06	6,11E-05

Table III.C.2: Geochemical data with trace and major elements results.

- *Authigenic enrichment: markers of paleoproductivity and redox conditions*

The Sr/Al, Cu/Al, Ni/Al P/Al, Mn/Al, and U/Al ratios are not significantly correlated with Al concentration (r = -0.47*** for Sr/Al, 0.26*** for Cu/Al, 0.52*** for Ni/Al, r = 0.45*** for P/Al, r = 0.27, *P* = 0.02 for Mn/Al, 0.59*** for U/Al). This indicates an authigenic origin for enrichment in these elements, in relation to variations in paleoenvironemental conditions (e.g., Sauvage *et al.*, 2013; Caravaca *et al.*, *in* press b, see section III.A). Cu/Al, Ni/Al and P/Al are usually interpreted as markers of the paleoproductivity, while Mn/Al, V/Al and U/Al are Redox Sensitive Trace Elements (RSTE), used to track down variations of the redox conditions at the bottom-water/sediment interface and in upper diagenetic sediments (e.g., Algeo & Meynard, 2004; Algeo & Lyons, 2006; Tribovillard *et al.*, 2006; Sauvage *et al.*, 2013; Caravaca *et al.*, *in* press b, see section III.A). However, due to its high correlation with Al, V/Al cannot be used as a redox marker and was therefore interpreted as a detrital flux marker (see above).

The Sr/Al ratio ranges from 2.83 x10-3 to 1.18, with a mean value of 1.70 x10-1 (± 2.70 x10-1, 1σ, Fig. III.C.4, Table III.C.2). The Cu/Al ratio ranges from 0.0 to 2.0 x10-2, with a mean value of 2.9 x10-3 (±3.3 x10-3, 1σ, Fig. III.C.4, Table III.C.2). The Ni/Al ratio ranges from 3.3 x10-3 to 2.9 x10-1, with a mean value of 2.7 x10-2 (±4.1 x10-2, 1σ, Fig. III.C.4, Table III.BC.2). The P/AL ratio ranges from 1.1 x10-3 to 5.6 x10-1, with a mean value of 6.8 x10-2 (± 9.7 x10-2, 1σ, Fig. III.C.4, Table III.C.2). The Mn/Al ratio ranges from 0.0 to 1.2, with a mean value of 0.2 (± 0.2, 1σ, Fig. III.C.4, Table III.C.2). Finally, the U/Al ratio ranges from 5.3 x10-5 to 9.5 x10-4, with a mean value of 2.3 x10-4 (± 1.6, 1σ, Fig. III.C.4, Table III.C.2).

It can be noticed that the Ni/Al and Cu/Al ratios show no significant variation, except for the SSB interval where the Cu/Al ratio seems to show a slight increase that may correspond to a short-lived enrichment in OM. The P/Al ratio evolves quite differently, with no marked variations within the Units A and C and SSB interval, but with two marked peaks within and at the top of the Unit B, just before the SSB transition. The concomitance of these two peaks with two shifts in the Mn/Al ratio (Fig. III.C.4) suggests a potential diagenetic origin for these variations through P remobilization. The most important peak (up to 0.6) at the top of the Unit B is also concomitant to a peak in TOC content (Figs. III.C.2 and III.C.4), pointing toward a primary origin for this shift. This is therefore interpreted as a pulse of paleoproductivity during this short-lived interval (Thomazo *et al.*, 2016). The paleoproductivity record for the Unit B remains nonetheless complex partly owe to secondary remobilization.

At MV, only Mn and U are available as RSTE. The Mn/Al ratio shows no marked variation through Unit A and first half of Unit B. Then, second part of Unit B is marked by two peaks, concomitant with those observed for the P/Al ratio. Mn/Al ratio is also somewhat scattered within the SSB interval and Unit C. Because of the poor correlation between Mn content and $CaCO_3$ content (r = -0.18***), most part of the Mn reservoir is thought to be of secondary origin (Thomazo *et al.*, 2016). Moreover, Mn-bearing carbonates also suggest a secondary origin for the Mn reservoir (see above; Thomazo *et al.*, 2016). This behavior also indirectly indicates that short-lived periodical suboxic conditions may have prevailed repeatedly during deposition of the MV section. The Mn/Al ratio thus cannot be retained as a reliable proxy, the U/Al ratio therefore remains as the sole marker for redox conditions. The U/Al ratio shows several (4) peaks within the Unit B (Fig. III.C.4). The rest of the section shows no marked variations. These peaks have been interpreted to reflect several episodes of suboxic to anoxic conditions at the bottom-water/sediment interface, which is in agreement with preservation issues discussed above (Thomazo *et al.*, 2016).

- Interpretation of the MV geochemical signal: only local?

While the $\delta^{13}C_{carb}$ seems to mirror the global carbon isotopic record known for the Smithian-Spathian interval, the $\delta^{13}C_{org}$ does not follow a parallel evolution. This decoupling between carbonate and OM reservoirs therefore highlights a relative absence of external forcing (i.e. exogenic carbon cycle) on the recorded local $\delta^{13}C$ signal (Thomazo *et al.*, 2016).

Trace and major elements show that no terrigenous influence is important enough to alter the $\delta^{13}C$ signal throughout this section. Additionally, despite the short-lived paleoproductivity pulses and short-lived suboxic to anoxic conditions at the bottom-water/sediment interface recorded within Unit B (middle to upper Smithian), these parameters apparently did not influence the carbon isotopic record, highlighting the role of secondary processes in this signal (Thomazo *et al.*, 2016).

An important remobilization is recorded in Unit B, taking place during episodic suboxic conditions. Thomazo *et al.* (2016) showed that bacterially-induced early diagenesis might had a crucial role in controlling this remobilization, and can be responsible for the observed shifts in the isotopic record. This highlights a strong role of the local conditions in controlling the overall pattern of the isotopic record in MV, rather than global forcing parameters even if their influence cannot be ruled out.

To sum up: local controls exerted by the depositional systems are here of prime importance on the observed geochemical signal, and therefore questions the global interpretation of the Smithian-Spathian carbon isotope record.

D. Characterization of the basin-scale geochemical signal

In order to highlight the similitudes and differences observed within the SFB, the three studied sections (MV, HS, LWC; Fig. III.D.1) were correlated using ammonoid biostratigraphy, the *Anasibirites* beds being the main temporal time line (Fig. III.D.1; see explanations in e.g., Brayard *et al*., 2013; Jattiot *et al.*, 2016, *in press*).

These sections show differential subsidence between South and North of the SFB (Caravaca *et al.*, *in* press a, see section IV) that does not seem to affect the geochemical record, and also a varying sedimentological record with differences in lithologies between MV, LWC and HS. Terrigenous and microbial deposits are present in MV while marine fine siltstones are present only in HS. LWC however displays terrigenous deposits similar to that of MV, MISS that are unique to this section, and marine bioclastic limestones close to that of HS, making LWC a “transitional” section in between northern and southern SFB. These sections also exhibit variable geochemical record and their carbon isotope signal and T&M elements concentrations are compared and discussed below.

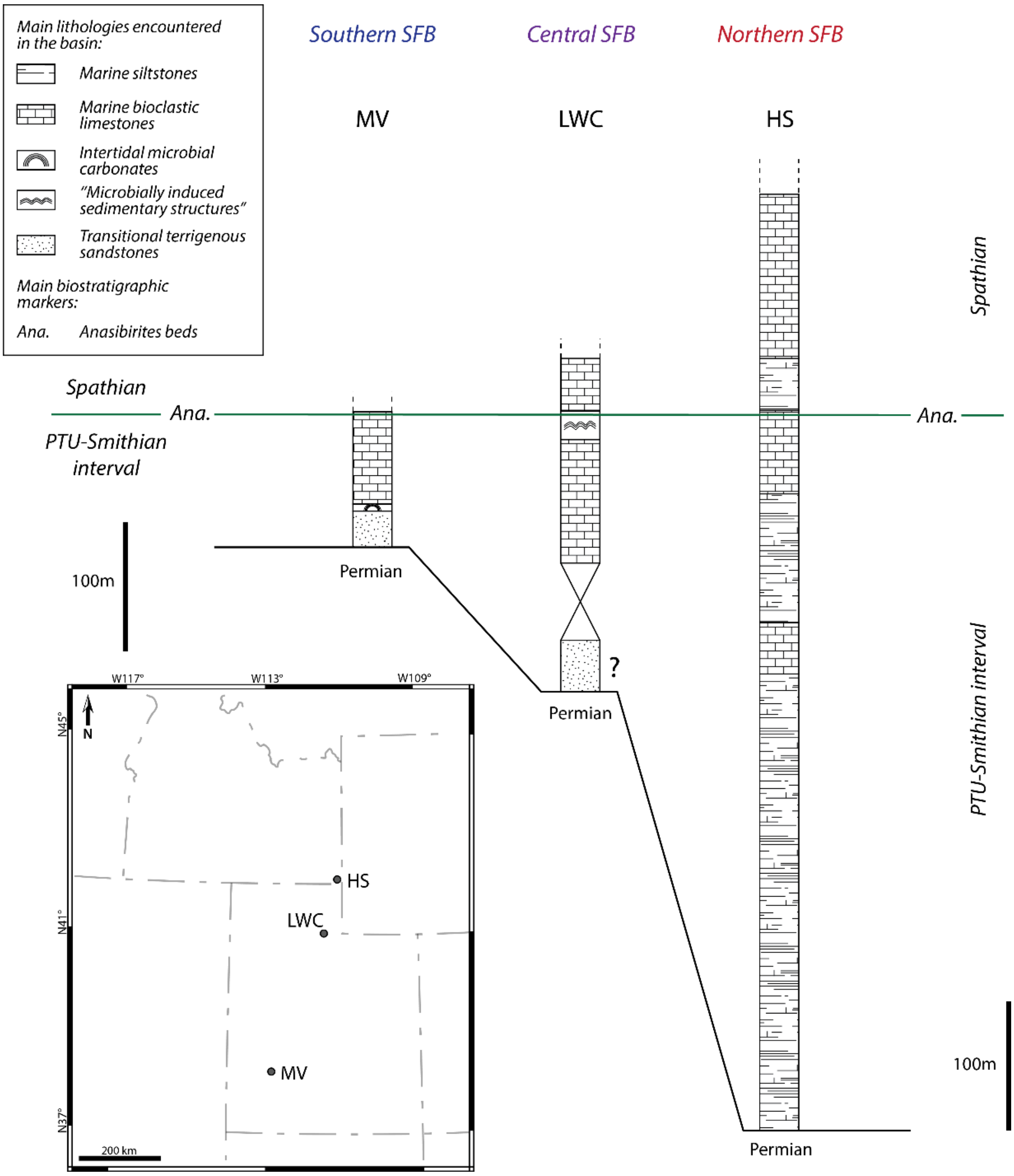

Figure III.D.1: Simplified lithological columns and biostratigraphic correlation based on Anasibirites beds for the Minersville, Lower Weber Canyon and Hot Springs sections, representing southern, central and northern parts of the SFB, respectively. The base of the sections corresponds to the regionally recognized Permian/Triassic unconformity (Brayard *et al.*, 2013).

Carbon isotopic record

- *Differential paired carbon isotopic signal*

When correlated and put side to side, the different studied sections in the SFB (HS, LWC and MV) show conspicuous differences in their paired carbon isotopic record for both carbonate and OM (Fig. III.D.2).

First, the overall shape of the globally recognized couplet of a negative/positive shift across the SSB (e.g., Payne *et al.*, 2004; Galfetti *et al.*, 2007b; Grasby *et al.*, 2013) is observed within the SFB. However, each section does not evidence this couplet in the same way, and differences in observed patterns arise from section to section (Fig. III.D.2).

More specifically, OM record in MV section shows no excursion within the SSB interval, contrary to the carbonate record that shows the expected signal (Fig. III.D.2). Conversely, in LWC section, it is the carbonate record that shows a dampened down and only positive excursion across the SSB, while the OM record displays the expected isotope couplet (Fig. III.D.2). Nevertheless, the latter is also dampened down compared to that of HS and MV for instance. Only the HS the carbon isotope record seems to follow the usually described pattern for both OM and carbonate signals across the SSB.

At a low temporal resolution, this negative/positive couplet is easily identifiable in all sections, arguing for a global paleoenvironmental forcing to imprint such a trend. Nevertheless, at a higher temporal resolution, each section shows a unique evolutionary pattern of the carbon isotope signal. Figure III.D.2 shows that amplitudes of the observed shifts greatly vary in OM signal from ~3 ‰ in LWC signal, up to ~7 ‰ in HS; but amplitudes also strongly varies in the carbonate signal, from ~4 ‰ in LWC up to ~12 ‰ in HS. This discrepancy is even more obvious when amplitudes in OM signals are compared to the carbonate signal (Fig. III.D.2).

Additionally, the local pattern of these couplets is different showing small-scale variations restricted to the SSB interval for both LWC and HS, while at MV the decrease in $\delta^{13}C_{carb}$ signal started below this interval (Fig. III.D.2). However, the precise timeline for these isotopic evolutions cannot be precisely constrained. Although showing discrepancies, a similarity between LWC and HS signals can be suggested given the similar evolutionary pattern and temporal extent observed for both these two signals. This is also supported by the similar sedimentary records of these two sections.

While these differences in shifts and amplitudes are mainly interpreted here to reflect secondary processes (see discussions about diagenetic overprint in sections above), it prevents the use of this geochemical record as main tool for detailed long-range chemostratigraphic correlations.

Additionally, the apparent lack of a parallel evolution between carbonate and OM isotopic record, except for HS section, also prevents the use of the paired carbon isotopic record for direct reconstruction of the past exogenic carbon cycle (e.g., Zeebe, 2012; Thomazo *et al.*, 2016). It therefore raises the question of the validity of the carbon isotopic record when addressing climatic changes in the Early Triassic.

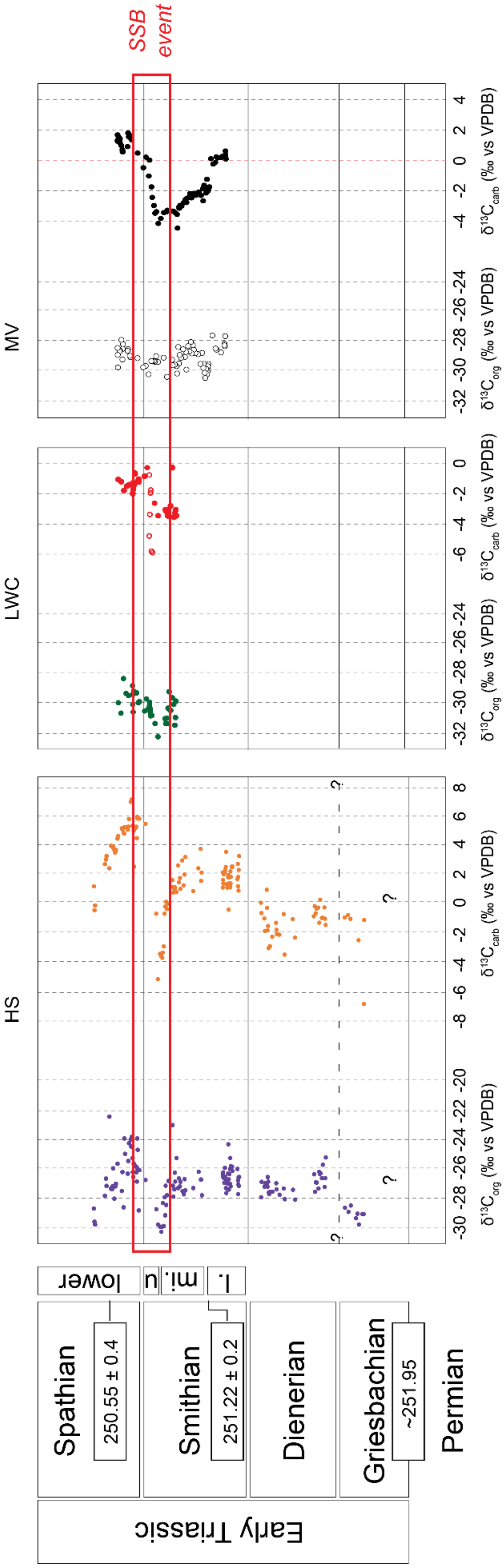

Figure III.D.2: Early Triassic variations of the δ13C signal for both carbonates and organic matter in the SFB based on the HS, LWC and MV studied sections. Open symbols in LWC record units bear uncertainties due to potential secondary alteration. Radiochronologic ages after Ovtcharova *et al*. (2006), Galfetti *et al*. (2007a) and Baresel *et al.* (2017). L.: lower; mi. middle; u. upper; SSB: Smithian/Spathian boundary.

Finally, the $\Delta^{13}C_{carb-org}$ (Fig. III.D.3) also supports the proposed distinctions within the SFB geochemical record. At LWC, the SSB signal is invariable and therefore cannot be interpreted nor compared to MV and HS. These latter however show marked variations, first in amplitudes being ~6 ‰ for MV *vs* ~12 ‰ for HS, in the same order than absolute amplitudes of the $\delta^{13}C_{carb}$ signals previously mentioned for MV and HS sections, suggesting a strong control of the $\delta^{13}C_{carb}$ signal variability over the $\Delta^{13}C_{carb-org}$ for these sections. Observed $\Delta^{13}C_{carb-org}$ patterns are also different indicating that their origin depends on various local processes. On the one hand, $\Delta^{13}C_{carb-org}$ from MV shows a general decreasing trend during the Smithian interval, followed by a steep increase across the SSB. However, as OM record shows no significant variation in MV, the $\Delta^{13}C_{carb-org}$ mainly mirrors the $\delta^{13}C_{carb}$ evolution, therefore restraining further interpretation about the significance of the $\Delta^{13}C_{carb-org}$ signal. On the other hand, HS $\Delta^{13}C_{carb-org}$ forms a marked couplet with a decrease followed by an increase centered across the SSB. There, $\Delta^{13}C_{carb-org}$ results from the difference of two varying carbonate and OM $\delta^{13}C$ signals, and it is therefore more likely to reflect the influence of the exogenic carbon cycle on both the OM and carbonate reservoirs.

These differences argue for a strong distinction between the southern and northern parts of the SFB regarding the geochemical parameters of the water-column, and emphasizes the local character of these controls.

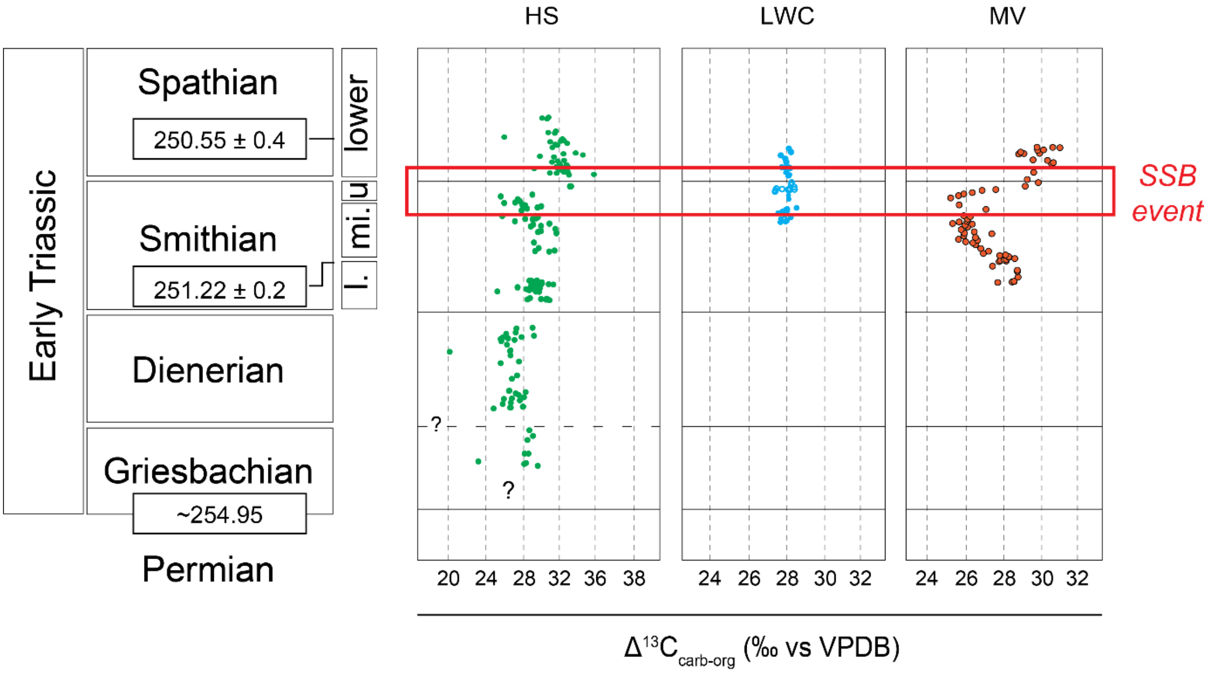

Figure III.D.3: Early Triassic variations of the Δ13C signal in the SFB based on the HS, LWC and MV studied sections. Open symbols in LWC record units bear uncertainties due to potential secondary alteration. Radiochronologic ages after Ovtcharova *et al*. (2006), Galfetti *et al.* (2007a) and Baresel *et al*. (2017). L.: lower; mi. middle; u. upper; SSB: Smithian/Spathian boundary.

- *Impact of diagenesis and secondary processes on the geochemical record*

The imprint of secondary processes on the isotopic record may lead to the obliteration of the primary signal, preventing any paleoenvironmental reconstruction and correlation. These secondary processes can also be triggered by local conditions (such as local suboxic/anoxic bottom-water/sediment interface), modifying the signal from section to section within the same sedimentary basin.

While the general shape of the isotopic record of the studied sections may have been influenced by the global exogenic carbon cycle (explaining the overall regional pattern of the isotopic record), local controlling factors also likely influenced the observed isotopic signals. Thus, the impact(s) of the secondary processes is even more important to constrain as to determine the message of the geochemical record, but also because secondary overprint might also give crucial information regarding early diagenesis and associated depositional settings.

In this way, the HS section apparently does not have undergone any major secondary overprint within its Triassic part. Its paired carbon isotopic record can therefore be considered to be pristine and reflecting the conditions during the time of deposition. However, in MV, diagnostic proxies (such as correlation of $\delta^{13}C_{carb}$ with $\delta^{18}O_{carb}$, or Mn-bearing authigenic carbonates precipitation) show a marked secondary overprint, notably due to recurrent suboxic conditions and the presence of bacterially-induced sulfato-reduction (BSR, Thomazo *et al.*, 2016). At LWC, no detailed study of the diagnostic proxies for secondary overprint are available by the time these lines are written (to be discussed in Grosjean *et al.*, *in prep.*). Nevertheless, the presence of several negative outliers within the $\delta^{13}C_{carb}$ signal around the SSB and the pattern of this signal argues for another strong influence of secondary probably early diagenetic processes.

It therefore appears that varying local conditions and early diagenetic processes acted within the SFB during the Early Triassic, with a southern part more prone to undergo e.g. remobilization, while the northern part was less influenced and better reflects the primary signal. More work is needed on the LWC section to confirm such a scenario. A distinction between the northern and southern parts of the SFB is nonetheless evidenced through the paired carbon isotopic record.

• Trace and major elements occurrences and concentrations

The same detrital and authigenic fractions are observed between MV and HS in spite of their distant position in the SFB (Fig. III.D.1a). Al, Fe, Zr and Th are strongly correlated to Al in both sections (see sections above; Fig. III.D.4). Ti is also well present in the detrital fraction of MV. Additionally, V is regarded as a detrital proxy and not as an authigenic enrichment in both sections. This particularity points toward a shared reservoir and/or similar terrigenous inputs within the entire SFB.

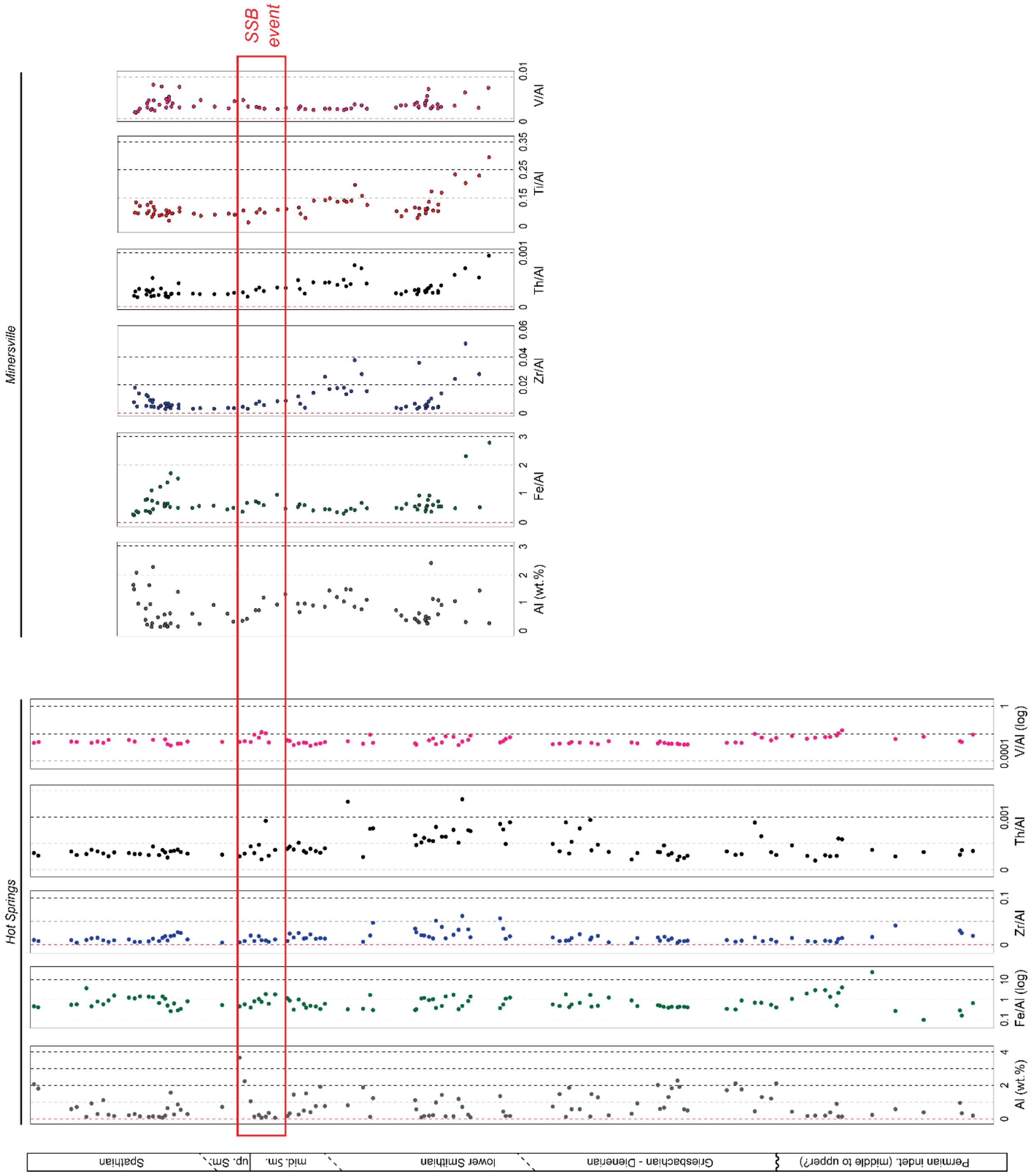

Figure III.D.4: Chemostratigraphy of the detrital trace and major elements in the HS and MV sections.

Consequently, the authigenic fraction remains unchanged between MV and HS with Sr, Ni, P, Mn and U present in both sections. Ni and P are interpreted as paleoproductivity proxies and Mn and U as paleoredox proxies (Fig. III.D.5). Cr also forms part of the authigenic fraction in HS with a similar behavior to that of Ni, which may have formed MeCrO4 complexes during suboxic early diagenesis (Tribovillard *et al.*, 2008; see Caravaca *et al.,* 2017, see section III.A). However, in MV, Cu has been measured and is associated to the paleoproductivity evolution.

The partitioning similarity of T&M elements between detrital and authigenic fractions is remarkable and argues for a stability in the elementary input and water geochemistry in the

SFB. It is also worth noting that the amplitudes of variation within these elementary records are of same order between the sections. In more details, evolution of these markers shows small-scale variations specific to each section and therefore reflect locally controlled influences upon these parameters.

Figure III.D.4 shows that no specific trend can be documented within the detrital fluxes in both MV and HS sections. Several small-scale variations can be observed, but they are rather due to local variations in lithology and/or mirroring local fluctuations of the depositional settings.

Figure III.D.5 shows a slightly different scheme for authigenic enrichments with conspicuous variations visible around the SSB in both sections. Regarding the paleoproductivity record, a peak in P/Al occurs at the top of the upper Smithian for both MV and HS sections (Fig. III.D.5.). This suggests a common perturbation in the form of an increasing primary productivity at the scale of the basin. However, the presence of a positive peak in the Ni/Al ratio at HS and its absence at MV indicate locally different processes (see discussion in Caravaca *et al*., 2017, see section III.A) and potential remobilization. Therefore, a basin-scale coeval paleoproductivity fluctuation at that time cannot be retained based solely on data from these two sections.

Within paleoredox markers, more differences can be documented between the two sections. If a peak in U/Al is present in HS and MV at the top of the upper Smithian (Fig. III.D.5), indicating potential suboxic to anoxic conditions, these perturbations are more recurrent in MV with at least four peaks observed in the U/Al ratio while the HS signal does not fluctuate as much. This highlights local differences within the water column (or upper sediments) chemistry (e.g., redox conditions) between both localities. Based on these elements, occurrence of a basin-scale event at the end of the Smithian that affected the entire SFB reservoir is not to be discarded so far.

Regarding Mn, both Mn/Al ratios in HS and MV exhibit a concomitant peak with U/Al at the top of the upper Smithian (Fig. III.D.5), and no other significant variations along the rest of the section. However, if the general behavior of the Mn seems similar, correlation of Mn with $CaCO_3$ content completely differs between HS and MV. A strong positive correlation between Mn and $CaCO_3$ is observed at HS (r = 0.91***) while no correlation is observed at MV (r = -0.18, p = 0.13).

Thomazo *et al.* (2016) showed that the Mn enrichment in MV is linked to suboxic diagenetic processes and has a mainly authigenic origin. Again, MV seems to have recorded more reducing conditions (bottom-water column or upper sediments) than HS leading to a strong secondary overprint reflecting early diagenetic processes. On the contrary, Mn at HS seems to be embedded into the carbonate deposits. This observation indicate that local conditions have a strong influence on the T&M elementary record from section to section in the SFB.

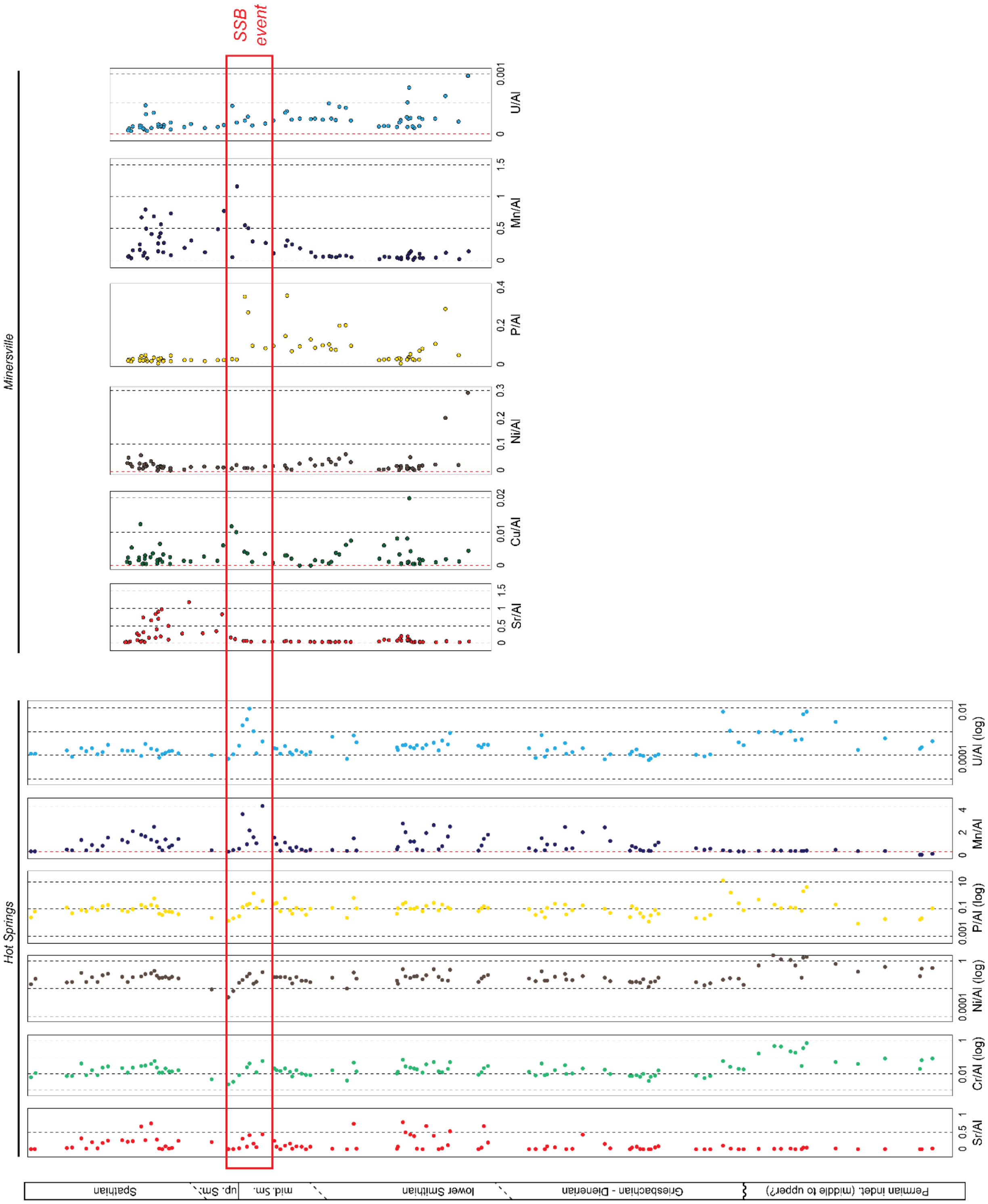

Figure III.D.5 Chemostratigraphy of the authigenic trace and major elements in the HS and MV sections. SSB: Smithian/Spathian boundary.

- Geochemical discrimination between a southern and a northern sub-basin in the SFB

Paired carbon isotopic record and T&M elements concentrations show both similarities and differences between the three studied sections in the SFB. The similarity of the various trends (e.g., overall temporal pattern of the paired carbon isotopes signal at the basin scale, differentiation between detrital and authigenic fractions) is obvious. Observed differences are likely the result of local forcing parameters varying from one part of the basin to another, or even the result of very local conditions.

The paired carbon isotopic record is similar to the globally-recognized trend for the Early Triassic, especially for the SSB interval (e.g., Galfetti *et al.*, 2007a; Hermann *et al.*, 2011; Sun *et al.*, 2012; Grasby *et al.*, 2013; see Fig. I.A.3). However, based on our SFB data, this evolution appears to be strongly influenced by local variations in the carbon reservoir and does not only fully reflect exogenic forcing. Local controls are therefore of prime importance in driving the carbon isotopic signal. They additionally well emphasize the differences between the northern and southern parts of the SFB: the southern signal is probably more diagenesis-driven (associated with episodic suboxic conditions), whereas the northern signal is probably more paleoenvironmentally-driven at a global scale.

A same North/South distinction can be documented based on T&M elements. Paleoredox proxies indicate that recurrent suboxic to anoxic conditions at the bottom-water/sediment interface took place in the southern part of the SFB while the northern part conditions remain oxic most of the time. These variations are likely to be linked to different local conditions, such as the presence or absence of BSR metabolisms (Thomazo *et al.*, 2016). Paleoproductivity markers indicate coeval events within the SFB reservoir, notably across the SSB with concomitant shifts in P/Al HS and MV. Finally, detrital proxies also show a similar nature of the terrigenous influxes at the basin scale, characterized by inputs in V whose enrichment is usually controlled by paleoredox conditions. Nevertheless, a detailed study of the provenance of the terrigenous fractions is necessary to determine their origin among the various potential sources around the SFB, using QFL diagrams (e.g., Dickinson *et al.*, 1983; Dickinson & Gehrels, 2010) or U-Pb ages of detrital zircons (e.g., Dickinson & Gehrels, 2008, 2010; Thomas, 2011).

No major variation in depositional environments is observed within the SFB, with dominantly shallow and inner to outer ramp conditions prevailing. Still, differences in terms of diagenetic processes, alkalinity, redox conditions, lithology and biotic communities (e.g., Blakey, 1977; Olivier *et al.*, 2014, 2016, see appendix 1; Vennin *et al.*, 2015; for southern SFB; Kummel, 1957; Paull & Paull, 1993; Caravaca *et al.*, 2017, see section III.A; Grosjean *et al.*, *in prep.*; for northern SFB) likely characterize and differentiate the northern and southern parts of the basin. This distinction is notably visible from a sedimentary point of view (e.g., presence/absence of red beds deposits and/or presence/absence of microbial carbonates), but also from a geochemical perspective (e.g., more or less pronounced impact of secondary processes).

These results strongly argue for a N/S partitioning of the SFB, and for the existence of two distinct sub-basins from at least a geochemical point of view.

- SFB *versus* global Early Triassic geochemical record

HS, LWC and MV sections show that the SFB paired carbon isotope records apparently mirrors the globally recognized ET trend characterized by the couplet of a positive and negative excursion before and across the SSB (e.g., Galfetti *et al.*, 2007b; Grasby *et al.*, 2013). The positive excursion potentially corresponding to the Dienerian/Smithian boundary (DSB) is also documented (in HS only). However, if an influence of the global exogenic carbon cycle on the SFB record cannot be completely discarded, documented signals among the studied sections were primarily influenced by locally controlled parameters.

Additionally, the commonly accepted transient ET marine anoxia (e.g., Grice *et al.*, 2005; Algeo *et al.*, 2011; Meyer *et al.*, 2011; Song *et al.*, 2012, 2014; Metcalfe *et al.*, 2013) has not been directly documented in the studied sections. The SFB geochemical record is therefore in opposition with the paradigm of a globally anoxic marine realm throughout the ET (e.g., Isozaki, 1997; Fraiser & Bottjer, 2007).

Episodic suboxic to slightly anoxic conditions (resulting from local forcing parameters) may have prevailed in the studied sections, as in MV and in a lesser extent in HS, but not in the same order of magnitude as observed in some other basins such as South China (Sun *et al.*, 2012) or Arctic Canada (Grasby *et al.*, 2013).

Some rare “black shales” and OM-rich deposits have been observed within the SFB sedimentary record (ongoing team work, unpublished data from a few other places). However, if these levels potentially result from suboxic conditions during deposition, they appear diachroneous within the basin, ranging e.g. from upper Smithian to lower Spathian in in Idaho. Consequently, they may not necessarily result from global deleterious conditions.

While studying the geochemical record within the SFB, both paired carbon isotopes and T&M elements show that local parameters of the depositional settings appear to locally overprint the SFB signature and the overall exogenic carbon cycle. Based on $\delta^{13}C$ and T&M records, similarities and differences are evidenced between records of distant sections, and allow to establish a North/South distinction within the basin, in agreement with the differences observed among the sedimentary records.

Globally recognized couplet of negative and positive isotopic excursions across the SSB is not equally recorded throughout the basin, being influenced by local depositional settings (e.g., in the northern part) and/or secondary alteration (in the southern part). Paleoredox markers suggest recurrent suboxic to anoxic conditions in the southern part of the basin while the northern part does not show any major perturbation in the oxygen concentration of the (bottom-)water column. A marked transient anoxia therefore cannot be firmly documented for this interval within the SFB.

Nevertheless, elementary records from distant sections in the basin show common characteristics too, such as the presence of V in the detrital fraction in both HS and MV. Also, concomitant peaks in P in both sections argues for a paleoproductivity event occurring throughout the basin. Common perturbations within several elementary reservoirs indicate that northern and southern parts of the basin share a common water column. Still, this geochemical signal is locally controlled and display small-scale variations specific to each section.

IV. CHARACTERIZATION OF THE MAIN CONTROLLING FACTORS OVER THE SFB SEDIMENTARY RECORD

The paleontological, sedimentary and geochemical record investigated in the SFB tends to demonstrate an obvious distinction between its southern and northern parts. However, current knowledge of the geodynamical framework and history of the basin does not allow to determine the origin of this N/S dichotomy that is particularly characterized by a marked discrepancy in spatial repartition of the sedimentary thickness within the PTB-Smithian interval.

An integrated study, using sedimentological paleontological, geodynamical, structural, cartographic and geophysical approaches, has been conducted, associated with numerical modeling of the rheological behavior of the lithospheric basement. This work aimed to decipher the processes involved in the formation and development of the SFB, and to seek out the controlling factors behind the differentiation of two distinct parts within the foreland basin.

Geol. Mag.: page 1 of 25 © Cambridge University Press 2017
doi:10.1017/S0016756817000164

Controlling factors for differential subsidence in the Sonoma Foreland Basin (Early Triassic, western USA)

GWÉNAËL CARAVACA*†, ARNAUD BRAYARD*, EMMANUELLE VENNIN*, MICHEL GUIRAUD*, LAETITIA LE POURHIET‡, ANNE-SABINE GROSJEAN*, CHRISTOPHE THOMAZO*, NICOLAS OLIVIER§, EMMANUEL FARA*, GILLES ESCARGUEL¶, KEVIN G. BYLUND‖, JAMES F. JENKS# & DANIEL A. STEPHEN**

*Biogéosciences UMR6282, CNRS, Université Bourgogne Franche-Comté, 21000 Dijon, France
‡Sorbonne Universités, UPMC Univ Paris 06, CNRS, Institut des Sciences de la Terre de Paris (iSTeP), 4 place Jussieu 75005 Paris, France
§Laboratoire Magmas et Volcans, CNRS, IRD, OPGC, Université Blaise Pascal, 63038 Clermont Ferrand, France
¶UMR 5023 LEHNA, Université Lyon 1, 69622 Villeurbanne Cedex, France
‖140 South 700 East, Spanish Fork, Utah 84660, USA
#1134 Johnson Ridge Lane, West Jordan, Utah 84084, USA
**Department of Earth Science, Utah Valley University, Orem, Utah 84058, USA

(*Received* 8 June 2016; *accepted* 15 February 2017)

Abstract – Sediments deposited from the Permian–Triassic boundary (~252 Ma) until the end-Smithian (Early Triassic; *c.* 250.7 Ma) in the Sonoma Foreland Basin show marked thickness variations between its southern (up to *c.* 250 m thick) and northern (up to *c.* 550 m thick) parts. This basin formed as a flexural response to the emplacement of the Golconda Allochthon during the Sonoma orogeny. Using a high-resolution backstripping approach, a numerical model and sediment thickness to obtain a quantitative subsidence analysis, we discuss the controlling factor(s) responsible for spatial variations in thickness. We show that sedimentary overload is not sufficient to explain the significant discrepancy observed in the sedimentary record of the basin. We argue that the inherited rheological properties of the basement terranes and spatial heterogeneity of the allochthon are of paramount importance in controlling the subsidence and thickness spatial distribution across the Sonoma Foreland Basin.

Keywords: Early Triassic, Sonoma orogeny, foreland basins, lithospheric strength, subsidence.

1. Introduction

The Sonoma Foreland Basin (SFB, western USA; Fig. 1a) provides an excellent Early Triassic fossil and sedimentary record (Hofmann *et al.* 2014; Brayard *et al.* 2015; Thomazo *et al.* 2016). This N–S-trending foreland system (*sensu* DeCelles & Giles, 1996) was located on the western Pangea margin and results from the emplacement of the Golconda Allochthon (GA) during the Sonoma orogeny around the Permian–Triassic boundary (Fig. 1; Burchfiel & Davis, 1975; Speed & Silberling, 1989; Ingersoll, 2008; Dickinson, 2013). Nevertheless, despite numerous studies, the geometry and the palaeogeography of this basin remain poorly constrained. The SFB covered a large area including present-day eastern Nevada, Utah, Idaho and parts of Wyoming (Marzolf, 1993; Dickinson, 2006, 2013; Ingersoll, 2008).

Foreland sedimentary basins are generally considered as passive systems resulting from the flexural subsidence of the elastic lithosphere in response to crustal thickening and sediment loading (e.g. DeCelles & Giles, 1996; Allen & Allen, 2005). If the flexural isostatic model is a reasonable first-order explanation for the overall shape of foreland basins, sediment thickness variations and peculiar stratigraphic successions involve a differential local subsidence. In order to decipher such potential mechanisms at the origin of the SFB structuring and sedimentary record variations, we use a multidisciplinary approach. We perform a subsidence analysis of the basin within a high-resolution biostratigraphically controlled time-frame from the Permian–Triassic unconformity (PTU) up until late Smithian time (a *c.* 1.3 Ma long interval; the Smithian is the third substage of the Early Triassic). This allows us to characterize the basin infill in relation to the emplacement of the Golconda Allochthon during the Sonoma orogeny. We also provide new evidence indicating that the studied area is a foreland basin. Using a complementary backstripping approach and numerical models we discuss the main factors controlling the subsidence variations observed in the SFB, including the impact of lithospheric and rheological features, on basement partitioning and sedimentation.

---

†Author for correspondence: gwenael.caravaca@u-bourgogne.fr

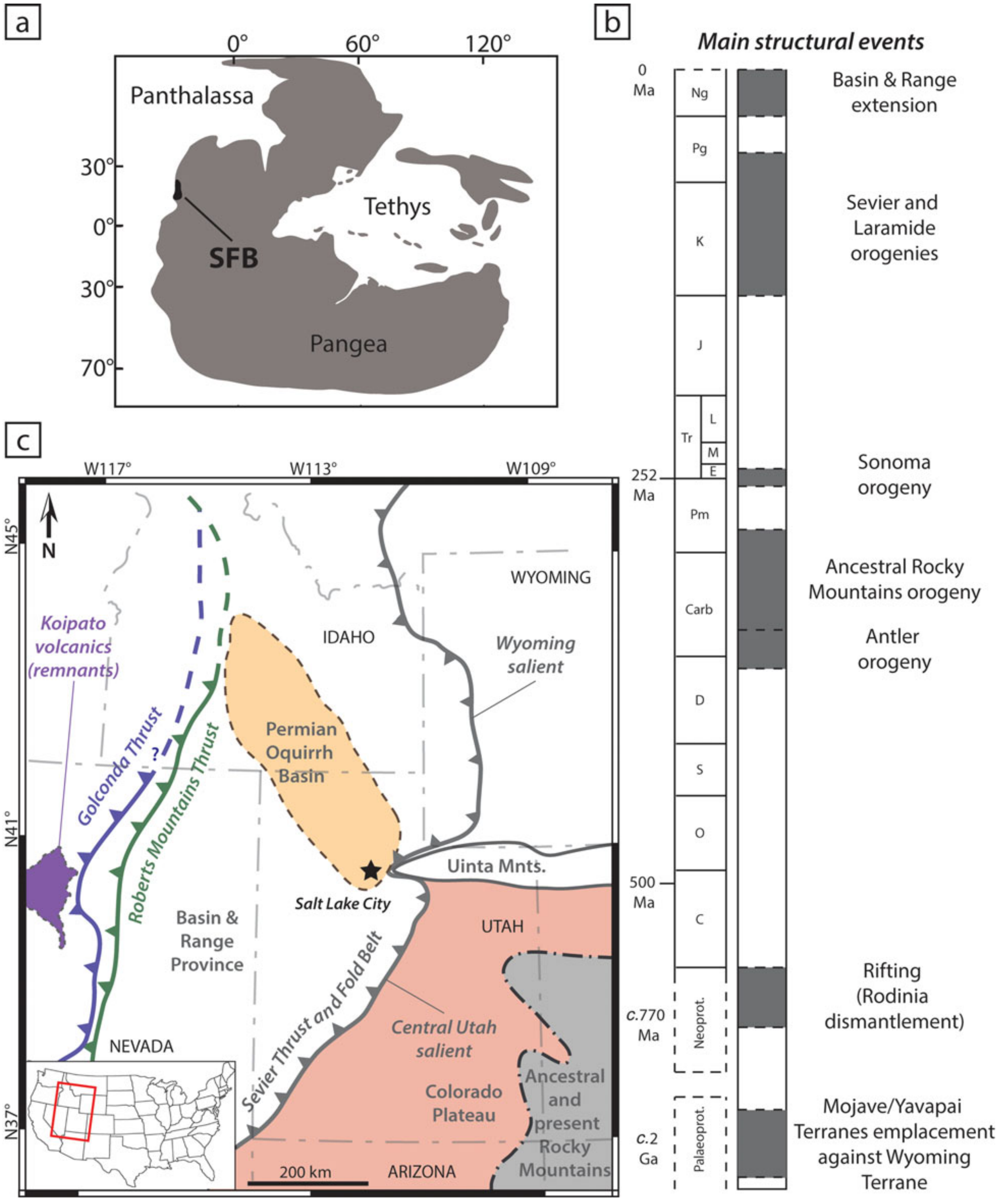

Figure 1. (Colour online) (a) Early Triassic location of the Sonoma Foreland Basin (SFB; after Brayard *et al.* 2013). (b) Simplified chronostratigraphy of the succession of structuring events in the studied area since Palaeoproterozoic time (after Oldow *et al.* 1989; Whitmeyer & Karlstrom, 2007; Dickinson, 2013). (c) Simplified map of the study area with location of the main structural elements discussed and mentioned in this work (after Bond *et al.* 1985; Walker, 1985; Dickinson, 2004, 2006, 2013; Vetz, 2011; Yonkee & Weil, 2015).

2. Geological setting

2.a. Brief geological history of the study area

The Sonoma Foreland Basin lies within a region of the North American continent showing a very long and complex tectonosedimentary history starting during Proterozoic time and still active today (e.g. Dickinson, 2013). The first documented structuring of the region dates back to the Palaeoproterozoic period when Mojave and Yavapai terranes were emplaced against the Archean Wyoming craton (Fig. 1b; Whitmeyer & Karlstrom, 2007; Lund *et al.* 2015). This event generated multiple crustal fault zones along which later reactivations were possible with deformational episodes (Oldow *et al.* 1989; Dickerson, 2003). At least two rifting events took place in this region during subsequent Proterozoic times (Burchfiel & Davis, 1975; Oldow *et al.* 1989), the most recent being during Neoproterozoic time (*c.* 770 Ma) and linked to the fragmentation of the supercontinent Rodinia (Fig. 1b; Dickinson, 2006). The long period of tectonic quiescence following the formation of this passive margin lasted until Late Devonian time (*c.* 380 Ma) and corresponds to the deposition of a thick sedimentary prism formerly known as the 'Cordilleran Miogeocline' (Clark, 1957; Paull & Paull, 1991; Dickinson, 2006, 2013).

Starting during Late Devonian time and lasting until late Early Carboniferous time, the Antler orogeny marks the beginning of a period of nearly continuous structural events that are still active today (Fig. 1b). The Antler orogeny was caused by the convergence and accretion of exotic island-arcs against the western margin of the North American Plate. This orogeny is characterized by the emplacement of a large obducted accretionary prism located in Central Nevada today (i.e. Roberts Mountains Thrust, Fig. 1c; Burchfiel & Davis, 1975; Speed & Sleep, 1982; Speed & Silberling, 1989; Burchfiel & Royden, 1991). The Roberts Mountains Allochthon led to the formation of the N–S-trending westwards-dipping Antler Foreland Basin (Speed & Sleep, 1982; Burchfiel & Royden, 1991; Blakey, 2008; Ingersoll, 2008; Dickinson, 2004, 2006, 2013).

Soon after the Antler orogeny the Ancestral Rocky Mountains (ARM) orogeny occurred on the eastern part of the region (Fig. 1c), ranging over Early Carboniferous to early–middle Permian time (*c.* 350–270 Ma; Fig. 1b). This mountain-building event resulted from a succession of crustal uplifts because of important long-range intracratonic deformations. There, transtensional and transpressional constraints occurred along with lithospheric buckling as a response to the Laurentia–Gondwana continental collision (Kluth & Coney, 1981; Ye *et al.* 1996; Geslin, 1998; Dickerson, 2003; Dickinson, 2006, 2013; Blakey, 2008). The resulting chain probably showed a marked topographic relief, some of which could have persisted until Early Triassic time (Kluth & Coney, 1981; Blakey, 2008). Most of these crustal uplifts were emplaced according to lithospheric weaknesses inherited from the Proterozoic structural events (Kluth & Coney, 1981; Dickerson, 2003).

Many sedimentary basins formed during the Carboniferous–Permian interval (Dickerson, 2003). For instance, the Permian Oquirrh Basin (Fig. 1c) probably resulted from the complex interplay between intracratonic deformations to the east and the reactivation of Antler faults to the west (Geslin 1998: fig. 12; Trexler & Nitchman, 1990; Dickerson, 2003; Blakey, 2008). This highly subsiding basin recorded up to 6 km of marine strata (Walker, 1985; Yonkee & Weil, 2015).

Similarly to the Antler orogeny, the Sonoma orogeny is the result of the eastwards migration and accretion of exotic island-arc systems belonging to the Sonomia microplate onto the North American Plate around the Permian–Triassic boundary (Burchfiel & Davis, 1975; Speed & Silberling, 1989; Dickinson, 2006, 2013; Blakey, 2008; Ingersoll, 2008). The Sonoma orogeny is characterized by the thrusting of an accretionary prism above continental crust, known as the Golconda Allochthon, and emplaced in the same area as the older Roberts Mountains Allochthon (Fig. 1c). The Golconda Allochthon is thought to have initiated the formation of a foreland basin – the Sonoma Foreland Basin (Dickinson, 2006, 2013; Blakey, 2008; Ingersoll, 2008) – which recorded sediments deposited during Early Triassic time. However, field evidence pointing towards the location and extension of the Golconda Allochthon is restricted to only a few remnants (e.g. 'Koipato volcanics') near the southern part of the basin, which are presently located in Central Nevada (Fig. 1c; Snyder & Brueckner, 1983; Walker, 1985; Schweickert & Lahren, 1987; Oldow *et al.* 1989; Dickinson, 2006, 2013; Blakey, 2008; Ingersoll, 2008). Remnants of the Golconda Allochthon, if any, are yet to be found in the northern part of the basin, especially in Idaho (Schweickert & Lahren, 1987; Oldow *et al.* 1989). This allochthon is sealed in present-day Nevada by the rhyolitic Koipato Formation volcanism, presumably emplaced by the end of the Sonoma orogeny (Vetz, 2011). A minimum age of Anisian (Middle Triassic) can be given to this volcanic formation using geochronology (Vetz, 2011) and due to the occurrence of Anisian ammonites in the unconformably overlying sedimentary series (Nichols & Silberling, 1977; Bucher, 1988; Vetz, 2011). The potential presence of older ammonoid faunas is not to be discarded.

The following Sevier orogeny is of Early Cretaceous – Eocene age (*c.* 140–50 Ma; Fig. 1b) and it originated from the subduction of the Farallon Plate under the North American continental plate (Burchfiel & Davis, 1975; Dickinson, 2006, 2013). E–W-directed compressive constraints resulted in the formation of a large Sevier thrust-and-fold belt which is still present today and constitutes the eastern border of the Great Basin (Fig. 1c; Dickinson, 2006, 2013; Yonkee & Weil, 2010; Yonkee *et al.* 2014). This thrust-and-fold belt is however not homogeneous along its N–S-trending front, and displays two convex-to-the-foreland 'salients' (Fig. 2) with varying estimated tectonic shortening and eastwards displacement of terrains reaching up to 140 km (DeCelles & Coogan, 2006; Schelling *et al.* 2007; Dickinson, 2006, 2013; Yonkee & Weil, 2010, 2015; Yonkee *et al.* 2014). These Wyoming and Central Utah salients are separated by a conspicuous recess formed by a lateral ramp and located west of the Uinta Mountains (Figs 1c, 2). Its formation results from inherited features of the basement (see Section 4.c; e.g. Lawton, Boyer & Schmitt, 1994; Mukul & Mitra, 1998; Paulsen & Marshak, 1999; Wilkerson, Apotria & Farid, 2002).

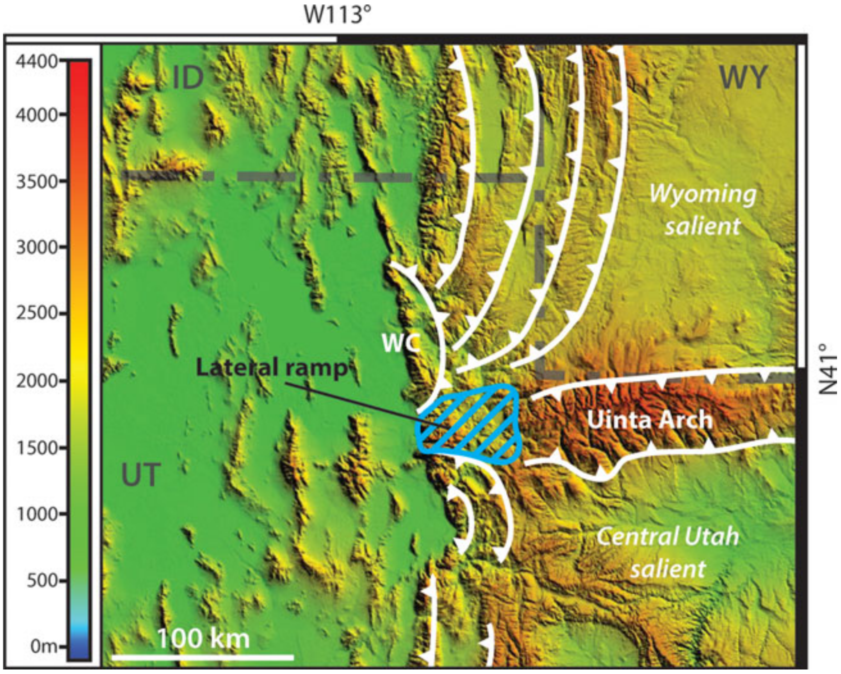

Figure 2. (Colour online) Topographic map of the central part of current-day Sevier thrust-and-fold belt with accentuation of the Wyoming and Central Utah salients thrusts. A lateral ramp is present between the two salients (after Paulsen & Marshak, 1999).

Also during Early Cretaceous – Eocene time, the eastern Laramide orogeny reactivated basal crustal uplifts set during the Ancestral Rocky Mountains orogeny. This led to the formation of the modern-day Rocky Mountains which overlapped older structures in the Colorado Plateau (Fig. 1b, c; Oldow *et al.* 1989; Ye *et al.* 1996; Dickinson, pers. comm. 2015).

Finally, the Basin and Range extension of the entire region started during Neogene time (*c.* 20 Ma; Fig. 1b) and is still active today (Oldow *et al.* 1989; DeCelles & Coogan, 2006; Dickinson, 2002, 2006, 2013). This extension is the result of internal forces (Kreemer & Hammond, 2007) that generated transtensional stresses and pure shear (Parsons, Thompson & Sleep, 1994; Gans & Bohrson, 1998; Dickinson, 2002, 2006). However, the origin of these extensional constraints is still being discussed. Several possible mechanisms have been proposed, including: (1) a mantellic ‘wide rift-like’ process with ascent and underplating of mantellic material leading to thermal lamination of the lithosphere (Lachenbruch & Morgan, 1990; Parsons, Thompson & Sleep, 1994, Gans & Bohrson, 1998); or (2) a mechanical origin with the extension occurring in a late orogenic context, due to the instability and gravity collapse of the thickened lithospheric crust present in Nevada and westernmost Utah (Fletcher & Hallet 1983; Malavieille, 1993; Zandt, Myers & Wallace, 1995). Nevertheless, the easternmost borders of the basin (e.g. Colorado Plateau or Uinta Mountains) are not affected by these displacements (Fig. 1c; Dickinson, 2006, 2013). It is also worth noting that this extension reactivates in inversion some of the thrust faults created during the Sevier orogeny (Coney, 1987; Dickinson, 2006, 2013).

2.b. Sedimentary record of the Sonoma Foreland Basin

Here we focus on the Early Triassic sedimentary record of the Sonoma Foreland Basin (Figs 3a, 4). The stratigraphic succession displays marked spatial differences in thickness and in dominant lithologies (Fig. 4). The sedimentary record is considered as almost continuous throughout the basin, with local erosion surfaces being under the temporal resolution of ammonoid biozones for this Early Triassic interval (e.g. Olivier *et al.* 2014, 2016; Vennin *et al.* 2015). In its southern part (Figs 3a, 4), the basin is mainly filled with transitional continental to marine coarse sandstones to conglomerates known as ‘red beds’ of the Moenkopi Group (Fig. 5a–c, e; *sensu* Lucas, Krainer & Milner, 2007; Brayard *et al.* 2013). At the top of the Moenkopi Group, metric-scale beds of intertidal microbial limestones can be observed (Figs 3a, 4, 5e; Brayard *et al.* 2013; Vennin *et al.* 2015; Olivier *et al.* 2016). The upper part of the sedimentary pile is characterized by open-marine bioclastic limestones (locally shales) of the Thaynes Group (Figs 3a, 4, 5d, f; *sensu* Lucas, Krainer & Milner, 2007), marking the maximum flooding of the Smithian third-order transgression (Embry, 1997; Vennin *et al.* 2015). This flooding event is characterized by the presence of the ammonoid genus *Anasibirites* (Figs 3a, 4; Lucas, Krainer & Milner, 2007; Brayard *et al.* 2013; Jattiot *et al.* 2015, in press). In the northern part of the basin (Figs 3a, 4) the sedimentary record differs at its base by the presence of the Dinwoody and Woodside formations, characterized by fine marine siltstones (Figs 3a, 4, 5g; Kummel, 1954, 1957; Sadler, 1981; Paull & Paull, 1991). Above these formations, the

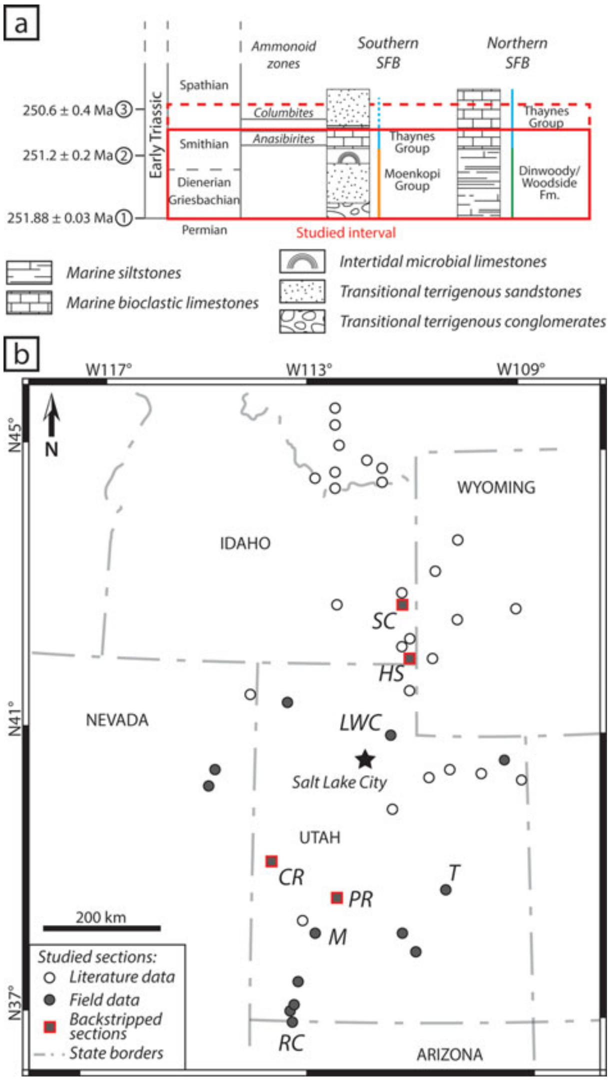

Figure 3. (Colour online) (a) Simplified litho- and chronostratigraphic subdivisions of the Early Triassic Sonoma Foreland Basin (SFB). This study encompasses the PTU-Smithian interval, with Spathian complement for the subsidence analysis. Main ammonoid markers used in this study are the *Anasibirites* beds and the *Columbites* beds. Radiometric ages: (1) from Burgess, Bowring & Shen (2014); (2) and (3) from Galfetti *et al.* (2007). (b) State map of the study area showing current location of the 43 studied sections, from both literature data (open circles) and field data (grey circles). Complete GPS coordinates and references are given in online Supplementary Table S2. Red outlines highlight the sections used for the subsidence analysis, and selected for their completeness, temporal resolution and spatial distribution. Sections detailed in Figure 4: SC: Sheep Creek; HS: Hot Springs; LWC: Lower Weber Canyon; CR: Confusion Range; T: Torrey area; PR: Pahvant Range; M: Minersville; RC: Rock Canyon.

sedimentary record resembles that observed in the southern part and corresponds to the open-marine bioclastic limestones and shales of the Thaynes Group (Figs 3a, 4, 5d, h). A basin-scale synthetic facies analysis with associated depositional environments and estimations of the palaeobathymetries can be found in online Supplementary Table S1 (available at http://journals.cambridge.org/geo).

3. Dataset and methods

3.a. Dataset

We compiled a comprehensive sedimentary and biostratigraphic dataset for the Early Triassic outcrops in the Sonoma Foreland Basin, including previously published works (e.g. Kummel, 1954, 1957; Paull & Paull, 1991; Goodspeed & Lucas, 2007; Heckert *et al.* 2015) together with new field data (Fig. 3b). We selected 43 biostratigraphically correlated sections documenting different parts of the basin in order to estimate the thickness (at the metre scale) of the sedimentary deposits (GPS coordinates and main characteristics of each section are provided in online Supplementary Table S2). The 43 studied sections correspond to the Early Triassic interval. The base of this interval is defined by a major regional PTU (Brayard *et al.* 2013). Its upper end is determined by the *Anasibirites* beds or the uppermost part of the *Owenites* beds as a surrogate, which are the main biostratigraphic markers of the end-Smithian (Figs 3a, 4; Brayard *et al.* 2013; Jattiot *et al.* 2015). Eleven sections were delimited using a high-resolution ammonoid zonation (e.g. sections in Fig. 4; Brayard *et al.* 2013). We conservatively used only minimum thickness values for the 32 sections taken from the literature because they are not always based on homogeneous sedimentary and biostratigraphical data (online Supplementary Table S2). For completeness of the subsidence analysis, we included when possible thickness data available for the lower part of the Spathian (fourth substage of the Early Triassic), the *Columbites* beds marking in this case the end of the studied interval (Fig. 3a).

3.b. Methods

3.b.1. Palinspastic reconstructions using retrodeformations

Post-Triassic times in the Sonoma Foreland Basin are characterized by important tectonic compressive and later extensive deformations. These successive deformations are mostly represented in the basin by the complex and heterogeneous Sevier thrust-and-fold belt. The palaeogeographic configuration of the Sonoma Foreland Basin was therefore different compared to the modern configuration. In order to resolve this issue, we performed a palinspastic reconstruction to estimate the Early Triassic palaeogeography of this basin.

Retrodeformations of observed structural features affecting the Triassic series were applied to several regional cross-sections using literature data (e.g. DeCelles & Coogan, 2006; Yonkee & Weil, 2010; Fig. 6). This method consists of the horizontalization of a selected layer (here the Triassic series) by virtually inverting all the structural features observed in the section between a fixed reference point named the 'pin line' and a mobile reference point named the 'loose line' (Fig. 6; see Groshong, 2006 for details). In the two regional cross-sections of the Sevier

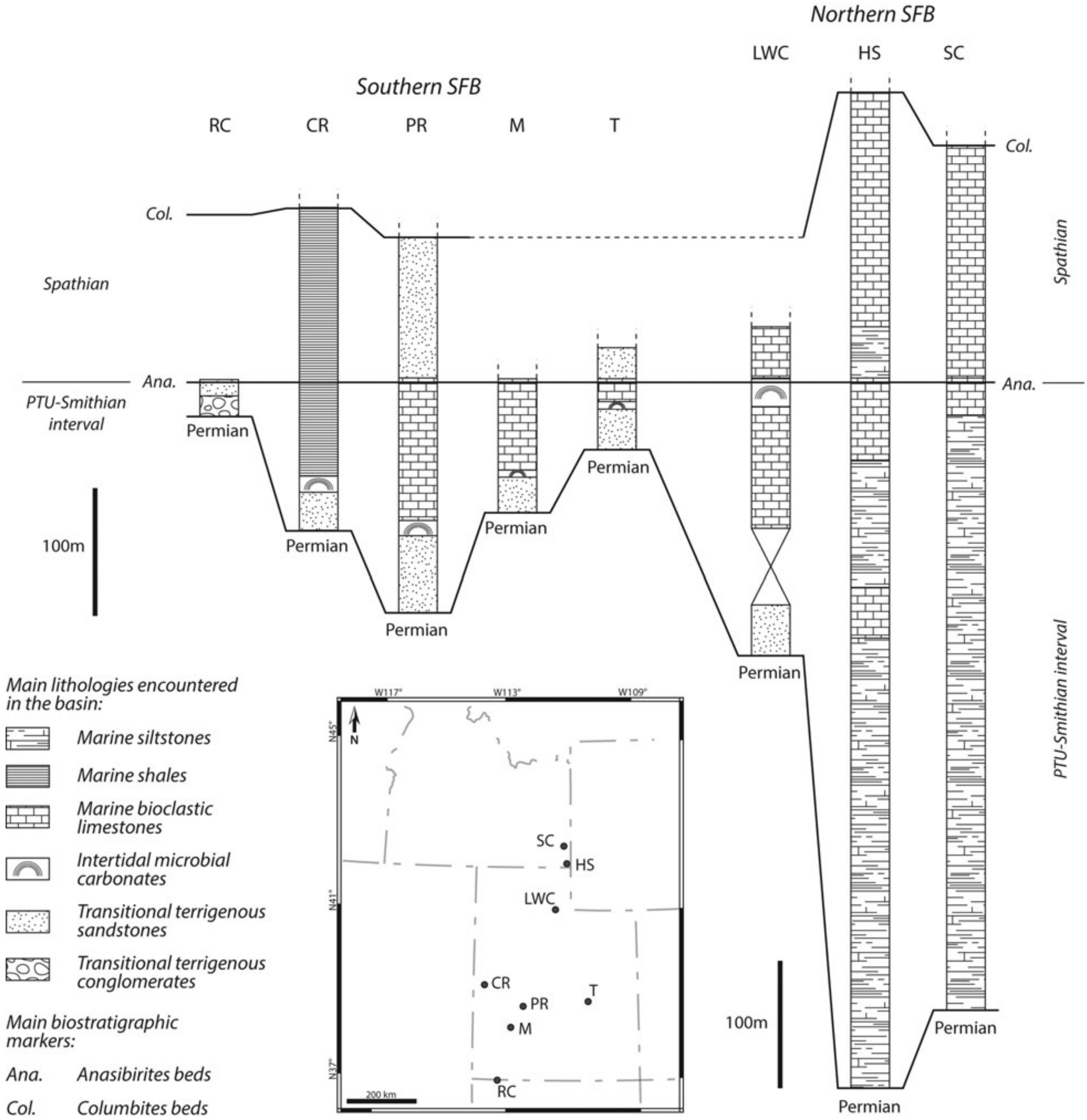

Figure 4. Biostratigraphic correlation based on the *Anasibirites* and *Columbites* beds observed in 8 of the 43 studied sections, illustrating the discrepancy in sedimentary thickness between the southern and northern parts of the Sonoma Foreland Basin (with simplified lithology). Base of the sections corresponds to the regionally recognized Permian–Triassic unconformity (Brayard *et al.* 2013).

thrust-and-fold belt illustrated in Figure 6, most structural features are thrust complexes; horizontalization therefore mainly consists of retrodeformation of the displacements along thrust planes. Finally, balanced cross-sections represent a good approximation of the geomorphological setting by the time of deposition. Based on this method, the direction and value of the estimated tectonic transport (ETT) underwent by the terrains can also be calculated (e.g. *c.* 140 km and *c.* 60 km for the cross-sections a and b in Fig. 6, respectively).

Due to the complex nature of the Sevier thrust-and-fold belt resulting from the inherited structure and thickness pattern of the pre-deformation basins (Paulsen & Marshak, 1999), and also the westwards focalization of the subsequent Basin and Range extension, ETT was spatially heterogeneous between Wyoming and Central Utah salients (Mukul & Mitra, 1998; DeCelles & Coogan, 2006; Schelling *et al.* 2007; Yonkee & Weil, 2010; Yonkee *et al.* 2014). We therefore defined seven sectors within our study area (sectors 1–7 in Fig. 7). These sectors were delimited based on similar ETT values (Table 1; Fig. 7). These values were determined from data available in the literature (references in Table 1) and checked with the retrodeformation of regional cross-sections taken from geological maps (cross-sections in Fig. 6).

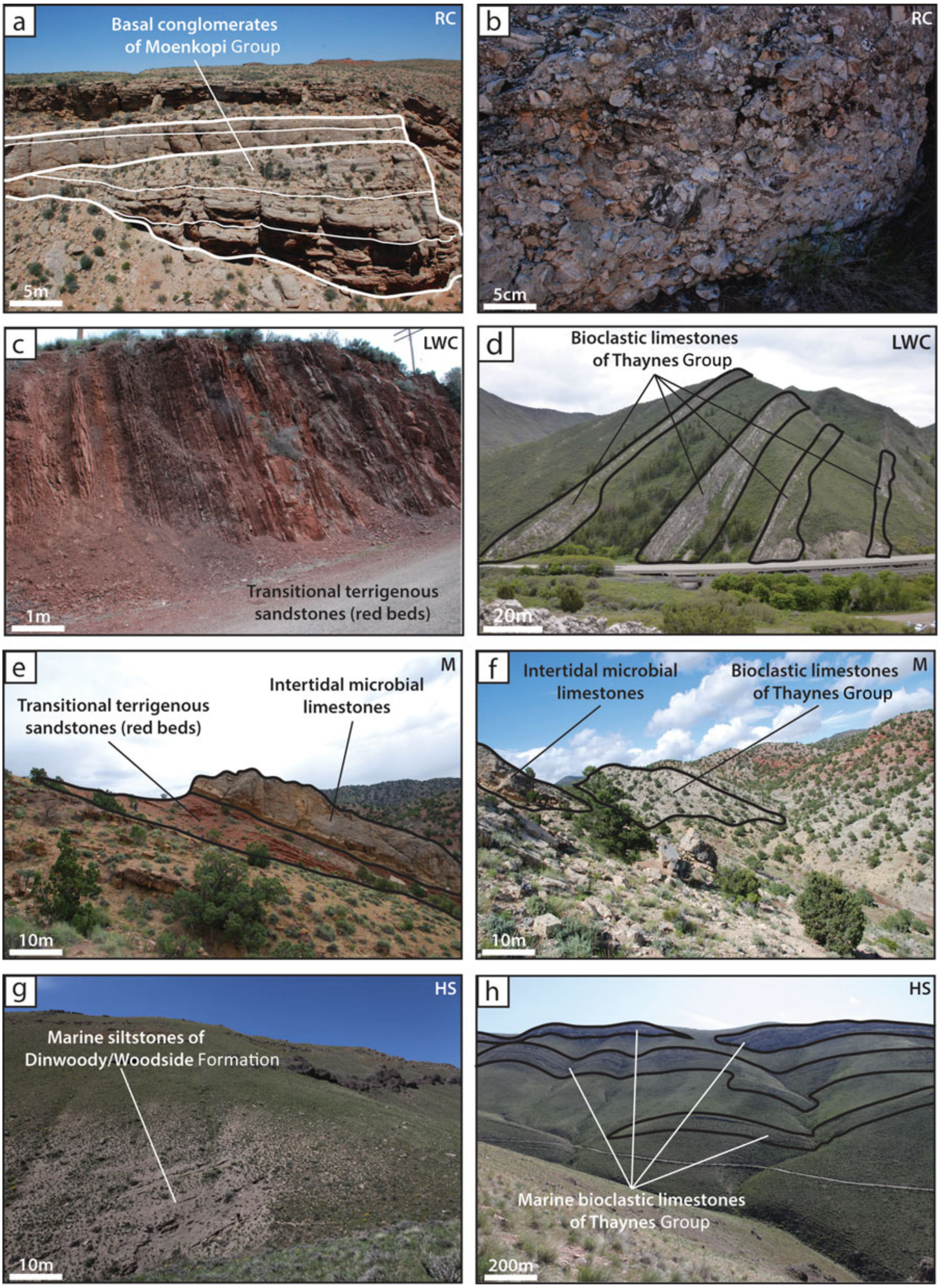

Figure 5. (Colour online) Photographs of different outcrops in the SFB, showing variations in dominant lithologies and sedimentary thicknesses encountered throughout the basin. (a) Panorama of Rock Canyon (RC) outcrop, showing the plurimetric beds of conglomerates from the basal Moenkopi Group. (b) Detail photograph of the conglomerate from Rock Canyon. (c) Photograph of the terrigenous red beds of the Moenkopi Group at Lower Weber Canyon (LWC). (d) Panorama of the limestones beds of the Thaynes Group limestones at Lower Weber Canyon. (e) Panorama of the Moenkopi Group at Minersville (M), showing succession of terrigenous red beds and microbial limestones. (f) Panorama of the transition between Moenkopi and Thaynes Group showing succession of microbial limestones and bioclastic limestones at Minersville. (g) Photograph of the marine siltstones of the Dinwoody and Woodside Formation at Hot Springs (HS). (h) Panorama of the Hot Springs section, showing succession of limestone levels of the Thaynes Group bioclastic limestones.

Table 1. Estimated tectonic transport values used for palinspastic reconstructions of each sectors defined within the SFB, and associated references.

Sector		Estimated tectonic transport (km)	References
1	Sevier foreland	0	DeCelles & Coogan, 2006; Schelling *et al.* 2007; Yonkee & Weil, 2010; Yonkee *et al.* 2014
2	Wyoming salient, north part	*c.* 100	Paull & Paull, 1991; Yonkee & Weil, 2010
3	Wyoming salient, central part	140	Yonkee & Weil, 2010
4	Wyoming salient, south part	95	Yonkee & Weil, 2010
5	Central Utah salient, north part	100	Schelling *et al.* 2007
6	Central Utah salient, south sector	*c.* 75	DeCelles & Coogan, 2006; Schelling *et al.* 2007
7	Sevier hinterland, Basin & Range province	*c.* 80	Yonkee *et al.* 2014

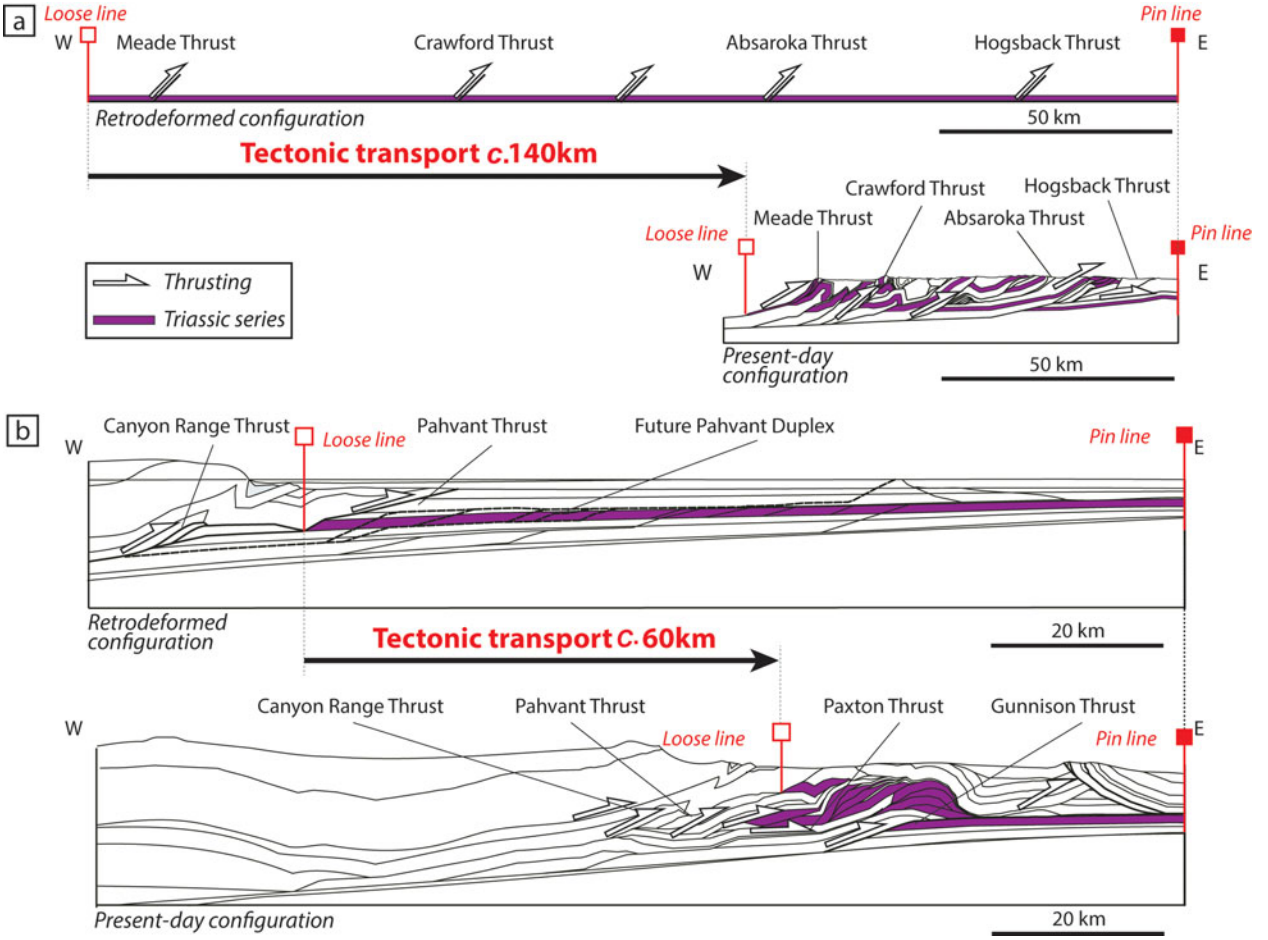

Figure 6. (Colour online) Present-day and retrodeformed (for the PTU-Smithian interval) configurations for two regional cross-sections in the (a) northern and (b) southern parts of the Sonoma Foreland Basin, illustrating the method used for palinspastic reconstruction (after Groshong, 2006). Balanced cross-sections adapted from (a) Yonkee & Weil (2010) and (b) DeCelles & Coogan (2006) illustrate the retrodeformation process used to estimate the value of the tectonic transport, and therefore the approximate original location of the sections during the studied interval. Triassic series (highlighted layers) are used as the basis for the retrodeformation process and are horizontalized between the designated Pin and Loose lines (see text for details). The two cross-sections are located in Figure 7.

3.b.2. *Subsidence analysis and backstripping*

Subsidence analysis quantifies the vertical movements underwent by a given sedimentary depositional surface through a graphic representation, by tracking the subsidence and uplift history of said surface (Van Hinte, 1978). This history is reconstructed based on sedimentary thickness, lithology, palaeo-sea level, palaeobathymetry and age data. This analysis also accounts for the mechanical compaction underwent by the sediments. The resulting curve provides a view of the total subsidence history for a given stratigraphic column (Van Hinte, 1978; Allen & Allen, 2005). Steckler & Watts (1978) showed that the local isostatic effect exerted by the sedimentary load can be removed. This ‘backstripping’ method can therefore help to characterize the tectonic subsidence only, as if the basin has been filled by air only and not by water and/or sediment during its history (Steckler & Watts, 1978; Xie & Heller, 2009). Backstripping is also

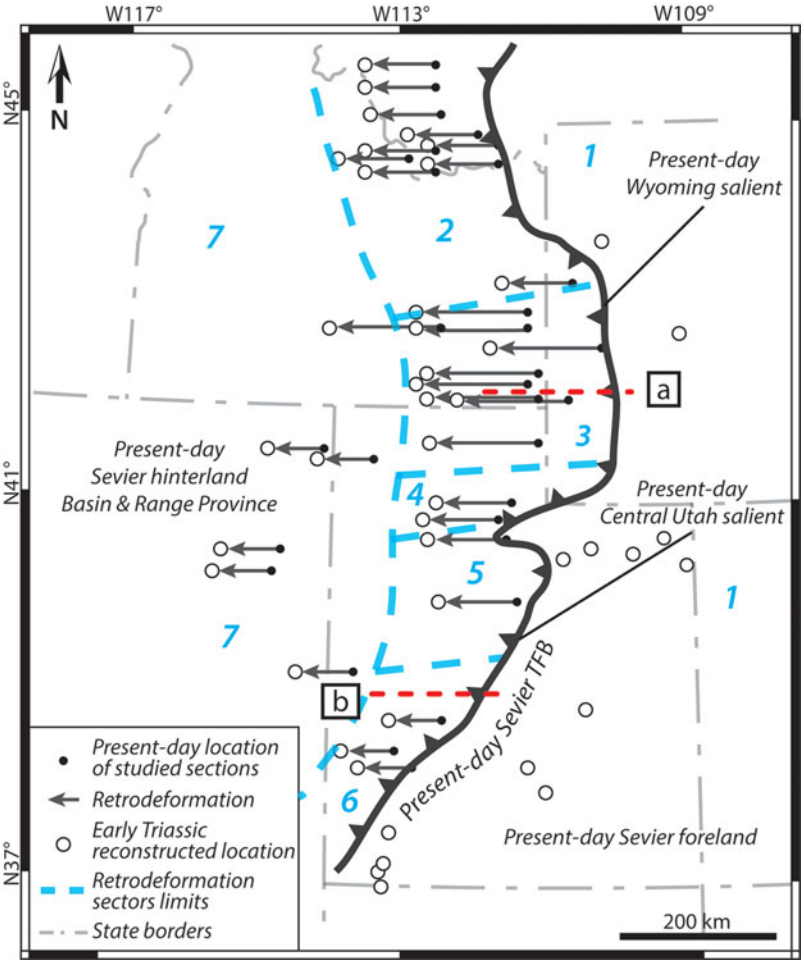

Figure 7. (Colour online) Map representing the present-day location of the studied sections (dots) and their reconstructed position (open circles) obtained after retrodeformation. Positions of balanced cross-sections (a) and (b) illustrated in Figure 6 are also indicated. The present-day Sevier Thrust-and-Fold Belt (TFB; after Yonkee *et al.* 2014) is the main structural element responsible for tectonic transport during post-Triassic times. Black arrows represent the retrodeformation values applied from the present-day location of the studied sections. Seven sectors of similar estimated tectonic transport are delimited by dashed lines (see Table 1). Sector 1: Sevier foreland; Sector 2: Wyoming salient, northern part; Sector 3: Wyoming salient, central part; Sector 4: Wyoming salient, southern part; Sector 5: Central Utah salient, northern part; Sector 6: Central Utah salient, southern part; Sector 7: Sevier hinterland.

used to restore the initial thickness of a sedimentary column (Angevine, Heller & Paola, 1990; Allen & Allen, 2005). Lithological compositions and palaeobathymetries have been checked using facies analysis (online Supplementary Table S1) or literature data (see analysed sections in Fig. 3b and online Supplementary Table S2). Porosity was quantified by comparison with experimental data (e.g. Van Hinte, 1978; Sclater & Christie, 1980) and represents an important proxy for compaction analysis. Additionally, Chevalier *et al.* (2003) and Lachkar *et al.* (2009) showed that a highly resolved biostratigraphic control is useful to define and quantify variations in subsidence at a fine spatio-temporal scale as it yields accurate subsidence rates. For the Early Triassic Sonoma Foreland Basin, the high-resolution ammonoid zonation by Brayard *et al.* (2013) serves as the main timeframe. Complementary absolute time lines were obtained from radiometric ages published from coeval beds in South China (Galfetti *et al.* 2007; Burgess, Bowring & Shen, 2014), whereas the duration of the studied intervals was interpolated from ammonoid biozone duration (after Brühwiler *et al.* 2010 and Ware *et al.* 2015). Palaeo-sea level curve is based on data from Haq, Hardenbol & Vail (1988), providing a quantitative representation of the reconstructed Early Triassic sea level.

We chose to not use the flexural backstripping method (Allen & Allen, 2005) due to the lack of appropriate data needed for such model (e.g. flexural rigidity data, regional distribution of the sedimentary load). Instead, we calculated the total and tectonic subsidence curves using the one-dimensional (1D) local isostatic approach of Steckler & Watts (1978). In addition, this method emphasizes the tectonic subsidence as ‘a way of normalizing subsidence in different basins that have undergone very different sedimentation histories’ (Xie & Heller, 2009). Our results for the tectonic subsidence history in the SFB can therefore be compared to the compilation of Xie & Heller (2009). Subsidence analyses were performed on four sections (Fig. 3b) using the OSXBackstrip software performing 1D Airy backstripping (after Watts, 2001; Allen

& Allen, 2005; available at: http://www.ux.uis.no/~nestor/work/programs.html). These sections were selected for their completeness (a complete and continuous sedimentary succession is reported from the PTU to at least lower Spathian stratigraphy), for the presence of biostratigraphic markers (ammonoid beds) and for their repartition within the SFB (representative of both the northern and southern areas). A complete set of initial parameters and detailed results of the subsidence analysis for each of the four sections are reported in online Supplementary Material S1.

This analysis bears limitations as some errors may arise from uncertainties around the data used for the subsidence analysis (Chevalier *et al.* 2003; Xie & Heller, 2009): (1) accuracy of the measurement and report of the sedimentary thickness; (2) backstripping calculation; (3) palaeo-bathymetry estimations; and (4) age control. Regarding the accuracy of the sediment thickness, all selected sections have been measured at a centimetric scale. Errors on measurements are therefore rather low, i.e. ±2 % of the total thickness. In the backstripping analysis, variables used for the calculation of the burial compaction are: thickness; the initial porosity of the sediment; and the lithological constant of corresponding lithologies. The latter two parameters are determined by comparison with experimental data (e.g. Van Hinte, 1978; Sclater & Christie, 1980). Error on sediment decompaction is therefore estimated to be low (*c.* ±5 %). Palaeobathymetry is hard to determine because of the paucity of discriminating indicators. We hypothesize that errors on depth estimations are about ±10 %. For age control, we used a compilation of biostratigraphic and radiochronological data, leading to a detailed timeframe with a maximum error of around 60 ka (Brühwiler *et al.* 2010).

3.b.3. *Spatial distribution of sedimentary thickness*

PTU-Smithian sedimentary thicknesses and their respective location within the SFB were integrated in Global Mapper v.16.2.3 GIS software (available at http://www.bluemarblegeo.com/products/global-mapper.php) to generate an isopach map by creating a 3D triangulated grid projection of thicknesses (online Supplementary Figure S1).

3.b.4. *Lithospheric heterogeneity of the basement*

To explore the nature of the SFB basement, a terrane map was constructed using previous published maps by Yonkee *et al.* (2014), Yonkee & Weil (2015) and Lund *et al.* (2015). In addition, we analysed several types of geophysical data: a raw regional Bouguer gravity anomaly map (Kucks, 1999); an aeromagnetic anomaly map from Bankey *et al.* (2002); and literature data (e.g. Gilbert, Velasco & Zandt, 2007). We also used published U/Pb radiochronological data to assess an age for each basement terrane defined in the basin (Foster *et al.* 2006; Fan *et al.* 2011; Mueller *et al.* 2011; Nelson, Hart & Frost, 2011; Strickland, Miller & Wooden, 2011). It is worth noting that Precambrian crystalline basements, lying under detachments and décollements responsible for nucleation of thrusting, are not affected by these 'thin-skin' thrust-induced displacements (DeCelles & Coogan, 2006; Schelling *et al.* 2007; Yonkee & Weil, 2010).

3.b.5. *Numerical model*

The flexural response of the SFB basement has been simulated using a 2D plane stress flexural model solved with a finite element method code written in Matlab®. This approach has been successfully used to model lithospheric deformation due to topographic and mantle loads (Le Pourhiet & Saleeby, 2013) and ice loads (Moreau *et al.* 2015). First, a model of the basin is made using field-based and literature data to characterize and quantify the flexural response of the modelled SFB basement. Three additional models are then proposed to test different scenarios regarding possible mechanisms controlling the flexure of the SFB basement.

4. Results

We first reconstructed the SFB palaeogeography and used lithological and stratigraphical analyses to constrain the spatial distribution of the sedimentary record across the basin. This approach provides estimations of subsidence rates in the SFB. Secondly, we identified and characterized the terranes that compose the SFB basement using geophysical and cartographic data, as well as previously published ages. We then reconstructed the morphology of the Golconda Allochthon in relation to the heritage of the basin. Finally, a 2D model is proposed to quantify the flexural behaviour of the basin.

4.a. Lithological and stratigraphical analyses

Previous palaeogeographic reconstructions of the SFB did not take tectonic events and the ensuing displacements into account (e.g. Paull & Paull, 1993). The palinspastic map of the basin with the initial locations of the studied sections is shown on Figure 7. For the first time post-Triassic displacements were accounted for, including: (1) the Sevier orogeny (Cretaceous–Eocene) and the associated regional shortening due to the setting of a thrust-and-fold belt (e.g. Yonkee & Weil, 2010); and (2) the later Neogene – present-day extension linked to the Basin and Range province (e.g. Yonkee *et al.* 2014).

Based on the palinspastic map, we constructed a palaeogeographic isopach map of the SFB (Fig. 8). The isopach map shows that the distribution of the sedimentary thickness for the PTU-Smithian interval is heterogeneous within the basin, showing a thicker succession in the northern than in the southern part. In the southern part, the thickness gradually varies along a roughly NW–SE-aligned transect, showing low

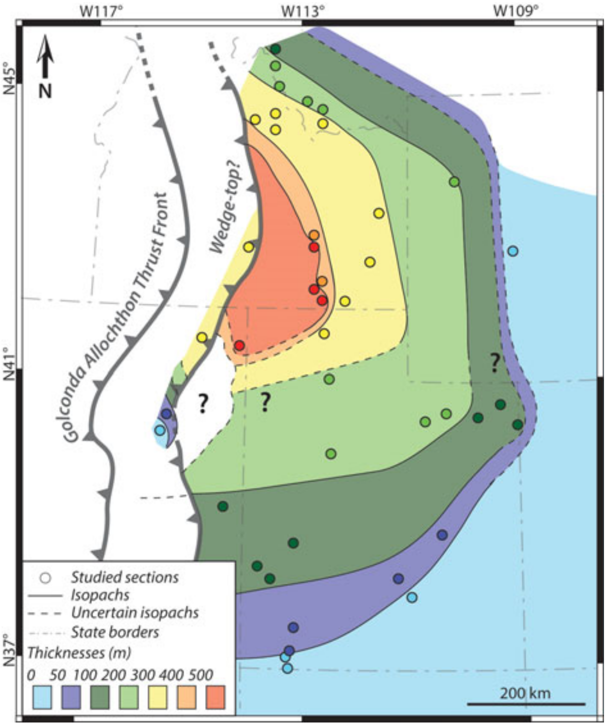

Figure 8. (Colour online) Isopach map of the sedimentary thicknesses recorded for the PTU-Smithian interval, showing marked differences in sedimentary thicknesses between northern and southern Sonoma Foreland Basin. The studied sections are shown at their palaeolocation (Fig. 7). The reconstructed Golconda Allochthon Thrust Front during the PTU-Smithian studied interval is also indicated (modified from Dickinson, 2013; see also Fig. 12). The position of the wedge-top is based on variations in the sedimentary thicknesses and on geophysical data (Fig. 10).

thicknesses over a large surface (*c.* 500 km from east to west). The thickness ranges from a few tenths of metres in south and SE Utah, up to 250 m around Salt Lake City. The westernmost area (NE Nevada) is also characterized by low thicknesses (<100 m thick). Conversely, the northern part of the basin exhibits a marked transition with thickness values broadly increasing from east to west. The easternmost area of the northern part (west Wyoming) shows sedimentary thicknesses similar to that of the southern part (<300 m thick; Fig. 8). The west-central area records the thickest succession of the SFB (up to *c.* 550 m thick), and is centred on present-day south-central Idaho. The westernmost area (west-central Idaho) shows similar thicknesses (up to *c.* 300 m thick; Fig. 8).

The subsidence analysis (Fig. 9) also shows a clear distinction between the northern and southern parts of the basin. Confusion Range (CR, Fig. 9a) and Pahvant Range (PR, Fig. 9b) sections exhibit relatively low subsidence curves during the studied interval, whereas Sheep Creek (SC, Fig. 9c) and Hot Springs (HS, Fig. 9d) sections show a high subsidence profile. The total and tectonic subsidence curves are similar and the tectonic subsidence is here a major component of the total subsidence, accounting for at least two-thirds of the total subsidence, if not more (e.g. in CR, Fig. 9a).

When looking at the dominant lithologies (Fig. 9e), the sections from the southern part of the basin display a sedimentary succession dominated by coarse conglomerates and sandstones and microbial limestones of the Moenkopi Group and the limestones/shales of the Thaynes Group (Figs 3, 4, 9e), while the total subsidence is low. By contrast, the sections from the northern part of the SFB are dominated by fine siltstones (Figs 3, 4, 9e) with an important subsidence.

Finally, the tectonic subsidence appears as a critical diagnostic feature for the basin (Fig. 9f). A marked difference exists between mean tectonic subsidence rates in the southern and northern parts of the basin (*c.* 100 m Ma^{-1} v. *c.* 500 m Ma^{-1}, respectively). The southern sections show a low-rate tectonic subsidence (50–200 m Ma^{-1}; Fig. 9e). Nevertheless, a marked increase in subsidence rate is recorded during early Spathian time for these sections (150–600 m Ma^{-1}; Fig. 9e). Conversely, the northern sections show a higher rate of tectonic subsidence during the PTU-Smithian interval (450–650 m Ma^{-1}; Fig. 9e), whereas early Spathian time is characterized by a decrease in subsidence rate (100–250 m Ma^{-1}; Fig. 9e).

4.b. Basement characterization

On the gravimetric anomaly map shown on Figure 10a, black lines outline the geophysical features that may represent traces of crustal/lithospheric faults or heterogeneities in the basement (Lowrie, 2007). The lowest Bouguer anomaly values (<150 mGal, Fig. 10a) suggest the presence of a thick crust, whereas moderate negative anomalies (between −65 and −135 mGal; white outlines) point towards a thinner crust and/or the presence of lower-crustal high-density bodies (e.g. Gilbert, Velasco & Zandt, 2007; Lowrie, 2007). The Snake River Plain (SRP in Fig. 10a) is a Yellowstone hotspot track-related basaltic province. This young (of Neogene age) structure influences neither the geometry nor the properties of the basement (Dickinson, 2013). The Farmington Anomaly (FA on Fig. 10a), located in the centre of the study area, may result from the presence of lower-crustal high-density mafic and/or ultramafic material emplaced during a thermal event dated at *c.* 1.64 Ga (Mueller *et al.* 2011). Alternatively, it can have originated from a more recent thermal event and/or the presence of a thin lithospheric crust (e.g. Gilbert, Velasco & Zandt, 2007; Lowrie, 2007). Remnants of an important thermal metamorphism including partial melting (*c.* 1.67 Ga) can also be observed in this area (red dots in Fig. 10c; Mueller *et al.* 2011). The Southern Anomaly (SA on Fig. 10a) is poorly documented and may result from variations in the crustal thickness of the terrane (e.g. Gilbert, Velasco & Zandt, 2007; Lowrie, 2007), possibly linked to the Ancestral Rocky Mountains orogeny or to the more recent Laramide orogeny and the building of the Rocky Mountains (Ye *et al.* 1996; Dickerson, 2003).

The aeromagnetic anomaly map presented in Figure 10b discriminates areas of contrasted

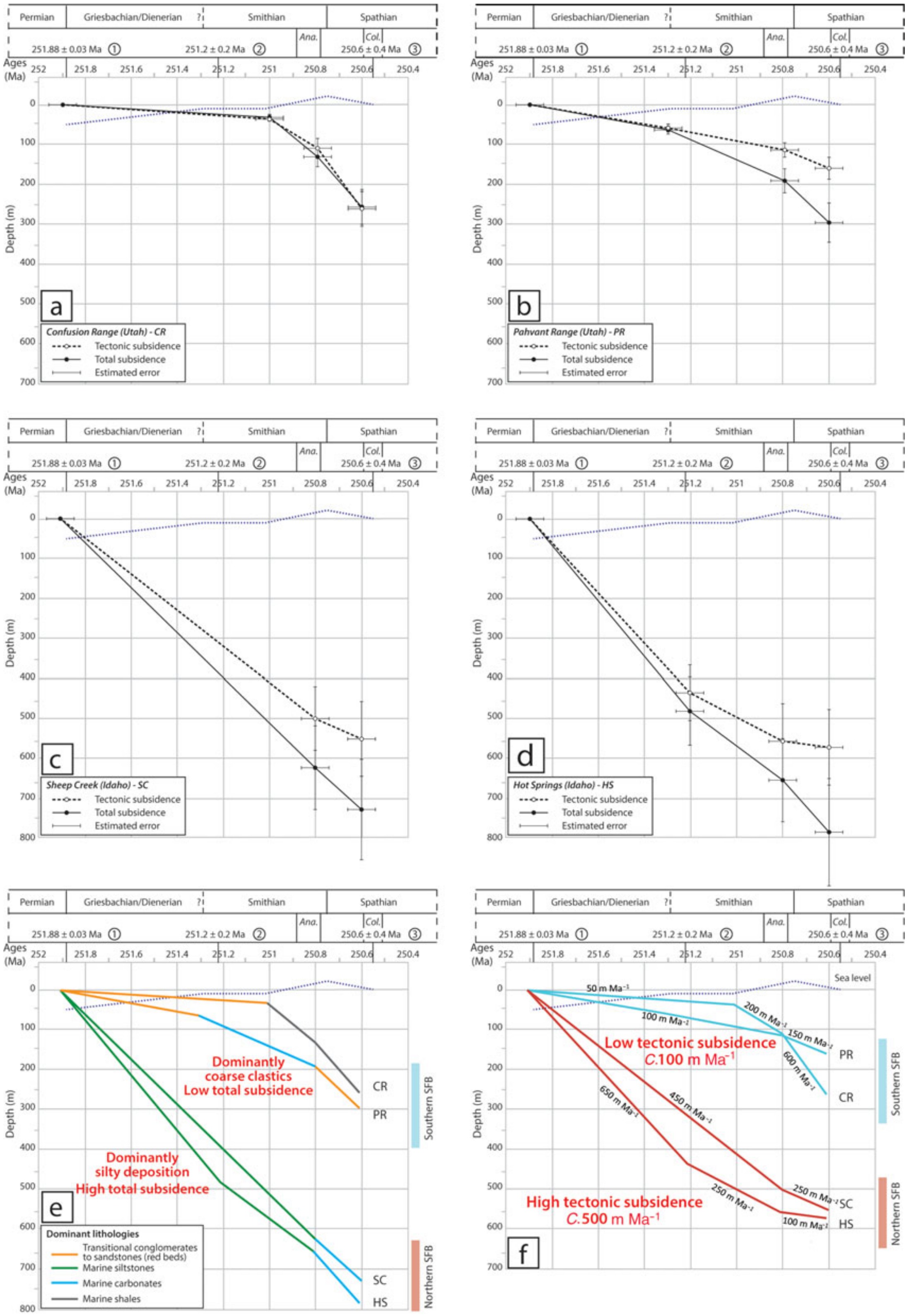

Figure 9. (Colour online) Subsidence analysis results obtained for the PTU-Smithian interval and early Spathian time using 1D backstripping (Steckler & Watts, 1978; Van Hinte, 1978; Allen & Allen, 2005). Locations of sections are given in Figure 3b. Ages for the bottom and top boundaries of the Smithian are interpolated from ammonoid biozone durations (after Brühwiler *et al.* 2010). Sea-level curve after Haq, Hardenbol & Vail (1988). *Ana.*: *Anasibirites* beds; *Col.*: *Columbites* beds. Radiometric ages from (1) Burgess, Bowring & Shen (2014); (2) and (3) Galfetti *et al.* (2007). Subsidence analysis for: (a) Confusion Range (CR) section; (b) Pahvant Range (PR) section; (c) Sheep Creek (SC) section; (d) Hot Springs (HS) section. (e) Total subsidence curves for all the CR, PR, SC and HS sections and associated dominant lithologies are indicated for each subinterval. (f) Tectonic subsidence curves for the CR, PR, SC and HS sections and associated mean tectonic subsidence rates. (e) and (f) allow two distinct subsidence dynamics to be discriminated between the southern and northern parts of the SFB.

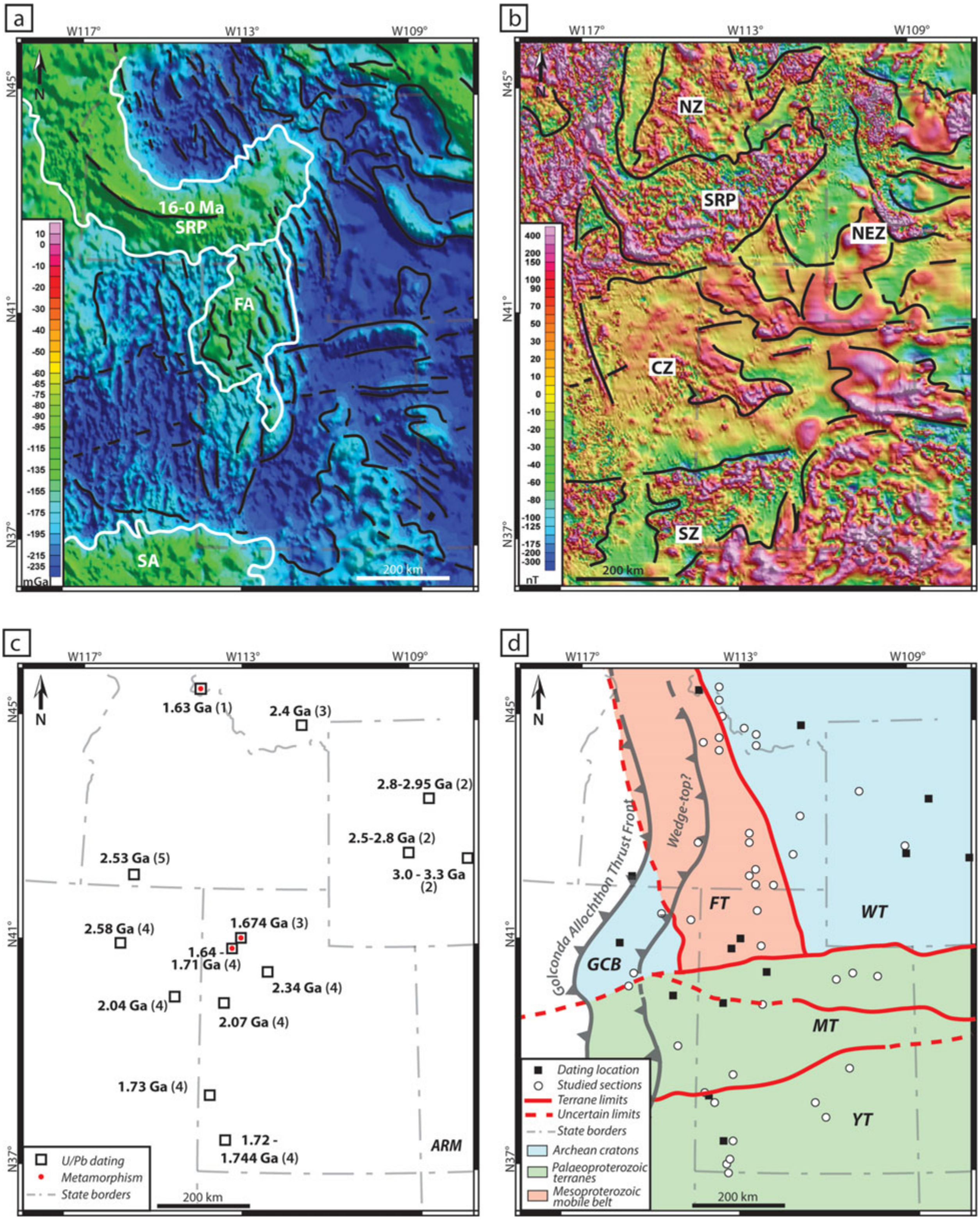

Figure 10. (Colour online) (a) Bouguer gravity anomaly map of the Sonoma Foreland Basin and its surroundings (in mGal; after Kucks, 1999). Notable moderate gravity anomalies are highlighted by a white contour. SRP: Snake River Plain; FA: Farmington Anomaly; SA: Southern Anomaly. Black lines represent the interpreted remnants of the main geophysical accidents, and limits between crustal features. (b) Aeromagnetic anomaly map of the Sonoma Foreland Basin and its surroundings (in nT; after Bankey *et al.* 2002). Black lines highlight areas of contrasted magnetic signatures: SRP: Snake River Plain; SZ: Southern magnetic Zone; CZ: Central magnetic Zone; NEZ: North-Eastern magnetic Zone; NZ: Northern magnetic Zone. (c) Map of the spatial location of the radiochronological ages (U/Pb ages) after: (1) Foster *et al.* 2006; (2) Fan *et al.* 2011; (3) Mueller *et al.* 2011; (4) Nelson, Hart & Frost, 2011; (5) Strickland, Miller & Wooden, 2011). Superimposed red dots indicate Mesoproterozoic metamorphism episodes (Mueller *et al.* 2011). (d) Map of basement terranes of the SFB according to their age and nature, with Archean terranes (pale blue), Palaeoproterozoic terranes (pale green) and Mesoproterozoic mobile belt (pale red). FT: Farmington Terrane; GCB: Grouse Creek Block; MT: Mojave Terrane; WT: Wyoming Terrane; YT: Yavapai Terrane.

magnetic signatures (separated by black lines on Fig. 10b). These disturbances in magnetic field are attributed to differences in the nature of the rocks composing the basement (Turner, Rasson & Reeves, 2007). We do not attempt to identify the exact nature of these rocks here; rather, we use these contrasted anomalies to characterize differences of rock types that compose the basement (Purucker & Whaler, 2007; Lund *et al.* 2015). As on the Bouguer gravity anomaly map, the presence of the Snake River Plane hotspot-track (SRP in Fig. 10a, b) is obvious on the aeromagnetic anomaly map. It features a strong positive magnetic anomaly signal (>150 nT, Fig. 10b). The Southern magnetic Zone (SZ on Fig. 10b) can be distinguished on the southern part of the studied area by contrasted anomalies with a wide range of variations (from *c.* –200 nT up to *c.* 400 nT). The Central magnetic Zone (CZ on Fig. 10b) occupies the central third of the map. It is characterized by generally neutral to (strongly) positive anomalies (from *c.* –10 nT to *c.* 60 nT, locally up to >150 nT). In the northeastern quarter of the studied area, the North-Eastern magnetic Zone (NEZ on Fig. 10b) is characterized by generally negative anomalies (between *c.* –80 nT and *c.* –10 nT). Some areas with strong positive anomalies (>150 nT) are also observed, whose shape and extension are very similar in the Bouguer gravity anomaly map (Fig. 10a). Finally, a small Northern magnetic Zone (NZ on Fig. 10b) is visible north to the SRP and west to the NZ. It shows contrasting anomalies, but with a less important range of variation than the SRP and less strongly positive values (from *c.* –60 nT to *c.* 150 nT only).

Figure 10c synthesizes the location and the different U/Pb radiochronological ages for the basement (Foster *et al.* 2006; Fan *et al.* 2011; Mueller *et al.* 2011; Nelson, Hart & Frost, 2011; Strickland, Miller & Wooden, 2011). Basement rocks of Archean, Palaeoproterozoic and Mesoproterozoic ages can be found throughout the entire studied area (Fig. 10c). Archean ages are found in Wyoming, southwestern Montana and northeastern Nevada (Fig. 10c; Fan *et al.* 2011; Mueller *et al.* 2011; Nelson, Hart & Frost, 2011; Strickland, Miller & Wooden, 2011). Palaeoproterozoic ages are found in Utah and eastern Nevada (Fig. 10c; Mueller *et al.* 2011; Nelson, Hart & Frost, 2011). Finally, Mesoproterozoic ages associated with metamorphism are found in northwestern Utah and northern Idaho (Fig. 10c; Foster *et al.* 2006; Mueller *et al.* 2011; Nelson, Hart & Frost, 2011).

Five different lithospheric terranes composing the SFB basement can therefore be identified: the Wyoming Terrane (WT); the Grouse Creek Block (GCB); the Mojave Terrane (MT); the Yavapai Terrane (YT); and the Farmington Terrane (FT; Fig. 10d). The GCB and WT are Archean terranes with ages of *c.* 2.5 Ga (Nelson, Hart & Frost, 2011; Strickland, Miller & Wooden, 2011) and 2.4–3.3 Ga (Fan *et al.* 2011; Mueller *et al.* 2011), respectively. The MT is a Palaeoproterozoic terrane of age 2.04–2.34 Ga, whereas the YT is a younger Palaeoproterozoic terrane of age 1.720–1.744 Ga (Nelson, Hart & Frost, 2011). The FT is a Mesoproterozoic intracratonic mobile belt (Lund *et al.* 2015) composed of reworked Archean crust (Whitmeyer & Karlstrom, 2007), with metamorphism ages between 1.63 and 1.71 Ga (Foster *et al.* 2006; Mueller *et al.* 2011; Nelson, Hart & Frost, 2011).

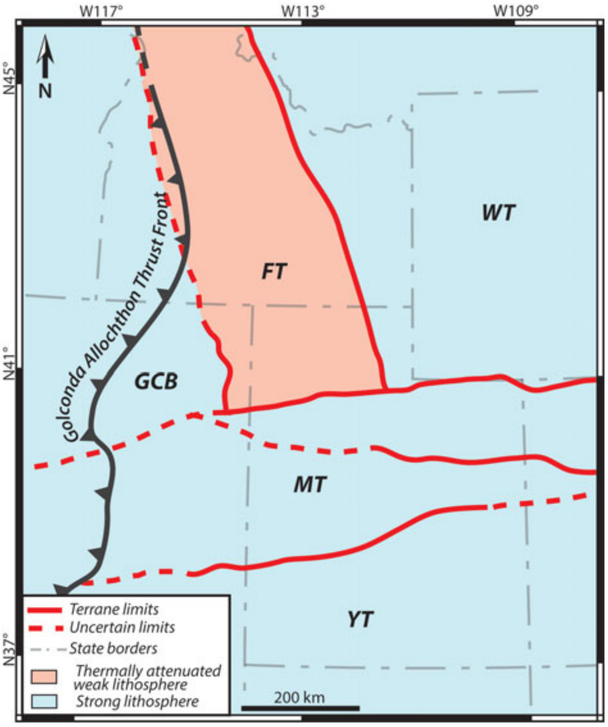

Figure 11. (Colour online) Map of the SFB basement (cf. Fig. 10d) after their heritage and therefore their rheological behaviour. Archean Grouse Creek Block and Wyoming Terrane, Palaeoproterozoic Mojave Terrane and Yavapai Terrane are considered 'strong' lithospheres with an important rigidity (pale blue), while the Mesoproterozoic mobile belt Farmington Terrane is considered a 'thermally attenuated weak' lithosphere due to its lesser rigidity (pale red).

4.c. Impact of the heritage on the SFB development

The fact that the basement of the SFB is composed of five Archean–Mesoproterozoic terranes questions the potentially crucial role of inherited lithospheric features on the formation and spatio-temporal evolution of the SFB.

Lithospheric strength (i.e. rigidity) of the terranes varies depending on their age and heritage (Poudjom Djomani *et al.* 2001; Artemieva & Mooney, 2002), with important changes in rheological behaviour and segregation between oldest (>1.7 Ga) and juvenile crusts (<1.7 Ga; Artemieva & Mooney, 2002). Since older lithospheres are more rigid than younger, Archean and Palaeoproterozoic basements such as the Wyoming Terrane, Grouse Creek Block, Mojave Terrane and Yavapai Terrane are defined here as 'strong' lithospheres (e.g. Cardozo & Jordan, 2001; Leever *et al.* 2006; Fig. 11). Conversely, the more recent Mesoproterozoic lithospheres such as the Farmington Terrane (Fig. 11) are characterized by a lower rigidity (e.g. Cardozo & Jordan, 2001; Leever *et al.* 2006; Fosdick, Graham & Hilley, 2014). Additionally, some lithospheres can be weaker than coeval ones due to their structural heritage and thermal history, and are assumed to be 'attenuated' (*sensu* Fosdick, Graham & Hilley, 2014). The Farmington Terrane was formed as a mobile belt between Archean GCB and WT and underwent at least one event of intense thermal metamorphism during Mesoproterozoic time (Mueller *et al.* 2011; Lund *et al.* 2015) Younger occurrences of similar events until Early Triassic time cannot be ruled out, especially given the Bouguer gravity anomaly hints of underplating dense material (see Section 4.b). The Farmington Terrane is therefore considered here as a 'thermally attenuated weak' lithosphere (Fig. 11).

Due to the lithospheric heterogeneity of the basement, the role of the boundary lithospheric faults can be considered as essential. Neoarchean–Palaeoproterozoic terranes are limited by mega-shear zones along with deep (nearly) vertical crustal and/or lithospheric faults (Figs 10d, 11). Terranes in the SFB display some characteristics (e.g. dimension, geometry) that are similar to the terranes associated with the Neoarchean–Palaeoproterozoic accretionary orogens (e.g. Chardon, Gapais & Cagnard, 2009; Cagnard, Barbey & Gapais, 2011). These lithospheric and crustal accidents have therefore been reactivated since their Precambrian onset (e.g. Bryant & Nichols, 1988; Paulsen & Marshak, 1999). Additionally, several authors (e.g. Eardley, 1939; Peterson, 1977) identified the presence of a topographic basement highland (pale blue area in Fig. 12a, in colour online) near the junction between the MT and the GCB/FT/WT during Palaeozoic time, separating the northern and southern areas of marked sedimentary accumulation. Eardley (1939) first introduced this feature as the 'Northern Utah Highland'. Peterson (1977) highlighted its presence on his palinspastic maps for the Palaeozoic stratigraphic record. Finally, this sedimentary and topographic pattern seems to have been the same in this basin since Proterozoic time (Paulsen & Marshak, 1999; Fig. 12a).

By the time of the initiation of the Sonoma orogeny, this difference in sedimentary accumulation was well marked in Palaeozoic series (Peterson, 1977). For instance, about 6 km of marine sediments accumulated in the Permian Oquirrh Basin in the northern part of the SFB (Fig. 12a; Yonkee & Weil, 2015), whereas the southern part of the SFB saw the deposition of only several hundred metres of marine and terrigenous sediments (e.g. *c.* 640 m in southwestern Utah; Rowley *et al.* 2005) during the same interval. The thick Palaeozoic sedimentary series in northern and southern parts of the foreland (Peterson, 1977) would have allowed the thrust belt to propagate, while the presence of the topographic basement highland characterized by a reduced sedimentary cover should have triggered the formation of a lateral ramp and a recess in the central part of the front (Fig. 12a). The presence of the topographic high is attested by the occurrence of shallow conglomerates in the western part of the SFB within the PTU-Smithian interval (Fig. 12a, b; e.g. Gabrielse, Snyder & Stewart, 1983; Lucas & Orchard, 2007; Jattiot *et al.*, in press). Previous reconstruction of the GA thrust front also accounted for the presence of a recess in the central part of the thrust front (e.g. Dickinson, 2006, 2013). Moreover, this mechanism underlying the

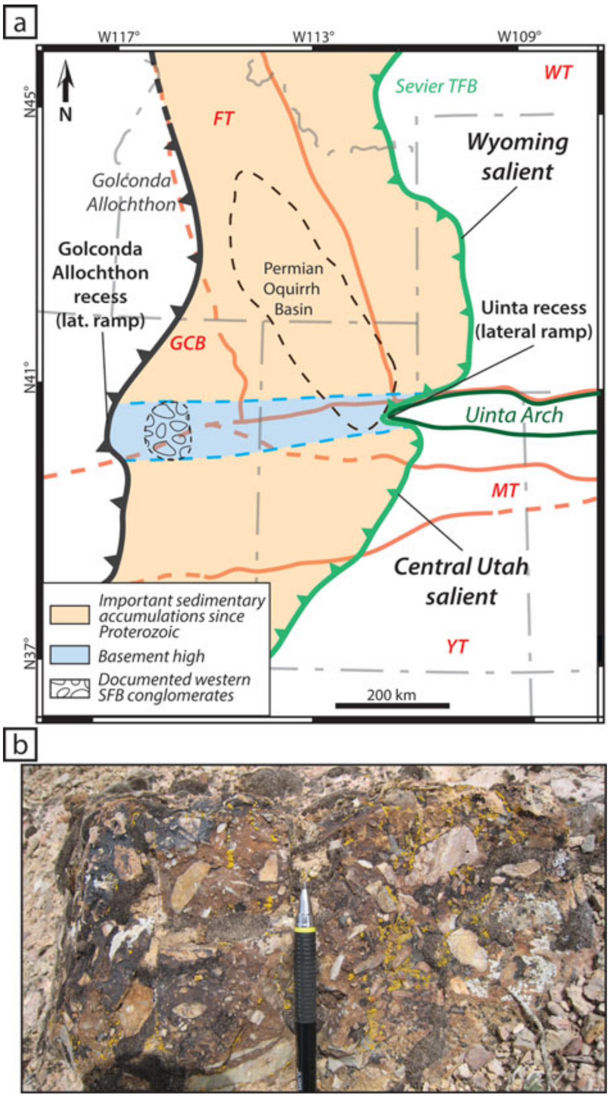

Figure 12. (Colour online) (a) Simplified map showing the position of the Uinta recess (lateral ramp) and Wyoming and Central Utah salients (frontal ramps) of the present-day Sevier TFB (after Paulsen & Marshak, 1999; Yonkee & Weil, 2010) and reconstructed Golconda Allochthon front and associated recess (lateral ramp). Sedimentary pattern since Proterozoic time shows two high accommodation zones separated by a topographic high close to the terrane boundaries (Peterson, 1977, Bryant & Nichols, 1988; Paulsen & Marshak, 1999). Palaeolocation of Permian Oquirrh Basin (e.g. Yonkee & Weil, 2015) and documented PTU-Smithian conglomerates in the western SFB (e.g. Gabrielse, Snyder & Stewart, 1983; Lucas & Orchard, 2007) are also included on the map. Red lines indicate limits of the basement terranes (cf. Fig 9d). (b) Photograph (courtesy of Hugo Bucher, Zürich) of the conglomerates found in the area delimited in (a), presumably a product of western relief dismantlement.

Table 2. Summary of model parameters for the SFB and tested scenarii.

Parameter	SFB model (Fig. 13)	Heterogeneous basement scenario (Fig. 14a)	Heterogeneous allochthon scenario (Fig. 14b)	Combined heterogeneities (basement & allochthon; Fig. 14c)
Young's modulus E (GPa)	80	80	80	80
Poisson's ratio, ν	0.25	0.25	0.25	0.25
Elastic thickness of 'strong' lithosphere, T_{e1} (km)	90	90	90	90
Elastic thickness of 'weak' lithosphere, T_{e2} (km)	30	30	n/a	30
Loading parameters				
Allochthon thickening, h (m)	1500	1500	1500	1500
Density of topographic load, ρ_t (kg m^{-3})	2700	2700	2700	2700
Density of the mantle, ρ_m (kg m^{-3})	3300	3300	3300	3300
Density of the sedimentary infill, ρ_i (kg m^{-3})	1600	1600	1600	1600
Gravitational acceleration, g (m s^{-2})	9.81	9.81	9.81	9.81

observed differential propagation has been proposed by Paulsen & Marshak (1999) for the Sevier thrust-and-fold belt which shows the presence of a lateral ramp in its central part (Fig. 2). This was explained by the pre-deformational sedimentary thicknesses pattern showing thrusts propagating further when emplaced upon a thicker sedimentary cover (Figs 2, 12a; Paulsen & Marshak, 1999). It is worth noting that both the lateral ramps of the Sevier and Golconda thrust-and-fold belt are located close to and along the lithospheric boundary between the MT and FT/WT (Figs 2, 12a).

The GA heterogeneity may therefore have played a role, complementary to the basement heritage, over the flexural response of the SFB. However, due to the scarcity of allochthon remnants, a numerical model is required to decipher its potential role.

4.d. Simulating the flexural response of the basin

All the data discussed above have been integrated in a 2D numerical flexural model. This approach allows us to quantify in a predictive way the flexural behaviour of the basin in relation to its basement heritage.

4.d.1. Numerical approach and setup

The 2D plane stress flexural models have been solved with a finite element method code written in Matlab® (Le Pourhiet & Saleeby, 2013; Moreau *et al.* 2015). It solves

$$\nabla^2\left(D\nabla^2\omega\right) = g\left(\rho_m - \rho_i\right) + q \qquad (1)$$

for flexural deflection ω of a thick elastic plate (Reissner–Mindlin approximation) using bilinear isoparametric elements with under integration technique for the shear terms (Zienkiewicz & Taylor, 2005). In Equation (1) the rigidity of the plate D, defined

$$D = \frac{E T_e^3}{12\left(1-\nu^2\right)},$$

depends solely on the effective elastic thickness T_e as the plate Young's modulus E and Poisson's ratio ν are fixed at 80 GPa and 0.25, respectively (Burov & Diament, 1995). The topographic loads $q = \rho_t\, g\, h$ account for the thickening h resulting from the orogeny and are computed using a density ρ_t = 2700 kg m^{-3}. The mantle restoring forces are computed assuming a density ρ_m = 3300 kg m^{-3}, while the infill is considered to be sediments of density ρ_i =1600 kg m^{-3}. We arbitrarily attributed a constant height h = 1500 m to the topographic load as we concentrate on the effect of heterogeneities of the allochthon morphology and rheology of the basement only. These initial parameters are summarized in Table 2.

The models are 907 km wide in the x direction, chosen to be normal to the trend of the orogenic belt, and 1166 km in the y direction. We assume that isostatic compensation is achieved underneath the orogen and, accordingly, we set the curvature normal to the right side to zero, $\partial\omega/\partial x = 0$. As the orogen is very long compared to the region where flexural subsidence is analysed, we enforce cylindrical boundary conditions on the side of normal y ($\partial\omega/\partial y = 0$). On the right boundary, that is, far from the orogeny, the effect of topographic loading can be considered null, corresponding to $\omega = 0$.

In this model, we used T_{e1} = 90 km for the 'strong' GCB, WT, MT and YT lithospheres (Table 2), which is a good approximation for cratonic T_e (Watts, 1992). The 'weak-attenuated' FT is expected to show a contrasted lower T_e value due to its assumed rheological weaknesses. This value was set at T_{e2} = 30 km (Table 2; e.g. Leever *et al.* 2006).

4.d.2. Model results

Figure 13 shows that the southern part of the front is reconstructed as less propagated into the foreland than the northern part (Fig. 12a; see Dickinson, 2006, 2013). In this model, the lateral ramp is spatially restricted along the limit between the FT/WT and MT (Fig. 13a). The northern part, emplaced mainly above the 'weak' FT and in front of the largest part of the GA, presents a narrower foredeep with λ ≈ 250 km (Fig. 13a, b). The steep foredeep is bordered by a well-expressed forebulge emplaced close to the FT/WT boundary (Fig. 13a; *XX'* in Fig. 13b). The southern

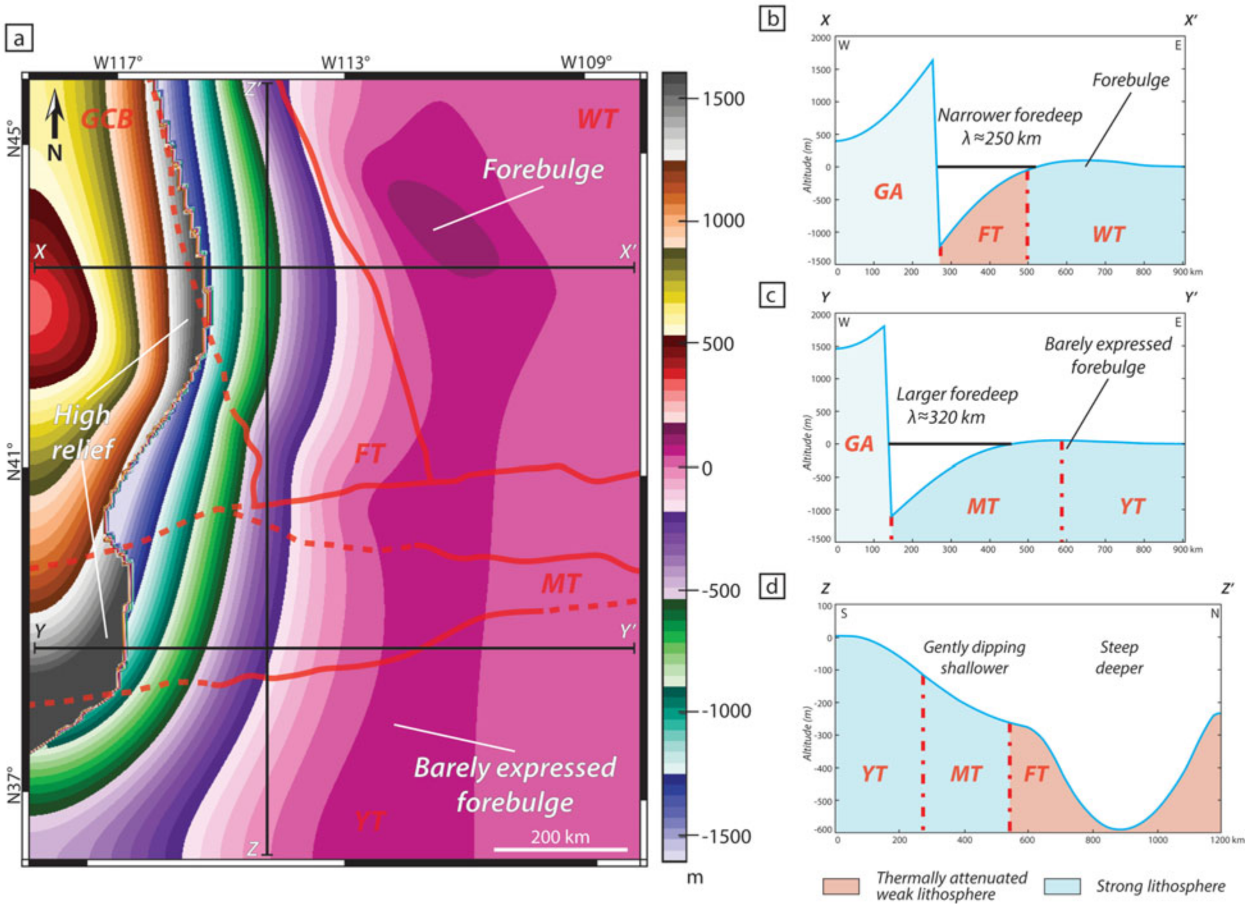

Figure 13. (Colour online) Numerical model of the SFB after the reconstructed palaeogeography and terranes map (cf. Figs 11, 12) with an heterogeneous basement ('strong' v. 'thermally attenuated weak' lithospheres) and an heterogeneous allochthon (recessed area in central part of the front). (a) Simulated map of the SFB. Thin black lines indicate the position of the 2D profiles; red lines indicate limits of the basement terranes (cf. Fig 10d). (b) 2D W–E profile of the northern part of the SFB model. The narrow foredeep is emplaced upon the 'thermally attenuated weak' FT and is bordered by a well expressed forebulge. (c) 2D W–E profile of the southern part of the SFB model. The wider foredeep is emplaced upon the 'strong' MT, and is bordered by a barely expressed forebulge. (d) 2D S–N profile of the SFB model. The two northern and southern parts of the basin are individualized with a limit near the MT/FT boundary.

part of the foreland is set upon 'strong' lithospheres (MT and YT) in front of the smallest and recessed parts of the GA (Fig. 13a, c). The foredeep in this part of the model is larger, with $\lambda \approx 320$ km, and its profile (*YY'* in Fig. 13c) also exhibits a weaker topography than in the northern part. We also notice the presence of a barely expressed forebulge in this area (Fig. 13a, c).

The dichotomy between the northern and southern parts is especially obvious on a S–N transect (*ZZ'* in Fig. 13d). A shallow southern sub-basin with a gentle northwards dip ($<$ *c.* 250 m deep) is identified, as well as a northern deeper basin with steep borders (*c.* 600 m deep). The limit between the northern and southern parts appears relatively close to the MT/FT boundary (Fig. 13d), suggesting a significant role for lithospheric boundaries in the differential flexuration of the SFB. This N–S differentiation is found not only in the foreland, but also within the allochthon itself as its simulated elevation is not continuous along its front (Fig. 13a). Two areas of important elevations ($>$1200 m) can be observed on both the northern and southern sides of the GA recess. This positive relief could have contributed as a significant source of terrigenous material, then being deposited in the proximal foreland.

5. Discussion

Our results highlight the spatial differences in subsidence within the SFB, especially between its northern and southern parts (Figs 8, 9). This differential subsidence is underlined by variations in the sedimentary record (Figs 4, 5). In addition, a highland was probably present in the central SFB and could physically have partly separated these two parts of the basin.

5.a. Evidence for a foreland basin

The convex 'lozenge shape' (*sensu* Miall, 2010) of the isopach map (Fig. 8) and the westwards-thickening pattern of the sedimentary record are in agreement with the common asymmetric geometry of foreland basins (Fig. 8; DeCelles & Giles, 1996; Miall, 2010). Additionally, the observed high-rate subsidence values (*c.* 100–500 m Ma^{-1}) agree with foreland basin dynamics, even if these values are greater in magnitude than values generally given in the literature for similar contexts (e.g. Xie & Heller, 2009). This difference in magnitude is interpreted by considering that estimations from backstripping analyses are generally proposed for continuous sedimentary series spanning several millions years, if not several tenth of millions years (e.g. Xie & Heller, 2009). Over such long time intervals, the subsidence rate values are less accurate. The high resolution of the timeframe used for the SFB mirrors short-acting structural events in the basin. Similar 'higher than average' values for subsidence rates have been calculated by Chevalier *et al.* (2003) and Lachkar *et al.* (2009) using high-resolution biostratigraphic time-calibrations, and also by Roddaz *et al.* (2010) with similar magnitude for the Miocene Amazonian Foreland Basin (*c.* 200–700 m Ma^{-1}; Roddaz *et al.* 2010). Moreover, values observed in the SFB (0.05–0.65 mm a^{-1}) are consistent with yearly deposition rates indicated by Allen & Allen (2005) for foreland basins (0.2–0.5 mm a^{-1}). Finally, the convex-up shape of the tectonic subsidence curves (Fig. 9f) is diagnostic of foreland basins and corresponds to the progressive flexural response of the lithosphere to the topographic load and/or sedimentary infill of the basin overtime (Angevine, Heller & Paola, 1990; Allen & Allen, 2005; Xie & Heller, 2009).

In the SFB, the topographic load is exerted by the GA. This allochthon has been emplaced on the North American continental margin, as evidenced by the geochemical signature of the Koipato Formation volcanics (Early Triassic) originating from the partial melting of a Palaeoproterozoic continental crust (likely the Mojave Terrane; Vetz, 2011).

The observed spatial heterogeneity of the sedimentary thickness in the SFB (Figs 4, 8) and the much higher tectonic subsidence rate detected in the northern part of the basin (*c.* 500 m Ma^{-1} v. *c.* 100 m Ma^{-1} in the southern part; Fig. 9f) are striking and raise the question of the controlling factor(s) responsible for this phenomenon, especially for such a short interval (*c.* 1.3 Ma).

5.b. Potential underlying mechanisms for observed variations in flexural subsidence

Spatial variations in subsidence within the SFB may result from different mechanisms that are inherent to the flexural nature of the foreland basin: (1) the sedimentary overload provoked by the continuous filling of the basin over time; (2) the spatial heterogeneity of the GA (topography and shape of the load); and/or (3) the differential flexural response of the lithosphere to this topographic load and linked to the rheology of the basement.

Considering point (1) above, in some cases the distributed vertical load exerted by the sedimentary filling of the basin might affect and amplify the flexuration in foreland basins over time (Shanmugam & Walker, 1980; Beaumont, 1981; Cardozo & Jordan, 2001; Allen & Allen, 2005). As this load depends mainly on the sedimentary fluxes and density of the filling, a denser deposited material leads to a more important flexuration of the lithosphere, as modelled by Angevine, Heller & Paola (1990) and Fosdick, Graham & Hilley (2014). The southern part of the SFB, characterized by low subsidence rates, exhibits coarse clastic sedimentation in the Moenkopi Group with the presence of conglomerates and sandstones (Figs 3a, 4, 5b, c, e, 12; e.g. Gabrielse, Snyder & Stewart, 1983; Olivier *et al.* 2016) of density 2.5–2.8 kg cm^{-3} (Manger, 1963; McCulloh, 1967; Sclater & Christie, 1980; Tenzer *et al.* 2011). The top of the Moenkopi Group consists of thick microbial limestone beds (Figs 3a, 4, 5e; e.g. Olivier *et al.* 2014, 2016; Vennin *et al.* 2015). These limestones bear a density of *c.* 2.6–2.8 kg cm^{-3} (Manger, 1963; McCulloh, 1967; Sclater & Christie, 1980; Tenzer *et al.* 2011). In contrast, the northern part which is characterized by high subsidence rates, is dominated by marine siltstones of the Dinwoody and Woodside Formation (Figs 3a, 4, 5g; e.g. Kummel, 1954, 1957). The density of this type of sediment is of 2.3–2.7 kg cm^{-3} (Manger, 1963; Sclater & Christie, 1980; Tenzer *et al.* 2011). Based on these data, the sedimentary filling should have had a higher impact on the flexuration in the southern part of the basin. However, we show that the most important subsidence during the PTU-Smithian interval took place in the northern part of the SFB (Figs 8, 9). Moreover, the difference between tectonic and total subsidence mainly consist of the local isostasy and compaction of the sediments (Allen & Allen, 2005). With the tectonic subsidence being the most important component of the total subsidence in the SFB (Fig. 9a), this argues for a weak potential role of the sedimentary load. The sedimentary overload therefore cannot be a major controlling factor explaining the differential flexuration observed within the basin.

Regarding points (2) and (3) above, while it is possible to discuss the role of the sedimentary overload using only field-based data, interpretations of the allochthon heterogeneity and the basement rheological behaviour require an additional model approach. We combine these in the following discussion. To that purpose, we used three different scenarios (Fig. 14) with the same initial setup (Section 4.d; Table 2) except for the x and y dimensions of the model that are set to 2000 km in the x direction and 1000 km in the y direction to avoid border effects.

The first scenario tests the impact of a rheologically heterogeneous basement loaded by a homogeneous allochthon (Fig. 14a). The rigidity of the terrane controls its capacity to flexure. The shape of ensuing flexural foreland basins and the distribution of their sedimentary records are therefore a direct consequence of the rheological behaviour of the basement (Angevine, Heller & Paola, 1990; Watts, 1992; Cardozo & Jordan, 2001; Allen & Allen, 2005; Leever *et al.* 2006; Fosdick, Graham & Hilley, 2014). Upon the high-rigidity part of the basement (T_{e1}), a wide foreland

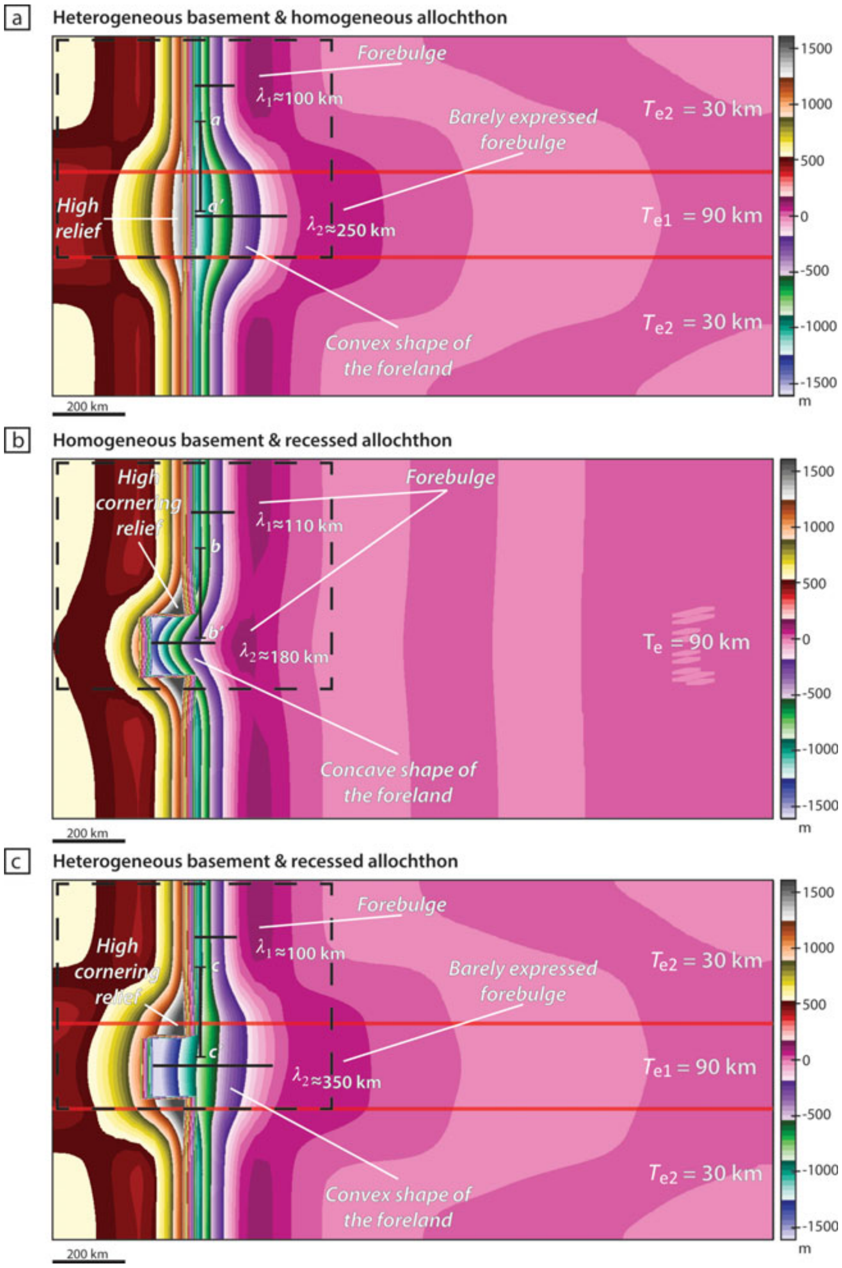

Figure 14. (Colour online) Numerical models showing the effects of the heterogeneities of the basement and of the topographic load over the formation of a foreland basin. Dashed lines represent an area analogue to the SFB configuration. (a) Scenario using a heterogeneous basement with contrasted elastic thicknesses ($T_{e1} = 3 \times T_{e2}$) and a homogeneous allochthon. A large convex foreland is formed upon the most rigid lithosphere. (b) Scenario using a heterogenous allochthon with a *c.* 100 km wide recess (lateral ramp) and a homogeneous fixed T_e lithosphere. A slightly wider concave foreland is formed within the recessed area and a cornering relief appears on both sides of the recessed area in the allochthon. (c) Scenario showing the combined effect of a heterogeneous basement with contrasted elastic thicknesses ($T_{e1} = 3 \times T_{e2}$) and a heterogeneous allochthon with a *c.* 100 km wide recess (lateral ramp). A much wider convex foreland is formed within the recessed area upon the rigid lithosphere, and a cornering relief on both sides of the recess in the allochthon is also visible.

($\lambda_2 \approx 250$ km) develops with a well-expressed convex shape in map view and a barely expressed forebulge. Upon the low-rigidity parts of the basement (T_{e2}), a narrower foreland ($\lambda_1 \approx 100$ km) is structured with a more pronounced forebulge. This is in agreement with the SFB observations. However, a N–S transect (*aa'*, Fig. 14a) shows that the wider area of the foreland basin is deeper than observed in the field and that only one high-relief area is individualized within the central part of the allochthon. Even if the rigidity does play a role in the development of the flexural foreland basin, as commonly assumed in the literature (Angevine, Heller & Paola, 1990; DeCelles & Giles, 1996; Cardozo & Jordan, 2001; Allen & Allen, 2005; Leever *et al.* 2006; Miall, 2010; Fosdick, Graham & Hilley, 2014), our results indicate that a rheological difference is not enough to control the variations in SFB.

The second scenario uses a heterogeneous topographic load exerted by the allochthon upon a homogeneous 'strong' lithosphere ($T_e = 90$ km; Fig. 14b).

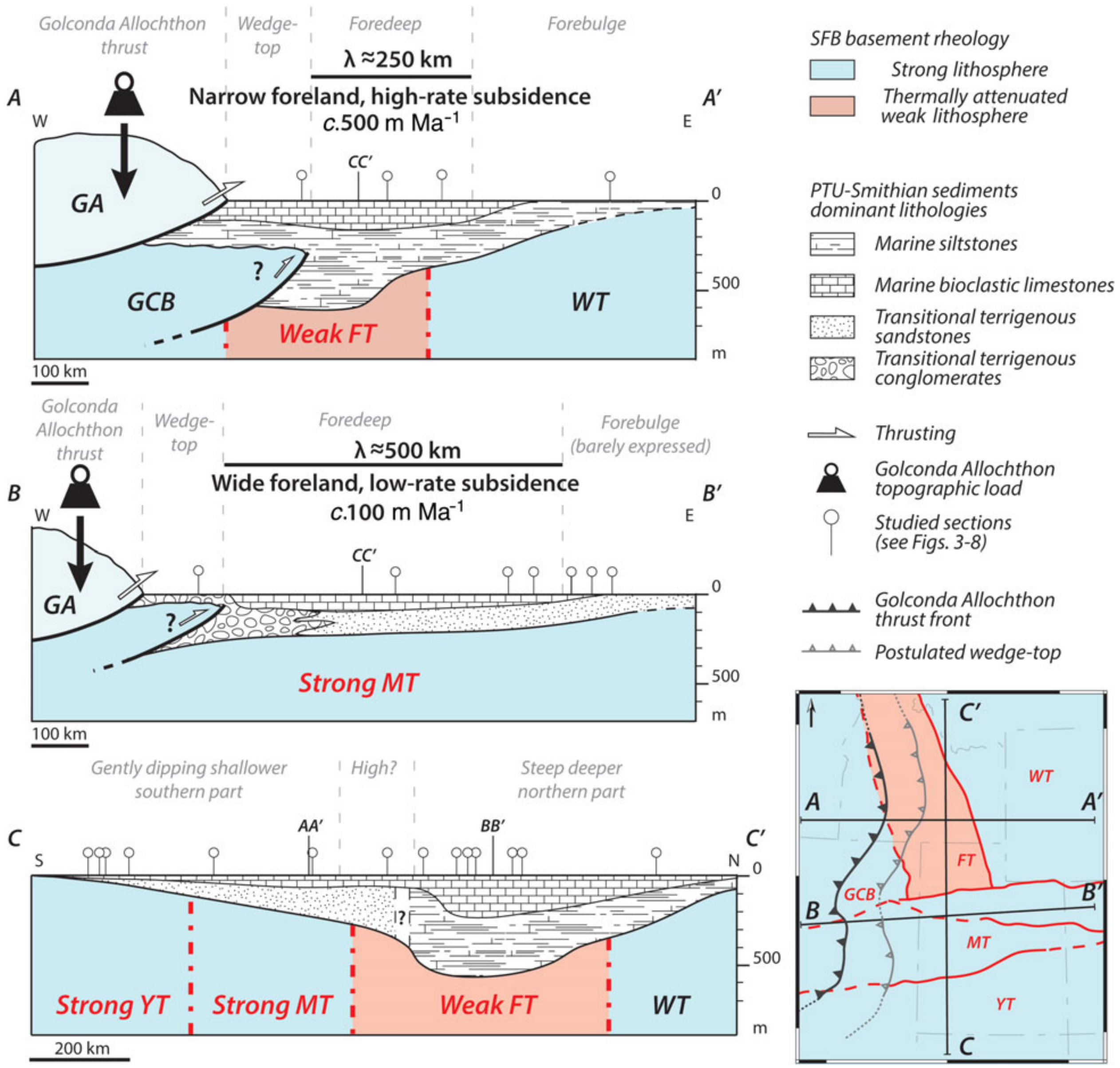

Figure 15. (Colour online) Cross-sections of the Sonoma Foreland Basin (SFB) illustrating variations in the subsidence and sedimentary accumulation pattern during the PTU-Smithian interval. The Golconda Allochthon (GA) is the main topographic load on the lithosphere (Dickinson, 2006, 2013; Marzolf, 1993); the postulated wedge-top is also represented. (*AA'*) W–E cross-section in the northern part of the basin exhibiting a narrow foreland with a high-rate tectonic subsidence with a developed silty and limestone sedimentation over the Mesoproterozoic 'thermally attenuated weak' Farmington Terrane (FT). (*BB'*) W–E cross-section in the southern part of the Sonoma Foreland Basin showing a wide foreland with a low-rate tectonic subsidence, forming a reduced deposition of mainly terrigenous clastic series upon the Palaeoproterozoic 'strong' Mojave Terrane (MT). A barely expressed forebulge borders this part of the SFB. (*CC'*). S–N cross-section of the basin, highlighting the differences between southern and northern parts of the SFB in terms of subsidence, sedimentation and geometry of the basin. The transition between these two parts is situated close to the terranes boundary between MT and FT. This area is postulated to be a basement topographic highland, as supported by the transition between southern terrigenous clastic series and northern silty sedimentation.

The heterogeneity in the allochthon is introduced in the form of a *c.* 100 km wide recess (i.e. a lateral ramp) along its front. The foreland basin shows a larger area ($\lambda_2 \approx 180$ km) in front of the lateral ramp compared to the northern and southern parts ($\lambda_1 \approx 110$ km). Moreover, a N–S transect (*bb'* in Fig. 14b) shows that the narrow northern part of the basin is deeper than in front of the recess. An important relief is also formed in the corners of the allochthon on both lateral borders of the recess. This is in agreement with SFB observations. However, the overall shape of the foreland basin is rather concave and penetrates significantly into the recessed area. Even if the morphology of the allochthon plays a role in the development of the foreland basin, this numerical scenario shows marked differences with the SFB.

The third scenario combines both previously tested heterogeneities (Fig. 14c). The graphic output exhibits a wider foreland ($\lambda_2 \approx 350$ km) emplaced above the 'strong' lithosphere in front of the recess, and a narrow foreland ($\lambda_1 \approx 100$ km) above 'weak' lithospheres. This model reproduces well the convex shape of the foreland basin with a marked forebulge development upon 'weak' lithospheres, whereas it is less pronounced upon the strong lithosphere. Moreover, a N–S transect (*cc'* in Fig. 14c) highlights a deeper area upon the 'weak' lithosphere. Finally, a prominent relief of the allochthon is observed on both corners bordering the recess.

To summarize, from the three possible mechanisms proposed to explain the origin of the differential flexural subsidence in the SFB, only the combined effect of the heterogeneous rheology of the basement and the spatial heterogeneity of the GA can be considered as the major controlling factors.

5.c. Combined outcomes of heterogeneities over differential subsidence

Our field data highlight the contrasted subsidence between the northern and southern parts of the SFB. The numerical model provides a complement to discuss the potential combined outcomes of rheology and allochthon heterogeneities. Congruent features between the numerical model of the SFB (Fig. 13), the tested scenarios (Fig. 14) and field data (Fig. 15) indeed argue for a major controlling role of the allochthon spatial heterogeneities and of the basement rheological behaviour on the formation and development of the SFB during Early Triassic time. As these two parameters are directly linked to the age, nature and pattern of the basement terranes, the lithosphere heritage likely controls the flexuration and therefore the subsidence variations documented for the Early Triassic SFB.

Combining all field data and numerical simulations, a model of the SFB is proposed in Figure 15. The northern part of the basin (section *AA'*) is characterized by a narrow foredeep ($\lambda \approx 250$ km) with a high-rate tectonic subsidence (*c.* 500 m Ma^{-1}) and high sedimentary thickness (up to *c.* 550 m of mostly fine siltstones deposits), which is located upon the 'weak/attenuated' Farmington Terrane and in front of the largest reconstructed part of the GA. The postulated wedge-top and forebulge are located above the 'strong' Archean lithospheres, that is, the GCB and WT, respectively. The southern part of the SFB exhibits a large foredeep ($\lambda \approx 500$ km, section *BB'*) with a relatively low-rate tectonic subsidence (*c.* 100 m Ma^{-1}) and a reduced sedimentary thickness (up to *c.* 250 m of mixed limestones and coarse clastic deposits). This part of the SFB is emplaced upon the 'strong' lithospheres of the Palaeoproterozoic MT and YT, in front of the thinnest reconstructed part of the GA. The southern SFB also shows a reduced postulated wedge-top to the west and a barely expressed forebulge to the east. These spatial variations in flexural subsidence and their good agreement with limits of the terranes composing the SFB basement are also evident along a S–N transect (section *CC'*). The spatial separation between the shallow and gently dipping southern part of the SFB and the deep and steep northern part is obvious. This separation is located close to the boundary between MT and FT.

6. Conclusion

In this study, we used an integrated approach to decipher the major role of the lithospheric heritage over the differential sedimentary deposition in the Sonoma Foreland Basin during Early Triassic time. Our approach used both field-based sedimentary data, calibrated within a highly resolved biostratigraphic framework, and numerical model to test the influence of several potential controlling factors. Palinspastic reconstructions were also performed to obtain an accurate palaeogeographic context.

Using high-resolution temporal data, the subsidence analyses help to identify the main controlling factors at the origin of the spatial variations of the Early Triassic sedimentary record in the SFB. The sedimentary overload cannot satisfactorily explain the observed variations in thickness of the sedimentary record throughout the basin. The combined effects of the contrasted lithospheric strength of the terranes ('weak' v. 'strong' lithospheres) composing the basement of the basin, and the spatial heterogeneity of the Golconda Allochthon (with the presence of a lateral ramp within the belt), best explain a differential flexural response of the SFB basement to the emplacement of the allochthon. Such a differential flexural response ultimately controls the overall geometry of the basin through spatially heterogeneous tectonic subsidence rates: *c.* 100 m Ma^{-1} in a wide southern part upon a 'strong' lithosphere loaded by a recessed and thin (in map-view) front belt, v. *c.* 500 m Ma^{-1} in a narrower northern part upon a 'weak/attenuated' lithosphere loaded by a larger front belt. Although field data highlight the potential role of the rheological behaviour of the basement based on observed differential subsidence rates, the numerical model approach suggests a combined effect of the latter and of the spatial heterogeneity of the allochthon.

As heterogeneities of the basement and in the morphology of the allochthon result from the nature and history of the different lithospheric terranes that compose the basement, the lithosphere heritage likely played a prime role in controlling the development of the Sonoma Foreland Basin during Early Triassic time, and consequently generated the observed variations of the sedimentary record through differential subsidence.

Acknowledgements. We particularly thank the late Professor W.R. Dickinson for constructive discussions. We also thank Hugo Bucher and Romain Jattiot (Zürich) for discussion on Nevada outcrops. This work is a contribution to the ANR project AFTER (ANR-13-JS06-0001-01). The study was also supported by ENGIE.

Supplementary material

To view supplementary material for this article, please visit https://doi.org/10.1017/S0016756817000164.

References

Allen, P. A. & Allen, J. R. 2005. *Basin Analysis: Principles and Applications*. Oxford: Blackwell Science Publishing.

Angevine, C. L., Heller, P. L. & Paola, C. 1990. *Quantitative Sedimentary Basin Modeling*. American Association of Petroleum Geologists.

Artemieva, I. M. & Mooney, W. D. 2002. On the relations between cratonic lithosphere thickness, plate motions, and basal drag. *Tectonophysics* **358**(1–4), 211–31.

Bankey, V. A., Cuevas, D., Daniels, A. A., Finn, C. A., Hernandez, I., Hill, P., Kucks, R., Miles, W., Pilkington, M., Roberts, C., Roest, W., Rystrom, V., Shearer, S., Snyder, S., Sweeney, R., Velez, J., Phillips, J. D. & Ravat, D. 2002. Digital data grids for the magnetic anomaly map of North America. Open-File Report 02-414: USGS.

Beaumont, C. 1981. Foreland basins. *Geophysical Journal International* **65**(2), 291–329.

Blakey, R. C. 2008. Pennsylvanian-Jurassic sedimentary basins of the Colorado Plateau and Southern Rocky Mountains. *Sedimentary Basins of the World*, pp. 245–96. Netherlands: Elsevier.

Bond, G. C., Christie-Blick, N., Kominz, M. A. & Devlin, W. J. 1985. An early Cambrian rift to post-rift transition in the Cordillera of western North America. *Nature* **315**, 742–46.

Brayard, A., Bylund, K. G., Jenks, J. F., Stephen, D. A., Olivier, N., Escarguel, G., Fara, E. & Vennin, E. 2013. Smithian ammonoid faunas from Utah: implications for Early Triassic biostratigraphy, correlation and basinal paleogeography. *Swiss Journal of Palaeontology* **132**(2), 141–219.

Brayard, A., Meier, M., Escarguel, G., Fara, E., Nuetzel, A., Olivier, N., Bylund, K. G., Jenks, J. F., Stephen, D. A., Hautmann, M., Vennin, E. & Bucher, H. 2015. Early Triassic 'Gulliver' gastropods; spatio-temporal distribution and significance for biotic recovery after the end-Permian mass extinction. *Earth-Science Reviews* **146**, 31–64.

Brühwiler, T., Bucher, H., Brayard, A. & Goudemand, N. 2010. High-resolution biochronology and diversity dynamics of the Early Triassic ammonoid recovery; the Smithian faunas of the northern Indian margin. *Palaeogeography, Palaeoclimatology, Palaeoecology* **297**(2), 491–501.

Bryant, B. & Nichols, D. 1988. Late Mesozoic and early Tertiary reactivation of an ancient crustal boundary along the Uinta trend and its interaction with the Sevier orogenic belt. *Geological Society of America Memoirs* **171**, 411–30.

Bucher, H. 1988. A new Middle Anisian (Middle Triassic) ammonoid zone from northwestern Nevada (USA). *Eclogae Geologicae Helvetiae* **81**(3), 723–62.

Burchfiel, B. & Davis, G. A. 1975. Nature and controls of Cordilleran orogenesis, western United States: Extensions of an earlier synthesis. *American Journal of Science* **275**, 363–96.

Burchfiel, B. & Royden, L. 1991. Antler orogeny: A Mediterranean-type orogeny. *Geology* **19**(1), 66–9.

Burgess, S. D., Bowring, S. & Shen, S.-Z. 2014. High-precision timeline for Earth's most severe extinction. *Proceedings of the National Academy of Sciences of the United States of America* **111**(9), 3316–21.

Burov, E. B. & Diament, M. 1995. The effective elastic thickness (T_e) of continental lithosphere: What does it really mean? *Journal of Geophysical Research: Solid Earth* **100**(B3), 3905–27.

Cagnard, F., Barbey, P. & Gapais, D. 2011. Transition between "Archaean-type" and "modern-type" tectonics: insights from the Finnish Lapland Granulite Belt. *Precambrian Research* **187**(1), 127–42.

Cardozo, N. & Jordan, T. 2001. Causes of spatially variable tectonic subsidence in the Miocene Bermejo Foreland Basin, Argentina. *Basin Research* **13**(3), 335–57.

Chardon, D., Gapais, D. & Cagnard, F. 2009. Flow of ultra-hot orogens: a view from the Precambrian, clues for the Phanerozoic. *Tectonophysics* **477**(3), 105–18.

Chevalier, F., Guiraud, M., Garcia, J. P., Dommergues, J. L., Quesne, D., Allemand, P. & Dumont, T. 2003. Calculating the long-term displacement rates of a normal fault from the high-resolution stratigraphic record (early Tethyan rifting, French Alps). *Terra Nova* **15**(6), 410–16.

Clark, D. L. 1957. Marine Triassic stratigraphy in eastern Great Basin. *AAPG Bulletin* **41**(10), 2192–222.

Coney, P. J. 1987. The regional tectonic setting and possible causes of Cenozoic extension in the North American Cordillera. *Geological Society Special Publications* **28**, 177–86.

DeCelles, P. G. & Coogan, J. C. 2006. Regional structure and kinematic history of the Sevier fold-and-thrust belt, central Utah. *Geological Society of America Bulletin* **118**(7–8), 841–64.

DeCelles, P. G. & Giles, K. A. 1996. Foreland basin systems. *Basin Research* **8**(2), 105–23.

Dickerson, P. W. 2003. Intraplate mountain building in response to continent-continent collision; the ancestral Rocky Mountains (North America) and inferences drawn from the Tien Shan (Central Asia). *Tectonophysics* **365**(1–4), 129–42.

Dickinson, W. R. 2002. The Basin and Range Province as a composite extensional domain. *International Geology Review* **44**(1), 1–38.

Dickinson, W. R. 2004. Evolution of the North American cordillera. *Annual Review of Earth and Planetary Sciences* **32**, 13–45.

Dickinson, W. R. 2006. Geotectonic evolution of the Great Basin. *Geosphere* **2**(7), 353–68.

Dickinson, W. R. 2013. Phanerozoic palinspastic reconstructions of Great Basin geotectonics (Nevada-Utah, USA). *Geosphere* **9**(5), 1384–96.

Eardley, A. J. 1939. Structure of the Wasatch-Great Basin region. *Geological Society of America Bulletin* **50**(8), 1277–310.

Embry, A. F. 1997. Global sequence boundaries of the Triassic and their identification in the Western Canada sedimentary basin. *Bulletin of Canadian Petroleum Geology* **45**(4), 415–33.

Fan, M., DeCelles, P. G., Gehrels, G. E., Dettman, D. L., Quade, J. & Peyton, S. L. 2011. Sedimentology, detrital zircon geochronology, and stable isotope geochemistry of the lower Eocene strata in the Wind River Basin, central Wyoming. *Geological Society of America Bulletin* **123**(5–6), 979–96.

Fletcher, R. C. & Hallet, B. 1983. Unstable extension of the lithosphere: A mechanical model for basin-and-range structure. *Journal of Geophysical Research: Solid Earth* **88**(B9), 7457–66.

Fosdick, J. C., Graham, S. A. & Hilley, G. E. 2014. Influence of attenuated lithosphere and sediment loading on flexure of the deep-water Magallanes retroarc foreland basin, Southern Andes. *Tectonics* **33**(12), 2505–25.

Foster, D. A., Mueller, P. A., Mogk, D. W., Wooden, J. L. & Vogl, J. J. 2006. Proterozoic evolution of the western margin of the Wyoming craton: implications for the tectonic and magmatic evolution of the northern Rocky Mountains. *Canadian Journal of Earth Sciences* **43**(10), 1601–19.

Gabrielse, H., Snyder, W. S. & Stewart, J. H. 1983. Sonoma orogeny and Permian to Triassic tectonism in western North America. *Geology* **11**(8), 484–86.

Galfetti, T., Bucher, H., Ovtcharova, M., Schaltegger, U., Brayard, A., Brühwiler, T., Goudemand, N., Weissert, H., Hochuli, P. A., Cordey, F. & Guodun, K. 2007. Timing of the Early Triassic carbon cycle perturbations inferred from new U-Pb ages and ammonoid biochronozones. *Earth and Planetary Science Letters* **258**(3–4), 593–604.

Gans, P. & Bohrson, W. 1998. Suppression of volcanism during rapid extension in the Basin and Range Province, United States. *Science* **279**(5347), 66–68.

Geslin, J. K. 1998. Distal ancestral Rocky Mountains tectonism: Evolution of the Pennsylvanian-Permian Oquirrh–Wood River basin, southern Idaho. *Geological Society of America Bulletin* **110**(5), 644–63.

Gilbert, H., Velasco, A. A. & Zandt, G. 2007. Preservation of Proterozoic terrane boundaries within the Colorado Plateau and implications for its tectonic evolution. *Earth and Planetary Science Letters* **258**(1–2), 237–48.

Goodspeed, T. H. & Lucas, S. G. 2007. Stratigraphy, sedimentology, and sequence stratigraphy of the Lower Triassic Sinbad Formation, San Rafael Swell, Utah. *Bulletin - New Mexico Museum of Natural History and Science* **40**, 91–101.

Groshong Jr, R. H. 2006. *3-D Structural Geology*. Berlin, Heidelberg: Springer.

Haq, B. U., Hardenbol, J. & Vail, P. R. 1988. Mesozoic and Cenozoic chronostratigraphy and cycles of sea-level change. In: *Sea-Level Changes: An Integrated Approach* (eds C. K. Wilgus, B. S. Hastings, H. Posamentier, J. Van Wagoner, C. A. Ross & C. G. St. C. Kendall), pp. 72–108. Society of Economic Paleontologists and Mineralogists, Special Publication no. 42.

Heckert, A. B., Chure, D. J., Voris, J. T., Harrison, A. A. & Thomson, T. J. 2015. Stratigraphy, correlation and age of the Moenkopi Formation in the vicinity of Dinosaur National Monument, Eastern Uinta Basin, Utah and Colorado, USA. In *Geology of Utah's Uinta Basin and Uinta Mountains* (eds M. D. Vanden Berg, R. Ressetar and L. P. Birgenheier), pp. 1–12. Utah Geological Association Publication.

Hofmann, R., Hautmann, M., Brayard, A., Nuetzel, A., Bylund, K. G., Jenks, J. F., Vennin, E., Olivier, N. & Bucher, H. 2014. Recovery of benthic marine communities from the end-Permian mass extinction at the low latitudes of eastern Panthalassa. *Palaeontology* **57**(3), 547–89.

Ingersoll, R. V. 2008. Subduction-related sedimentary basins of the USA Cordillera. In: *Sedimentary Basins of the World*, pp. 395–428. Amsterdam, Netherlands: Elsevier.

Jattiot, R., Bucher, H., Brayard, A., Brosse, M., Jenks, J. & Bylund, K. G. In press. Smithian ammonoid faunas from northeastern Nevada: implications for Early Triassic biostratigraphy and correlation within the western USA basin. *Palaeontographica Abteilung A*.

Jattiot, R., Bucher, H., Brayard, A., Monnet, C., Jenks, J. F. & Hautmann, M. 2015. Revision of the genus *Anasibirites* Mojsisovics (Ammonoidea): an iconic and cosmopolitan taxon of the late Smithian (Early Triassic) extinction. *Papers in Palaeontology* **2**(1), 155–188.

Kluth, C. F. & Coney, P. J. 1981. Plate tectonics of the ancestral Rocky Mountains. *Geology* **9**(1), 10–15.

Kreemer, C. & Hammond, W. C. 2007. Geodetic constraints on areal changes in the Pacific–North America plate boundary zone: What controls Basin and Range extension? *Geology* **35**(10), 943–46.

Kucks, R. P. 1999. Bouguer gravity anomaly data grid for the conterminous US. US Geological Survey Digital Data Series DDS-9: USGS.

Kummel, B. 1954. *Triassic Stratigraphy of Southeastern Idaho and Adjacent Areas*. Washington: US Government Printing Office.

Kummel, B. 1957. Paleoecology of Lower Triassic formations of southeastern Idaho and adjacent areas. In: *Treatise on Marine Ecology and Paleocology* (ed. H. S. Ladd), pp. 437–68. Geological Society of America, Memoir no. 67.

Lachenbruch, A. H. & Morgan, P. 1990. Continental extension, magmatism and elevation; formal relations and rules of thumb. *Tectonophysics* **174**(1), 39–62.

Lachkar, N., Guiraud, M., El Harfi, A., Dommergues, J.-L., Dera, G. & Durlet, C. 2009. Early Jurassic normal faulting in a carbonate extensional basin; characterization of tectonically driven platform drowning (High Atlas rift, Morocco). *Journal of the Geological Society of London* **166**(3), 413–30.

Lawton, T. F., Boyer, S. E. & Schmitt, J. G. 1994. Influence of inherited taper on structural variability and conglomerate distribution, Cordilleran fold and thrust belt, western United States. *Geology* **22**(4), 339–42.

Le Pourhiet, L. & Saleeby, J. 2013. Lithospheric convective instability could induce creep along part of the San Andreas fault. *Geology* **41**(9), 999–1002.

Leever, K., Matenco, L., Bertotti, G., Cloetingh, S. & Drijkoningen, G. 2006. Late orogenic vertical movements in the Carpathian Bend Zone–seismic constraints on the transition zone from orogen to foredeep. *Basin Research* **18**(4), 521–45.

Lowrie, W. 2007. *Fundamentals of Geophysics*. Cambridge: Cambridge University Press.

Lucas, S. G., Krainer, K. & Milner, A. R. 2007. The type section and age of the Timpoweap Member and stratigraphic nomenclature of the Triassic Moenkopi Group in Southwestern Utah. Triassic of the American West. *New Mexico Museum of Natural History and Science Bulletin* **40**, 109–18.

Lucas, S. G. & Orchard, M. J. 2007. Triassic lithostratigraphy and biostratigraphy north of Currie, Elko County, Nevada. *Bulletin - New Mexico Museum of Natural History and Science* **40**, 119–26.

Lund, K., Box, S. E., Holm-Denoma, C. S., San Juan, C. A., Blakely, R. J., Saltus, R. W., Anderson, E. D. & Dewitt, E. H. 2015. Basement domain map of the conterminous United States and Alaska. Reston, VA, United States: US Geological Survey.

Malavieille, J. 1993. Late orogenic extension in mountain belts: insights from the Basin and Range and the late Paleozoic Variscan belt. *Tectonics* **12**(5), 1115–30.

Manger, G. E. 1963. Porosity and bulk density of sedimentary rocks. Report published by US Government Printing Office, Washgington.

Marzolf, J. E. 1993. Palinspastic reconstruction of early Mesozoic sedimentary basins near the latitude of Las Vegas; implications for the early Mesozoic Cordilleran cratonal margin. In: *Mesozoic Paleogeography of the Western United States*, vol. II (eds G. C. Dunn & K. A. McDougall), pp. 433–62. Pacific Section, Society of Economic Paleontologists and Mineralogists, Field Trip Guidebook 71.

McCulloh, T. H. 1967. Mass properties of sedimentary rocks and gravimetric effects of petroleum and natural-gas reservoirs. Report published by US Government Printing Office, Washington.

Miall, A. 2010. *The Geology of Stratigraphic Sequences*. Berlin, Heidelberg: Springer Science & Business Media.

Moreau, J., Le Pourhiet, L., Huuse, M., Gibbard, P. L. & Grappe, B. 2015. The impact of the lithospheric flexure during the Elsterian glacial maximum on post-/proglacial systems in the southern North Sea area. In *Quaternary Research Association, Annual Discussion Meeting*, Edinburgh, 5–8 January 2015.

Mueller, P. A., Wooden, J. L., Mogk, D. W. & Foster, D. A. 2011. Paleoproterozoic evolution of the Farmington Zone; implications for terrane accretion in southwestern Laurentia. *Lithosphere* **3**(6), 401–08.

Mukul, M. & Mitra, G. 1998. Finite strain and strain variation analysis in the Sheeprock Thrust Sheet: an internal thrust sheet in the Provo salient of the Sevier Fold-and-Thrust belt, Central Utah. *Journal of Structural Geology* **20**(4), 385–405.

Nelson, S. T., Hart, G. L. & Frost, C. D. 2011. A reassessment of Mojavia and a new Cheyenne Belt alignment in the eastern Great Basin. *Geosphere* **7**(2), 513–27.

Nichols, K. M. & Silberling, N. J. 1977. *Stratigraphy and Depositional History of the Star Peak Group (Triassic), Northwestern Nevada*. Geological Society of America Special Paper no. 178, 74 pp.

Oldow, J. S., Bally, A. W., Avé Lallemant, H. & Leeman, W. P. 1989. Phanerozoic evolution of the North American Cordillera; United States and Canada. In: *The Geology of North America* (eds A. W. Bally & A. R. Palmer), 139–232. Boulder: Geological Society of America.

Olivier, N., Brayard, A., Fara, E., Bylund, K. G., Jenks, J. F., Vennin, E., Stephen, D. A. & Escarguel, G. 2014. Smithian shoreline migrations and depositional settings in Timpoweap Canyon (Early Triassic, Utah, USA). *Geological Magazine* **151**(5), 938–55.

Olivier, N., Brayard, A., Vennin, E., Escarguel, G., Fara, E., Bylund, K. G., Jenks, J. F., Caravaca, G. & Stephen, D. A. 2016. Evolution of depositional settings in the Torrey area during the Smithian (Early Triassic, Utah, USA) and their significance for the biotic recovery. *Geological Journal* **51**(4), 600–26.

Parsons, T., Thompson, G. A. & Sleep, N. H. 1994. Mantle plume influence on the Neogene uplift and extension of the US western Cordillera? *Geology* **22**(1), 83–6.

Paull, R. A. & Paull, R. K. 1991. Allochthonous rocks from the western part of the early Triassic miogeocline; Hawley Creek area, east-central Idaho. *Contributions to Geology* **28**(2), 145–54.

Paull, R. A. & Paull, R. K. 1993. Interpretation of Early Triassic nonmarine–marine relations, Utah, USA. *New Mexico Museum of Natural History and Science Bulletin* **3**, 403–09.

Paulsen, T. & Marshak, S. 1999. Origin of the Uinta recess, Sevier fold–thrust belt, Utah: influence of basin architecture on fold–thrust belt geometry. *Tectonophysics* **312**(2), 203–16.

Peterson, J. A. 1977. Paleozoic shelf-margins and marginal basins, western Rocky Mountains–Great Basin, United States. In: *Rocky Mountain Thrust Belt, Geology and Resources* (eds E. L. Helsey et al.), 135–53. Wyoming Geological Association, Casper, Guidebook 29.

Poudjom Djomani, Y. H., O'Reilly, S. Y., Griffin, W. L. & Morgan, P. 2001. The density structure of subcontinental lithosphere through time. *Earth and Planetary Science Letters* **184**(3–4), 605–21.

Purucker, M. & Whaler, K. 2007. Crustal magnetism. *Treatise on Geophysics* **5**, 195–237.

Roddaz, M., Hermoza, W., Mora, A., Baby, P., Parra, M., Christophoul, F., Brusset, S. & Espurt, N. 2010. Cenozoic sedimentary evolution of the Amazonian foreland basin system. In: *Amazonia, Landscape and Species Evolution: A Look into the Past* (eds C. Hoorn & F. P. Wesselingh), pp. 61–88. Hoboken: Blackwell-Wiley.

Rowley, P. D., Vice, G. S., Mcdonald, R. E., Anderson, J. J., Machette, M. N., Maxwell, D. J., Ekrem, E. B., Cunningham, C. G., Steven, T. A. & Wardlaw, B. R. 2005. Interim geologic map of the Beaver 30'x60' Quadrangle, Beaver, Piute, Iron, and Garfield Counties, Utah. Utah Geological Survey, Open-File Report 454, scale 1:100,000.

Sadler, R. K. 1981. Structure and stratigraphy of the Little Sheep Creek area, Beaverhead County, Montana. M.Sc. thesis, United States. Published thesis.

Schelling, D. D., Strickland, D. K., Johnson, K. R. & Vrona, J. P. 2007. Structural geology of the central Utah thrust belt. In: *Central Utah: Diverse Geology of a Dynamic Landscape* (eds G. C. Willis, M. D. Hylland, D. L. Clark & T. C. Chidsey), pp. 1–29. Salt Lake City, UT: Utah Geological Association, Publication 36.

Schweickert, R. A. & Lahren, M. M. 1987. Continuation of Antler and Sonoma orogenic belts to the eastern Sierra Nevada, California, and Late Triassic thrusting in a compressional arc. *Geology* **15**(3), 270–73.

Sclater, J. G. & Christie, P. A. F. 1980. Continental stretching: an explanation of the post-Mid-Cretaceous subsidence of the central North Sea basin. *Journal of Geophysical Research* **85**(B7), 3711–39.

Shanmugam, G. & Walker, K. R. 1980. Sedimentation, subsidence, and evolution of a foredeep basin in the Middle Ordovician, southern Appalachians. *American Journal of Science* **280**(6), 479–96.

Snyder, W. S. & Brueckner, H. K. 1983. Tectonic evolution of the Golconda allochthon, Nevada: problems and perspectives. In: *Pre-Jurassic Rocks in Western North American Suspect Terranes* (ed. C. H. Stevens), pp. 103–23. Pacific Section, SEPM, Upland, CA.

Speed, R. & Silberling, N. J. 1989. IGC Field Trip T122: Early Mesozoic tectonics of the Western Great Basin, Nevada. In *Early Mesozoic Tectonics of the Western Great Basin, Nevada: Battle Mountain to Yerington District*, Nevada, July 1–7, 1989, 1.

Speed, R. & Sleep, N. 1982. Antler orogeny and foreland basin: a model. *Geological Society of America Bulletin* **93**(9), 815–28.

Steckler, M. & Watts, A. 1978. Subsidence of the Atlantic-type continental margin off New York. *Earth and Planetary Science Letters* **41**(1), 1–13.

Strickland, A., Miller, E. L. & Wooden, J. L. 2011. The timing of Tertiary metamorphism and deformation in the Albion-Raft River-Grouse Creek metamorphic core complex, Utah and Idaho. *Journal of Geology* **119**(2), 185–206.

Tenzer, R., Sirguey, P., Rattenbury, M. & Nicolson, J. 2011. A digital rock density map of New Zealand. *Computers & Geosciences* **37**(8), 1181–91.

Thomazo, C., Vennin, E., Brayard, A., Bour, I., Mathieu, O., Elmeknassi, S., Olivier, N., Escarguel, G., Bylund, K. & Jenks, J. 2016. A diagenetic control on the Early Triassic Smithian–Spathian carbon isotopic excursions recorded in the marine settings of the Thaynes Group (Utah, USA). *Geobiology* **14**(3), 220–36.

Trexler, J. H. & Nitchman, S. P. 1990. Sequence stratigraphy and evolution of the Antler foreland basin, east-central Nevada. *Geology* **18**(5), 422–25.

Turner, G., Rasson, J. & Reeves, C. 2007. Observation and measurement techniques. *Treatise in Geophysics, Geomagnetism* **5**, 93–146.

Van Hinte, J. 1978. Geohistory analysis: application of micropaleontology in exploration geology. *AAPG Bulletin* **62**(2), 201–22.

Vennin, E., Olivier, N., Brayard, A., Bour, I., Thomazo, C., Escarguel, G., Fara, E., Bylund, K. G., Jenks, J. F., Stephen, D. A. & Hofmann, R. 2015. Microbial deposits in the aftermath of the end-Permian mass extinction; a diverging case from the Mineral Mountains (Utah, USA). *Sedimentology* **62**(3), 753–92.

Vetz, N. Q. 2011. Geochronologic and isotopic investigation of the Koipato Formation, northwestern Great Basin, Nevada: implications for Late Permian–Early Triassic tectonics along the Western US Cordillera. M.Sc. thesis. Boise State University. Published thesis.

Walker, J. D. 1985. Permo-Triassic paleogeography and tectonics of the Southwestern United States. Ph.D. thesis. Cambridge: Massachusetts Institute of Technology. Published thesis.

Ware, D., Bucher, H., Brayard, A., Schneebeli-Hermann, E. & Brühwiler, T. 2015. High-resolution biochronology and diversity dynamics of the Early Triassic ammonoid recovery: the Dienerian faunas of the Northern Indian Margin. *Palaeogeography, Palaeoclimatology, Palaeoecology* **440**, 363–73.

Watts, A. 1992. The effective elastic thickness of the lithosphere and the evolution of foreland basins. *Basin Research* **4**(3–4), 169–78.

Watts, A. B. 2001. *Isostasy and Flexure of the Lithosphere*. Cambridge: Cambridge University Press.

Whitmeyer, S. J. & Karlstrom, K. E. 2007. Tectonic model for the Proterozoic growth of North America. *Geosphere* **3**(4), 220–59.

Wilkerson, M. S., Apotria, T. & Farid, T. 2002. Interpreting the geologic map expression of contractional fault-related fold terminations: lateral/oblique ramps versus displacement gradients. *Journal of Structural Geology* **24**(4), 593–607.

Xie, X. & Heller, P. L. 2009. Plate tectonics and basin subsidence history. *Geological Society of America Bulletin* **121**(1–2), 55–64.

Ye, H., Royden, L., Burchfiel, C. & Schuepbach, M. 1996. Late Paleozoic deformation of interior North America: the greater Ancestral Rocky Mountains. *AAPG bulletin* **80**(9), 1397–432.

Yonkee, W. A., Dehler, C. D., Link, P. K., Balgord, E. A., Keeley, J. A., Hayes, D. S., Wells, M. L., Fanning, C. M. & Johnston, S. M. 2014. Tectono-stratigraphic framework of Neoproterozoic to Cambrian strata, west-central US: protracted rifting, glaciation, and evolution of the North American Cordilleran margin. *Earth-Science Reviews* **136**, 59–95.

Yonkee, W. A. & Weil, A. B. 2010. Reconstructing the kinematic evolution of curved mountain belts: Internal strain patterns in the Wyoming salient, Sevier thrust belt, USA. *Geological Society of America Bulletin* **122**(1–2), 24–49.

Yonkee, W. A. & Weil, A. B. 2015. Tectonic evolution of the Sevier and Laramide belts within the North American Cordillera orogenic system. *Earth-Science Reviews* **150**, 531–93.

Zandt, G., Myers, S. C. & Wallace, T. C. 1995. Crust and mantle structure across the Basin and Range-Colorado Plateau boundary at 37 N latitude and implications for Cenozoic extensional mechanism. *Journal of Geophysical Research: Solid Earth* **100**(B6), 10529–48.

Zienkiewicz, O. C. & Taylor, R. L. 2005. *The Finite Element Method for Solid and Structural Mechanics*. Oxford: Butterworth-Heinemann.

The integrated study of the SFB allowed to confirm the previously discussed foreland nature of this basin and its formation as a flexural response to the emplacement of the Golconda Allochthon during the Sonoma orogeny. However, this process could not account for the observed discrepancy between northern and southern parts of the basin. We notably show that the sedimentary overload is not responsible for the observed variation in subsidence within the basin, but that inherited rheological properties of the basement are the main controlling factors involved there. Indeed, the differential resistance of the terranes that compose the basement of the SFB is responsible for a differential resistance to the flexuration provoked by the allochthon, and therefore influences the tectonic subsidence rates. Moreover, inherited basement pattern is also responsible for spatial heterogeneity of the allochthon, leading to a differential topographic load exerted onto the flexure basement of the basin, also accounting for the differential subsidence observe in the SFB.

We therefore highlight a major role of the heritage over the subsidence and spatial distribution of the sedimentary thickness across the SFB.

V. SYNTHESIS/CONCLUSIONS

SFB OR SFBs?

The Early Triassic Sonoma Foreland Basin is a key area showing an excellent record of the biotic recovery after the Permian-Triassic mass extinction (e.g., Kummel, 1954, 1957; Blakey, 1974; Schubert & Bottjer, 1995; Paull & Paull, 1997; Pruss & Bottjer, 2004, 2005; Mata & Bottjer, 2011). Several recent works (e.g., Brayard *et al.*, 2017, Jattiot *et al.*, *in prep.*) especially well highlighted the exceptional diversity documented in the SFB compared to some other basins and its importance in reinterpreting the paradigms commonly assumed until now on the ET recovery (e.g., "disaster taxa", Schubert & Bottjer, 1992, 1995; He *et al.*, 2007; "anachronistic facies", Woods *et al.*, 1999; Pruss *et al.*, 2005; Woods, 2009; "Lilliput effect", Urbanek, 1993; Payne, 2005, Twitchett, 2007; Fraiser *et al;*, 2011; "global anoxia/euxinia", Isozaki, 1997; Meyer *et al.*, 2011; Grasby *et al.*, 2013; see section I.B.1).

However, the detailed paleoenvironmental and geodynamical framework and the 4D evolution of the SFB was poorly constrained up to now. This original integrated work brings new insights on the controlling physical and chemical mechanisms over the spatio-temporal variations of the geological record observed within the SFB.

A. Evidence for two sub-basins

- Paleontological record

The paleontological record within the SFB is heterogeneous in terms of diversity and preservation and show marked variations according to the studied interval (e.g., Lucas *et al.*, 2007; Romano *et al.*, 2012; Hofmann *et al.*, 2013; Jenks *et al.*, 2013; Zatoń, *et al.*, 2013). However, some highly diversified and complex assemblages (e.g., Brayard *et al.*, 2011), as well as the occurrence of unexpected organisms and ecosystems for the ET (e.g., Brayard *et al.*, 2010, 2015, 2017; Villier *et al.*, *in press*), represent convincing examples of advanced recovery steps rapidly after the PTB crisis. The SFB may therefore appear as an exception to the "delayed recovery" scenario commonly assumed (e.g., Fraiser & Bottjer, 2007; Meyer *et al.*, 2011; Song *et al.*, 2012; Pietsch *et al.*, 2014) although many ET paradigms were paradoxically seminally proposed from earlier observations in the SFB (e.g., Schubert & Bottjer, 1992; Fraiser & Bottjer, 2004; Pruss & Bottjer, 2004). Overall, several biological communities show the co-occurrence of abundant benthic (e.g., bivalves, gastropods, echinoderms, sponges; e.g., Brayard *et al.*, 2010, 2017; Hofmann *et al.*, 2013) and nekto-pelagic organisms (e.g., fishes, ammonoids; e.g., Romano *et al.*, 2012; Brayard *et al.*, 2013; Jattiot *et al.*, *in press, in prep.*). Numerous abundant and large-sized trace fossils at different places in the SFB also indicate important infaunal assemblages (e.g., Vennin *et al.*, 2015; Caravaca *et al.*, 2017, see section III.A). Different microbial communities were also present in the SFB, and are documented by massive microbial carbonate levels with different morphologies (Pruss & Bottjer, 2004; Marenco *et al.*, 2012; Woods, 2013; Vennin *et al.*, 2015; Olivier *et al.*, 2016, see appendix 1), and by microbially-induced sedimentary structures (MISS) at some places (Grosjean *et al.*, *in prep.*).

Nevertheless, these **assemblages are not spatio-temporally homogeneous within the basin**. If some organisms indeed show a wide distribution at the basin-scale (e.g., presence of siliceous sponges in both the southern and northern parts of the SFB, Brayard *et al.*, 2011, 2017), some others exhibit distribution patterns restricted to the northern or to the southern part of the SSB.

This is the case for massive microbial deposits that are observed in the southern part of the SFB (e.g., MV, see section III.C, and Torrey area, see appendix 1; Fig. V.A.1), but lack from the central Utah and northern part of the SFB. In the latter area, deposition of MISS and the absence of carbonated beds are observed at some places (see section III.B; Fig. V.A.1). A North/South opposition can also be observed for metazoan organisms. This is the case for ammonoids, which show spatially-restricted distribution of some genera into a specific part of the SFB (Fig. V.A.1; Jattiot *et al.*, *in prep.* and ongoing work).

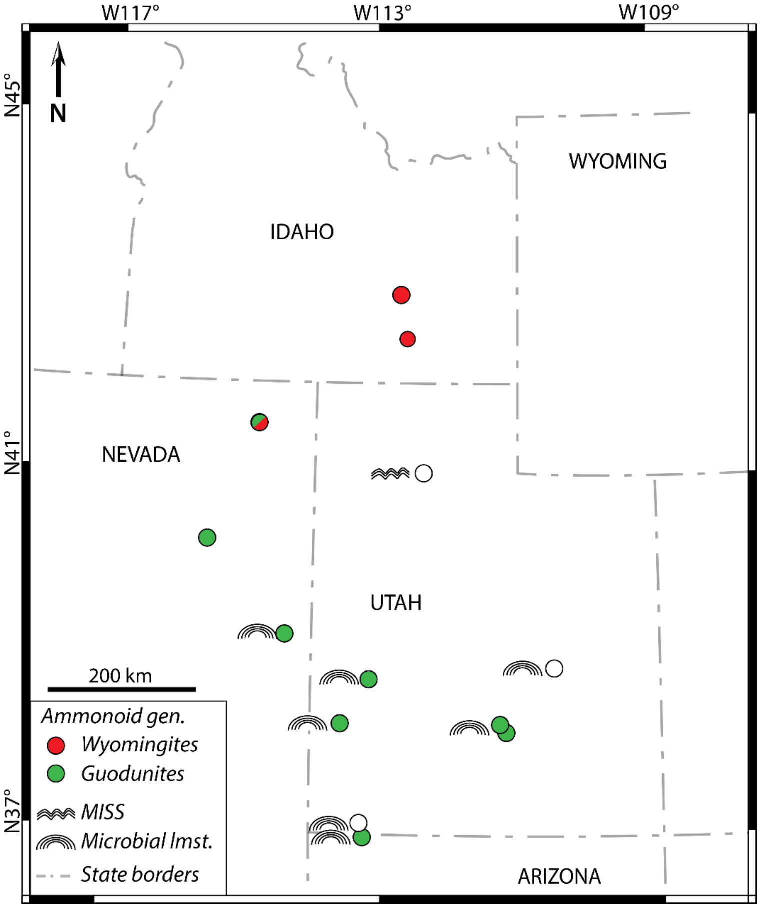

Figure V.A.1: Paleogeographic map illustrating the spatial distribution of some ammonoids genera and microbial deposits and displaying a segregation between the northern and southern parts of the basin (after Brayard *et al.*, 2013; Olivier *et al.,* 2014, 2016; Vennin *et al.,* 2015; Grosjean *et al., in prep*.; Jattiot *et al., in prep*.).

This distinction based on biotic data between different parts of the basin is striking and may be linked to local environmental conditions (e.g., depositional settings, nutrient and clastic influxes, etc.) allowing for instance the onset and proliferation of microbial communities and their preservation, or the flourishing of nekto-pelagic organisms.

Thus, **a N/S SFB partitioning is visible in the paleontological record**.

- Sedimentary record

In the SFB, the ET sedimentary record is represented by 3 main interfingering entities represented by the following simplified scheme:

- The Moenkopi Group (*sensu* Lucas *et al.*, 2007), characterized by transitional continental to marine (dolo-)siltstones and sandstones (locally conglomerates) that compose "red beds" (e.g., Blakey, 1974, Lucas *et al.,* 2007; Vennin *et al.*, 2015; Olivier *et al.*, 2016, see appendix 1). On top of these terrigenous sediments lies meter-thick beds of peritidal to intertidal microbial limestones with various internal structures according to the depositional setting (e.g., thrombolitic, stromatolitic; e.g., Vennin *et al.*, 2015).
- The Griesbachian to early/middle Smithian Dinwoody and Woodside formations, characterized by marine fine (dolo-)siltstones series of tidal flat settings, and locally carbonated shoal deposits (e.g., Kummel, 1954, 1957, Paull & Paull, 1983, 1993, 1994). The Dinwoody and Woodside formations are very close in lithology and often hard to distinguish. They are also described (particularly the Woodside) as being similar to the Moenkopi red beds without the typical red coloration (e.g., Kummel, 1957, Paull & Paull, 1993). However, these two formations bear an obvious marine affinity (e.g., Paull & Paull, 1994) rather than a transitional character like the Moenkopi's red beds.
- The Thaynes Group (*sensu* Lucas *et al.*, 2007), formed by metric to plurimetric beds of bioclastic limestones deposited under shoreface to upper offshore conditions. Locally, storm-induced and shoal deposits are recorded.

Until the middle-late Smithian, the SFB sedimentary record can be well divided between its southern and northern part: the Moenkopi Group red beds are characteristic of the southern transitional deposits, while the northern part of the basin is filled with Dinwoody and Woodside marine sediments (Fig. V.A.2a). From the middle-late Smithian, the Thaynes Group is emplaced in both the northern and southern parts of the basin, and represents the dominant sedimentary record of the entire SFB (Fig. V.A.2b). The Moenkopi Group is found in the most proximal localities (Fig. V.A.2b). The Thaynes marine bioclastic sedimentation is thought to be emplaced in relation to a regional third order transgression whose maximum flooding is reached just before the SSB (e.g., Embry, 1997; Brayard *et al.*, 2013; Vennin *et al.*, 2015; Olivier *et al.*, 2016, see appendix 1). A subsequent spatially-varying regression occurs between the northern and southern parts of the basin. In the south, rapidly retreating marine conditions allow deposition of a renewed unit of red beds during the early Spathian (e.g., Blakey, 1974; Lucas *et al.*, 2007; Olivier *et al.*, 2014), whereas marine conditions last longer in the northern part of the SFB (e.g., Kummel, 1957; Caravaca *et al.*, 2017, see section III.A).

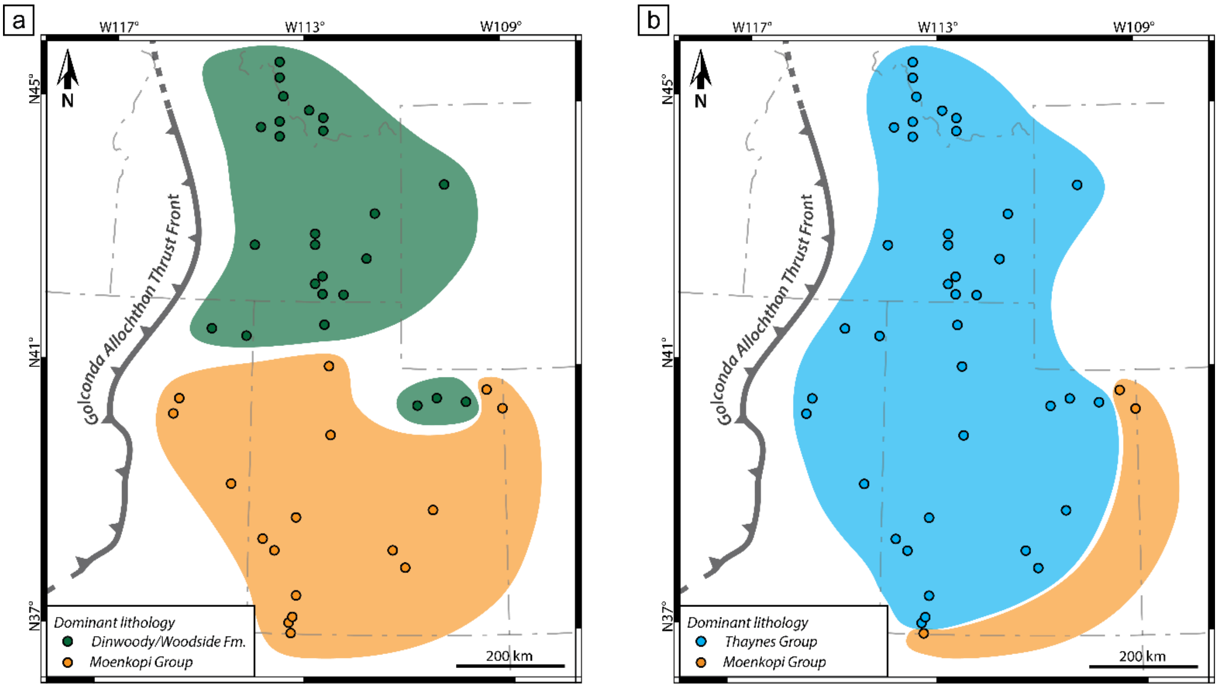

Figure V.A.2: Paleogeographic maps of the spatial distribution of the Early Triassic dominant lithological formations in the SFB. a) Spatial distribution of the Dinwoody and Woodside formations and of the Moenkopi Group until the middle-late Smithian. b) Spatial distribution of the remaining Moenkopi Group and of the Thaynes Group during late Smithian and early Spathian.

Sedimentary deposition in the SFB is therefore diachroneous, and argues for the importance of local controls on the depositional setting. The SFB was a very flat large wavelength basin, where small variation in accommodation have great and rapid consequences upon migration of facies belts, resulting in a patchy sedimentary record (e.g., the Torrey area evidencing a mosaic facies pattern; Olivier *et al.*, 2016, see appendix 1).

The sedimentary record, therefore, highlights **a North/South dichotomy in terms of sedimentary deposition within the SFB** (Fig. V.A.2).

- Geochemical record

Geochemical analyses at the basin-scale were lacking up to now, and only few studies were available (e.g., Marenco *et al.*, 2008, 2012; Thomazo *et al.*, 2016).

The study of the geochemical record of three distant sections, and more particularly of the T&M elements indicates that the **entire SFB has comparable water column chemistry and inputs** as suggested by detrital elementary ratios. T&M elements also show that while dysoxic conditions may have been present episodically, **no marked anoxia can be observed in the shallow deposits of the SFB**. Anoxia may therefore not drive the sedimentary record of the ET in the SFB basin which contrast from the common interpretation found in the literature based on other basins localities (e.g., South China, Sun *et al.*, 2012; Arctic Canada; Grasby *et al.*, 2013).

The **carbon isotope record exhibits marked differences among sections**. While a global, first order, influence of the exogenic carbon cycle is observed (couplet of negative and positive shifts before and across the SSB), it appears that the main controlling factors behind these variations within the basin are of local origin and linked to the depositional setting.

The southern and northern geochemical records could therefore be differentiated based on C isotope data (Fig. V.A.3). In the southern part, the MV section shows a marked influence of secondary diagenetic processes altering the original carbon isotope signal. Several and recurrent suboxic to anoxic conditions at the bottom-water/sediment interface are suggested by T&M elements concentrations. In the northern part of the basin, the record of the HS section appears more pristine. Only a few episodes of potential suboxic conditions at the bottom-water/sediment interface are documented. The LWC section has not yet been tested for alteration of the signal using T&M elements. However, based on the observed carbon isotope signal, secondary processes have most probably, at least partly, altered the original signal.

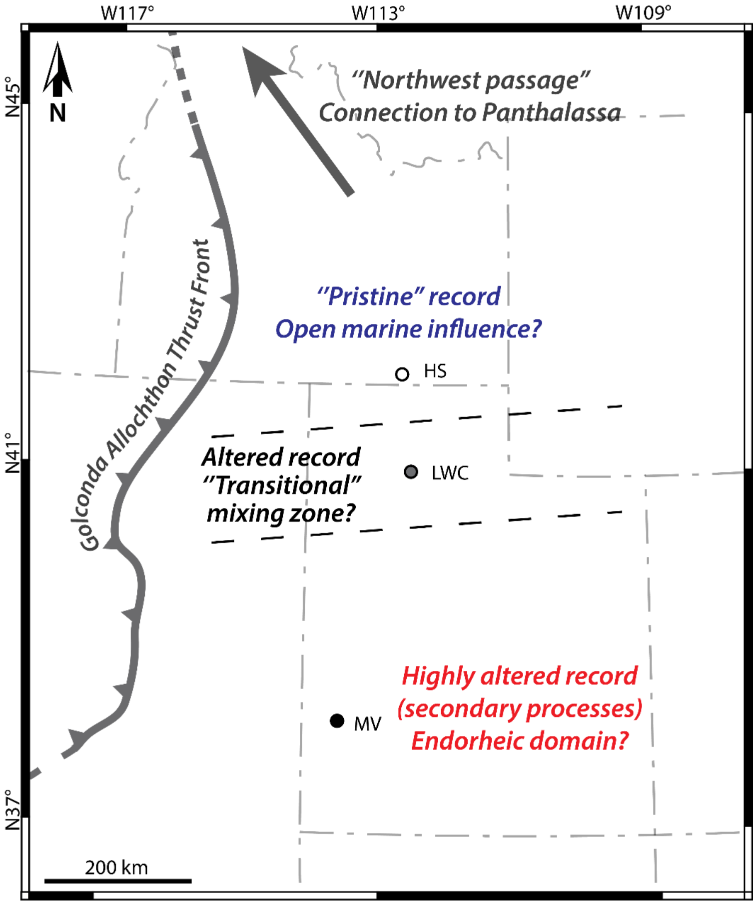

Figure V.A.3: Map of the studied area with location of the HS, LWC and MV section, representing northern, central "transitional" and southern parts of the SFB, respectively. SFB geochemical signals record differential preservation of the primary depositional signatures and imprint by local secondary processes.

To sum up, we suggest that **two sub-basins can be identified within the SFB based on the geochemical record.** Local controls are responsible for observed differences. However, mechanisms underlying this differentiation remain to investigate in further details: provenance analyses can help sorting out the precise nature and origin of the fluxes entering the SFB reservoirs. The northern part of the basin is thought to have been connected to the open Panthalassa Ocean via a northwestern passage (Fig. V.A.3, Colpron & Nelson, 2009). This communication with the open sea and its continuous marine influences upon the sedimentary deposition may have been a key factor explaining the presence of a more pristine signal in the northern sub-basin and providing a well-preserved paired carbon isotopic record. The southern sub-basin, as exemplified by the MV record, shows important alterations of the geochemical signal owe to remobilization and fluid circulation (e.g., generating Mn-bearing carbonates; Thomazo *et al.*, 2016). As this part of the SFB is more distant and disconnected from the open sea until the late Smithian maximum of transgression, endorheic conditions may have prevailed, leading to more accentuated diagenetic alterations and/or fluctuations of water column hydrochemistry such as the alkalinity, thus leading to local modifications of the water column geochemistry (e.g., El Tabakh & Schreiber, 1998). The “transitional” central part of the basin remains to be further study and could represent a “mixing” zone.

• Geodynamical framework of the SFB

The spatial distribution of the sedimentary thickness record was analyzed at the basin scale and showed marked differences between the southern and the northern parts. The southern part, mainly covering southern and central Utah, displays sedimentary deposits with a thickness from a few meters up to no more than 250 m in central Utah, with an average around a few to several tenths of meters (Fig. V.A.4). On the contrary, the northern part, centered in northern Utah and southern Idaho, shows sedimentary successions no less than 300 m-thick and up to ~600 m (Fig. V.A.4).

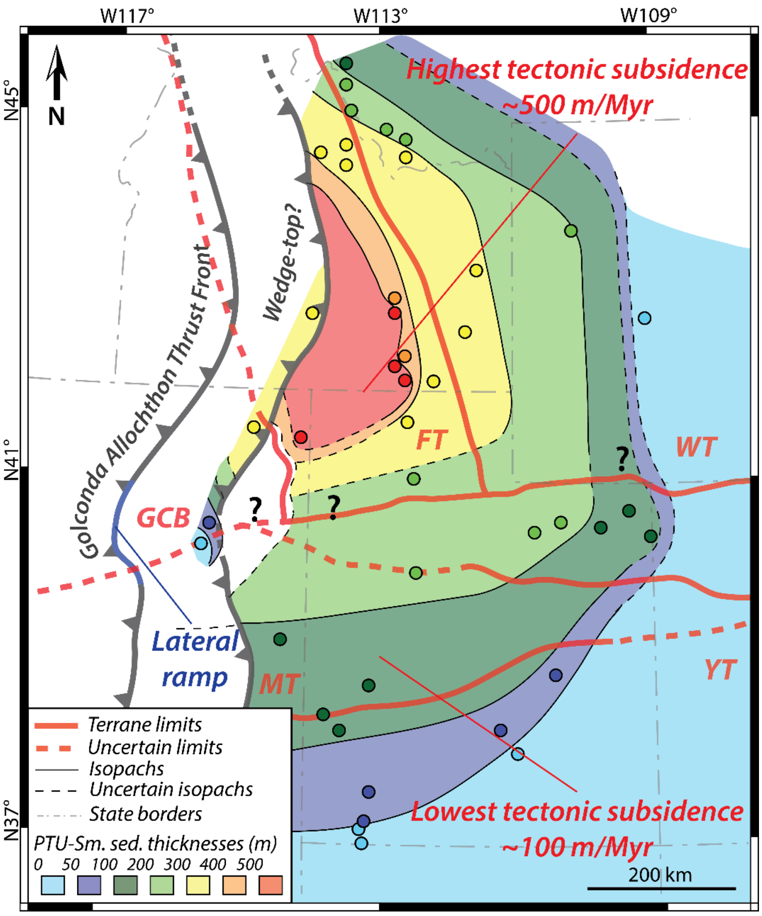

Figure V.A.4: Isopach map of the sedimentary thicknesses recorded for the PTU-Smithian interval, showing marked differences in sedimentary thicknesses between northern and southern parts of the SFB (after Caravaca *et al.*, *in press*, see section IV). Red lines indicate the limits of lithospheric terranes; GCB: Grouse Creek Block; FT: Farmington Terrane; WT: Wyoming Terrane; MT: Mojave Terrane; YT: Yavapai Terrane.

As these series were deposited under shallow shoreface to upper offshore environments in both parts of the SFB, it raises the question of the subsidence rates providing such different records of thickness. Sedimentary successions in both parts of the basin were backstripped and subsidence rates of ~100 m/Myr in the southern part, and ~500 m/Myr in the northern part, with a preponderant tectonic subsidence driver were deduced (Caravaca *et al.*, *in press*, see section IV). Such important rates and the typical convex-up shape of the backstripping curves (see Caravaca *et al.*, *in press,* see section IV) strongly suggest that **this basin was a foreland basin**.

The basement of the SFB is composed of 5 different lithospheric terranes of various ages: the Archean Wyoming Terrane and Grouse Creek Block, the Paleoproterozoic Mojave and Yavapai Terranes, and the Mesoproterozoic Farmington Terrane (Fig; V.A.4). Age differences among these terranes are responsible for differences in their rheological behavior. The Archean and Paleoproterozoic Terranes are old and thick lithospheric terranes with a limited elasticity and enhanced rigidity: those are identified as “strong” terranes. On the contrary, the Farmington Terrane is a “juvenile”, thin, mobile belt, and underwent high tectonic constrains and an intense thermal metamorphism: it is considered as a “weak” lithosphere.

The discrepancies between “strong” and “weak” lithospheres appeared to be a major controlling factor over the spatio-temporal evolution of the SFB for two main reasons:

- First, the Farmington “weak” lithosphere, given its reduced rigidity, likely accommodated more flexural deformation provoked by the westward emplacement of the Golconda Allochthon. It therefore allowed a mere five times more important tectonic subsidence than in the southern part of the basin, emplaced above “strong” lithospheres with higher rigidity.
- Second, as this lithospheric differentiation dates back to the Proterozoic, inherited features have played a preponderant role in the history of the basin before the onset of the Sonoma Orogeny and emplacement of the Golconda Allochthon. The E/W limit between the southern Mojave Terrane and the northern Grouse Creek Block, Farmington and Wyoming Terranes was in place for ~2Gyr and formed a topographic high, which was at the origin of the formation of a lateral ramp along the front of the Golconda Allochthon (Fig. V.A.4). This resulted in a spatial heterogeneity of the allochthon, and consequently, on spatial variations of the topographic load exerted by the Golconda Allochthon, contributing to the differential subsidence observed in the SFB (Caravaca *et al.*, *in press*, see section IV).

Inherited properties of the lithospheric basement therefore appear as a first order driver over the subsidence and spatial pattern of the sedimentary deposition across the SFB.

• Perspectives on basin paleogeography

The Sonoma Foreland Basin appears to be more complex than commonly assumed (e.g., Paull & Paull, 1993; Dickinson, 2006, 2013; Goodspeed & Lucas, 2007; Blakey, 2008; Ingersoll, 2008; Brayard *et al.*, 2013), with an internal differential evolution through space and time. Heritage and lithospheric parameters are a first order controlling factor underlying the North/South subsidence differences within the basin. This differentiation is also visible in the sedimentary, geochemical and paleontological records. **Therefore, two distinct parts can be defined: the North-SFB and South-SFB sub-basins** (Fig. V.A.5).

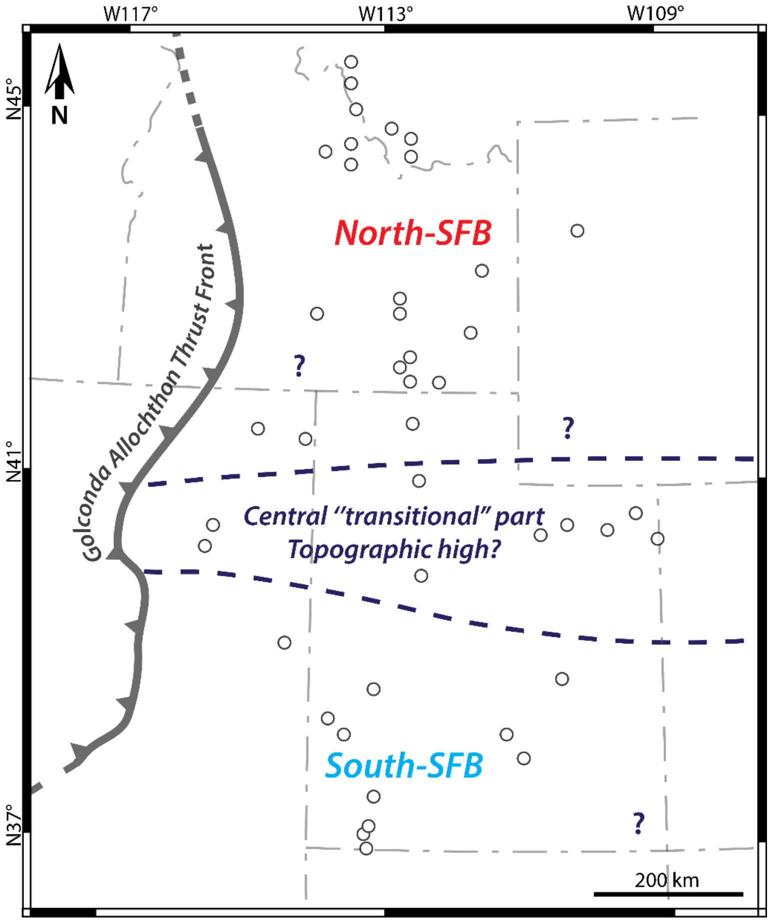

Figure V.A.5: Revised paleogeography for the SFB, showing a distinction between the North-SFB and South-SFB, delimited by a central "transitional" part (potentially a topographic high).

Nevertheless, the detailed paleogeography of the SFB remains not completely resolved. Indeed, several areas lack data to understand their evolution during the Early Triassic although they may be important to the understanding of the basin's dynamic. One of this key area is the central "transitional" domain that is located in North-central Utah (Fig. V.A.5). Being **a potential topographic high delimiting the North-SFB from the South-SFB**, this area has to be thoroughly investigated, but exposures and good outcrops are very rare. A drilling campaign to access preserved Early Triassic record could thus be considered. The Eastern and southern bordering areas of the SFB (Fig. V.A.5) are also not well constrained, mostly because of their continental settings. However, a better knowledge of these areas would help to delimit the maximum extension of the marine influence into the basin, and especially to resolve the question of **the provenance of the terrigenous inputs into the SFB**. For instance, Banham & Mountney (2013) described the presence of ET salt-walled mini-basins in southeasternmost Utah controlling the local fluvial network that directly contributed into the SFB. Finally, the area situated at the triple-junction of Nevada, Idaho and Utah is also lacking new field data **while being modeled as the most accommodating and potentially deepest part of the basin** (Fig. V.A.5; Caravaca *et al.*, *in press,* see section IV).

B. Ongoing work: expected impact on the 4D evolution of depositional settings in the North- and South-SFB

The existence of two distinct sub-basins within the SFB (North-SFB and South-SFB) is visible through variation in geodynamical, geochemical and paleontological records. This distinction is also remarkable in the sedimentary record of the basin, and therefore has major consequences on the depositional settings and their evolution during the entire Early Triassic. It is therefore of paramount interest to observe, describe and understand these local variations and the local evolution of the depositional setting for precise paleoenvironmental reconstruction.

This ongoing project relies on this work and on the many sections of the SFB to be interpreted. However, results gathered until now already gave an idea of the general evolution of the paleoenvironmental conditions in several distinct parts of the basin (e.g., Brayard *et al.*, 2013, 2017; Olivier *et al.*, 2014, 2016, see appendix 1; Vennin *et al.*, 2015; Grosjean *et al.*, *in prep.*; Jattiot *et al.*, *in prep.*).

A preliminary synthesis of the evolution of depositional setting and migration of the facies belts during the middle to late Smithian allows to recognize seven main facies association (FA1 to FA7, Fig. V.B.1, Table V.B.1), characterizing seven successive depositional settings throughout the whole SFB evolving from the proximal transitional environments to outer platform conditions (Fig. V.B.1; Table V.B.1).

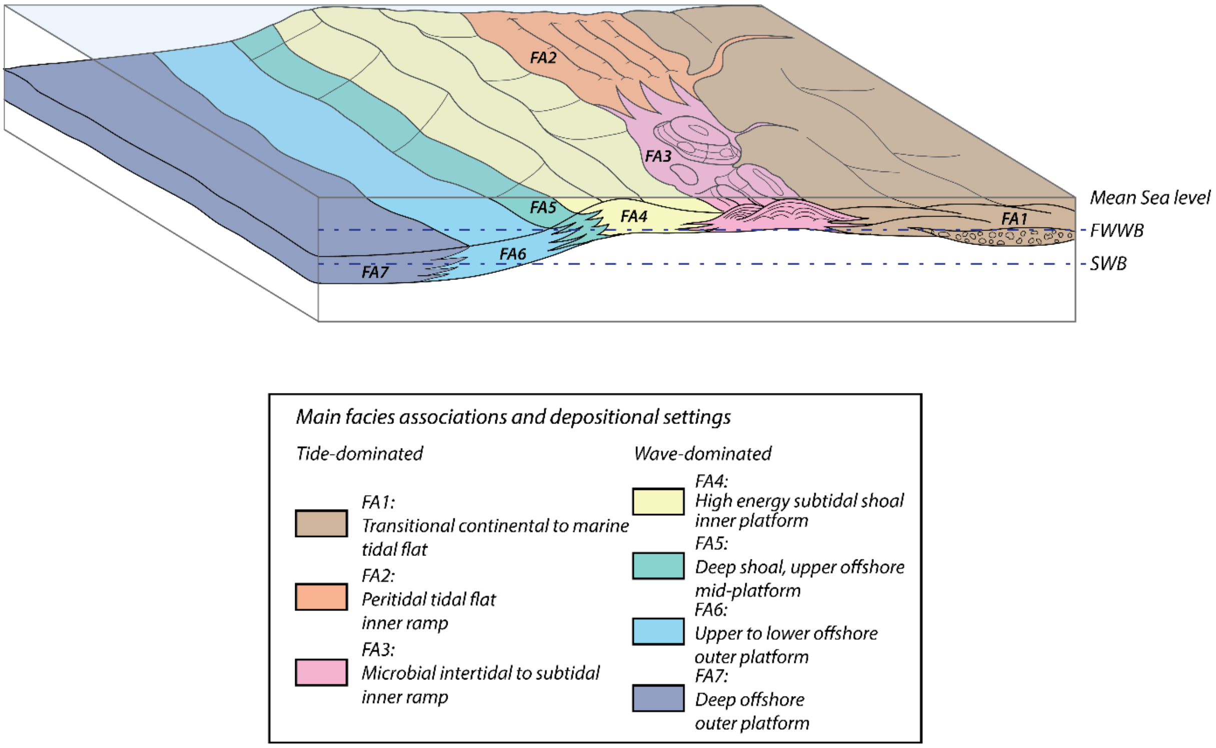

Figure V.B.1: Simplified synthetic depositional model for the main facies associations FA1 to FA7 (Table 7.B.1) described for the middle-late Smithian interval in the SFB. FWWB: Fair weather wave base; SWB: Storm wave base.

We suggest to define seven main facies associations at the SFB scale as following: Facies FA1 is characteristic of the Moenkopi Group “red beds”, and consists in siltstones and sandstones, locally conglomerates, representing shallow transitional continental to marine conditions (Fig. V.B.1; Table V.B.1). Facies FA2 consists in fine (dolo-)siltstones and calcarenites deposited on a peritidal flat of inner ramp (Fig. V.B.1; Table V.B.1). This association is of marine affinity with a sustained bioclastic content (Table V.B.1), and is restricted to the North-SFB (Figs. V.B.2 and V.B.3) where it represents the main facies associated with the Dinwoody and Woodside formations. Facies FA3 is characterized by massive intertidal to subtidal microbial limestones beds of an inner ramp (Fig. V.B.1; Table V.B.1). This association is restricted to the South-SFB (Figs. V.B.2 and V.B.3). Facies FA4 represents high energy ooidic shoals of inner platform (Fig. V.B.1; Table V.B.1). Facies FA5 is a continuity of the latter, and represent deeper wave-dominated mid-platform conditions (Fig. V.B.1; Table V.B.1). Finally, FA6 and FA7 represent mud-dominated deposition of upper to lower and deep offshore conditions, respectively (Fig. V.B.1; Table V.B.1). Both these associations represent lower energy deposition, with locally episodic storm-induced bioaccumulations (Fig. V.B.1; Table V.B.1).

These depositional settings are common to both the two sub-basins, and for the two time-intervals considered here (*Owenites* and *Anasibirites* beds). This highlights a continuity in the lateral and vertical evolution of the depositional settings, following a transgressive pattern, compatible with the third-order transgressive sequence known for the Smithian, with a maximum flooding attained around the *Anasibirites* beds (e.g., Embry, 1997; Brayard *et al.*, 2013; Vennin *et al.*, 2015; Olivier *et al.*, 2016, see appendix 1).

Figures V.B.2 and V.B.3 show the spatial repartition of the identified main depositional settings observed throughout the SFB for the interval corresponding to the *Owenites* beds (~middle Smithian; Fig. V.B.2) and the *Anasibirites* beds (~late Smithian; Fig. V.B.3), respectively.

Figure V.B.2 illustrates the globally shallow and tide-dominated deposition of the SFB during the *Owenites* beds (middle Smithian) time-interval. A westward and northward deepening trend is observed, as expected due to the foreland nature of the basin and the northwestern open marine influence. In South-SFB, depositional settings evolve along a SE/NW transect from the transitional red beds, restricted to the southern and eastern borders of the sub-basin, to upper offshore mud-dominated outer platforms in northwestern part of the South-SFB. In the North-SFB, the depositional settings evolve from terrigenous transitional deposits in its southeastern part, but reach deeper offshore conditions in the westernmost part.

Main facies association		Biotic components	Non-biotic elements	Structures	Energy	Main depositional setting	Refs.
FA1	"Red beds" siltstones/sandstones (locally conglomerates) to dolosiltstone	Rare fragmented bivalves	Subrounded to subangular quartz grains and micas (locally conglomerates with moderately to well-sorted pebbles to granules), peloids	Erosive sandstones with basal lags, plane-parallel stratified conglomerates, trough crossed bedded sands to silts, ripple-laminated sands with silt and clay alternations, mud-cracks and rootlets	Low to moderate energy (locally high)	Transitional continental to marine tidal flat	Blakey, 1974; Lucas *et al.*, 2007; Olivier *et al.*, 2014, 2016 (cf. appendix 1); Vennin *et al.*, 2015
FA2	(Dolo-)siltstones to calcarenites	Bivalves, gastropods, echinoderms	Subrounded silty quartz grains	Asymmetric ripples and megaripples, flat pebbles, mud flakes, intraformationnal breccias, planar to trough cross-beddings; rare to common bioturbation	Low to moderate energy, locally high (and storm-influenced)	Peritidal flat, inner ramp	Kummel, 1957; Olivier *et al.*, 2016 (cf. appendix 1); Vennin *et al.*, 2015; Grosjean *et al.*, *in prep.*
FA3	Microbial limestones	Associations of siliceous sponges, gastropods, bivalves, echinoderms and ostracods	Peloids, oncoids, mud-clasts	Macrostructure: pluri-dm to m coalescent domes; planar to wavy undulated laminations. Mesostructure: stromatolitic and/or thrombolitic, presence of numerous fenestrae	Low to moderate energy (tide-dominated)	Intertidal to subtidal inner ramp	Brayard *et al.*, 2013; Olivier *et al.*, 2014, 2016 (cf. appendix 1); Vennin *et al.*, 2015
FA4	Ooidic/cortoidic and/or bioclastic-rich packstones to grainstones	Bivalves, gastropods, echinoderms, vertebrate fragments	Ooids (usually type 1, Strasser, 1986), cortoids, peloids, locally phosphatic grains, clastic grains	Asymmetric and climbing ripples, through cross-bedding, planar to oblique lamination, metric to pluri-metric megaripples, bioturbation	High energy (wave-dominated)	Subtidal shoal, inner platform	Olivier *et al.*, 2014; 2016 (cf. appendix 1); Vennin *et al.*, 2015; Grosjean *et al.*, *in prep.*; Jattiot *et al.*, *in prep.*

Main facies association		Biotic components	Non-biotic elements	Structures	Energy	Main depositional setting	Refs.
FA5	Bioclastic wackestones to floatstones	Thick-shelled bivalves, gastropods, echinoderms, ammonoids	Rare peloids	M-thick megaripples, bioturbation (locally intense), local storm-induced bioaccumulations (with erosional base)	Moderate to high energy (wave-dominated) with storm-induced episodes	Deep shoal, upper offshore, mid-platform	Olivier *et al.*, 2014; 2016 (cf. appendix 1); Vennin *et al.*, 2015; Grosjean *et al.*, *in prep.*; Jattiot *et al.*, *in prep.*
FA6	Ammonoid floatstones in wackestone matrix	Ammonoids, thin-shelled bivalves, gastropods, echinoderms	Rare fine silty grains	Storm-induced bioaccumulations, bioturbation	Low energy, with storm-induced deposits	Upper to lower offshore, mud-dominated outer platform with amalgamated storm-induced deposits	Olivier *et al.*, 2014; 2016 (cf. appendix 1); Vennin *et al.*, 2015; Grosjean *et al.*, *in prep.*; Jattiot *et al.*, *in prep.*
FA7	Ammonoid floatstones in mudstone matrix	Ammonoids, thin-shelled bivalves, gastropods	Micrite	Rare storm-induced bioaccumulations, bioturbation	Low energy	Deep offshore, mud-dominated outer platform	Olivier *et al.*, 2014; 2016 (cf. appendix 1); Vennin *et al.*, 2015; Grosjean *et al.*, *in prep.*; Jattiot *et al.*, *in prep.*

Table V.B.1: Main facies associations and depositional settings observed in the SFB during the middle-late Smithian interval (references are given within the table).

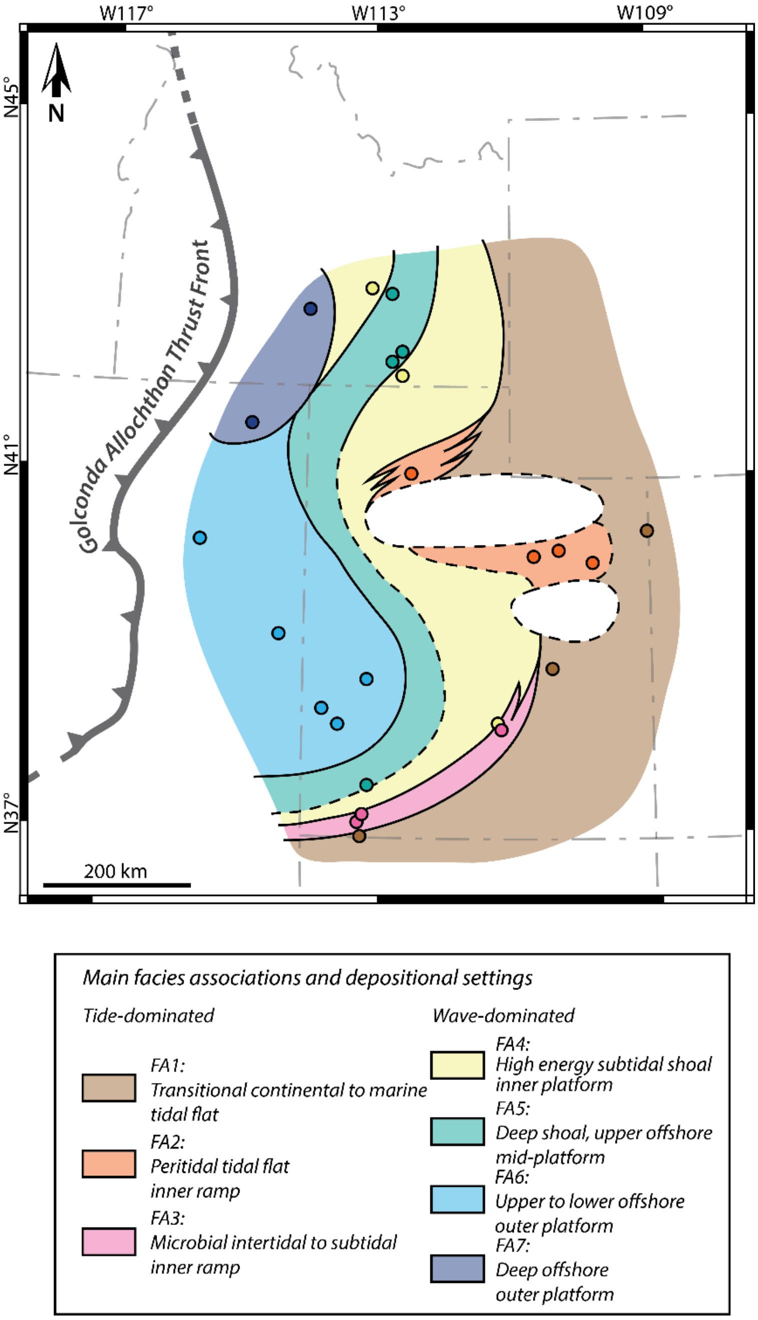

Figure V.B.2: Preliminary representation of the spatial distribution of the main depositional settings in the SFB during the *Owenites* beds (middle Smithian, after Brayard *et al*., 2013). A North/South distinction is evidenced by this map, with restriction of the FA3 microbial association to the South-SFB, while the North-SFB exclusively displays the FA2 peritidal association and FA7 deep offshore conditions.

Figure V.B.3 illustrates the SFB during the late Smithian associated with *Anasibirites* beds, during the maximum flooding of the basin. Paleoenvironments in South-SFB range from transitional continental (red beds) to marine outer platforms series (mud-dominated), while the North-SFB displays mainly outer platform mud-dominated sedimentation. A general transgressive trend is evidenced throughout the whole SFB with southwards and southeastwards migration of the facies belts. More open marine conditions prevailed during this interval, as evidenced by prominence of offshore facies FA6 and FA7 in both North-SFB and South-SFB.

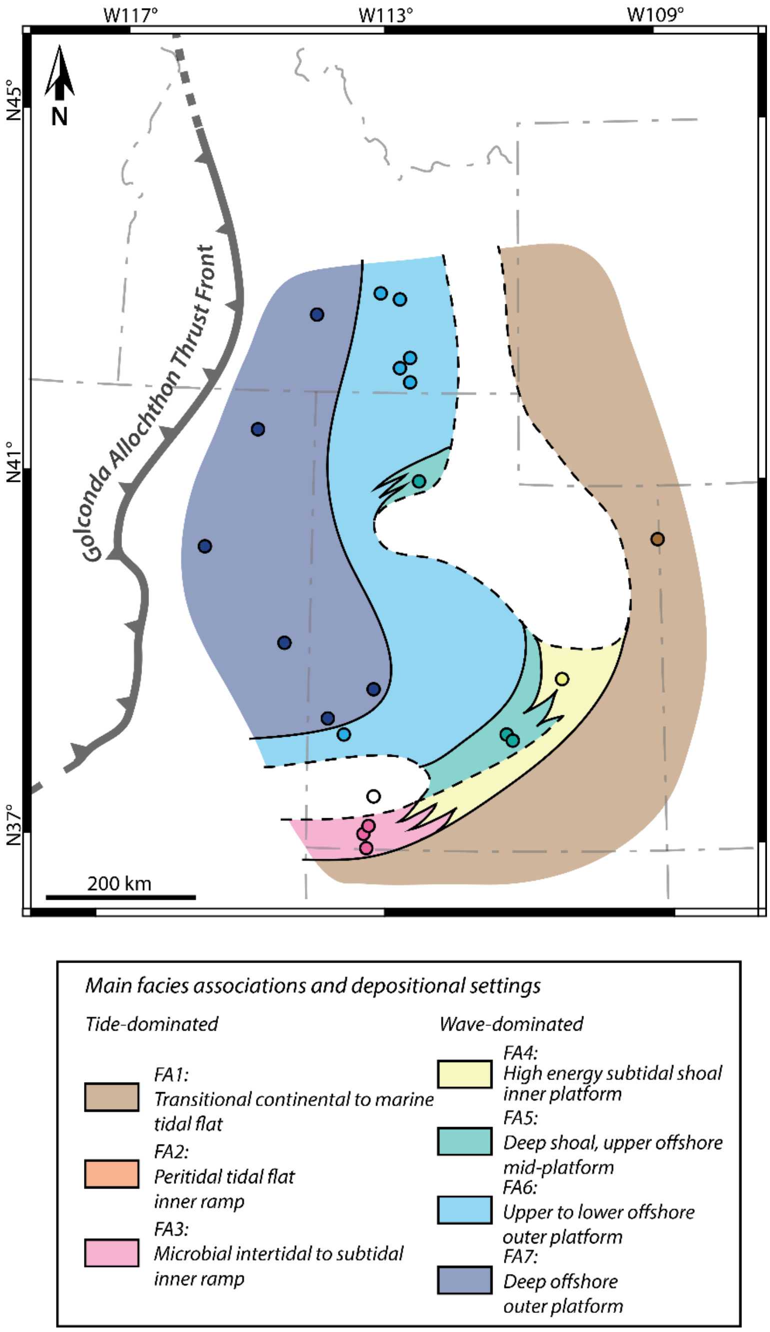

Figure V.B.3: Preliminary representation of the spatial distribution of the main depositional settings in the SFB during the *Anasibirites* beds (late Smithian, after Brayard *et al.,* 2013). Southeastward migration of the FA5 is clearly evidenced by this map and marks lateral evolution and migration of specific depositional conditions with time.

On these maps, a strict differentiation is observed between North-SFB and South-SFB in terms of repartition of the paleoenvironments. Nevertheless, the precise paleogeography remains to be further investigate (Figs. V.B.2 and V.B.3). This N/S difference in spatial repartition of the depositional settings follows the N/S distinction observed for the different proxies studied within this work. Noteworthy, some facies associations are restricted to either the North-SFB or the South-SFB. They thus may reflect specific conditions that are locally controlled. Microbial limestones of the FA3 association are only found in South-SFB (Figs. V.B.2 and V.B.3). We can hypothesize that the shallow conditions, such as the geochemistry of the water column and the low-rate subsidence, may have been among important factors in the installation and proliferation of these microbially driven deposits. Another example is given by the FA2, which is found only in North-SFB and in the transitional zone (Figs. V.B.2 and V.B.3). While the depositional settings of this association are similar to that of the red beds of FA1, a strong marine affinity is observed for this facies characterized by its bioclastic content (bivalves, gastropods, echinoderms; Table V.B.1). FA1 association is thus probably strongly influenced by terrigenous fluxes. The spatial repartition of these two facies associations consequently appears to be controlled by local parameters such as terrigenous input and connection to the open marine realm. It is therefore not surprising that FA2 is only found in the northern part of the SFB that seems to be connected to the Panthalassa during the whole ET, whereas FA1 is most prominently found in the southern part of the SFB and on its borders. Finally, deepest depositional conditions are found (association FA7) in the North-SFB throughout the middle-late Smithian interval (Figs. V.B.2. and V.B.3). This must probably owe to the continuous marine influences in this area, associated with the most important subsidence rate in the entire basin, allowing such sustained deep and quiet deposition. Local controls that are spatially differentiated between different parts of the SFB therefore have a major influence on the spatial pattern of the depositional setting and subsequent geological record.

The spatio-temporal evolution and the migration of the facies belt in the SFB is particularly well established for the Smithian and well exemplified by facies belts representing specific depositional conditions. The FA5 association, representing deep shoal conditions (Table V.B.1; Figs. V.B.1 to V.B.3) illustrates this migrating trend. This association represents specific bathymetric and hydrodynamic conditions that were subject to very quick changes when accommodation fluctuated. From the middle (Fig. V.B.2) to the late Smithian (Fig. V.B.3), the facies belt migrates southeastward in both North-SFB and South-SFB. As a consequence, this migration physically marks the lateral evolution of the paleoenvironmental conditions consecutive to changes in bathymetry and energy of the water column. The same evolution can be observed using the FA3 microbial association as a reference, given the specific conditions required for deposition of these limestones. Migration of this facies belt thus represents the lateral migration of specific conditions. This phenomenon also highlights the evolution of the local controlling factors. Indeed, it materializes the setting, development and cessation of a particular set of local influences.

The Early Triassic 4D evolution of the paleoenvironments in the SFB appears to strongly influence the pattern observed for the biotic recovery (presence/absence of fauna, preservation, etc.). Indeed, feedbacks between local conditions and biotic communities might be one of the keys to explain the explosive recovery observed for many organisms at a regional scale, and more largely, might shed new light on the importance of the local paleoenvironmental conditions during the Early Triassic.

The two preliminary maps of the spatial repartition of the Smithian depositional settings (Figs. V.B.2 and V.B.3) are only a small part of the larger work remaining to understand the evolution of paleoenvironments in the SFB during the entire Early Triassic. Additionally, extensive prospective work has to be done in the still under sampled areas of the SFB to further complete our database. Correlation of the existing data must also be done to analyze and decipher the sequential framework at different scales. Aside these studies, provenance analyses (using the QFL method of Dickinson *et al.*, 1983) must be shortly performed to discriminate potentially different sources for the terrigenous material and associated watersheds.

Finally, impact of other locally evolving parameters could be evidenced. As an example, the differential subsidence observed between North-SFB and South-SFB could explain the presence or absence of microbial carbonates. Indeed, the low subsidence and accommodation in the South-SFB is probably a helping factor allowing installation and growth of microbial communities. On the contrary, the rapidly subsiding environment and continued terrigenous inputs in the North-SFB could prevent installation of precipitating communities. Another hypothesis to be explored concerning these particular deposits, is the potential influence of the alkalinity of the water column, and variation of this parameter between North-SFB and South-SFB should be investigated.

C. Larger implications for the Early Triassic time interval

Ongoing works of the research team on the SFB are showing that most models and paradigms commonly accepted for the Early Triassic remain hypothetical, have likely to be reinterpreted or are simply incorrect. In a more problematic fashion, it appears that most of these models were established on the basis of local data that were then extrapolated at a global scale. In this context, several questions arose concerning the accuracy of these models, their regional or global significance, or the impact of potential biases (e.g., sub-sampling, rough time frame).

In order to decipher the complex history of the Early Triassic biotic recovery, from both the biological and paleoenvironemental points of view, a large set of parameters has to be integrated (e.g., sedimentary, geochemical, geodynamical) because of the obvious and complex interplay between each of these parameters, and their influences on the observed diversity.

Our multidisciplinary approach well highlights the necessity to take into account the different potential data from studied sections, and to propose a detailed reconstruction of these sites. Also, the use of different methods allows to reduce potential biases (e.g., sub-sampling, preservation bias), as well as making analyses at various scales. Moreover, potential unexpected feedbacks between discrete parameters (e.g., influence of bacterial sulfato-reduction metabolisms on the preservation of the geochemical record during early diagenesis) can therefore be deciphered.

This work therefore demonstrates the need for complete reinvestigation using similar integrated study of other Early Triassic basins worldwide to discriminate the local, regional and expected global influences on paleoenvironments, and their impacts on the biotic recovery.

By this way, a global and accurate scenario, minimizing potential biases or misinterpretations due to local specific conditions, can be obtain to bring further insights on the biotic recovery after the Permian/Triassic mass extinction event.

D. Other general and conceptual perspectives

Aside its potential (yet requested) use for a broader understanding of the Early Triassic interval, the integrated method developed during the work in studying sedimentary basins may find other applications to answer diverse scientific questions.

Due to this approach involving different parameters as several scales, which is the main interest of the method, it might be used to help discriminate the influence of each distinct controlling parameter.

A similar work can be achieved for other critical time periods, such as the aftermath of the late-Devonian mass extinction (due to the important reefal microbial carbonates found in these deposits, Riding, 2006). Additionally, the microbial communities are not an exclusive tool, and influences of other organisms can be determined, such as during the aftermath of the end-Cretaceous mass extinction, where microbial deposits are not reported (Riding, 2006).

Moreover, integrated study of the Sonoma Foreland Basin allows to understand the conditions behind the development and spatio-temporal extension of several specific ecosystems (e.g., the microbial communities). These data (e.g., sedimentary conditions, water column geochemistry) could be therefore used and transferred to other basins to predict the presence of similar deposits/communities (e.g., microbialites distribution in the Great Salt Lake, Bouton *et al.*, 2016). Numerical modelling and study of analog basins (such as the Miocene Amazon Foreland Basin, being a large shallow foreland basin sit on a lithospherically-heterogeneous basement, and is influenced by the heterogeneous Andean Cordillera, Roddaz *et al.*, 2010) could therefore be used to decipher the timely-controlled evolution of forcing parameters in these basins. This approach can be useful in oil and gas exploration as basin-scale analyses of reservoir sedimentary basins prevent a thoroughly detailed field study.

Finally, this integrated approach was rather successful in deciphering the long-lost Sonoma Foreland Basin, whose remnants are very scattered and limited. Using a complete set of data through varied methods (sedimentological, paleontological, geochemical, cartographic, structural, etc.), we were able to reconstruct its history and constrain its evolution at a high resolution. We hope that this work will open the way to new possibilities for studies of very ancient and/or nearly obliterated basins with few available remnants to understand their past history (e.g., Paleozoic Williston Basin or Devonian Amazon Basin; e.g., Ahern & Mrkvicka, 1984; Isaacson & Sablock, 1990). Growing use of remote sensing data and their present-day resolution also allow to apply this approach to merely accessible basins where access to field data can be compromised, such as basins situated in remote areas, or even to the field of planetary geology to reconstruct the past histories of extra-terrestrial sedimentary basins, such as the deltaic basin of Gale Crater on Mars.

REFERENCES

AHERN, J.L. & MRKVICKA, S.R., 1984. A mechanical and thermal model for the evolution of the Williston Basin. *Tectonics* **3**(1), 79-102.

ALGEO, T.J. & LYONS, T.W., 2006. Mo–total organic carbon covariation in modern anoxic marine environments: Implications for analysis of paleoredox and paleohydrographic conditions. *Paleoceanography*, **21**(1).

ALGEO, T.J. & MAYNARD, J.B., 2004. Trace-element behavior and redox facies in core shales of Upper Pennsylvanian Kansas-type cyclothems. *Chemical geology*, **206**(3), 289-318.

ALGEO, T.J. & TWITCHETT, R.J., 2010. Anomalous Early Triassic sediment fluxes due to elevated weathering rates and their biological consequences. *Geology* **38**(11), 1023-1026.

ALGEO, T.J., CHEN, Z.Q., FRAISER, M.L., TWITHCETT, R.J., 2011. Terrestrial-marine teleconnections in the collapse and rebuilding of Early Triassic marine ecosystems. *Palaeogeography, Palaeoclimatology, Palaeoecology* **308**(1-2), 1-11.

ARP, G., REIMER, A., REITNER, J., 2003. Microbialite formation in seawater of increased alkalinity, Satonda crater Lake, Indonesia. *Journal of Sedimentary Research* **73**(1), 105-127.

ASAACSON, P.E. & SABLOCK, P.E., 1990. Devonian palaeogeography and palaeobiogeography of the central Andes. *Geological Society, London, Memoirs* **12**(1), 431-435.

BARESEL, B., BUCHER, H., BROSSE, M., CORDEY, F., GUODUN, K., SCHALTEGGER, U., 2007. Precise age for the Permian-Triassic boundary in South China from high-precision U-Pb geochronology and Bayesian age-depth modeling. *Solid Earth*, **8**(2), 361-378.

BEATTY, T.W., ZONNELVELD, J.-P., HENDERSON, C.M., 2008. Anomalously diverse Early Triassic ichnofossil assemblages in northwest Pangea: A case for a shallow-marine habitable one. *Geology* **36**(10), 771-774.

BEAUCHAMP, B. & BAUD, A., 2002. Growth and demise of Permian biogenic chert along northwest Pangea: evidence for end-Permian collapse of thermohaline circulation. *Palaeogeography, Palaeoclimatology, Palaeoecology* **184**(1-2), 37-63.

BECKER, L., POREDA, R.J., BASU, A.R., POPE, K.O., HARRISON, T.M., NICHOLSON, C., IASKY, R., 2004. Bedout: A possible End-Permian impact crater offshore of northwestern Australia. *Science* **304**(5676), 1469-1476.

BEERLING, D.J., HARFOOT, M., LOMAX, B., PYLE, J.A., 2007. *Philosophical transactions of the Royal Society A* **365**(1856) 1843-1866.

BENTON, M.J. & NEWELL, A.J., 2014. Impacts of global warming on Permo-Triassic terrestrial ecosystems. *Gondwana Research* **25**(4), 1308-1337.

BENTON, M.J. & TWITCHETT, R.J., 2003. How to kill (almost) all life: the end-Permian extinction event. *Trends in Ecology & Evolution* **18**(7), 358-365.

BENTON, M.J., TVERDOKHLEBOV, V.P., SURKOV, M.V., 2004. Ecosystem remodeling among vertebrates at the Permian-Triassic boundary in Russia. *Nature* **432**, 91-100.

BLAKEY, R.C., 1974. Stratigraphic and Depositional Analysis of the Moenkopi Formation, Southeastern Utah. *Utah Geological Mineral Survey Bulletin* **104**, 81 pp.

BLAKEY, R.C., 1977. Petroliferous lithosomes in the Moenkopi Formation, southern Utah. *Utah Geology* **4**(2), 67-84

BLAKEY, R.C., 2008. Pennsylvanian-Jurassic sedimentary basins of the Colorado Plateau and Southern Rocky Mountains. *Sedimentary basins of the world*, pp. 245-296. Netherlands: Elsevier.

BLAKEY, R.C., 2013. Southwestern North America Paleogeographic maps. Retrieved 03/15/2017, http://cpgeosystems.com/swnam.html .

BOND, D.P.G. & WIGNALL, P.B., 2014. Large igneous provinces and mass extinctions: An update. *Geological Society of America Special Papers*, 505.

BÖNING, P., BRUMSACK, H-J., BÖTTCHER, M.E., SCHNETGER, B., KRIETE, C., KALLMEYER, J., BORCHERS, S.L., 2004. Geochemistry of Peruvian near-surface sediments. *Geochimica et Cosmochimica Acta* **68**(21), 4429-4451.

BOTTJER, D.J., CLAPHAM, M.E., FRAISER, M.L., POWERS, C.M., 2008, Understanding mechanisms for the end-Permian mass extinction and the protracted Early Triassic aftermath and recovery. *GSA Today* **18**(9), 4-10

BOUTON, A., VENNIN, E., BOULLE, J., PACE, A., BOURILLOT, R., 2016. Linking the distribution of microbial deposits from the Great Salt Lake (Utah, USA) to tectonic and climatic processes. *Biogeosciences* **13**(19), 5511-5526.

BRAYARD, A. & BUCHER, H., 2015. Permian-Triassic extinctions and rediversifications. *Ammonoid paleobiology: From macroevolution to paleogeography*, pp. 465-473. Netherlands: Springer.

BRAYARD, A., 2015. *La rediversification du Trias inférieur : entre paradigmes, paradoxes et réalités du terrain.* Mémoire d'Habilitation à Diriger les Recherches, Université de Bourgogne, 01/2015.

BRAYARD, A., BUCHER, H., ESCARGUEL, G., FLUTEAU, F., BOURQUIN, S., GALFETTI, T., 2006. The Early Triassic ammonoid recovery: Paleoclimatic significance of diversity gradients. *Palaeogeography, Palaeoclimatology, Palaeoecology* **239**(3-4), 374-395.

BRAYARD, A., BYLUND, K.G., JENKS, J.F., STEPHEN, D.A., OLIVIER, N., ESCARGUEL, G., FARA, E., VENNIN, E. 2013. Smithian ammonoid faunas from Utah: implications for Early Triassic biostratigraphy, correlation and basinal paleogeography. *Swiss Journal of Palaeontology* **132**(2), 141-219.

BRAYARD, A., ESCARGUEL, G., BUCHER, H., MONNET, C., BRÜHWILER, T., GOUDEMAND, N., GALFETTI, T., GUEX, J., 2009. Good genes and good luck: ammonoid diversity and the end-Permian mass extinction. *Science*, **325**(5944), 1118-1121.

BRAYARD, A., KRMENACKER, L.J., BOTTING, J/P/, JENKS, J.F., BYLUND, K.G., FARA, E., VENNIN, E., OLIVIER, N., GOUDEMAND, N., SAUCEDE, T., CHARBONNIER, S., ROMANO, C., DOGUZHAEVA, L., THUY, B., HAUTMANN, M., STEPHEN, D.A., THOMAZO, C., ESCARGUEL, G., 2017. Unexpected Early Triassic marine ecosystem and the rise of the Modern evolutionary fauna. *Science Advances* **3**(2). DOI: 10.1126/sciadv.1602159

BRAYARD, A., MEIER, M., ESCARGUEL, G., FARA, E., NUETZEL, A., OLIVIER, N., BYLUND, K. G., JENKS, J. F., STEPHEN, D. A., HAUTMANN, M., VENNIN, E., BUCHER, H. 2015. Early Triassic 'Gulliver' gastropods; spatio-temporal distribution and significance for biotic recovery after the end-Permian mass extinction. *Earth-Science Reviews* **146**, 31-64.

BRAYARD, A., NÜTZEL, A., STEPHEN, D.A., BYLUND, K.G., JENKS, J., BUCHER, H., 2010. Gastropod evidence against the Early Triassic Lilliput effect. *Geology* **38**(2), 147-150.

BRAYARD, A., VENNIN, E., OLIIER, N., BYLUD, K.G., JENKS, J., STEPHEN, D.S., BUCHER, H., HOFMANN, R., GOUDEMAND, N., ESCARGUEL, G., 2011. Transient metazoan reefs in the aftermath of the end-Permian mass extinction. *Nature Geoscience* **4**, 693-697.

BROOKFIELD, M.E., ALGEO, T.J., HANNIGAN, R., WILLIAMS, J., BHAT, G.M., 2013. Shaken and stirred: Seismites and tsunamites at the Permian-Triassic boundary, Guryul Ravine, Kashmir, India. *Palaios* **28**, 568-582.

BRÜHWILER, T., BUCHER, H., BRAYARD, A., GOUDEMAND, N. 2010. High-resolution biochronology and diversity dynamics of the Early Triassic ammonoid recovery; the Smithian faunas of the northern Indian margin. *Palaeogeography, Palaeoclimatology, Palaeoecology* **297**(2), 491-501.

BUCHER, H. 1988. A new Middle Anisian (Middle Triassic) ammonoid zone from northwestern Nevada (USA). *Eclogae Geologicae Helvetiae* **81**(3), 723-762.

BURCHFIEL, B. & DAVIS, G. A. 1975. Nature and controls of Cordilleran orogenesis, western United States: Extensions of an earlier synthesis. *American Journal of Science* **275**, 363-396.

BURCHFIEL, B. & ROYDEN, L. 1991. Antler orogeny: A Mediterranean-type orogeny. *Geology* **19**(1), 66-69.

CAGNARD, F., BARBEY, P., GAPAIS, D. 2011. Transition between “Archaean-type” and “modern-type” tectonics: insights from the Finnish Lapland Granulite Belt. *Precambrian Research* **187**(1), 127-142.

CALVERT, S., BUSTIN, R., INGALL, E., 1996. Influence of water column anoxia and sediment supply on the burial and preservation of organic carbon in marine shales. *Geochimica et Cosmochimica Acta* **60**(9), 1577-1593.

CARAVACA, G., BRAYARD, A., VENNIN, E., GUIRAUD, M., LE POURHIET, L., GROSJEAN, A.S., THOMAZO, C., OLIVIER, N., FARA, E., ESCARGUEL, G., BYLUND, K.G., JENKS, J.F., STEPHEN, D.A., *in press*. Controlling factors for differential subsidence in the Sonoma Foreland Basin (Early Triassic, western USA). *Geological Magazine*, 1-25. DOI: 10.1017/S0016756817000164

CARAVACA, G., THOMAZO, C., VENNIN, E., OLIVIER, N., COQUEREZ, T., ESCARGUEL, G., FARA, E., JENKS, J.F., BYLUND, K.G., STEPHEN, D.A., BRAYARD, A., 2017. Early Triassic fluctuations of the global carbon cycle: new evidence from paired carbon isotopes in the western USA Basin. *Global and Planetary Change* 154**, 10-22. DOI: 10.1016/j.gloplacha.2017.05.005**

CHARDON, D., GAPAIS, D., CAGNARD, F. 2009. Flow of ultra-hot orogens: a view from the Precambrian, clues for the Phanerozoic. *Tectonophysics* **477**(3), 105-118.

CHEN, Z.Q. & BENTON, M.J., 2012. The timing and pattern of biotic recovery following the end-Permian mass extinction. *Nature Geoscience* **5**, 375-383.

CHEN, Z.Q., FRAISER, M.J., BOLTON, C., 2012. Early Triassic fossils from Gondwana Interior Sea: Implication for ecosystem recovery following the end-Permian mass extinction in south high-latitude region. *Gondwana Research* **22**(1), 238-255.

CLARK, D.L. 1957. Marine Triassic stratigraphy in eastern Great Basin. *AAPG Bulletin* **41**(10), 2192-2222.

CLARKSON, M.O., KASERMANN, S.A., WOD, R.A., LENTON, T.M., DAINES, S.J., ROCHOZ, S., OHNEMUELLER, F., MEIXER, A., POLTON, S.W., TPPER, E.T., 2015. Ocean acidification and the Permo-Triassic mass extinction. *Science* **348**(6231), 229-232.

COCKS, L.R.M. & TORSVIK, T.H., 2011. The Palaeozoic geography of Laurentia and western Laurussia: A stable craton with mobile margins. *Earth-Science Reviews* **106**(1-2), 1-51.

COLPRON, M. & NELSON, J.L., 2009. A Palaeozoic Northwest Passage: incursion of Caledonian, Baltican and Siberian terranes into eastern Panthalassa, and the early evolution of the North American Cordillera. *Geological Society, London, Special Publications,* **318**(1), 273-307.

COLPRON, M., NELSON, J.L., MURPHY, D.C., 2007. North Cordilleran terranes and their interaction through time. *GSA Today* **17**(4/5), 4-10.

CONEY, P.J. 1987. The regional tectonic setting and possible causes of Cenozoic extension in the North American Cordillera. *Geological Society Special Publications* **28**, 177-186.

COWEN, R., 2013. *History of life*. John Wiley & Sons.

DAVIDSON, E.S., 1967. Geology of the Circle Cliffs Area, Garfield and Kane Counties, Utah. *Geological Survey Bulletin* **1229**, US Government Printing Office.

DAVYDOV, V.I., CROWLEY, J.L., SCHMITZ, M.D., SNYDER, W.S., 2016. New U-Pb constraints identify the end-Guadalupian and possibly end-Lopingian extinction events conceivably preserved in the passive margin of North America: implication for regional tectonics. *Geological Magazine*, 1-13. DOI: 10.1017/S0016756816000959

DECELLES, P.G. & COOGAN, J.C. 2006. Regional structure and kinematic history of the Sevier fold-and-thrust belt, central Utah. *Geological Society of America Bulletin* **118**(7-8), 841-864.

DICKERSON, P.W. 2003. Intraplate mountain building in response to continent-continent collision; the ancestral Rocky Mountains (North America) and inferences drawn from the Tien Shan (Central Asia). *Tectonophysics* **365**(1-4), 129-142.

DICKINSON, W.R. & GEHRELS, G.E., 2008. U-Pb ages of detrital zircons in relation to paleogeography: Triassic paleodrainage networks and sediment dispersal across southwest Laurentia. *Journal of Sedimentary Research* **78**(12), 745-764.

DICKINSON, W.R. & GEHRELS, G.E., 2010. Insights into North American paleogeography and paleotectonics from U-Pb ages of detrital zircons in Mesozoic strata of the Colorado Plateau, USA. *International Journal of Earth Sciences* **99**(6), 1247-1265.

DICKINSON, W.R. 2002. The Basin and Range Province as a composite extensional domain. *International Geology Review* **44**(1), 1-38.

DICKINSON, W.R. 2004. Evolution of the North American cordillera. *Annu. Rev. Earth Planet. Sci.* **32**, 13-45.

DICKINSON, W.R. 2006. Geotectonic evolution of the Great Basin. *Geosphere* **2**(7), 353-368.

DICKINSON, W.R. 2013. Phanerozoic palinspastic reconstructions of Great Basin geotectonics (Nevada-Utah, USA). *Geosphere* **9**(5), 1384-1396.

DICKINSON, W.R., BEARD, L.S., BRAKENRIDGE, G.R., ERJAVEC, J.L., FERGUSON, R.C., INMAN, K.F., KNEPP, R.A., LINDBERG, F.A., RYBERG, P.T., 1983. Provenance of North American Phanerozoic sandstones in relation to tectonic setting. *Geological Society of America Bulletin* **94**(2), 222-235.

DUPRAZ, C., VISSCHER, P.T., BAUMGARTNER, L.K., REID, R.P., 2004. Microbe-mineral interactions: early carbonate precipitation in a hypersaline lake (Eleuthera Island, Bahamas). *Sedimentology* **51**(4), 745-765.

EL TABAKH, M. & SCHREIBER, B.C., 1998. Diagenesis of the Newark rift basin, eastern North America. *Sedimentology* **45**, 855-874.

EMBRY, A.F. 1997. Global sequence boundaries of the Triassic and their identification in the Western Canada sedimentary basin. *Bulletin of Canadian Petroleum Geology* **45**(4), 415-433.

ERWIN, D.H., 2006. *Extinction: how life on Earth nearly ended 250 million years ago.* Princeton University Press, 296 pp.

EVANS, J.P., MARTINDALE, D.C., KENDRICK, R.D., 2003. Geologic setting of the 1884 Bear Lake, Idaho, earthquake; rupture in the hanging wall of a basin and range normal fault revealed by historical and geological analyses. *Bulletin of the Seismological Society of America* **93**(4), 1621-1632.

FLETCHER, R.C. & HALLET, B. 1983. Unstable extension of the lithosphere: A mechanical model for basin-and-range structure. *Journal of Geophysical Research: Solid Earth* **88**(B9), 7457-7466.

FLÜGEL, E., 2002. Triassic reef patterns. *SEPM Special Publications* **72**, 391-463.

FOLEY, D.J., UMHOEFER, P.J., LEARY, R.J., BURR, G.L.E., SMITH, M.E., 2016. Regional scale Ancestral Rocky Mountains tectonics: relation to associated Pennsylvanian-Permian southeastern and southwestern basins and plate margins. *Geological Society of America Abstracts with programs* **48**(7), DOI: 10.1130/abs/2016AM-288016

FRAISER, M.L. & BOTTJER, D.J., 2004. The non-actualistic Early Triassic gastropod fauna: a case study of the Lower Triassic Sinbad limestone member. *Palaios* **19**(3), 259-275.

FRAISER, M.L. & BOTTJER, D.J., 2007. Elevated atmospheric CO 2 and the delayed biotic recovery from the end-Permian mass extinction. *Palaeogeography, Palaeoclimatology, Palaeoecology* **252**(1), 167-175.

FRAISER, M.L., TWITCHETT, R.J., FREDERICKSON, J.A., METCALFE, B., BOTTJER, D.J., 2011. Gastropod evidence against the Early Triassic Lilliput effect: COMMENT. *Geology* **39**(1), e232-e232.

GABRIELSE, H., SNYDER, W.S., STEWART, J. H. 1983. Sonoma orogeny and Permian to Triassic tectonism in western North America. *Geology* **11**(8), 484-486.

GALFETTI, T., BUCHER, H., OVTCHAROVA, M., SCHALTEGGER, U., BRAYARD, A., BRÜHWILER, T., GOUDEMAND, N., WEISSERT, H., HOCHULI, P.A., CORDEY, F., GUODUN, K., 2007a. Timing of the Early Triassic carbon cycle perturbations inferred from new U-Pb ages and ammonoid biochronozones. *Earth and Planetary Science Letters*, **258**(3-4), 593-604.

GALFETTI, T., HOCHULI, P.A., BRAYARD, A., BUCHER, H., WEISSERT, H., VIGRAN, J.O., 2007b. Smithian-Spathian boundary event: Evidence for global climatic change in the wake of the end-Permian biotic crisis. *Geology*, **35**(4), 291-294.

GANS, P. & BOHRSON, W. 1998. Suppression of volcanism during rapid extension in the Basin and Range Province, United States. *Science* **279**(5347), 66-68.

GESLIN, J.K. 1998. Distal Ancestral Rocky Mountains tectonism: Evolution of the Pennsylvanian-Permian Oquirrh–Wood River basin, southern Idaho. *Geological Society of America Bulletin* **110**(5), 644-663.

GOODSPEED, T.H. & LUCAS, S.G. 2007. Stratigraphy, sedimentology, and sequence stratigraphy of the Lower Triassic Sinbad Formation, San Rafael Swell, Utah. *Bulletin - New Mexico Museum of Natural History and Science* **40**, 91-101.

GOUDEMAND, N., OCHARD, M., BUCHER, H., BRAYARD, A., BRÜHWILER, T., GALFETTI, T., HOCHULI, P.A., HERMANN, E., WARE, D., 2008. Smithian-Spathian Boundary: the biggest crisis in Triassic conodont history. *Geological Society of America Abstracts with programs* **40**(6), 505.

GRASBY, S., BEAUCHAMP, B., EMBRY, A., SANEI, H., 2013. Recurrent Early Triassic ocean anoxia. *Geology*, **41**(2), 175-178.

GRICE, K., CAO, C., LOVE, G.D., BÖTTCHER, M.E., TWITCHETT, R.J., GROSJEAN, E., SUMMONS, R.E., TRGEIN, S.C., DUNNING, W., JIN, Y., 2005. Photic zone euxinia during the Permian-Triassic superanoxic event. *Science* **307**(5710), 706-709.

GROSJEAN, A.S., VENNIN, E., OLIVIER, N., CARAVACA, G., THOMAZO, C., FARA, E., ESCARGUEL, G., BYLUND, K.G., JENKS, J.F., STEPHEN, D.A, BRAYARD, A., *in prep.*, Early Triassic environmental dynamics and microbial development during the Smithian-Spathian transition (Lower Weber Canyon, Utah, USA).

HAUTMANN, M. & NÜTZEL, A., 2005. First record of a heterodont bivalve (Mollusca) from the Early Triassic: palaeoecological significance and implications for the 'Lazarus problem'. *Palaeontology* **48**(6), 1131-1138.

HAUTMANN, M., BUCHER, H., BRÜHWILER, T., GOUDEMAND, N., KAIM, A., N¨TZEL, A., 12011. An unusually diverse mollusk fauna from the earliest Triassic of South China and its implication for benthic recovery after the end-Permian biotic crisis. *Geobios* **44**(1), 71-85.

HAYS, L.E., BEATTY, T., HENDERSON, C.M., LOVE, G.D., SUMMONS, R.E., 2007. Evidence for photic zone euxinia through the end-Permian mass extinction in the Panthalassic Ocean (Peace River Basin, Western Canada). *Palaeoworld* **16**(1), 39-50

HE, W., SHI, G.R., FENG, Q., CAMPI, M.J., GU, S., BU, J., PENG, Y, MENG, Y., 2007. Brachiopod miniaturization and its possible causes during the Permian-Triassic crisis in deep water environments. *Palaeogeography, Palaeoclimatology, Palaeoecology* **252**(1), 145-163.

HECKERT, A. B., CHURE, D. J., VORIS, J. T., HARRISON, A. A., THOMSON, T. J. 2015. Stratigraphy, Correlation and Age of the Moenkopi Formation in the Vicinity of Dinosaur National Monument, Eastern Uinta Basin, Utah and Colorado, USA. In *Geology of Utah's Uinta Basin and Uinta Mountains* eds M. D. Vanden Berg, R. Ressetar and L. P. Birgenheier). pp. 1-12. Utah Geological Association Publication.

HERMANN, E., HOCHULI, P.A., MÉHAY, S., BUCHER, H., BRÜHWILER, T., WARE, D., HAUTMANN, M., ROOHI, G., YASEEN, A., 2011. Organic matter and palaeoenvironmental signals during the Early Triassic biotic recovery: The Salt Range and Surghar Range records. *Sedimentary Geology*, **234**(1), 19-41.

HOFMANN, R., GOUDEMAND, N., WASMER, M., BUCHER, H., HAUTMANN, M., 2011. New trace fossil evidence for an early recovery signal in the aftermath of the end-Permian mass extinction. *Palaeogeography, Palaeoclimatology, Palaeoecology* **310**(3-4), 216-226.

HOFMANN, R., HAUTMANN, M., BRAYARD, A., NUETZEL, A., BYLUND, K. G., JENKS, J. F., VENNIN, E., OLIVIER, N., BUCHER, H. 2014. Recovery of benthic marine communities from the end-Permian mass extinction at the low latitudes of eastern Panthalassa. *Palaeontology* **57**(3), 547-589.

HUANG, B., HARPER, D.A., ZHAN, R., RONG, J., 2010. Can the Lilliput Effect be detected in the brachiopod faunas of South China following the terminal Ordovician mass extinction? *Palaeogeography, Palaeoclimatology, Palaeoecology* **285**(3), 277-286.

IACONO-MARZIANO, G., MARECAL, V., PIRRE, M., GAILALRD, F., ARTETA, J., SCAILLET, B., ARNDT, N.T, 2012. Gas emissions due to magma-sediment interactions during flood magmatism at the Siberian Traps: Gas dispersion and environmental consequences. *Earth and Planetary Science Letters* **357**, 308-318.

INGERSOLL, R.V. 2008. Subduction-related sedimentary basins of the USA Cordillera *Sedimentary basins of the world*. pp. 395-428. Netherlands: Elsevier: Amsterdam, Netherlands.

INNOCENT, C., BRIQUEU, L., CABANIS, B., 1994. Sr-Nd isotope and trace-element geochemistry of the Late Variscan volcanism in the Pyrenees: Magmatism in post-orogenic extension? Tectonophysics 238(1-4), 161-181.

ISAACSON, P. E., & Sablock, P. E., 1990. Devonian palaeogeography and palaeobiogeography of the central Andes. *Geological Society, London, Memoirs* **12**(1), 431-435.

ISOZAKI, Y., 1997. Permo-Triassic boundary superanoxia and stratified superocean: records from lost deep sea. *Science* **276**(5310), 235-238.

IVANOV, A.V., HE, H., YAN, L., RYABOV, V.V., SHEVKO, A.Y., PALESSKII, S.V., NIKOLAEVA, I.V., 2013; Siberian Traps large igneous province: Evidence for two flood basalt pulses around the Permo-Triassic boundary and in the Middle Triassic, and contemporaneous granitic magmatism. *Earth-Science Reviews* **122**, 58-76.

IVANOV, A.V., HE, H., YANG, L., NIKOLAEVA, I.V., PALESSKII, S.V., 2009. 40Ar/39Ar dating of intrusive magmatism in the Angara-Taseevskyaya syncline and its implication for duration of magmatism of the Siberian Traps. *Journal of Asian Earth Sciences* **35**(1), 1-12.

JATTIOT R., BUCHER H., BRAYARD A., BROSSE M., JENKS J. & BYLUND K. G. (in press). Smithian ammonoid faunas from northeastern Nevada: implications for Early Triassic biostratigraphy and correlation within the western USA basin. *Palaeontographica Abteilung A*. DOI: 10.1127/pala/2017/0070

JATTIOT, R., BRAYARD, A., ESCARGUEL, G., BUCHER, G., CARAVACA, G., VENNIN, E., JENKS, J.F., BYLUND, K.G., *in prep.* Biogeography of Smithian (Early Triassic) ammonoid faunas within the western USA basin and controlling parameters.

JATTIOT, R., BUCHER, H., BRAYARD, A., MONNET, C., JENKS, J. F., HAUTMANN, M. 2016. Revision of the genus *Anasibirites* Mojsisovics (Ammonoidea): an iconic and cosmopolitan taxon of the late Smithian (Early Triassic) extinction. *Papers in Palaeontology* **2**(1), 155-188.

JENKS, J., GUEX, J., HUNGERBÜHLER, A., TAYLOR, D.G., BUCHER, H., 2013. Ammonoid biostratigraphy of the Early Spathian *Columbites parisianus* Zone (Early Triassic) at Bear Lake Hot Springs, Idaho. *New Mexico Museum of Natural History and Science Bulletin*, **61**(61), 268-283.

JOHNSTON, S.T. & BOREL, G.D., 2007. The odyssey of the Cache Creek terrane, Canadian Cordillera: Implications for accretionary orogens, tectonic setting of Panthalassa, the Pacific superwell, and break-up of Pangea. *Earth and Planetary Science Letters* **253**(3), 415-428.

JONES, C.H., Jones, 2013. Tectonics of the Western U.S., Retrieved 03/10/2017. http://www.colorado.edu/geolsci/Resources/WUSTectonics/tectonics.html

KAIHO, K. & KOGA, S., 2013. Impacts of a massive release of methane and hydrogen sulfide on oxygen and ozone during the late Permian mass extinction. *Global and Planetary Change* **107**, 91-101.

KAIHO, K., KAJIWARA, Y., NAKANO, T., MIURA, Y., KAWAHATA, H., TAZAKI, K., UESHIMA, M., CHEN, Z., SHI, G.R., 2001. End-Permian catastrophe by a bolide impact: Evidence of a gigantic release of sulfur from the mantle. *Geology* **29**(9), 815-818.

KAIM, A., NÜTZEL, A., BUCHER, H., BRÜHWILER, T., GOUDEMAND? N., 2010. Early Triassic (Late Griesbachian) gastropods from South China (Shanggan, Guangxi). *Swiss Journal of Geosciences* **103**(1), 121-128.

KATO, Y., NAKAO, K., ISOZAKI, Y., 2002. Geochemistry of late Permian to Early Triassic pelagic cherts from southwest Japan: implications for an oceanic redox change. *Chemical Geology* **182**(1), 15-34.

KAUFMANN, A.J. & KNOLL, A.H., 1995. Neoproterozoic variations in the C-isotopic composition of seawater: stratigraphic and biogeochemical implications. *Precambrian Research* **73**(1-4), 27-49.

KERSHAW, S., CRASQUIN, S., COLLIN, P.Y., LI, Y., FENG, Q., FOREL, M.B., 2009. Microbialites as disaster forms in anachronistic facies following the end-Permian mass extinction: a discussion. *Australian Journal of Earth Sciences* **56**(9), 809-813.

KERSHAW, S., LI, Y., CRASQUIN-SOLEAU, S., FENG, Q., MU, X., COLLIN, P.Y., REYNOLDS, A., GUO, L., 2007. Earliest Triassic microbialites in the South China block and other areas: controls on their growth and distribution. *Facies* **53**(3), 400-425.

KLAEBE, R., KENNEDY, M., JARRETT, A., BROCKS, J., 2017. Local paleoenvironmental controls on the carbon - isotope record defining the Bitter Springs Anomaly. *Geobiology*, **15**(1), 65-80.

KLUTH, C.F. & CONEY, P.J. 1981. Plate tectonics of the ancestral Rocky Mountains. *Geology* **9**(1), 10-15.

KNOLL, A.H., BAMBACH, R.K., PAYNE, J.L., PRUSS, S., FISHCER, W.W., 2007. Paleophysiology and the end-Permian mass extinction. *Earth and Planetary Science letters* **256**(3), 295-313.

KONSTANTINOV, K.M., BAZHENOV, M/L/, FETISOVA, A.M., KHUTORSKOY, M.D., 2014. Paleomagnetism of trap intrusions, East Siberia: Implications to flood basalt emplacement and the Permo-Triassic crisis of biosphere. *Earth and Planetary Science Letters* **394**, 242-253.

KORTE, C., PANDE, P., KALIA, H.W., JOACHIMSKI, M.M., OBERHÄNSLI, H., 2010. Massive volcanism at the Permian-Triassic boundary and its impact on the isotopic composition of the ocean and atmosphere. *Journal of Asian Earth Sciences* **37**(4), 293-311.

KREEMER, C. & HAMMOND, W.C. 2007. Geodetic constraints on areal changes in the Pacific–North America plate boundary zone: What controls Basin and Range extension? *Geology* **35**(10), 943-946.

KRULL, E.S. & RETALLACK, G.J., δ13C depth profiles from paleosols across the Permian-Triassic boundary: evidence for methane release. *Geological Society of America Bulletin* **112**(9), 1459-1472.

KRULL, E.S., RETALLACK, G.J., CAMPBELL, H.J., LYON, G.L., 2000. δ13Corg chemostratigraphy of the Permian-Triassic boundary in the Maitai Group, New Zealand: evidence for high-latitudinal methane release. *New Zealand Journal of Geology and Geophysics* **43**(1), 21-32.

KRYSTYN, L., HORACEK, M., BRANDNER, R., PARCHA, S., 2014, Late Permian tsunamites in Guryul Ravine (Kashmir, India)-revisited and rejected. *EGU General Assembly Conference Abstracts* **16**, 15312.

KUMMEL, B. 1954. *Triassic stratigraphy of southeastern Idaho and adjacent areas*. US Government Printing Office.

KUMMEL, B. 1957. Paleoecology of Lower Triassic formations of southeastern Idaho and adjacent areas. *Geological Society of America Memoirs* **67**, 437-468.

LABANDEIRA, C.C. & SEPKOSKI Jr, J.J., 1993. Insect diversity in the fossil record. *Science* **261**(5119), 310-315.

LACHENBRUCH, A.H. & MORGAN, P. 1990. Continental extension, magmatism and elevation; formal relations and rules of thumb. *Tectonophysics* **174**(1), 39-62.

LAMARQUE, J.F., KIEHL, J.T., ORLANDO, J.J., 2007. Role of hydrogen sulfide in a Permian-Triassic boundary ozone collapse. *Geophysical Research letters* **34**(2).

LAWTON, T.F., BOYER, S.E., SCHMITT, J.G. 1994. Influence of inherited taper on structural variability and conglomerate distribution, Cordilleran fold and thrust belt, western United States. *Geology* **22**(4), 339-342.

LUCAS, S.G., KRAINER, K., MILNER, A.R. 2007. The type section and age of the Timpoweap Member and stratigraphic nomenclature of the Triassic Moenkopi Group in Southwestern Utah. *Triassic of the American West. New Mexico Museum of Natural History and Science Bulletin* **40**, 109-118.

LUND, K., BOX, S.E., HOLM-DENOMA, C.S., SAN JUAN, C.A., BLAKELY, R.J., SALTUS, R.W., ANDERSON, E.D., DEWITT, E.H. 2015. Basement domain map of the conterminous United States and Alaska. United States: U. S. Geological Survey: Reston, VA, United States.

MAJOROWICZ, J., GRASBY, S.E., SAFANDA, J., BEAUCHAMP, B., 2014. Gas hydrate contribution to Late Permian global warming. *Earth and Planetary Science Letters* **393**, 243-253.

MALAVIEILLE, J. 1993. Late orogenic extension in mountain belts: insights from the Basin and Range and the late Paleozoic Variscan belt. *Tectonics* **12**(5), 1115-1130.

MALAVIEILLE, J., GUIHOT, P., COSTA, S., LARDEAUX, J.M., GARDIEN, V., 1990. Collapse of the thickened Variscan crust in the French Massif Central: Mont Pilat extensional shear zone and St Etienne Late Carboniferous Basin. *Tectonophysics* **177**(1-3), 139-149.

MARENCO, P.J., CORSETTI, F.A., HAMMOND, D.E., KAUFMAN, A.J., BOTTJER, D.J., 2008. Oxidation of pyrite during extraction of carbonate associated sulfate. *Chemical Geology* **247**(7), 124-132.

MARENCO, P.J., GRIFFIN, J.M., FRAISER, M.L., CLAPHAM, M.E., 2012. Paleoecology and geochemistry of Early Triassic (Spathian) microbial mounds and implications for anoxia following the end-Permian mass extinction. *Geology* **40**(8), 715-718.

MARY, M. & WOODS, A.D., 2008. Stromatolites of the Lower Triassic Union Wash Formation, CA: evidence for continued post-extinction environmental stress in western North America through the Spathian. *Paleogeography, Palaeoclimatology, Palaeoecology* **261**(1), 78-86.

MASSARE, J.A. & CALLAWAY, J.M., 1994. Cymbospondylus (Ichthyosauria: Shastasauridae) from the Lower Triassic Thaynes Formation of southeastern Idaho. *Journal of Vertebrate Paleontology* **14**(1), 139-141.

MATA, S.A. & BOTTJER, D.J., 2011. Origin of Lower Triassic microbialites in mixed carbonate-siliciclastic successions: ichnology, applied stratigraphy, and the end-Permian mass extinction. *Palaeogeography, Palaeoclimatology, Palaeoecology* **300**(1), 158-178.

MCGOWAN, A.J., SMITH, A.B., TAYLOR, P.D., 2009. Faunal diversity, heterogeneity and body size in the Early Triassic: testing post-extinction paradigms in the Virgin Limestone of Utah, USA. *Australian Journal of Earth Sciences* **56**(6), 859-872.

METCALFE, B., TWITHCETT, R.J., PRICE-LLOYD, N., 2011. Changes in size and growth rate of 'Lilliput' animals I the earliest Triassic. *Palaeogeography, Palaeoclimatology, Palaeoecology* **308**(1), 171-180.

METCALFE, I., 1994. Late Paleozoic and Mesozoic palaeogeography of eastern Pangea and Tethys. *Pangea: Global Environments and Resources* **17**, 97-111.

METCALFE, I., NICOLL, R., WILLINK, R., LADJAVADI, M., GRICE, K., 2013. Early Triassic (Induan–Olenekian) conodont biostratigraphy, global anoxia, carbon isotope excursions and environmental perturbations: New data from Western Australian Gondwana. *Gondwana Research*, **23**(3), 1136-1150.

MEYER, K., YU, M., JOST, A., KELLEY, B., PAYNE, J., 2011. δ 13 C evidence that high primary productivity delayed recovery from end-Permian mass extinction. *Earth and Planetary Science Letters*, **302**(3), 378-384.

MIALL, A. 2010. *The geology of stratigraphic sequences*. Springer Science & Business Media.

MUELLER, P.A., WOODEN, J.L., MOGK, D.W., FOSTER, D.A. 2011. Paleoproterozoic evolution of the Farmington Zone; implications for terrane accretion in southwestern Laurentia. *Lithosphere* **3**(6), 401-408.

MUKUL, M. & MITRA, G. 1998. Finite strain and strain variation analysis in the Sheeprock Thrust Sheet: an internal thrust sheet in the Provo salient of the Sevier Fold-and-Thrust belt, Central Utah. *Journal of Structural Geology* **20**(4), 385-405.

MURPHY, J.B. & NANCE, R.D., 2008. The Pangea conundrum. *Geology* 36(9), 703-706.

MURPHY, J.B., NANACE, R.D., CAWOOD, P.A., 2009. Contrasting modes of supercontinent formation and the conundrum of Pangea. *Gondwana Research* **15**(3), 408-420.

MYSHRALL, K.L., MOBBERLEY, J.M., GREEN, S.J., VISSCHER, P.T., HAVEMANN, S.A., REID, R.P., FOSTER, J.S., 2010. Biogeochemical cycling and microbial diversity in the thrombolitic microbialites of Highborne Cay, Bahamas. *Geobiology* 8(4), 337-354.

NEWELL, N.D. & KUMMEL, B. 1942. Lower Eo-Triassic stratigraphy, western Wyoming and southeast Idaho. *Geological Society of America Bulletin* **53**(6), 937-996.

NICHOLS, K.M. & SILBERLING, N.J. 1977. Stratigraphy and depositional history of the Star Peak Group (Triassic), northwestern Nevada. *Geological Society of America Special Papers* **178**, 1-74.

OGDEN, D.E. & SLEEP, N.H., 2012. Explosive eruption of coal and basalt and the end-Permian mass extinction. *Proceedings of the National Academy of Sciences* **109**(1), 59-62.

OLDOW, J.S., BALLY, A.W., AVÉ LALLEMANT, H., LEEMAN, W.P. 1989. Phanerozoic evolution of the North American Cordillera; United States and Canada. *The Geology of North America*, 139-232.

OLIVIER, N., BRAYARD, A., FARA, E., BYLUND, K. G., JENKS, J. F., VENNIN, E., STEPHEN, D. A., ESCARGUEL, G. 2014. Smithian shoreline migrations and depositional settings in Timpoweap Canyon (Early Triassic, Utah, USA). *Geological Magazine* **151**(5), 938-955.

OLIVIER, N., BRAYARD, A., VENNIN, E., ESCARGUEL, G., FARA, E., BYLUND, K. G., JENKS, J. F., CARAVACA, G., STEPHEN, D. A. 2016. Evolution of depositional settings in the Torrey area during the Smithian (Early Triassic, Utah, USA) and their significance for the biotic recovery. *Geological Journal* 51(4), 600-626.

ORCHARD, M.J., 2007. Conodont diversity and evolution through the latest Permian and Early Triassic upheavals. *Palaeogeography, Palaeoclimatology, Palaeoecology*, **252**(1), 93-117.

ORIEL, S.S. & PLATT, L.B., 1980. Geologic map of the Preston 1 degree by 2 degrees Quadrangle, southeastern Idaho and western Wyoming. *U.S. Geological Survey Publication* **1127**. U.S. Government Printing Office.

OVTCHAROVA, M., BUCHER, H., SCHALTEGGER, U., GALFETTI, T., BRAYARD, A., GUEX, J., 2006. New Early to Middle Triassic U–Pb ages from South China: calibration with ammonoid biochronozones and implications for the timing of the Triassic biotic recovery. *Earth and Planetary Science Letters*, **243**(3), 463-475.

PARRISH, J.T., 1993. Climate of the supercontinent Pangea. *The Journal of Geology* **101**(2), 215-233.

PARSONS, T., THOMPSON, G. A., SLEEP, N. H. 1994. Mantle plume influence on the Neogene uplift and extension of the US western Cordillera? *Geology* **22**(1), 83-86.

PAULL, R.A. & PAULL, R.K. 1991. Allochthonous rocks from the western part of the early Triassic miogeocline; Hawley Creek area, east-central Idaho. *Contributions to Geology* **28**(2), 145-54.

PAULL, R.A. & PAULL, R.K. 1993. Interpretation of Early Triassic nonmarine–marine relations, Utah, USA. *New Mexico Museum of Natural History and Science Bulletin* **3**, 403-09.

PAULL, R.K. & PAULL, R.A., 1994. Shallow marine sedimentary facies in the earliest Triassic (Griesbachian) Cordilleran miogeocline, USA. *Sedimentary Geology* **93**(3-4), 181-191.

PAULL, R.K. & PAULL, R.A., 1997. Transgressive conodont fauna of the early Triassic: an opportunity for correlation in the Tethys and the circum-Pacific. *Late Palaeozoic and Early Mesozoic Circum-Pacific Events and their Global Correlations*. Cambridge University Press

PAULL, R.K. & PAULL., R.A., 1983. Revision of type Lower Triassic Dinwoody Formation, Wyoming, and designation of principal reference section. *Rocky Mountain Geology* **22**(2), 83-90.

PAULSEN, T. & MARSHAK, S. 1999. Origin of the Uinta recess, Sevier fold–thrust belt, Utah: influence of basin architecture on fold–thrust belt geometry. *Tectonophysics* **312**(2), 203-216.

PAYEN, J.L., 2005. Evolutionary dynamics of gastropod size across the end-Permian extinction and through the Triassic recovery interval. *Paleobiology* **31**(2), 269-290.

PAYNE, J.L. & CLAPHAM, M.E., 2012. End-Permian mass extinction in the oceans: an ancient analog for the twenty-first century? *Annual Review of Earth and Planetary Sciences* **40**, 89-111.

PAYNE, J.L. & KUMP, L.R., 2007. Evidence for recurrent Early Triassic massive volcanism from quantitative interpretation of carbon isotope fluctuations. *Earth and Planetary Science Letters*, **256**(1), 264-277.

PAYNE, J.L., LEHRMANN, D.J., CHRISTENSEN, S., WEI, J., KNOLL, A., 2006. Environmental and biological controls on the initiation and growth of a Middle Triassic (Anisian) reef complex on the Great Bank of Guizhou, Guizhou Province, China. *Palaios* **21**(4), 325-343.

PAYNE, J.L., LEHRMANN, D.J., WEI, J., ORCHARD, M.J., SCHRAG, D.P., KNOLL, A.H., 2004. Large perturbations of the carbon cycle during recovery from the end-Permian extinction. *Science* **305**(5683), 506-509.

PAYNE, J.L., TURCHYN, A.V., PAYTAN, A., DEPAOLO, D.J., LEHRMANN, D.J., YU, M., WEI, J., 2010. Calcium isotope constraints on the end-Permian mass extinction. *Proceedings of the National Academy of Sciences* **107**(19), 8543-8548.

PETERSON, J.A. 1977. Paleozoic shelf-margins and marginal basins, western Rocky Mountains-Great Basin, United States. In: Helsey, E.L. et al. (Eds.), *Rocky Mountain Thrust Belt, Geology and Resources*. Guidebook Wyo. Geol. Assoc. Annu. Field Conf. **29**, 135–153.

PIETSCH, C. & BOTTJER, D.J., 2014. The importance of oxygen for the disparate recovery patterns of the benthic macrofauna in the Early Triassic. *Earth-Science Reviews* **137**, 65-84.

PRUSS, S.B. & BOTTJER, D.J., 2004. Early Triassic trace fossils of the western United States and their implication for prolonged environmental stress from the end-Permian mass extinction. *Palaios* **19**(6), 551-564.

PRUSS, S.B. & BOTTJER, D.J., 2005. The reorganization of reef communities following the end-Permian mass extinction. *Comptes Rendus Palevol* **4**(6), 553-568.

PRUSS, S.B. & PAYNE, J.L., 2009. Early Triassic microbial spheroids in the Virgin Limestone Member of the Moenkopi Formation, Nevada, USA. *Palaios* **24**(2), 131-136.

PRUSS, S.B., CORSETTI, F.A., BOTTJER, D.J., 2005. The unusual sedimentary rock record of the Early Triassic: a case study from the southwestern United States. *Paleogeography, Palaeoclimatology, Palaeoecology* **222**(1), 33-52.

RACHOLD, V. and BRUMSACK, H.J., 2001. Inorganic geochemistry of Albian sediments from the Lower Saxony Basin NW Germany: palaeoenvironmental constraints and orbital cycles. Palaeogeography, Palaeoclimatology, Palaeoecology, **174**(1), 121-143.

RAUP, D.M., 1979. Size of the Permo-Triassic bottleneck and its evolutionary implications. *Science* **206**(4415), 217-218.

RETALLACK, G.J., VEEVERS, J.J., MORANTE, R., 1996. Global coal gap between Permian-Triassic extinction and Middle Triassic recovery of peat-forming plants. *Geological Society of America Bulletin* **108**(2), 195-207.

RIDING, R., 2006. Microbial carbonate abundance compared with fluctuations in metazoan diversity over geological time. *Sedimentary Geology* 185(3), 229-238.

RILEY, T.R., LEAT, P.T., PANKHURST, R.J., HARRIS, C., 2001. Origins of large volume rhyolitic volcanism in the Antarctic Peninsula and Patagonia by crustal melting. *Journal of Petrology* **42**(6), 1043-1065.

RODDAZ, M., HERMOZA, W., MORA, A., BABY, P., PARRA, M., CHRISTOPHOUL, F., BRUSSET, S., ESPURT, N. 2010. Cenozoic sedimentary evolution of the Amazonian foreland basin system. *Amazonia, landscape and species evolution: a look into the past. Blackwell-Wiley, Hoboken*, 61-88.

RODLAND, D.L. & BOTTJER, D.J., 2001. Biotic recovery from the end-Permian mass extinction: behavior of the inarticulate brachiopod Lingula as a disaster taxon. *Palaios* **16**(1), 95-101.

ROMANO, C., GOUDEMAND, N., VENNEMANN, T.W., WARE, D., SCHNEEBELI-HERMANN, E., HOCHULI, P.A., BRÜHWILER, T., BRINKMANN, W., BUCHER, H., 2013. Climatic and biotic upheavals following the end-Permian mass extinction. *Nature Geoscience* **6**(1), 57-60.

ROMANO, C., KOGAN, I., JENKS, J., JERJEN, I., BRINKMANN, W., 2012. Saurichthys and other fossil fishes from the late Smithian (Early Triassic) of bear Lake County (Idaho, USA), with a discussion of saurichthyid palaeogeography and evolution. *Bulletin of Geosciences* **87**(3), 543-570.

ROTHMAN, D.H., FOURNIER, G.P., FRENCH, K.L., ALM, E.J., BOYLE, E.A, CAO, C., SUMMONS, R.E., 2014. Methanogenic burst in the end-Permian carbon cycle. *Proceeding of the National Academy of Sciences* **111**(15), 5462-5467.

SADLER, R.K. 1981. Structure and stratigraphy of the Little Sheep Creek area, Beaverhead County, Montana. United States. Master of Science thesis of the Oregon State University, 06/1981.

SAUVAGE, L., RIQUIER, L., THOMAZO, C., BAUDIN, F., MARTINEZ, M., 2013. The late Hauterivian Faraoni “Oceanic Anoxic Event” at Río Argos (southern Spain): An assessment on the level of oxygen depletion. *Chemical Geology*, **340**, 77-90.

SCHELLING, D.D., STRICKLAND, D.K., JOHNSON, K.R., VRONA, J.P. 2007. Structural geology of the central Utah thrust belt. *Utah Geological Association Publication* **36**, 1-29.

SCHUBERT, J.K. & BOTTJER, D.J., 1992. Early Triassic stromatolites as post-mass extinction disaster forms. *Geology* **20**(10), 883-886.

SCHUBERT, J.K. & BOTTJER, D.J., 1995. Aftermath of the Permian-Triassic mass extinction event: Paleoecology of Lower Triassic carbonates in the western USA. *Palaeogeography, Palaeoclimatology, Palaeoecology* **116**(1-2), 1-39.

SCHWEICKERT, R. A. & LAHREN, M. M. 1987. Continuation of Antler and Sonoma orogenic belts to the eastern Sierra Nevada, California, and Late Triassic thrusting in a compressional arc. *Geology* **15**(3), 270-273.

SEPKOSKI Jr, J.J., 2002. A compendium of fossil marine animal general. *Bulletins of American paleontology* **363**, 1-560.

SMITH, M.T., DICKINSON, W.R., GEHRELS, G.E., 1993. Contractional nature of Devonian-Mississippian Antler tectonism along the North American continental margin. *Geology* **21**(1), 21-24.

SNYDER, W.S. & BRUECKNER, H.K. 1983. Tectonic evolution of the Golconda allochthon, Nevada: problems and perspectives. *Pre-Jurassic Rocks in Western North American Suspect Terranes*, Pacific Section SEPM.

SNYDER, W.S., TREXLER, J.H., DAVYDOV, V.I., CASHMAN, P., SCHIAPPA, T.A., SWEET, D., 2003. Upper Paleozoic tectonostratigraphic framework for the Western Margin of North America. AAPG Hedberg Conference, July 21-26, 2002, Vail, Colorado.

SOBOLEV, S.V., SOBOLEV, A.V., KUZMIN, D.V., KRIVOLUTSKAYA, N.A., PETRUNIN, A.G., ARNDT, N.T., RADKO, V.A, VASILIEV, Y.R., 2011. Linking mantle plumes, large igneous provinces and environmental catastrophes. *Nature*, **477**(7364), 312-316.

SONG, H., TONG, J., CHEN, Z.Q., 2011. Evolutionary dynamics of the Permian-Triassic foraminifer size: evidence for Lilliput effect in the end-Permian mass extinction and its aftermath. *Palaeogeography, Palaeoclimatology, Palaeoecology* **308**(1), 98-110.

SONG, H., WIGNALL, P.B., CHU, D., TONG, J., SUN, Y., SONG, H., HE, W., TIAN, L., 2014. Anoxia/high temperature double whammy during the Permian-Triassic marine crisis and its aftermath. *Scientific Reports* **4**, 4132.

SONG, H., WIGNALL, P.B., TONG, J., BOND, D.P.G., SONG, H., LAI, X., ZHANG, K., WANG, H., CHEN, Y., 2012. Geochemical evidence from bio-apatite for multiple oceanic anoxic events during Permian–Triassic transition and the link with end-Permian extinction and recovery. *Earth and Planetary Science Letters* **353**, 12-21.

SPEED, R.C. & SILBERLING, N.J. 1989. IGC Field Trip T122: Early Mesozoic Tectonics of the Western Great Basin, Nevada. *Early Mesozoic Tectonics of the Western Great Basin, Nevada: Battle Mountain to Yerington District, Nevada, July 1-7, 1989*, 1.

SPEED, R.C. & SLEEP, N. 1982. Antler orogeny and foreland basin: A model. *Geological Society of America Bulletin* **93**(9), 815-28.

SPEED, R.C., 1979. Collided Paleozoic microplate in the western United States. *The Journal of Geology* **87**(3), 279-292.

SPERLING, E.A. & INGLE, J.C., 2006. A Permian-Triassic boundary section at Quinn River Crossing, northwestern Nevada, and implications for the cause of the Early Triassic chert gap on the western Pangean margin. *Geological Society of America Bulletin* **118**(5-6), 733-746.

SPRACHTA, S., CAMOIN, G., GOLUBIC, S., LE CAMPION, T., 2001. Microbialites in a modern lagoonal environment: nature and distribution. *Palaeogeography, Palaeoclimatology, Palaeoecology* **175**(1), 103-124.

STAMPFLI, G.M., HOCHARD, C./, VERARD, C., WILHEM, C., 2013. The formation of Pangea. *Tectonophysics* **593**, 1-19.

STRASSER, A., 1986. Ooids in Purbeck limestones (lowermost Cretaceous) of the Swiss and French Jura. *Sedimentology* **33**(5), 711-727.

SUN, Y., JOACHIMSKI, M.M., WIGNALL, P.B., YAN, C., CHEN, Y., JIANG, H., WANG, L., LAI, X., 2012. Lethally hot temperatures during the Early Triassic greenhouse. *Science* **338**(6105), 366-370.

SUN, Y., WIGNALL, P.B., JOACHIMSKI, M.M., BOND, D.P.G., GRASBY, S.E., SUN, S., YAN, C.B., WANG, L.N., CHEN, Y.L., LAI, X.L., 2015. High amplitude redox changes in the late Early Triassic of South China and the Smithian–Spathian extinction. *Palaeogeography, Palaeoclimatology, Palaeoecology* **427**, 62-78.

SVENSEN, H., PLANKE, S., POLOZOV, A.G., SCHMIDBAUER, N., CORFU, F., PODLADCHIKOV, Y.Y., JAMTVEIT, B., 2009. Siberian gas venting and the end-Permian environmental crisis. *Earth and Planetary Science Letters* **277**(3), 490-500.

TABOR, N.J. & MONTAÑEZ, I.P., 2002. Shifts in late Paleozoic atmospheric circulation over western equatorial Pangea: Insights from pedogenetic mineral δ18O compositions. *Geology* **30**(12), 1127-1130.

THOMAS, W.A., 2011. Detrital-zircon geochronology and sedimentary provenance. *Lithosphere* **3**(4), 304-308.

THOMAZO, C., ELMELNASSI, S., BRAYARD, A., VENNIN, E., CARAVACA, G., OLIVIER, N., ESCARGUEL, G., BYLUND? K.G., JENKS, J., STEPHEN, D.A., FARA, E., SANSJOFRE, P., KILLINGSWORTH, B., CARTIGNY, P., *in prep.* Multiple sulfur isotope signals associated with the end-Permian mass extinction recovery.

THOMAZO, C., VENNIN, E., BRAYARD, A., BOUR, I., MATHIEU, O., ELMEKNASSI, S., OLIVIER, N., ESCARGUEL, G., BYLUND, K., JENKS, J. 2016. A diagenetic control on the Early Triassic Smithian–Spathian carbon isotopic excursions recorded in the marine settings of the Thaynes Group (Utah, USA). *Geobiology* **14**(3), 220-236.

THORPE, R.S., LEAT, P.T., BEVINS, R.E., HUGHES, D.J., 1989. Late-orogenic alkaline/subalkaline Silurian volcanism of the Skomer Volcanic Group in the Caledonides of south Wales. *Journal of the Geological Society* **146**(1), 125-132.

TOHVER, E., CAWOOD, P.A., RICCOMONI, C., LANA, C., TRINDALE, R.I.F.D., 2013. Shaking a methane fizz: Seismicity from the Araguainha impact event and the Permian-Triassic global carbon isotope record. *Palaeogeography, Palaeoclimatology, Palaeoecology* **387**, 66-75.

TOHVER, E., LANA, C., CAWOOD, P.A., FLETCHER, I.R., JOURDAN, F., SHERLOCK, S., RASMUSSEN, B., TRINDALE, R.I.F., YOKOYAMA, E., SOUZA FILHO, C.R., MARANGONI, Y., 2012. Geochronological constraints on the age of a Permo-Triassic impact event: U-Pb and 40Ar/39Ar results for the 40km Araguainha structure of central Brazil. *Geochimica et Cosmochimica Acta* **86**, 214-227.

TREXLER, J.H. & NITCHMAN, S.P. 1990. Sequence stratigraphy and evolution of the Antler foreland basin, east-central Nevada. *Geology* **18**(5), 422-425.

TRIBOVILLARD, N., ALGEO, T.J., LYONS, T., RIBOULLEAU, A., 2006. Trace metals as paleoredox and paleoproductivity proxies: an update. *Chemical Geology* **232**(1), 12-32.

TRIBOVILLARD, N., BOUT-ROUMAZEILLES, V., ALGEO, T., LYONS, T.W., SIONNEAU, T., MONTERO-SERRANO, J.C., RIBOULLEAU, A., BAUDIN, F., 2008. Paleodepositional conditions in the Orca Basin as inferred from organic matter and trace metal contents. *Marine Geology* **254**(1), 62-72.

TWITCHETT, R.J., 1999. Palaeoenvironments and faunal recovery after the end-Permian mass extinction. *Palaeogeography, Palaeoclimatology, Palaeoecology* **154**(1), 27-37.

TWITCHETT, R.J., 2007. The Lilliput effect in the aftermath of the end-Permian extinction event. *Palaeogeography, Palaeoclimatology, Palaeoecology* **252**(1), 132-144.

TWITHCETT, R.J. & WIGNALL, P.B., 1996. Trace fossils and the aftermath of the Permo-Triassic mass extinction: evidence from northern Italy. *Palaeogeography, Palaeoclimatology, Palaeoecology* **124**(1-2), 137-151.

URBANEK, A., 1993. Biotic crisis in the history of Upper Silurian graptoloids: a palaeobiological model. *Historical Biology* **7**(1), 29-50.

VALENZUELA, A., DONAIRE, T., PIN, C., TOSCANO, M., HAMILTON, M.A., PASCUAL, E., 2011. Geochemistry and U-Pb dating of felsic volcanic rocks in the Riotinto-Nerva unit, Iberian Pyrite Belt, Spain: crustal thinning, progressive crustal melting and massive sulphide genesis. *Journal of the Geological Society* **168**(3), 717-732.

VEEVERS, J.J., 1994. Pangea: Evolution of a supercontinent and its consequences for Earth's paleoclimate and sedimentary environments. *Geological Society of America Special paper* **288**, 13-28.

VEEVERS, J.J., CONAGHAN, P.J., SHAW, S.E., 1994. Turning point in Pangean environemental history at the Permian/Triassic (P/Tr) boundary. *Geological Society of America Special Papers* **288**, 187-196.

VENNIN, E., OLIVIER, N., BRAYARD, A., BOUR, I., THOMAZO, C., ESCARGUEL, G., FARA, E., BYLUND, K. G., JENKS, J. F., STEPHEN, D. A., HOFMANN, R. 2015. Microbial deposits in the aftermath of the end-Permian mass extinction; a diverging case from the Mineral Mountains (Utah, USA). *Sedimentology* **62**(3), 753-792.

VERMEIJ, G.J., 1977. The Mesozoic marine revolution: evidence from snails, predators and grazers. *Paleobiology* **3**(03), 245-258.

VETZ, N.Q. 2011. Geochronologic and isotopic investigation of the Koipato Formation, northwestern Great Basin, Nevada: implications for Late Permian-Early Triassic tectonics along the Western US Cordillera. Boise State University. Master of Science thesis of Boise State University, 08/2011.

VILLIER, L., BRAYARD, A., BYLUND, K.G., JENKS, J.F., ESCARGUEL, G., OLIVIER, N., STEPHEN, D.A., VENNIN, E., FARA, E., *in press*. Superstesaster promissor gen. et sp. Nov., a new starfish (Echinodermata, Asteroidea) from the Early Triassic of Utah, USA, filling a major gap in the phylogeny of asteroids. *Journal of Systematic Paleontology*, 1-21. DOI: 10.1080/14772019.2017.1308972

WALKER, J.D. 1985. Permo-Triassic paleogeography and tectonics of the Southwestern United States. Cambridge: Massachusetts Institute of Technology. PhD thesis of the Massachusetts Institute of Technology, 06/1985.

WEIDLICH, O., KIESSLING, W., FLÜGEL, E., 2003. Permian-Triassic boundary interval as a model for forcing marine ecosystem collapse by long-term atmospheric oxygen drop. *Geology* **31**(11), 961-964.

WHEELEY, J. & TWITCHETT, R., 2005. Palaecological significance of a new Griesbachian (Early Triassic) gastropod assemblage from Oman. *Lethaia* **38**(1), 37-45.

WHITMEYER, S.J. & KARLSTROM, K.E. 2007. Tectonic model for the Proterozoic growth of North America. *Geosphere* **3**(4), 220-259.

WIGNALL, P.B., 2001. Large igneous provinces and mass extinctions. *Earth-Science Reviews* **53**(1), 1-33.

WIGNALL, P.B., 2007. The End-Permian mass extinction-how bad did it get? *Geobiology* **5**(4), 303-309.

WILKERSON, M.S., APOTRIA, T., FARID, T. 2002. Interpreting the geologic map expression of contractional fault-related fold terminations: lateral/oblique ramps versus displacement gradients. *Journal of Structural Geology* **24**(4), 593-607.

WILKIN, R.T. & BARNES, H.L., 1997. Formation processes of framboidal pyrite. *Geochimica et Cosmochimica Acta* **61**(2), 323-339.

WOODS, A.D., Anatomy of an anachronistic carbonate platform: Lower Triassic carbonates of the southwestern United states. *Australian Journal of Earth Sciences* **56**(6), 825-839.

WOODS, A.D., BOTTJER, D.J., MUTTI, M., MORRISON, J., 1999. Lower Triassic large sea-floor carbonate cements: Their origin and a mechanism for the prolonged biotic recovery from the end-Permian mass extinction. *Geology* **27**(7), 645-648.

WOODS, A.D., Microbial ooids and cortoids from the Lower Triassic (Spathian) Virgin Limestone, Nevada, USA: evidence for an Early Triassic microbial bloom in shallow depositional environments. *Global and Planetary Change* **105**, 91-101.

WU, Y.S., YU, G.L., LI, R., SONG, L.R., JIANG, H.X., RIDING, R., LIU, L.J., ZHAO, R., 2014. Cyanobacterial fossils from 252 Ma old microbialites and their environmental significance. *Scientific Reports* **4**. DOI: 10.1038/srep03820

WYLD, S.J., 1991. Permo-Triassic tectonism in volcanic arc sequences of the western US Cordillera and implications for the Sonoma orogeny. *Tectonics* **10**(5), 1007-1017.

YANG, J.H., WU, F.Y., WILDE, S.A., CHEN, F., LIU, X.M., XIE, L.W., 2008. Petrogenesis of an alkali syenite-granite-rhyolite suite I the Yanshan Fold and Thrust Belt, Eastern North China Craton: geochronological, geochemical and Nd-Sr-Hf isotopic evidence for lithospheric thinning. *Journal of Petrology* **49**(2), 315-351.

YE, H., ROYDEN, L., BURCHFIEL, C., SCHUEPBACH, M. 1996. Late Paleozoic deformation of interior North America: the greater Ancestral Rocky Mountains. *AAPG bulletin* **80**(9), 1397-1432.

YONKEE, W.A. & WEIL, A.B. 2010. Reconstructing the kinematic evolution of curved mountain belts: Internal strain patterns in the Wyoming salient, Sevier thrust belt, USA. *Geological Society of America Bulletin* **122**(1-2), 24-49.

YONKEE, W.A. & WEIL, A.B. 2015. Tectonic evolution of the Sevier and Laramide belts within the North American Cordillera orogenic system. *Earth-Science Reviews* **150**, 531-593.

YONKEE, W.A., DEHLER, C.D., LINK, P.K., BALGORD, E.A., KEELEY, J.A., HAYES, D.S., WELLS, M.L., FANNING, C.M., JOHNSTON, S.M. 2014. Tectono-stratigraphic framework of Neoproterozoic to Cambrian strata, west-central U. S.; protracted rifting, glaciation, and evolution of the North American Cordilleran margin. *Earth-Science Reviews* **136**, 59-95.

ZANDT, G., MYERS, S.C., WALLACE, T.C. 1995. Crust and mantle structure across the Basin and Range-Colorado Plateau boundary at 37 N latitude and implications for Cenozoic extensional mechanism. *Journal of Geophysical Research: Solid Earth* **100**(B6), 10529-10548.

ZATOŃ, M., TAYLOR, P.D., VINN, O., 2013. Early Triassic (Spathian) post-extinction microconchids from western Pangea. *Journal of Paleontology* **87**(1), 159-165.

ZEEBE, R.E., 2012. History of seawater carbonate chemistry, atmospheric CO2, and ocean acidification. Annual Review of Earth and Planetary Sciences, 40, 141-165.

ZONNEVELD, J.P., GINGRAS, M.K., BEATTY, T.W., 2010. Diverse ichnofossil assemblages following the PT mass extinction, Lower Triassic, Alberta and British Columbia, Canada: evidence for shallow marine refugia on the northwestern coast of Pangaea. *Palaios* **25**(6), 368-392.

APPENDICES

Appendix 1: Characterization of the sedimentary record and depositional environments of the Torrey area (south-central Utah)

This work focuses on the Smithian-Spathian sedimentary succession outcropping in the Torrey area (south-central Utah). Detailed study of three outcrops (French Fork, Beas Lewis Flats and Pleasant Creek) allowed to characterize the main depositional settings of this area. They evolve into a sedimentary system ranging from tidal flats of interior platform to a bioclastic mid-shelf.

This study notably demonstrated that microbial deposits were contemporaneous and co-occurring with a well-diversified marine fauna. Therefore, the presence and distribution of the microbial deposits does not follow/is not restricted to the expected deleterious paleoenvironemental conditions during this time interval (e.g., Pruss & Bottjer, 2004; Mata & Bottjer, 2011). On the contrary, local depositional conditions drove their distribution. Additionally, we identified several multi-scale sequences, whose large- and medium scales are consistent with known eustatic changes (e.g., Embry, 1997; Vennin *et al*., 2015), while small-scale and elementary sequences relied on local autocyclic processes highlighting the important role of local conditions.

GEOLOGICAL JOURNAL
Geol. J. **51**: 600–626 (2016)
DOI: 10.1002/gj.2663

Evolution of depositional settings in the Torrey area during the Smithian (Early Triassic, Utah, USA) and their significance for the biotic recovery

NICOLAS OLIVIER[1]*, ARNAUD BRAYARD[2], EMMANUELLE VENNIN[2], GILLES ESCARGUEL[3], EMMANUEL FARA[2], KEVIN G. BYLUND[4], JAMES F. JENKS[5], GWÉNAËL CARAVACA[2] and DANIEL A. STEPHEN[6]

[1] Laboratoire Magmas et Volcans, Université Blaise Pascal – CNRS – IRD, OPGC, Clermont-Ferrand, France
[2] UMR CNRS 6282 Biogéosciences, Université de Bourgogne, Dijon, France
[3] Laboratoire de Géologie de Lyon: Terre, Planètes, Environnement, UMR CNRS 5276, Université Lyon 1, Villeurbanne, France
[4] 140 South 700 East, Spanish Fork, Utah, USA
[5] 1134 Johnson Ridge Lane, West Jordan, Utah, USA
[6] Department of Earth Science, Utah Valley University, 800 West University Parkway, Orem, Utah, USA

This work focuses on well-exposed Lower Triassic sedimentary rocks in the area of Torrey (south-central Utah, USA). The studied Smithian deposits record a large-scale third-order sea-level cycle, which permits a detailed reconstruction of the evolution of depositional settings. During the middle Smithian, peritidal microbial limestones associated with a rather low-diversity benthic fauna were deposited seaward of the tidal flat siliciclastic red beds. Associated with siliceous sponges, microbial limestones formed small m-scale patch reefs. During the late middle to late Smithian interval, the sedimentary system is characterized by tidal flat dolostones of an interior platform, ooid-bioclastic deposits of a tide-dominated shoal complex, and mid-shelf bioclastic limestones. Microbial deposits, corresponding to sparse stromatolites formed in the interior platform, are contemporaneous with a well-diversified marine fauna living in a seaward shoal complex and mid-shelf area. The nature and distribution of these Smithian microbial deposits are not related to any particular deleterious environmental condition, highlighting that observed patterns of biotic recovery after the end-Permian mass extinction were directly influenced by depositional settings. Facies evolution and stratal stacking patterns allow us to identify large, medium and small-scale, as well as elementary depositional sequences. Large- and medium-scale sequences are consistent with sea-level changes, whereas small-scale and elementary sequences are better explained by autocyclic processes.

Received 5 June 2014; accepted 21 January 2015

KEY WORDS Early Triassic; Smithian; Utah; microbialites; depositional environments; biotic recovery; bioconstructions

1. INTRODUCTION

Deleterious oceanic conditions are generally associated with the aftermath of the Permian–Triassic mass extinction, the most devastating biotic crisis in the Phanerozoic (Raup, 1979; Erwin, 2006). Indeed, large environmental perturbations, combining ocean acidification, anoxia, euxinia, and fluctuating productivity (Payne *et al.*, 2004; Galfetti *et al.*, 2007; Grasby *et al.*, 2013), likely constrained the biotic recovery during the Early Triassic. Until recently, post-crisis environments appeared to be particularly suitable for widespread development of abiotic and microbial deposits (Schubert and Bottjer, 1992; Baud *et al.*, 1997, 2007; Mata and Bottjer, 2012; Woods, 2013), whereas the metazoan recovery was assumed to be delayed. However, for some marine groups such as ammonoids (Brayard *et al.*, 2009a) and conodonts (Orchard, 2007), or where permitted by favourable environmental conditions (Krystyn *et al.*, 2003; Twitchett *et al.*, 2004; Chen *et al.*, 2007; Beatty *et al.*, 2008; Zonneveld *et al.*, 2010; Brayard *et al.*, 2011; Hautmann *et al.*, 2011, 2013; Kaim *et al.*, 2010; Hofmann *et al.*, 2011, 2013 a, b), life seems to have recovered rapidly in the Early Triassic. The timing and modalities of the biotic recovery are therefore still debated, highlighting the importance of its spatio-temporal variations, especially from the point of view of the underlying depositional settings (Pruss *et al.*, 2006; Beatty *et al.*, 2008; Galfetti *et al.*, 2008; Brühwiler *et al.*, 2009; Mata and Bottjer, 2011, 2012;

---

*Correspondence to: N. Olivier, Laboratoire Magmas et Volcans, Université Blaise Pascal – CNRS – IRD, OPGC, 5 rue Kessler, 63038 Clermont-Ferrand, France. E-mail: n.olivier@opgc.fr

Kershaw *et al.*, 2012; Sano *et al.*, 2012; Komatsu *et al.*, 2014; Olivier *et al.*, 2014; Pietsch and Bottjer, 2014). Therefore, detailed sedimentological studies and palaeoenvironmental reconstructions are of primary importance for improving our knowledge of the Early Triassic biotic recovery.

In the Torrey area (south central Utah, USA), excellent, widespread exposures of Lower Triassic deposits occur within and near Capitol Reef National Park (Fig. 1). In this area, the lithological succession includes Permian limestones, red beds of the Black Dragon Formation, microbial and bioclastic limestones of the Smithian Sinbad Formation, and sediments up to and including the red beds of the Spathian Torrey Formation (Stewart *et al.*, 1972; Blakey, 1974, 1977; Dean, 1981). The variety of deposits and number of potential sections represent a good opportunity for detailed three-dimensional analysis of rapid lateral and vertical facies changes (Dean, 1981). However, the only previous attempt at section correlation in the Torrey area was largely based on a lithostratigraphic approach (Dean, 1981). This work presents a detailed bed-by-bed sedimentological analysis of three sections in the area southeast of Torrey (Fig. 1a). Its main objectives include: (i) analyse the nature and diversity of facies in order to obtain robust depositional environmental reconstructions; (ii) achieve sequential analysis of these sections in order to obtain highly-resolved correlation and discuss the effect of relative sea-level fluctuations on sedimentation with regard to autocyclic and allocyclic processes; and (iii) discuss the evolution of local depositional settings and its potential influence on biotic recovery at the regional level.

2. GEOLOGICAL SETTING

The three studied outcrops are located near the town of Torrey (Wayne County, southern Utah, USA; Fig. 1a) as follows: (i) French Fork section (38°15′32.11″N, 111°24′

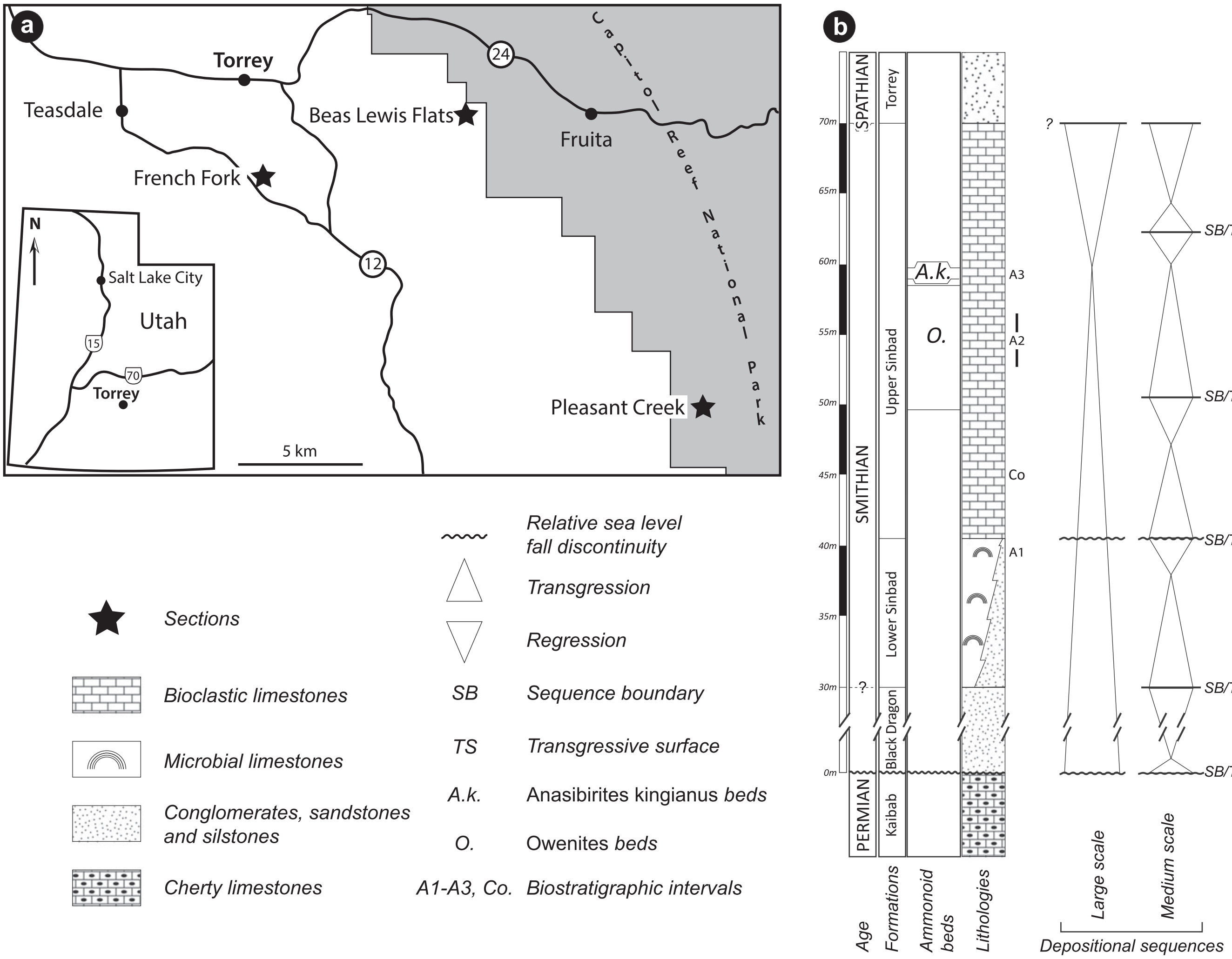

Figure 1. (a) Geographic location of the French Fork, Beas Lewis Flats and Pleasant Creek sections in the Torrey area (southern Utah). (b) Synthetic lithological succession of the Torrey area and its depositional sequence interpretation.

DOI: 10.1002/gj

36.31″W), situated 4 km south of Torrey; (ii) Beas Lewis Flats section (38°17′0.98″N, 111°18′49.07″W), located about 6 km west of the small town of Fruita; and (iii) Pleasant Creek section (38°10′21.58″N, 111°11′54.89″W), situated within Capitol Reef National Park, 13 km south of Fruita.

In the Torrey area, the Lower Triassic sedimentary succession is represented by interfingered siliciclastic and carbonate deposits (Blakey, 1974; Dean, 1981; Goodspeed and Lucas, 2007). These sediments belong to the Moenkopi and Thaynes groups (*sensu* Lucas *et al.*, 2007), which unconformably overly the Permian carbonate Kaibab Formation (Blakey, 1974; Dean, 1981). Directly above the Permian rocks, the Black Dragon Formation corresponds to the first occurrence of red beds (Fig. 1b). These siliciclastic deposits correspond to reddish to brownish siltstones, sandstones and even conglomerates (Blakey, 1974; Dean, 1981). The transition to the carbonate deposits of the Smithian Sinbad Formation can be gradual. Although Dean (1981) placed the boundary between the Black Dragon and the Sinbad formations below the first carbonate bed, other workers considered transitional carbonate beds observed within the red beds as part of the Black Dragon Formation (Blakey, 1974; Goodspeed and Lucas, 2007). This work follows the lithostratigraphical definition of Dean (1981). The Sinbad Formation can be readily subdivided into two main units (Fig. 1b): a massive microbial limestone unit (lower Sinbad Formation) and a bioclastic limestone unit (upper Sinbad Formation). Contact with the overlying deposits of the Spathian Torrey Formation is classically described as a conformable surface between the bioclastic limestones of the Sinbad Formation and a second occurrence of red beds (Blakey, 1974; Dean, 1981).

During the Early Triassic, the western USA basin was located at a near-equatorial position on the western margin of the Pangea. A large epicontinental sea about 500 to 600 km-wide and extending from southern Utah to British Columbia, exhibited a deepening trend from the south-east to the north-west (Blakey, 1974; Paull and Paull, 1993; Goodspeed and Lucas, 2007). Thus, most of the terrigenous sediments belonging to the Moenkopi Group can be found in southern and southeastern Utah and they represent the most proximal settings and palaeoshoreline positions (Olivier *et al.*, 2014). Carbonate deposits of the Thaynes Group represent more open-marine conditions and can be found mainly in central and northwestern Utah, southeastern Idaho and northeastern Nevada (Kummel, 1954; Blakey, 1974; Collinson and Hasenmueller, 1978; Dean, 1981; Goodspeed and Lucas, 2007; Guex *et al.*, 2010; Brayard *et al.*, 2011, 2013).

Preliminary information regarding regional ammonoid and conodont biostratigraphy, from previous studies indicate that the Sinbad Formation in the Torrey area is late Smithian (*sensu* Brühwiler *et al.*, 2010) in age due to the occurrence of the *Anasibirites kingianus* Zone (Stewart *et al.*, 1972; Blakey, 1974; Dean, 1981; Goodspeed and Lucas, 2007; Lucas *et al.*, 2007). Several new ammonoid specimens, collected bed-by-bed from the Torrey area, have been integrated with the new regional biostratigraphic framework proposed by Brayard *et al.* (2013). *Juvenites* aff. *spathi*, *Parussuria compressa*, *Meekoceras gracilitatis* and *Lanceolites compactus* occur in the uppermost part of the lower Sinbad Formation (interval A1; Fig. 1b), suggesting a likely middle Smithian age (basal *Owenites* beds by comparison with neighbouring localities; see Brayard *et al.*, 2013). Interval A2, situated in the middle of the upper Sinbad Formation, yields ammonoids identified as *Lanceolites compactus*, *Hedenstroemia kossmati*, *Churkites noblei*, *Guodunites hooveri* and *Dieneroceras dieneri*. Such an assemblage is diagnostic of the *Owenites* beds, which are typically middle Smithian in age (Brayard *et al.*, 2009b, 2013). Interval A3 includes *Wasatchites perrini* and *Anasibirites kingianus*, indicating a late Smithian age (Brayard *et al.*, 2013). Rare conodonts occurring near the base of the upper Sinbad Formation are represented by *Furnishius triserratus*, *Parachirognathus ethingtoni* and some ellisonids, also indicating a Smithian age (N. Goudemand, personal communication 2012).

3. SECTIONS AND FACIES DESCRIPTION

3.1. French Fork section

The Permian Kaibab limestones are not exposed at the base of the French Fork section (Fig. 2a). The entire section can be subdivided into three main lithological units (Figs. 3 and 4). The first unit includes the uppermost 12 m of red beds of the Black Dragon Formation (Fig. 1b). Facies (F1) consists of mm- to cm-thick red, dolosiltstone beds with small asymmetrical ripples (Table 1). Some muddy sheets display mud cracks locally. Other observed sedimentary structures include megaripples and climbing ripples. Quartz grains are abundant and subangular to subrounded. Also present are few cm- to dm-thick beds particularly rich in secondary gypsum.

The second unit occupying the interval between 12 and 23 m consists of two main limestone facies, which constitute the lower Sinbad Formation. Facies F2, which occurs only as a thin cm-thick interval at the base of this second lithological unit, corresponds to an intraclastic floatstone, with frequent basal erosive surfaces. Flat pebbles made of peloidal wackestone (locally mudstone or packstone) and exhibiting desiccation cracks are also present. Smaller intraclasts are poorly sorted and subangular to subrounded. A few domal stromatolites are visible locally.

DOI: 10.1002/gj

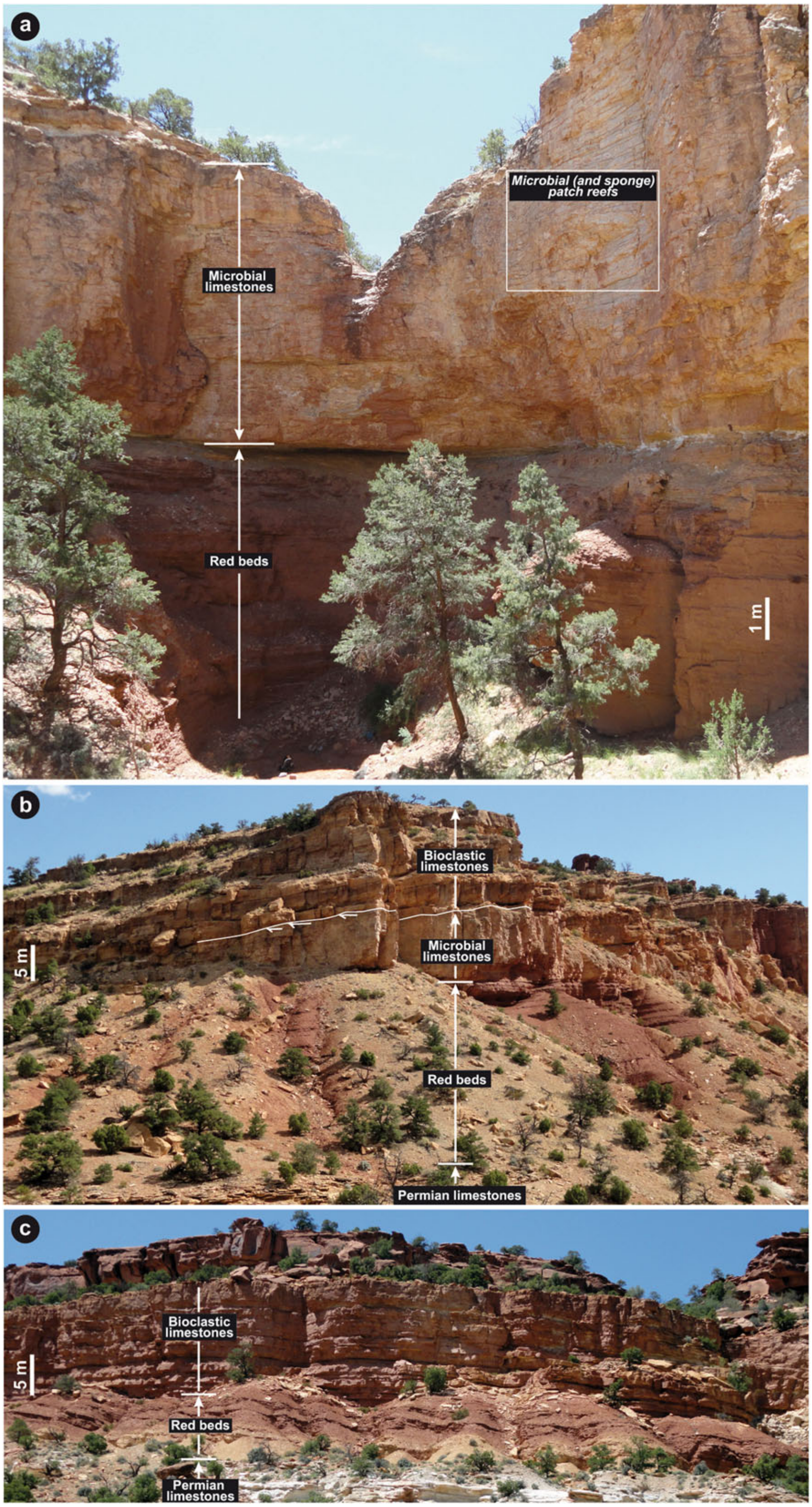

Figure 2. Field views of the three studied sections and their main lithological units. (a) Lower part of the French Fork section. Note the patchy morphology visible locally in the microbial unit. (b) Beas Lewis Flats section. Note the truncation surface at the top of the microbial limestone unit (white arrows: stratal terminations). (c) Pleasant Creek section. The microbial limestone unit documented both at French Fork and Beas Lewis Flats is absent here. This figure is available in colour online at wileyonlinelibrary.com/journal/gj

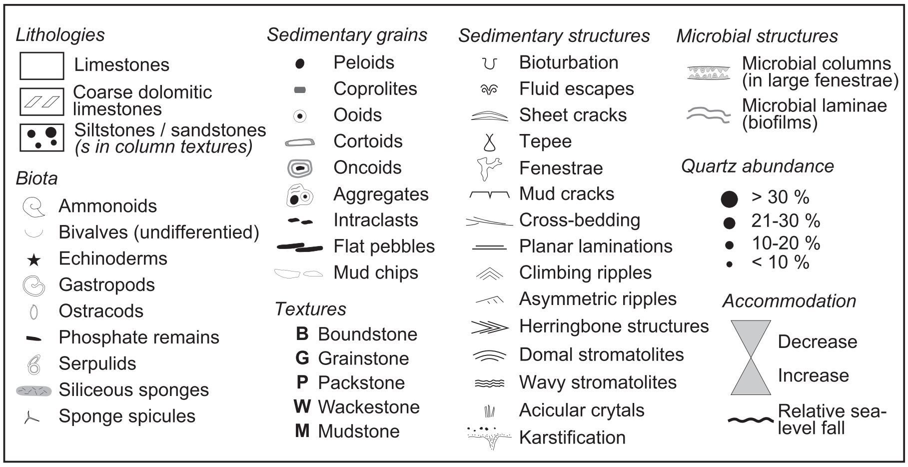

Figure 3. Legends for French Fork, Beas Lewis Flats and Pleasant Creek log sections.

Facies F3 corresponds to a massive peritidal limestone interval (Fig. 2a). Several undulating surfaces can be followed laterally along the cliff, permitting the identification of 6 m-scale subunits (Fig. 4). These subunits consist of cm- to dm-thick beds that show important lateral variations in thickness. These variations tend to form local metre-scale patches (Figs. 2a and 5a and b). In greater detail, two main subfacies can be identified at French Fork (Fig. 5c and d). The first fenestral limestone subfacies (F3b) is made of fenestrae, oncoids, peloids, aggregate grains, and some ooids and cortoids. Locally, some undulating laminated crusts binding the different grains are present (Fig. 5e and f). The sizes of the fenestrae are classically mm-scale, but some can be coalescent and form dm-scale aligned structures (Fig. 6a and d). Within these large fenestrae, microbialitic crusts are observed on the walls and roofs of the cavities with upward and downward growth direction (Fig. 6b and c, e). The relatively poor fauna is composed only of gastropods, bivalves, ostracods and siliceous sponges (Fig. 6f). Some fenestrae exhibit vadose silts (Fig. 7c). The second subfacies (F3c) consists of laminated micrites with domal and horizontal sheet cracks, and tepee structures (Figs. 5g and h and 7d). Some stromatolites are also observed locally. The biota is sparse, consisting mainly of ostracods, gastropods, and siliceous sponges (Fig. 6g). Subfacies F3b and F3c can either be observed juxtaposed or superimposed (Fig. 7).

The third lithological unit, observed from 23 to 45 m, represents the upper Sinbad Formation. At French Fork, seven facies are identified in this uppermost lithological unit (Facies F5 and F8–F13; Fig. 4; Table 1). Facies F5 corresponds to dm- to m-thick intervals of dolostones with common cm-thick intercalations of siltstones and rare sandstones. Peloids and common-to-abundant subrounded quartz grains mainly represent non-biotic grains. This facies generally appears barren of organisms, but some ostracods and bivalve moldic voids can be observed. Evidence of infaunal activity is uncommon; only rare and localized trace fossils can be observed. Sedimentary structures are common and correspond to low-angle cross-laminations. Facies F8 consists of ooid-bioclastic grainstone, which is only observed in a thin interval between 27 and 27.5 m. Facies F9 corresponds to peloid-bioclastic grainstone, which is also only observed within a thin interval at the top of the section (close to 45 m). Facies F10 is more frequent within the section, consisting of a grainstone (locally packstone) made of abundant gastropods and bivalves. Dense, deep bioturbation can also be present, and trough cross-stratifications are common. Facies F11 consists of grainstone to packstone with bivalves, serpulids, rare echinoderm plates and peloids. This facies is only observed in the interval between 25 and 27 m in the section. Facies F12 is composed of a peloid-bioclastic packstone with abundant bivalves, gastropods, and echinoderm plates associated with some ammonoids and serpulids. This facies is observed at two intervals within the section (~35 m and 43.5 m). Facies F13 consists of a peloid-bioclastic wackestone to packstone. This intensely and deeply bioturbated facies is observed in two thin intervals within the section (~32 m and 37.5 m). Ammonoids are observed in three intervals within the third lithological unit (Fig. 4). *Meekoceras* is documented between 34.5 and 35 m in facies F12. The second main occurrence consists of *Guodunites* and *Churkites*, observed in facies F10 and F13, between 36.5 and 37.5 m. The uppermost occurrence of common *Anasibirites* and *Wasatchites* is observed in facies F10 between 41 and 42 m.

3.2. *Beas Lewis Flats section*

This section can be subdivided into four lithological units (Figs. 2b and 8). The first unit, which is beyond the scope

DOI: 10.1002/gj

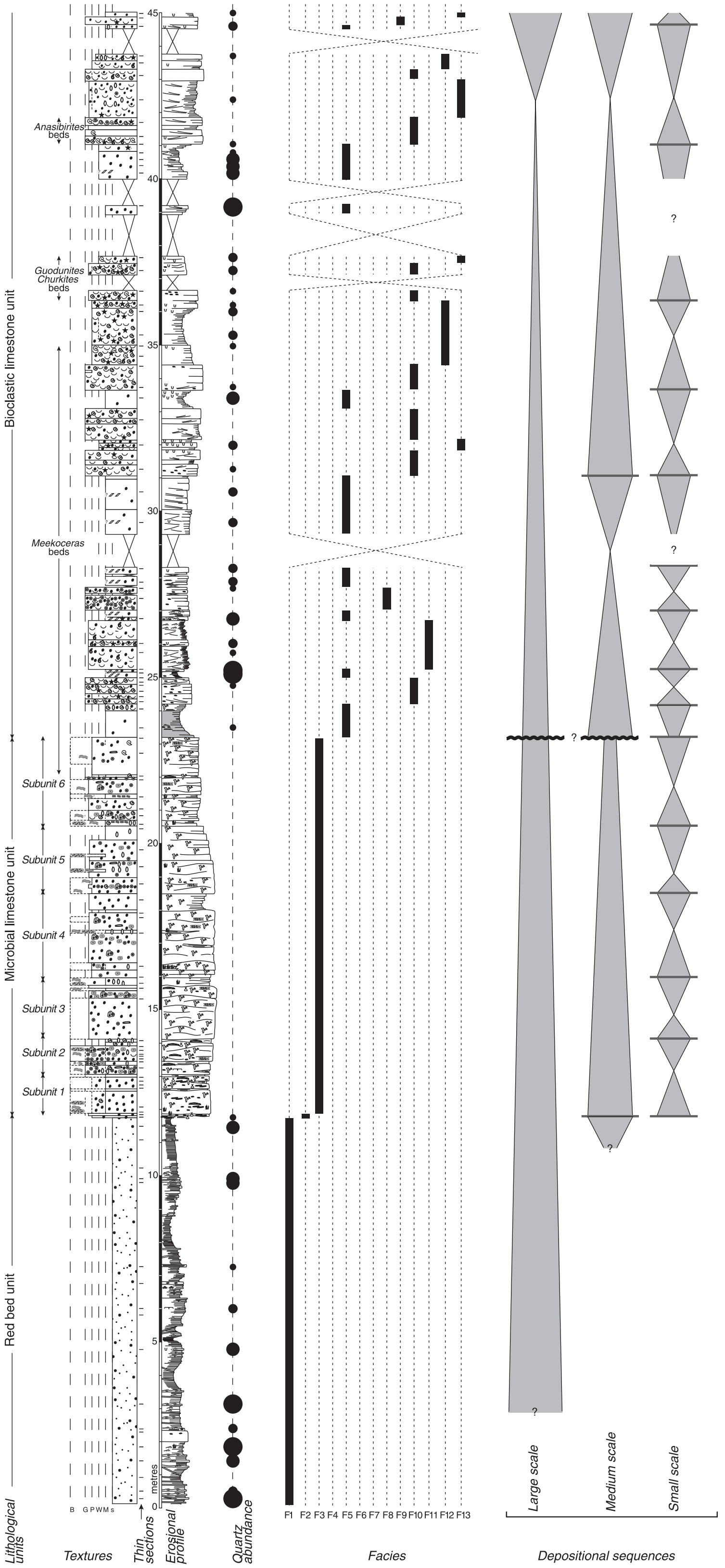

Figure 4. Log of the French Fork section including lithology, texture and relative abundance of quartz grains. Facies distribution and depositional sequence interpretation is also indicated. See Table 1 for facies descriptions and Figure 3 for legend.

DOI: 10.1002/gj

Table 1. Facies descriptions and depositional settings

Facies		Textures	Biotic/non biotic grains	Matrix/cements	Bedding/sedimentary structures	Zones	Environments
F1 Red beds		Dolosiltstones/ dolosandstones (conglomerates)	No biota Abundant quartz grains (subrounded to subangular), rare micas and some intraclasts (cm-scale sub-angular to sub-rounded mud chips and mud pebbles). Locally rare primary gypsum needles	Microdolomitic cement	Thin cm-thick (rarely dm-thick) beds. Asymmetrical ripples, climbing ripples, planar and crossed lamination. Tepees, convolutes and very rare and localized bioturbation in the transition beds to F3	Lower intertidal (to shallow subtidal)	Tidal flat
F2 Intraclastic limestones		F	Rare gastropods and siliceous sponge spicules Frequent cm-scale flat pebbles and subangular to subrounded intraclasts, common peloids, rare ooids and oncoids, aggregate grains. Presence of quartz grains and rare micas	Micritic matrix	Thin cm-thick beds with frequent basal erosive surfaces. Presence of tepees, desiccation cracks, fenestrae and few cm-scale stromatolitic domes. Bioturbation. Some crossed lamination and asymmetrical ripples	Subtidal to intertidal	Peritidal/ interior platform
F3 Peritidal limestones	F3a – Gastropod-rich	P (G/B)	Abundant gastropods, common ostracods and some siliceous sponges Abundant intraclasts and peloids	Micritic matrix, sparitic cement	Basal bed (cm-thick) intervals, lateraly discontinuous. Basal erosive surfaces. Some fenestrae, micritic geopetal filling of gastropod cavities	Subtidal to intertidal	Peritidal
	F3b – Fenestral	G/P/B	Rare gastropods, ostracods, siliceous sponges and bivalves Abundant oncoids, peloids, aggregate grains. Some ooids and cortoids	Peloidal micrite, sparitic cement	Cm- to dm-thick beds (strong lateral thickness variations). Abundant fenestrae and undulated laminated biofilms	Intertidal	
	F3c – Muddy sheet-cracked	M (W/B)	Rare ostracods, small gastropods and siliceous sponges Some intraclasts and mud flakes	Micritic matrix	Dm-thick beds. Laminations with tepee structures and sheet cracks. Some stromatolites, fenestrae and rare bioturbation	Intertidal to supratidal	
	F3d – Oo-pel-oncoidal	G	No biota Abundant peloids, oncoids and ooids	Sparitic cement	Microbial lamination. Some fenestrae	Subtidal gullies	
	F3e – Onco-fenestral	P/G (B)	Common gastropods, some serpulids and ostracods Abundant peloids and oncoids. Some ooids, aggregate grains and mud clasts	Micritic matrix, sparitic cement	Cm- to dm-thick beds. Cm- to dm-long fenestrae with internal stromatolitic crusts (with upward and downward growth) and stromatactis. Locally, microbial laminated biofilms	Subtidal	
F4 Stromatolitic beds		W/P	No biota Common peloids, some intraclasts	Clotted micritic matrix	Undulated and domal microbial laminations. Tepee structures and fenestrae	Intertidal (supratidal)	Interior platform (tide dominated)
F5 Dolostones		M/W	Rare bivalves, gastropods and ostracods, often as moldic voids. Rare echinoderms Rare to common, locally abundant, quartz grains (sub-rounded to sub-angular). Some intraclasts, mud flakes and peloids. Rare micas	Microdolomitic matrix or cement	Dm- to m-thick intervals of dolostones with cm-thick intercalations of siltstones (more rarely sandstones). Trough cross-stratification, horizontal to low angle planar lamination. Rare bioturbation	Subtidal to intertidal	

(Continues)

Table 1. (Continued)

Facies	Textures	Biotic/non biotic grains	Matrix/cements	Bedding/sedimentary structures	Zones	Environments
F6 Peloidal-intraclastic limestones	P/G	Common bivalves and presence of gastropods Abundant peloids and intraclasts, common cortoids, ooids and aggregate grains. Some oncoids. Rare quartz grains	Peloidal matrix and sparitic cement	Dm- to m-thick beds. Trough cross-stratification and asymmetrical ripples. Some bioturbation	Subtidal to intertidal channels	Tide-dominated shoal complex
F7 Intraclastic rudstone	R	Rare echinoderms (fragments) Common intraclasts (sub-rounded to sub-angular). Some lithoclasts, peloids and ooids	Dolomitized sparitic cement	Cm-thick beds. Asymmetrical ripples and planar horizontal lamination		
F8 Oo-bioclastic grainstone	G	Common bivalves and gastropods fragments Abundant ooids, some peloids and intraclasts, aggregate grains, oncoids, cortoids and mud flakes. Rare quartz grains	Sparitic cement (micrite matrix)	Dm-thick beds. Asymmetrical ripples and low-angle cross-stratification. Rare bioturbation	Subtidal bars	
F9 Pel-bioclastic grainstone	G	Abundant bivalve fragments, some gastropods and rare echinoderms Abundant peloids. Some ooids, oncoids, cortoids and intraclasts	Sparitic cement (micrite matrix)	Cm- to dm-thick beds. Asymmetrical ripples and low-angle cross-stratification. Rare bioturbation		
F10 Bioclastic grainstone	G (P)	Abundant bivalves and gastropods. Common echinoderms (fragments) and some serpulids and ammonoids Common peloids and micritic intraclasts. Rare ooids and phosphate grains. Presence of quartz grains	Sparitic to microsparitic cement (peloidal matrix)	Cm- to dm-thick beds. Trough cross-stratification, small asymmetrical ripples. Bioturbation is present		
F11 Bivalve-rich limestones	P/G	Abundant bivalves. Some serpulids, rare gastropods and echinoderms Abundant peloids. Rare intraclasts and phosphate grains. Common sub-rounded quartz grains	Sparitic cement and micritic (peloidal) matrix	Cm- to dm-thick beds. Trough cross-stratification, small asymmetrical ripples. Bioturbation is rare to present		
F12 Bioclastic packstone	P	Abundant bivalves, gastropods and echinoderms. Some ammonoids, serpulids and siliceous sponges Common peloids. Some phosphate grains. Quartz grains are common	Micritic matrix, and locally sparitic cement	Cm-thick beds. Trough cross-stratification, small asymmetrical ripples, horizontal to low-angle oblique planar lamination. Common bioturbation	Inner- to mid-shelf transition	Open wave-dominated marine setting
F13 Peloidal-bioclastic limestones	W/P	Common bivalves. Some serpulids, echinoderms, ammonoids, gastropods and siliceous sponges (cf. Dean, 1981) Common peloids, some intraclasts. Common quartz grains, rare micas and very rare detrital dolorhombs	Micritic matrix	Cm-thick beds. Rare trough cross-stratification and asymmetrical ripples. Intense bioturbation	Mid shelf	

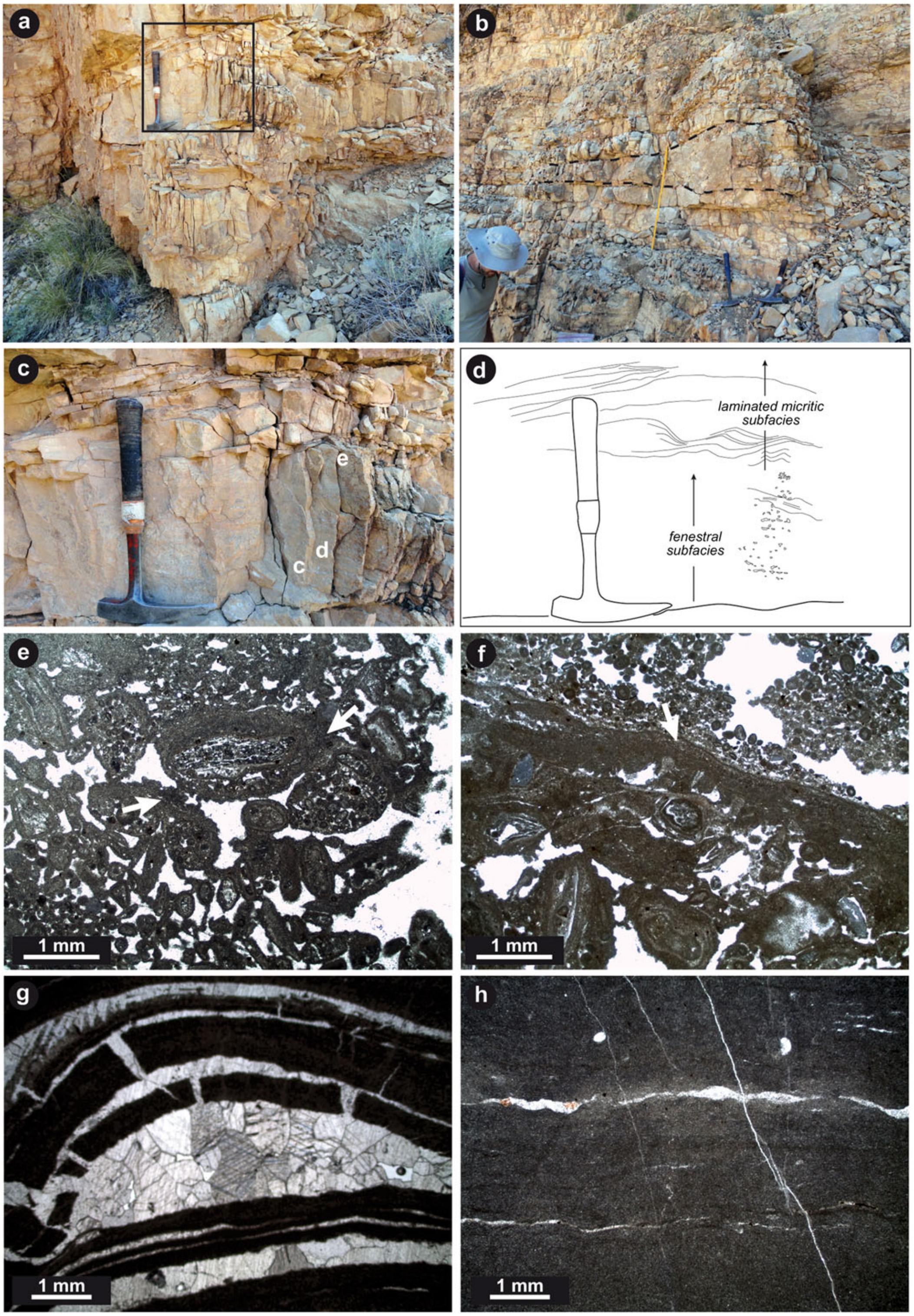

Figure 5. (a) and (b) Field views of the bedding stacking pattern of the microbial limestone unit in the French Fork section. In (a) the black window represents photograph in (c) hammer scale is 32 cm. Some beds show important lateral thickness variations (dashed lines in b) generating dm-patch reef morphologies. (c) and (d) Field view and sketch of a bed that displays a lateral thickness variation in the microbial limestone unit at French Fork. Note that this bed can be subdivided into two subunits: a lower part made of a fenestral limestone subfacies (F3b) and an upper part made of a laminated mudstone subfacies (F3c). (e) Oncoid–ooid–peloidal–intraclast grainstone with fenestrae (F3b). Note the laterally discontinuous stromatolitic crusts that coated some grains (white arrows). (f) Microbial laminae or crusts (F3b; white arrow). (g) Large domal spar-filled sheet cracks (F3c). (h) Mudstone with sparse and laterally discontinuous horizontal cracks, small gastropods and ostracods (F3c). This figure is available in colour online at wileyonlinelibrary.com/journal/gj

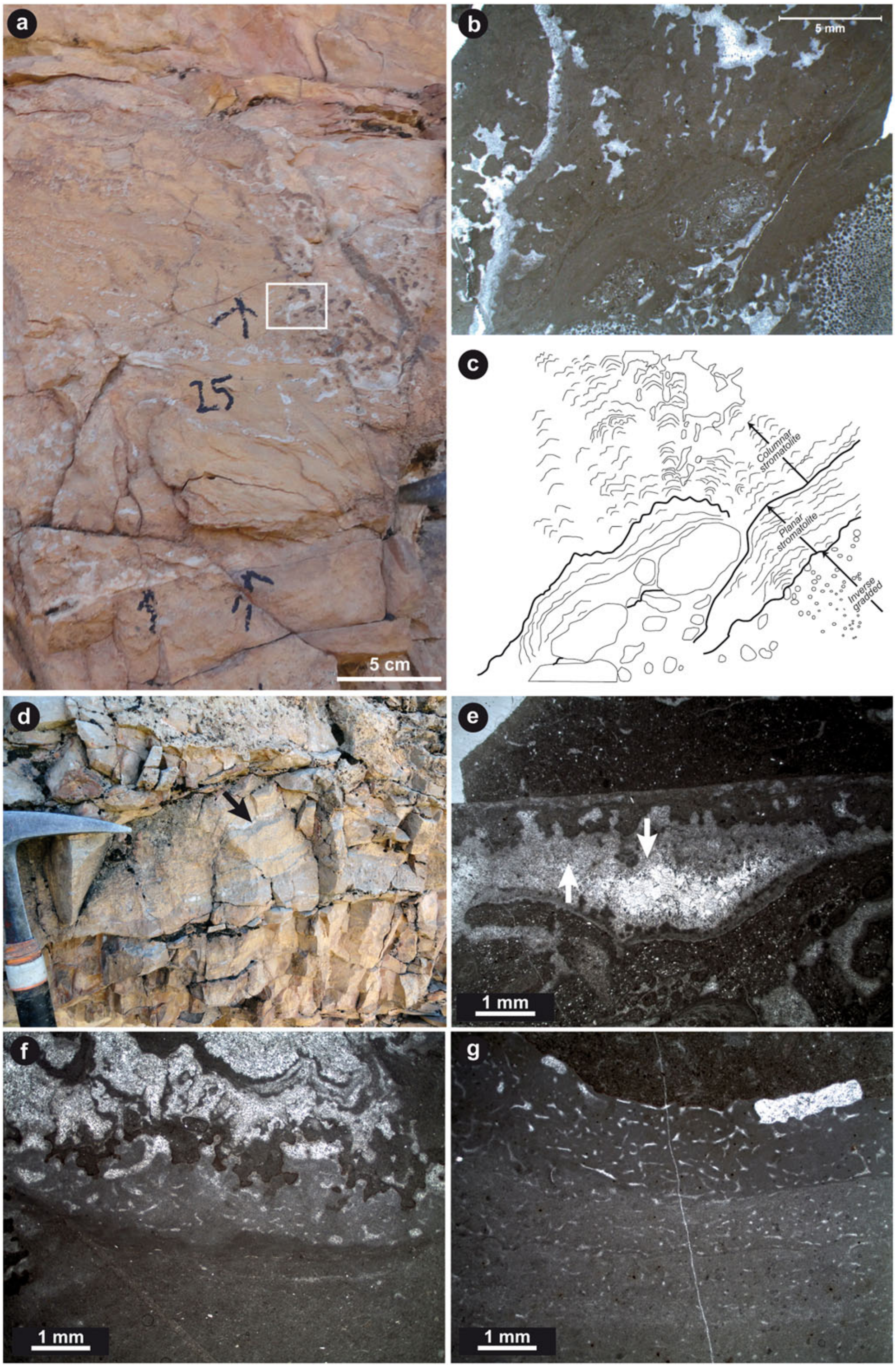

Figure 6. (a) Field view of a fenestral-rich bed in microbial limestone unit at French Fork. (b) and (c) Thin section and sketch of microbial crusts (both planar and columnar) in a large fenestrae illustrated in (a) (white window). Note that planar stromatolites bind an oolitic grainstone or an oncolitic floatstone and are overlain by columnar stromatolites, which exhibit an upward growth direction inside the fenestrae. (d) Field view of large fenestrae (black arrow) in a bed of the microbial limestone unit at French Fork. (e) Thin section of large fenestrae with downward and upward microbial growth (white arrows). (f) and (g) Siliceous sponges in the microbial limestone unit at French Fork section. (f) Sponge in the fenestral limestone subfacies (F3b). The sponge is partially dissolved and replaced by a cavity infilled by microbes and cements. (g) Sponge in the laminated mudstone subfacies (F3c). This figure is available in colour online at wileyonlinelibrary.com/journal/gj

DOI: 10.1002/gj

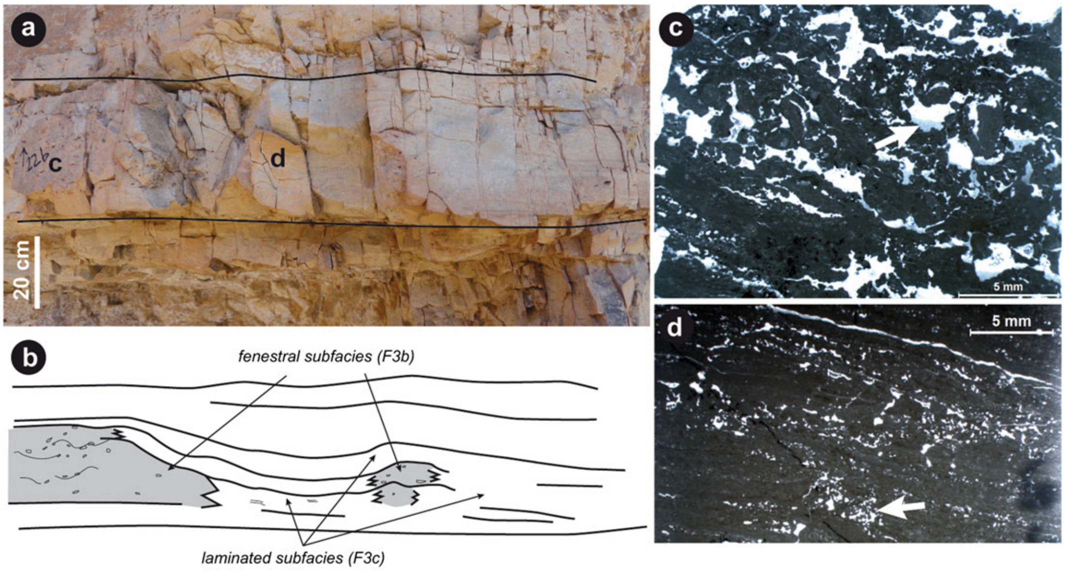

Figure 7. (a) and (b) Lateral facies variations observed in a bed of the microbial limestone unit at French Fork. (c) Fenestral limestone subfacies (F3b). Note the internal vadose silts preserved in some fenestrae (white arrow). (d) Laminated facies (F3c) with local small fenestrae and tepee structures (white arrow). This figure is available in colour online at wileyonlinelibrary.com/journal/gj

of this work, corresponds to the Permian bioclastic and bioturbated limestones of the Kaibab Formation. The base of the section displays a 20 m-thick interval composed mainly of dolomitized and silicified limestones. Only the uppermost 7 m of this lithological unit are illustrated in Figure 8. An intense bioturbation emphasized by silicification is recorded in these Permian limestones. Two bioclastic-rich intervals with cross bedding are observed at about 15 m above the base of the section. These Permian limestones are also locally affected by intense karstification (Fig. 8).

The second lithological unit is 34 m thick and corresponds to the red beds of the Black Dragon Formation. These red beds (Facies F1) are similar to those observed at the base of the French Fork section. The Beas Lewis Flats section exhibits a progressive transition between the second and the third lithological units.

The ~6 m-thick third lithological unit corresponds to the massive peritidal limestones (F2 and F3) of the lower Sinbad Formation. This unit is only half as thick as corresponding beds in the French Fork section; it does not exhibit conspicuous m-scale patchy microbial structures. It can be subdivided into three subunits (Fig. 8). The basal subunit (between 53.5 m and 56 m) includes the first limestone beds that interfinger with the dolosiltstones (F1) of the red bed unit. These uppermost red bed intercalations are notably richer in micritic intraclasts. This first subunit is comprised of floatstone with some localized small cm- to dm-large domal stromatolites (F2; Figs. 9a and 10). Rare gastropods and siliceous sponges also occur. Additionally, even though burrows could not be clearly identified, the distribution of sedimentary grains tends to record an apparent infaunal activity. The second subunit (between 56 m and 58.5 m) corresponds to relatively well-bedded limestone (F3), including three main subfacies (F3a–c; Fig. 10). Each bed exhibits a basal part with abundant gastropods (F3a; Figs. 9b and 11). This subfacies can also be rich in intraclasts and it also includes some rare siliceous sponges (Fig. 10k–m). The middle part of these beds corresponds to fenestral limestone subfacies (F3b; Figs. 10h–j and 12), and the upper part displays laminated mudstones with sheet cracks (F3c; Figs. 10e–g and 11). The third subunit (between 58.5 m and 60 m) consists of oncoid-fenestral limestones (F3e) with abundant peloids and some ooids, aggregate grains, gastropods, serpulids and ostracods (Fig. 10b–d). This subfacies is characterized by large fenestrae that display internal stromatolites with upward and downward growth.

The fourth lithological unit of the Beas Lewis Flats section is characterized by a succession of dolostone intervals (F5) with various bioclastic, oolitic or peloidal limestones (F6–F10, F12 and F13). This bioclastic limestone unit comprises the upper 30 m of the section. From 61.5 to 65 m, two m-thick beds correspond to a peloid-intraclastic grainstone (F6). From 65 to 69.5 m, ooid-bioclastic grainstone (F8) and peloid-bioclastic grainstone (F9) are particularly well represented, interfingering with thin intervals of dolostones (F5). At about 70 m, a thin dm-thick interval of intraclastic grainstone (F7) is observed, in which subangular to angular limestone intraclasts are associated with well-rounded lithoclasts. The first occurrence of peloidal and bioclastic wackestone (F13) is documented above this intraclastic

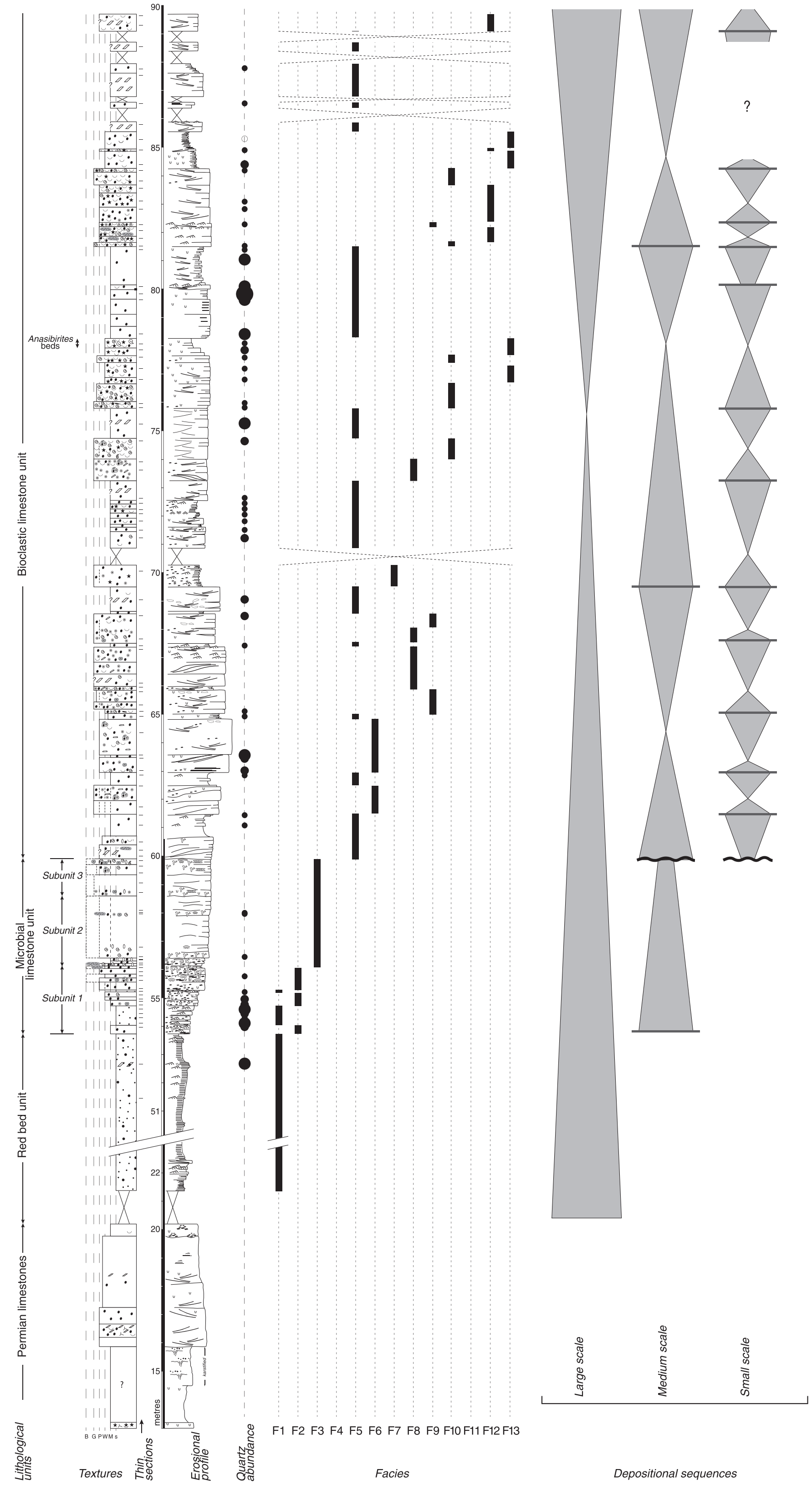

Figure 8. Log of the Beas Lewis Flats section including lithology, texture and relative abundance of quartz grains. Facies distribution and depositional sequence interpretation is also indicated along the section. See Table 1 for facies descriptions and Figure 3 for legends.

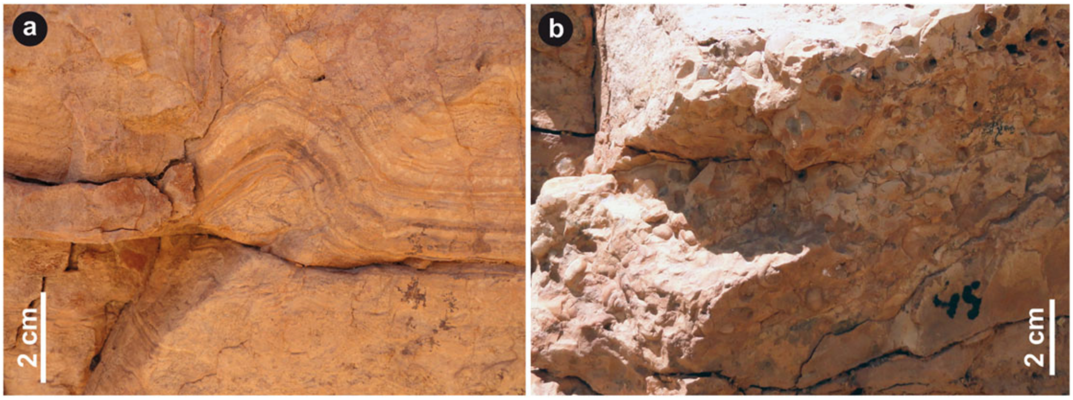

Figure 9. Field views of (a) a cm-scale domal stromatolite (55.6 m, F2, subunit 1) and (b) subfacies F3a with dense accumulation of gastropods (56.1 m). Beas Lewis Flats section. This figure is available in colour online at wileyonlinelibrary.com/journal/gj

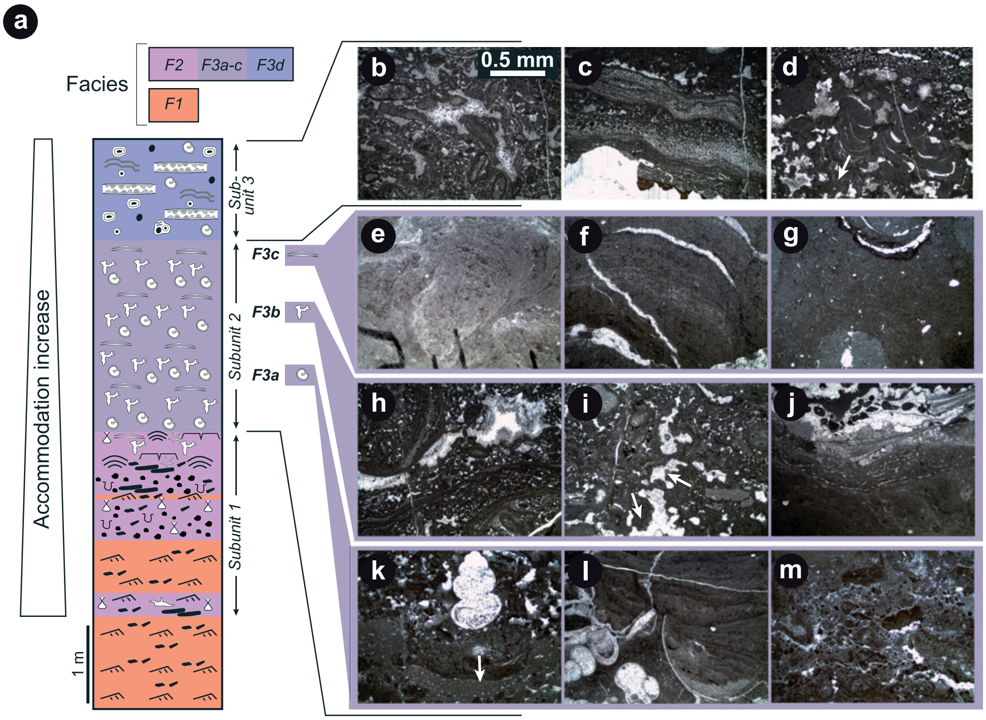

Figure 10. Schematic evolution of the main facies types in the microbial limestone unit at Beas Lewis Flats. (a) Synthetic log of the microbial limestone unit (F3) subdivided into three subunits. Each bed of the second subunit (see Figures 8, 11) includes a succession of the three subfacies (F3a–c). (b–d) Subfacies F3e, subunit 3. (b) Peloidal, oncoidal, fenestral fabric. (c) Stromatolitic crust showing the alternation of thin dark microbial lamina with ooid–peloidal grainstone. (d) Downward growth of stromatolitic columns with horizontal cracked lamina at the roof of large fenestrae. (e–g) Subfacies F3c, subunit 2. (e) Small columnar to domal stromatolite. (f) Domal muddy sheet cracks. (g) Micrite with gastropods and ostracods. (h–j) Subfacies F3b, subunit 2. (h) Peloid–oncoid–ooid–fenestral grainstone intervals coated with thin microbial lamina. (i) Irregular fenestrae with downward and lateral microbial growth. (j) Subfacies F3c with micrite, ostracods and siliceous sponge (lower-half thin section) and subfacies F3b with peloidal–fenestral fabric (upper-half thin section). (k–m) Subfacies F3a, subunit 2. (k) Siliceous sponge (white arrow) overlains by gastropod-rich subfacies F3a. (l) Gastropod-rich subfacies F3a directly overlays by planar stromatolites. (m) Intraclastic deposits in subfacies F3a. All thin section illustrations have similar scale bar to (b). This figure is available in colour online at wileyonlinelibrary.com/journal/gj

interval. From 74 m, dolostone intervals interfinger with bioclastic limestone beds of facies F10, F12 and F13. At about 78 m, specimens of the ammonoid *Anasibirites kingianus* are observed in a thin dm-thick interval within facies F13.

3.3. *Pleasant Creek section*

The Pleasant Creek section is subdivided into three lithological units (Fig. 12). Permian limestones of the Kaibab Formation are visible within a 15 m interval at the base of the

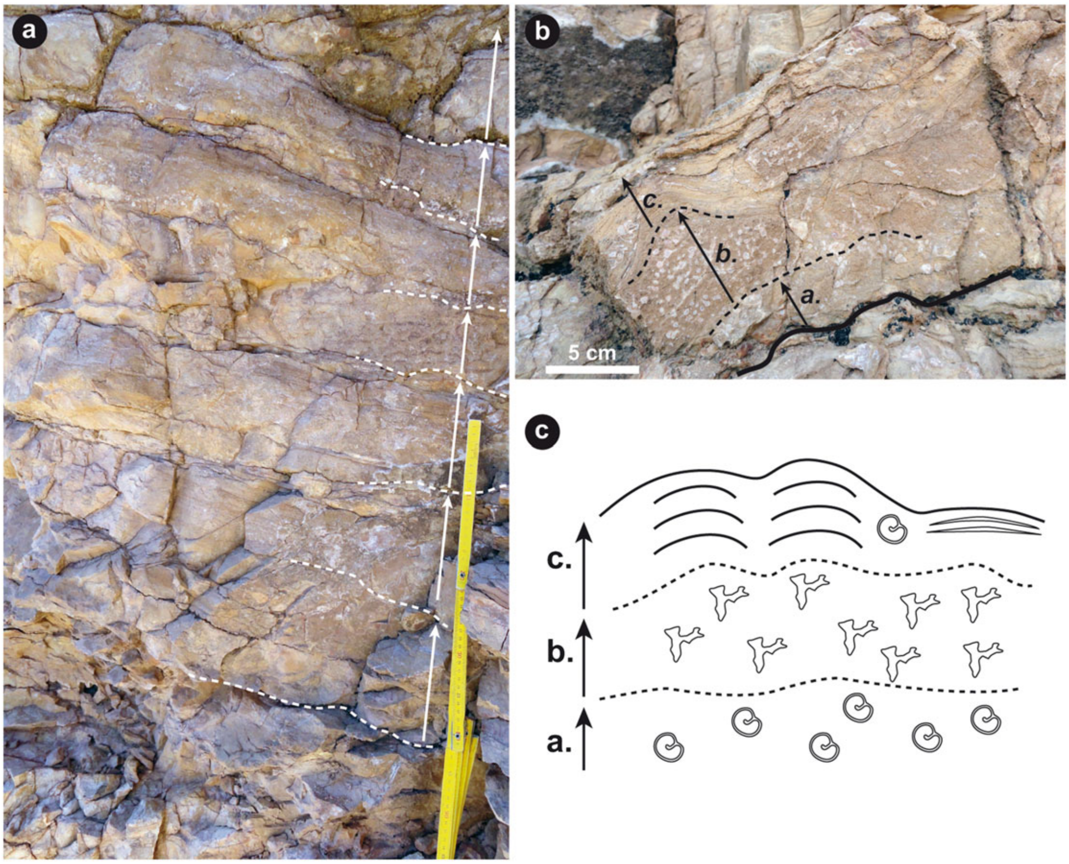

Figure 11. Bed stacking pattern of the microbial limestone unit (subunit 2) at Beas Lewis Flats. (a) Field view of several dm-thick beds displaying similar internal organization. (b) and (c) Field view and schematic sketch of a bed-scale depositional sequence. a.: gastropod-rich basal interval (F3a); b.: fenestral-rich intermediate interval (F3b); c.: Mud sheet crack or stromatolite upper interval (F3c). This figure is available in colour online at wileyonlinelibrary.com/journal/gj

section (Fig. 2c). These limestones are strongly dolomitized and no fossil grains could be identified. Nonetheless, some sedimentary structures are still recognizable, such as abundant planar laminations, small asymmetrical ripples, and some trough cross-bedding.

Above a stratigraphic gap of 5 m, a 15 m-thick red bed unit of the Black Dragon Formation is documented. The uppermost part of this unit corresponds to F1 that displays frequent conglomeratic intervals. Some tepee structures and desiccation cracks are also observed.

The third lithological unit corresponds to the bioclastic limestone unit of the upper Sinbad Formation. The thick microbial limestone unit of the lower Sinbad Formation observed at French Fork and Beas Lewis Flats is therefore not recorded at Pleasant Creek. In the basal 5 m, several intervals of intraclastic limestone (F2) are interfingered with dolostones (F5). At 38.5 m, a dm-thick bed exhibits domal stromatolites (F4; Fig. 13a). Microscopically, these stromatolites consist of dense micritic laminae, which sometimes reveal desiccation cracks, alternating with fenestral laminae (Fig. 13b). From 40 to 45 m, dolostones (F5) are interfingered with dm- to m-thick peloidal-intraclastic limestones (F6). These beds display internal cross bedding, frequent mudclasts, and important changes in lateral thickness. A second occurrence of intraclastic limestones (F2) and stromatolites (F4) is recorded between 45 m and 46 m. In this case, the stromatolitic interval can be subdivided into a lower bed characterized by dm-scale wavelength domal stromatolites and an upper stratiform bed displaying a wavy laminated structure (Fig. 13c). Microscopically, these wavy microbial carbonates are comprised of an alternation of dense micritic laminae with clotted laminae (Fig. 13d).

The rest of the section is characterized by a succession of dolostones (F5) with various bioclastic, ooidal, and peloidal limestones. From 46 m to 48 m, a thick ooid-peloidal grainstone (Facies F8) displays herringbone cross-stratification in its uppermost part (Fig. 13e). It is characterized by well-sorted ooids associated with some gastropods (Fig. 13f). From 49.5 m to 52.5 m, the section displays an

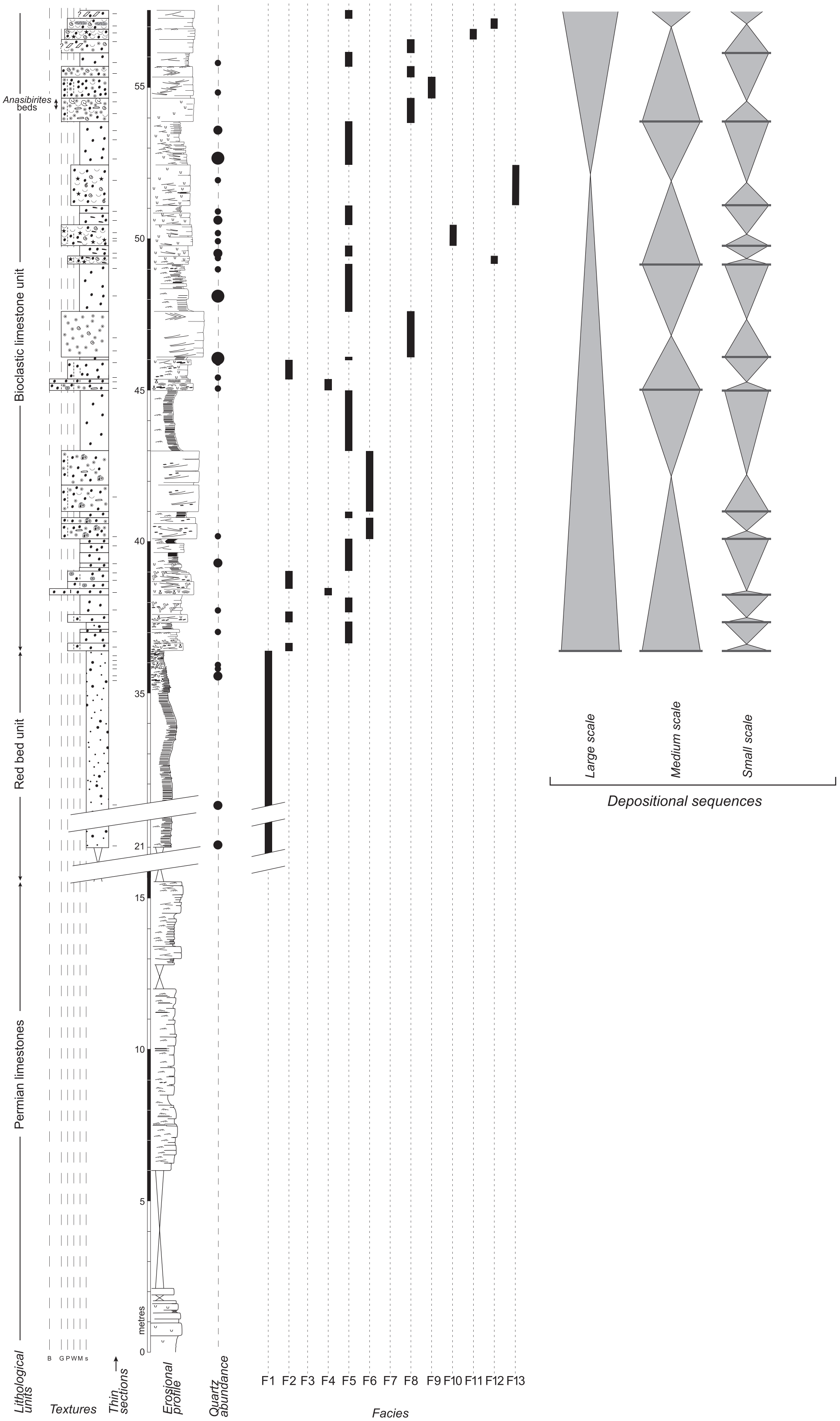

Figure 12. Log of the Pleasant Creek section including lithology, texture and relative abundance of quartz grains. Facies distribution and depositional sequence interpretation is also indicated along the section. See Table 1 for facies descriptions and Figure 3 for legends.

DOI: 10.1002/gj

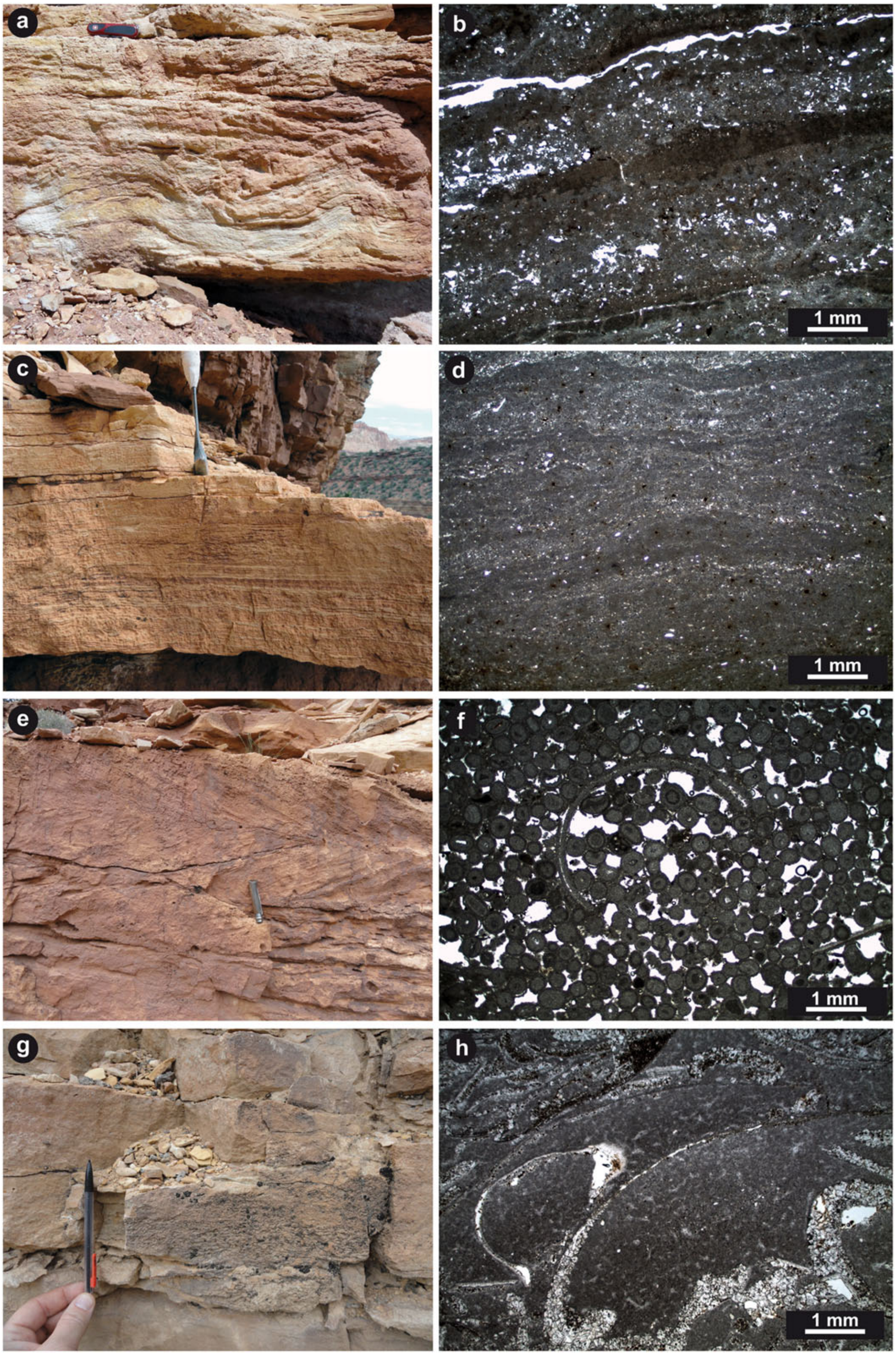

Figure 13. Field views and thin section illustrations of microbialites observed in the upper Sinbad Formation at Pleasant Creek. (a) Dm-scale domal stromatolites (F4 at around 38.5 m in Figure 12). (b) Laminated microfabric of stromatolites illustrated in (a). (c) Laminated wavy structures in a dm-thick microbialitic bed (F4 at 45 m in Fig. 14). (d) Laminated microfabric of stromatolites illustrated in (c). (e) Field view of bidirectional cross bedding in oolitic grainstone (F9) in the upper Sinbad Formation. (f) Thin section of oolitic grainstone (F9) with gastropods. (g) Field view and (h) thin section of a peloidal and bioclastic packstone (F13) with bivalves that display umbrella structures with underlying siliceous sponges. Pleasant Creek section. This figure is available in colour online at wileyonlinelibrary.com/journal/gj

interval characterized by an alternation of dolostones (F5) with bioclastic facies (F10, F12, and F13). This interval is notably characterized by its intense bioturbation and the presence of echinoderm fragments (Fig. 12; Table 1). At about 55 m, an oolite-rich bed (F8) contains abundant *Anasibirites kingianus*. In the uppermost part of the section (at 57 m), some cm-scale beds with basal erosive parts are particularly rich in bivalves (F11 and F12; Fig. 13g) that exhibit siliceous sponges under their disarticulated valves (Fig. 13h).

4. FACIES MODELS AND DEPOSITIONAL ENVIRONMENTS

For the studied stratigraphic interval, the 13 identified facies can be placed into two facies models (Fig. 14; Table 1). The first model is characterized by the red beds (F1) of the Black Dragon Formation and the microbial limestones (F2 and F3) of the lower Sinbad Formation (Fig. 14a). Progressive gradation between the red bed deposits and the microbial limestones observed in the Beas Lewis Flats section supports a common facies model for these deposits. Previous workers mentioned the vertical interfingering between the Black Dragon red beds and the Sinbad carbonates (Blakey, 1974, 1977; Dean, 1981; Goodspeed and Lucas, 2007). Red beds may have originated in various depositional environments such as marginal marine, deltaic, and coastal plain settings (Voigt *et al.*, 2013; Thomson and Lovelace, 2014). In this first depositional model, the red beds display both cm-scale planar- or ripple-bedding structures and climbing ripples that are consistent with a tide-dominated setting. Rippled siltstones and fine sandstones are interpreted as deposits of

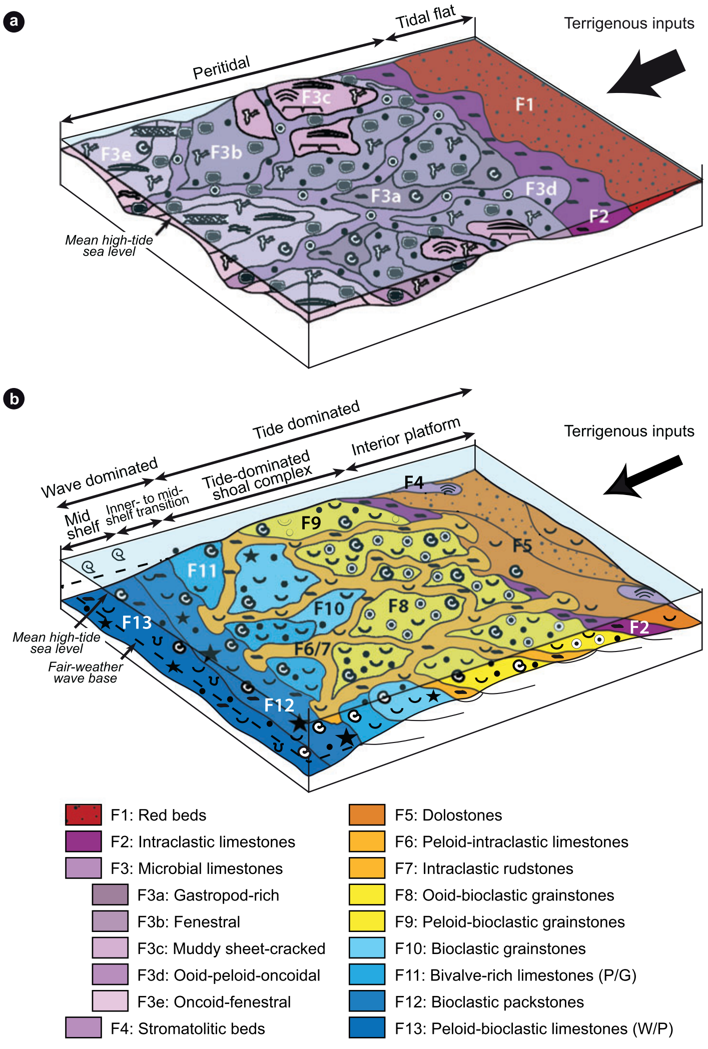

Figure 14. Depositional models (a) for the red beds of the Black Dragon Formation and microbial limestone unit of lower Sinbad Formation (middle Smithian) and (b) for the bioclastic limestone unit of the upper Sinbad Formation (late middle to late Smithian). See Table 1 for facies description and Figure 3 for legends. This figure is available in colour online at wileyonlinelibrary.com/journal/gj

DOI: 10.1002/gj

the lower intertidal (low tidal flats) to shallow subtidal zone, where bedload transport occurs during moderate tidal activity (Alam, 1995). The paucity of tidal channels in the red beds can be considered as an evidence of a low palaeotidal range (Walker and Harms, 1975). It may also indicate a gentle palaeoslope, such as a low gradient inner shelf or embayment, in which the tidal currents were not strong enough to develop tidal channels (Alam, 1995). Limestones (F2 and F3) of the lower Sinbad Formation represent a facies association interpreted as peritidal, which formed in environments around the tidal zone (Wright, 1984; Flügel, 2004). The rarity of siliciclastic grains suggests a position still under terrigenous influence, but sufficiently removed from the terrigenous sources. *In situ* and reworked desiccation cracks observed in F2 provide evidence of at least temporarily emerged small islands. Small cm-scale stromatolitic domes observed locally in this facies highlight some zones of higher accommodation, also allowing for an infaunal activity. The peritidal limestones (F3) are subdivided into five subfacies (F3a–e; Table 1). These subfacies vary both laterally and vertically in the same bed, suggesting a patchy facies distribution (facies mosaic; Wright and Burgess, 2005; Strasser and Védrine, 2009). Gastropod-rich packstone (F3a), which show important lateral thickness changes, may represent winnowed subtidal skeletal deposits in zones of gently sloping gully surfaces (Fig. 14a). These gastropods can also be found in the margin of small ponds that merged with surrounding intertidal flats (Shinn, 1969). The fenestral limestones (F3b) are the most common deposits of the peritidal facies association and represent supratidal or intertidal sediments (Shinn, 1968). With biofilms that coated numerous fenestrae and diverse grains, this subfacies commonly developed a small synoptic relief above the sea floor. Vadose silts observed in some fenestrae are consistent with areas intermittently exposed at the time of deposition. Mudstone deposits (F3c) with sheet-cracks, a restricted fauna (ostracods and gastropods), and some stromatolites reflect supratidal to intertidal low-energy settings. Ooid–oncoid–peloidal grainstone (F3d) was deposited in subtidal high-energy gullies. The latter may have enhanced the patchy geometry of these peritidal deposits. Large sheet-like fenestrae limestones with oncoids and sparse ooids (F3e) are interpreted to reflect more distal shallow subtidal settings. The presence of siliceous sponges and gastropods in these peritidal limestones (F3) is also indicative of marine conditions and thus, of a seaward position of the lower Sinbad limestones as compared to the red beds of the Black Dragon Formation.

The second facies model is characterized by deposits of the bioclastic limestone unit (i.e. the upper Sinbad Formation; Fig. 14b). The 11 facies included in this model can be grouped into three facies associations typical of the following three different depositional settings: (i) tide-dominated interior platform; (ii) tide-dominated shoal complex; and (iii) open wave-dominated marine platform. Dolostones (F5) represent internal muddy and low-energy depositional settings, recording variable amount of terrigenous inputs. It differs from the red beds (F1) by recording obvious marine influences shown by the presence of bivalves, gastropods and echinoderm plates. These dolostones are consistent with deposition on a vast interior platform or a large embayment system. Stromatolites made of small domes and wavy laminated structures (F4) may have formed in upper intertidal and supratidal zones within this interior platform. Ooid-bioclastic grainstone with some bivalves (F8) is probably indicative of stronger tidal currents, and possibly wave action that impacted the shoal complex area. As observed on both the ocean-ward and platform-ward sides of the oolitic shoal, the peloid-bioclastic grainstone with bivalves and sparse ooids (F9) logically points to less vigorous tidal currents. Well-marked herringbone cross-stratifications observed in these shoal deposits (F8 and F9) indicate a tide-dominated process. Intraclastic rudstone (F7) and peloid-intraclastic limestones (F6) were deposited in channels that cut across the shoal. Seaward of the tidal-dominated shoal complex, sediments may have evolved from peloidal and ooidal sands into a mixture of skeletal (gastropods, bivalves, serpulids and echinoderms) and peloidal sands (Halley *et al.*, 1983, p. 472). More abundant bioclasts recorded in grain-supported sediments (F10 and F11) may have been deposited on the seaward side of the tide-dominated shoal complex. An inner- to mid-shelf transition zone is marked by the deposition of bioclastic packstone (F12). Mud-supported texture and intense bioturbation that characterize peloidal-bivalve wackestone (F13) indicate deposition below the fair-weather wave base in an offshore position. The record of vertically oriented bivalves in F12 and F13 suggests local turbulent and rotary flows during storms (Pérez-López and Pérez-Valera, 2011). The frequent record of ammonoids in these facies also confirms an open-ocean influence. Thus, in a large embayment system, the shoal complex can be considered as tide dominated, even if its seaward margin was impacted by open-sea waves.

5. SECTION CORRELATION AND DEPOSITIONAL SEQUENCES

The only previous attempt to correlate sections in the Torrey area was largely based on a lithostratigraphic approach (Dean, 1981). For the herein studied sections, age assignments are nevertheless possible owing to conodont and ammonoid occurrences. Conodonts from the base of the upper Sinbad Limestone at French Fork yield a Smithian age. However, no definite conodont zonation and correlation are possible between the French Fork, Beas Lewis Flats and Pleasant Creek sections. Therefore, the record of the *Anasibirites* fauna within dm-scale levels in the upper part of these three sections is the only correlation timeline available within the Torrey area (Fig. 15). Based on these *Anasibirites* beds, it is possible to recognize distinct hierarchical stacking patterns and facies evolution in the sedimentary succession, thus allowing for the identification of large-, medium-, and small-scale depositional sequences. At each hierarchical level, the facies evolution of depositional sequences generally indicates deepening and shallowing trends defined by transgressive surfaces (Strasser *et al.*, 1999).

The Black Dragon and Sinbad formations reflect a large-scale depositional sequence, which is similar to the facies evolution previously described in the San Rafael Swell area (Goodspeed and Lucas, 2007). The Black Dragon red beds, which represent clastic tidal-flat deposition (Blakey, 1974), mark the beginning of the transgressive trend. Maximum accommodation corresponds to the *Anasibirites* beds observed in the uppermost Sinbad Formation. The sequence boundary may either be at the top of the Sinbad Formation or in the lower part of the Spathian Torrey Formation, in agreement with the interpretation of Goodspeed and Lucas (2007).

Five medium-scale sequences are identified (S.I–V; Fig. 15). The first sequence is initiated at the top of the Permian limestones, but no clear facies evolution can be observed in the dolosiltstones of the red beds. The second medium-scale depositional sequence is well visible at French Fork and Beas Lewis Flats. Intraclastic limestones (F2) observed at the base of the microbial unit of the lower Sinbad

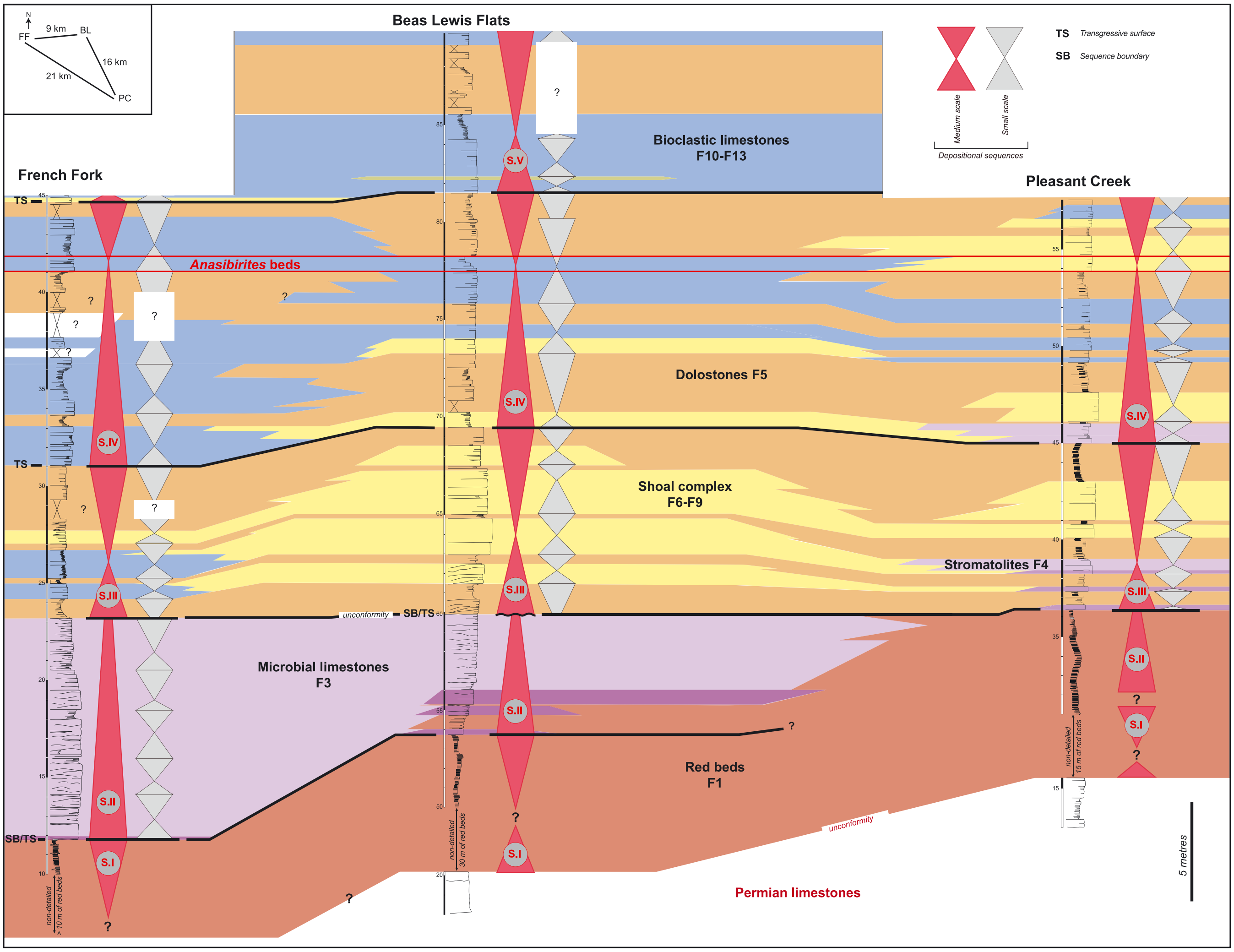

Figure 15. Correlation of the French Fork, Beas Lewis Flats and Pleasant Creek sections illustrating the general facies architecture of the Torrey area during the Smithian. S.I to S.V: medium-scale depositional sequences. This figure is available in colour online at wileyonlinelibrary.com/journal/gj

Formation mark the transgressive interval of this second medium-scale depositional sequence. The sparse ammonoid record at French Fork and the presence of large fenestrae and oncoids (F3e) in the uppermost part of the microbial limestone unit at Beas Lewis Flats underline the maximum flooding interval (Figs. 4 and 8). This second depositional sequence is more difficult to observe at Pleasant Creek, where the microbial limestone unit is absent (Fig. 15). The progressive decrease in thickness of the microbial limestone unit between French Fork and Beas Lewis Flats and its absence in Pleasant Creek is consistent with a general retrogradational pattern of this facies towards the southeast (Dean, 1981). The erosional surface at the top of the microbial limestone unit at Beas Lewis Flats marks the sequence boundary of this second medium-scale sequence. The remaining three medium-scale depositional sequences are characterized by a facies evolution with deepening-shallowing trends marked by a complex interplay between lower shoreface, shoal, and tidal flat deposits. Thus, the third medium-scale sequence displays a basal transgressive interval, well recorded at Pleasant Creek with stromatolitic (F4) and intraclastic (F2) deposits. The progressive incursion of seaward bioclastic shoal deposits at French Fork and of shoal complexes at Beas Lewis flats is consistent with a deepening trend. The maximum flooding interval is marked by the presence of subtidal bars made of bivalve-rich limestones (F11) at French Fork, allowing the accumulation of thick ooidic shoal deposits at Beas Lewis Flats. A thick interval of interior platform dolostones (F5) underlines the progradational trend at the end of this third medium-scale sequence. During the initiation of the deepening trend of the fourth medium-scale depositional sequence, lower shoreface deposits with ammonoids are recorded at French Fork, whereas at Beas Lewis Flats, only a thin oolitic interval is observed. In a more proximal setting, stromatolitic (F4) and intraclastic (F2) deposits mark this transgressive interval at Pleasant Creek. The record of the *Anasibirites* ammonoid fauna in the three sections indicates the maximum flooding interval. The shallowing trend is characterized by the presence of ooidic shoal deposits in Pleasant Creek and then dolostones (F5), which are relatively thick at Beas Lewis Flats. The fifth medium-scale depositional sequence is well visible only at Beas Lewis Flats. Seaward bioclastic shoal deposits (F9–F12) mark the deepening trend. Offshore deposits (F13) underline the maximum flooding interval. The shallowing trend is evidenced by deposition of a thick interval of dolostones (F5), and the sequence boundary corresponds to the limit between the deposits of the Sinbad and Torrey formations.

Within such large- and medium-scale hierarchical stacking patterns, more than fifteen small-scale depositional sequences can be identified. In the middle Smithian microbial limestones of the French Fork section, five small-scale sequences can be recognized. Dm-thick intervals of thin laminated beds (F3c) or erosive surfaces delimit these sequences in which m-scale patch reefs developed (Fig. 2a). Such a stacking pattern is not observed at Beas Lewis Flats, where facies evolution reflects a medium-scale increase in accommodation (Figs. 8 and 10). With the change of depositional settings during the late middle to late Smithian (Fig. 14), small-scale sequences are marked by rapid facies shifts between offshore, shoal and interior platform deposits. In some intervals, correlation between these small-scale sequences is apparently possible, but for other intervals, their numbers and thicknesses differ greatly between the three studied sections, making their correlation difficult (Fig. 15).

Depositional sequences characterized by a facies evolution corresponding to the shortest recognizable cycle of environmental change are called elementary sequences (Strasser *et al.*, 1999). These elementary sequences, which generally correspond to one bed, are observed within 13 successive beds of the microbial limestone unit at Beas Lewis Flats (Fig. 11). Facies evolution of these elementary sequences involves a succession of gastropod-rich accumulations (F3a), fenestral limestones (F3b), and laminated mudstones (F3c; Fig. 11).

6. ORIGINS OF DEPOSITIONAL SEQUENCES

Global sea-level curves indicate a general rise during the Permian–Triassic transition (Haq and Al-Qahtani, 2005; Haq and Shutter, 2008). During this global trend, several world-wide localities record third-order sea-level cycles in Lower Triassic rocks (Embry, 1997; Vigran *et al.*, 1998; Lehrmann *et al.*, 2001, 2007a, 2007b). In the western USA basin, the Lower Triassic sedimentary succession records three third-order transgressive–regressive sequences, namely in the Griesbachian, Smithian and earliest-middle Spathian (Paull and Paull, 1993, 1997). In southern Utah, the Early Triassic transgression began in the early middle Smithian (Goodspeed and Lucas, 2007; Brayard *et al.*, 2013). The large-scale depositional sequence recognized in the Torrey area is consistent with this Smithian third-order sea-level cycle.

The medium-scale sequences can be correlated across the three studied sections. Indeed, they display relatively close bed-stacking patterns and facies evolution (e.g. the progressive retrogradation of offshore deposits in the bioclastic limestone unit; Fig. 15) that are congruent with a sea-level control. Based on published U/Pb ages and the comparison of average Smithian ammonoid zone durations inclusive of separation intervals (see Brühwiler *et al.*, 2010 for details), the Sinbad Formation likely represents a duration less than 490 kyr in the Torrey area. Thus, observed medium-scale depositional sequences may reflect the orbital cycle of eccentricity. The lack of a regressive trend in the second medium-scale depositional sequence coupled with the presence of a truncated surface at the top of the microbial limestone unit of the lower Sinbad Formation is consistent with a sudden drop in sea level, which may have a tectonic origin. A regional tectonic uplift probably related to the Sonoma Orogeny (Collinson *et al.*, 1976) has also been identified at the top of fenestral–microbial limestones of the Sinbad Formation in southwest Utah (Olivier *et al.*, 2014). Additionally, a local inherited topography at the top of the microbial limestone unit may also explain the formation of a thick ooidic shoal system in the Beas Lewis Flats area.

The origin of small-scale sequences is often more difficult to assess because autocyclic processes inherent in the depositional system also played a role in their formation (Strasser *et al.*, 2012). These autocyclic processes, including progradation or lateral migration of sedimentary bodies (tidal flats, shoals or delta lobes), can lead to the formation of shallowing-up depositional sequences (Ginsburg, 1971; Pratt and James, 1986; Drummond and Wilkinson, 1993; Satterley, 1996; Burgess, 2006). At Beas Lewis Flats, the upper Sinbad Formation consists of tide-dominated ooidic shoal deposits that actually reflect important lateral facies migration. Along the three studied sections, small-scale sequences show a disordered pattern and a limited lateral consistency. All these observations argue for a preponderant role by autocyclic processes rather than putative orbitally-forced sea-level changes in the formation of small-scale depositional sequences.

Observed elementary sequences reflect a facies evolution corresponding to the succession of gastropod-rich accumulations (F3a), fenestral limestones (F3b), and laminated mudstones (F3c; Fig. 11). This shortest recognizable cycle of environmental change is relatively similar to the Alpine Late Triassic Lofer (Dachstein) cycles originally described in the Austrian northern calcareous Alps (Fischer, 1964). Interpretation of these peritidal cyclic carbonate sequences is controversial. They can be interpreted as reflecting a deepening-upward cycle (Fischer, 1964 – Symposium on Cyclic Sedimentation), a shallowing-upward cycle (Goldhammer *et al.*, 1990; Satterley, 1996; Cozzi *et al.*, 2005), or as a structure formed in tune with autocyclic processes (Enos and Samankassou, 1998). Even though such sequences are now largely documented in Middle and Late Triassic deposits, they are generally considered as unknown in Lower Triassic sedimentary successions (Weidlich and Bernecker, 2007). However, one site in the Smithian–Spathian strata of the Great Bank of Guizhou (South China) records thrombolitic reef mounds within peritidal cyclic limestones (Lehrmann *et al.*, 1998, 2001). These deposits display a typical thrombolite-bearing parasequence – i.e. another term illustrating the fundamental building block of sequences (Mitchum and Van Wagoner, 1991) – that consists in the upward succession of a basal oolitic grainstone overlain by skeletal packstone, thrombolite reef mounds, and capped by flaser-bedded limestones. Such a parasequence (0.2 to 7.4 m-thick) has been interpreted as reflecting low-amplitude, high frequency (fifth order, 0.01–0.1 my) sea-level fluctuations resulting from greenhouse conditions (Lehrmann *et al.*, 2001). At Beas Lewis Flats, gastropod accumulations are laterally discontinuous, suggesting a concentration in subtidal local topographic low points. It may also represent lag deposits during phases of lateral migration of gullies (Fig. 14a). Subfacies F3b, with abundant fenestrae, some microbial deposits and sparser gastropods, represents intertidal deposits that progressively filled available space in local ponds or abandoned gullies. Subfacies F3c, with abundant sheet cracks, some stromatolites and a restricted fauna (some ostracods and gastropods), reflects an intertidal to supratidal area prone to record intermittent exposure and desiccation. At French Fork, fenestral (F3b) and muddy laminated (F3c) subfacies are laterally observed in the same bed (Fig. 7). Such an observation, coupled with the limited lateral consistency of these subfacies between French Fork and Beas Lewis Flats, supports an autocyclic origin of the observed elementary sequences.

7. SIGNIFICANCE OF MICROBIAL DEPOSITS: ARE THEY LINKED TO DELETERIOUS ENVIRONMENTS?

It is classically assumed that a return to pre-extinction levels in taxonomic and functional diversity after the end-Permian mass extinction did not occur until the end of the Early Triassic (Schubert and Bottjer, 1995; Lehrmann *et al.*, 2006; Chen and Benton, 2012; Pietsch and Bottjer, 2014). Lower Triassic rocks are thus often considered to record low-diversity benthic faunas (Lehrmann *et al.*, 2001; Fraiser and Bottjer, 2004; Pruss *et al.*, 2006). In this context, microbialites are thought to have flourished as a consequence of continuous or recurrent environmental stresses such as anoxia or high water temperature (Pietsch *et al.*, 2014; Song *et al.*, 2014) and in the absence of developed benthic faunas (Schubert and Bottjer, 1992, 1995). Indeed, several microbialite pulses have been identified in Lower Triassic rocks (Baud *et al.*, 2007; Algeo *et al.*, 2011; Mata and Bottjer, 2012). It has therefore been suggested that these microbialite episodes may reflect the unusual chemistry of Lower Triassic oceans (Pruss and Bottjer, 2004; Woods, 2014). However, recent studies have demonstrated that the rediversification of some nekto-pelagic organisms such as ammonoids (Brayard *et al.*, 2009a) and conodonts (Orchard, 2007) was explosive after the mass extinction. The consensual view of widespread depauperate benthic faunas throughout the entire Early Triassic is now obsolete, as shown by the diversified assemblages recently described from various time intervals and latitudes (Twitchett *et al.*, 2004; Beatty *et al.*, 2008; Kaim *et al.*, 2010; Hautmann *et al.*, 2011, 2013; Hofmann *et al.*, 2011, 2013a, b, 2014).

In the Torrey area, the observed lithological succession is consistent with two depositional models (middle and late middle to late Smithian, respectively; Fig. 14). The first model implies an extension of peritidal microbial limestones (F3) over tens of kilometres (see also Dean, 1981), which laterally pass to more internal tidal-flat red beds (F1; Fig. 14a). Within these microbial limestones, the associated fauna, although common, is of relatively low diversity and is mainly represented by ostracods, gastropods, some bivalves and rare foraminifers. Such a biotic assemblage could be interpreted as representing an impoverished and low-complexity marine ecosystem, typified by primary producers and opportunistic consumers (Lehrmann *et al.*, 2001; Chen and Benton, 2012; Crasquin and Forel, 2014). In this context, microbialites are expected to be widespread and capable of forming patch reefs (Schubert and Bottjer, 1992, 1995; Lehrmann, 1999; Pruss and Bottjer, 2004). Nevertheless, at French Fork, the occurrence of frequent siliceous sponges in the reef framework confirms the existence of an advanced ecological step above microbe-only constructions early in the Early Triassic (Pruss *et al.*, 2007; Brayard *et al.*, 2011; Marenco *et al.*, 2012; Pandolfi and Kiessling, 2014; Vennin *et al.*, in press). Similar sponge-microbe reefs have already been reported from the early Smithian of central Utah (Brayard *et al.*, 2011), thus demonstrating that the Smithian occurrence is not anecdotal in the western USA basin. Their diachronous formation during the Smithian transgression also suggests that they are probably linked to water depth/energy/nutrient conditions.

The record of the Early Triassic biotic recovery appears to be strongly dependent on the type of depositional setting (Pruss *et al.*, 2006; Beatty *et al.*, 2008; Mata and Bottjer, 2011; Olivier *et al.*, 2014). In the Torrey area, previous studies interpreted the sediments of the Black Dragon and Sinbad formations as part of the same depositional model (Blakey, 1974; Dean, 1981). However, high-resolution correlation between the three studied sections does not support such a lateral facies distribution between microbial limestones (F3) of the lower Sinbad Formation and the more diversified bioclastic limestones (F10–F13) of the upper Sinbad Formation (Fig. 14a and b). Such a lateral facies variation was nevertheless assumed in southwestern Utah in time-equivalent Sinbad limestones (Olivier *et al.*, 2014). The lack of a fauna in the Black Dragon Formation red beds (F1) must be considered from the perspective that these deposits formed in a tidal-system reflecting important terrigenous inputs (Fig. 14a). In such depositional settings, significant sediment mobility (caused by tidal currents) and abundant suspended sediment particles (that prevent the colonization by filter-feeding organisms) may cause intertidal settings to be prohibitive environments for common benthic organisms (Davis and Fitzgerald, 2004). Indeed, the western USA basin corresponds to a narrow epicontinental shallow sea that progressively transgressed southward during the Smithian (Paull and Paull, 1993; Goodspeed and Lucas, 2007; Brayard *et al.*, 2013). Abundant lower–middle Smithian terrigenous red-bed deposits in central and southern Utah indicate the existence of complex topographic highs as well as significant continental erosion along the margins of an epicontinental sea tongue or embayment system (Blakey, 1974; Dean, 1981; Nielson, 1991; Olivier *et al.*, 2014). Thus, the intense microbial development in the lower Sinbad Formation coupled with the lack of a fauna in the contemporaneous red beds of the Black Dragon Formation may be explained by specific local environmental conditions. Microbialites are not consistent with high rates of sedimentation (Kershaw *et al.*, 1999), and therefore microbial limestones (F3) could not have formed very close to the terrigenous sources where the red beds were deposited. On the other hand, associated with the terrigenous flux in marine systems, nutrient-rich conditions may have appeared, thus favouring the formation of microbial deposits (Dupraz and Strasser, 2002; Olivier *et al.*, 2004). Red beds were favoured by an intense weathering of silicate rocks, which could have increased the amount of carbonate minerals delivered to the oceans (Ferris *et al.*, 1994; Locklair and Lerman, 2005). Carbonate precipitation depends on carbonate alkalinity and the availability of free calcium (Dupraz and Visscher, 2005; Aloisi, 2008). The intense erosion of calcareous Permian deposits of the Kaibab Formation also supports the existence of seawaters enriched in Ca^{2+} (Arp *et al.*, 2003). Coupled with the rare skeletal carbonate sinks during the middle Smithian, a shift in the carbonate saturation of seawater can help to explain the intense development of microbialites (Pruss *et al.*, 2005; Payne *et al.*, 2007). Thus, the formation of middle Smithian microbial deposits in the lower Sinbad Formation may have occurred in a specific depositional window corresponding to a peritidal setting sufficiently distant from terrigenous sources but still under the influence of alkaline and/or nutrient-rich waters.

During the late–middle to late Smithian, the depositional environment changed drastically. Faunas, which are notably more abundant and diversified, include bivalves, gastropods, echinoderms, ammonoids and serpulids. An intense infaunal activity is also recorded (Fig. 14b). This environmental change may be explained by an acceleration of the transgression following a significant sea-level drop of probable tectonic origin at the top of the microbial limestone unit. The inherited topography probably allowed the formation of an oolitic shoal complex in the Beas Lewis Flats area (Fig. 15). It also permitted recurrent incursions of seaward shoal complex deposits characterized by a more diversified fauna.

DOI: 10.1002/gj

These ooid-bioclastic limestones comprise the upper Sinbad Limestone Formation. This unit exhibits a relatively high diversity and abundant fauna up to the *Anasibirites kingianus* beds (Brayard *et al.*, 2013; Hofmann *et al.*, 2014; Pietsch *et al.*, 2014). These bioclastic limestones (F10–13) interfinger with intertidal interior platform dolostones (F5) that contain a sparse and poorly preserved fauna. In the upper Sinbad facies model (Fig. 14b), microbial deposits are still documented, but their nature and depositional setting strongly differ from their lower Sinbad counterparts. In the youngest case, dm-thick beds of domal stromatolites or wavy carbonate structures (F4) display a laminated micritic fabric. Such microbial carbonates may have played a stabilizing role on the internal part of the shoal complex such as do modern seagrass communities (Rankey, 2014). However, modern and ancient microbialites observed near high-energy shoals incorporate sand-size detrital particles (Riding *et al.*, 1991; Feldmann and McKenzie, 1998; Planavsky and Ginsburg, 2009). Fine-grained microbial deposits closely associated with high-energy shoals are known in the Middle Jurassic and they are interpreted as being deposited in tune with sea-level fluctuations (Tomás *et al.*, 2013). This is not the case in the Torrey area where depositional sequences, including microbial, oolitic and dolostone deposits, are better explained by autocyclic processes. Early Triassic wrinkle structures have also been described associated with cross-laminated siltstones interbedded with shales on supratidal flat environments (Hips, 1998; Pruss *et al.*, 2004; Mata and Bottjer, 2012). Late middle to late Smithian dolostones (F5) in the Torrey area reflect a tide-dominated interior platform with minor terrigenous influences. Thus, observed wavy microbial carbonates can display structures similar to their wrinkle siliciclastic analogues. However, since they formed in a mud-dominated setting, they could not have integrated siliciclastic grains (Luo *et al.*, 2013). Observed wavy microbial carbonates may therefore reflect local low-energy topographic highs in the interior platform, whereas dm-scale domal stromatolites probably formed in an area characterized by a slightly higher accommodation (Fig. 14b). All of these microbial limestones (F4) are clearly contemporaneous with the more distal and more diversified bioclastic limestones (F10–13) of the upper Sinbad Formation. They can be considered as reflecting marine and oxic waters, as previously suggested for younger Spathian microbialites in the Virgin Limestone Formation in western USA (Schubert and Bottjer, 1992, 1995). Thus, both lower and upper Sinbad microbialites (F3 and F4) observed in the Torrey area indicate that Early Triassic microbialites were able to form in various depositional settings that did not necessarily reflect deleterious environments.

8. CONCLUSIONS

The lithological succession in the Torrey area represents a general transgression after the Permian–Triassic mass extinction. This transgression corresponds to the middle Smithian third-order sea-level cycle. The stacking pattern of the studied stratigraphical interval allows the identification of large, medium, small-scale and elementary depositional sequences. While one particular medium-scale depositional sequence observed in the lower Sinbad Formation (middle Smithian) may reflect a regional tectonic uplift, others possibly formed in tune with orbitally (eccentricity) controlled sea-level fluctuations within the upper Sinbad Limestone Formation (late middle to late Smithian). Autocyclic processes better explain small-scale and elementary depositional sequences.

During the Smithian, the sedimentary systems documented in the Torrey area show depositional settings characteristic of an embayment or a sea tongue. The sedimentation reflects a tide-dominated regime that displays wave influences only during major phases of transgression. The first depositional model highlights the juxtaposition between the Black Dragon (red beds) and Lower Sinbad formations, corresponding to a siliciclastic tidal flat and peritidal microbial limestones, respectively. Microbial limestones developed m-scale patch reefs and display a rather low-diversity benthic fauna with gastropods, ostracods, rare foraminifers, and common siliceous sponges. The contribution of siliceous sponges to the reef framework indicates an advanced ecological step above microbial-only reefs. Similar sponge–microbe associations were also documented from older beds of the early Smithian of central Utah, indicating that these bioconstructions were probably common within the western USA basin. The second upper Sinbad depositional model is characterized by three main facies associations: (i) tidal flat dolostones of the interior platform; (ii) ooid-bioclastic deposits of a tide-dominated shoal complex; and (iii) bioclastic limestones of open wave dominated marine settings.

Microbialites occur in both lower and upper Sinbad depositional models. During deposition of the lower Sinbad, the initiation of the transgression allowed the development of a large microbial-dominated peritidal area seaward of a siliciclastic tidal flat in which red beds devoid of any fauna were being deposited. The formation of these microbialites seems to have occurred in a specific depositional window sufficiently far from terrigenous sources, but still under the influence of alkaline and/or nutrient-rich waters. During the upper Sinbad deposition, the sea-level rise permitted the formation of a mixed wave-tide dominated sedimentary system and the microbialitic growth was limited to a small area in the dolostone interior platform. A rather low-diversity fauna characterizes the lower Sinbad microbial

DOI: 10.1002/gj

deposits, whereas upper Sinbad stromatolites are contemporaneous with a much more diversified and abundant fauna. The nature of microbialites and their formation apparently depend strongly on the type of depositional setting. These Smithian microbialites do not reflect the peculiar deleterious environmental conditions that are classically assumed for the Early Triassic time interval.

ACKNOWLEDGEMENTS

This work is a contribution to the ANR project AFTER (ANR-13-JS06-0001-01). The Région Bourgogne and the CNRS INSU Interrvie also supported this study. N. Goudemand (Zurich) is thanked for his help with conodont determinations. D.A. Stephen is grateful for the ongoing financial support of the College of Science & Health at Utah Valley University. Beas Lewis Flats and French Fork sections are located on US public land under the stewardship of the Bureau of Land Management (BLM) of the US Department of the Interior, their management and access to these lands is much appreciated. The Pleasant Creek section is located in Capitol Reef National Park, and was studied and collected under Permit # CARE-2013-SCI-0005, thanks to Sandy Borthwick for her help with the permitting process. Pedro Marenco and Spencer G. Lucas are thanked for their helpful comments on the manuscript.

REFERENCES

Alam, M.M. 1995. Tide-dominated sedimentation in the Upper Tertiary succession of the Sitapahar anticline, Bangladesh. In: *Tidal Signatures in Modern and Ancient Sediments*, Flemming, B.W., Bortholoma, A. (eds). International Association of Sedimentologists, Special Publication **24**, 329–341.

Algeo, T., **Kuwahara, K.**, **Sano, H.**, **Bates, S.**, **Lyons, T.**, **Elswick, E.**, **Hinnov, L.**, **Ellwood, B.**, **Moser, J.**, **Maynard, J. 2011**. Spatial variation in sediment fluxes, redox conditions, and productivity in the Permian–Triassic Panthalassic Ocean. *Palaeogeography, Palaeoclimatology, Palaeoecology* **308**, 65–83.

Aloisi, G. 2008. The calcium carbonate saturation state in cyanobacterial mats throughout Earth's history. *Geochimica and Cosmochimica Acta* **72**, 6037–6060.

Arp, G., **Reimer, A.**, **Reitner, J. 2003**. Microbialite formation in seawater of increased alkalinity, Satonda Crater Lake, Indonesia. *Journal of Sedimentary Research* **73**, 105–127.

Baud, A., **Cirilli, S.**, **Marcoux, J.**, **1997**. Biotic response to mass extinction: the lowermost Triassic microbialites. *Facies* **36**, 238–242.

Baud, A., **Richoz, S.**, **Pruss, S.B. 2007**. The Lower Triassic anachronistic carbonate facies in space and time. *Global and Planetary Change* **55**, 81–89.

Beatty, T.W., **Zonneveld, J.P.**, **Henderson, C.M. 2008**. Anomalously diverse Early Triassic ichnofossil assemblages in northwest Pangea: a case for a shallow-marine habitable zone. *Geology* **36**, 771–774.

Blakey, R.C. 1974. Stratigraphic and depositional analysis of the Moenkopi Formation, Southeastern Utah. *Utah Geological and Mineral Survey Bulletin* **104**, 1–81.

Blakey, R.C. 1977. Petroliferous lithosomes in the Moenkopi Formation, Southern Utah. *Utah Geology* **4**, 67–84.

Brayard, A., **Escarguel, G.**, **Bucher, H.**, **Monnet, C.**, **Brühwiler, T.**, **Goudemand, N. Galfetti, T.**, **Guex, J. 2009a**. Good genes and good luck: ammonoid diversity and the end-Permian mass extinction. *Science* **325**, 1118–1121.

Brayard, A., **Brühwiler, T.**, **Bucher, H.**, **Jenks, J. 2009b**. *Guodunites*, a low-palaeolatitude and trans-panthalassic Smithian (Early Triassic) ammonoid genus. *Palaeontology* **52**, 471–481.

Brayard, A., **Vennin, E.**, **Olivier, N.**, **Bylund, K.G.**, **Jenks, J.**, **Stephen, D.A.**, **Bucher, H.**, **Hofmann, R.**, **Goudemand, N.**, **Escarguel, G. 2011**. Transient metazoan reefs in the aftermath of the end-Permian mass extinction. *Nature Geoscience* **4**, 693–697.

Brayard, A., **Bylund, K.G.**, **Jenks, J.**, **Stephen, D.**, **Olivier, N.**, **Escarguel, G.**, **Fara, E.**, **Vennin, E. 2013**. Smithian ammonoid faunas from Utah: implications for Early Triassic biostratigraphy, correlation and basinal paleogeography. *Swiss Journal of Palaeontology* **132**, 141–219.

Brühwiler, T., **Goudemand, N.**, **Galfetti, T.**, **Bucher, H.**, **Baud, A**, **Ware, D.**, **Hermann, E.**, **Hochuli, P.A.**, **Martini, R. 2009**. The Lower Triassic sedimentary and carbon isotope records from Tulong (South Tibet) and their significance for Tethyan palaeoceanography. *Sedimentary Geology* **222**, 314–332.

Brühwiler, T., **Bucher, H.**, **Brayard, A.**, **Goudemand, N. 2010**. High-resolution biochronology and diversity dynamics of the Early Triassic ammonoid recovery: The Smithian faunas of the Northern Indian Margin. *Palaeogeography, Palaeoclimatology, Palaeoecology* **297**, 491–501.

Burgess, P.M. 2006. The signal and the noise: forward modeling of allocyclic and autocyclic processes influencing peritidal carbonate stacking patterns. *Journal of Sedimentary Research* **76**, 962–977.

Chen, Z.Q., **Benton, M.J. 2012**. The timing and pattern of biotic recovery following the end-Permian mass extinction. *Nature Geoscience* **5**, 375–383.

Chen, Z.Q., **Tong, J.**, **Kaiho, K.**, **Kawahata, H. 2007**. Onset of biotic and environmental recovery from the end-Permian mass extinction within 1–2 million years: a case study of the Lower Triassic of the Meishan section, south China. *Palaeogeography, Palaeoclimatology, Palaeoecology* **252**, 176–187.

Collinson, J.W., **Hasenmueller, W.A. 1978**. Early Triassic paleogeography and biostratigraphy of the Cordilleran miogeosyncline. In *Mesozoic Paleogeography of the West–Central United States*, Howell, D.G., McDougall, K.A. (eds). Society of Economic Paleontologists and Mineralogists, Pacific Coast Paleogeography Symposium **2**, Society of Economic Paleontologists and Mineralogists: Los Angeles, Pacific Section.175–187.

Collinson, J.W., **Kendall, C.G.S.C.**, **Marcantel, J. B. 1976**. Permian–Triassic boundary in eastern Nevada and west–central Utah. *Bulletin of the Geological Society of America* **87**, 821–824.

Cozzi, A., **Hinnov, L.A.**, **Hardie, L.A. 2005**. Orbitally forced Lofer cycles in the Dachstein Limestone of the Julian Alps (northeastern Italy). *Geology* **33**, 789–792.

Crasquin, S., **Forel, M.B. 2014**. Ostracods (Crustacea) through Permian-Triassic events. *Earth-Science Reviews* **137**, 52–64.

Davis, R., **Fitzgerald, D.M. 2004**. *Beaches and Coasts*. Wiley-Blackwell: New York.

Dean, J.S. 1981. Carbonate petrology and depositional environments of the Sinbad Limestone Member of the Moenkopi Formation in the Teasdale Dome Area, Wayne and Garfield Counties, Utah. *Brigham Young University Geology Studies* **28**, 19–51.

Drummond, C.N. Wilkinson, B.H. 1993. Carbonate cycle stacking patterns and hierarchies of orbitally forced eustatic sea level change. *Journal of Sedimentary Petrology* **63**, 369–377.

Dupraz, C., **Strasser, A. 2002**. Nutritional modes in coral-microbialite reefs (Jurassic, Oxfordian, Switzerland): evolution of trophic structure as a response to environmental change. *Palaios* **17**, 449–471

Dupraz, C., **Visscher, P.T. 2005**. Microbial lithification in marine stromatolites and hypersaline mats. *Trends in Microbiology* **13**, 429–438.

Embry, A.F. 1997. Global sequence boundaries of the Triassic and their identification in the western Canada sedimentary basin. *Canadian Petroleum Geology Bulletin* **45**, 415–433.

Enos, P., **Samankassou, E. 1998**. Lofer cyclothems revisited (Late Triassic, Northern Alps, Austria). *Facies* **38**, 207–228.

Erwin, D.H. 2006. *Extinction. How Life on Earth nearly ended 250 million years ago*. Princeton University Press: New York.

Feldmann, M., **McKenzie, J.A. 1998**. Stromatolite–thrombolite associations in a modern environment, Lee Stocking Island, Bahamas. *Palaios* **13**, 201–212.

Ferris, G.F., **Wiese, R.G.**, **Fyfe, W.S. 1994**. Precipitation of carbonate minerals by microorganisms: implications for silicate weathering and the global carbon dioxide budget. *Geomicrobiology Journal* **12**, 1–13.

Fischer, A.G. 1964. The Lofer cyclothems of the Alpine Triassic. In: Merrian, D.F. (Ed.), *Symposium on Cyclic Sedimentation*. Kansas Geological Survey, Bulletin **23**. 107–149.

Flügel, E. 2004. *Microfacies of carbonate rocks*. Springer: Berlin.

Fraiser, M.L., **Bottjer, D.J. 2004**. The non-actualistic Early Triassic gastropod fauna: a case study of the Lower Triassic Sinbad Limestone Member. *Palaios* **19**, 259–275.

Galfetti, T., **Bucher, H.**, **Ovtcharova, M.**, **Schaltegger, U.**, **Brayard, A.**, **Brühwiler, T.**, **Goudemand, N.**, **Weissert, H.**, **Hochuli, P.A.**, **Cordey, F.**, **Guodun, K. 2007**. Timing of the Early Triassic carbon cycle perturbations inferred from new U–Pb ages and ammonoid biochronozones. *Earth and Planetary Science Letters* **258**, 593–604.

Galfetti, T., **Bucher, H.**, **Martini, R.**, **Hochuli, P.A.H.**, **Weissert, H.**, **Crasquin-Soleau, S.**, **Brayard, A.**, **Goudemand, N.**, **Brühwiler, T.**, **Guodun K. 2008**. Evolution of Early Triassic outer platform paleoenvironments in the Nanpanjiang Basin (South China) and their significance for the biotic recovery. *Sedimentary Geology* **204**, 36–60.

Ginsburg, R.N. 1971. Landward movement of carbonate mud: new model for regressive cycles in carbonates (abstract). *American Association of Petroleum Geologist, Bulletin* **55**, 340.

Goldhammer, R.K., **Dunn, P.A.**, **Hardie, L.A. 1990**. Depositional cycles, composite sea-level changes, cycle stacking patterns, and the hierarchy of stratigraphic forcing: examples from Alpine Triassic platform carbonates. *Geological Society of America Bulletin* **102**, 535–562.

Goodspeed, T.H., **Lucas, S.G. 2007**. Stratigraphy, sedimentology, and sequence stratigraphy of the Lower Triassic Sinbad Formation, San Rafael Swell, Utah. *New Mexico Museum of Natural History and Science Bulletin* **40**, 91–101.

Grasby, S.E., **Beauchamp, B.**, **Embry, A.**, **Sanei, H. 2013**. Recurrent Early Triassic ocean anoxia. *Geology* **41**, 175–178.

Guex, J., **Hungerbühler, A.**, **Jenks, J.F.**, **O'Dogherty, L.**, **Atudorei, V.**, **Taylor, D.G.**, **Bucher, H.**, **Bartolini, A. 2010**. Spathian (Lower Triassic) ammonoids from western USA (Idaho, California, Utah and Nevada). *Mémoires de Géologie de Lausanne* **49**, 1–81.

Halley, R.B., **Harris, P.M.**, **Hine, A.C. 1983**. Bank margin environment. In: *Carbonate Depositional Environments*, Scholle P.A., Bebout, D.G., Moore, C.H. (eds). American Association of Petroleum Geologists Memoir **33**, 464–506.

Haq, B.U., **Al-Qahtani, A.M. 2005**. Phanerozoic cycles of sea-level change on the Arabian Platform. *Geoarabia* **10**, 127–60.

Haq, B.U., **Shutter, S.R. 2008**. A chronology of Paleozoic sea-level changes. *Science* **322**, 64–68.

Hautmann, M., **Bucher, H.**, **Brühwiler, T.**, **Goudemand, N.**, **Kaim, A.**, **Nützel, A. 2011**. An unusually diverse mollusc fauna from the earliest Triassic of south China and its implications for benthic recovery after the end-Permian biotic crisis: *Geobios* **44**, 71–85.

Hautmann, M., **Smith, A.B.**, **McGowan, A.J.**, **Bucher, H. 2013**. Bivalves from the Olenekian (Early Triassic) of south-western Utah: systematics and evolutionary significance. *Journal of Systematic Palaeontology* **11**, 263–293.

Hips, K. 1998. Lower Triassic storm-dominated ramp sequence in northern Hungary: an example of evolution from homoclinal through distally steepened ramp to Middle Triassic flat-topped platform. In: *Carbonate Ramps*, Wright, V.P., Burchette, T.P. (eds). Geological Society, London, Special Publication **149**, 315–338.

Hofmann, R., **Goudemand, N.**, **Wasmer, M.**, **Bucher, H.**, **Hautmann, M. 2011**. New trace fossil evidence for an early recovery signal in the aftermath of the end-Permian mass extinction. *Palaeogeography, Palaeoclimatology, Palaeoecology* **310**, 216–226.

Hofmann, R., **Hautmann, M.**, **Bucher, H. 2013a**. A new paleoecological look at the Dinwoody Formation (Lower Triassic, Western U.S.): intrinsic versus extrinsic controls on ecosystem recovery after the end-Permian mass extinction. *Journal of Paleontology* **87**, 854–880.

Hofmann, R., **Hautmann, M.**, **Wasmer, M.**, **Bucher, H. 2013b**. Palaeoecology of the Virgin Formation (Utah, USA) and its implications for the Early Triassic recovery. *Acta Palaeontologica Polonica* **58**, 149–173.

Hofmann, R., **Hautmann, M.**, **Brayard, M.**, **Nützel, A.**, **Bylund, K.G.**, **Jenks, J.F.**, **Vennin, E.**, **Olivier, N.**, **Bucher, H. 2014**. Recovery of benthic marine communities from the end-Permian mass extinction at the low latitudes of eastern Panthalassa. *Palaeontology* **57**, 547–589.

Kaim, A., **Nützel, A.**, **Bucher, H.**, **Brühwiler, T.**, **Goudemand, N.**, **2010**. Early Triassic (Late Griesbachian) gastropods from South China (Shanggan, Guangxi). *Swiss Journal of Geosciences* **103**, 121–128.

Kershaw, S., **Zhang, T.**, **Lan, G. 1999**. A ?microbialite carbonate crust at the Permian–Triassic boundary in South China, and its paleoenvironmental significance. *Palaeogeography, Palaeoclimatology, Palaeoecology* **146**, 1–18.

Kershaw, S., **Crasquin, S.**, **Li, Y.**, **Collin, P.Y.**, **Forel, M.B.**, **Mu, X.**, **Baud, A.**, **Wang, Y.**, **Xie, S.**, **Guo, L.**, **Maurer, F. 2012**. Microbialites and global environmental change across Permian–Triassic boundary: a synthesis. *Geobiology* **10**, 25–47.

Komatsu, T., **Naruse, H.**, **Shigeta, Y.**, **Takashima, R.**, **Maekawa, T.**, **Dang, H.T.**, **Dinh, T.C.**, **Nguyen, P.D.**, **Nguyen, H.H.**, **Tanaka, G.**, **Sone M. 2014**. Lower Triassic mixed carbonate and siliciclastic setting with Smithian–Spathian anoxic to dysoxic facies, An Chau basin, northeastern Vietnam. *Sedimentary Geology* **300**, 28–48.

Krystyn, L., **Richoz, S.**, **Baud, A.**, **Twitchett, R.J. 2003**. A unique Permian–Triassic boundary section from the Neotethyan Hawasina basin, central Oman mountains. *Palaeogeography, Palaeoclimatology, Palaeoecology* **191**, 329–344.

Kummel, B., **JR**. **1954**. Triassic stratigraphy of southeastern Idaho and adjacent areas. *U.S. Geological Survey Professional Paper* **254-H**, 165–194.

Lehrmann, D.J. 1999. Early Triassic calcimicrobial mounds and biostromes of the Nanpanjiang basin. south China. *Geology* **27**, 359–362.

Lehrmann, D.J., **Wei, J.**, **Enos, P. 1998**. Controls on facies architecture of a large Triassic carbonate platform: the Great Bank of Guizhou, Nanpanjiang Basin, South China. *Journal of Sedimentary Research* **68**, 311–326.

Lehrmann, D.J., **Wang, Y.**, **Wei, J.**, **Yu, Y.Y.**, **Xiao, J. 2001**. Lower Triassic peritidal cyclic limestone: an example of anachronistic carbonate facies from the Great Bank of Guizhou, Nanpanjiang Basin, Guizhou province, South China. *Palaeogeography, Palaeoclimatology, Palaeoecology* **173**, 103–123.

Lehrmann, D.J., **Ramezani, J.**, **Bowring, S.A.**, **Martin, M.W.**, **Montgomery, P.**, **Enos, P.**, **Payne, J.L.**, **Orchard, M.J.**, **Wang, H.**, **Wei, J. 2006**. Timing of recovery from the end-Permian extinction: geochronologic and bio-stratigraphic constraints from south China. *Geology* **34**, 1053–1056.

Lehrmann, D.J., **Pei, D.H.**, **Enos, P.**, **Minzoni, M.**, **Ellwood, B.B.**, **Orchard, M.J.**, **Zhang, J.Y.**, **Wei, J.Y.**, **Dillett, P.**, **Koenig, J.**, **Steffen, K.**, **Druke, D.**, **Druke, J.**, **Kessel, B.**, **Newkirk, T. 2007a**. Impact of differential tectonic subsidence on isolated carbonate platform evolution: Triassic of the Nanpanjiang Basin, south China. *American Association of Petroleum Geologists Bulletin* **91**, 287–320.

Lehrmann, D.J., **Payne, J.L.**, **Donghong, P.**, **Enos, P.**, **Druke, D.**, **Steffen, K.**, **Jinan, Z.**, **Jiayong, W.**, **Orchard, M.J.**, **Ellwood, B. 2007b**. Record of the end-Permian extinction and Triassic biotic recovery in the Chongzuo–Pingguo platform, southern Nanpanjiang basin, Guangxi, south China. *Palaeogeography, Palaeoclimatology, Palaeoecology* **252**, 200–217.

Locklair, R.E., **Lerman, A. 2005**. A model of Phanerozoic cycles of carbon and calcium in the global ocean: Evaluation and constraints on ocean chemistry and input fluxes. *Chemical Geology* **217**, 113–126.

Lucas, S.G., **Goodspeed, T.H.**, **Estep, J.W. 2007**. Ammonoid biostratigraphy of the Lower Triassic Sinbad Formation, East–Central Utah. *New Mexico Museum of Natural History and Science Bulletin* **40**, 103–108.

Luo, M., Chen, Z.Q., Hu, S., Zhang, Q., Benton, M.J., Zhou, C., Wen, W., Huang, J.Y. 2013. Carbonate reticulated ridge structures from the lower Middle Triassic of the Luoping area, Yunnan, southwestern China: geobiologic features and implications for exceptional preservation of the Luoping Biota. *Palaios* **28**, 541–551.

Marenco, P.J., Griffin, J.M., Fraiser, M.L., Clapham, M.E. 2012. Paleoecology and geochemistry of Early Triassic (Spathian) microbial mounds and implications for anoxia following the end-Permian mass extinction. *Geology* **40**, 715–718.

Mata, S.A., Bottjer, D.J. 2011. Origin of Lower Triassic microbialites in mixed carbonate–siliciclastic successions: ichnology, applied stratigraphy, and the end-Permian mass extinction. *Palaeogeography, Palaeoclimatology, Palaeoecology* **300**, 158–178.

Mata, S.A., Bottjer, D.J. 2012. Microbes and mass extinctions: paleoenvironmental distribution of microbialites during times of biotic crisis. *Geobiology* **10**, 3–24.

Mitchum, R.M., van Wagoner, J.C. 1991. High-frequency sequences and their stacking patterns: sequence-stratigraphic evidence of high-frequency eustatic cycles. *Sedimentary Geology* **70**, 131–160.

Nielson, R.L. 1991. Petrology, sedimentology and stratigraphic implications of the Rock Canyon conglomerate, southwestern Utah. *Utah Geological Survey, Miscellaneous Publication* **91**, 1–65.

Olivier, N., Carpentier, C., Martin-Garin, B., Lathuilière, B., Gaillard, C., Ferry, S., Hantzpergue, P., Geister, J. 2004. Coral-microbialite reefs in pure carbonate versus mixed carbonate–siliciclastic depositional environments: the example of the Pagny-sur-Meuse section (Upper Jurassic, northeastern France). *Facies* **50**, 229–255.

Olivier, N., Brayard, A., Fara, E., Bylund, K.G., Jenks, J. F., Vennin, E., Stephen, D.A., Escarguel, G. 2014. Smithian Shoreline migrations and depositional settings in Timpoweap Canyon (Early Triassic, Utah, USA). *Geological Magazine* **151**, 938–955.

Orchard, M. J. 2007. Conodont diversity and evolution through the latest Permian and Early Triassic upheavals. *Palaeogeography, Palaeoclimatology, Palaeoecology* **252**, 93–117.

Pandolfi, J.M., Kiessling, W. 2014. Gaining insights from past reefs to inform understanding of coral reef response to global climate change. *Current Opinion in Environmental Sustainability* **7**, 52–58.

Paull, R.A., Paull, R.K. 1993. Interpretation of Early Triassic nonmarine–marine relations, Utah, U.S.A. *New Mexico Museum of Natural History and Science Bulletin* **3**, 403–409.

Paull, R.K., Paull, R.A. 1997. Transgressive conodont faunas of the early Triassic: an opportunity for correlation in the Tethys and the circum-Pacific. In: *Late Palaeozoic and Early Mesozoic Circum-Pacific Events and their Global Correlation*, Dickins, J.M., Zunyi, Y., Hongfu, Y., Lucas, S.G., Acharyya S.K. (eds). Cambridge University Press, World and Regional Geology **10**, 158–167.

Payne, J.L., Lehrmann, D.J., Wei, J., Orchard, M.J., Schrag, D.P., Knoll, A.H. 2004. Large perturbations of the carbon cycle during recovery from the end-Permian extinction. *Science* **305**, 506–509.

Payne, J.L., Lehrmann, D.J., Follett, D., Seibel, M., Kump, L.R., Riccardi, A., Altiner, D., Sano, H., Wei, J. 2007. Erosional truncation of uppermost Permian shallow-marine carbonates and implications for Permian–Triassic boundary events. *Geological Society of America Bulletin* **119**, 771–784.

Pérez-López, A., Pérez-Valera, F. 2011. Tempestite facies model for the epicontinental Triassic carbonates of the Betic Cordillera (southern Spain). *Sedimentology* **59**, 646–78.

Pietsch, C., Bottjer, D.J. 2014. The importance of oxygen for the disparate recovery patterns of the benthic macrofauna in the Early Triassic. *Earth Science Reviews* **137**, 65–84.

Pietsch, C., Mata, S.A., Bottjer, D.J. 2014. High temperature and low oxygen perturbations drive contrasting benthic recovery dynamics following the end-Permian mass extinction. *Palaeogeography, Palaeoclimatology, Palaeoecology* **399**, 98–113.

Planavsky, N., Ginsburg, R.N. 2009. Taphonomy of modern marine Bahamian microbialites. *Palaios* **24**, 5–17.

Pratt, B.R., James, N.P. 1986. The St George Group (Lower Ordovician) of western Newfoundland: tidal flat island model for carbonate sedimentation in shallow epeiric seas. *Sedimentology* **33**, 313–343.

Pruss S.B., Bottjer D.J. 2004. Late Early Triassic microbial reefs of the western United States: a description and model for their deposition in the aftermath of the end-Permian mass extinction. *Palaeogeography, Palaeoclimatology, Palaeoecology* **211**, 127–137.

Pruss, S.B., Fraiser, M., Bottjer, D.J. 2004. Proliferation of Early Triassic wrinkle structures: implications for environmental stress following the end-Permian mass extinction. *Geology* **32**, 461–464.

Pruss, S.B., Corsetti, F.A., Bottjer, D.J. 2005. The unusual sedimentary rock record of the Early Triassic: a case study from the southwestern United States. *Palaeogeography, Palaeoclimatology, Palaeoecology* **222**, 33–52.

Pruss, S.B., Bottjer, D.J., Corsetti, F.A., Baud, A. 2006. A global marine sedimentary response to the End-Permian mass extinction: examples from southern Turkey and the western United States. *Earth-Science Reviews* **78**, 193–206.

Pruss, S.B., Payne, J.L. Bottjer, D.J. 2007. *Placunopsis* bioherms: the first metazoan buildups following the End-Permian mass extinction. *Palaios* **22**, 17–23.

Rankey, E.C. 2014. Contrasts between wave- and tide-dominated oolitic systems: Holocene of Crooked–Acklins Platform, southern Bahamas. *Facies* **60**, 405–428.

Raup, D.M. 1979. Size of the Permo-Triassic bottleneck and its evolutionary implications. *Science* **206**, 217–218.

Riding, R., Braga, J.C., Martín, J.M. 1991. Oolite stromatolites and thrombolites, Miocene, Spain: analogues of Recent giant Bahamian examples. *Sedimentary Geology* **71**, 121–127.

Sano, H., Onoue, T., Orchard, M., Martini R. 2012. Early Triassic peritidal carbonate sedimentation on a Panthalassan seamount: the Jesmond succession, Cache Creek Terrane, British Columbia, Canada. *Facies* **58**, 113–130.

Satterley, A.K. 1996. The interpretation of cyclic successions of the Middle and Upper Triassic of the Northern and Southern Alps. *Earth-Science Reviews* **40**, 181–207.

Schubert, J.K., Bottjer, D.J. 1992. Early Triassic stromatolites as post-mass extinction disaster forms. *Geology* **20**, 883–886.

Schubert, J.K., Bottjer, D.J. 1995. Aftermath of the Permian–Triassic mass extinction event: paleoecology of Lower Triassic carbonates in the western USA. *Palaeogeography, Palaeoclimatology, Palaeoecology* **116**, 1–39.

Shinn, E.A. 1968. Practical significance of birdseye structures in carbonate rocks. *Journal of Sedimentary Petrology* **38**, 215–223.

Shinn, E.A. 1969. Anatomy of modern carbonate tidal-flat, Andros Island, Bahamas. *Journal of Sedimentary Petrology* **39**, 1202–1228.

Song, H., Wignall, P.B., Chu, D., Tong, J., Sun, Y., Song, H., He, W., & Tian, L. 2014. Anoxia/high temperature double whammy during the Permian–Triassic marine crisis and its aftermath. *Scientific Report* **4**, 4132.

Stewart, J.H., Poole, F.G., Wilson, R.F. 1972. Stratigraphy and origin of the Triassic Moenkopi formation and related strata in the Colorado Plateau region. *Geological Survey Professional Paper* **691**, 1–195.

Strasser, A., Védrine, S. 2009. Controls on facies mosaics of carbonate platforms: a case study from the Oxfordian of the Swiss Jura. *International Association of Sedimentologists. Special Publication* **41**, 199–213.

Strasser, A., Pittet, B., Hillgärtner, H., Pasquier, J.B. 1999. Depositional sequences in shallow carbonate-dominated sedimentary systems: concepts for a high-resolution analysis. *Sedimentary Geology* **128**, 201–221.

Strasser, A., Védrine, S., Stienne, N. 2012. Rate and synchronicity of environmental changes on a shallow carbonate platform (Late Oxfordian, Swiss Jura Mountains). *Sedimentology* **59**, 185–211.

Thomson, T.J., Lovelace, D.M. 2014. Swim track morphotypes and new track localities from the Moenkopi and Red Peak formations (Lower–Middle Triassic) with preliminary interpretations of aquatic behaviors. In: *Fossil Footprints of Western North America*, Lockley, M.G., Lucas, S.G. (eds). NMMNHS Bulletin **62**, 103–128.

Tomás, S., Homann, M., Mutti, M., Amour, F., Christ, N., Immenhauser, A., Agar, S.M., Kabiri, L. 2013. Alternation of microbial mounds and ooid shoals (Middle Jurassic, Morocco): response to paleoenvironmental changes. *Sedimentary Geology* **294**, 68–82.

Twitchett, R.J., **Krystyn, L.**, **Baud, A.**, **Wheeley, J.R.**, **Richoz, S. 2004**. Rapid marine recovery after the end-Permian mass-extinction event in the absence of marine anoxia. *Geology* **32**, 805–808.

Vennin, E., **Olivier, N.**, **Brayard, A.**, **Bour, I.**, **Thomazo, C.**, **Escarguel, G.**, **Fara, E.**, **Bylund, K.G.**, **Jenks, J.F.**, **Stephen, D.A.**, **Hofmann, R**. (in press). Microbial deposits in the aftermath of the end-Permian mass extinction: a diverging case from Mineral Mountains (Utah, USA). DOI: 10.1111/Sed12166.

Vigran, J.O., **Mangerud, G.**, **Mørk, A.**, **Bugge, T.**, **Weitschat, W. 1998**. Biostratigraphy and sequence stratigraphy of the Lower and Middle Triassic deposits from the Svalis Dome, central Barents Sea, Norway. *Palynology* **22**, 89–141.

Voigt, S., **Lucas, S.G.**, **Krainer, K. 2013**. Coastal-plain origin of trace-fossil bearing red beds in the Early Permian of Southern New Mexico, U.S.A. *Palaeogeography, Palaeoclimatology, Palaeoecology* **369**, 323–334.

Walker R.G., **Harms, J.C. 1975**. Shorelines of weak tidal activity: Upper Devonian Catskill Formation; Central Pennsylvania. In: *Tidal Deposits: a Casebook of Recent Examples and Fossil Counterparts*, Ginsburg, R.N. (ed). Springer-Verlag: New-York. 103–108.

Weidlich, O., **Bernecker, M. 2007**. Differential severity of Permian–Triassic environmental changes on Tethyan shallow-water carbonate platforms. *Global and Planetary Change* **55**, 209–235.

Woods, A.D. 2013. Microbial ooids and cortoids from the Lower Triassic (Spathian) Virgin Limestone, Nevada, USA: evidence for an Early Triassic microbial bloom in shallow depositional environments. *Global and Planetary Change* **105**, 91–101.

Woods, A.D. 2014. Assessing Early Triassic paleoceanographic conditions via unusual sedimentary fabrics and features. *Earth-Science Reviews* **137**, 6–18.

Wright, V.P. 1984. Peritidal carbonate facies models: A review. *Geological Journal* **19**, 309–325.

Wright, V.P., **Burgess, P.M. 2005**. The carbonate factory continuum, facies mosaics and microfacies: an appraisal of some of the key concepts underpinning carbonate sedimentology. *Facies* **51**, 17–23.

Zonneveld, J.P., **Gingras, M.K.**, **Beatty, T.W. 2010**. Diverse ichnofossil assemblages following the P–T mass extinction, Lower Triassic, Alberta and British Columbia, Canada: evidence for shallow marine refugia on the northwestern coast of Pangaea. *Palaios* **25**, 368–392.

Scientific editing by Zhong Chen

Appendix 2: Supplementary material belonging to the article “Early Triassic fluctuations of the global carbon cycle: new evidence from paired carbon isotopes in the western USA basin” (see section III.A)

This supplementary material provides additional data used to perform the integrated study presented in Caravaca *et al.*, 2017 (see section III.A). It includes the complete geochemical data for the paired carbon isotopes, TOC and carbonate contents (Table ST1) and for the trace and major elements concentrations (Table ST2).

EARLY TRIASSIC FLUCTUATIONS OF THE GLOBAL CARBON CYCLE: NEW EVIDENCE FROM PAIRED CARBON ISOTOPES IN THE WESTERN USA BASIN

Gwénaël Caravaca[1, *], Christophe Thomazo[1], Emmanuelle Vennin[1], Nicolas Olivier[2], Théophile Cocquerez[1], Gilles Escarguel[3], Emmanuel Fara[1], James F. Jenks[4], Kevin G. Bylund[5], Daniel A. Stephen[6] and Arnaud Brayard[1]

APPENDIX A: SUPPLEMENTARY GEOCHEMICAL DATA

Supplementary Table S1. Geochemical data with carbonate, organic matter and net isotopic effect results, Total Organic Carbon (TOC) content, carbonate $\delta^{18}O$ values and carbonate content.

	Sample	$\delta^{13}C_{carb}$ ‰ vs VPDB	$\delta^{13}C_{org}$ ‰ vs VPDB	$\Delta^{13}C_{carb-org}$ ‰ vs VPDB	TOC ppm	$\delta^{18}O_{carb}$ ‰ vs VPDB	$CaCO_3$ %
Permian (middle to upper?)	HSP 1	-7.97	-27.57	19.60	4.78	-14.90	81.97
	HSP 2	-4.11	-27.49	23.38	N/A	-10.28	32.61
	HSP 3	-5.39	-26.68	21.29	N/A	-9.43	37.08
	HSP 4	-5.84	-27.21	21.37	N/A	-10.18	40.39
	HSP 5	-5.43	-26.57	21.14	N/A	-10.08	35.24
	HSP 6	-3.45	-25.60	22.15	N/A	-9.36	20.04
	HSP 7 b	-5.64	-27.46	21.82	N/A	-9.68	14.46
	HSP 8	-5.36	-27.17	21.81	N/A	-10.17	37.17
	HSP 10	-0.06	-27.02	26.96	N/A	-2.34	89.94
	HSP 11	N/A	-27.16	27.16	N/A	N/A	11.30
	HSP 12	-5.89	-28.14	22.25	59.47	N/A	92.27
	HSP 14	1.83	-27.09	28.92	N/A	N/A	13.16
	HSP 15	3.23	-27.71	30.94	N/A	-0.61	7.06
	HSP 13	N/A	-27.85	27.85	N/A	N/A	27.53
	HSP 16	N/A	-27.72	27.72	N/A	N/A	8.75
	HSP 17	-1.56	-26.50	24.94	N/A	-3.93	6.83
	HSP 18	N/A	-28.31	28.31	N/A	N/A	2.14
	HSP 19	N/A	-26.80	26.80	N/A	N/A	4.98
	HSP 20	N/A	-27.58	27.58	N/A	N/A	5.64
	HSP 21	N/A	-28.84	28.84	N/A	N/A	6.22
	HSP 22	N/A	-28.15	28.15	18.35	N/A	8.24
	HSP 23	-0.56	-29.06	28.50	N/A	-2.19	19.53
Griesbachian - Dienerian	HSP 24	-1.44	-28.48	27.04	17.78	-3.12	11.09
	HSP 25	-1.38	-28.64	27.26	47.81	-3.69	13.85
	HSP 26	-6.84	-28.92	22.08	N/A	-3.17	49.97
	HSP 186	N/A	-28.94	28.94	N/A	N/A	13.27
	HSP 187	-2.44	-29.60	27.16	N/A	-9.63	39.62
	HSP 27	N/A	-28.86	28.86	39.66	N/A	78.62
	HSP 28	N/A	-29.21	29.21	44.35	N/A	78.31
	HSP 29	-1.00	-28.37	27.37	N/A	-4.99	39.58
	HSP 30	-0.74	-28.74	28.00	N/A	-3.31	39.59
	HSP 31	-0.91	-28.51	27.60	N/A	-3.98	41.93
	HSP 32	-1.42	-25.16	23.74	N/A	-9.89	81.52
	HSP 145	-0.95	-26.54	25.59	N/A	-8.28	37.25
	HSP 146	-0.19	-27.13	26.94	N/A	-8.44	85.33
	HSP 147	-0.92	-25.65	24.73	N/A	-8.89	33.09
	HSP 33	-0.92	-26.51	25.59	N/A	-8.03	39.25
	HSP 34	0.33	-26.22	26.55	N/A	-8.26	79.43
	HSP 148	-0.58	-26.26	25.68	N/A	-8.03	29.03
	HSP 149	-1.24	-26.12	24.88	N/A	-8.48	31.41

	HSP 35	-0.23	-27.21	26.98	N/A	-8.28	60.65
	HSP 150	-0.30	-26.84	26.54	N/A	-8.87	75.64
	HSP 151	-0.61	-26.82	26.21	N/A	-8.23	31.19
	HSP 152	-0.13	-27.44	27.31	N/A	-8.64	85.38
	HSP 153	-0.80	-26.28	25.48	N/A	-8.34	32.53
	HSP 36	-2.30	-27.97	25.67	N/A	-8.72	65.92
	HSP 37	-1.02	-27.23	26.21	3.76	-8.63	93.34
	HSP 39	-3.46	-27.93	24.47	N/A	-8.17	91.79
	HSP 38	-0.67	-27.17	26.50	3.10	-8.59	97.10
	HSP 40	-2.04	-27.64	25.60	N/A	-8.20	42.70
	HSP 41	-2.06	-21.01 *	18.95	N/A	-8.16	43.11
	HSP 43	-1.76	-27.25	25.49	N/A	-8.87	79.18
	HSP 42	-1.24	-26.88	25.64	N/A	-7.94	90.88
	HSP 45	-2.23	-27.40	25.17	4.61	-8.67	75.06
	HSP 44	-2.87	-27.44	24.57	N/A	-8.06	80.69
	HSP 154	-1.61	-27.61	26.00	N/A	-8.43	63.86
	HSP 46	-3.01	-27.51	24.50	N/A	-11.46	39.88
	HSP 155	-1.49	-26.78	25.29	N/A	-7.13	32.01
	HSP 156	-1.80	-26.47	24.67	N/A	-6.53	41.82
	HSP 47	-0.18	-26.92	26.74	1.56	-8.50	98.14
	HSP 157	0.99	-27.11	28.10	4.83	-9.31	97.57
	HSP 48	-1.83	-26.88	25.05	N/A	-5.65	44.56
	HSP 158	-0.98	-27.10	26.12	N/A	-5.82	35.91
	HSP 159	-0.60	-26.79	26.19	N/A	-6.91	68.29
	HSP 160	0.10	-27.81	27.91	2.66	-7.10	95.49
Lower Smithian	HSP 161	3.31	-26.47	29.78	1.99	-9.40	95.89
	HSP 162	2.35	-27.06	29.41	N/A	-10.01	67.96
	HSP 163	0.93	-26.48	27.41	N/A	-11.45	33.90
	HSP 164	1.87	-26.96	28.83	1.12	-8.84	97.89
	HSP 165	1.24	-27.61	28.85	N/A	-9.92	32.05
	HSP 166	2.77	-26.69	29.46	N/A	-9.70	82.83
	HSP 167	1.73	-25.93	27.66	N/A	-8.88	33.54
	HSP 49	2.60	-26.05	28.65	N/A	-9.77	99.04
	HSP 50	2.54	-25.78	28.32	2.81	-9.60	98.49
	HSP 168	2.58	-21.55 *	24.13	2.68	-9.98	93.05
	HSP 169	1.88	-25.73	27.61	N/A	-9.03	61.62
	HSP 51	1.56	-27.09	28.65	N/A	-9.10	69.73
	HSP 52	2.26	-25.20	27.46	3.38	-9.42	96.40
	HSP 170	1.16	-26.92	28.08	N/A	-9.19	39.75
	HSP 53	1.34	-25.93	27.27	N/A	-8.83	38.35
	HSP 54	1.85	-26.27	28.12	N/A	-9.25	95.79
	HSP 55	1.43	-27.31	28.74	N/A	-9.40	84.29
	HSP 56	-0.32	-26.62	26.30	N/A	-11.78	97.90
	HSP 57	2.00	-24.28	26.28	N/A	-9.72	97.91
	HSP 171	1.85	-26.23	28.08	0.96	-9.00	98.37
	HSP 58	1.25	-26.91	28.16	N/A	-9.04	33.55
	HSP 59	1.14	-26.66	27.80	N/A	-8.53	41.21

	HSP 172	1.36	-27.53	28.89	N/A	-9.31	44.79
	HSP 173	3.60	-26.63	30.23	N/A	-6.48	87.49
	HSP 60 b	2.57	-27.20	29.77	N/A	-8.46	80.78
	HSP 175	2.36	-26.44	28.80	N/A	-9.24	95.73
	HSP 174	2.20	-25.84	28.04	N/A	-9.40	63.32
	HSP 176	2.13	-26.85	28.98	2.99	-8.90	96.42
	HSP 61	2.05	-26.45	28.50	1.31	-8.69	97.66
	HSP 62	1.42	-26.46	27.88	N/A	-9.05	77.61
	HSP 177	1.66	-26.16	27.82	N/A	-9.01	77.01
	HSP 63	1.16	-26.40	27.56	N/A	-7.30	43.32
	HSP 178	2.18	-26.27	28.45	N/A	-8.37	53.34
	HSP 64	2.18	-27.65	29.83	N/A	-13.44	48.56
	HSP 65	1.60	-26.64	28.24	N/A	-13.31	90.51
	HSP 66	3.75	-26.63	30.38	1.33	-9.51	98.38
	HSP 179	2.47	-26.09	28.56	N/A	-9.22	32.93
	HSP 69	0.91	-27.21	28.12	N/A	-13.38	62.87
Middle Smithian	HSP 70	3.27	-27.35	30.62	N/A	-8.63	80.45
	HSP 180	2.03	-26.60	28.63	N/A	-8.83	65.25
	HSP 181	1.31	-27.62	28.93	N/A	-10.62	28.29
	HSP 71	3.01	-27.40	30.41	3.92	-8.58	75.49
	HSP 72	1.06	-26.71	27.77	N/A	-10.52	83.76
	HSP 73	1.80	-27.07	28.87	N/A	-9.50	37.57
	HSP 182	1.53	-26.56	28.09	N/A	-9.41	49.45
	HSP 74	2.67	-27.13	29.80	2.67	-8.74	87.27
	HSP 75	0.83	-25.18	26.01	3.86	-8.96	91.32
	HSP 76	1.17	-26.75	27.92	N/A	-9.00	95.51
	HSP 183	1.03	-26.18	27.21	N/A	-8.58	31.83
	HSP 77	1.06	-27.24	28.30	N/A	-9.98	47.04
	HSP 78	0.80	-27.73	28.53	2.67	-9.17	91.09
	HSP 79	1.19	-27.05	28.24	N/A	-9.10	95.80
	HSP 184	1.65	-23.25	24.90	2.62	-9.33	97.08
	HSP 80	0.04	-26.70	26.74	N/A	-7.93	99.15
	HSP 144	-0.33	-27.68	27.35	4.19	-8.47	86.02
	HSP 81	0.16	-28.32	28.48	3.20	-8.55	93.54
	HSP 82	-0.16	-27.05	26.89	N/A	-8.21	98.49
	HSP 83	-0.15	-29.01	28.86	3.89	-8.61	98.32
	HSP 84	-0.63	-27.79	27.16	2.25	-8.58	98.21
	HSP 85	-2.90	-29.72	26.82	N/A	-7.84	99.43
	HSP 86	-3.32	-28.19	24.87	N/A	-8.06	94.71
	HSP 87	-3.67	-29.76	26.09	3.38	-7.74	96.43
	HSP 89	-3.57	-30.11	26.54	1.56	-6.93	98.59
Up. Sm.	HSP 90	-3.40	-29.77	26.37	N/A	-8.28	66.86
	HSP 142	-5.08	-29.62	24.54	23.23	-7.10	45.97
	HSP 143	-0.65	-28.60	27.95	32.00	-8.37	28.89
	HSP 140	5.50	-26.67	32.17	6.14	-7.66	88.74
Lower	HSP 91	5.86	-26.01	31.87	3.82	-8.59	95.48
	HSP 92	5.89	-28.69	34.58	5.49	-9.16	95.60

HSP 93	5.91	-24.66	30.57	3.05	-10.27	98.33
HSP 94	5.99	-23.88	29.87	1.26	-10.02	96.55
HSP 96	5.91	-25.83	31.74	3.46	-8.35	80.20
HSP 95	4.53	-26.77	31.30	N/A	-11.21	80.28
HSP 97	5.31	-26.15	31.46	N/A	-8.30	69.65
HSP 185	5.21	-25.73	30.94	N/A	-9.50	91.66
HSP 98	2.58	-25.55	28.13	N/A	-8.23	33.25
HSP 99	5.06	-25.58	30.64	N/A	-7.58	60.70
HSP 100	5.38	-26.43	31.81	4.40	-8.43	79.54
HSP 101	5.38	-26.14	31.52	4.79	-8.64	88.86
HSP 102	5.38	-25.21	30.59	N/A	-10.12	94.23
HSP 103	7.17	-23.81	30.98	1.36	-7.47	99.12
HSP 104	7.17	-24.44	31.61	1.44	-8.72	98.97
HSP 105	7.02	-23.88	30.90	3.70	-8.18	97.69
HSP 106	5.85	-24.21	30.06	N/A	-8.20	96.14
HSP 107	5.32	-25.36	30.68	2.17	-9.78	96.83
HSP 108	5.12	-26.23	31.35	3.75	-9.57	97.61
HSP 109	5.30	-24.93	30.23	N/A	-9.51	97.24
HSP 110	4.85	-23.90	28.75	7.81	-7.86	86.76
HSP 111	4.89	-28.48	33.37	7.54	-8.26	94.96
HSP 112	5.14	-26.14	31.28	N/A	-8.52	86.47
HSP 113	5.20	-27.35	32.55	5.14	-8.22	94.94
HSP 114	4.68	N/A	N/A	N/A	-8.36	99.40
HSP 115	4.54	-25.58	30.12	N/A	-8.90	95.04
HSP 116	3.73	-26.89	30.62	4.61	-8.97	85.12
HSP 117	3.40	-27.06	30.46	2.14	-8.15	90.70
HSP 118	3.75	-27.91	31.66	N/A	-8.09	50.00
HSP 119	3.95	-25.89	29.84	2.59	-9.75	90.76
HSP 120	3.91	-27.08	30.99	N/A	-8.76	89.03
HSP 121	4.02	-27.29	31.31	N/A	-7.46	89.14
HSP 122	4.00	-27.23	31.23	9.76	-7.98	66.36
HSP 123	2.46	-22.44	24.90	N/A	-10.21	94.81
HSP 124	3.31	-27.05	30.36	N/A	-8.35	79.68
HSP 125	3.07	-26.57	29.64	5.94	-9.02	92.44
HSP 126	2.72	-27.72	30.44	5.16	-8.49	86.05
HSP 127	-0.08	-29.57	29.49	12.88	-6.59	30.40
HSP 128	-0.40	-29.37	28.97	5.80	-7.90	67.80
HSP 130	1.22	-28.55	29.77	75.56	-8.32	31.31

VPDB: Vienna Pee Dee Belemnite; *: outliers removed from graphical representation on Fig. 7; N/A: sample below the detection level.

Supplementary Table S2. Geochemical data with trace and major elements results.

	Sample	Al (Wt. %)	Fe/Al	Zr/Al	Th/Al	V/Al	Sr/Al	Cr/Al	Ni/Al	P/Al	Mn/Al	U/Al
Permian (middle to upper?)	HSP 1	0.167	0.67	1.92E-02	3.60E-04	8.40E-03	3.12E-02	7.80E-02	2.94E-01	0.12	0.09	5.40E-04
	HSP 3	0.323	0.16	2.54E-02	3.72E-04	2.48E-03	7.43E-03	6.19E-02	2.85E-01	0.02	0.02	3.10E-04
	HSP 4	0.931	0.28	3.02E-02	2.90E-04	2.79E-03	4.19E-03	1.83E-02	7.51E-02	0.02	0.01	2.58E-04
	HSP 6	0.357	0.10	8.57E-02 *	3.36E-04	5.88E-03	8.40E-03	7.28E-02	3.44E-01	0.02	0.01	5.04E-04
	HSP 7 b	0.545	0.28	4.16E-02	2.57E-04	4.22E-03	6.24E-03	3.85E-02	1.58E-01	0.01	0.01	1.65E-04
	HSP 10	0.209	21.43	1.67E-02	3.83E-04	1.06 *	2.87E-02	4.78E-02	5.45E-01	0.22	0.11	2.58E-03
	HSP 11	0.122	3.85	1.48E-02	5.75E-04	1.81E-02	5.18E-02	6.65E-01	1.80E+00	4.52	0.08	6.90E-03
	HSP 14	0.135	2.10	1.26E-02	5.93E-04	1.11E-02	4.37E-02	3.41E-01	1.64E+00	2.22	0.05	5.41E-03
	HSP 15	0.855	0.51	5.26E-03	2.69E-04	7.49E-03	8.77E-03	2.81E-02	5.50E-02	0.08	0.05	4.56E-04
	HSP 17	0.352	1.35	7.67E-03	2.56E-04	6.25E-03	1.05E-02	1.73E-01	4.43E-01	0.12	0.04	4.26E-04
	HSP 18	0.177	2.80	9.02E-03	2.82E-04	5.64E-03	1.47E-02	2.14E-01	1.14E+00	0.14	0.05	1.02E-03
	HSP 19	0.167	2.81	6.60E-03	1.80E-04	5.40E-03	1.32E-02	4.08E-01	1.21E+00	0.12	0.08	8.40E-04
	HSP 20	0.151	1.90	7.96E-03	2.65E-04	4.64E-03	2.19E-02	4.57E-01	2.49E+00	0.22	0.08	9.94E-04
	HSP 22	0.408	1.09	1.47E-02	4.66E-04	7.12E-03	1.52E-02	1.60E-01	4.47E-01	0.52	0.05	9.57E-04
Griesbachian - Dienerian	HSP 25	2.114	0.41	7.43E-03	2.84E-04	4.82E-03	3.78E-03	1.80E-02	1.75E-02	0.08	0.02	2.65E-04
	HSP 186	1.209	0.55	1.13E-02	3.39E-04	3.31E-03	8.19E-03	1.90E-02	5.04E-02	0.28	0.02	3.47E-04
	HSP 187	1.307	0.67	7.27E-03	6.35E-04	5.05E-03	2.44E-02	2.45E-02	5.35E-02	1.68	0.03	1.06E-03
	HSP 28	0.445	0.68	1.53E-02	9.00E-04	1.03E-02	1.18E-01	5.62E-02	4.27E-02	13.47	0.10	6.84E-03
	HSP 29	1.744	0.89	8.49E-03	3.04E-04	2.18E-03	7.11E-03	6.88E-03	2.52E-02	0.04	0.23	1.03E-04
	HSP 30	2.104	0.33	7.70E-03	2.90E-04	2.33E-03	5.37E-03	5.23E-03	1.66E-02	0.02	0.16	9.03E-05
	HSP 31	1.715	0.34	1.06E-02	3.50E-04	2.22E-03	6.36E-03	7.58E-03	2.86E-02	0.02	0.27	1.05E-04
	HSP 32	0.482	0.43	8.72E-03	2.70E-04	1.66E-03	9.86E-02	1.45E-02	6.02E-02	0.05	0.79	1.04E-04
	HSP 146	0.542	0.42	7.93E-03	2.21E-04	1.66E-03	5.99E-02	7.37E-03	3.13E-02	0.08	0.56	9.22E-05
	HSP 147	1.905	0.42	8.24E-03	2.57E-04	1.78E-03	7.45E-03	6.30E-03	2.89E-02	0.03	0.06	7.35E-05
	HSP 33	2.284	0.41	4.42E-03	1.88E-04	1.84E-03	6.26E-03	3.50E-03	1.36E-02	0.01	0.07	6.13E-05
	HSP 148	1.818	0.42	1.30E-02	3.19E-04	1.87E-03	7.04E-03	9.35E-03	4.84E-02	0.03	0.05	9.35E-05
	HSP 35	1.302	0.38	1.11E-02	2.84E-04	1.92E-03	1.84E-02	6.14E-03	2.61E-02	0.05	0.14	9.98E-05
	HSP 150	0.651	0.42	1.67E-02	4.61E-04	2.15E-03	7.93E-02	7.68E-03	3.07E-02	0.10	0.32	1.69E-04
	HSP 152	0.566	0.48	9.18E-03	3.36E-04	2.65E-03	6.16E-02	7.06E-03	2.83E-02	0.17	0.47	1.41E-04
	HSP 153	2.024	0.52	1.62E-02	3.41E-04	2.07E-03	5.98E-03	6.92E-03	3.16E-02	0.03	0.06	1.09E-04
	HSP 36	0.924	0.45	1.43E-02	3.25E-04	1.95E-03	4.09E-02	8.66E-03	3.46E-02	0.05	0.93	1.08E-04
	HSP 37	0.296	0.88	3.71E-03	2.02E-04	2.36E-03	1.50E-01	1.69E-02	6.41E-02	0.11	2.11	6.75E-05
	HSP 38	0.204	1.22	5.40E-03	3.44E-04	2.94E-03	4.18E-01	1.96E-02	7.85E-02	0.19	1.70	1.96E-04
	HSP 40	1.270	0.48	1.95E-02	4.80E-04	1.73E-03	1.39E-02	1.02E-02	4.17E-02	0.08	0.26	1.34E-04
	HSP 41	1.469	0.45	1.50E-02	3.74E-04	2.04E-03	1.26E-02	9.53E-03	4.22E-02	0.04	0.22	1.16E-04
	HSP 42	0.127	1.65	1.18E-02	9.45E-04	N/A	1.02 *	3.15E-02	1.10E-01	0.22	2.15	3.15E-04
	HSP 45	0.564	0.70	2.22E-02	7.81E-04	2.31E-03	6.62E-02	1.60E-02	6.92E-02	0.25	0.62	1.95E-04
	HSP 154	0.564	0.55	1.47E-02	5.32E-04	2.48E-03	8.91E-02	8.87E-03	3.73E-02	0.13	0.61	1.60E-04
	HSP 155	1.858	0.42	9.21E-03	3.12E-04	2.05E-03	5.49E-03	8.07E-03	3.88E-02	0.02	0.10	8.61E-05
	HSP 157	0.101	1.77	8.95E-03	8.95E-04	N/A	1.23 *	3.98E-02	1.79E-01	0.07	1.14	6.96E-04
	HSP 158	1.463	0.46	8.13E-03	3.49E-04	1.85E-03	4.92E-03	7.52E-03	3.35E-02	0.04	0.08	7.52E-05
	HSP 159	0.712	0.56	1.63E-02	4.92E-04	1.69E-03	9.55E-03	1.26E-02	5.48E-02	0.10	0.28	1.97E-04
Lo	HSP 161	0.146	1.23	1.79E-02	8.93E-04	5.50E-03	1.90E-01	2.75E-02	9.62E-02	0.12	1.45	2.75E-04

	HSP 164	0.143	1.08	1.33E-02	4.90E-04	4.20E-03	6.60E-01	2.10E-02	7.00E-02	0.17	1.12	2.80E-04
	HSP 166	0.421	0.56	3.40E-02	7.61E-04	2.85E-03	5.94E-02	1.19E-02	5.23E-02	0.12	0.53	2.14E-04
	HSP 167	1.350	0.38	5.66E-02	8.67E-04	2.37E-03	6.59E-03	8.15E-03	2.96E-02	0.07	0.07	2.52E-04
	HSP 49	0.082	1.41	1.71E-02	7.31E-04	7.31E-03	5.18E-01	4.88E-02	2.19E-01	0.11	2.20	8.53E-04
	HSP 168	0.214	0.83	3.27E-02	7.46E-04	3.73E-03	1.30E-01	1.87E-02	3.73E-02	0.12	1.31	2.80E-04
	HSP 169	0.693	0.48	6.16E-02	1.33E-03	2.74E-03	2.58E-02	1.15E-02	3.89E-02	0.22	0.48	4.18E-04
	HSP 170	1.180	0.34	3.22E-02	5.17E-04	1.53E-03	9.15E-03	1.36E-02	6.69E-02	0.08	0.19	1.61E-04
	HSP 54	0.119	1.70	2.18E-02	7.56E-04	5.88E-03	3.88E-01	5.04E-02	2.44E-01	0.29	2.31	3.36E-04
	HSP 171	0.111	1.38	1.35E-02	6.30E-04	6.30E-03	6.64E-01	3.60E-02	9.00E-02	0.18	1.64	2.70E-04
	HSP 59	1.426	0.48	3.85E-02	6.24E-04	2.24E-03	1.08E-02	1.12E-02	4.63E-02	0.07	0.11	1.96E-04
	HSP 172	0.953	0.39	5.11E-02	8.08E-04	1.68E-03	1.61E-02	1.78E-02	7.87E-02	0.14	0.20	2.62E-04
	HSP 60 b	0.201	1.03	1.39E-02	5.47E-04	4.48E-03	3.76E-01	1.99E-02	7.46E-02	0.11	0.85	1.99E-04
	HSP 175	0.180	0.95	1.72E-02	5.56E-04	3.33E-03	4.17E-01	2.22E-02	6.11E-02	0.11	0.90	2.22E-04
	HSP 176	0.148	1.16	2.02E-02	6.07E-04	N/A	4.89E-01	2.70E-02	7.42E-02	0.31	1.68	2.70E-04
	HSP 61	0.077	1.14	2.08E-02	5.21E-04	N/A	7.71E-01	6.52E-02	2.48E-01	0.23	2.44	2.61E-04
	HSP 177	0.550	0.32	2.71E-02	4.72E-04	1.64E-03	7.70E-02	1.27E-02	2.18E-02	0.11	0.37	1.64E-04
	HSP 178	1.117	0.30	3.51E-02	6.54E-04	1.97E-03	1.71E-02	9.85E-03	3.76E-02	0.05	0.19	2.15E-04
	HSP 64	1.217	0.29	4.68E-02	7.80E-04	2.22E-03	1.33E-02	1.31E-02	5.18E-02	0.12	0.06	3.53E-04
	HSP 66	0.090	1.67	2.00E-02	7.78E-04	8.89E-03	7.28E-01	4.45E-02	1.44E-01	0.70	1.14	6.67E-04
	HSP 179	1.879	0.35	6.81E-03	2.45E-04	1.86E-03	6.44E-03	3.73E-03	1.01E-02	0.02	0.03	6.92E-05
	HSP 69	0.802	0.32	1.11E-01	1.28E-03	2.74E-03	2.03E-02	1.62E-02	5.99E-02	0.12	0.12	5.99E-04
Middle Smithian	HSP 70	0.741	0.60	1.32E-02	4.05E-04	2.43E-03	8.06E-02	8.10E-03	2.83E-02	0.11	0.15	1.35E-04
	HSP 181	1.913	0.33	1.47E-02	3.29E-04	1.93E-03	5.70E-03	8.36E-03	3.50E-02	0.04	0.03	1.05E-04
	HSP 71	0.749	0.44	1.30E-02	3.61E-04	1.74E-03	7.74E-02	9.35E-03	3.61E-02	0.09	0.15	1.34E-04
	HSP 72	0.376	0.47	2.26E-02	3.99E-04	1.33E-03	8.44E-02	1.60E-02	6.65E-02	0.13	0.39	1.60E-04
	HSP 182	1.522	0.39	1.45E-02	3.29E-04	2.17E-03	1.40E-02	6.57E-03	2.37E-02	0.04	0.07	1.05E-04
	HSP 74	0.471	0.59	1.40E-02	3.61E-04	2.34E-03	1.65E-01	1.27E-02	5.10E-02	0.08	0.30	1.27E-04
	HSP 75	0.254	0.98	2.52E-02	5.12E-04	1.97E-03	1.06E-01	1.97E-02	6.69E-02	0.62	0.79	2.36E-04
	HSP 183	1.432	0.31	1.58E-02	3.84E-04	1.54E-03	8.59E-03	1.40E-02	6.71E-02	0.07	0.08	1.12E-04
	HSP 78	0.315	0.84	2.41E-02	4.45E-04	2.86E-03	8.03E-02	1.59E-02	6.35E-02	0.29	0.65	1.91E-04
	HSP 184	0.151	1.11	7.96E-03	3.98E-04	3.31E-03	2.53E-01	1.99E-02	6.63E-02	0.26	1.21	1.99E-04
	HSP 80	0.053	1.78	1.13E-02	3.78E-04	N/A	4.31E-01	5.67E-02	1.51E-01	0.41	4.01	3.78E-04
	HSP 81	0.333	0.61	6.90E-03	2.70E-04	2.40E-03	6.99E-02	1.20E-02	3.00E-02	0.14	0.72	1.20E-04
	HSP 83	0.130	1.86	9.25E-03	9.25E-04	1.08E-02	1.66E-01	N/A	2.31E-02	1.48	1.24	1.00E-03
	HSP 85	0.050	0.77	9.94E-03	1.99E-04	1.39E-02	4.00E-01	3.98E-02	1.19E-01	0.26	1.85	9.15E-03
	HSP 86	0.209	1.04	1.91E-02	4.78E-04	5.26E-03	8.95E-02	2.39E-02	7.65E-02	0.21	0.65	3.30E-03
	HSP 89	0.093	0.79	8.64E-03	3.24E-04	8.64E-03	3.02E-01	N/A	4.32E-02	0.14	3.26	1.84E-03
Up. Sm.	HSP 90	1.024	0.40	1.94E-02	4.39E-04	2.54E-03	3.33E-02	7.81E-03	2.64E-02	0.03	0.25	2.54E-04
	HSP 142	2.228	0.57	7.90E-03	3.05E-04	2.83E-03	6.91E-03	3.14E-03	6.73E-03	0.02	0.12	1.08E-04
	HSP 143	3.668	0.46	5.29E-03	2.59E-04	2.54E-03	3.98E-03	2.18E-03	2.45E-03	0.01	0.02	6.82E-05
	HSP 140	0.691	0.53	4.20E-03	2.90E-04	2.61E-03	2.13E-01	4.34E-03	8.69E-03	0.02	0.09	1.01E-04
Lower	HSP 91	0.257	0.83	1.17E-02	3.12E-04	2.73E-03	2.40E-01	1.56E-02	5.45E-02	0.04	1.08	1.17E-04
	HSP 96	0.521	0.36	2.55E-02	3.45E-04	1.92E-03	5.10E-02	1.34E-02	6.91E-02	0.06	0.52	1.53E-04
	HSP 97	0.834	0.29	2.65E-02	3.84E-04	1.80E-03	2.56E-02	1.32E-02	5.28E-02	0.07	0.39	1.44E-04
	HSP 185	0.246	0.64	2.03E-02	3.66E-04	N/A	8.33E-02	2.03E-02	6.91E-02	0.07	1.07	1.22E-04

HSP 98	1.567	0.25	1.86E-02	3.57E-04	1.40E-03	7.21E-03	1.15E-02	6.06E-02	0.04	0.10	1.09E-04
HSP 100	0.638	0.51	9.41E-03	2.35E-04	1.72E-03	3.18E-02	1.10E-02	5.80E-02	0.04	0.37	7.84E-05
HSP 102	0.183	1.09	1.86E-02	3.29E-04	3.83E-03	2.79E-01	2.19E-02	8.22E-02	0.17	0.85	1.64E-04
HSP 103	0.053	1.39	1.51E-02	3.78E-04	N/A	1.57 *	5.67E-02	1.89E-01	0.58	2.18	N/A
HSP 105	0.106	0.66	8.50E-03	2.83E-04	N/A	7.43E-01	3.78E-02	1.23E-01	0.21	1.02	1.89E-04
HSP 106	0.135	1.27	1.33E-02	4.45E-04	3.70E-03	2.58E-01	2.96E-02	1.11E-01	0.15	1.31	2.96E-04
HSP 108	0.108	1.32	7.37E-03	2.77E-04	N/A	6.54E-01	2.77E-02	7.37E-02	0.20	1.46	9.22E-05
HSP 109	0.132	1.40	6.05E-03	3.02E-04	N/A	2.40E-01	2.27E-02	6.80E-02	0.10	1.76	1.51E-04
HSP 111	0.267	1.11	6.73E-03	2.99E-04	2.62E-03	2.26E-01	1.12E-02	2.99E-02	0.07	0.81	1.50E-04
HSP 113	0.185	1.25	1.19E-02	3.24E-04	3.24E-03	2.66E-01	2.16E-02	7.02E-02	0.08	1.01	1.62E-04
HSP 115	0.148	1.53	9.45E-03	3.37E-04	N/A	2.54E-01	2.70E-02	1.15E-01	0.21	1.20	2.70E-04
HSP 116	0.228	0.89	6.59E-03	2.64E-04	3.52E-03	1.87E-01	2.20E-02	8.79E-02	0.16	0.50	1.32E-04
HSP 118	1.117	0.58	9.76E-03	3.13E-04	2.15E-03	3.32E-02	8.06E-03	2.96E-02	0.09	0.10	1.07E-04
HSP 120	0.257	0.80	1.56E-02	3.51E-04	2.73E-03	2.10E-01	1.56E-02	6.62E-02	0.13	0.56	1.95E-04
HSP 122	0.902	0.46	1.41E-02	3.77E-04	2.22E-03	3.04E-02	7.76E-03	2.99E-02	0.07	0.11	1.44E-04
HSP 123	0.101	3.55	1.09E-02	2.98E-04	N/A	3.16E-01	3.98E-02	1.29E-01	0.09	1.00	1.99E-04
HSP 124	0.707	0.58	5.24E-03	2.83E-04	2.26E-03	5.52E-02	7.08E-03	2.97E-02	0.05	0.10	8.49E-05
HSP 126	0.574	0.55	1.08E-02	3.48E-04	2.61E-03	4.25E-02	6.97E-03	2.79E-02	0.13	0.16	1.57E-04
HSP 127	1.789	0.41	7.83E-03	2.74E-04	2.46E-03	8.50E-03	1.06E-02	5.03E-02	0.07	0.03	1.12E-04
HSP 130	2.059	0.44	9.91E-03	3.21E-04	2.09E-03	7.19E-03	5.83E-03	1.99E-02	0.02	0.02	1.12E-04

*: outliers removed from graphical representation on Fig. 3; N/A: sample below the detection level.

Appendix 3: Supplementary material belonging to the article "Controlling factors for differential subsidence in the Sonoma Foreland Basin (Early Triassic, western USA)" (see section IV)

This supplementary material provides additional data used to perform the integrated study presented in Caravaca *et al.*, *in press* (see section IV). It includes a synthetic facies table of the main lithologies found in the SFB (Appendix 2.1), the exhaustive list of studied outcrops (Appendix 2.2), the complete and detailed set of initial parameters and results for the backstripping analyses performed on four selected sections of the SFB (Appendix 2.3), and the preliminary isopach map of the spatial distribution of the sedimentary thickness recorded during the Permian/Triassic unconformity-Smithian interval obtained using Global Mapper GIS software (Appendix 2.4).

Geological Magazine

Controlling factors for differential subsidence in the Sonoma Foreland Basin (Early Triassic, western USA)

Gwénaël Caravaca[1], Arnaud Brayard[1], Emmanuelle Vennin[1], Michel Guiraud[1], Laetitia Le Pourhiet[2], Anne-Sabine Grosjean[1], Christophe Thomazo[1], Nicolas Olivier[3], Emmanuel Fara[1], Gilles Escarguel[4], Kevin G. Bylund[5], James F. Jenks[6], Daniel A. Stephen[7].

Supplementary material

Appendix 1

Synthetic facies table of the main lithologies present in Lower Triassic Sonoma Foreland Basin and associated depositional environment, and estimated Paleobathymetric ranges, as used in the backstripping analysis. References are given in the table accordingly.

Lithologies (formation)	Geographic extension (estimated temporal	Diagnostic features	Sedimentary structures	Depositional Settings	References	Paleobathymetric range
"Red Beds" (Moenkopi Group)	Southern SFB (Griesbachian to lower/middle Smithian)	a) Conglomerates (locally), moderately to well-sorted pebble to grabule assemblages b) Cm- to dm- beds of fine to medium siltstones and sandstones with subrounded to subangular quartz grains and micas	a) Channelizing erosion base b) Planar and cross-bedded laminations, asymmetric and climbing ripples. Bioturbation, locally intense	a) Transitional continental to marine flood plain, embayement b) intertidal mud flat	Goodspeed & Lucas, 2007; Brayard *et al.* , 2013; Olivier *et al.* , 2014, 2016; Vennin *et al.* , 2015	1 to 2.5m
Microbial limestones (Moenkopi Group)	Southern SFB (Lower/middle Smithian)	M- beds of microbial carbonates (peloidal, clotted micritic or micritic laminae textures). Associated with sponges, gastropods, ostracods, bivalves and echinoderms.	Macrostructure: pluri-dm to m-coalescent domes; planar to wavy undulated laminations. Mesostructure: stromatolitic and/or thrombolitic, presence of numerous fenestrae	Intertidal to subtidal inner ramp	Brayard et al., 2013; Olivier et al., 2014, 2016; Vennin et al., 2015	2.5 to 10m
Siltstones (Dinwoody & Woodside Formations)	Northern SFB (Griesbachian to middle Smithian)	Cm- to dm beds of fine (dolo-)siltstones with sub-rounded quartz grains and micas	Planar to oblique laminations, asymmetric ripples, megaripples	Intertidal inner ramp	Newell & Kummel, 1942; Kummel, 1954, 1957, Chamberlain *et al*, 1980	5 to 30m
Bioclastic limestones and shales (Thaynes Group)	Entire SFB (Middle/upper Smithian to Spathian)	a) Dm- to metric bioclasts supported limestone beds with bivalves, gastropods, serpulids, echinoderms in a peloidal to micritic matrix. Locally ooidic and cortoidic beds are present as well. b) Fine shales	a) Planar, trough and hummocky cross-bedding, asymmetric ripples, megaripples and tempestites, normal and inverse grading. Bioturbation b) No distinctive structures	a) Subtidal to upper offshore ramp b) Shale dominated outer ramp	Brayard et al., 2013; Olivier et al., 2014, 2016; Vennin et al., 2015	a) 5 to 50m b) 50 to 90m

Appendix 2

List of studied sections, with GPS coordinates and references when data are taken from literature. An asterisk (*) indicates a minimum thickness value. Initials for sections illustrated in the manuscript are also indicated.

Locality	GPS coordinates (approximate for literature data)	PTU-Smithian interval thickness	Notes	References	Retrodeformation sector (Table 1)
Gros Ventre Canyon	43.775185° -110.333094°	241*	Dinwoody and Woodside Fm. only, misses Smithian part of Thaynes Fm.	Kummel, 1954, 1957	1
Wind River Canyon	42.767269° -109.217611°	36*	Dinwoody Fm. only, Woodside Fm. not measured (Red Peak Fm.)	Newell & Kummel, 1942	1
Brush Creek	40.598932° -109.463689°	123		Field measurement	1
Lake Fork	40.517877° -110.435441°	207*	Woodside Fm. only, misses Smithian part of the Thaynes Fm.	Kummel, 1954, 1957	1
White Rocks	40.574083° -109.820793°	158*	Woodside Fm. only, misses Smithian part of the Thaynes Fm.	Kummel, 1954, 1957	1
Duchesne River	40.436090° -110.817317°	242*	Woodside Fm. only, misses Smithian part of the Thaynes Fm.	Kummel, 1954, 1957	1
Bourdette Draw	40.373293° -109.209247°	114*		Heckert *et al.*, 2015	1
San Rafael Swell	38.872793° -110.558438°	70		Goodspeed & Lucas, 2007	1
Torrey area (T; Beas Lewis Flats)	38.283606° -111.313631°	57		Field measurement (Olivier *et al.*, 2015)	1
Circle Cliffs	37.992881° -111.128166°	~15		Field measurement	1
Kannaraville	37.519590° -113.181241°	~80		Field measurement	1
Virgin Dam	37.196480° -113.234689°	55		Field measurement (Olivier *et al.*, 2014)	1
Black Rock Canyon	37.099110° -113.294606°	~35		Field measurement	1

Rock Canyon (RC)	36.976783° -113.261400°	23,5		Field measurement	1
Trapper Creek	45.683504° -112.762157°	194*	Dinwoody Fm. only	Kummel, 1954, 1957	2
Greenstone Gulch	45.374291° -112.704205°	214*	Dinwoody Fm. only	Kummel, 1954, 1957	2
Dalys Spur	45.072219° -112.692223°	288*	Dinwoody Fm. only	Kummel, 1954, 1957	2
Hogback Mountain	44.865113° -112.130820°	255*	Dinwoody and Woodside Fm. only, misses Smithian part of Thaynes Fm.	Kummel, 1954, 1957	2
Fossil Creek	44.764825° -111.852615°	192*	Dinwoody and Woodside Fm. only, misses Smithian part of Thaynes Fm.	Kummel, 1954, 1957	2
Little Water Canyon	44.660495° -112.747416°	332		Kummel, 1954, 1957	2
Hawley Creek	44.625504° -113.143714°	300*	Only Smithian part of the Thaynes Fm.	Paull & Paull, '91	2
Odell Creek	44.561568° -111.863906°	310*	Dinwoody and Woodside Fm. only, misses Smithian part of Thaynes Fm.	Kummel, 1954, 1957	2
Little Sheep Creek	44.523573° -112.696346°	296*	Dinwoody and Woodside Fm. only, misses Smithian part of Thaynes Fm.	Sadler, 1981	2
Bear Gulch	43.312260° -110.730134°	294*	Dinwoody and Woodside Fm. only, misses Smithian part of Thaynes Fm.	Kummel, 1954, 1957	2
Grays Range	42.935617° -111.366417°	450*		Field measurement	3
Sheep Creek (SC)	42.868187° -111.372443°	~500	Dinwoody Fm. measure from geologic map, Smithian part of Thaynes Fm. from Kummel	Kummel, 1954, 1957; Rioux *et al.*, 1975	3
Fort Hall Reservation	42.841336° -112.584126°	360		Kummel, 1954, 1957	3
North Piney Creek	42.637904° -110.325953°	345*	Dinwoody and Woodside Fm. only, misses Smithian part of Thaynes Fm.	Kummel, 1954, 1957	3
Montpellier Canyon	42.344409° -111.203904°	337*	Dinwoody and Woodside Fm. only, misses Smithian part of Thaynes Fm.	Newell & Kummel, 1942; Kummel, 1954, 1957	3

Paris Canyon	42.220270° -111.415473°	~460	Smithian part from correlative Georgetown section	Field measurement; Kummel, 1954, 1957	3
Hot Springs (HS)	42.112226° -111.255145°	540		Field measurement	3
Cokeville	42.074825° -110.817294°	345*	Misses limestones part of Smithian Thaynes Fm.	Kummel, 1954, 1957	3
Rex Peak	41.654641° -111.095798°	374*	Dinwoody and Woodside Fm. only, misses Smithian part of Thaynes Fm.	Chamberlain *et al.*, 1980	3
Lower Weber Canyon (LWC)	41.063626° -111.570078°	210*		Field measurement	4
Diamond Fork	40.030004° -111.508545°	130-235*	Woodside Fm. only, misses Smithian part of the Thaynes Fm.	Constenius *et al.*, 2011	5
Pahvant Range (PR; Dog Valley)	38.674360° -112.521926°	185		Field measurement (Brayard *et al.*, 2013)	6
Star Range	38.357141° -113.129252°	110*	Lower boundary not visible	Field measurement (Brayard *et al.*, 2013)	6
Minersville (M)	38.225545° -112.888220°	105		Field measurement (Vennin *et al.*, 2015)	6
Crittenden Springs	41.546087° -114.184977°	300*		Field measurement	7
Terrace Mountain	41.454115° -113.487207°	534		Doelling, 1980	7
Pequop Mountain	40.500000° -114.750000°	~20		Lucas & Orchard, 2007	7
Palomino Ridge	40.240326° -114.858275°	~70		Field measurement	7
Confusion Range (CR)	39.232513° -113.686809°	120		Field measurement (Brayard *et al.*, 2013)	7

Appendix 3

Subsidence analysis data with complete set of initial parameters and results of the analysis. A. Data and results from the Confusion Range (CR) section. B. Data and results from the Pahvant Range (PR) section. C. Data and results from the Sheep Creek (SC) section. D. Data and results from the Hot Springs (HS) section. E. Synthesis of the tectonic subsidence results for each sections. For location of the analyzed sections, see Fig. 3b and Appendix 2. Radiometric ages

after Burgess *et al.* (2014) and Galfetti *et al.* (2007); age interpolation of ammonoid biozone durations after Brühwiler *et al.*, (2010). Sea level curve after Haq *et al.* (1988).
Subsidence analyses were performed using "OSXBackstrip" software and performing 1D Airy backstripping (after, Allen & Allen, 1990, and Watts, 2001; available at: http://www.ux.uis.no/~nestor/work/programs.html).

Parameters:
Base and top: depth (in km) of the limits of the considered members from top of the section. Age (base and top, in Ma): radiometric or estimated ages for the limits of considered members. Sea level (base and top, in km): estimated paleo-sea level compared to present day, as depths (negative values are above present-day sea-level). Water depth (base and top, in km): paleobathymetry estimated after facies and paleoenvironments characterization. Rho (in g.m^{-3}): density of the dominant lithology. C (in .10^{-5} cm^{-1}): coefficient of exponential relation between depth and porosity (Sclater & Christie, 1980). Phy0 (in %): estimated final porosity of the dominant lithology. Type: 0 for marine deposits, 1 for continental deposits.

A. Data and results from the Confusion Range section (CR in Figs. 3b, 9a, 9e and 9f).

Name	Base (km)	Age base (Ma)	Sea Level base (km)	Water depth base (km)	Top (km)	Age top (Ma)	Sea Level top (km)	Water depth top (km)	Rho (g.m^-3)	C	Phy 0	type
Moenkopi red beds	0,255	251,88	-0,05	0,0025	0,225	251,019	-0,01	0,001	2650	0,27	50%	0
Thaynes shales (Smithian)	0,225	251,019	-0,01	0,001	0,135	250,751	0,2	0,05	2750	0,51	60%	0
Thaynes shales (Spathian)	0,135	250,751	0,2	0,05	0	250,55	0	0,09	2750	0,51	60%	0
	0	250,55	0	0,09								
	0	0	0	0								

Results	Age (Ma)	Compacted thickness (m)	Total subsidence (m)	Tectonic subsidence (m)
	251,9	0	0	0
	251	30	32	36
	250,8	120	130	108
	250,6	255	256	260

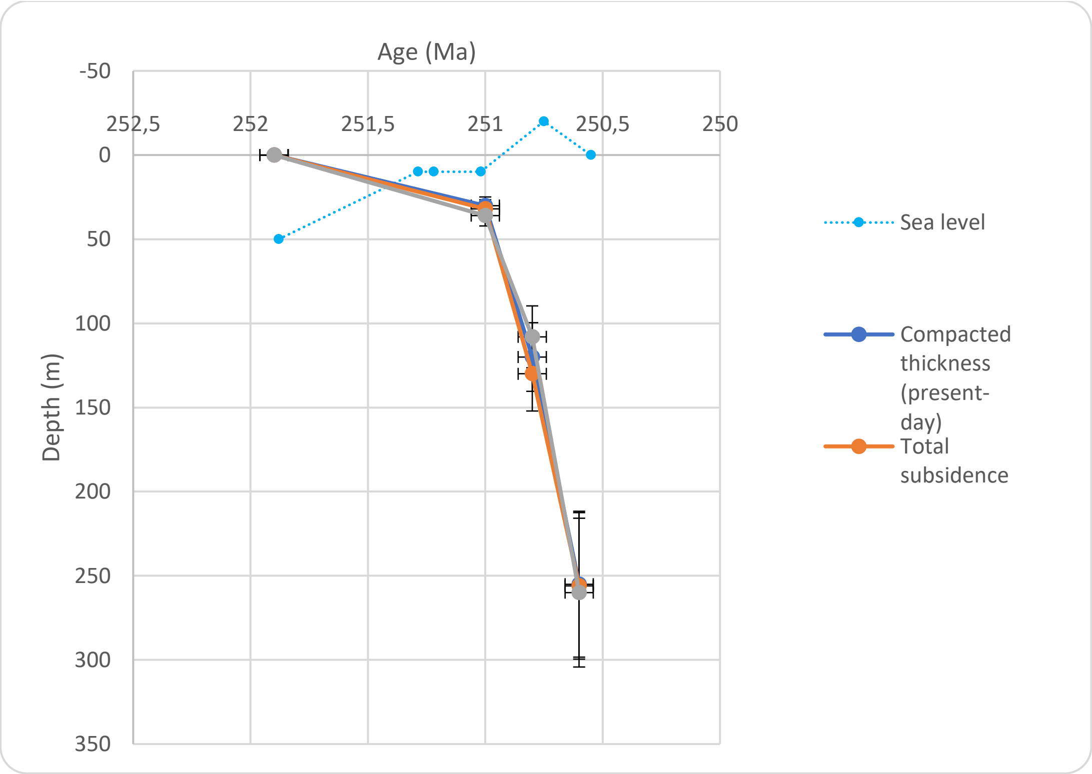

B. Data and results from the Pahvant Range section (PR in Figs. 3b, 9b, 9e and 9f).

Name	Base (km)	Age base (Ma)	Sea Level base (km)	Water depth base (km)	Top (km)	Age top (Ma)	Sea Level top (km)	Water depth top (km)	Rho (g.m^-3)	C	Phy 0	type
Moenkopi red beds	0,295	251,88	-0,05	0,0025	0,235	251,287	-0,01	0,0025	2650	0,27	50	0
Thaynes carbonates	0,235	251,287	-0,01	0,0025	0,11	250,751	0,02	0,05	2750	0,71	25	0
Spathian red beds	0,11	250,751	0,02	0,05	0	250,55	0	0,0025	2650	0,27	50	0

Results	Age (Ma)	Compacted thickness (m)	Total subsidence (m)	Tectonic subsidence (m)
	251,9	0	0	0
	251,3	60	64	58
	250,8	185	190	114
	250,6	295	296	161

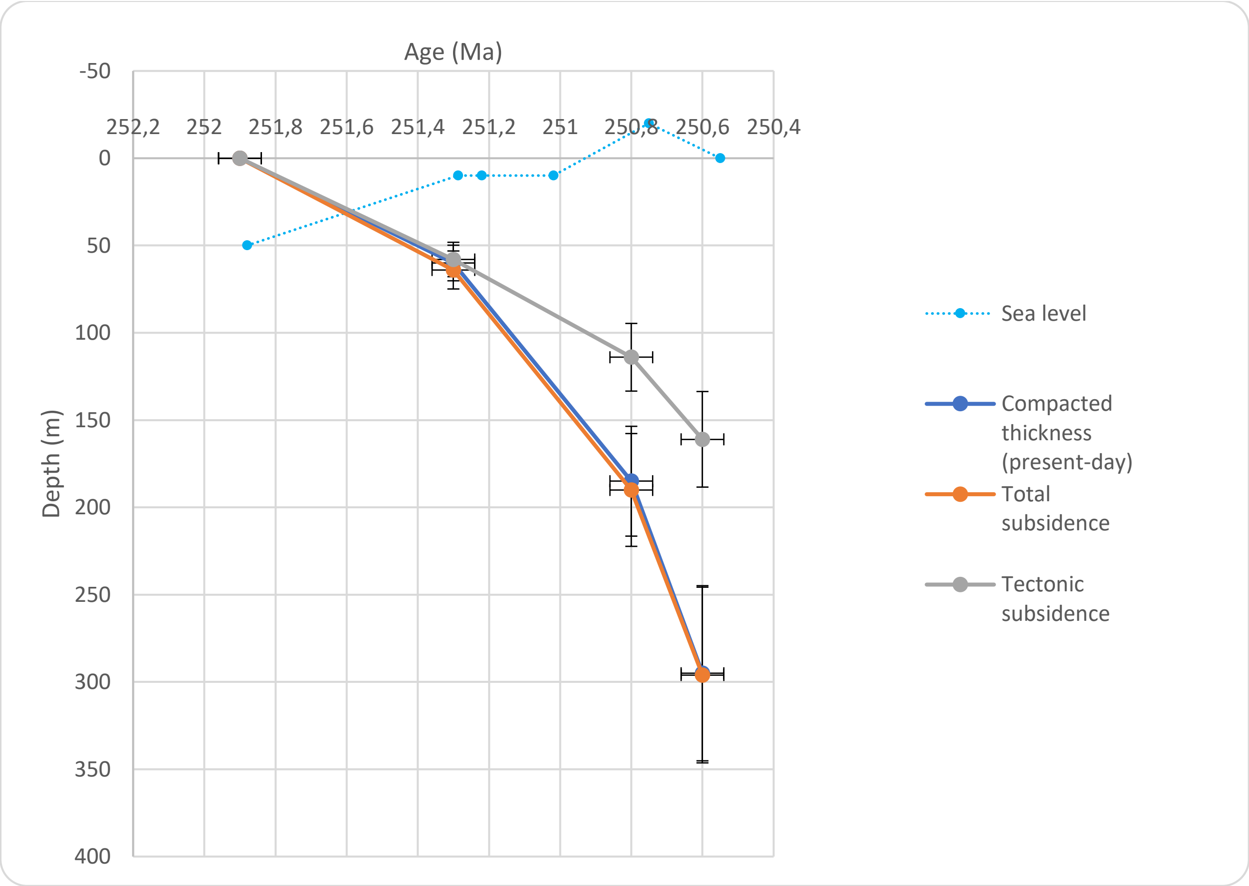

C. Data and results from the Sheep Creek section (SC in Figs. 3, 89c, 9e and 9f).

Name	Base (km)	Age base (Ma)	Sea Level base (km)	Water depth base (km)	Top (km)	Age top (Ma)	Sea Level top (km)	Water depth top (km)	Rho (g.m^-3)	C	Phy 0	type
Dinwoody + Woodside siltstones	0,732	251,88	-0,5	0,005	0,182	250,751	0,02	0,005	2650	0,27	85%	0
Thaynes carbonates	0,182	250,751	0	0,005	0	250,55	0	0,025	2750	0,71	25%	0

Results	Age (Ma)	Compacted thickness (m)	Total subsidence (m)	Tectonic subsidence (m)
	251,9	0	0	0
	250,8	550	627	505
	250,6	732	733	554

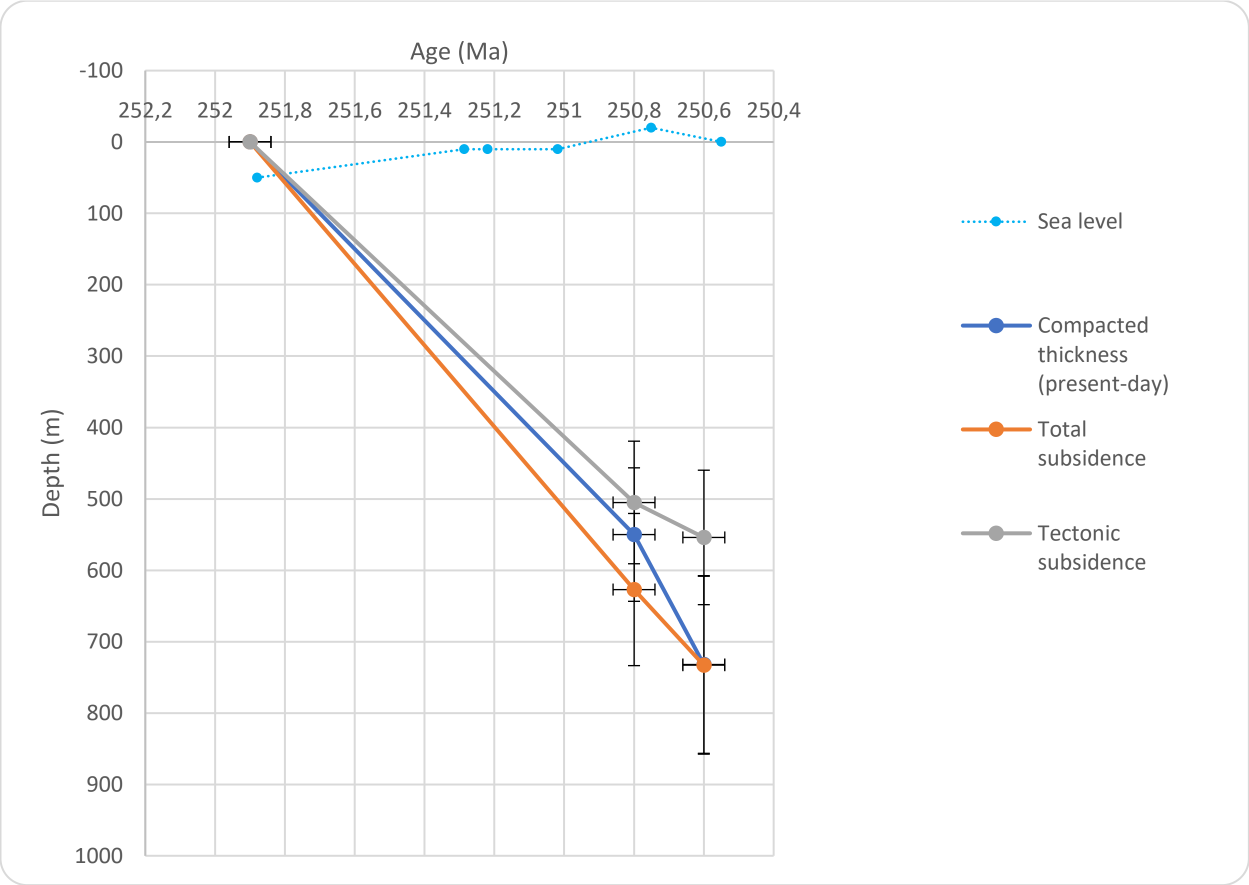

D. Data and results from the Hot Springs section (HS in Figs. 3b, 9d, 9e and 9f).

Name	Base (km)	Age base (Ma)	Sea Level base (km)	Water depth base (km)	Top (km)	Age top (Ma)	Sea Level top (km)	Water depth top (km)	Rho (g.m^-3)	C	Phy 0	type
Dinwoody siltstones	0,79	251,88	-0,05	0	0,435	251,22	-0,01	0,01	2650	0,27	85%	0
Woodside (?) siltstones	0,435	251,22	-0,01	0,01	0,23	250,751	0,02	0,03	2650	0,27	85%	0
Thaynes carbonates	0,23	250,751	0,02	0,03	0	250,55	0	0,025	2750	0,71	25%	0

Results	Age (Ma)	Compacted thickness (m)	Total subsidence (m)	Tectonic subsidence (m)
	251,9	0	0	0
	251,2	355	488	441
	250,8	560	657	559
	250,6	790	792	578

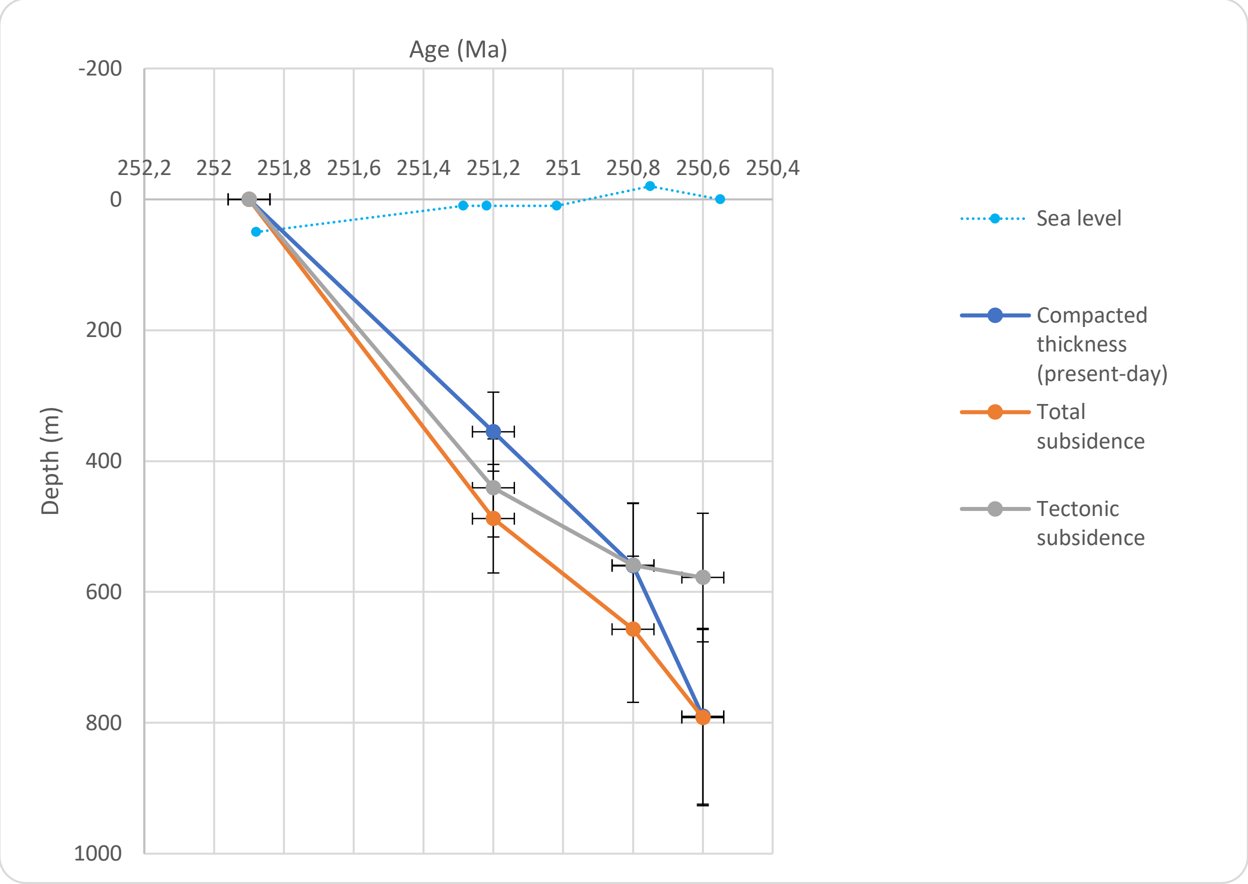

E. Synthesis of the tectonic subsidence results for each section (as presented in Fig. 9e).

	Depth (m) (tectonic subsidence only)				Sea level
Age (Ma)	Confusion Range	Pahvant Range	Sheep Creek	Hot Springs	
251,88	0	0	0	0	50
251,287		58			10
251,22				441	10
251,019	36				10
250,751	108	114	505	559	-20
250,55	260	161	554	578	0

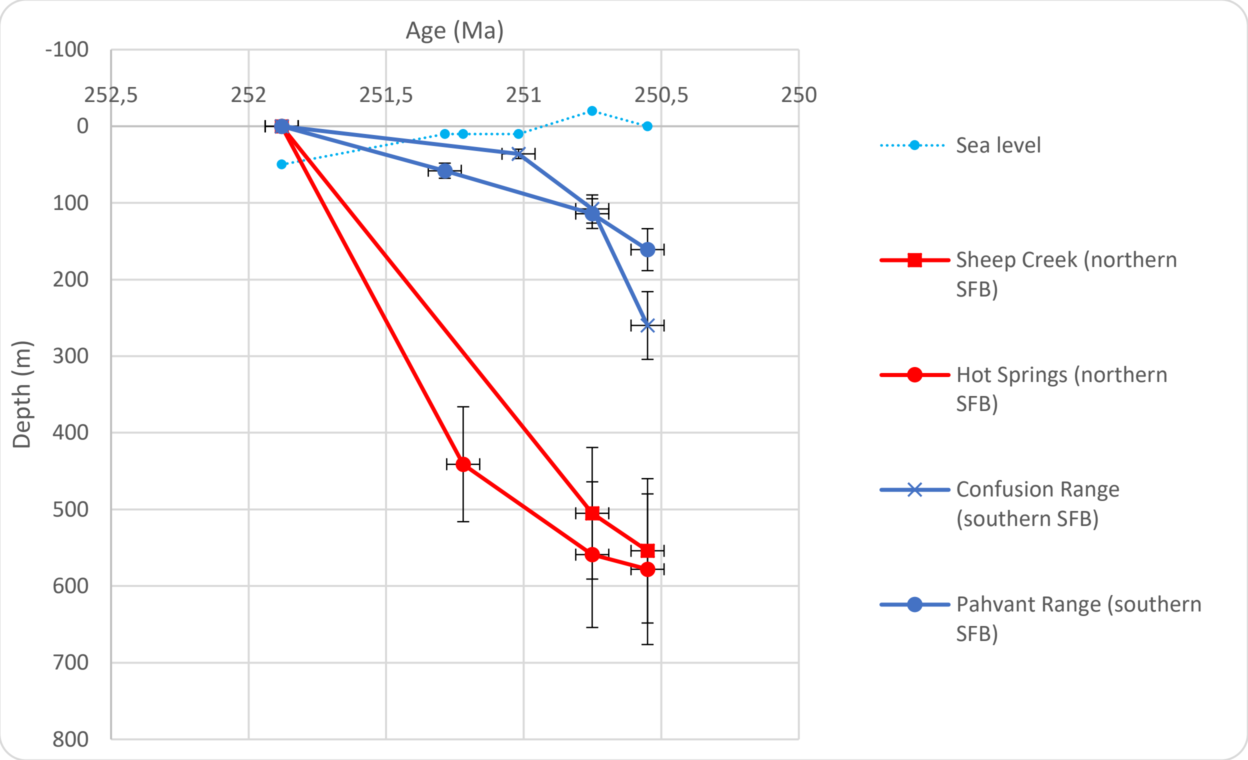

Appendix 4

Preliminary isopach map obtained by 3D interpolation and triangulation of georeferenced (and retrodeformed after palinspastic reconstruction) sedimentary thickness data for the PTU/Smithian interval, under the Global Mapper v.16.2.3 GIS software.

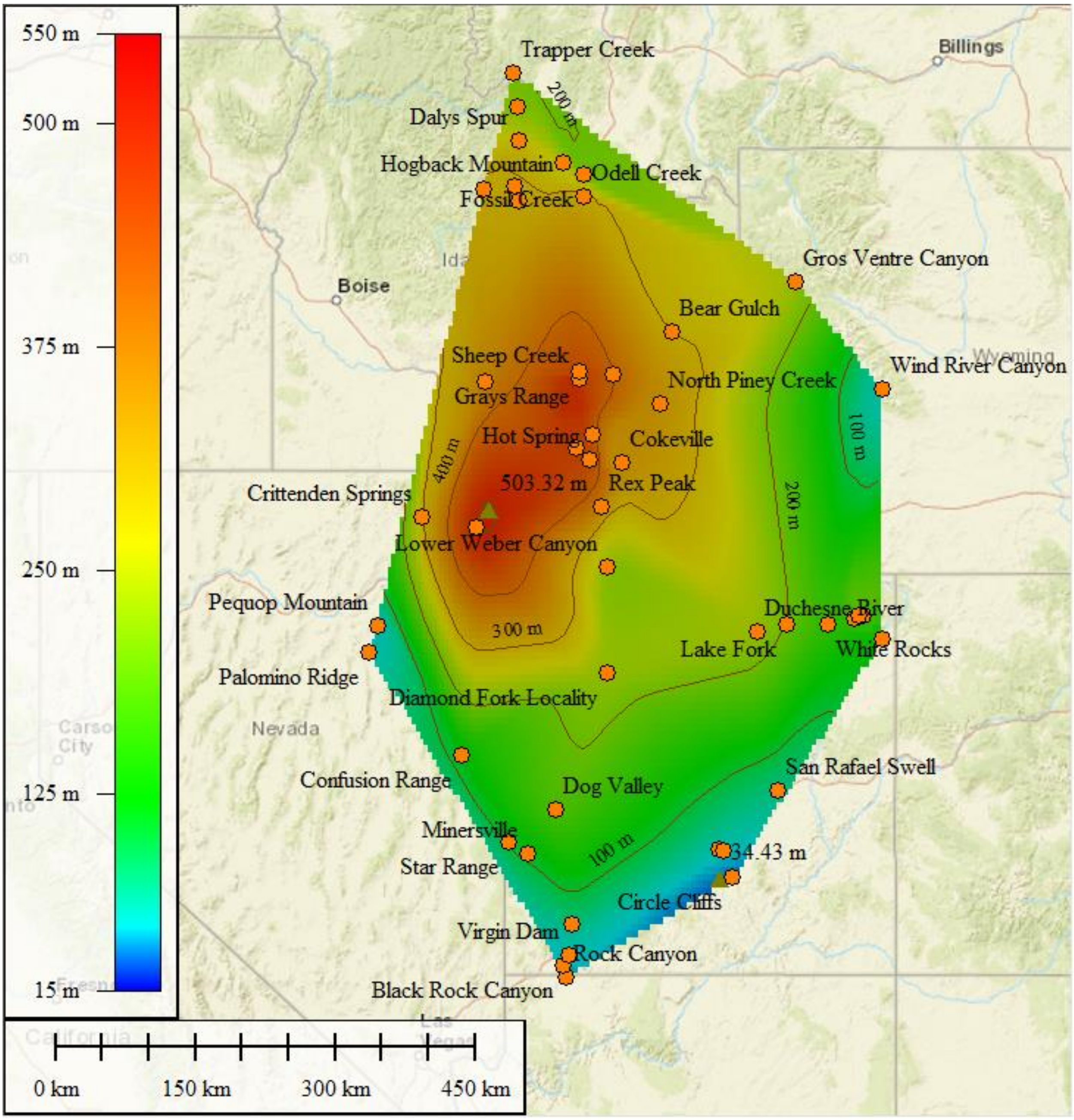

‘’Il n’y a pas que les aigles qui atteignent les sommets. Les escargots aussi.

Mais ils en bavent… comme moi !’’